Determination of Nonlinear Optical Properties of Phthalocyanine Regioisomers Using Computational Models

Marcel Louzada

A thesis presented for the degree of
Doctor of Philosophy
of Rhodes University
February 2020

Abstract

This work investigates the effects of the nonlinear optical properties of four different constitutional isomers (C_{4h}, C_{2v}, C_s, and D_{2h}) of a series of tetrasubstituted phthalocyanines (free-base 3-4-tert-butylphenoxyether phthalocyanines, free-base 4-4-tert-butylphenoxyether phthalocyanines, $SnCl_2$ tetra substituted 3-4-tert-butylphenoxyether phthalocyanine, and $SnCl_2$ tetra substituted 4-4-tert-butylphenoxyether phthalocyanine). The properties investigated were the real and imaginary components of the 3^{rd} order hyperpolarizability, as well as the excited state absorption and refraction cross sections. The investigations were performed with a z-scan over a range of laser beam intensities. This work determined the imaginary component of the 3^{rd} order hyperpolarizability for the free-base and $SnCl_2$ 3-4-tert-butylphenoxyether phthalocyanines and 4-4-tert-butylphenoxyether phthalocyanines to be highly dependent on the excited state cross sections. The refraction caused due to the real component of the 3^{rd} order hyperpolarizability of the phthalocyanines was also investigated, however, the values found were strongly dependent on the laser beam intensity and the cause of this was investigated. A five-level model was developed and run on GPGPU computing devices in order to isolate the absorption and refractive cross sections. The effects of the regio substitution on the excited state cross sections were also investigated, and the 1^{st} singlet excited state and 1^{st} triplet state absorption cross sections were calculated for all constitutional isomers. It was found that the symmetry of the constitutional isomers have a disproportionately large effect on the excited state absorption when compared to the ground state absorption. The nonlinear refractive properties of all constitutional isomers were also investigated, and the values of the parametric susceptibility are reported herein. The nonlinear refraction was found to have less effect than was seen in the nonlinear absorption. The 1^{st} singlet excited state and 1^{st} triplet state refractive cross sections of all constitutional isomer was determined. The results indicated that if more than one excited state was present and contributing to the nonlinear refraction, then more data than was collected here would be required. However, the 1^{st} singlet excited state cross section were successfully determined for the free-base constitutional isomers. This work concluded that the region substitution affected the excited states more than the ground state.

Acknowledgements

I would like to thank all those who have helped me through this work. The words here cannot do justice to the extent that I have been helped and assisted by you all. Firstly, I would like to thank my supervisor Prof Sam Khene, for facilitating this work and providing guidance and advice when needed. I would like to thank Dennis Barrett specifically, for aiding in the mathematical and computational problems encountered in the course of this work. I would like to thank the NIC, for allowing me access to their laser, the data from which this work is built around, as well as their other various instruments. I also wish to thank the Computer Science Department for loaning me some of the GPGPU instrumentation used in this work, and the Chemistry department for the use of lab space. I wish to thank my supervisor and lab mates for a pleasant working environment. I wish to also thank Arthur, Vincent and Sisa, for making coffee breaks that much more interesting and entire days that much more bearable. And finally, I would also like to thank NIC, for providing the funding for this research project.

Contents

Symbols

$\mathbf{P}$	Polarisation vector
$\mathbf{E}$	Electric field vector
χ	Susceptibility
μ_0	Permeability of free space
ε_0	Permittivity of free space
$\chi^{(3)}$	3^{rd} order susceptibility
I	Intensity
n_2	Nonlinear refraction index
$Re[\chi^{(3)}]$	Real 3^{rd} order susceptibility
$Im[\chi^{(3)}]$	Imaginary 3^{rd} order susceptibility
P	Power
α	Linear absorption coefficient
β	Nonlinear absorption coefficient
T_{n}	Normilised transmittance
$\omega^2(z)$	Beam width at z
$\mathrm{z_R}$	Rayleigh range
$\mathrm{z_0}$	Focal position
$q_0(z)$	Transformed transmittance at z
$\mathrm{Q_0}$	Peak transformed transmittance
$Im[\gamma]$	Imaginary 2^{nd} order hyperpolarisability
$Re[\gamma]$	Real 2^{nd} order hyperpolarisability
S_0	Ground state
S_1	First singlet state
S_{n}	n^{th} singlet state
T_1	First triplet state
T_{n}	n^{th} triplet state
σ_1	Ground state absorption cross section
σ_2	Singlet excited state absorption cross section
σ_3	Triple excited state absorption cross section
σ_{r1}	Ground state cross refraction section
σ_{r2}	Singlet excited state refraction cross section
σ_{r3}	Triple excited state refraction cross section

Abbreviations

NLO Nonlinear Optics

DC Direct Current

Nd:YAG Neodymium-doped yttrium aluminium garnet

KTP Potassium titanyl phosphate

LBO Lithium triborate

PMD Polarization mode dispersion

TPA Two-photon absorption

RSA Reverse Saturable Absorption

SA Saturable Absorption

EPNLR Electronic polarisation induced nonlinear refraction

CW Continuous-wave

Pcs Phthalocyanines

MPcs Metalated phthalocyanines

HOMO Highest occupied molecular orbital

LUMO Lowest unoccupied molucular orbital

ESA Excited state absorption

TCSPC Time correlated single photon counting

GPGPU General-purpose graphics processing units

CHPC Centre of High Performance Computing

QMM Quantum molecular modelling

DFT Density functional theory

TD-DFT Time dependent-density functional theory

RTTD-DFT Real time-time dependent-density functional theory

MCD Magnetic circular dichroism

DCM Dichloromethane

List of Figures

List of Schemes

List of Tables

1 Introduction

1.1 Nonlinear Optics

In classical optics, properties are defined by the adherence to Maxwell's equations[1] and the field has been well studied since Newton defined it in 1666[2]. The field of Nonlinear Optics (NLO) is the study of phenomena caused by the nonlinear optical response of material to light, more specifically the response of a material (from either its atomic or molecular composition) to an applied electromagnetic field[3]. Almost all materials that possess optical properties also possess NLO properties, with the latter only coming into effect when the strength of the applied electromagnetic fields approach that of the order of the interatomic field strength[4]. This results in NLO materials, even those with extreme nonlinearities, to behave in a characteristically linear fashion under most light sources. The first reported observation of an NLO property was the change in refraction index that John Kerr observed when he applied a direct current (DC) field to some materials[5]. However, the electric fields that Kerr applied were stronger than most light sources at the time could produce, so the study of self-induced NLO properties could only begin with the invention of the laser in 1960.

1.1.1 Application of Nonlinear Optics in Technology

Due to the dependence of NLO studies on the laser, it becomes obvious that many of the applications of NLO involve or are directly related to lasers and fields in which lasers are used[6]. The earliest examples of NLO applications are their uses in second harmonic generation where a longer wavelength laser beam (typically the 1064 nm emitted by a neodymium-doped yttrium aluminium garnet (Nd:YAG)) is passed through a material such as potassium titanyl phosphate (KTP) or lithium triborate (LBO), and this generates an output laser beam with twice the frequency[7]. Another early example of an NLO effect that is still used today is the passive Q-switch[8], which uses a light-absorbing material that will optically bleach once an intensity threshold is reached (this is discussed in greater detail later) whereby the lasing material can emit its stored energy. The absorbing material then regains its absorbing capabilities and this cycle repeats. Similar to Q-switching, mode-locking is the technique wherein multiple oscillation modes are used within a laser cavity, such that a fixed-phase relationship between these modes results in very short emission pulses (as low as 10 fs)[9]. The pulses generated from mode-locking tend to be far shorter, with a higher repetition rate than those made by Q-switching; however, they will have a lower peak intensity. Modern uses of NLO effects can be seen in the use of pumped multi-photon absorption machining, allowing for the three-dimensional milling of materials (additive or subtractive depending on the media)[10]. This same multi-photon technique can also be used at much lower intensities as a non-destructive method of imaging[11]. NLO properties are also encountered in information technologies where they are found to be the limiting factor in the data transmission rate of a single optical fibre. As the data transmission rate through an optical fibre directly corresponds

to the time-averaged intensity of the laser, the NLO properties can begin to affect the signal passing through the fibre. This same effect was seen when the length of the fibres was increased, as higher power lasers need to be used to transmit signals over larger distances. These effects observed in optical fibres are due to several NLO mechanisms. Among them are stimulated Brillion scattering and (to a lesser extent) stimulated Raman scattering, both of which cause a reflection of part of the signal back to the emitter. Another problem encountered in fibre-based telecommunications was the self-induced phase change, due to polarization mode dispersion (PMD), of all or some of the signal pulse due to small imperfections in the fibre[12].

1.1.2 Causes of Optical Nonlinearities

The effects of NLO materials are typically categorised by the mechanisms responsible for the behaviour, though a single mechanism can be responsible for multiple effects[13]. From an experimental standpoint, however, it is more practical to group NLO phenomena as the sum of the processes that give rise to it. The interaction of light with a material is best described by the Taylor series expansion of the polarisation vector $\mathbf{P}(t)$'s response to the electric field $\mathbf{E}(t)$[14]:

$$\mathbf{P}(t) = \mu_0 + \varepsilon_0(\chi^{(1)}\mathbf{E}(t) + \chi^{(2)}\mathbf{E}^2(t) + \chi^{(3)}\mathbf{E}^3(t) + ...) \tag{1}$$

Where the different χ(s) are the complex susceptibilities, μ_0 is the permeability of free space, and ε_0 is the permittivity of free space. The first order susceptibility, $\chi^{(1)}$, governs the response to $\mathbf{E}(t)$, with the imaginary component describing the absorption of light and the real component related to its refraction index. Equation 1 also shows higher-order terms for χ and their dependence on higher-order terms of $\mathbf{E}(t)$. These are the terms that define the nonlinearity of the media, scaling with the exponent of $\mathbf{E}(t)$. However, in order to be valid, the values of the increasing orders of χ must diminish suitably, else they will dominate $\mathbf{P}(t)$ at small values of $\mathbf{E}(t)$. Boyd[14] shows the approximate values of $\chi^{(1)}$, $\chi^{(2)}$ and $\chi^{(3)}$ to be of the orders

$$\chi^{(1)} \simeq 1 \tag{2a}$$

$$\chi^{(2)} \simeq \frac{(4\pi\varepsilon_0)^3\hbar^4}{m^2e^5}\,\mathrm{m/V} \tag{2b}$$

$$\chi^{(3)} \simeq \frac{(4\pi\varepsilon_0)^6\hbar^8}{m^8e^{10}}\,\mathrm{m^2/V^2} \tag{2c}$$

with m and e the mass and charge of an electron respectively. This separates the magnitudes of each order of χ by 10^{-12}, thus the presence of each successive nonlinearity will only manifest at increasing values of $\mathbf{E}(t)$. The term $\chi^{(2)}$, called the second order

susceptibility, is responsible for several distinct NLO processes, including second-harmonic generation, sum-frequency generation, difference-frequency generation, and Rayleigh scattering (they will not, however, be discussed in this work). The term $\chi^{(3)}$, called the third order susceptibility is similar to the first order susceptibility, with the imaginary component related to some absorption processes and the real component related to refraction. This work focuses on effects due to or related to $\chi^{(3)}$ (such as multiphoton absorption nonlinear refraction or excited state absorption, which will be detailed below) and attempts to separate and quantify each component. Higher order susceptibilities will contribute in some way to the effects studied here, such as effects from the fifth order susceptibility($\chi^{(5)}$) as it shares optical characteristics with $\chi^{(3)}$[13]. Due to the scaling of $\mathbf{E}$, these effects are expected to be negligible at the values of $\mathbf{E}$ used in this work.

1.1.3 Nonlinear Attenuation

The nonlinear loss of transmittance at higher powers is a well-studied property of some NLO materials, as it is easy to observe and measure. The properties that give rise to NLO attenuation are often nonparametric (their final state differs from their first) in nature and change in the properties of the excited state, with respect to the ground state, allows the measurement of each processes' contribution[15]. The calculation of the energy of these states, their density, and their relative populations, require extensive measurements and knowledge of the associated states, and despite the information available the computational costs for these calculations are still high[16].

1.1.3.1 Multi-photon Absorption

Multi-photon absorption is the simultaneous absorption of two or more photons via intermediary states. Multi-photon absorption occurs where there is no allowed one-photon transition, as the change of the orbital angular quantum number ($\Delta\ell$) of the first and final state, governed by Equation 3, is limited to 1 for single photon absorption.

$$\Delta\ell = 0, \pm n \tag{3}$$

Here, n is the number of photons being absorbed and each photon carries with it one unit of momentum. For a multi-photon process, the value n is greater than 1, and this precludes a one photon and multiphoton transition overlap. As each successive photon absorption becomes less and less likely, the most common multi-photon absorption observed is two-photon absorption (TPA). TPA cross sections are generally reported with the units GM, after Maria Göppert-Mayer who predicted the process in 1930[17]. The units GM can be expresed in SI units as:

$$1\,\mathrm{GM} = 10^{-58}\,\mathrm{m}^4\,\mathrm{photon}^{-1}\,\mathrm{s} \tag{4}$$

These units are the result of the product of the two cross sections, the initial state and the virtual state, and the lifetime of the virtual state. Due to the per photon dependancy of the TPA cross section, the amount of light absorbed by TPA scales with the fluence of the incident light, and the effects of TPA will only be seen at very high intensities. It is possible to enhance the TPA cross section, either by increasing one of the cross sections (initial to virtual, or virtual to final) or by stabilising the virtual state with an existing state of similar energy: so-called resonance enhancement[18].

1.1.3.2 Excited State Absorption

NLO materials can receive their nonlinearity from the differences in their ground state and excited state properties. Absorption, in particular, can often increase due to the increase in the density of states at higher orders, with triplet absorption being the most well-known example. In general, excited state absorption is separated into two groups: Reverse Saturable Absorption (RSA) and Saturable Absorption (SA)[14]. RSA is the NLO phenomenon where the effective light attenuation of the material increases due to an increase in the excited state population. SA is the reverse of RSA, whereby the excited state possesses a smaller cross section than the ground state, leading to an overall attenuation decrease with the increase in the excited state population.

1.1.4 Nonlinear Refraction

The change in the refractive index of a media in response to light intensity for most materials can be described by the relation in Equation 5[14]

$$n = n_0 + n_2 I \tag{5}$$

with I the intensity of the light passing through the media, n_0 the linear refraction index (weak-field refraction index) and n_2 the nonlinear refraction index. Equation 5 shows how the total refractive index can change in response to the light intensity. There are many mechanisms that can contribute to n_2, such as molecular orientation[19], electrostriction[20], the photorefractive effect[21], thermal effects[22], and electronic polarisation[23]. This work will only focus on two of these mechanisms: thermal effects via the thermal lensing effect, and electronic polarisability.

1.1.4.1 Electronic Polarisation Induced Nonlinear Refraction

As the nonlinear refraction mechanism with the fastest response time, as well as the smallest effect on the refractive index[14], the electronic polarisation induced nonlinear refraction (EPNLR) can be more challenging to measure than the other mechanisms of nonlinear refraction. However, due to its quick response time, it can cause phase interference and signal distortion through certain nonlinear materials[24]. As it is a result of the electronic polarisation, the contribution to n_2 from EPNLR can be

related back to the susceptibility of the material expressed in Equation 1 with the relation

$$n_2 = \frac{3}{2{n_0}^2 \varepsilon_0 c} \chi^{(3)} \tag{6}$$

with c the speed of light in a vacuum[15]. $\chi^{(3)}$ is a complex term, and both the real and the imaginary term contribute to EPNLR[14]. $Re[\chi^{(3)}]$ is generally the term used to describe the parametric mechanisms of measured EPNLR, while the change in refraction due to absorption processes are tied to $Im[\chi^{(3)}]$.

1.1.4.2 Thermal Lensing

The thermal effects on nonlinear refraction, caused by thermal lensing, contrast strongly with EPNLR, as thermal lensing has a long response time (up to 10^{-3}s) but has effects orders of magnitude larger than EPNLR (10^{-16} for EPNLR vs 10^{-6} for thermal lensing)[14]. Thermal lensing is caused by the excitation and subsequent relaxation of the optical material by an intense light source (laser). For condensed matter, this change in the material's temperature gives rise to a change in the refractive index. The change in refraction index with the change in the temperature of a material can be related directly[25]by the equation:

$$n = n_0 + (\frac{dn}{dT}) T_1 \tag{7}$$

Where the value $\frac{dn}{dT}$ describes the temperature dependence of the refractive index, and T_1 is the light induced change in temperature. As laser beams are not uniform, with the intensity of the beam often possessing a Gaussian profile as shown in Figure 1, the change in temperature will correspond to the radial profile of the beam.

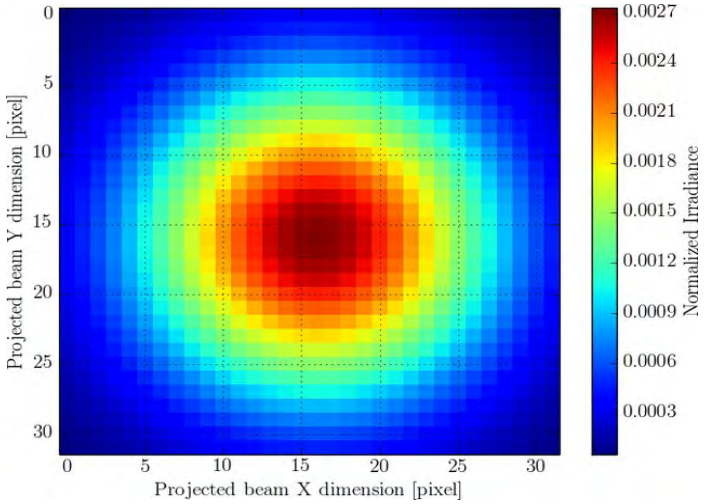

Figure 1: The spatial cross section the Irradiance distribution of a laser beam[26].

Depending on the material, the thermal lensing will lead to effects known as self-focusing or self-defocusing[27]. Due to the nature of thermal dissipation, thermal lensing is seperated into two cases: that for a continuous-wave (CW) laser, and the case for a pulsed laser. In the case of CW lasers, the thermal energy deposited into the material is allowed to build up, making this case the best suited for observing thermal lensing effects. In the case of pulsed laser beams the energy of one pulse is often dissipated by the next one (assuming a repetition rate lower than $\tilde{1}00$ Hz). However, as pulsed beams are often more intense and short, the heat deposited in the material will not have time to dissipate, and can affect the rest of the laser pulse; this still requires the excitation energy to be converted to thermal energy.

1.2 Phthalocyanines

Phthalocyanines (Pcs) are macrocyclic compounds, known for their distinct blue-green colour and their unique spectroscopic properties. Discovered in 1927[28], Pcs have since found use in dyes[28,29], catalysis[30–32], optical-based electronics[33,34], electro-sensing[35], photovoltaic cells[36,37] and even medicine[38,39]. These uses for Pcs all stem from their extended π electron system, shown in Figure 2, which contributes to all of the Pcs' optical and physical characteristics and plays a part in a theoretical or experimental consideration for the use of Pcs[40].

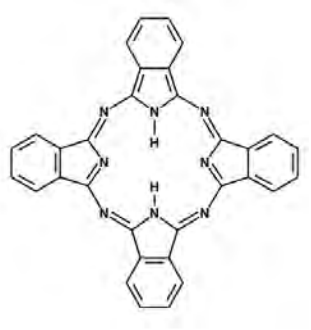

Figure 2: A free-base phthalocyanine.

1.2.1 Phthalocyanines' Photophysical Properties

First noted for their strong colour, Pc have a distinctive ground state spectrum, with two regions of intense absorption peaks separated by an optical window in the 500 nm range. As shown in Figure 3, Pcs' primary absorption peaks lie in the 600-700 nm range; this absorption gives them their blue-green colouration.

Dubbed the Q-band, this absorption corresponds to the transition from the highest occupied molecular orbital (HOMO) to the lowest unoccupied molecular orbital (LUMO) and LUMO+1. The small shoulder on the Q-band is a vibronic peak, and the small peaks found at the 350 nm region are called the Soret bands and are due

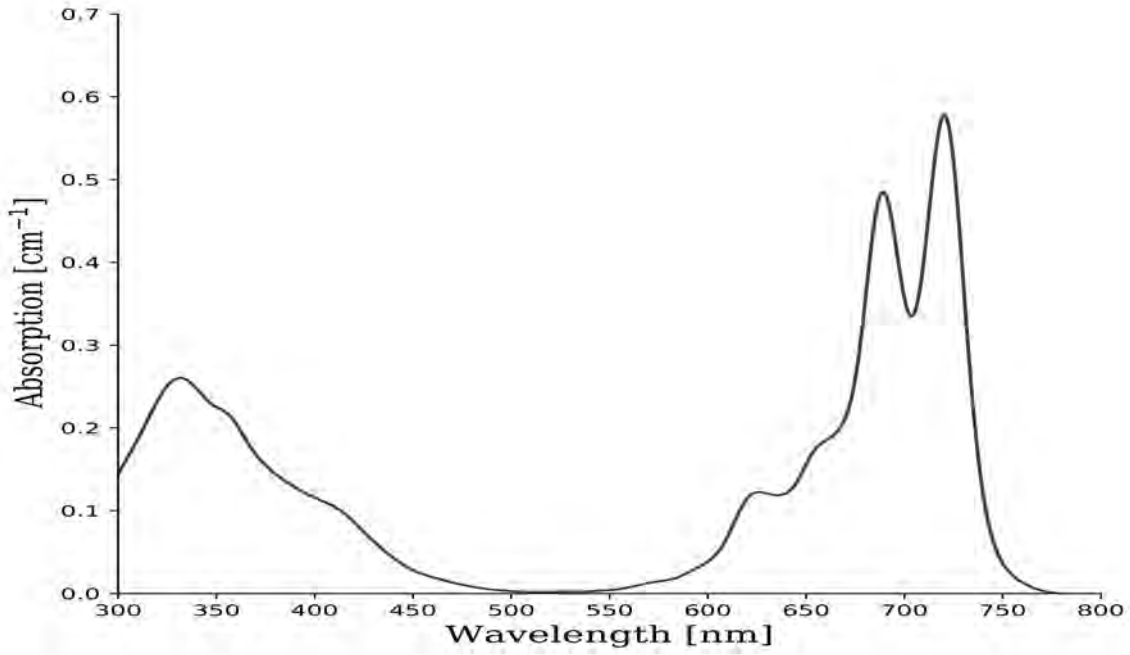

Figure 3: UV/Vis spectrum of a free-base phthalocyanine.

to transitions from lower-lying orbitals. The four frontier orbitals shown in Figure 4 as defined by Michl[41] are generally used to describe these transitions. Michl assigned the orbitals based on the presence of the orbital nodes on the x or y axis. From these orbitals, Michl assigned the $a \rightarrow$ -a and $a \rightarrow$ -s transitions to the Q-band and the $a \rightarrow$-a and $a \rightarrow$-s to the Soret band.

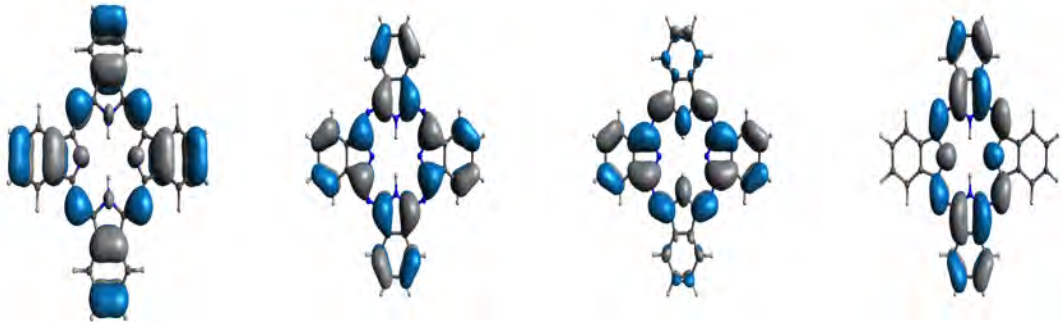

s *a* -*a* -*s*

Figure 4: The Four Michl Orbitals.

1.2.2 Modifying Phthalocyanine Properties

A Pc can be modified by one or a combination of three methods; these all maintain the core atomic configuration of the central Pc. Deviations from the Pc configuration,

such as sub- and super-phthalocyanines, corrals, and porphyrins will not be discussed in this work.

1.2.2.1 Metalation

The central two hydrogen atoms in a Pc can be replaced with any 2+ cation of appropriate size. For most cases, this cation is a transition metal and as shown from Figure 4, this modification will affect the *s*, *-a*, and *-s* orbitals and any other transitions that use one of these orbitals. Regardless of whether the central atom is a metal or semi-metal, the resulting Pc is referred to as a metalated Pc (MPc)[42]. The inclusion of a central metal can also introduce alternative electronic transition pathways within the Pc through the heavy-atom effect which increases the rate of spin-forbidden processes. The addition of the central atom adds one other property to the MPc: it adds a centre of inversion, which makes the *-a*, and *-s* orbitals degenerate and thus removes the splitting of the Q-band[43] as shown in Figure 5. Should the central cation be too large to fit into the central cavity, it will sit out of plane of the Pc, removing planar symmetry but leaving most other properties unchanged. For some 4+ cations, most notably very large ones, it becomes possible to sit between 2 Pcs simultaneously, creating sandwich MPcs which have their own set of properties[44].

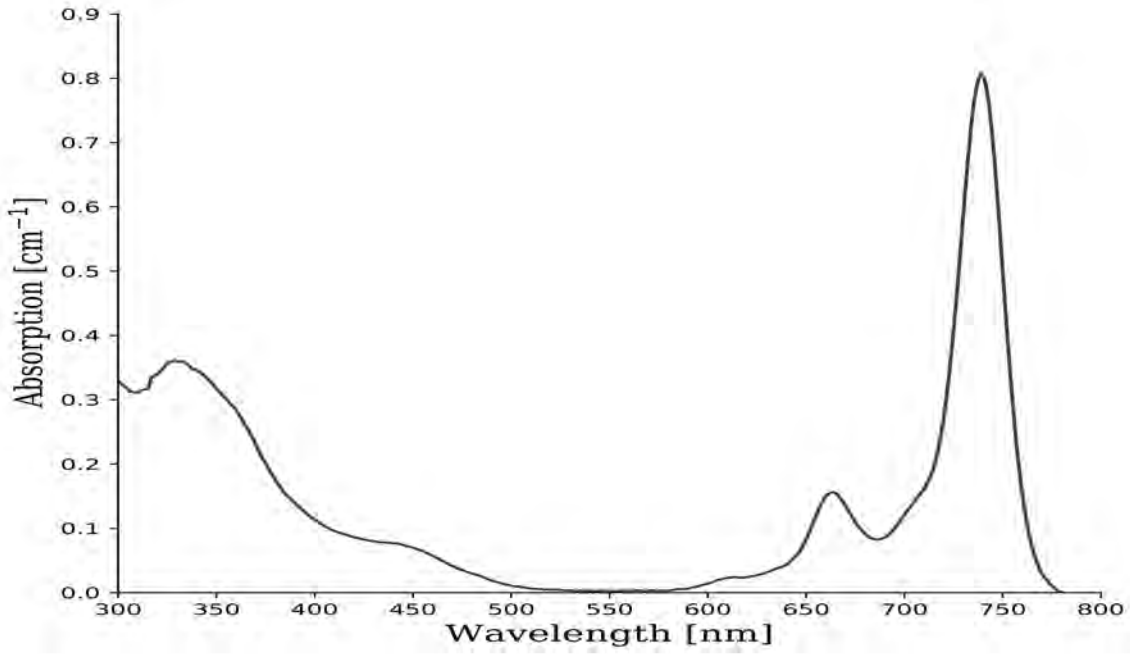

Figure 5: UV/Vis spectrum of a metalated phthalocyanine.

1.2.2.2 Axial Substitution

Should the central atom in an MPc possess other oxidation states higher than 2+, it becomes possible to add axial ligands to the MPc. These can be useful in attaching

the MPc to electrodes or other electrocatalytic surfaces. The axial ligand is also useful in conjugating the MPc to other molecules or surfaces through the central metal. The axial substitution has also been found to reduce Pc aggregation[45], and can also affect the energies of the MPc's molecular orbitals. The change in a MPc's molecular orbital's energies can be a minor or major change depending on the axial ligand choice[46].

1.2.2.3 Perimeter Substitution

The most versatile method of modifying a Pc's properties comes from the Pc's 16 different perimeter substitution points, Figure 6, as these allow the addition of substituents of almost any composition, electron affinity, polarity, and size. These substituents are what allow Pcs to perform the host of functions that they are used for in modern industry; from the highly stable and insoluble Phthalocyanine Green G[47] used in inks and cosmetics, to water-soluble Pcs used in photovoltaic films[48]. Some

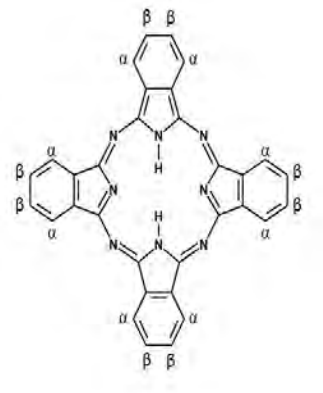

Figure 6: Unsubstituted free-base Pc with the possible substitution points α and β.

properties introduced by the substituents are a consequence of their size and/or solubility, and these properties are not sensitive to the exact position of the substituent and will not impact the photophysical properties of the Pc. Substituents that carry properties affecting the electron distribution of the Pc can however affect the Pc's photophysical properties and are position sensitive. Comparing Figure 6 with Figure 4 we see that substitution position will affect different orbitals. The s orbital does not interact directly with any α substituent, whereas the -a and -s orbitals are only affected by substituents on the -y and -x axis respectively, with little to no effect from the substituents on the opposite axis. These asymmetrical substitution positions can create a considerable variety in the properties of Pcs. Due to the possible asymmetry of the change induced by substituents, specific substitutions were used to deconvolute the Soret band into its component bands[49]. The variety of substitution positions result in Pcs exhibiting isomerisation, with two types of isomerisation being

seen: structural- and regioisomers. In structural isomers, the Pc is only substituted at either the α or β positions as seen in Figure 7.

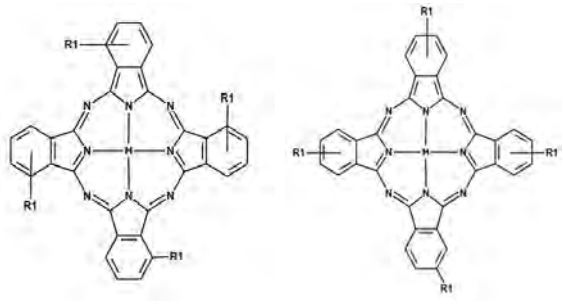

Figure 7: The two possible structural isomers for a tetra substituted MPc.

regioisomers are far more similar to each other than structural isomers[50]. The regioisomers, of which there are four per structural isomer of a planar Pc, are also difficult to isolate, as tetra-substituted Pcs are normally synthesised as a mixture and there is no method available to synthesise the isomers individually, and in a one pot synthesis are synthesised at a 1:1:2:4 ratio, excluding electronic and steric effects[42]. However, for most applications, the regioisomers mixture is not seperated, due to their small photophysical differences not impacting most experimental results. The regioisomers of planar Pcs have the symmetries D_{2h}, C_{4h}, C_{2v}, and C_s.

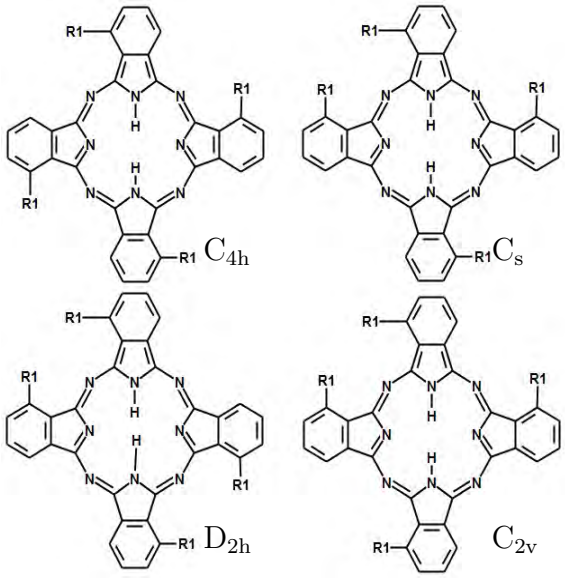

Figure 8: The four possible regioisomers for an *alpha* structural isomer.

1.2.3 Phthalocyanines in Nonlinear Optics

As dyes, Pcs also exhibit strong NLO properties at certain wavelengths[46]. Structural modifications to Pcs correspond to changes in their photophysical properties, similarly, the NLO properties of Pcs are also affected. However, the degree that the NLO properties are changed are not directly proportional to the changes in the linear optical properties[51], with a small shift in linear optical properties sometimes correlating to a large change in the Pcs NLO properties or vice versa. Studies to determine the most effective method of modifying Pcs for NLO have shown that axial substitutions[52], asymmetric and symmetric peripheral substitutions[53], and any method that extends the π conjugation system of the Pc[54] greatly affect the NLO properties of a Pc. Most interest in Pcs' NLO properties are concerned with their non-absorbing optical window found around 530 nm (see Figure 3) as any NLO effects seen at these wavelengths will reduce the Pc's transparency at non-normal light intensities. As such, there are two properties of a Pc that must be considered when evaluating its NLO response at its optical window. Firstly, Pcs are semiconductors with large band gaps, and the NLO response in the Pc's optical window will involve transitions to virtual states in between existing states[55,56]. Secondly, as there is no natural resonance in the Pc's optical window, the NLO response can be considered a nonresonant nonlinearity. However, due to the Pc's delocalised π electron system, the NLO response can still be large (as high as $\gamma \approx 10^{-32}$ esu)[57]. This is why extending the Pc's π conjugation system is the most efficient method of controlling a Pc's NLO properties in the Pc's optical window. Being a nonresonant nonlinearity, the processes that give rise to the nonlinear behaviour are virtual[14] in nature, and this allows Pcs to have very fast responses to optical stimuli[14]. This property is the main benefit of using Pc as NLO materials. Pcs The relation of a Pcs optical properties in the ground state to Pcs' NLO properties is varied. Very blue shifted MPcs can show low values of nonlinear absorption[58], while possessing very high ground state absorption cross sections. It has been reported that creating a large dipole via selective asymmetric substitution can increase the nonlinear absorption properties of Pcs[53]. In two studies on Pc regioisomers, Ngubeni[50] and Gouden[59] found that the NLO properties for the four regioisomers of two Pcs had dissimilar values, despite the regioisomers possessing ground state optical properties within 2-5% of each other.

1.3 Magnetic Circular Dichroism

Magnetic circular dichroism (MCD)is a technique that has been used since the 1960s to analyse various chromophores the exhibit different responses to left and right hand circularly polarised light (lcp and rcp respectively), among other uses[60]. This is done by inducing a Zeeman splitting of state of a chromophore (in this work, a Pc or MPc) by an applied magnetic field (B). This allows differential absorption of lcp and rcp resulting in a splitting of degenerate absorption spectra, as shown in Figure 9. The MCD spectra of a Pc is due to the general symmetry of each Pc molecule. MPcs,

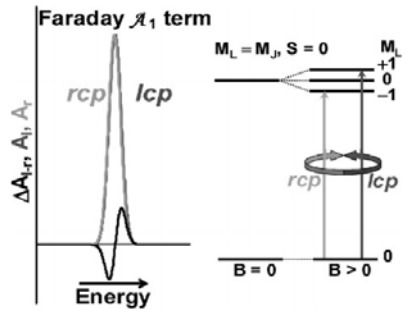

Figure 9: The result of a magnetic field on an orbital, resulting in Zeeman splitting into two states[60].

with a D_{4h} symmetry, show a $\mathbf{A}_1$ Faraday term due to the splitting of the x and y polarised Q-bands. A free-base Pc, with a D_{2h} symmetry, exhibits $\mathbf{B}_0$ Faraday terms, as the Q-band was already split before the induced Zeeman effect. These two terms are shown in Figure 10. As MCD spectra can be used to separate and

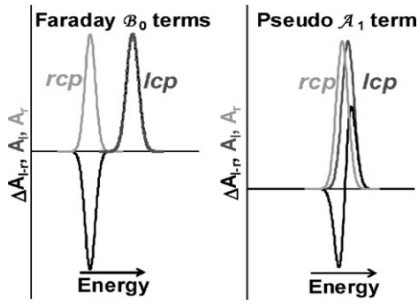

Figure 10: The $\mathbf{B}_0$ Faraday terms (left) and $\mathbf{A}_1$ Faraday term (right) in an MCD[60].

identify absorption transitions that are degenerate, and it is used in the study of Pc's photophysical properties[61].In this work, MCD spectra are used to accurately assign and identify absorption transitions.

1.4 Z-Scan

The primary method for measuring NLO properties in this work is the z-scan, originally developed by Sheik-Bahae[62] in 1990. The z-scan moves a sample along a single focused beam, such that the sample experiences a change in the beam's intensity (I [W.m^{-2}]) without a change in the power (P [W]) of the beam. This has the benefit of allowing high light intensities (over 10^{13} W.m^{-2}) at the focal point, without putting large amounts of energy into the sample, illustrated in Figure 11. The z-scan

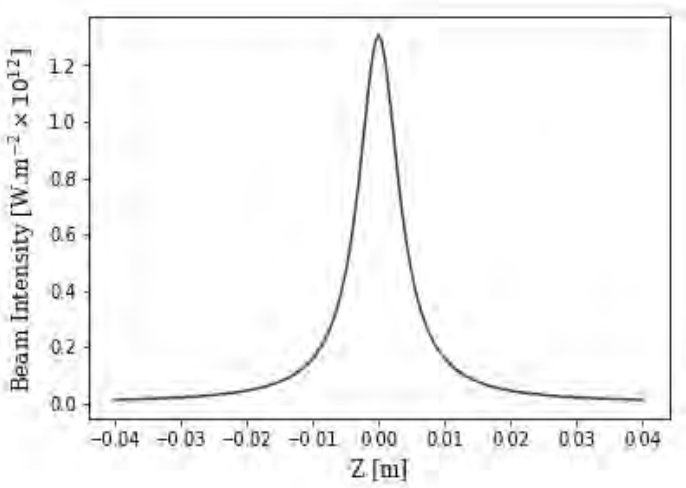

Figure 11: The beam intensity at each point in a z-scan for a 10 μJ, 10 ns pulse.

has two primary modes of operation: open aperture and closed aperture, with each allowing a measurement of a different type of nonlinearity. The 'aperture' in both closed aperture and open aperture refers to a variable aperture near the detector in a z-scan apparatus, shown in Figure 12: In the z-scan's first mode of operation, the aperture is left wide open, and does not interact with the beam in any way. The open aperture mode is then able to ignore all but the most extreme refractive properties of the sample, only being affected when the end position beam area becomes larger than the detector. This allows the mode to take measurements and observe the change in the linear absorption of the sample as it moves along a focused laser beam. This change in the absorption (if any) can be shown as an addition to Beer-Lambert's law:

$$\frac{dI}{dz} = -\alpha I + \beta I^2 \tag{8}$$

In Equation 8, α the linear absorption coefficient, and β is the nonlinear absorption coefficient. The dependence on I^2 for the change in intensity gives the sample its nonlinearity. For a sample exhibiting a negative β this will manifest as SA, but for positive values of β, this will manifest as RSA, shown in Figure 13. The second operational mode of the z-scan is the measurement of the change in the refraction

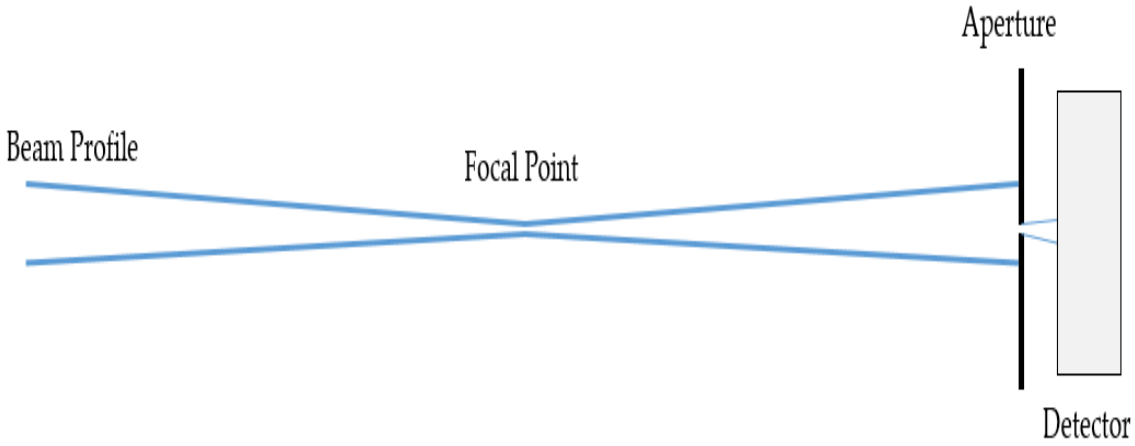

Figure 12: A closed aperture z-scan setup.

index of a sample as it moves along a focused laser beam. In open aperture mode, the aperture does not interfere with the beam at all, while in a closed aperture, the aperture is closed such that it only allows a small fraction of the beam through. The ratio of this fraction to the beam, normally 0.1-0.5 of the original beam, is named S and will be used in subsequent calculations. As a small portion of the beam is allowed through in a closed aperture, any effect that focuses or defocuses the beam at the aperture position will affect the measured transmittance. Since a focused beam is not parallel, any sample possessing a refraction index larger than the media the beam is passing through (typically atmospheric air, though some setups can use N_2

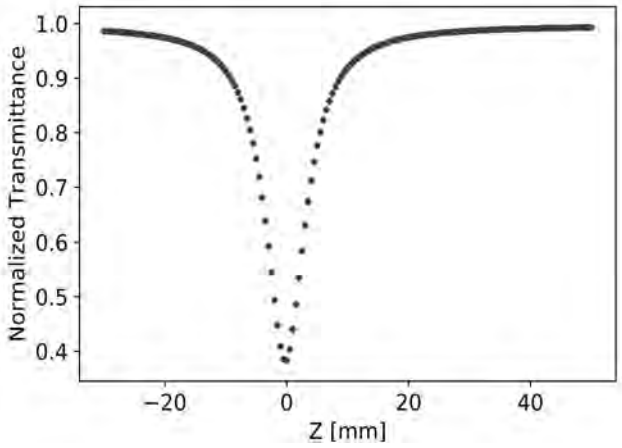

Figure 13: The normalised transmittance of a Pc due to RSA at 532 nm.

or a noble gas) will shift the focal point via Snell's law:

$$\vec{v}_{\text{refract}} = r\,\vec{l} + (rc - \sqrt{1 - r^2(1 - c^2)})\vec{n} \tag{9}$$

In Equation 9, $\vec{l}$ is the normalised incident light vector, $\vec{n}$ the normal of the sample, $r = n_1/n_2$, and $c = -\vec{n} \cdot \vec{l}$. For linear refraction, Equation 9 describe refraction well, but if the effects of nonlinear refraction are included, characteristic changes in the resulting transmittance will be observed. As shown in Equation 5, the nonlinear refraction will change with I and this change will increase in magnitude toward the focal point. As n_2 can be both positive and negative this can manifest as two types of transmittance that are shown in Figure 14. Unlike the open aperture mode,

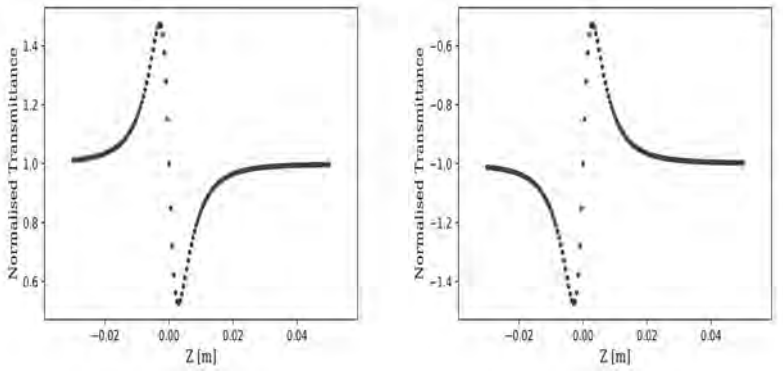

Negative n_2. Positive n_2.

Figure 14: Closed aperture z-scan for a positive and a negative nonlinear refraction index.

closed aperture cannot be run independently, as there is no way to remove the nonlinear absorption effects from the sample. Thus every closed aperture measurement requires another open aperture measurement. The effects of the nonlinear refraction are isolated by subtracting the open aperture measurements from the closed aperture measurements, shown in Figure 15. As discussed above, z-scan measurements are

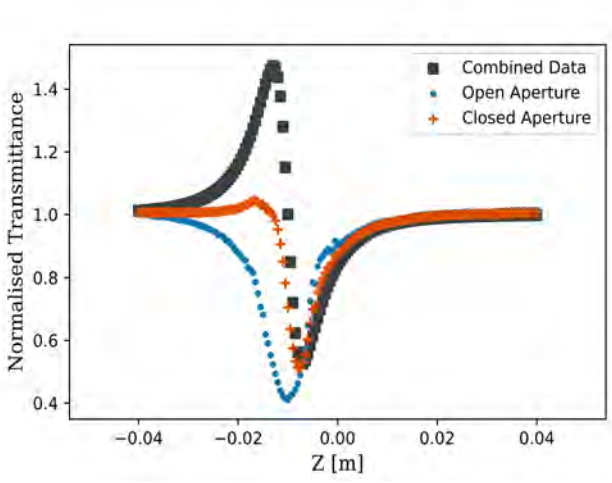

Figure 15: Isolating refractive response from a closed aperture measurement.

limited to two classes of nonlinearities, namely: nonlinear refraction and nonlinear absorption. Considering Equation 1, the parameters that gives rise to the properties measured with z-scan are predominantly $\chi^{(3)}$ and to some lesser extent higher order susceptibilities[13]. This work will utilise two models to isolate the refractive and absorption nonlinearities stemming from $\chi^{(3)}$, and these will be called the parametric models. However, as the parametric models cannot distinguish between different processes giving rise to the same type of property, such as an RSA and an SA process both contributing to the nonlinear absorption, two further models will be discusses as well. These models will focuses on excited state populations and specific cross sections, for both refractive and absorption processes.

1.4.1 Parametric Nonlinear Absorption Model

The parametric model of nonlinear absorption relates the transmittance seen in Figure 13 with Equation 1. To do this, the model will first find a numerical solution for Equation 8, and then transform each parameter with physical constants as needed. There are many methods for solving the parametric model of nonlinear absorption, fitting the data shown in Figure 13, but this work will use the method developed by Tsigaridas and co-workers[63], as this model has two large benefits which will be discussed below. The basis for this model is shown in Equation 10.

$$T_{\mathrm{n}}(z) = \frac{1}{Aq_0(z_0)} \int_{-\infty}^{\infty} ln[1 + q_0(z_0)f(\tau)]d\tau \tag{10}$$

Equation 10 describes the transmittance (T_{n}) as a function of the position along the beam (z), and the normalisation constant (A) defined in Equation 11 as:

$$A = \int_{-\infty}^{\infty} f(\tau) d\tau \tag{11}$$

Where $f(\tau)$ is a function describing the temporal profile of the laser pulse. The parameter $q_0(z_0)$ is a position dependant absorption parameter which we can relate to β with Equation 12:

$$q_0(z_0) = \frac{2\beta P_0 L_{\mathrm{eff}}}{\pi \omega^2(z)} \tag{12}$$

Here, β is the nonlinear absorption coefficient, L_{eff} is the effective path length of the sample, P_0 is the power of the laser pulse, and $\omega^2(z)$ is the beam width at position z, defined in Equation 13 as:

$$\omega(z) = \omega_0 \sqrt{1 + \frac{z - z_0}{z_{\mathrm{R}}}} \tag{13}$$

with ω_0 the beam width at focus, $\mathrm{z_0}$ the position of the focus (normally set to 0 either by adjusting the z-scan itself, or by translating the experimental data along the z-axis), and $\mathrm{z_R}$ is the Rayleigh range of the beam, defined in Equation 14 as:

$$z_{\mathrm{R}} = \frac{\pi {\omega_0}^2}{\lambda} \tag{14}$$

λ is the wavelength of the laser. In order to isolate β from Equation 10 a numerical fitting must be done, though from inspection of Equation 10 this is not a simple fit. Tsigaridas and co-worker's method redefines $q_0(z)$ using experimentally determined parameters, with the values of $q_0(z)$ depending on the amount of transmittance, shown in Equation 15 as:

$$q_0(z) = \begin{cases} a_0 + a_1 T_{\mathrm{n}}(z) + a_2 {T_{\mathrm{n}}}^2(z) + a_3 {T_{\mathrm{n}}}^3(z), & \text{if } T_{\mathrm{n}}(z) \leq 0.75 \\ c_0 + c_1 [T_{\mathrm{n}}(z)]^{c_2}, & \text{if } T_{\mathrm{n}}(z) \geq 0.75 \end{cases} \tag{15}$$

with the parameters a_0, a_1, a_2, a_3, c_0, c_1, and c_2 being experimentally determined by Tsigaridas and co-workers. Combining Equation 12 and Equation 15 another

definition of $q_0(z)$ can be defined as:

$$q_0(z) = \frac{Q_0}{1 + (\frac{z - z_0}{z_\mathrm{R}})^2} \tag{16}$$

The only new value in Equation 16 is Q_0, which is a constant grouping of experimental or physical constants defined in Equation 17:

$$Q_0 = \frac{2\beta P_0 L_\mathrm{eff}}{\lambda z_\mathrm{R}} \tag{17}$$

This value corresponds to the value of q_0 at $q_0(z_0)$. The result of this method is shown in Figure 17, noting that Tsigaridas's method has transformed the values using Equation 15; this is not a plot of normalised transmittance versus position, but a plot of q_0 versus position. As the values of the peak of the transformed curve can be

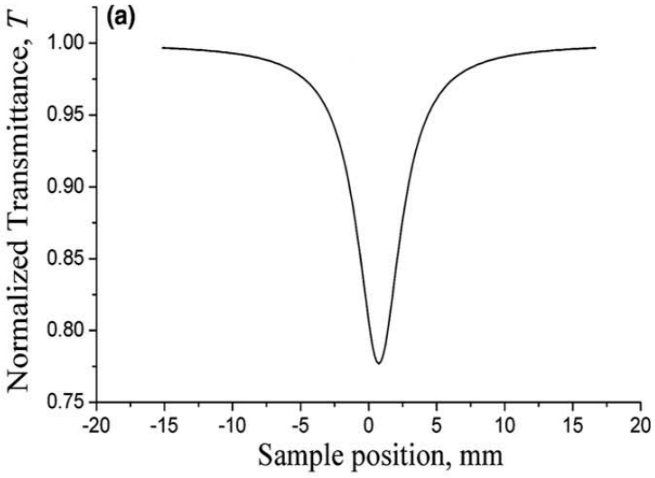

Figure 16: An open aperture z-scan fitted with Tsigaridas's method[63].

read off Figure 17 directly, a fitting of the transmittance curve is no longer necessary, minimising computation time and sensitivity to noise in the experiment. Rearranging Equation 17, we can determine β:

$$\beta = \frac{Q_0 \lambda z_\mathrm{R} 2}{P_0 L_\mathrm{eff}} \tag{18}$$

Having determined a value for β, it can then be related back to $Im[\chi^{(3)}]$ using Equation 19:

$$Im[\chi^{(3)}] = \frac{n\varepsilon_0 c^2 \lambda \beta}{2\pi} \tag{19}$$

In Equation 19, c is the speed of light in a vacuum. This can be related directly to Equation 1. $Im[\chi^{(3)}]$ describes the nonlinear response of the sample as a whole. In order to determine the equivalent response of each individual molecule giving rise to $Im[\chi^{(3)}]$, another equation is used to isolate the imaginary component of the third-order polarisability, more often called the second-order hyperpolarisability ($Im[\gamma]$).

$$Im[\gamma] = \frac{Im[\chi^{(3)}]}{f^4 N N_{\mathrm{A}}} \tag{20}$$

In Equation 20, f is the Lorentz local field factor, N the concentration, and N_{A} is Avogadro's number. The parametric nonlinear absorption model offers an interpretation for nonlinear absorption, with the two values $Im[\chi^{(3)}]$ and $Im[\gamma]$ responsible for all nonlinear absorption observed. These two values are generally reported in electrostatic units (esu), though they can also be reported in the International System of Units (SI) as ($m^2.V^2$). The two units can be related using Equation 21[64]:

$$Im[\chi^{(3)}](m^2.V^2) = \frac{4\pi}{9} 10^{-8} Im[\chi^{(3)}](esu) \tag{21}$$

Typical values for $Im[\chi^{(3)}]$ for Pcs and similar molecules[65] can range from 10^{-14} to 10^{-08}. A collection of values for $Im[\chi^{(3)}]$ of Pcs and other compounds are shown in Table 2:

Table 2: Examples of $Im[\chi^{(3)}]$ for Pcs from literature.

Central Metal	Substituent	Axial Ligand	$Im[\chi^{(3)}]$ esu	Reference
Zn(II)	N.A.	N.A.	1.13×10^{-10}	[66]
H_2	-OC_7H_{15}	N.A.	4.86×10^{-11}	[66]
Sn(IV)	Cl	F	2.09×10^{-12}	[67]
Sn(IV	F	Cl	5.58×10^{-12}	[67]
Sn(IV)	-NO_2	Cl	1.26×10^{-12}	[67]
Sn(IV)	-$O(C_6H_4)NO_2$	Cl	4.05×10^{-12}	[67]
Ge(IV)	-$O(C_6H_4)CHO$	Cl	4.05×10^{-12}	[67]
Sn(IV)	-$O(C_6H_4)CHO$	Cl	2.93×10^{-12}	[67]
In(III)	-$C(CH_3)_3$	Cl	1.60×10^{-11}	[46]
Ga(III)	-$C(CH_3)_3$	Cl	1.10×10^{-11}	[46]
Ga(III)	-$C(CH_3)_3$	Cl	1.20×10^{-11}	[46]
Pd	N.A.	N.A.	6.50×10^{-12}	[54]
Si	N.A.	N.A.	2.00×10^{-09}	[54]

1.4.2 Parametric Nonlinear Refraction Model

Unlike the previous model used for nonlinear absorption, the model used for nonlinear refraction in this work is relatively simple. Its main objective is to calculate the effects seen in Figure 14 in terms of Equation 1. As shown in Equation 5, the nonlinear refraction will increase with I and thus will increase toward the focal point. This model assumes the total refractive change (Δn) in the z-scan sample is homogenous, and entirely due to $\chi^{(3)}$, as higher order nonlinearities will give rise to nonlinear refraction that scales with higher order intensities[62]. Acquiring n_2 from the data can then be done using either a numerical[68] fit or a peak to peak fit[69]. The peak to peak fit is far simpler, as shown by Equation 22:

$$\Delta T_{\text{pv}} \cong 0.406(1-S)^{0.27}|\Delta\Phi_0| \tag{22}$$

With ΔT_{pv} being the valley-height difference of the curve (see Figure 14), S the ratio of light passing the aperture, and $|\Delta\Phi_0|$ the induced phase distortion, described in Equation 23:

$$\Delta\Phi_0 = \frac{2\pi}{\lambda} n_2 I_0 L_{\text{eff}} \tag{23}$$

n2 can be determined using Equation 23, since all other parameters are known. The benefits of choosing a peak fit over curve fitting the entire z-scan measurements are shown in Figure 17, with the peak fit matching the measured data closer than a full fit. This is mostly due to the measurements further from the peak being irrelevant to the nonlinear refraction, but having equal weight in a full curve fit. Equation 22 has

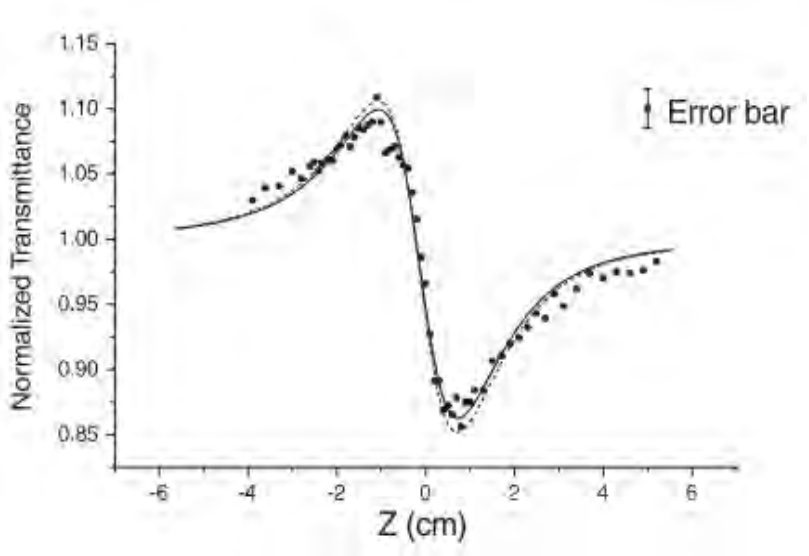

Figure 17: A fitted closed aperture z-scan[70].

two conditions: it loses accuracy for values of $\Delta T_{pv} > 1$[13] and is generally only useful for instantaneous nonlinearities[14]. The peak to peak fit also gives no information on the sign of n_2, which must be inferred by the shape of the transmittance curve. With n_2 known, the calculation of $Re[\chi^{(3)}]$ becomes possible, and is shown in Equation 24:

$$Re[\chi^{(3)}] = 10^{-4} \frac{{n^2}_0 \varepsilon_0 c^2 n_2}{\pi} \tag{24}$$

Like the nonlinear absorption equivalent $Im[\chi^{(3)}]$, the sample's $Re[\chi^{(3)}]$ can be converted into a molecular specific third order hyperpolarisability ($Re[\gamma]$) for solution based samples:

$$Re[\gamma] = \frac{Re[\chi^{(3)}]}{f^4 N N_A} \tag{25}$$

The values for both $Re[\chi^{(3)}]$ and $Re[\gamma]$ are calculated here in esu, and the convertion SI units can be done using Equation 26[64]:

$$Re[\chi^{(3)}](m^2.V^2) = \frac{4\pi}{9} 10^{-8} Re[\chi^{(3)}](esu) \tag{26}$$

With $Re[\chi^{(3)}]$ calclulated from Equation 26, and $Im[\chi^{(3)}]$ calculated from Equation 20 it becomes possible to determine the full $\chi^{(3)}$ using Equation 27[71]:

$$\chi^{(3)} = \sqrt{(Re[\chi^{(3)}])^2 + (Im[\chi^{(3)}])^2} \tag{27}$$

As the calculation of $Re[\chi^{(3)}]$ was done on measurements that had the open aperture measurements incorporated, literature will often report on either the full value of $\chi^{(3)}$ or simply on the change in refraction observed. As the $|\Delta\Phi_0|$ is directly responsible for other nonlinear properties, like phase mode distortion, literature focused on these effects will report the values for $|\Delta\Phi_0|$ directly[72,73]. Listed in Table 3 are some reported literature values of $\chi^{(3)}$ for compounds similar to those used in this work.

Table 3: Examples of $\chi^{(3)}$ for Pcs from literature.

Central Metal	Substituent	Axial Ligand	$\chi^{(3)}$ esu	Reference
H_2	$OCH_3(CH_2)_6OC_6H_4$	N.A.	4.86×10^{-11}	[74]
H_2	$-C(CH_3)_3$	N.A.	3.71×10^{-11}	[74]
Zn(II)	$-OCH_3(CH_2)_6OC_6H_4$	N.A.	1.13×10^{-10}	[74]
Zn(II)	$-C(CH_3)_3$	N.A.	2.10×10^{-11}	[74]
Cu(II)	$-C_6H_8S$	N.A.	3.2×10^{-13}	[75]
Ni(II)	$-C_6H_8S$	N.A.	2.1×10^{-13}	[75]
Zn(II)	$-O(C_6H_4)NN(C_6H_4)OH$	N.A.	5.1×10^{-13}	[75]
V(IV)	$-S(C_6H_{13})$	O	3.9×10^{-10}	[76]

1.4.3 Non-Parametric Nonlinear Absorption Model

If a material exhibits slow response NLO properties then the parametric nonlinear absorption model will fail to adequately explain experimental results. Previously, discussion of RSA and SA was limited to their effects on β, however these processes are independent of one another. A material with equal contributions of RSA and SA at a certain I will result in an apparent lack of NLO properties. This may lead to further uncertainty with regards to the nonlinear behaviour of the material should one of the processes favour a higher or lower I. In order to accurately simulate and explain the effects of multiple competing processes, the need for a more computationally complex model becomes apparent[15]. The non-parametric nonlinear absorption model's objective is to simulate the NLO properties of a material using multiple photophysical interactions that combine to create a sophisticated model. While this may be more computationally expensive than the parametric model, it is also more descriptive of a material's qualitative NLO properties. The most typical method of mapping out all possible photophysical processes for Pcs is with the use of a Perrin – Jablonski diagram[77], Figure 18. A Perrin–Jablonski diagram visualises allowed tran-

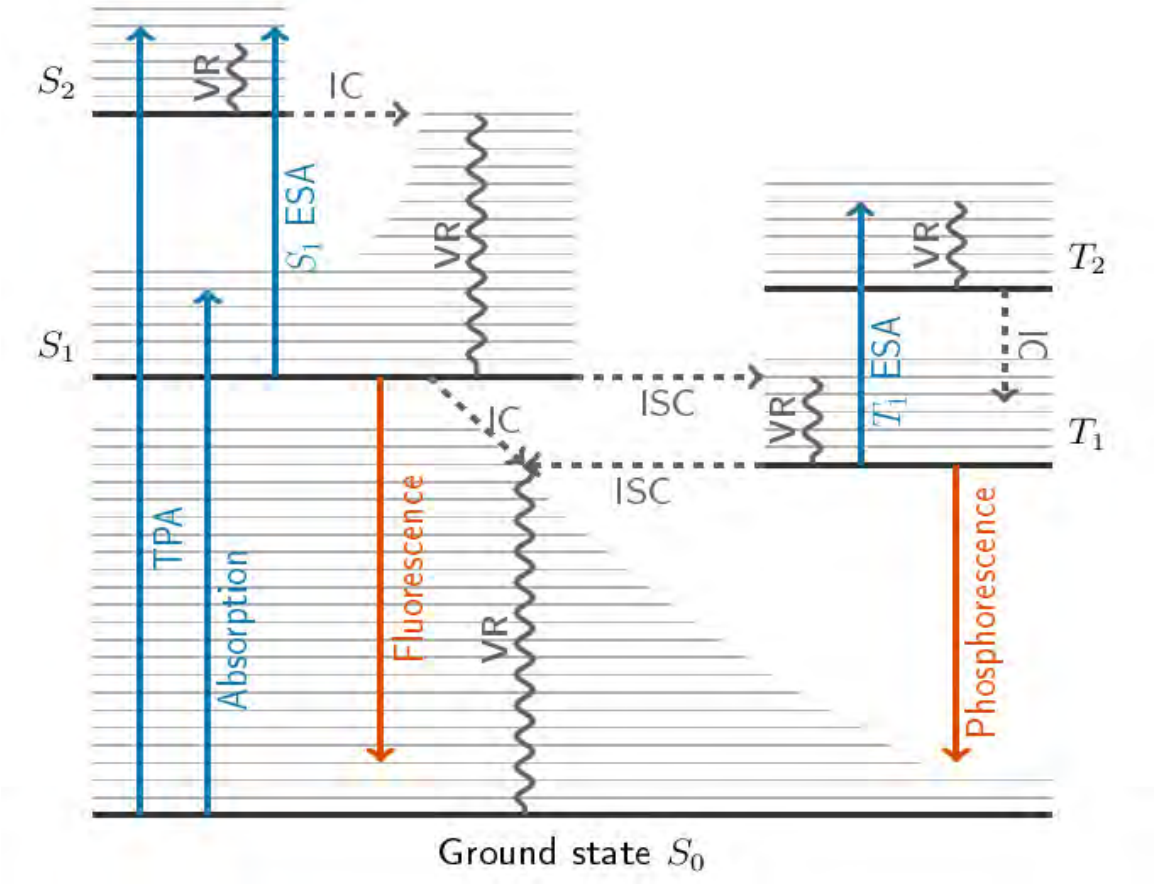

Figure 18: Perrin – Jablonski diagram mapping out photophysical processes for a Pc.

sitions and relative energy levels of the states. The states shown in Figure 18 are the ground state (S_0), the first singlet excited state (S_1), the n$^{\text{th}}$ singlet excited state (S_n), the fist triplet state (T_1), and the n$^{\text{th}}$ triplet excited state (T_1). The absorbing transitions (shown in blue with upward arrows) are the $S_0 \rightarrow S_1$ absorption, the $S_0 \rightarrow S_\text{n}$ two photon absorption (TPA), the $S_1 \rightarrow S_\text{n}$ excited state absorption (S_1 ESA), and the $T_1 \rightarrow T_\text{n}$ excited state absorption (T_1 ESA). The vibronic relaxation (VR) pathways are shown in gray curly lines, and the internal conversion (IC) and intersystem crossing (ISC) pathways are shown in dashed gray arrows. The emitting transitions (shown in orange downward arrows) are the $S_1 \rightarrow S_0$ (Fluorescence), and the $T_1 \rightarrow S_0$ (Phosphorescence). Some approximations are made in order to not obscure the relevant transitions: the Q_x transition is not shown as the S_2 in a Pc will be, for the purposes of this work, functionally the same as the S_1[78]. All of the Soret band transitions are also omitted as they have much higher energies than the transition of interest; the ISC transitions are also not shown for states higher than S_1 and T_1. These approximations are optional, the more energy levels included in the model the more accurate it will be in simulating the experimental results, however the computational costs scale roughly with (N!), with N being the number of energy levels[79]. The model used in this work employs five energy levels (N=5), and the population dynamics of these levels are described in Equations 28–32.

$$\frac{\partial}{\partial t}N_{\text{S}_0} = -\sigma_1\frac{IN_{\text{S}_0}}{h\nu} - \sigma_{\text{TPA}}\frac{I^2N_{\text{S}_0}}{(h\nu)^2} + \frac{N_{\text{S}_1}}{\tau_{\text{S}_1,\text{S}_0}} + \frac{N_{\text{T}_1}}{\tau_{\text{T}_1,\text{S}_0}} \tag{28}$$

$$\frac{\partial}{\partial t}N_{\text{S}_1} = \sigma_1\frac{IN_{\text{S}_0}}{h\nu} - \sigma_\text{n}\frac{IN_{\text{S}_1}}{h\nu} - \frac{N_{\text{S}_1}}{\tau_{\text{S}_1,\text{S}_0}} - \frac{N_{\text{S}_1}}{\tau_{\text{S}_1,\text{T}_1}} \tag{29}$$

$$\frac{\partial}{\partial t}N_{\text{S}_\text{n}} = \sigma_{\text{TPA}}\frac{I^2N_{\text{S}_0}}{(h\nu)^2} + \sigma_\text{n}\frac{IN_{\text{S}_1}}{h\nu} - \frac{N_{\text{S}_\text{n}}}{\tau_{\text{S}_\text{n},\text{S}_1}} \tag{30}$$

$$\frac{\partial}{\partial t}N_{\text{T}_1} = -\sigma_3\frac{IN_{\text{T}_1}}{h\nu} + \frac{N_{\text{S}_1}}{\tau_{\text{S}_1,\text{T}_1}} + \frac{N_{\text{T}_\text{n}}}{\tau_{\text{T}_\text{n},\text{T}_1}} - \frac{N_{\text{T}_1}}{\tau_{\text{T}_1,\text{S}_0}} \tag{31}$$

$$\frac{\partial}{\partial t}N_{\text{T}_\text{n}} = \sigma_3\frac{IN_{\text{T}_1}}{h\nu} - \frac{N_{\text{T}_\text{n}}}{\tau_{\text{T}_\text{n},\text{T}_1}} \tag{32}$$

$$N_{\text{total}} = N_{\text{S}_0} + N_{\text{S}_1} + N_{\text{S}_\text{n}} + N_{\text{T}_1} + N_{\text{T}_\text{n}} \tag{33}$$

In the equations above, $N_{\text{S}_0}, N_{\text{S}_1}, N_{\text{S}_\text{n}}, N_{\text{T}_1}$, and N_{T_n} are the populations of the $S_0, S_1, S_\text{n}, T_1$, and T_n states respectively, while N_{total} is the total population of all states. The absorption cross sections, σ_1, σ_2, and σ_3 are for the ground state, singlet state, and triplet state single photon absorptions respectively. σ_{TPA} is the two photon absorption cross section, h is Planck's constant, and ν the frequency of the light. The

values τ_{S_1,S_0}, τ_{T_1,S_0}, τ_{S_1,T_1}, τ_{S_n,S_1}, and τ_{T_n,T_1} are inverses of the rates of the $S_1 \rightarrow S_0$, $T_1 \rightarrow S_0$, $S_1 \rightarrow T_1$, $S_n \rightarrow s_1$, and $T_n \rightarrow T_1$ transitions respectively. With this model, Equation 8 can be rewritten as Equation 34.

$$\frac{dI}{dz'} = -I(\sigma_1 N_{S_0} + \sigma_2 N_{S_1} + \sigma_3 N_{T_1} + \sigma_{TPA} N_{S_0} I) \tag{34}$$

While Equation 34 may be simple to solve numerically, solving Equations 28–32 requires knowledge of the material's photophysical properties, namely the state lifetimes, τ_{T_1,S_0}, τ_{S_1,T_1}, τ_{S_n,S_1}, and τ_{T_n,T_1}. Equation 34 also has three unknown variables, compared to Equation 8's one unknown variable. This implies that at least three measurements at different points must be taken, varying only one parameter. Among the possible parameter that can be varied for this purpose are the pulse duration, laser pulse intensity, z_R, and concentration. As the laser pulse intensity is relatively easy to vary, keeping all others constant, it is prudent to use it as the parameter of variation. A simultaneous solution for the separate measurements can then be found with Equation 34. As mentioned, the units of TPA are reported in either GM or in $10^{-58}\,m^4\,photon^{-1}\,s$, while single photon cross sections are generally reported in cm^2. Most molecules possess excited state cross sections ranging between 10^{-19} cm^2 to $10^{-14}\,cm^2$[80]. As most Pcs possess σ_1 of the order $10^{-18}\,cm^2$ in the green wavelength region due to the gap in their absorption bands[81], any excited state cross section greater than $10^{-18}\,cm^2$ will provide noticeable nonlinear absorption. In the case of Pcs, σ_2 is typically found to be smaller than the values of σ_3 due to the semiconductor nature of the Pcs and the density of its triplet states[40]; however populating N_{T_1} requires the ISC from S_1 to T_1. This limits the effects observed from triplet absorption to measurements where the laser pulse time is of the order of the $S_1 \rightarrow T_1$ ISC time. The efficacy of the material as a nonlinear absorber depends on how large the difference is between the ground state absorption and the excited state absorption, as well as factors controlling the population of the excited state[80,82], the figure of merit for a material with RSA as its primary nonlinear absorption process is the ratio of the effective excited state cross section (σ_{eff}) to σ_1[83].This relationship is defined by Equation 35:

$$\frac{\sigma_{eff}}{\sigma_1} \approx \frac{\sigma_2 \frac{N_{S_1}}{N_{totaEl}} + \sigma_3 \frac{N_{T_1}}{N_{totalE}}}{\sigma_1} \tag{35}$$

In Equation 35, N_{totalE} is the total excited state population ($N_{T_1} + N_{S_1}$). While the RSA of a Pc in its optical window is noticeable due to its lack of ground state absorption, the transmittance attenuation due to TPA processes are minimal. This is primarily due to the TPA process in the Pcs optical window being a off resonant transition, possessing smaller σ_{TPA} values (typically 20 GM to 1000 GM)[80] than those seen in resonant enhanced TPA transitions (values exceeding 10 000 GM)[84]. As the

values for σ_{TPA} may be too low to noticeably affect the nonlinear absorption directly, it can still contribute to RSA process by populating states that have a higher cross section than the ground state[85].Table 4 contains literature values reported for 532 nm σ_{TPA} of Pcs from literature, and Table 5 contains reported values for excited state triplet and singlet cross sections.

Table 4: Examples of σ_{TPA} found it literature for Pcs at 532 nm.

Central Metal	Substituent	Axial Ligand	σ_{TPA} GM	Reference
Al(II)	-SO_3Na	N.A.	12.4	[86]
Al(II)	Cl	N.A.	11.1	[86]
Zn(II)	-S_3C_9	N.A.	12.1	[86]
Zn(II)	-S_4	N.A.	28.6	[86]
Pb(II)	-$O(C_5NH_4)$	N.A.	456	[87]
Pb(II)	-$O(C_5NH_4)$ *mono*	N.A.	45.3	[87]
Pb(II)	-$O(C_5H_4N)$ *mono*	N.A.	533	[87]

Table 5: Examples of σ_2 and σ_3 at 532 nm for Pcs reported in literature.

Central Metal	Substituent	Axial Ligand	σ_2 cm^2	σ_3 cm^2	Reference
Si(IV)	N.A.	-OSi(C_6H_{13})$_(3)$	39×10^{-18}	90×10^{-18}	[88]
Si(IV)	N.A.	-OSi(C_6H_{13})$_(3)$	30×10^{-18}	48×10^{-18}	[88]
Ge(IV)	N.A.	-OSi(C_6H_{13})$_(3)$	30×10^{-18}	51×10^{-18}	[88]
Sn(IV)	N.A.	-OSi(C_6H_{13})$_(3)$	22×10^{-18}	67×10^{-18}	[88]
Pb(II)	-C(CH_3)$_3$	N.A.	42×10^{-18}	33×10^{-18}	[88]
Zn(II)	-O(C_6H_4)COOH α	N.A.	4.0×10^{-17}	4.5×10^{-17}	[89]
Zn(II)	-O(C_6H_4)COOH β	N.A.	3.0×10^{-17}	17.0×10^{-17}	[89]
Zn(II)	-O(C_6H_4)COO$C_5H_1$1	N.A.	1.8×10^{-17}	40.0×10^{-17}	[89]
Al(III)	N.A.	Cl	18×10^{-18}	N.A.	[65]
Cu(II)	-OCH_2OCN(C_8H_{17})$_2$	N.A.	1.4×10^{-18}	N.A.	[65]
Pd(II)	-O$C_{10}H_{21}$	N.A.	75×10^{-18}	N.A.	[65]
Ni(II)	-O$C_{10}H_{21}$	N.A.	55×10^{-18}	N.A.	[65]
Co(II)	-O$C_{10}H_{21}$	N.A.	90×10^{-18}	N.A.	[65]
Cu(II)	-O$C_{10}H_{21}$	N.A.	72×10^{-18}	N.A.	[65]
Pb(II)	-O$C_{12}H_{25}$	N.A.	60×10^{-18}	N.A.	[65]

1.4.4 Non-Parametric Nonlinear Refraction Model

Analogous to the inter-dependence of the two parametric models, both non-parametric models depend on the state populations of the species that comprise them. The fundamental difference between the parametric and non-parametric refraction models are the adoption of refractions cross sections by the latter. This is a useful change of perspective for two reasons. First, it allows the sample to be treated as an ensemble of species, allowing measurements of each species' properties to be taken more accurately; and secondly, as a cross section, this model allows the modification of the input light with a statistical approach, allowing measurement of the phase shift due to each species. This was valid for the non-parametric absorption model as well, however, as the transmittance amplitude is a scalar, this bore no implications. For nonlinear refraction, and the processes that derive from it, like the $|\Delta\Phi_0|$, this can be used to model effects that influence only part of an input laser pulse, or for higher power, multiple parts of a laser pulse[90]. To that end, the non-parametric refraction model applies a multi-level model to Equation 5. This results in an equation directly analogous to Equation 34, which describes change in Φ_0 with respect to the populations of the excited species in the sample, Equation 36:

$$\frac{d\Phi}{dz'} = -\sigma_{\mathrm{r1}} N_{\mathrm{S}_0} + \sigma_{\mathrm{r2}} N_{\mathrm{S}_1} + \sigma_{\mathrm{r3}} N_{\mathrm{T}_1} + \sigma_{\mathrm{rker}} N_{\mathrm{S}_0} I \tag{36}$$

The new cross sections in Equation 36 (σ_{r1}, σ_{r2}, and σ_{r3}) are the respective refractive cross sections for the N_{S_0}, N_{S_1}, and N_{T_1}. The final cross section (σ_{rker}) represents the Kerr nonlinear cross section[90], with units $\mathrm{cm}^4\mathrm{W}^{-1}$ it is more dependent on the fluence of then the incident laser beam than the I[91]. As shown in Equation 36, the effects of the first three cross sections are independent of I, and thus have the units cm^2. The refraction due to these effects can be considered linear, with the nonlinearity being caused by the change in the state populations. This is not the case for σ_{rker} as its effects scale with I, however as this term depends on N_{S_0} and decreases with a decrease in N_{S_0}, its effects will mostly be seen in very short and/or highly intense laser pulses. Table 6 show values of refractive cross sections reported in literature.

Table 6: Examples of Pc refracive cross sections reported at 532 nm in literature.

Central Metal	Substituent	Axial Ligand	σ_{r1} cm^2	σ_{r2} cm^2	σ_{r3} cm^2	σ_{rker} $cm^4.W^{-1}$	Reference
Al(III)	N.A.	Cl	0	1.4×10^{-17}	N.A.	1.81×10^{-28}	[90]
Cu(II)	-O($C_{10}H_{12}$)($C_{10}H_{12}$)CHO ('R)	N.A.	-5.0×10^{-17}	N.A.	N.A.	N.A.	[92]
Cu(II)	-O($C_{10}H_{12}$)($C_{10}H_{12}$)CHO ('S)	N.A.	-2.1×10^{-17}	N.A.	N.A.	N.A.	[92]
Ni(II)	-OC_8H_{17}	N.A.	2.4×10^{-16}	N.A.	N.A.	N.A.	[93]
H_2	-OC_8H_{17}	N.A.	1.6×10^{-17}	N.A.	N.A.	N.A.	[93]

1.5 Research Goals

This works aims for the first to investigate the effects of symmetry on NLO properties of Pcs sterioisomers using computational methods and z-scan analysis of cross sections. This work is broken down into five goals. These goals include a) synthesizing a series of Pc isomers, specifically two types of Pcs, one free-base and one metalated with $SnCl_2$, with two structural isomers, alpha and beta substituted, each with four constitutional isomers ($SnCl_2$ was chosen as it is a good canditate for enhancing the intersystem crossing rate and is relatively stable), b) purifying and characterizing the constitutional isomers, c) studying their NLO properties, d) creating implementations of computational models to extract information from the experimental data, and e) utilising theoretical modelling methods to determine or predict the nature of the NLO behaviour observed. This process is illustrated in Scheme 1.

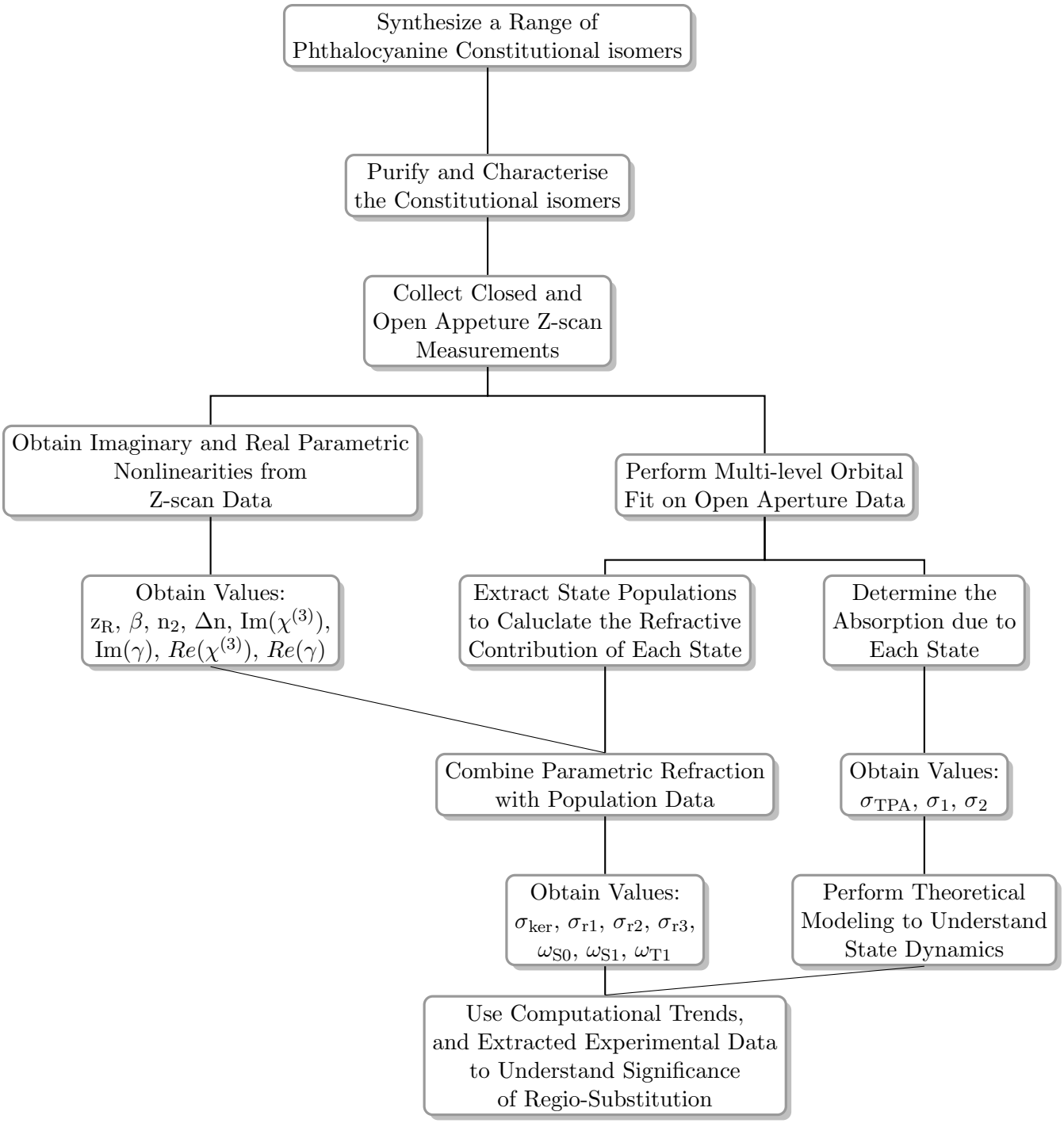

Scheme 1: Flow diagram illustrating the research methodology followed in this work.

2 Experimental

2.1 Synthesis

2.1.1 Free-base tetra substituted 3-4-tert-butylphenoxy Phthalocyanines (αH_2Pcs)

3-(4-tert-butylphenoxy) phthalonitrile (1.0 g; 1.4 mmol) was added to boiling 1-pentanol and stirred under nitrogen for 20 minutes. Catalytic amounts of metallic lithium were added to the reaction and it was left to reflux for 3 hours. The reaction was then cooled, and acetic acid was added to remove the excess lithium. Methanol was added to precipitate the product out of solution. The mixture was then filtered and washed with cold methanol. The isomers were separated using DCM for the C_{4h}(1^{st} fraction), C_{2v}(2^{nd} fraction), C_s(3^{rd} fraction) and methanol/DCM (1:9) to isolate D_{2h} (4^{th} fraction). What follows are the spectroscopic (IR and UV/Vis), elemental and mass spectra results for the respective regioisomers.

αH_2Pc C_{4h}

IR[cm^{-1}]:1244 (C-O-C); 1360 (CH_3); 1483, 1501, 1582 (C=C); 2850, 2929, 2959 (C-H); 3060, 3289 (=C-H) UV/Vis (chloroform) [nm (log(ε))]: 720.5 (5.14), 689.5 (5.07), 626 (4.47), 535.5 (2.98), 418 (3.12), 360 (4.11), 332 (4.80) MS (MALDI-TOF) $[M+2H]^+$: Calculated: 1107 m/z. Found: 1109 m/z. Elemental % (calc) : C 77.7 (78.1), H 5.7 (6), N 9.9 (10.1).

αH_2Pc C_{2v}

IR[cm^{-1}]:1246 (C-O-C); 1362 (CH_3); 1486, 1506, 1583 (C=C); 2865, 2955 (-C-H); 3036, 3290 (=C-H) UV/Vis (chloroform) [nm (log(ε))]: 723 (5.16), 691 (5.11), 626 (4.47), 536.5 (2.89), 419 (3.08), 361 (4.12), 331 (4.89) MS (MALDI-TOF) $[M+2]^+$: Calculated: 1107 m/z. Found: 1109 m/z. Elemental % (calc) : C 77.7 (78.1), H 5.7 (6), N 9.8 (10.1).

αH_2Pc C_s

IR[cm^{-1}]: 247 (C-O-C); 1362 (CH_3); 1485, 1506, 1583 (C=C); 2865, 2957, (-C-H); 3036, 3288 (=C-H) UV/Vis (chloroform) [nm (log(ε))]: 725 (5.02), 692.5 (4.97), 661 (4.48), 627 (4.33), 409 (4.12), 324 (4.61) MS (MALDI-TOF) $[M+2H]^+$: Calculated: 1107 m/z. Found: 1109 m/z. Elemental % (calc) : C 77.6 (78.1), H 5.7 (6), N 9.7 (10.1).

αH_2Pc D_{2h}

IR[cm^{-1}]: 248 (C-O-C); 1362 (CH_3); 1477, 1506, 1589 (C=C); 2856, 2924, 2957 (-C-H); 3297 (=C-H) UV/Vis (chloroform) [nm (log(ε))]: 728 (5.03), 695 (4.99), 663 (4.48), 629 (4.34), 409 (4.12), 325 (4.61) MS (MALDI-TOF) $[M+2H]^+$: Calculated:

1107 m/z. Found: 1109 m/z. Elemental % (calc) : C 77.7 (78.1), H 5.7 (6), N 9.7 (10.1).

2.1.2 Free-base tetra substituted 4-4-tert-butylphenoxy Phthalocyanines (βH_2Pcs)

The reaction was similar to that of the αH_2Pcs, however, it was refluxed for 4 hours, instead of the 3 hours used in the βH_2Pcs.

βH_2Pc C_{4h}

UV/Vis (chloroform) [nm (log(ε))]: 704 (5.01), 668 (4.93), 642 (4.46),606.5 (4.24), 400 (4.32) ,341 (4.66) 702 (4.69); 667 (4.63); 641(4.20); 607(4.01); 401 (4.01); 340(4.38). IR[cm^{-1}]: 1234 (C-O-C); 1363 (CH_3); 1465, 1506, 1602 (C=C);2853, 2922, 2955 (-C-H); 3043, 3287 (=C-H) MS (MALDI-TOF) $[M+H]^+$: Calculated: 1107 m/z. Found: 1108 m/z. Elemental % (calc) : C 77.6 (78.1), H 5.7 (6), N 9.8 (10.1).

βH_2Pc C_{2v}

UV/Vis (chloroform) [nm (log(ε))]: 704 (4.69), 668.5 (4.62), 642 (4.18), 607 (4.24), 399 (4.02) ,341 (4.36) IR[cm^{-1}]: 1238 (C-O-C); 1368(CH_3); 1465, 1507, 1604 (C=C); 2853, 2923, 2955 (-C-H) 3043, 3287 (=C-H) MS (MALDI-TOF) $[M+H]^+$: Calculated: 1107 m/z. Found: 1108 m/z. Elemental % (calc) : C 77.7 (78.1), H 5.3 (6), N 9.6 (10.1).

βH_2Pc C_s

UV/Vis (chloroform) [nm (log(ε))]: 704 (4.95), 668.5 (4.89), 642 (4.44), 607.5 (4.23), 399 (4.33) ,342 (4.66) IR[cm^{-1}]: 1234 (C-O-C); 1363 (CH_3); 1465, 1506, 1602 (C=C); 2853, 2922, 2955 (-C-H); 3043, 3287 (=C-H) MS (MALDI-TOF) $[M+2H]^+$: Calculated: 1107 m/z. Found: 1109 m/z. Elemental % (calc) : C 77.1 (78.1), H 5.7 (6), N 9.8 (10.1).

βH_2Pc D_{2h}

UV/Vis (chloroform) [nm (log(ε))]: 705 (4.85), 670 (4.80), 648 (4.46), 608 (4.25), 399 (4.42) ,342 (4.70) IR[cm^{-1}]: 1231 (C-O-C); 1366 (CH_3); 1474, 1505, 1601 (C=C); 2851, 2921, 2955 (-C-H); 3041, 3286 (=C-H) MS (MALDI-TOF) $[M+H]^+$: Calculated: 1107 m/z. Found: 1108 m/z. Elemental % (calc) : C 77.5 (78.1), H 5.2 (6), N 9.7 (10.1).

2.1.3 $SnCl_2$ tetra substituted 3-4-tert-butylphenoxy Phthalocyanines ($\alpha SnCl_2Pcs$)

The followed procedure was the same as that of αH_2Pcs. The resulting αH_2Pc regioisomer mixture was then cleaned, dried and added to boiling 1-Octanol under nitrogen. $SnCl_2$ (0.2 mg, 1 mol) was then added and the reaction was left to reflux for 2 hours. The green product was precipitated with methanol and washed with cold methanol. The isomers were separated using DCM for the C_{4h}(1^{st} fraction), C_{2v}(2^{nd} fraction), C_s(3^{rd} fraction) and methanol/DCM (1:9) to isolate D_{2h} (4^{th} fraction). What follows are the spectroscopic (IR and UV/Vis), elemental and mass spectra results for the respective regioisomers.

$\alpha SnCl_2Pc$ C_{4h}

UV/Vis (chloroform) [nm (log(ε))]: 739 (5.29), 664 (4.60), 414 (4.32), 339 (4.93) IR[cm^{-1}]: 1247(C-O-C); 1323 (CH_3); 1476, 1511, 1607 (C=C); 2926, 3105 (-C-H); MS (MALDI-TOF) $[M-2H]^+$: Calculated: 1294.8 m/z, Found: 1292.1 m/z. Elemental % (calc) : C 65.4 (66.8), H 4.4 (5), N 7.4 (8).

$\alpha SnCl_2Pc$ C_{2v}

UV/Vis (chloroform) [nm (log(ε))]: 741 (5.49), 664 (4.71), 420(4.21), 353 (4.87), 345 (4.86) IR[cm^{-1}]: 1247(C-O-C); 1323 (CH_3); 1476, 1511, 1607 (C=C); 2926, 3105 (-C-H); MS (MALDI-TOF) $[M-H]^+$: Calculated: 1294.8 m/z, Found: 1293.2 m/z. Elemental % (calc) : C 65.2 (66.8), H 4.7 (5), N 7.1 (8).

$\alpha SnCl_2Pc$ C_s

UV/Vis (chloroform) [nm (log(ε))]: 741 (4.91), 664 (4.65), 414 (4.29), 357 (4.38) IR[cm^{-1}]: 1247(C-O-C); 1323 (CH_3); 1476, 1511, 1607 (C=C); 2926, 3105 (-C-H); MS (MALDI-TOF) $[M-2H]^+$: Calculated: 1294.8 m/z, Found: 1292.4 m/z. Elemental % (calc) : C 65.4 (66.8), H 4.4 (5), N 7.4 (8).

$\alpha SnCl_2Pc$ D_{2h}

UV/Vis (chloroform) [nm (log(ε))]: 741 (4.84), 664 (4.55), 414 (4.35), 350 (4.30) IR[cm^{-1}]: 1247(C-O-C); 1323 (CH_3); 1476, 1511, 1607 (C=C); 2926, 3105 (-C-H); MS (MALDI-TOF) $[M-4H]^+$: Calculated: 1294.8 m/z, Found: 1290.6 m/z. Elemental % (calc) : C 65.9 (66.8), H 4.7 (5), N 7.3 (8)

2.1.4 $SnCl_2$ tetra substituted 4-4-tert-butylphenoxy Phthalocyanines ($\beta SnCl_2Pcs$)

Procedure was the same as the $\alpha SnCl_2Pc$ regioisomers

$\beta SnCl_2Pc$ C_{4h}

UV/Vis (chloroform) [nm ($\log(\varepsilon)$)]: 711 (5.29), 664 (4.60), 414 (4.32), 339 (4.93) IR[cm^{-1}]: 1242(C-O-C); 1326 (CH_3); 1473, 1501, 1598 (C=C); 2926, 3105 (-C-H); MS (MALDI-TOF) $[M\text{-}2H]^+$: Calculated: 1294.8 m/z, Found: 1292.1 m/z. Elemental % (calc) : C 65.4 (66.8), H 4.4 (5), N 7.4 (8).

$\beta SnCl_2Pc$ C_{2v}

UV/Vis (chloroform) [nm ($\log(\varepsilon)$)]: 711 (5.60), 640 (4.92), 420 (4.79), 361 (4.96) IR[cm^{-1}]: 1242(C-O-C); 1326 (CH_3); 1473, 1501, 1598 (C=C); 2926, 3105 (-C-H); MS (MALDI-TOF) $[M\text{-}2H]^+$: Calculated: 1294.8 m/z, Found: 1292.1 m/z. Elemental % (calc) : C 65.2 (66.8), H 4.7 (5), N 7.1 (8).

$\beta SnCl_2Pc$ C_s

UV/Vis (chloroform) [nm ($\log(\varepsilon)$)]: 711 (5.41), 640 (4.92), 420 (4.54), 361 (4.76) IR[cm^{-1}]: 1242(C-O-C); 1326 (CH_3); 1473, 1501, 1598 (C=C); 2926, 3105 (-C-H); MS (MALDI-TOF) $[M\text{-}2H]^+$: Calculated: 1294.8 m/z, Found: 1292.1 m/z. Elemental % (calc) : C 65.4 (66.8), H 4.4 (5), N 7.4 (8).

$\beta SnCl_2Pc$ D_{2h}

UV/Vis (chloroform) [nm ($\log(\varepsilon)$)]: 711 (5.22), 640 (4.56), 454 (4.56), 426 (4.56), 353 (4.71) IR[cm^{-1}]: 1242(C-O-C); 1326 (CH_3); 1473, 1501, 1598 (C=C); 2926, 3105 (-C-H); MS (MALDI-TOF) $[M\text{-}2H]^+$: Calculated: 1294.8 m/z, Found: 1293.6 m/z. Elemental % (calc) : C 65.9 (66.8), H 4.7 (5), N 7.3 (8).

2.2 Instrumentation

Ground-state absorption spectra were acquired on a PerkinElmer LAMBDA^{TM} 950 in spectroscopic grade chloroform. Elemental analyses were done using a Vario-Elemental Microcube ELIII. Mass spectra data were collected on a Bruker AutoFLEX III Smart-beam MALDI-TOF mass spectrometer using various matrices and modes of operation depending on the sample. Fluorescence lifetimes and isometric lifetimes were measured with a FluoTime 300 'EasyTau' spectrometer (PicoQuant GmbH) using time correlated single photon counting (TCSPC). The samples were excited at 670 nm with a diode laser (LDH-P-670, 20 MHz repetition rate, 44 ps pulse width, PicoQuant GmbH). The detector employed was a Peltier cooled photomultiplier (PMA-C 192-M, PicoQuant GmbH). Z-scans done in this study were performed with either a frequency-doubled Nd:YAG laser (Quanta-Ray, 1.5 J /10 ns FWHM pulse duration), or a frequency-doubled Nd:YAG laser (Quanta-Ray, 1.5 J /7 ns FWHM pulse duration) as the excitation source. The laser was operated in a near Gaussian transverse mode at 532 nm (second harmonic), with a pulse repetition rate of 10 Hz and energy range of 5-45 μJ. The beam was spatially filtered to remove the higher-order modes and tightly focused with a 15 cm focal length lens. The effects due to damage between runs was mitigated by replacing the sample. Magnetic circular dichroism (MCD) spectra were measured using a Chirascan plus spectrodichrometer equipped with a 1 T (Tesla) permanent magnet by using both the parallel and antiparallel fields.

2.3 Computation

2.3.1 Computational Hardware

The bulk of the calculations for this work that required open source or in-house scripts that utilised general-purpose graphics processing units (GPGPU) were done on a local Beowulf cluster consisting of four machines (3 slave nodes and 1 master node), each consisting of an Intel i5 3550 CPUs at 3.30 GHz, and 12 GB DDR3 Ram with three GPGPU cards (2 NVIDIA Tesla 1060c and 1 AMD WX 5100) that were distributed among the slave nodes. The cluster ran on the Rocks Cluster Distribution operating system. For large scale and memory-intensive calculations the Centre of High Performance Computing (CHPC) in Cape Town. The Lengau section of the CHPC cluster that was used in this work, consisted of 148.5 TB ram and 1368 nodes, with Intel Xeon (24 core) CPUs at 2.6 GHz.

2.3.2 Computational Software

The various quantum molecular modelling (QMM) suites used for this work were chosen based on their applicability to the type of calculation required. In addition, some other programs were used to handle and input data for the QMM suites, such

as GaussView 05, Avogadro, Visual Molecular Dynamics (VMD), ArgusLab, and the GNU Image Manipulation Program (GIMP).

2.3.2.1 Gaussian 09

Gaussian 09[94], version E01, was used to perform two types of calculations for this work, and was run on the CHPC. The first was the ground state geometry calculation for all molecules using density functional theory (DFT), using the B3LYP[95] functional and the CC-PVTZ[96] basis set, with an ultrafine grid. The second calculation type Gaussian 09 was utilised for were the time dependent-density functional theory (TD-DFT) calculations for the ground state absorption of all molecules, either the CAM-B3LYP[97] or M06-HF[98] functionals, as the CAM-B3LYP is the standard for DFT work with Pcs[99,100] an the M06-HF was found to give more accurate results for lower energy transitions, with the CC-PVDZ[96] basis set for both, solving for the first 30 states. Coupled-perturbed Hartree Fock (CPHF) was used to determine the second-order hyperpolarisability of each molecule, using the CC-PVDZ basis set.

2.3.2.2 NWChem

NWChem 6.8[101] was used to perform the real time-time dependent-density functional theory (RTTD-DFT), with the M06[98] functional, due to functionals with higher levels of exchange not being implemented in the RTTD-DFT module, and the CC-PVDZ basis set. Calculation of the ground state, as well as the excited state (singlet and triplet) absorptions, for all molecules were carried out on the CHPC.

2.3.2.3 Orca

Orca 4[102] was used for the investigation of small conformational issues that were encountered as well as used in the visualisation of orbitals and transitions. Orca was run off the local Beowulf cluster.

2.3.2.4 Custom Calculations

Some calculations were created during the course of this work, to calculate molecular cross sections. These calculations were carried out using the python library pandas to handle data transfer and either the python library numpy or the GPGPU language OpenCL to perform calculations, theses were run on the local Beowulf cluster.

3 Characterisation

3.1 Synthesis and Analysis

3.1.1 Synthesis of the Free-base Regioisomers of the βH_2Pc and αH_2Pc

The synthetic routes for the free-base Pcs are shown in Figures 2 and 3. The formation of the Pc macrocycle was confirmed by the absence of the CN IR peak at $\approx$ 2230 cm^{-1}. The IR spectra also confirm the presence of the substituent's tert-butyl peaks at $\approx$ 2850, 2929, and 2959 cm^{-1}. The presence of the IR peak at $\approx$ 1244 cm^{-1} confirms the substituents are bound via an ether. The lack of an IR peak for either a NO_2 at $\approx$ 1530 and 1350 cm^{-1} or a broad OH peak at $\approx$ 3030 cm^{-1} confirm that all four arms of the Pc are correctly substituted. The composition of the molecules was confirmed with elemental analysis and the mass of each regioisomer was found to be within 1 or 2 protons from their calculated mass of 1107 m/z. The UV/Vis of each regioisomer is central to this work and will be discussed in detail in the following section.

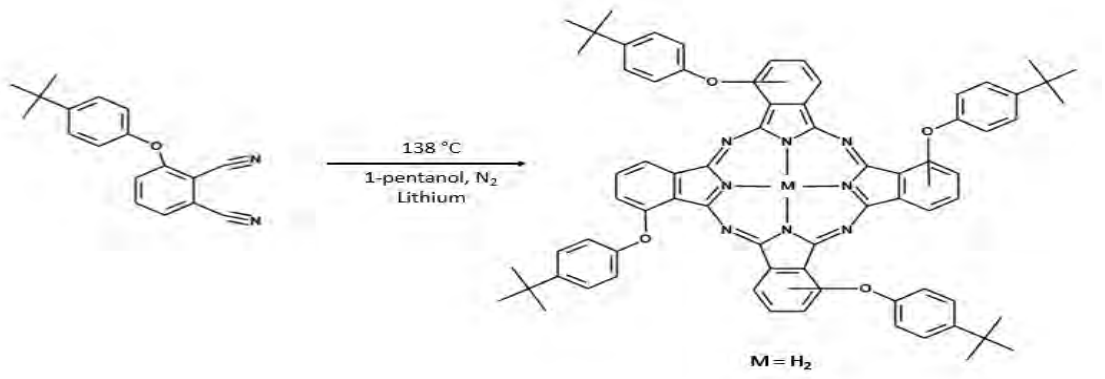

Scheme 2: Synthetic route for the αH_2Pc regioisomers.

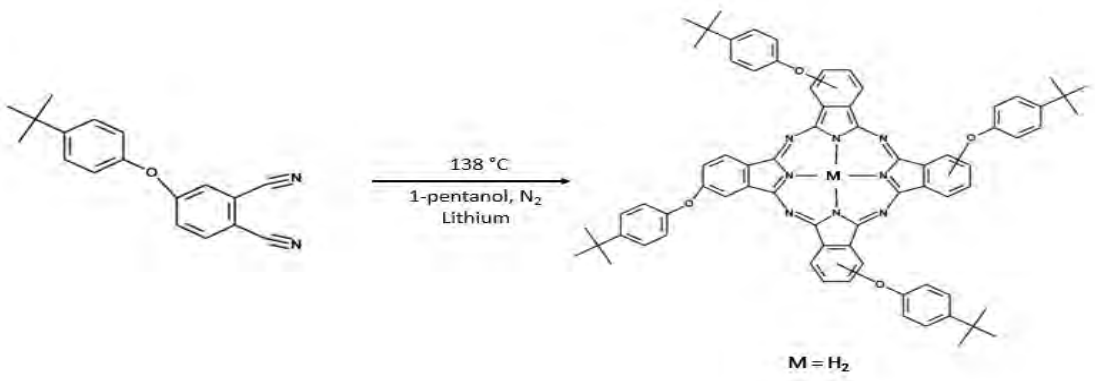

Scheme 3: Synthetic route for the βH_2Pc regioisomers.

3.1.2 Synthesis of the $SnCl_2$ Regioisomers of the $\beta SnCl_2Pc$ and $\alpha SnCl_2Pc$

The metalation of the regioisomers synthetic route is shown in Figures 4 and 5. The characterisation for the MPc regioisomers was the same as that for the free-base regioisomers, with slight shifts in the IR spectra observed. The elemental composition differed due to the introduced $SnCl_2$, however, elemental analysis confirmed that the measured composition matched the calculated (within 3-5%). The mass of each regioisomer was run in positive ion mode, and the results were found to be within 1 or 2 protons from their calculated mass. like the free-base regioisomers, the UV/Vis of each $SnCl_2$ regioisomers central to this work and will be discussed in detail in the following section.

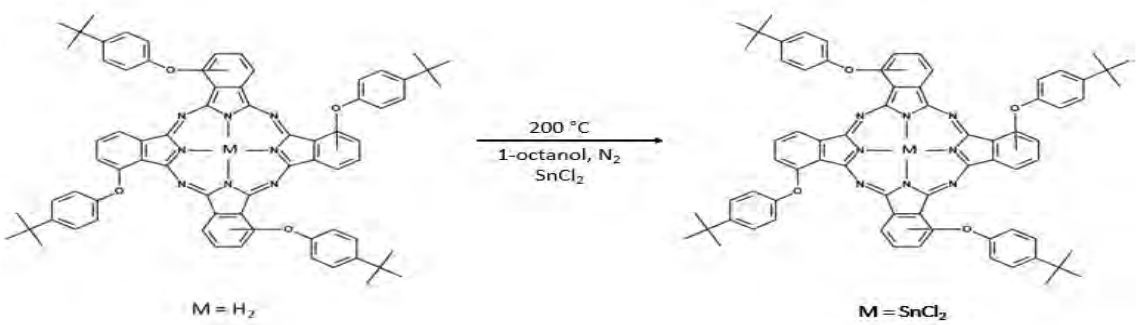

Scheme 4: Synthetic route for the αH_2Pc regioisomers.

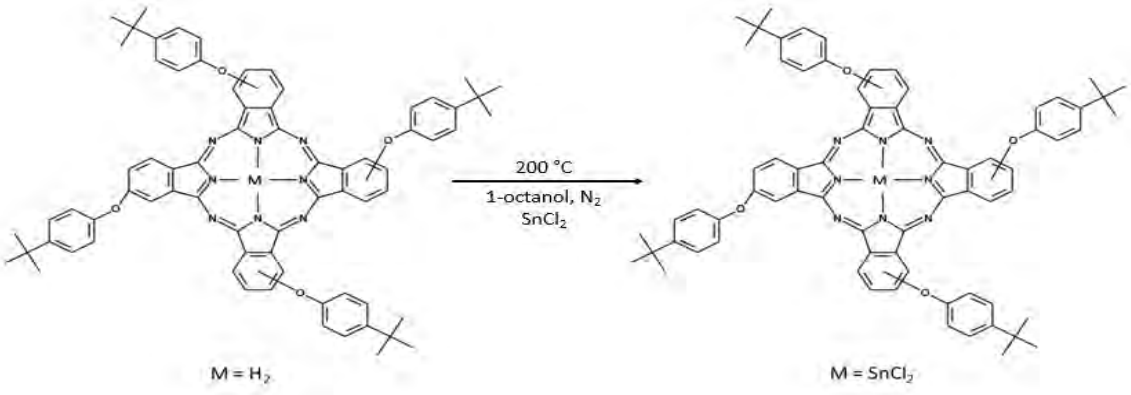

Scheme 5: Synthetic route for the βH_2Pc regioisomers.

3.2 Ground State Absorption

The ground state absorption cross sections were acquired using UV/Vis spectroscopy. The results were as expected for the structural isomers, however, the regioisomers exhibited minor deviation and these will be described below. A full analysis of the ground state absorption spectra and the transitions that they are composed of for all Pcs can be found in Appendix A.

3.2.1 Ground State Absorption of the free-base Regioisomers of the βH_2Pc and αH_2Pc

The beta substituted free-base Pc regioisomers exhibited very similar ground state absorption to each other, possessing absorption peaks that could not be differentiated with UV/Vis spectroscopy. The ground state absorption of one of the regioisomers, C_{4h}, is shown in Figure 19,

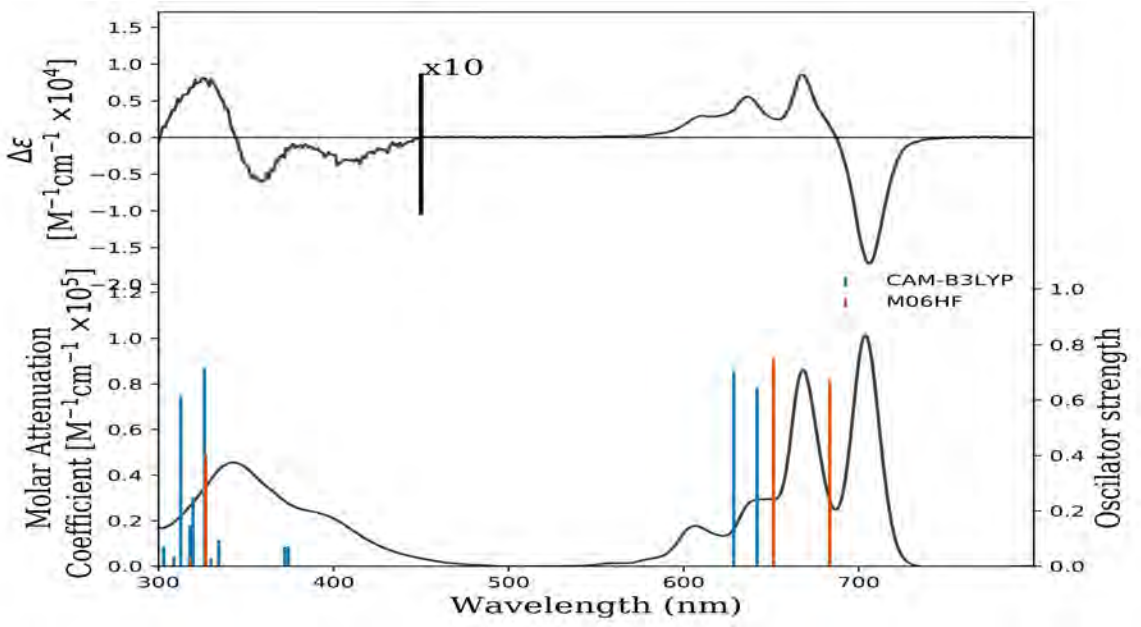

Figure 19: Ground state absorption of the βH_2Pc's C_{4h} regioisomer.

and it is typical of the beta free-base structural isomers substituted with tert-butyl phenoxyether, with the split Q-band around 700 nm, the Soret band at 350 nm and an optical window in the 500 nm range. Figure 19 also shows the MCD of the C_{4h}, depicting the polarisation of the absorption band and the intense Faraday $\mathbf{B}_0$ term that is characteristic of free-base Pcs[103].

The free-base alpha substituted Pc regioisomers showed more dramatic shifting of their Q-bands than the beta substituted equivalents. For a tert-butyl phenoxyether

substituent, this results in more red-shifted peaks, giving the sample a more green appearance as can be seen in Figure 20.

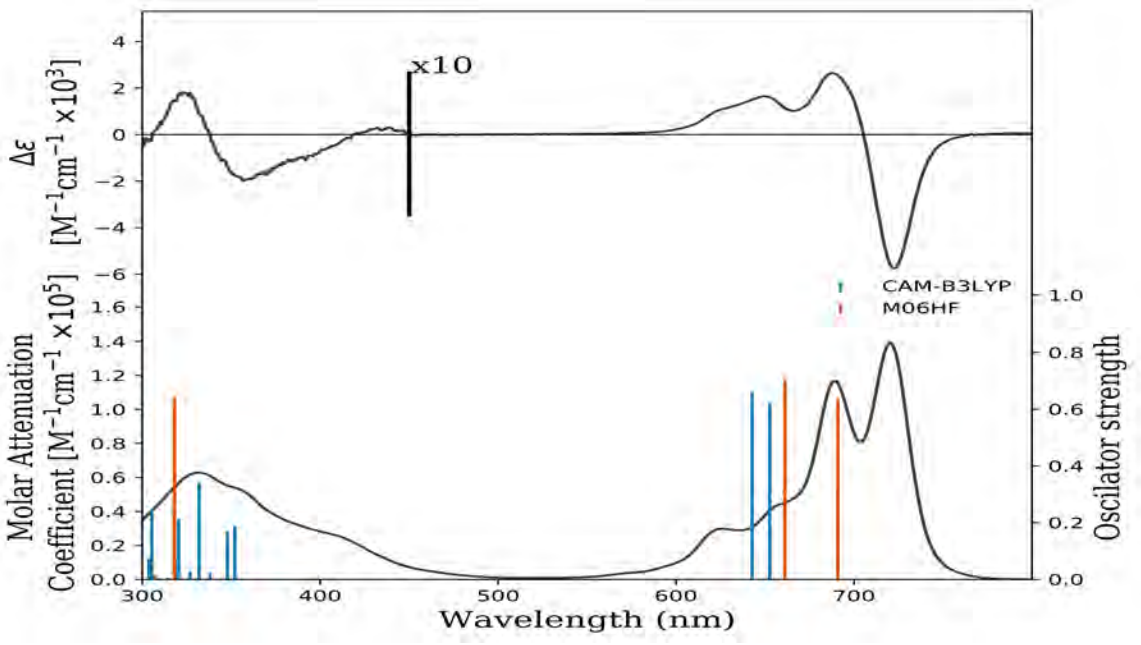

Figure 20: Ground state absorption of the αH_2Pc's C_{4h} regioisomer.

The lack of variation in the beta regioisomers is expected, as the beta substitution position is on the periphery of the Pc molecule, reducing the strength of its electronic effects. Aside from increasing the distance for any electronic-based effects, the beta position also does not sterically hinder the planar conformation of the ring, reducing the differences seen in the central Pc structure. The result of this can be seen in Table 8. Also shown are the calculated transition wavelengths for each band, and these too show the similarity of the position of the peaks across the regioisomers.

The spectral bands observed in the αH_2Pc regioisomers were more redshifted compared to the βH_2Pc's regioisomers. This resulted from a smaller HOMO-LUMO band gap than those observed in the βH_2Pc's regioisomers due to the proximity of the substituent to the central π electron system. As the Q-band is a π to π^* transition this will influence the transition energy of the band. The regioisomers experienced a small increasing trend in the position of the Q-band as well, shown in Table 7, with C_{4h} yielding the lowest, C_{2v} and C_s giving similar in-between values and D_{2h} at the highest wavelength.

Table 7 also shows the calculated energy for the Q-band transition, which follow this experimental trend. As the most notable absorption bands are a consequence of transitions between the four Michl frontier orbitals, Figure 21 shows how the orbitals are shifted equally, either to higher or lower energies, resulting in a HOMO-LUMO band gap remaining similar for all beta regioisomers.

Table 7: Ground state absorption peaks for the βH_2Pc's regioisomers

Isomer	Assignment	Experimental Wavelength[nm]	Cam-B3LYP Wavelength[nm]	M06-HF Wavelength[nm]
C4h	Q x	704.0	637	677
	Q y	668.0	621	644
	Soret y	401.0	310	290
	Soret x	340.0	304	286
C2v	Q x	704.0	633	677
	Q y	668.5	623	644
	Soret y	399.0	318	286
	Soret x	341.0	312	278
Cs	Q x	704.0	638	677
	Q y	668.5	622	644
	Soret y	399.0	313	285
	Soret x	342.0	310	278
D2h	Q x	705.0	670	716
	Q y	670.0	633	661
	Soret y	399.0	324	296
	Soret x	342.0	316	285

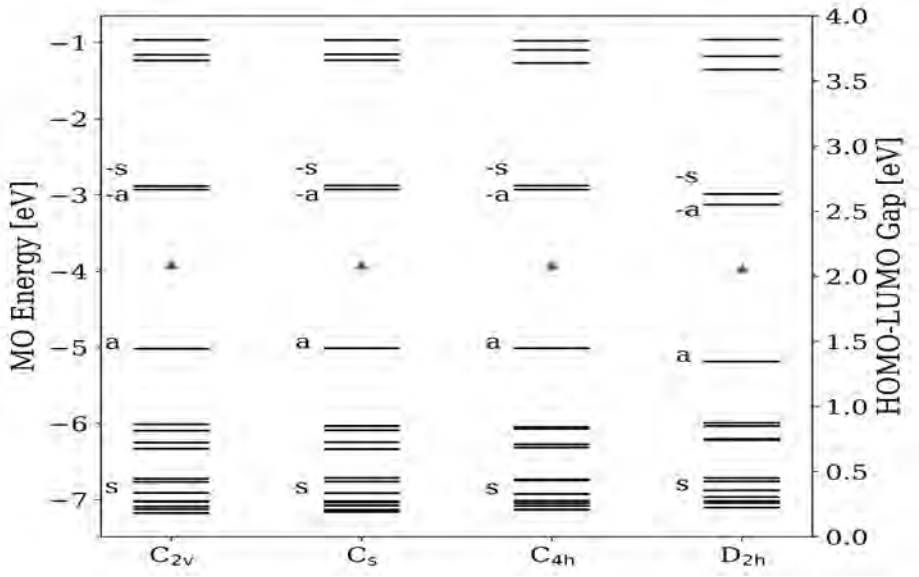

Figure 21: Calculated energy levels for the 4 Michl frontier orbitals of the βH_2Pc regioisomers.

Table 8: Ground state absorption peaks for the αH_2Pc's regioisomers

Isomer	Assignment	Experimental Wavelength[nm]	Cam-B3LYP Wavelength[nm]	M06-HF Wavelength[nm]
C4h	Q x	720.5	663	699
	Q y	689.5	650	670
	Soret y	418.0	353	322
	Soret x	360.0	335	308
C2v	Q x	723.0	665	696
	Q y	691.0	652	667
	Soret y	419.0	343	290
	Soret x	361.0	334	284
Cs	Q x	725.0	666	702
	Q y	692.5	652	670
	Soret y	409.0	352	292
	Soret x	325.0	339	283
D2h	Q x	728.0	670	705
	Q y	695.0	646	666
	Soret y	409.0	334	319
	Soret x	325.0	323	290

The energies for the βH_2Pc regioisomers' Michl orbitals are higher than those seen in the four Michl orbitals for the αH_2Pc's regioisomers, shown in Figure 22. However, the energy between the orbitals is lower for the αH_2Pc's regioisomers as is shown by their lower HOMO-LUMO band gap energies.

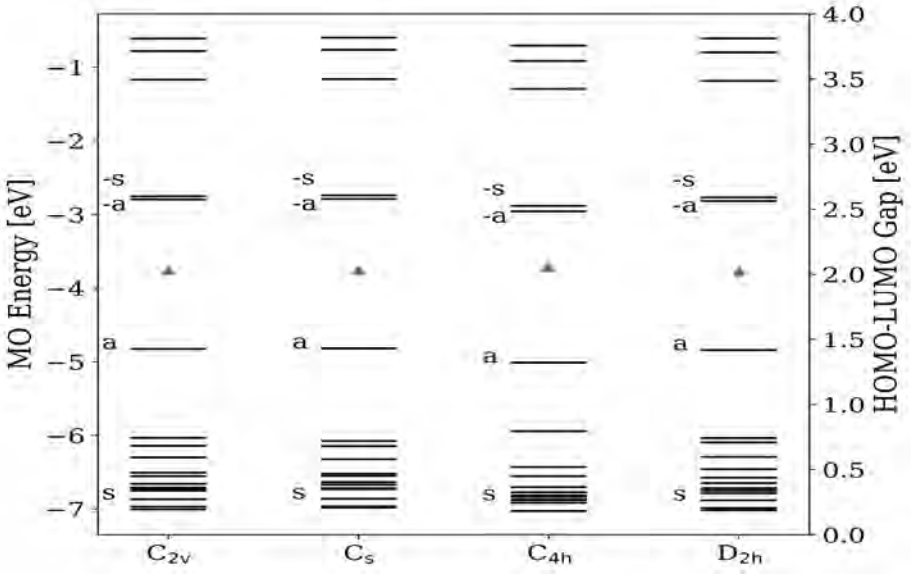

Figure 22: Molecular orbital energy levels for the 4 Michl frontier orbitals of the αH_2Pc's regioisomers.

3.2.2 Ground State Absorption of the $SnCl_2$ MPcs Regioisomers of $\alpha SnCl_2Pc$ and $\beta SnCl_2Pc$

Unlike the free-base Pcs, the $SnCl_2$ Pcs posses' a single Q-band. As discussed in Chapter 1, this is due to the first two Pc unoccupied orbitals of the free-base Pc (denoted by b_{2g} and b_{3g}) becoming degenerate (now denoted by e_{gy} and e_{gx}). This unified Q-band can, however, be separated with the use of MCD which shows a very strong Faraday **A** term for the $SnCl_2$ Pcs' Q-band, seen in Figure 23. Another effect of replacing the two central protons with $SnCl_2$ is the redshifting of the absorption peaks seen in both MCD and UV/Vis. This effect is a result of the electronegativity of the central $SnCl_2$ and its effects on the four frontier orbitals.

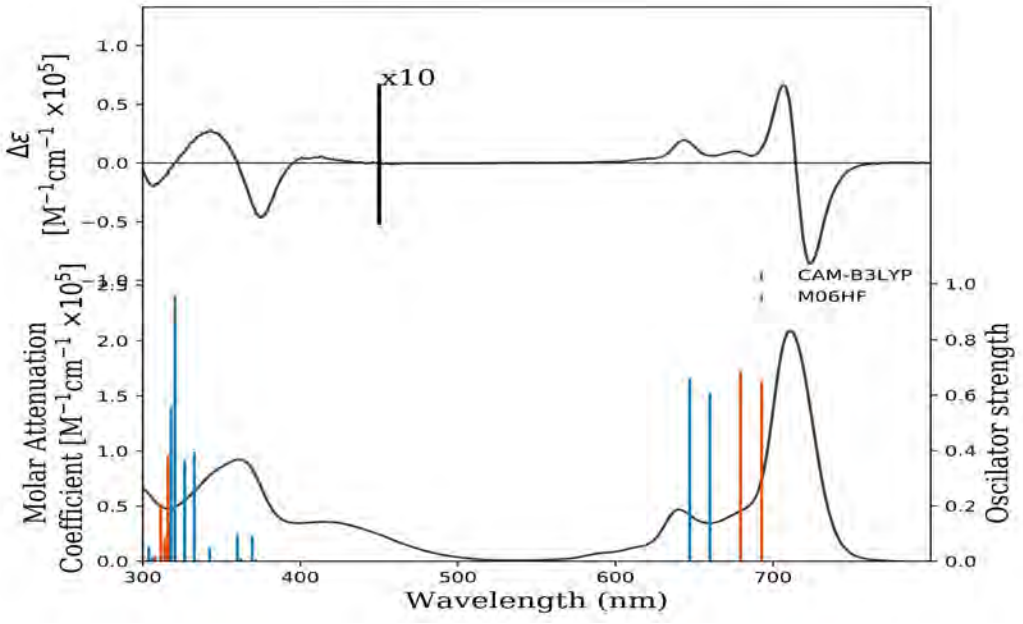

Figure 23: Ground state absorption of the $\beta SnCl_2Pc$'s C_{4h} regioisomer.

The $\alpha SnCl_2Pcs$ are the most redshifted regioisomers studied in this work, due to the electron affinity of both the central $SnCl_2$ and the tert-butyl phenoxyether substitution for this specific structural regioisomer. Like the $\beta SnCl_2Pcs$' regioisomers the $\alpha SnCl_2Pcs$' regioisomers all showed a single Q-band, but for the $\alpha SnCl_2Pcs$' regioisomers the Q-band was shifted to around 740 nm, and possessed a smaller and broader Soret band at 350 nm, as can be seen by the UV/Vis absorption of C_{4h} in Figure 24.

Like the βH_2Pc's regioisomers, the $\beta SnCl_2Pc$'s regioisomers did not exhibit a large shift between their respective absorption peaks. As shown in Table 9 the four regioisomers exhibited very similar Q-band absorption wavelengths with the Soret band showing some differences in values across the regioisomers. The TD-DFT calculations (both M06-HF and CAM-B3LYP functionals) fail to represent the exact transition energy, with the calculations predicting a larger degree of splitting in the peaks than

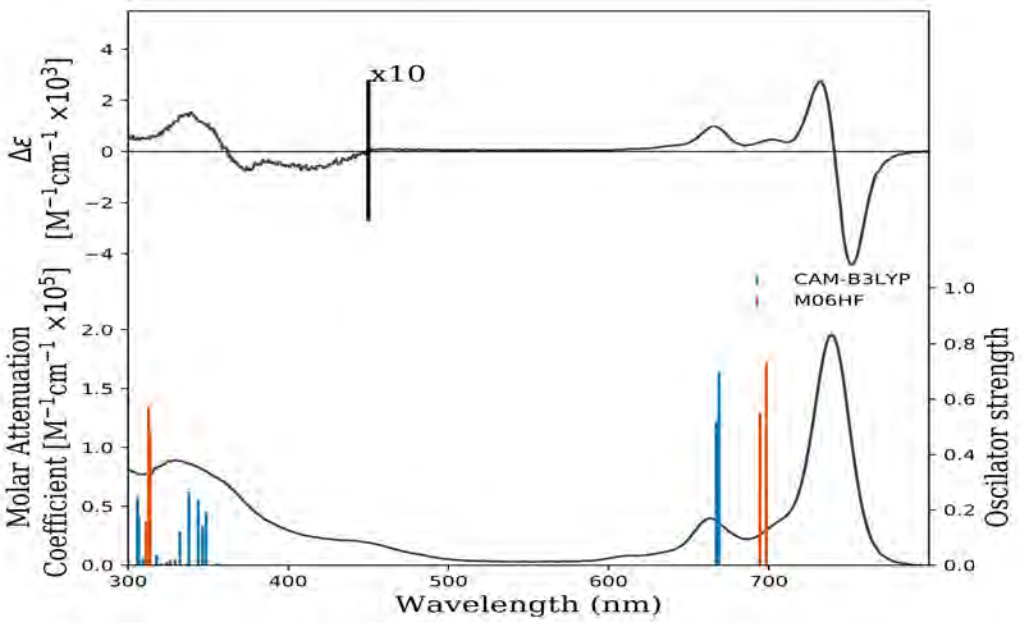

Figure 24: Ground state absorption of the $\alpha SnCl_2Pc$'s C_{4h} regioisomer.

is observed. The cause of this is likely due to the overly sensitive nature of DFT based calculations to geometry[104], which works in favour of the alpha structural isomers, but leads to incorrect conclusion for the more spectrally similar beta isomers.

The $\alpha SnCl_2Pc$ exhibited far more variation in the absorption peaks between the regioisomers than was seen in the beta structural isomer analogues, and this was seen also seen in the αH_2Pc's regioisomers. Unlike the $\beta SnCl_2Pcs$' regioisomers, the calculated transitions for the $a \rightarrow$ *-a* and $a \rightarrow$ *-s* orbitals for the $\alpha SnCl_2Pcs$ are closer in energy for both the M06-HF and CAM-B3LYP functionals used, as seen in Table 10.

The energy levels calculated by the non-time dependent DFT calculations, shown in Figure 25, explain the cause of the failure of the TD-DFT functionals to predict the transition degeneracy. The DFT also shows how the e_{gy} and e_{gx} orbitals are very sensitive to the structural symmetry of the molecule, causing the calculated transitions with TD-DFT to be less accurate. This is a known limitation of TD-DFT, especially when working within a 0.2 eV energy range[105].

While the DFT calculations overestimated the splitting in the $\beta SnCl_2Pcs$, for the $\alpha SnCl_2Pc$, the structural differences were large enough to yield an accurate replication of the e_g orbitals degeneracy as shown by Figure 26.

Table 9: Ground state absorption peaks for the $\beta SnCl_2Pc$ regioisomers.

Isomer	Assignment	Experimental Wavelength[nm]	Cam-B3LYP Wavelength[nm]	M06-HF Wavelength[nm]
C4h	Q x	711.0	654	688
	Q y	711.0	654	688
	Soret y	414.0	361	313
	Soret x	339.0	360	313
C2v	Q x	711.0	653	686
	Q y	711.0	652	683
	Soret y	420.0	364	314
	Soret x	361.0	362	311
Cs	Q x	711.0	660	693
	Q y	711.0	647	679
	Soret y	420.0	362	316
	Soret x	361.0	360	312
D2h	Q x	711.0	667	702
	Q y	711.0	641	674
	Soret y	454.0	361	317
	Soret x	353.0	360	307

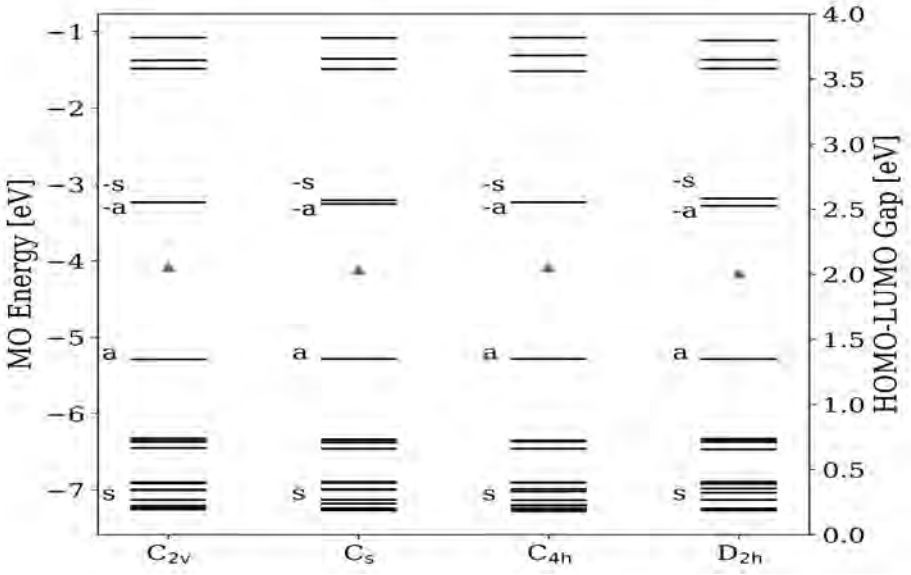

Figure 25: Molecular orbital energy levels for the 4 Michl frontier orbitals of the $\beta SnCl_2Pc$ regioisomers.

Table 10: Ground state absorption peaks for the $\alpha SnCl_2Pc$ regioisomers.

Isomer	Assignment	Experimental Wavelength[nm]	Cam-B3LYP Wavelength[nm]	M06-HF Wavelength[nm]
C4h	Q x	739.0	664	694
	Q y	739.0	659	691
	Soret y	414.0	328	276
	Soret x	339.0	333	263
C2v	Q x	741.0	668	697
	Q y	741.0	668	696
	Soret y	420.0	347	314
	Soret x	353.0	343	313
Cs	Q x	741.0	669	698
	Q y	741.0	667	695
	Soret y	414.0	332	314
	Soret x	357.0	329	313
D2h	Q x	741.0	671	702
	Q y	741.0	668	694
	Soret y	414.0	335	313
	Soret x	350.0	329	312

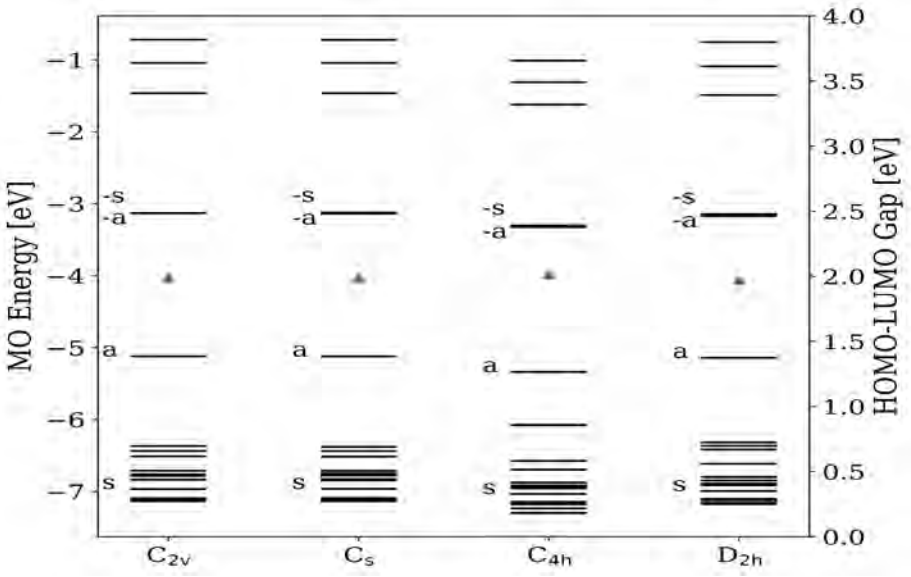

Figure 26: Molecular orbital energy levels for the 4 Michl frontier orbitals of the $\alpha SnCl_2Pcs$ regioisomers.

3.3 Fluorescence Studies

To better understand the excited state dynamics of the Pc isomers, a series of experiments were run on a TCSPC. Among the parameters sought were the Pcs' fluorescent lifetimes (τ), their isometric decay lifetime (ϕ) as well as the molecular rotational volumes (V_m). These values would be necessary for investigating the Pcs' NLO properties in Chapter 4 and provide a better understanding of the total molecular response to light in general. Also measured, though not used in the NLO calculations, are the emission and excitation spectra and their corresponding Stokes shifts. Though these parameters are not used in this study, they have been reported here for the sake of completeness.

3.3.1 Fluorescence Studies of the βH_2Pc Regioisomers

The fluorescence values of the βH_2Pc's regioisomers have been reported previously by Gouden[59], though the reported study used dichloromethane (DCM) as the solvent. The reported fluorescent values are in agreement with the ones found here, with the reported values of both τ and ϕ for the respective regioisomers being within margin of error of those reported, as can be seen in Table 11. Small changes in the ϕ are observed, and these are attributed to the differences in the viscosity difference between DCM and chloroform (0.401 mPa.s vs 0.530 mPa.s respectively)[106,107].

Table 11: TCSPC data of the βH_2Pc regioisomers in chloroform.

Isomer	Qy	Exc	Em	τ			ϕ			V_m
	nm	nm	nm	ns			ns			$10^{-27}m^3$
C4h	704	702	713	5.36	±	0.05	0.6	±	0.07	4.60
C2v	704	701	710	5.53	±	0.04	0.61	±	0.11	4.68
Cs	704	705	710	5.35	±	0.04	0.62	±	0.07	4.76
D2h	705	704	712	5.27	±	0.05	0.71	±	0.11	5.45

As the excitation and emission spectra for the values reported by Gouden were recorded in DCM, their wavelengths will not correspond directly to the ones found here in chloroform, and this is an expected result of solvent peak shifting[108]. Shown in Figure 27 are the normalised emission and excitation spectra of the C_{4h} regioisomer of the βH_2Pc plotted against its normalised ground state absorption. As can be shown, the excitation peaks correspond well to the absorption peaks, with the emission showing a slight Stokes shift that is similar to those reported by Gouden[59]. The τ is of interest to this study and was done in triplicate, though the results did not significantly vary between runs. Shown in Figure 28 and Figure 29 are the fluorescent decay and fluorescent isometric decay curves for the C_{4h} regioisomer of the βH_2Pc, and these graphs are typical of the structural isomers' other regioisomers. The values for τ shows some variation between regioisomers (5.27 ns - 5.53 ns), though it is small,

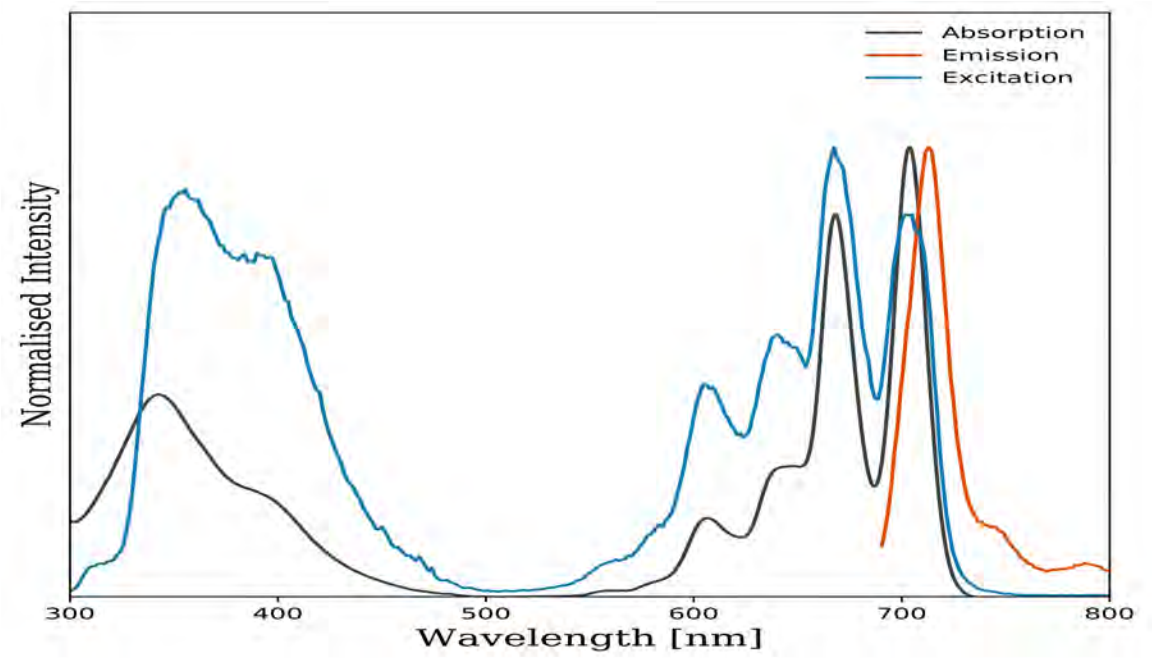

Figure 27: Fluorescence excitation and emission spectra of the βH_2Pc's C_{4h} regioisomer in chloroform.

the difference was found to be significant. The values for ϕ of the βH_2Pcs' regioisomers were found to be slightly similar to each other, though there they possessed a greater relative range than the values for τ (0.6 ns - 0.71 ns). Inspection of the structure of the four regioisomers geometry suggests that this is to be expected.

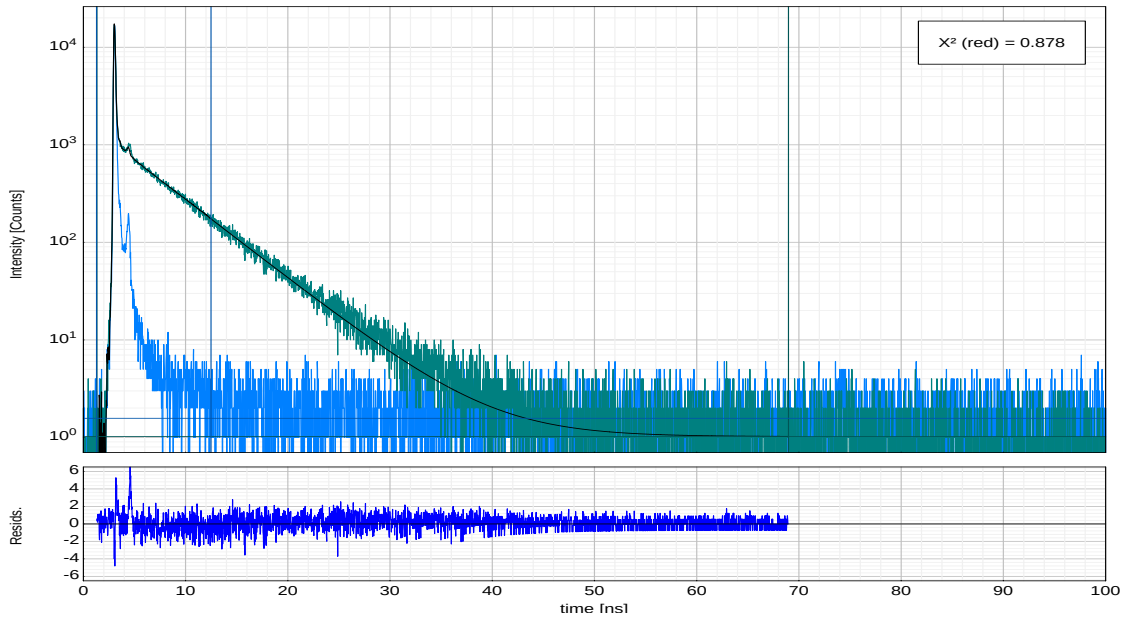

Figure 28: Fluorescence decay of the βH_2Pc's C_{4h} regioisomer.

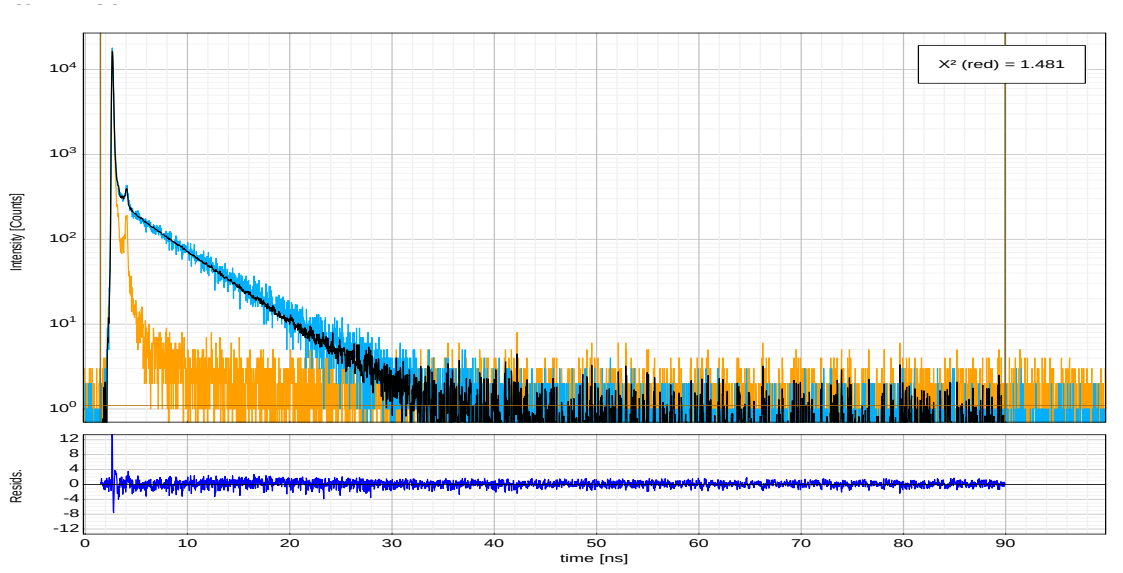

Figure 29: Fluorescence isometric decay of the βH_2Pc's C_{4h} regioisomer in chloroform.

3.3.2 Fluorescence Studies of the αH_2Pc Regioisomers

The regioisomers of the αH_2Pc exhibit behaviour that is is expected of their parent structural isomer, with longer wavelength excitation and emission peaks, as well as a shorter ϕ. The only differences between the alpha and beta structural isomers that is more difficult to predict from inspection of their respective geometries is the change in the τ values, which are found to be smaller, as shown in Table 12. These regioisomers have been reported in literature by Ngubeni[50], though the reported study was done in DCM. Despite this, the values are comparable to the ones found in this work.

Table 12: TCSPC Data of the αH_2Pc regioisomers in chloroform.

Isomer	Qy nm	Exc nm	Em nm	τ ns			ϕ ns			V_m $10^{-27}m^3$
C4h	721	719	727	5.11	±	0.02	0.43	±	0.06	3.30
C2v	723	720	734	5.12	±	0.02	0.42	±	0.09	3.22
Cs	725	728	736	5.03	±	0.03	0.43	±	0.05	3.30
D2h	728	720	731	4.92	±	0.02	0.45	±	0.08	3.45

Like the ground state absorption, the excitation and emission wavelengths are more redshifted compared to the βH_2Pc regioisomers. As shown in Figure 30, the excitation spectra has a good correspondence with the absorption spectra, though the Soret band does not seems to contribute significantly to the emission as the βH_2Pc Soret band does to its emission. The emission spectra can also be seen at slightly higher wavelengths. The vibronic bands, which were discussed in chapter 1.2.1, also contribute to the fluorescence. Differences in the emission and excitation wavelengths are observed, though they follow the absorption wavelength, shown in Table 12. The ϕ values for the αH_2Pc regioisomers vary as expected from their respective geometries, with values between 0.43 ns and 0.45 ns, these are all smaller than the βH_2Pcs' regioisomers values. The τ values shown in Table 12 are within range (4.92 ns - 5.12 ns) of a free-base Pc, and they are also similar to those reported by Ngubeni. The decay curves that were acquired for the fluorescent decay and isometric fluorescent decay of the αH_2Pc's regioisomers are very similar to those found for the βH_2Pc's regioisomers.

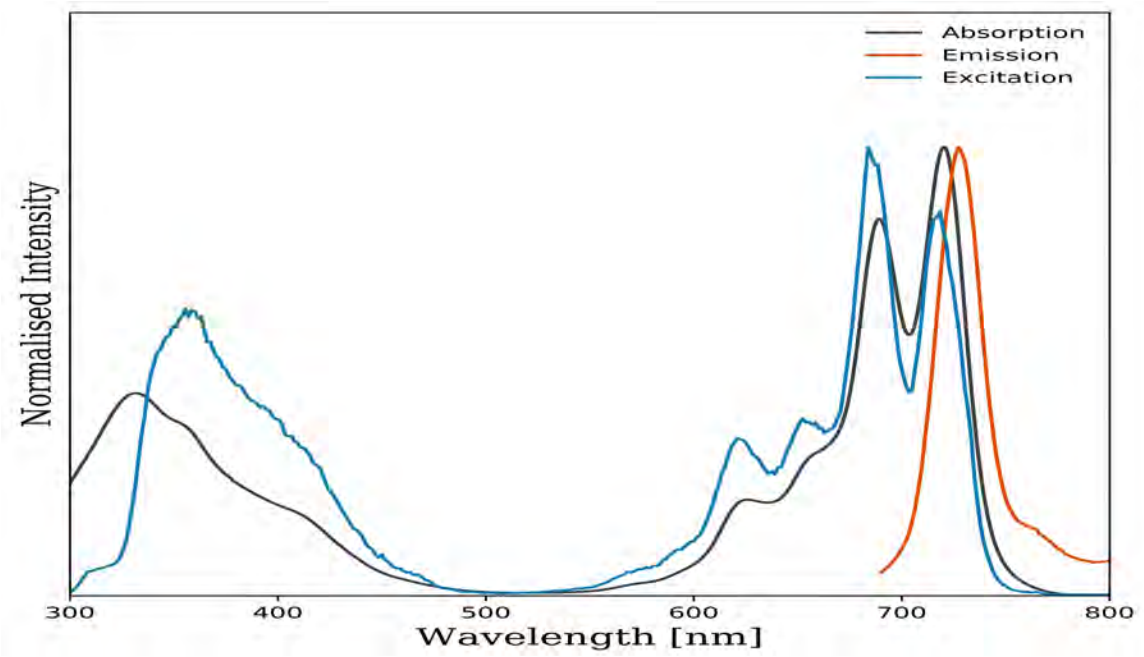

Figure 30: Fluorescenceexcitation and emission spectra of the αH_2Pc's C_{4h} regioisomer.

3.3.3 Fluorescence Studies of the $\beta SnCl_2Pc$ Regioisomers

The addition of a central metal, $SnCl_2$ in this case, has been shown to affect the fluorescent properties of Pcs[109], and this was observed for the $\beta SnCl_2Pc$ regioisomers in this work. Along with the redshfting of the absorption peak wavelengths, the excitation and emission peak wavelengths were equally shifted from those seen in βH_2Pc regioisomers. As can be seen in Table 13, all lifetimes were increased over the free-base structural regioisomers.

Table 13: TCSPC data of the $\beta SnCl_2Pc$'s regioisomers in chloroform.

Isomer	Qy nm	Exc nm	Em nm	τ ns			ϕ ns			V_m $10^{-27}m^3$
C4h	711	710	722	5.94	±	0.44	0.62	±	0.03	4.76
C2v	711	711	716	5.69	±	0.03	0.66	±	0.05	5.07
Cs	711	713	722	5.73	±	0.1	0.66	±	0.03	5.07
D2h	711	711	712	5.54	±	0.04	0.73	±	0.05	5.60

As discussed in Chapter 2.1.5, the inclusion of $SnCl_2$ into the Pc redshifts the absorption peaks strongly, as well as increasing the symmetry of the molecule and thus making many absorption transitions degenerate. These effects are also observed in the excitation and emission spectra of the $\beta SnCl_2Pc$ regioisomers, shown in Figure 31, with the Q, Soret, and vibronic bands showing the same decrease of peaks in their absorption.

The ϕ values observed were slightly increased from the values seen in the βH_2Pc regioisomers. The inclusion of the Cl axial groups do not significantly change the rotational radius of the molecule, leaving ϕ only slightly larger. The τ values were also observed to increase (ranging from 5.94 ns to 5.54 ns). Both fluorescent decay and fluorescent isometric decay curves for the other regioisomers are very similar to the decay curves shown in Figure 28 and Figure 29.

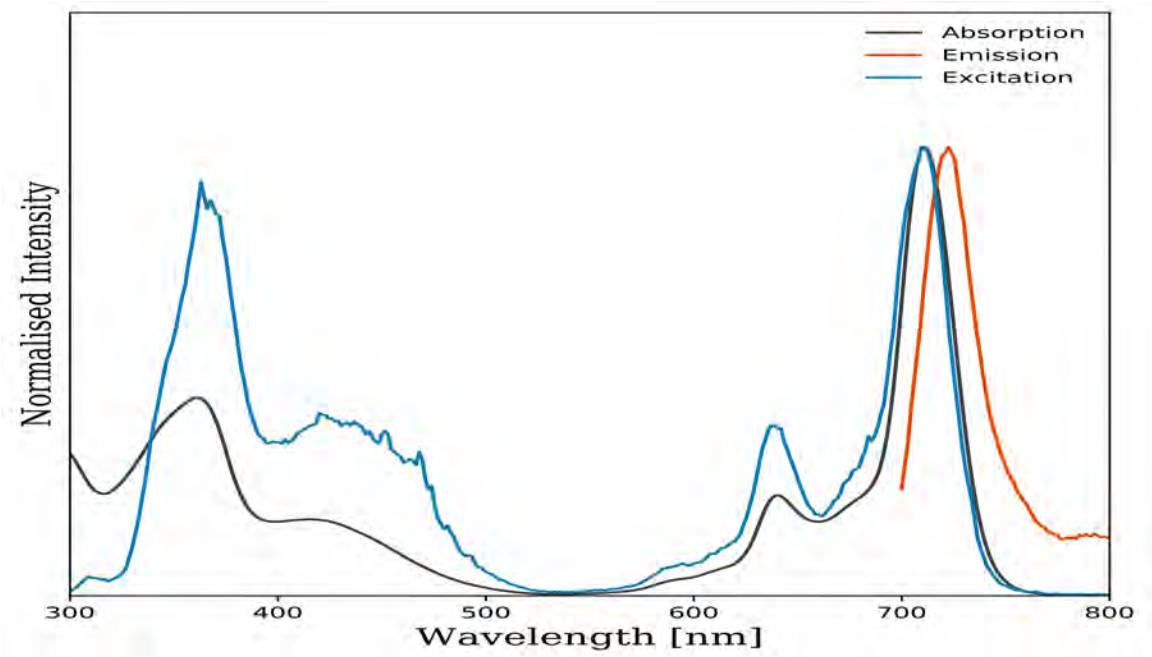

Figure 31: Fluorescence excitation and emission spectra of the $\beta SnCl_2Pc$'s C_{4h} regioisomer in chloroform.

3.3.4 Fluorescence Studies of the $\alpha SnCl_2Pc$ Regioisomers

As both a metallated Pc and alpha structural isomers, the $\alpha SnCl_2Pc$ regioisomers possess the most redshifted peaks and the smallest band gaps. Like the$\beta SnCl_2Pc$'s regioisomers, the $\alpha SnCl_2Pc$'s regioisomers have fluorescent values at higher wavelength and longer lifetimes than its unmetallated counterpart, the αH_2Pc regioisomers. Further, as seen in Table 14 the $\alpha SnCl_2Pc$ regioisomers show a similar trend in values after metallation to the $\beta SnCl_2Pc$ regioisomers. This results in the $\alpha SnCl_2Pc$ regioisomers having the longest wavelength emission peaks of all the Pc isomers in this work.

Table 14: TCSPC data of the $\alpha SnCl_2Pc$ regioisomers in chloroform.

Isomer	Qy	Exc	Em	τ			ϕ			V_m
	nm	nm	nm	ns			ns			$10^{-27}m^3$
C4h	739	734	753	5.44	$\pm$	0.03	0.449	$\pm$	0.03	3.45
C2v	741	735	755	5.46	$\pm$	1.41	0.459	$\pm$	0.05	3.52
Cs	741	741	752	5.37	$\pm$	1.32	0.477	$\pm$	0.03	3.66
D2h	741	741	753	5.71	$\pm$	0.53	0.496	$\pm$	0.06	3.81

The $\alpha SnCl_2Pc$ regioisomers also show redshifted emission and excitation peak wavelengths, as can be seen in Figure 32. Like the $\beta SnCl_2Pc$ regioisomers, the number of peaks are reduced compared to the non-metallated Pc analogue ($\alpha H2l_2Pc$), due to an increase in the structural symmetry of the central Pc ring.

Following the trend seen in the $\beta SnCl_2Pc$ regioisomers the $\alpha SnCl_2Pc$ shows values very close to the $\alpha H2_2Pc$ stereosiomers, but slightly higher. The values for ϕ were very similar to $\alpha H2_2Pcs$ due to their dependence on the geometry of the molecule. The values for τ were found to be slightly higher than those found for the $\alpha H2_2Pc$. The fluorescent decay and fluorescent isometric decay curves for the $\alpha SnCl_2Pc$'s regioisomers are very similar to those shown in Figure 28 and Figure 29.

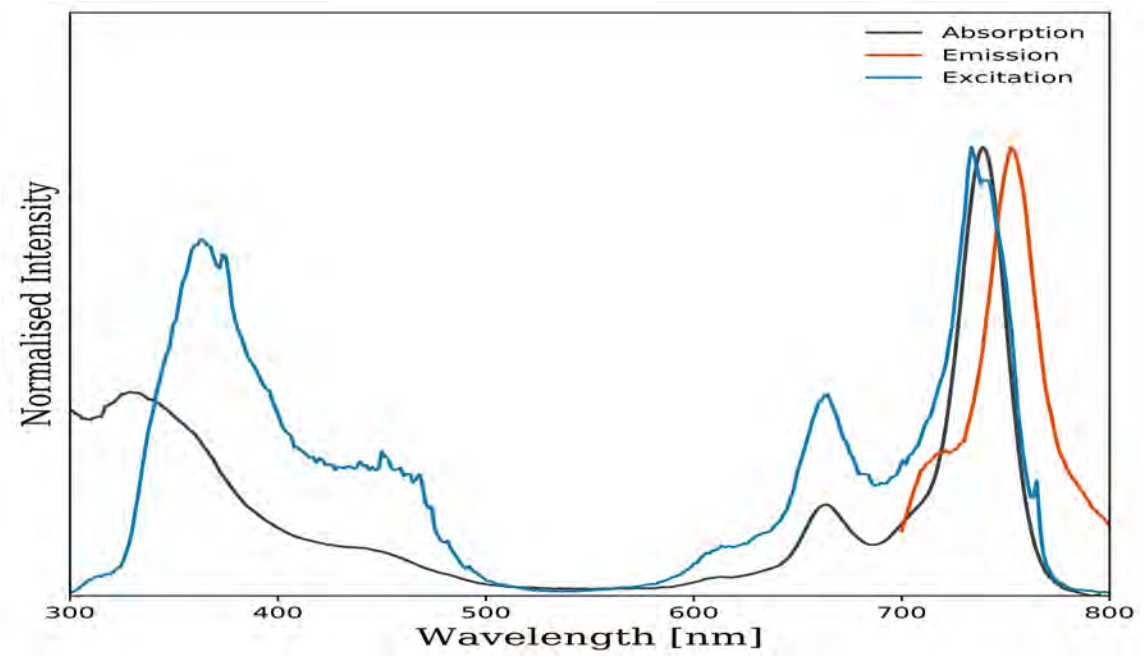

Figure 32: Fluorescence excitation and emission spectra of the $\alpha SnCl_2Pc$'s C_{4h} in chloroform.

3.4 Published Work

Part of the results discussed in this chapter have been published in a peer-reviewed journal:

- Marcel Louzada, Jonathan Britton, Tebello Nyokong, and Samson Khene.Solvent Effect on the Third-Order Nonlinear Optical Properties of α-and-β Tertbutyl Phenoxy-Substituted Tin (IV) Chloride Phthalocyanines. J. Phys.Chem. A, 121(38):7165-7175, 2017.

The computational methods developed in this work have been used in the following papers:

- Makinde, Z. O., Louzada, M., Mashazi, P., Nyokong, T., & Khene, S. (2017). Electrocatalytic behavior of surface confined pentanethio cobalt (II) binuclear phthalocyanines towards the oxidation of 4-chlorophenol. Applied Surface Science, 425, 702-712
- Mwanza, D., Louzada, M., Britton, J., Sekhosana, E., Khene, S., Nyokong, T., & Mashazi, P. (2018). The effect of the cobalt and manganese central metal ions on the nonlinear optical properties of tetra (4-propargyloxyphenoxy) phthalocyanines. New Journal of Chemistry, 42(12), 9857-9864.
- Kabwe, K. P., Louzada, M., Britton, J., Olomola, T. O., Nyokong, T., & Khene, S. (2019). Nonlinear optical properties of metal free and nickel binuclear phthalocyanines. Dyes and Pigments, 168, 347-356.
- Makinde, Z. O., Louzada, M. S., Britton, J., Nyokong, T., & Khene, S. (2019). Spectroscopic and nonlinear optical properties of alkyl thio substituted binuclear phthalocyanines. Dyes and Pigments, 162, 249-256.
- Gounden, D., Ngubeni, G. N., Louzada, M. S., Khene, S., Britton, J., & Nombona, N. (2017). Synthesis, spectroscopic and DFT characterization of 4 β-(4-tert-butylphenoxy) phthalocyanine positional isomers for non-linear optical absorption. South African Journal of Chemistry, 70, 49-59.
- Nwaji, N., Oluwole, D. O., Mack, J., Louzada, M., Khene, S., Britton, J., & Nyokong, T. (2017). Improved nonlinear optical behavior of ball type indium (III) phthalocyanine linked to glutathione capped nanoparticles. Dyes and Pigments, 140, 417-430.

4 Nonlinear Studies

4.0.1 Theoretical considerations

The calculation of the NLO parameters of each of the Pc regioisomer from all z-scan data sets were passed through both parametric and non-parametric computational models. The data sets used were derived from the average of three repeat runs that were done at each laser beam intensity. For open aperture z-scan measurements this only served to remove random detector error spikes. The closed aperture z-scan measurements were inherently noisy and the averaging was found to make the data more workable. The theoretical calculations were determined using RTTD-DFT for nonparametric results and CPHF for the parametric results. The computational scripts used for data handling can be found in the Supplementary Data, along with the scripts used to generate the CPHF and RTTD-DFT input files and the scripts used to extract results from the CPHF and RTTD-DFT output files.

4.0.2 Application of Parametric Models

Both the closed and open aperture data were fitted with Python, using the same script. The fitting was done using the Python library scipy's minimise function as both open and closed aperture models require only single variable fits (see Chapter 1.4.1 and 1.4.2). However, as both models relied on the accuracy of a single point in the data sets, a Savitzky–Golay filter[110] (window size 7) was applied. This smoothed data was only used for fitting purposes and was discarded after the fitting was complete. The raw data was used for plotting against the theoretical curve for all plots. All data shown in this chapter will be in the transformed value of q_0 as defined in Equation 15 (this transformation is visualised in Figure 33) and the parametric fits for the nonlinear absorption will be performed on the transformed data.

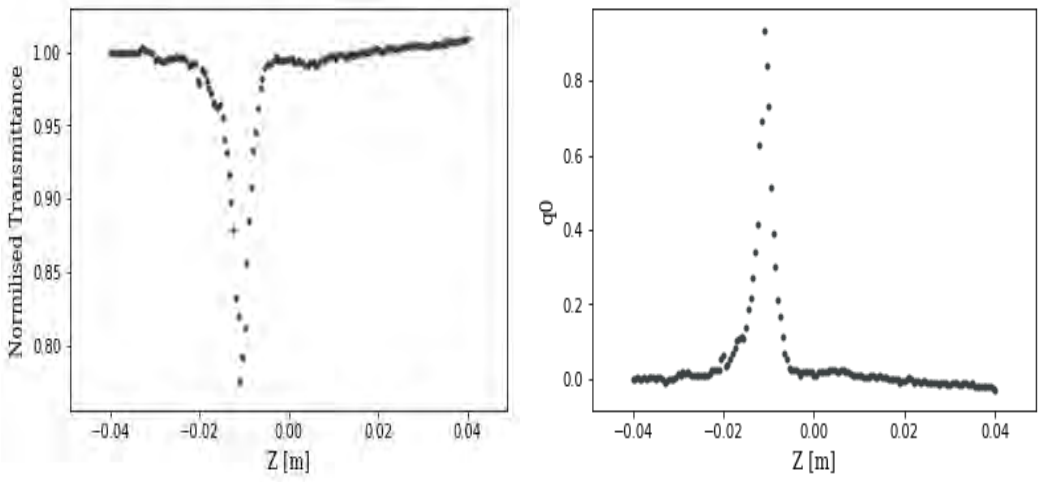

Figure 33: Raw z-scan transmittance (left) and the tranformed q0 of the same data (right).

4.0.3 Application of Non-Parametric Models

The open aperture non-parametric model used to fit the experimental data sets was written on an OpenCl kernel. The results of the model were then fitted with the LMFIT[111] package for Python, using the Differential Evolution[112] method. The methodology of this model is outlined in Scheme 6. The general approach to the calculation of the non-parametric parameters is allowing LMFIT to control the 3 compute nodes, each with their own respective GPGPU device. Information about each data point is sent to the nodes and the simulation is run in its entirety for each data point. The result of the simulation is passed to LMFIT, which then modifies the parameters and sends the calculation request back to the nodes. The simulation itself runs on a GPGPU device written as a kernel in OpenCL. The code for this can be found in Appendix B. As an additional result of the implementation develop for this work the relative contribution of each process to the nonlinear absorption are also calculated. These are normalised relative to the expected transmittance of the beam, however as the transmittance due to ground state absorption is nonzero, the scaling of the effects of SA are different to that of the nonlinear absorption processes. Figure 34 illustrates this, as the contribution from the singlet state RSA exceeds the total nonlinear absorption. The difference is due to the loss of ground state absorption, which is nonzero at all positions along the z-scan (assuming no ground state depletion). Thus, the magnitude of the SA is misleading, due to the ground state possessing linear absorption, skewing its normalisation and magnifying the apparent effect of the SA. The scaling left unmodified, to better visualise all absorption effects, and the inaccuracy is only for this visualisation. State population is also calculated, however it is only taken at the end of the simulation, due to the technical limitations of utilising GPGPU computation. This implies that the shorter lived S_1 state will be slightly under represented, and the long lived T_1 state will be over represented. Thus the population analysis should only be used as a rough guide to the state dynamics, however as the populations can differ by orders of magnitudes, they can still provide some understanding of the influence each state will have on a process. As is shown in Figure 35, the S_1 state population (blue) peaks at $\approx 10^{10}$, as this is calculated at the tail end of the pulse, the population during the pulse peak can be assumed to be $\approx 10^{11}$. Conversely, while Figure 35 shows the T_1 state population (red) peaks at $\approx 10^{8}$, due to the long lifetime of the T_1 state, its actual population during peak I would be an order of magnitude lower, around $\approx 10^{7}$.

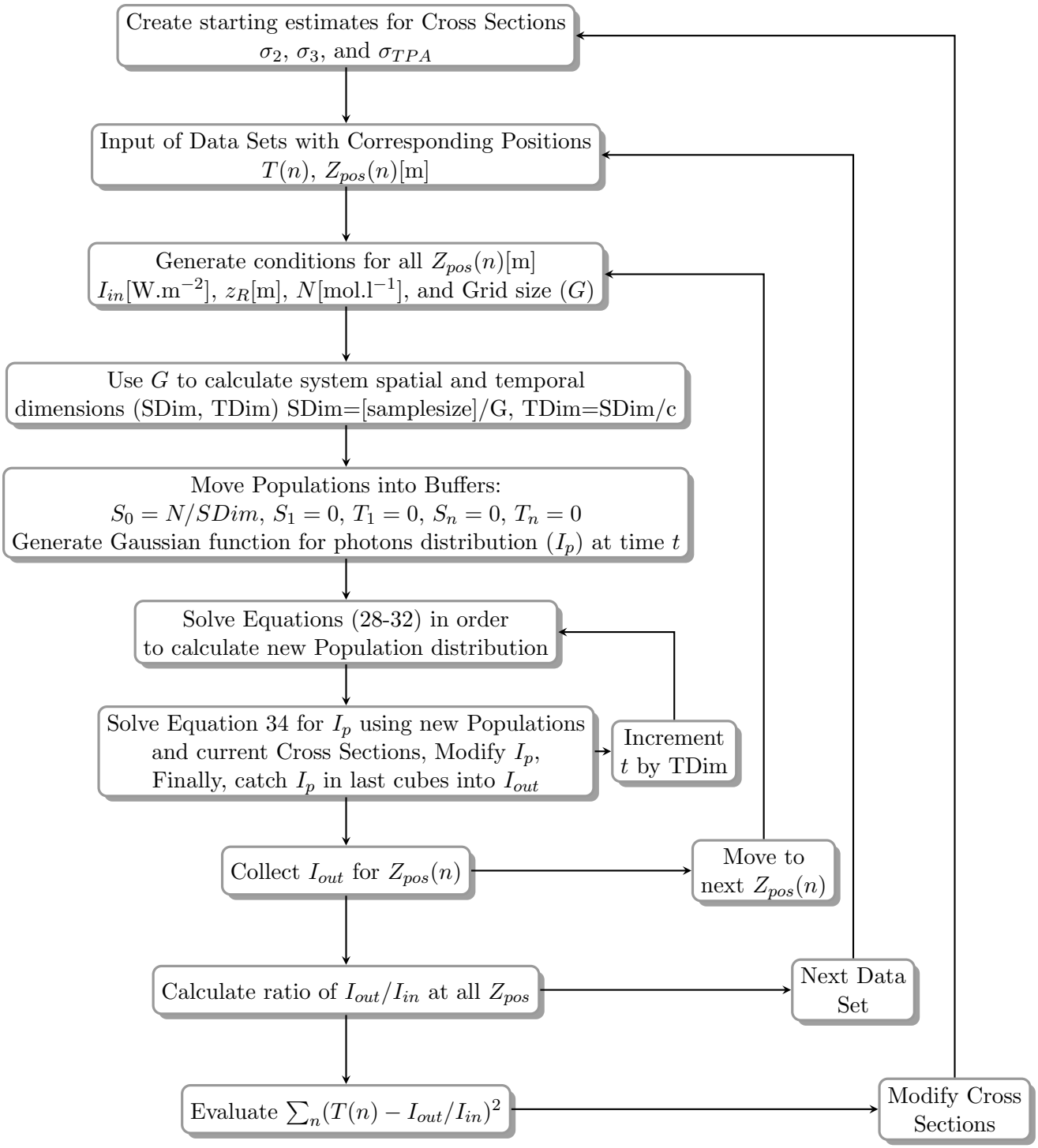

Scheme 6: Outline of the computational methodology used in the five level non-parametric model.

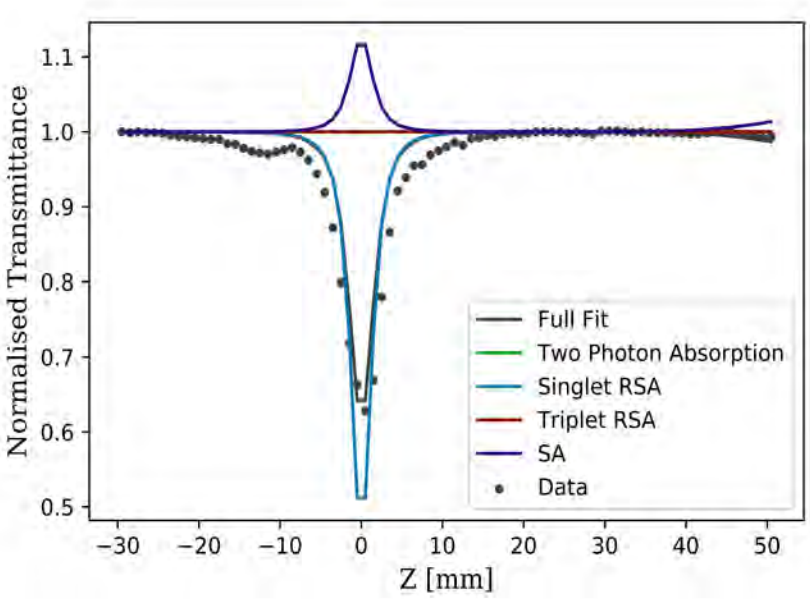

Figure 34: A typical result of the five level model fit of αH_2Pc's C_{4h} regioisomerat a focal intensity of 0.8×10^{12} W.m^{-2}.

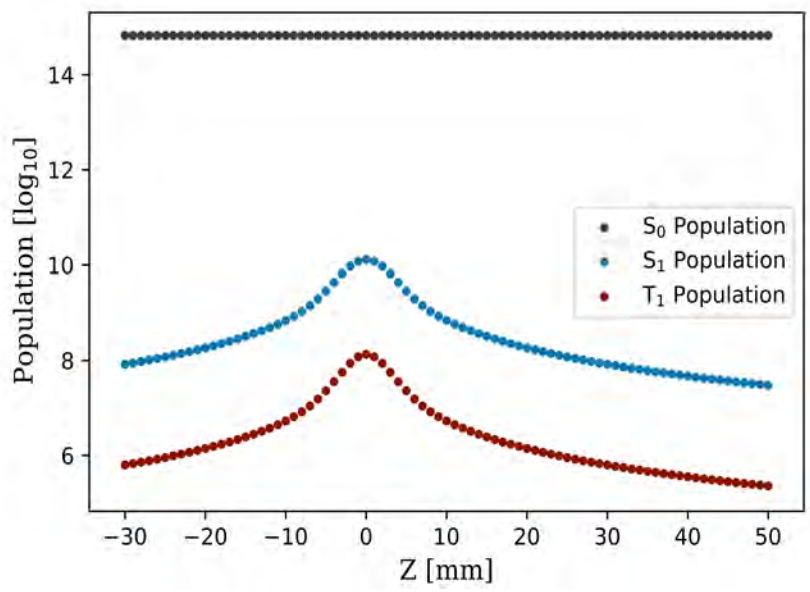

Figure 35: A typical result of the five level model populations of αH_2Pc's C_{4h} regioisomerat a focal intensity of 0.8×10^{12} W.m^{-2}.

4.0.4 Theoretical Calculation of Nonlinear Properties

CPHF calculations were used in order to determine theoretical values for the second-order hyperpolarisability(defined in Chapter 1.3.2 as γ) of each isomer. The calculations where done using Gassian09 and the results were extracted using a custom Python script. The excited state absorption was calculated using the RTTD-DFT method on NWChem6.8. The ground state absorption was also performed in the same manner for comparison. The results were extracted using a Python library, numpy's fft (a discrete Fourier transform) function. This was done once for two different light polarisations (x, y only as the z polarisation was not done for the excited states in order to reduce computational costs) for each state. The response to each polarisation was combined to give the total response.

4.1 αH_2Pcs regioisomers's Nonlinear Optical Properties

The NLO response of the αH_2Pc's regioisomers where measured with z-scan with multiple beam pulse energies. First the open aperture z-scan was run, and this showed a strong nonlinear attenuating response, with a positive nonlinear absorption coefficient (defined in Chapter 1.3.1 as β), for all the regioisomers, and this β remained positive as the beam's pulse energy was increased, as shown in Figure 36. Figure 36

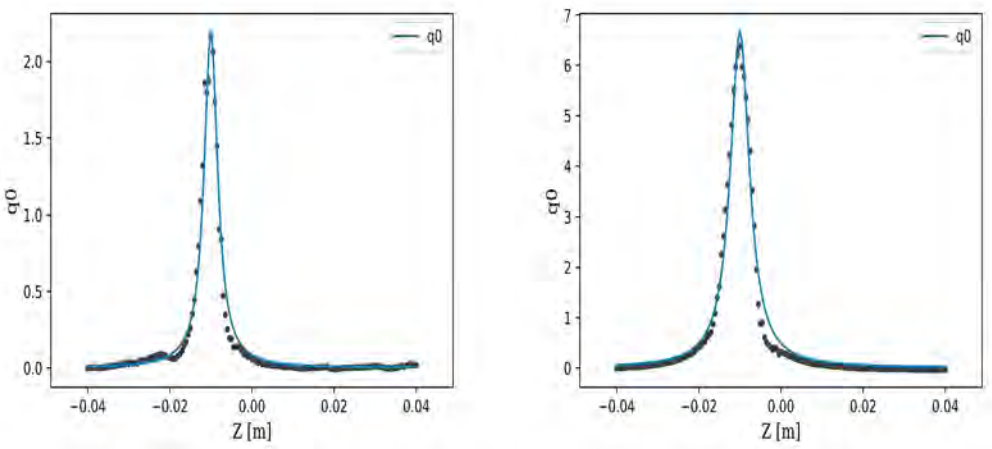

Figure 36: The values of q0 for αH_2Pc C_{4h} regioisomer at a focal intensity of 0.8×10^{12} W.m^{-2} (left), and 4.6×10^{12} W.m^{-2} (right).

illustrates Tsigaridas's method of fitting the parametric model, and theoretical fit has little deviation from the experiential z-scan data. Four open aperture z-scan measurements were repeated at increasing pulse energy levels ($\approx$8 μJ to $\approx$40 μJ), and the calculated values of the β and the $Im[\gamma]$ are shown in Figure 37. The nonlinear attenuation for the αH_2Pc's regioisomers were found to be a first order nonlinearity ($\frac{dI}{dz} \propto I$), this is seen in the lack of a significant relationship between β and the intensity. As β (and therefore $Im[\gamma]$) do not scale with I the average response of each regioisomer can be obtained, in order to rank their effectiveness for $Im[\gamma]$ induced NLO behaviour. The αH_2Pc regioisomer with the highest $Im[\gamma]$ is found to be the C_{4h} isomer, with the C_s and D_{2h} isomers having the lowest values of $Im[\gamma]$ as shown in Table 15. The ground state absorption of the αH_2Pc's regioisomers at 532 nm are low, as shown in Table 16, thus the results shown in Table 15 indicate that any of the regioisomers have possible use cases as optical limiters for light at 532 nm[75]. The regioisomers having small ground state cross sections has implications for any excited state absorption, as the probability of the excited state possessing a larger absorption cross section is high. As a semiconductor, the isomers have a large energy band gap between the occupied and unoccupied orbitals. However, once in the excited state (S_n or T_n) the total available states within a 2.33 eV transition become much larger, allowing more pathways for photon absorption. In order to determine

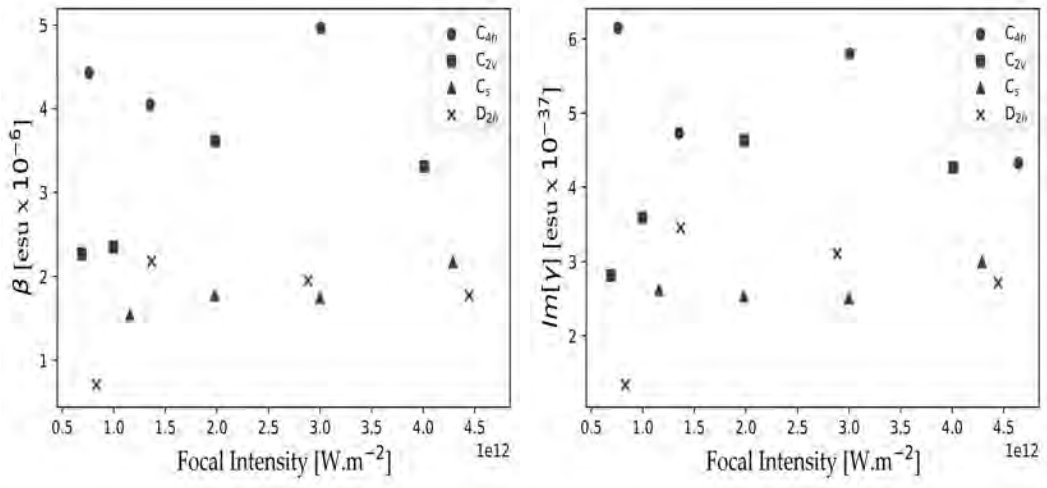

Figure 37: Calculated values of β(left), and $Im[\gamma]$(right) for the αH_2Pc's regioisomers.

the αH_2Pc's response to light in its triplet and singlet excited states, RTTD-DFT calculations were performed, and the results for the C_{4h} regioisomer are shown in Figure 38. The S_1 state has a strong resemblance to the ground state absorption, however the S_1 state has some responses in the 400-550 nm region. The combined effect of these responses will give rise to the excited state absorption for 2.33 eV light, however with the current level of theory it is not possible to determine the excitation pathways to which these resonances correspond. As such, the singlet RSA is simply referred to as $S_1 \rightarrow S_n$ transition as the exact state that S_n corresponds to has not been determined. The triplet response seen in Figure 38 shows a response analogous to the ground state response, only at lower wavelengths. The distinctive and strong response around 500 nm is typical for Pcs (often used in applications such as photo dynamic therapy[86]), and this response is analogues to the grounds state's HOMO-LUMO transition, $S_0 \rightarrow S_1$, that gives rise to the Q-band. In order to determine the relative populations of each state that contributes to the nonlinear absorption a five level fitting of the open aperture z-scan were performed. This was done as a simultaneous fit of the measurements of all four pulse energies, and resulted in the calculation of the cross sections σ_2, σ_3, and σ_{tpa} as well as the populations of

Table 15: Averaged values of the measured $Im[\gamma]$ for the αH_2Pc regioisomers.

regioisomer	$Im[\gamma]$ esu
C_{4h}	5.25E-37
C_{2v}	3.82E-37
C_s	2.67E-37
D_{2h}	2.65E-37

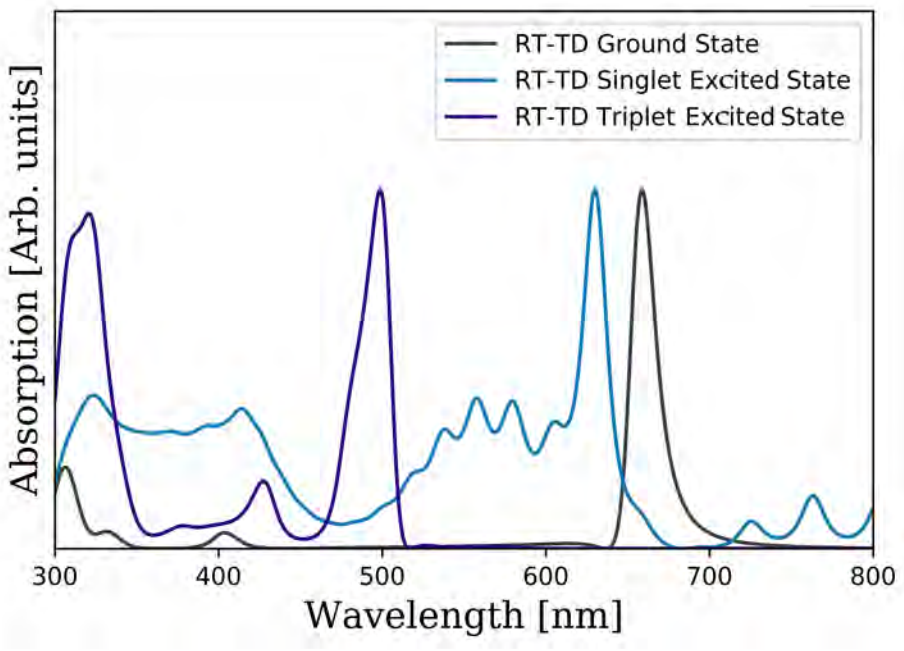

Figure 38: RTTD-DFT dipole response of the C_{4h} regioisomer of αH_2Pc in the UV/Vis region.

each state along the z-scan measurement. The result of one such fit, with a focal I of $0.8{\times}10^{12}$ W.m^{-2}, is shown in Figure 39, and this demonstrates that the RSA from the S_1 state to be the dominant factor in the particular regioisomers' nonlinear absorption. Figure 39 also shows the absorption due to the ground state decreases slightly towards the focus exhibiting some SA, while the singlet RSA increase to a greater degree. The total nonlinear response is due to the combination of these two processes, with the contributions from the triplet RSA being very low due to the T_1 states low population. This is due, in part, to the αH_2Pc structural isomers lack of a heavy atom, lowering the ISC rate and making it improbable that the T_1 state will become significantly populated. However, the contribution from the TPA to the nonlinear absorption is unexpectedly small. Though the TPA was not expected to be the dominant factor in the nonlinear absorption, the TPA contribution is negligibly small, with its only contribution in providing an excitation pathway to populate the S_1 state. The calculated cross sections are reported in Table 16, and the ratio of $\sigma_{\text{eff}}/\sigma_1$ can be reduced down to σ_2/σ_1 as the population of the T_1 state is three orders of magnitude lower than the population of the S_1 state, shown in Figure 40. Ranking the values of $\sigma_{\text{eff}}/\sigma_1$, it can be seen that there is a direct correspondence between the rankings of the regioisomers' $Im[\gamma]$. The variation of σ_1 seen in the regioisomers is likely to be due to a $S_1 \rightarrow S_{\text{n}}$ transition in the vicinity of 2.33 eV. With each regioisomer, the transition could be being closer to, or further away from resonances, depending on the exact energy of the transition. The values of the σ_3

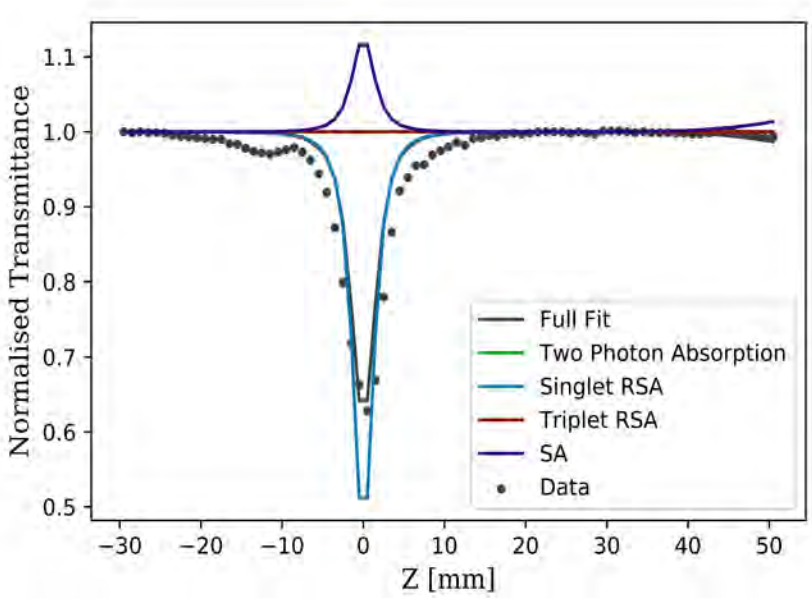

Figure 39: The five level model fit of αH_2Pc's C_{4h} regioisomer at a focal intensity of 0.8×10^{12} W.m^{-2}.

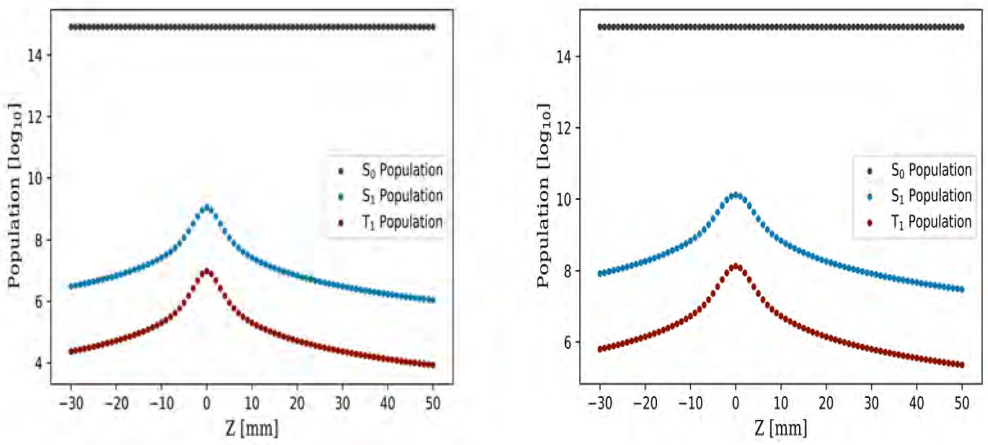

Figure 40: The five level model populations of αH_2Pc's C_{4h} regioisomer at a focal intensity of 0.8×10^{12} W.m^{-2} (left), and 4.6×10^{12} W.m^{-2} (right).

and σ_{tpa} have no direct relation to the calculated $Im[\gamma]$ and this is likely due to their low contribution to the total nonlinear absorption. In the case of the σ_2 having a low value, the fit minimised the value of the calculated cross section, in order to minimise error[111]. A final note on the cross sections is that σ_1 was found to have the largest values for the regioisomers with high $Im[\gamma]$ and this is a large contributor in the

effective nonlinear absorption, as a large $\sigma_1$will reduce the measured values of $Im[\gamma]$ and $\sigma_{\text{eff}}/\sigma_1$.

Table 16: Calculated cross sections from the fivel level model for the αH_2Pc regioisomers.

regioisomer	σ_{tpa} GM	σ_2 cm^2	σ_3 cm^2	σ_1 cm^2	$\sigma_{\text{eff}}/\sigma_1$
C_{4h}	111.22	2.03E-17	1.64E-18	3.63E-18	5.58
C_{2v}	181.31	2.02E-17	1.28E-20	2.77E-18	7.29
C_s	155.58	1.09E-17	6.11E-19	4.26E-18	2.55
D_{2h}	123.15	1.72E-17	9.73E-19	6.04E-18	2.84

To complement the results of the open aperture z-scan, four corresponding closed aperture z-scans were performed at the same beam pulse energy levels. The data acquired from the open aperture z-scan were subtracted from the closed aperture data and the results were fitted using the parametric nonlinear refraction model. Unlike the open aperture results, the close aperture results showed some deviation at higher beam energies. Shown in Figure 41 are the refractive responses at a low focal $I(0.8\times10^{12}$ W.m$^{-2})$ and a higher focal $I(4.6\times10^{12}$ W.m$^{-2})$. While the lower I show a well-behaved refractive response with a strong negative value for n_2, and thus $Re[\gamma]$, the higher I shows the presence of a competing refractive element, with a positive $Re[\gamma]$, not present in the measurements at low I. The competing refractive element

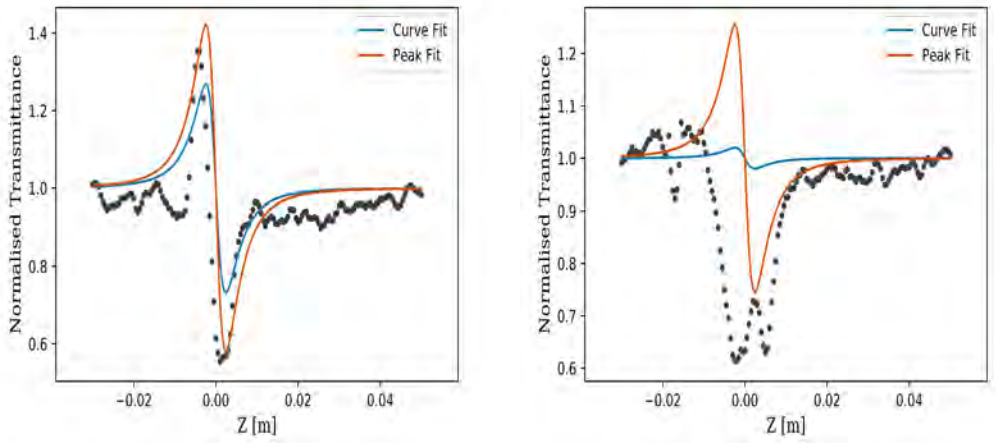

Figure 41: Closed aperture results for αH_2Pc C_{4h} regioisomerat a focal intensity of 0.8×10^{12} W.m^{-2} (left), and 4.6×10^{12} W.m^{-2} (right).

in Figure 41 is unlikely to be due to the ground state refraction, as CPHF determined the sign of the ground state refractive index to be negative, in line with the low I

result. The CPHF results are shown in Table 17, but due to limitation on the CPHF method, only the ground state was be calculated. This leaves the positive refractive contribution to be due to either excited state refraction or thermal lensing. Thermal

Table 17: Theoretical values for γ, calculated with CPHF, for the αH_2Pc regioisomers.

regioisomer	γ esu ($\times 10^{-36}$)
C_{4h}	-1.41E+03
C_{2v}	-1.39E+03
C_s	-1.37E+03
D_{2h}	-1.36E+03

lensing however, can be discounted for two reasons: the first is that the thermal lensing effect in chloroform would produce a negative refractive change, and the second being its response time is far longer than the laser pulse used in this study (10^{-3} s vs (10^{-8} s)[14]. This leaves the excite state refraction as the most likely contributor to the positive nonlinear refraction. The populations, shown in Figure 40, only differ by one order of magnitude between the high I and the low I. This is sufficient to account for the contribution however, as the observed refraction seen in Figure 41 has roughly equal contribution from the positive and negative nonlinear refractive components. This progression of the nonlinear refractive index to one consisting of almost equivalent positive and negative components can be seen in Figure 42 as the $Re[\gamma]$ decreases with an increase in I.

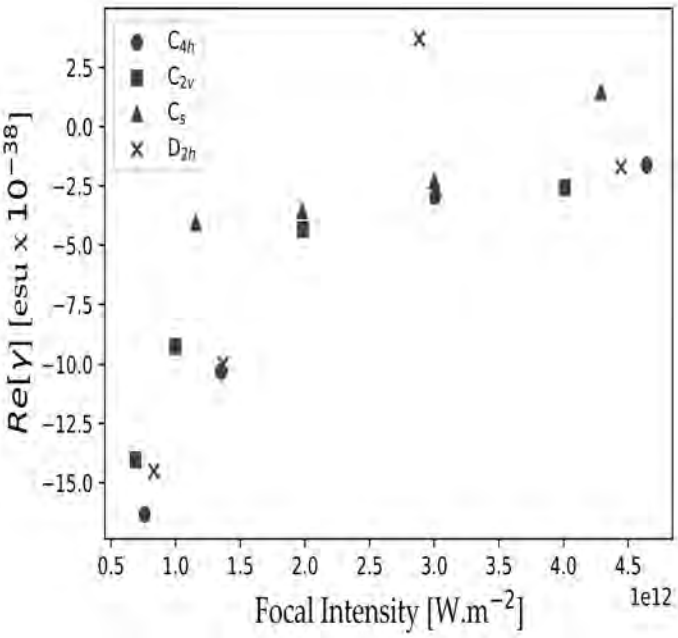

Figure 42: $Re[\gamma]$ for the regioisomers of αH_2Pc plotted against focal intensity.

Unlike the imaginary components of γ, the real components differ at each I and an average of the values would not yield usable information. The calculated values for β, the susceptibilities, and the hyperpolarizability can be found in Table 19 along with the total effective Δn as well as $W = \Delta n/\sigma_1$. To account for the additional contributions, the data from the five level non-parametric fit was done to determine the effective refractive cross sections (σ_{r1}, σ_{r2}, σ_{r3}, and σ_{rker}) shown in Table 18. Similar to the absorption results, the triplet contribution is found to be minimal

Table 18: Calculated values of the refractive cross section for the αH_2Pc regioisomers.

regioisomer	σ_{r1} cm^2	σ_{r2} cm^2	σ_{r3} cm^2
C_{4h}	-4.43E-19	7.23E-17	*N.A.*
C_{2v}	-3.93E-19	6.95E-17	*N.A.*
C_s	-3.73E-19	7.11E-17	*N.A.*
D_{2h}	-4.21E-19	6.83E-17	*N.A.*

due to the low population of the T_1 state and the values for σ_{r3} thus can swing to improbably large values without affecting the calculated refraction. Similarly, the contribution due to σ_{rker} was found to be insignificant and was not reported. The values of σ_{r1} are small as expected for a non-resonant refraction cross section, but the values of σ_{r2} are quite large, more than three order of magnitude larger. This is congruent with reported behaviour[14], as the S_1 has a transition peak around 532 nm, making the refraction at this wavelength a resonant refraction. Even though the σ_{r2} was calculated to be very large, the population of T_1 is so low that no effect is observed from them, thus the values of σ_{r2} were not reported for the αH_2Pc regioisomers.

Table 19: Parametric model results of the αH_2Pc regioisomers.

regioisomer	I W.m^{-2}	z_R m	β m.W^{-1}	$Im[\chi^{(3)}]$ esu	$Im[\gamma]$ esu	n_2 m^2.W^{-1}	$Re[\chi^{(3)}]$ esu	$Re[\gamma]$ esu	Δn	W
C_{4h}	1.35E+12	3.12E-03	4.05E-06	9.63E-11	4.73E-37	-3.74E-13	-2.10E-11	-1.03E-37	-8.42E-02	-3.7E-01
	3.01E+12	2.44E-03	4.96E-06	1.18E-10	5.80E-37	-1.07E-13	-6.02E-12	-2.96E-38	-5.37E-02	-2.4E-01
	4.64E+12	2.23E-03	3.84E-06	9.13E-11	4.32E-37	-6.08E-14	-3.42E-12	-1.62E-38	-4.70E-02	-2.0E-01
	7.60E+11	3.79E-03	4.43E-06	1.05E-10	6.15E-37	-4.98E-13	-2.80E-11	-1.63E-37	-6.32E-02	-3.3E-01
C_{2v}	1.98E+12	2.63E-03	3.61E-06	8.60E-11	4.63E-37	-1.44E-13	-8.07E-12	-4.35E-38	-4.75E-02	-3.2E-01
	4.01E+12	2.51E-03	3.31E-06	7.88E-11	4.26E-37	-8.45E-14	-4.75E-12	-2.57E-38	-5.65E-02	-3.8E-01
	6.90E+11	2.32E-03	2.27E-06	5.39E-11	2.81E-37	-4.79E-13	-2.69E-11	-1.40E-37	-5.50E-02	-3.6E-01
	9.98E+11	3.28E-03	2.35E-06	5.59E-11	3.59E-37	-2.57E-13	-1.44E-11	-9.26E-38	-4.27E-02	-3.4E-01
C_s	1.98E+12	3.07E-03	1.78E-06	4.23E-11	2.53E-37	-1.06E-13	-5.94E-12	-3.55E-38	-3.48E-02	-2.5E-01
	3.00E+12	2.44E-03	1.75E-06	4.17E-11	2.51E-37	-6.81E-14	-3.83E-12	-2.30E-38	-3.40E-02	-2.5E-01
	4.29E+12	2.08E-03	2.18E-06	5.18E-11	3.00E-37	4.51E-14	2.53E-12	1.47E-38	3.22E-02	2.3E-01
	1.16E+12	3.01E-03	1.54E-06	3.68E-11	2.62E-37	-1.01E-13	-5.70E-12	-4.06E-38	-1.95E-02	-1.7E-01
D_{2h}	1.37E+12	5.71E-03	2.18E-06	5.19E-11	3.45E-37	-2.67E-13	-1.50E-11	-9.99E-38	-6.08E-02	-5.2E-01
	2.88E+12	2.81E-03	1.95E-06	4.65E-11	3.11E-37	9.86E-14	5.54E-12	3.70E-38	4.73E-02	3.6E-01
	4.44E+12	3.53E-03	1.77E-06	4.22E-11	2.71E-37	-4.72E-14	-2.65E-12	-1.71E-38	-3.50E-02	-2.9E-01
	8.32E+11	3.62E-03	7.08E-07	1.69E-11	1.34E-37	-3.26E-13	-1.83E-11	-1.45E-37	-4.52E-02	-3.6E-01

4.2 βH_2Pcs regioisomer's Nonlinear Optical Properties

The NLO response of the βH_2Pc's regioisomer were measured with z-scan for multiple beam powers. As was done for the αH_2Pc regioisomer, first open aperture and then closed aperture measurements were performed at all four beam powers. Similar to the αH_2Pc regioisomer, positive β were observed at all beam powers, fitted with Tsigaridas's method and shown in Figure 43. This demonstrated the efficacy of Tsi-

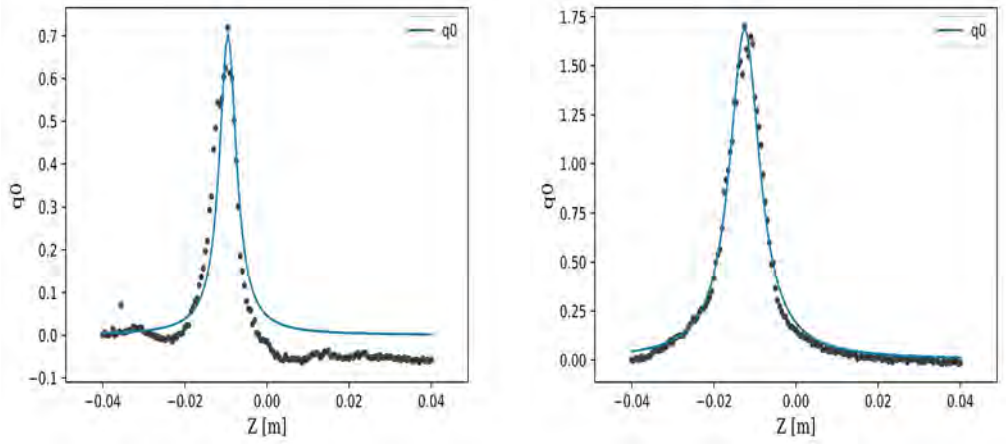

Figure 43: q0 for βH_2Pc C_{4h} constitutional isomer at a focal intensity of 1.2×10^{12} W.m^{-2} (left), and 5.6×10^{12} W.m^{-2}(right).

garidas's method for fitting the parametric model and describes the observed open aperture z-scan data at all beam powers. Similar to the results calculated for αH_2Pc, the values of β and $Im[\gamma]$ were found to not vary as the value of I was increased. However, the βH_2Pc's regioisomer did exhibit reduced nonlinear absorption, as shown in Figure 44, of both β and $Im[\gamma]$ than the αH_2Pc's regioisomer. As was seen in the αH_2Pc regioisomer, the lack of scaling with I allows an average of all measured values of $Im[\gamma]$ for each constitutional isomer, shown in Table 20. For βH_2Pc the constitutional isomer with the highest $Im[\gamma]$ (ignoring the D_{2h} outlier found at 3.5×10^{-37} esu) was found to be the D_{2h} constitutional isomer, followed by C_s and C_{2v} and finally C_{4h} with the lowest average value of $Im[\gamma]$. This is almost the inverse of the trend found in the αH_2Pc regioisomer and further investigation is required to explain this behaviour. The ground state absorption of the βH_2Pc's regioisomer, shown in Table 21, are smaller than those for the corresponding cross sections for αH_2Pcs regioisomer. This goes against the observation that the αH_2Pcs regioisomer are more effective at nonlinear absorption, as a lower ground state absorption should increase the observed nonlinearity. To better understand the dynamics of nonlinear absorption, RTTD-DFT calculations were performed and results were examined, shown in Figure 45. Unfortunately the RTTD-DFT results were very similar to those of the αH_2Pcs regioisomer, and were not accurate enough to discreet descriptions of the

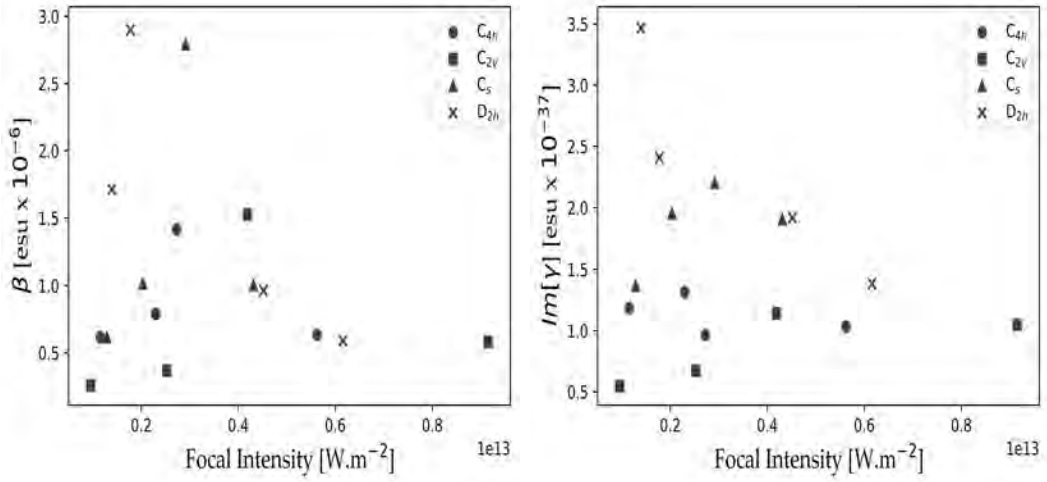

Figure 44: Calculated values of β(left), and $Im[\gamma]$(right) for the βH_2Pc's regioisomer.

exact energy of excited state transitions. However, the RTTD-DFT does still predict excited state transitions for both $S_1 \rightarrow S_n$ and $T_1 \rightarrow T_n$, that are not present in the ground state RTTD-DFT calculations. As found in the αH_2Pc, the states involved in the excited state absorption are not easily discernible from the RTTD-DFT. However, the triplet response shows strong peaks that are analogues to the grounds states' response. The singlet response is much lower, though there are 3 small peaks in the 520 —- 550 nm range that could comprise the $S_1 \rightarrow S_n$ transition. A simultaneous fit of the five level model was performed on the open aperture z-scan, resulting in the calculation of the βH_2Pc regioisomer' cross sections: σ_2, σ_3, and σ_{tpa}, as well as the populations of each state along the z-scan measurement. The result of the C_{4h} constitutional isomer, with a focal intensity of 1.2×10^{12} W.m^{-2}, is shown in Figure 46. As was found in all the αH_2Pc regioisomer, the nonlinear absorption is dominated by RSA due to absorption of the S_1 state, shown by Figure 46. The triplet absorption contribution was also shown to be negligible, this is believed to be due to the βH_2Pc possessing no heavy atom, leaving the T_1 state to be relatively under populated when compared to the S_1 state. The absorption contribution from the TPA to the nonlinear absorption was as negligible as the triplet absorption, however, as the TPA process

Table 20: Averaged values of the measured $Im[\gamma]$ for the βH_2Pc regioisomer.

Constitutional isomer	$Im[\gamma]$ esu
C_{4h}	1.12E-37
C_{2v}	8.52E-38
C_s	1.86E-37
D_{2h}	2.30E-37

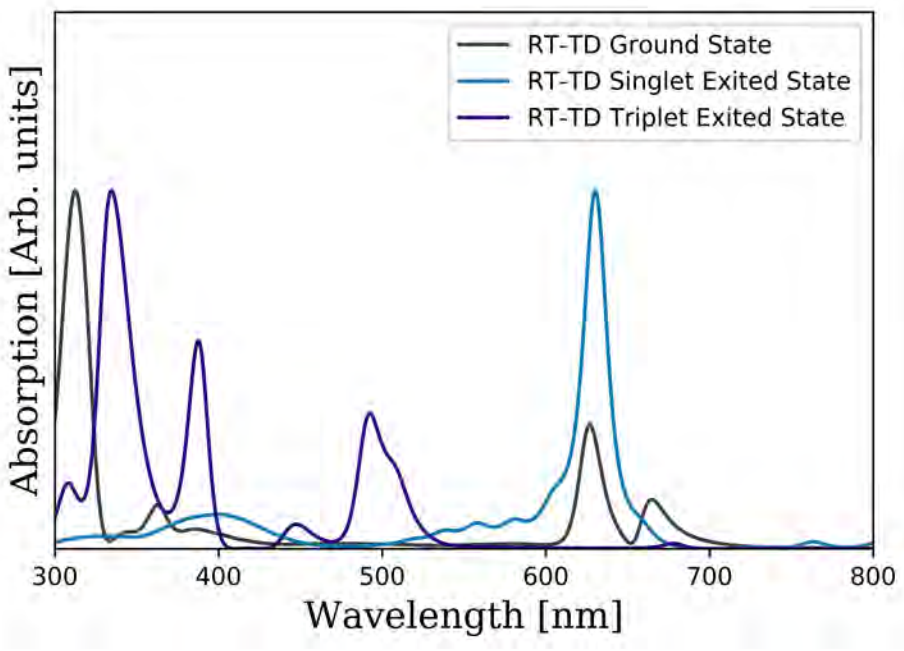

Figure 45: RTTD-DFT dipole response of the C_{4h} constitutional isomer of βH_2Pc in the UV/Vis region.

can populate the S_1 state, the fitting did not find the σ_{tpa} to be inconsequential.

As was found in the αH_2Pc regioisomer, due to the dominance of the $S_1 \rightarrow S_n$ absorption in the nonlinear absorption, the effective excited state absorption is simply σ_2. The population results of the αH_2Pc regioisomer also found that the S_1 state population represents a similar portion of the total state population, T_1 state again yielding a population three orders of magnitude lower, shown in Figure 47. The values of $\sigma_{\text{eff}}/\sigma_1$, shown in Table 21, follow the trend seen in the regioisomer' $Im[\gamma]$, and similarly do not correspond to the trend seen in the αH_2Pc regioisomer. With the αH_2Pc regioisomer the variation in the σ_1 calculated were attributed to slight shifts in the transition energies with the states associated with the singlet RSA. It is likely that the blue shift associated with the ground state also translated into the excited state spectra, and the $S_1 \rightarrow S_n$ transition for the βH_2Pc regioisomer is not close to 2.33 eV, reducing their effective area. Table 21 also shows the calculated values for σ_3 and σ_{tpa}, however, as the former was found to have a small degree of influence on the nonlinear absorption at the current population of T_1, its value was minimised to reduce apparent error. The TPA was found to be significant to the nonlinear absorption even though it did not absorb a significant part of the light. The primary role the TPA in the nonlinear behaviour is believed to be as a pathway to populating the S_1 state.

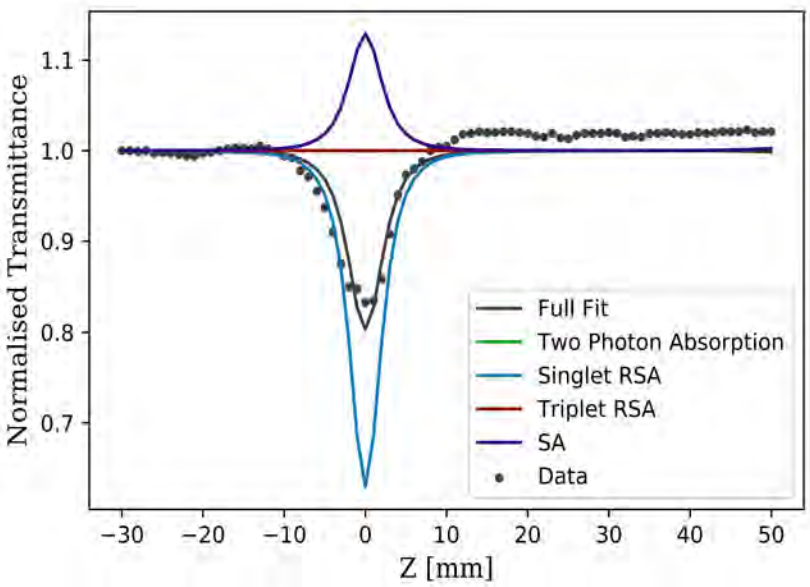

Figure 46: The five level model fit of βH_2Pc's C_{4h} constitutional isomer at a focal intensity of 1.2×10^{12} W.m^{-2}.

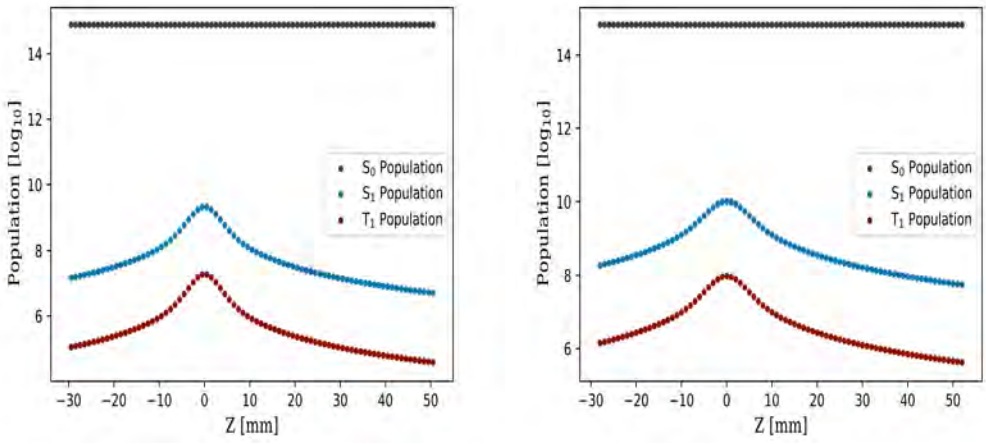

Figure 47: The five level model populations of βH_2Pc's C_{4h} constitutional isomer at a focal intensity of 1.2×10^{12} W.m^{-2} (left), and 5.6×10^{12} W.m^{-2} (right).

Table 21: Calculated cross sections from the fivel level model for the βH_2Pc regioisomer.

Constitutional isomer	σ_{tpa} GM	σ_2 cm^2	σ_3 cm^2	σ_1 cm^2	$\sigma_{\text{eff}}/\sigma_1$
C_{4h}	110.06	2.18E-17	2.06E-19	2.95E-18	7.39
C_{2v}	55.01	1.72E-17	5.18E-24	2.97E-18	5.78
C_s	105.46	1.64E-17	6.31E-23	2.72E-18	6.04
D_{2h}	111.24	1.97E-17	4.68E-19	2.39E-18	8.25

Closed aperture z-scans were performed on the βH_2Pc regioisomer at the same beam pulse energy levels that the open aperture z-scan were run. The βH_2Pc regioisomer also showed the same deviation at higher beam powers that was seen in the αH_2Pc regioisomer. This deviation can be shown with the two most extreme beam intensities in Figure 48. The theoretical values of γ were calculated with CPHF and shown in

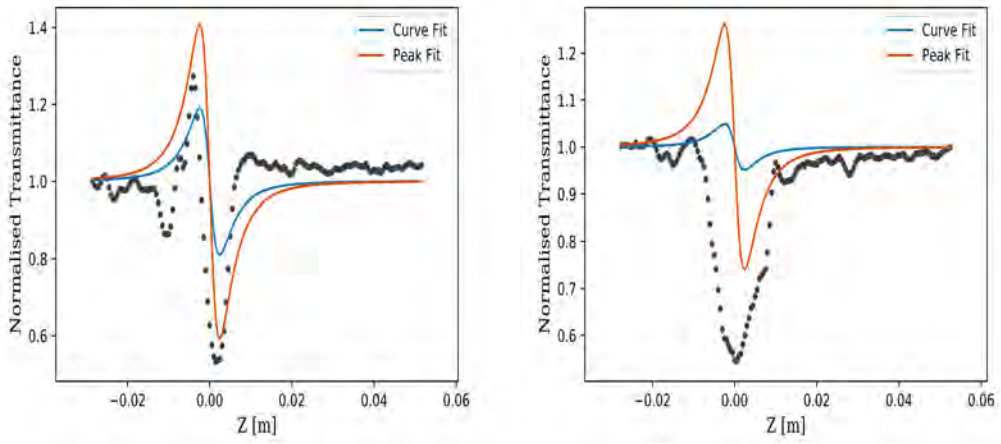

Figure 48: Closed aperture results for βH_2Pc C_{4h} constitutional isomer at a focal intensity of 1.2×10^{12} W.m^{-2} (left), and 5.6×10^{12} W.m^{-2} (right).

Table 22. The theoretical values of γ suggest that the sign of the ground state $Re[\gamma]$ of the βH_2Pc regioisomer should be negative, and this matches the closed aperture results. The calculated values for $Re[\gamma]$ are recorded in Table 24, but the

Table 22: Theoretical values for γ, calculated with CPHF, for the βH_2Pc regioisomer.

Constitutional isomer	γ esu ($\times10^{-36}$)
C_{4h}	-1.45E+03
C_{2v}	-1.52E+03
C_s	-1.49E+03
D_{2h}	-1.11E+03

behaviour of $Re[\gamma]$ is best illustrated in Figure 49 which demonstrates the gradual shift from a mostly negative $Re[\gamma]$ to a $Re[\gamma]$ that has almost equal positive and negative components. The trend seen in Figure 49 for the βH_2Pc regioisomer is very similar to the αH_2Pc regioisomer' trend seen in Figure 42. As seen in Figure 49 calculating the average values for $Re[\gamma]$ would have no significance, with the only conclusion that can be taken from the values of $Re[\gamma]$ is that the values for the βH_2Pc regioisomer are lower than those for the αH_2Pc regioisomer. In order to calculate each regioisomer

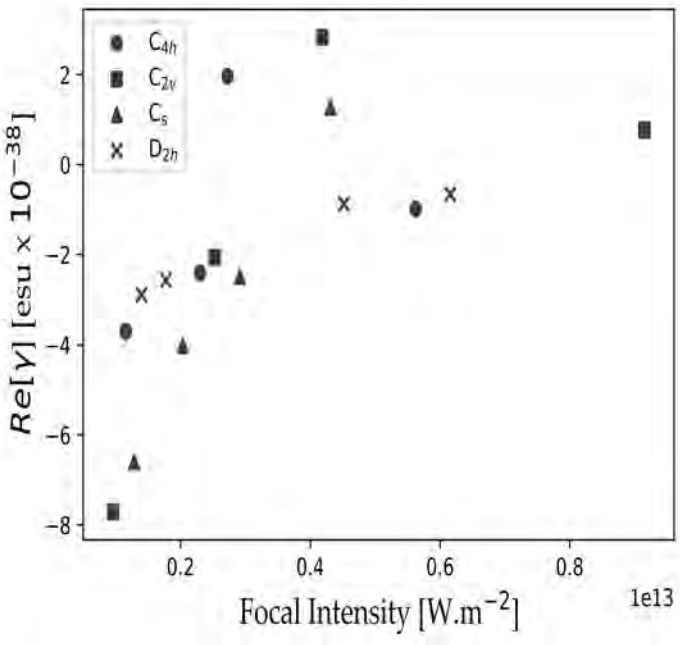

Figure 49: $Re[\gamma]$ for the regioisomer of βH_2Pc plotted against focal intensity.

effectiveness at nonlinear refraction, the data from the populations calculated from the five level model, shown in Figure 47, are used to isolate σ_{r1}, σ_{r2}. As was found in the αH_2Pc regioisomer, the triplet refraction contribution and those from the Kerr effect were found to be negligible.It is likely that this is due to the duration of the laser pulse (7 ns) and the Kerr effect would become more prominent with a shorter pulse length. The results from the non-parametric refraction model can be found in Table 23. The values of σ_{r2} are smaller than the values seen for the αH_2Pc regioisomer.

Table 23: Calculated values of the refractive cross section for the βH_2Pc regioisomer.

Constitutional isomer	σ_{r1} cm^2	σ_{r2} cm^2	σ_{r3} cm^2
C_{4h}	-2.13E-19	3.83E-17	*N.A.*
C_{2v}	-2.21E-19	5.02E-17	*N.A.*
C_s	-1.96E-19	4.11E-17	*N.A.*
D_{2h}	-2.45E-19	4.89E-17	*N.A.*

This is expected as the αH_2Pc regioisomer refraction was closer to resonant transition than the refractions of βH_2Pc, as is shown by the size of their respective σ_2. Similar reasoning can apply to the off resonant σ_{r1} refraction which is also smaller than the αH_2Pc regioisomer's σ_{r1}.

Table 24: Parametric model results of the βH_2Pc regioisomer.

Constitutional isomer	I W.m^{-2}	z_R m	β m.W^{-1}	$Im[\chi^{(3)}]$ esu	$Im[\gamma]$ esu	n_2 m^2.W^{-1}	$Re[\chi^{(3)}]$ esu	$Re[\gamma]$ esu	Δn	W
C_{4h}	2.30E+12	3.12E-03	7.89E-07	1.88E-11	1.31E-37	-6.14E-14	-3.45E-12	-2.41E-38	-2.35E-02	-2.04E-
	2.72E+12	2.44E-03	1.41E-06	3.36E-11	9.63E-38	1.22E-13	6.84E-12	1.96E-38	5.53E-02	1.97E-
	5.62E+12	2.23E-03	6.33E-07	1.51E-11	1.03E-37	-2.56E-14	-1.44E-12	-9.89E-39	-2.40E-02	-2.05E-
	1.16E+12	3.79E-03	6.15E-07	1.46E-11	1.18E-37	-8.17E-14	-4.59E-12	-3.71E-38	-1.57E-02	-1.58E-
C_{2v}	2.53E+12	2.63E-03	3.68E-07	8.75E-12	6.72E-38	-4.78E-14	-2.68E-12	-2.06E-38	-2.02E-02	-1.87E-
	4.19E+12	2.51E-03	1.52E-06	3.63E-11	1.14E-37	1.60E-13	8.98E-12	2.83E-38	1.12E-01	3.79E-
	9.15E+12	2.32E-03	5.82E-07	1.38E-11	1.05E-37	1.80E-14	1.01E-12	7.66E-39	2.75E-02	2.52E-
	9.59E+11	3.28E-03	2.57E-07	6.13E-12	5.44E-38	-1.54E-13	-8.68E-12	-7.71E-38	-2.47E-02	-2.66E-
C_s	2.04E+12	3.07E-03	1.02E-06	2.42E-11	1.95E-37	-8.82E-14	-4.96E-12	-4.01E-38	-2.98E-02	-3.07E-
	2.91E+12	2.44E-03	2.79E-06	6.65E-11	2.20E-37	-1.33E-13	-7.50E-12	-2.49E-38	-6.48E-02	-2.73E-
	4.31E+12	2.08E-03	1.01E-06	2.39E-11	1.90E-37	2.84E-14	1.60E-12	1.27E-38	2.03E-02	2.06E-
	1.29E+12	3.01E-03	6.15E-07	1.46E-11	1.37E-37	-1.25E-13	-7.05E-12	-6.60E-38	-2.70E-02	-3.20E-
D_{2h}	1.40E+12	5.71E-03	1.71E-06	4.07E-11	3.47E-37	-6.05E-14	-3.40E-12	-2.90E-38	-1.41E-02	-3.26E-
	1.77E+12	2.81E-03	2.90E-06	6.90E-11	2.41E-37	-1.31E-13	-7.38E-12	-2.58E-38	-3.88E-02	-3.68E-
	4.52E+12	3.53E-03	9.63E-07	2.29E-11	1.92E-37	-1.87E-14	-1.05E-12	-8.78E-39	-1.41E-02	-3.19E-
	6.16E+12	3.62E-03	5.91E-07	1.41E-11	1.38E-37	-1.21E-14	-6.78E-13	-6.68E-39	-1.24E-02	-3.31E-

4.3 $\alpha SnCl_2Pcs$ regioisomer's Nonlinear Optical Properties

The metalated Pc, $\alpha SnCl_2Pc$, regioisomer NLO properties were measured with z-scan. For open aperture z-scan the $\alpha SnCl_2Pc$ regioisomer showed strong nonlinear absorption. The z-scan data was fitted using Tsigaridas's method, shown in Figure 50. As was seen in both free base isomers, the nonlinear absorption exhibited a positive β. From the parametric fittings, the values of β and $Im[\gamma]$ were calculated. As was

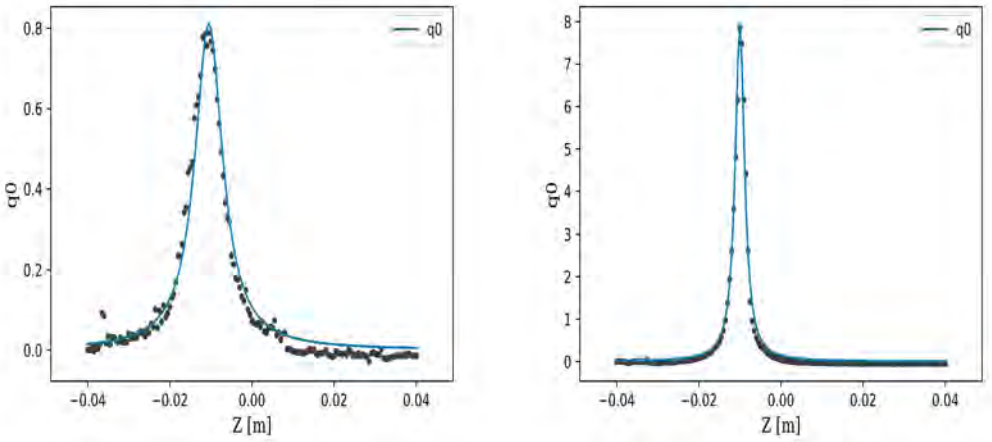

Figure 50: q0 for $\alpha SnCl_2Pc$ C_{4h} regioisomer at a focal intensity of 0.8×10^{12} W.m^{-2} (left), and 7.5×10^{12} W.m^{-2}(right).

seen in the free-base Pc isomers, the laser I had minimal effect on the values of β and $Im[\gamma]$, shown in Figure 51. Like the free-base Pcs, this implies that the nonlinear absorption seen in the $\alpha SnCl_2Pc$'s regioisomer is mostly intensity dependent, such as RSA, and not a fluence dependent process, such as TPA. The linearity of the nonlinear absorption results allows an average value of $Im[\gamma]$ to be taken. Table 25 shows the averaged values for $Im[\gamma]$ of each regioisomer, and it was found that the C_{4h} regioisomer has the highest $Im[\gamma]$, followed by C_{2v} then C_s and finally D_{2h} with the lowest average value of $Im[\gamma]$. This was the same trend found in the αH_2Pc regioisomer. As shown in the previous chapter, the addition of $SnCl_2$ to the centre

Table 25: Averaged values of the measured $Im[\gamma]$ for the $\alpha SnCl_2Pc$ regioisomer.

regioisomer	$Im[\gamma]$ esu
C_{4h}	2.92E-37
C_{2v}	1.30E-37
C_s	9.30E-38
D_{2h}	5.28E-38

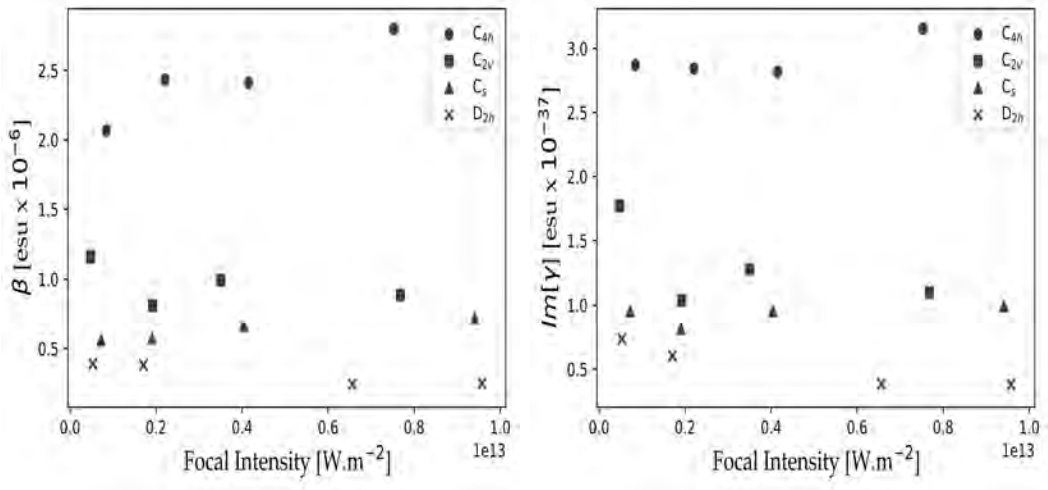

Figure 51: Calculated values of β(left), and $Im[\gamma]$(right) for the $\alpha SnCl_2Pc$'s regioisomer.

of the Pc has two significant effects on the optical properties of the Pc. The first is a redshift in its Uv/vis spectra due to the HOMO-LUMO gap being decreased, and the second in the increase in molecular symmetry, leading to a degeneracy of the x-axis and y-axis of the Pc (the symmetrical effects of the regioisomer notwithstanding). This has significance in the excited state absorption, due to the lower distribution of state transitions (half as many due to the new x/y symmetry) and it becomes less likely that there is a transition in the region of 2.33 eV. This can be illustrated with the RTTD-DFT results shown in Figure 52. The RTTD-DFT results indicate that there are multiple weak $S_1 \rightarrow S_n$ transitions around the 500-600 nm region. For the $T_1 \rightarrow S_n$ transitions there appear to be two strong bands around 500 nm that could contribute to the excited state absorption. Due to the ground state absorption results from the RTTD-DFT being blueshifted 80 nm from the measured experimental position (at around 740 nm), it is likely that σ_3,will be significantly larger than σ_1.

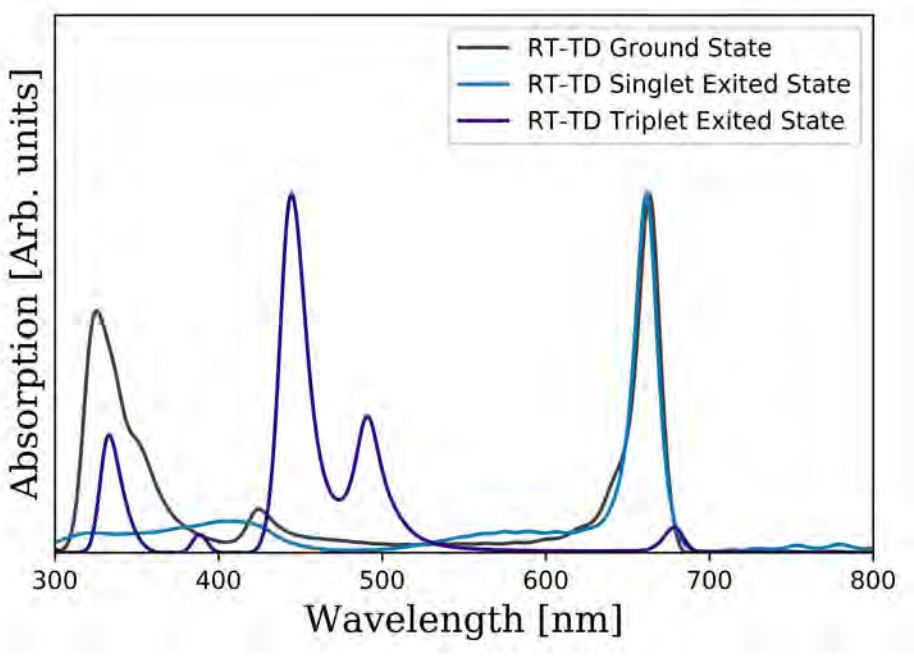

Figure 52: RTTD-DFT dipole response of the C_{4h} regioisomer of $\alpha SnCl_2Pc$ in the UV/Vis region.

In order to calculate the excited state contribution to the nonlinear absorption of the $\alpha SnCl_2Pc$'s regioisomer, the experimental data from multiple intensity open aperture z-scan measurements was passed to the five level non-parametric model. As can be seen from Figure 53, the dominant process in the nonlinear absorption is the singlet RSA, arising from the $S_1 \rightarrow S_n$ transition, the triplet RSA contributes a significant portion of the nonlinear absorption. As with the free-base Pc isomers, the TPA did not significantly contribute to the nonlinear absorption, but the TPA process was found to be significant to the total nonlinear absorption. The triplet RSA

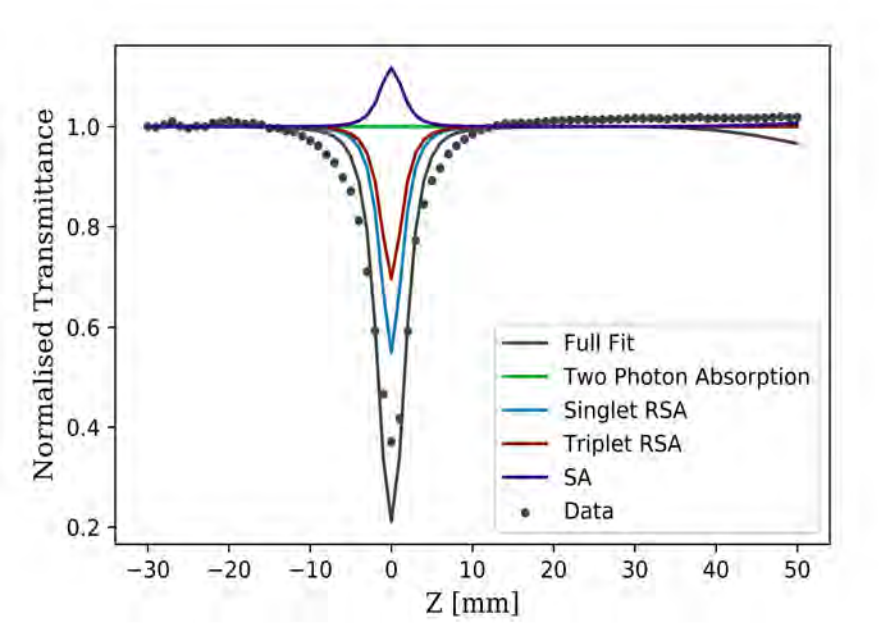

Figure 53: The five level model fit of $\alpha SnCl_2Pc$'s C_{4h} regioisomer at a focal intensity of 0.8×10^{12} W.m^{-2}.

process was expected to be the dominant absorption, however this was not found to be the case with the singlet RSA still contributing more to the nonlinear absorption, though the triplet RSA did still contribute to the total nonlinear absorption. This is likely due to the relative population size of the T_1 state to the population of the S_1. As shown in Figure 54, the population of the T_1 state smaller than the S_1 state population by approximately two orders of magnitude (considering the population biases mentioned at the start of this chapter). The cross sections calculated for the $\alpha SnCl_2Pc$ regioisomer are shown in Table 26. The σ_3 was found to be significant for the total absorption, exhibiting values almost one order of magnitude larger than σ_2. As the absorption due to σ_3 is significant, Equation 35 can no longer be reduced to σ_2/σ_1 as was done with the αH_2Pc and βH_2Pc regioisomer. Due to the ratio of T_1 to S_1 changing I, as shown by Figure 54, the cross sections along with σ_{eff}, are calculated using a single value of I, and these are tabulated in Table 26.

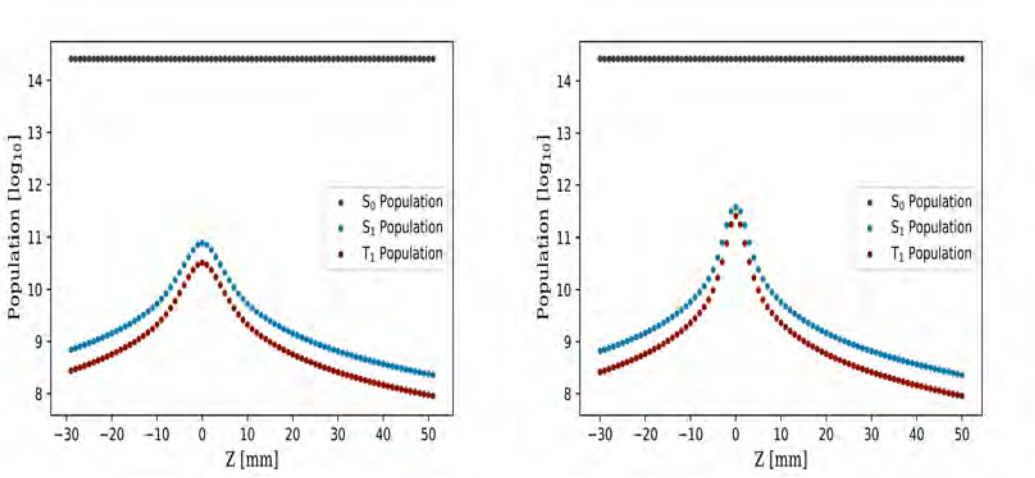

Figure 54: The five level model populations of $\alpha SnCl_2Pc$'s C_{4h} regioisomer at a focal intensity of 0.8×10^{12} W.m^{-2} (left), and 5.6×10^{12} W.m^{-2} (right).

Table 26: Calculated cross sections from the five level model for the $\alpha SnCl_2Pc$ regioisomer.

regioisomer	σ_{tpa} GM	σ_2 cm^2	σ_3 cm^2	σ_1 cm^2	$\sigma_{\text{eff}}/\sigma_1$
C_{4h}	26.69	1.73E-17	5.60E-17	3.19E-18	9.84
C_{2v}	87.93	1.71E-17	5.61E-17	5.63E-18	5.61
C_s	25.68	1.64E-17	5.87E-17	6.89E-18	4.52
D_{2h}	47.07	1.61E-17	6.31E-17	4.10E-18	7.56

The closed aperture z-scan results of the $\alpha SnCl_2Pc$ regioisomer were collected and the measurements were then fitted using the parametric closed aperture model. The nonlinear refraction response for the $\alpha SnCl_2Pc$ regioisomer are less dominated by negative values of n_2 than the αH_2Pc and βH_2Pc regioisomer, with the refractive response showing a dominant positive n_2 at higher values of I, as seen in Figure 55. The fits shown in Figure 55 suggest a reversal of the sign of n_2 at the higher I. In this

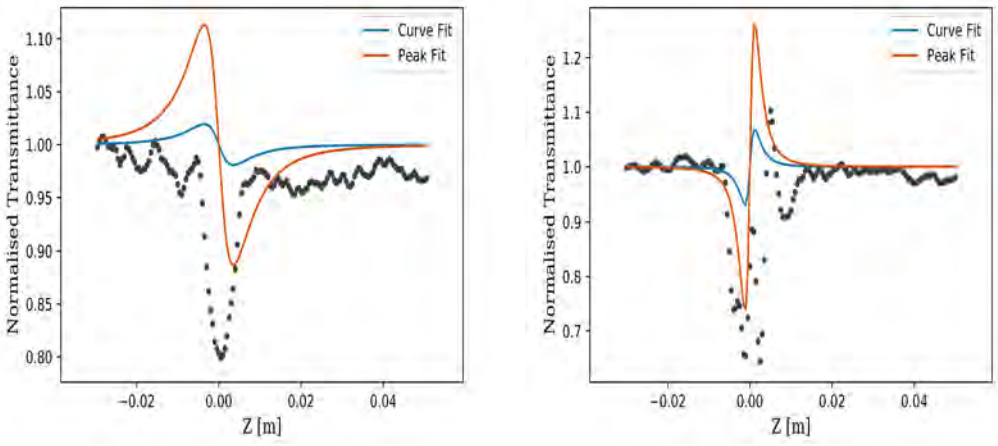

Figure 55: Closed aperture results for $\alpha SnCl_2Pc$ C_{4h} regioisomer at a focal intensity of 0.8×10^{12} W.m^{-2} (left), and 7.5×10^{12} W.m^{-2} (right).

case, the nonlinear refractive response is dominated by a negative process at 0.8×10^{12} W.m^{-2} and by a positive refractive process at 7.5×10^{12} W.m^{-2}. The populations calculated during the five level model show there is a significant population of both S_1 and T_1 states. Further, as is shown by the RTTD-DFT calculations, the T_1 state has a strong response very near the 532 nm wavelength at which this study was done. Thus the refraction due to the T_1 state can be considered an on resonance response, like the response due to the S_1 state. It can be concluded that the negative contribution in the nonlinear refraction is due to the ground state, as the positive nonlinear refraction contribution decreases with a decrease in I. The negative contribution to the refractive index diminishes as I increases, and this is attributed to excited state refraction contributions. For the $\alpha SnCl_2Pc$ regioisomer the relative population of the S_1 state is comparable to the populations seen in both the αH_2Pc and βH_2Pc regioisomer. However the T_1 state population is greatly increased, thus N_{totalE} is larger for the $\alpha SnCl_2Pc$ regioisomer so is any nonlinear effect to which they contribute. To investigate the sources of each process, CPHF calculations were performed for γ on the S_0 and the T_1 state of each regioisomer, the results are tabulated in Table 27. Similar to previous regioisomer, the S_0 state is shown to have a negative γ at 532 nm, while the triplet state shows a positive value of γ. The results of the closed aperture fitting for the $\alpha SnCl_2Pc$'s regioisomer are shown in Figure 56, with the val-

Table 27: Theoretical values for γ, calculated with CPHF, for the $\alpha SnCl_2Pc$ regioisomer.

regioisomer	γ_{S_0} esu ($\times 10^{-36}$)	γ_{T_1} esu ($\times 10^{-36}$)
C_{4h}	-1.22E+03	7.78E+02
C_{2v}	-1.22E+03	7.17E+02
C_s	-1.20E+03	7.88E+02
D_{2h}	-1.20E+03	7.76E+02

ues of $Re[\gamma]$ recorded in Table 29. Unlike the results seen in the αH_2Pc and βH_2Pc regioisomer, the values for $Re[\gamma]$ seen in the $\alpha SnCl_2Pc$ regioisomer are more sporadic, and show smaller absolute values of $Re[\gamma]$. As seen in Figure 56 the values of $Re[\gamma]$

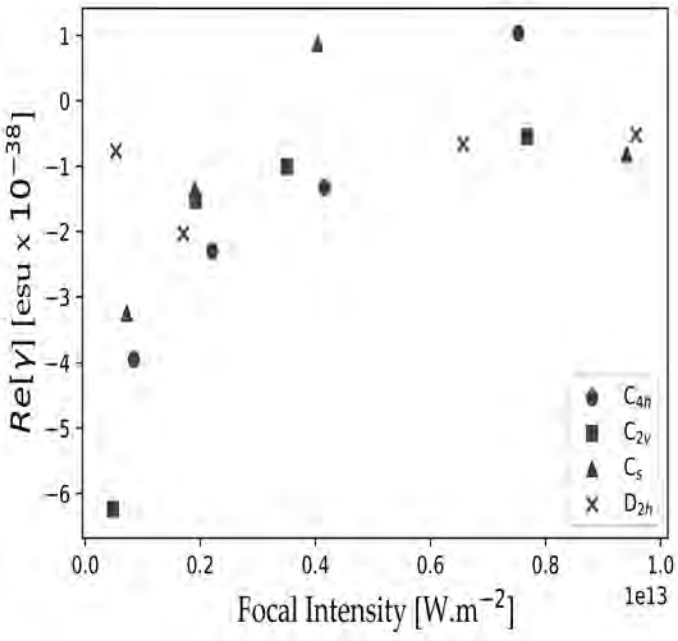

Figure 56: $Re[\gamma]$ for the regioisomer of $\alpha SnCl_2Pc$ plotted against focal intensity.

are smaller than expected, and one possible explanation for this is the relative state populations. When analysed using the populations from the five level model, shown in Figure 54, the values of σ_{r1}, σ_{r2} can be found. However, unlike the deconvolution of the grounds state, isolating the contribution from a separate refractive component proved difficult, with the fitting dividing the simulated refraction equally between σ_{r1} and σ_{r2}. The result is tabulated in Table 28. As was found in the αH_2Pc and βH_2Pc regioisomer, the Kerr effect on nonlinear refraction was found to be negligible. The values of σ_{r2} and σ_{r3} are as expected, considering the populations of their respective

Table 28: Calculated values of the refractive cross section for the $\alpha SnCl_2Pc$ regioisomer.

regioisomer	σ_{r1} cm^2	σ_{r2} cm^2	σ_{r3} cm^2
C_{4h}	-3.52E-19	5.60E-17	2.75E-16
C_{2v}	-2.07E-19	7.39E-17	1.51E-16
C_s	-3.17E-19	2.01E-17	5.59E-16
D_{2h}	-3.20E-19	7.43E-17	2.04E-16

states. The size of the σ_{r3} values is attributed resonance with the large σ_3, similar to the behaviour seen for the σ_{r2} induced refraction seen in the free-base Pcs. The relative sizes of σ_{r2} and σ_{r3} are not as expected, and this is mostly due to the fit not being constrained to not allocate their contributions equally. This is indicitive of a lack of sufficent data required for an accurate fit of these variables, as such the values of of σ_{r2} and σ_{r3} are to be regarded as inaccurate.

Table 29: Parametric model results of the $\beta SnCl_2Pc$ regioisomer.

regioisomer	I W.m^{-2}	z_R m	β m.W^{-1}	$Im[\chi^{(3)}]$ esu	$Im[\gamma]$ esu	n_2 m^2.W^{-1}	$Re[\chi^{(3)}]$ esu	$Re[\gamma]$ esu	Δn	W
C_{4h}	1.52E+12	3.43E-03	1.49E-06	3.55E-11	2.48E-37	-8.33E-14	-4.68E-12	-3.27E-38	-2.10E-02	-1.82E-01
	4.83E+12	2.08E-03	2.76E-06	6.57E-11	1.88E-37	-6.07E-14	-3.41E-12	-9.78E-39	-4.88E-02	-1.74E-01
	7.97E+12	1.66E-03	1.15E-06	2.74E-11	1.88E-37	2.03E-14	1.14E-12	7.83E-39	1.62E-01	2.29E-01
	6.75E+11	4.78E-03	1.63E-06	3.88E-11	3.14E-37	-8.18E-14	-4.60E-12	-3.71E-38	-9.20E-03	9.24E-02
C_{2v}	2.24E+12	2.47E-03	1.05E-06	2.51E-11	1.93E-37	-9.25E-14	-5.20E-12	-4.00E-38	-3.45E-02	-3.22E-01
	3.63E+12	2.23E-03	2.37E-06	5.65E-11	1.78E-37	-1.48E-13	-8.30E-12	-2.61E-38	-8.93E-02	-3.41E-01
	6.13E+12	1.84E-03	9.69E-07	2.31E-11	1.74E-37	-2.82E-14	-1.58E-12	-1.20E-38	-1.73E-01	-2.64E-01
	8.32E+11	3.76E-03	9.24E-07	2.20E-11	1.95E-37	-9.37E-14	-5.27E-12	-4.68E-38	-1.30E-02	-1.40E-01
C_s	1.83E+12	3.34E-03	8.22E-07	1.96E-11	1.58E-37	-5.40E-14	-3.03E-12	-2.45E-38	-1.65E-02	-1.69E-01
	5.76E+12	2.07E-03	1.83E-06	4.34E-11	1.44E-37	-5.74E-14	-3.23E-12	-1.07E-38	-5.52E-02	-2.32E-01
	1.02E+13	1.37E-03	6.71E-07	1.60E-11	1.27E-37	-1.17E-14	-6.56E-13	-5.22E-39	-1.98E-02	-2.00E-01
	8.17E+11	3.22E-03	1.23E-06	2.93E-11	2.74E-37	-1.56E-13	-8.76E-12	-8.20E-38	-2.12E-02	-2.52E-01
D_{2h}	6.08E+11	8.63E-03	9.67E-07	2.30E-11	1.96E-37	-3.14E-14	-1.76E-12	-1.50E-38	-3.18E-03	-7.36E-02
	2.81E+12	2.82E-03	5.03E-07	1.20E-11	4.18E-38	-4.41E-14	-2.48E-12	-8.65E-39	-2.07E-02	-1.95E-01
	2.93E+12	4.25E-03	2.79E-07	6.63E-12	5.55E-38	3.13E-14	1.76E-12	1.47E-38	9.16E-02	3.47E-01
	6.53E+11	4.45E-03	1.29E-07	3.08E-12	3.03E-38	-5.49E-14	-3.09E-12	-3.04E-38	-5.98E-03	-1.60E-01

4.4 $\beta SnCl_2Pcs$ regioisomers's Nonlinear Optical Properties

The last isomers studied were the $\beta SnCl_2Pc$'s regioisomers. As was done for the other isomers, both open and closed z-scan were performed at four intensities, and the $\beta SnCl_2Pc$'s regioisomers were found to behave in a similar manner to the $\alpha SnCl_2Pc$. For the open aperture z-scan, the $\beta SnCl_2Pc$'s regioisomers exhibited a positive β at all four values of I. Figure 43, shows two sets of data from the C_{4h} regioisomer's open aperture z-scan fitted using Tsigaridas' method. The parametric fitting model used

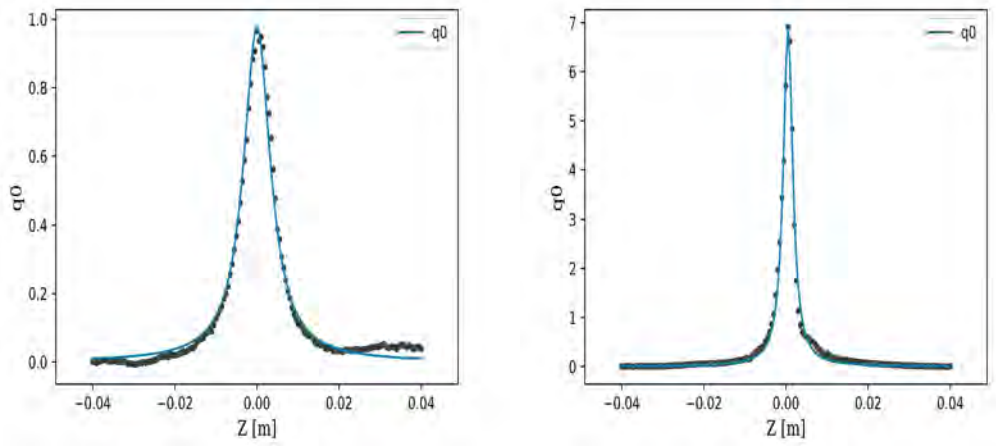

Figure 57: q0 for $\beta SnCl_2Pc$ C_{4h} regioisomer at a focal intensity of 0.7×10^{12} W.m^{-2} (left), and 8.0×10^{12} W.m^{-2}(right).

to fit the open aperture z-scan data calculates values for $Im[\gamma]$ with slight clustering for each regioisomer. Similar to the other isomers studied above, the regioisomers of $\beta SnCl_2Pc$ show negligible relation to I and the values of $Im[\gamma]$ can be averaged, allowing investigation of the specific regioisomer properties. The averaged values for $Im[\gamma]$ are tabulated in Table 20. The C_{4h} regioisomer was found to possesses the largest averaged value of $Im[\gamma]$, followed by the C_{2v} then C_s and finally D_{2h} regioisomers. This is the same trend found in the $\alpha SnCl_2Pc$ and αH_2Pc regioisomers but does not follow the trend of the other β structural isomer, $\beta SnCl_2Pc$. The RTTD-DFT calculations,

Table 30: Averaged values of the measured $Im[\gamma]$ for the $\beta SnCl_2Pc$ regioisomers.

regioisomer	$Im[\gamma]$ esu
C_{4h}	2.35E-37
C_{2v}	1.85E-37
C_s	1.76E-37
D_{2h}	8.09E-38

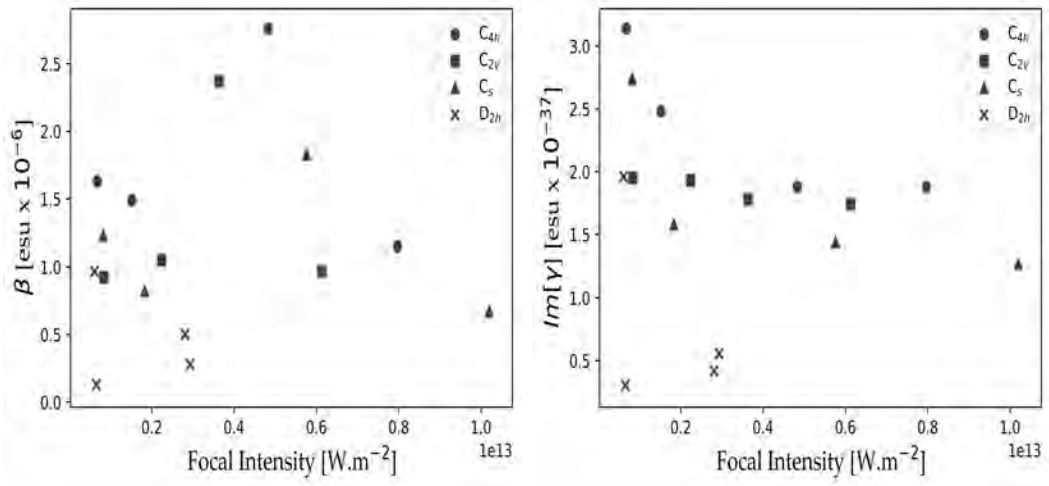

Figure 58: Calculated values of β(left), and $Im[\gamma]$(right) for the $\beta SnCl_2Pc$'s regioisomers.

shown in Figure 59, indicate multiple possible singlet transitions that can contribute to the singlet RSA while the triplet has its typical strong absorption band in the 500 nm region. While the RTTD-DFT has redshifted the ground state absorption, (both excited state spectra are assumed to be redshifted as well) the optical window for the Pc's ground state absorption is found by the RTTD-DFT to be between 400 nm and 500 nm (experimentally found at 500 nm to 600 nm). The experimental ground state absorption is very low in this window, shown in Table 31, and the excited state absorption in the same region is expected to be the primary cause of the nonlinear absorption seen at 532 nm. A five level fit was performed on the open aperture z-scan data. The results of the C_{4h} regioisomer, at a focal intensity of 0.8×10^{12} W.m^{-2}, is shown in Figure 60. Once more, the excited state absorption due to the S_1 state was responsible for most of the nonlinear absorption for the $\beta SnCl_2Pc$ regioisomers. Like the $\alpha SnCl_2Pc$, the triplet RSA was found to comprise a significant amount of the total nonlinear absorption while the contribution of the TPA was minimal. In the case of TPA, the contribution was found to be significant as a excitation pathway for the $S_0 \rightarrow S_1$ transition, thereby helping populate the S_1 state. Similar to the other metalated Pc isomers, the $\beta SnCl_2Pc$ regioisomers exhibited higher populations of the T_1 state relative to the free-base Pc isomers. This allowed effects from the T_1 state, like absorption or refraction, to be observed even if its magnitude was lower than that of the nonlinear absorption due to the S_1 state. Figure 61 shows the populations of each state during the calculation for the data used in Figure 60. As can be seen, T_1 is a significant fraction of the N_{totalE}. The percentage of N_{totalE} seen in $\beta SnCl_2Pc$ is almost double the percentage found in the free-base Pc isomers, due to the increase in the population of T_1. As a result of the five level model, the values of the excited state and TPA cross sections, σ_2, σ_3, and σ_{tpa}, were calculated and are tabulated in Table 31. The trend seen in the values of $\sigma_{\text{eff}}/\sigma_1$ resemble the trend seen

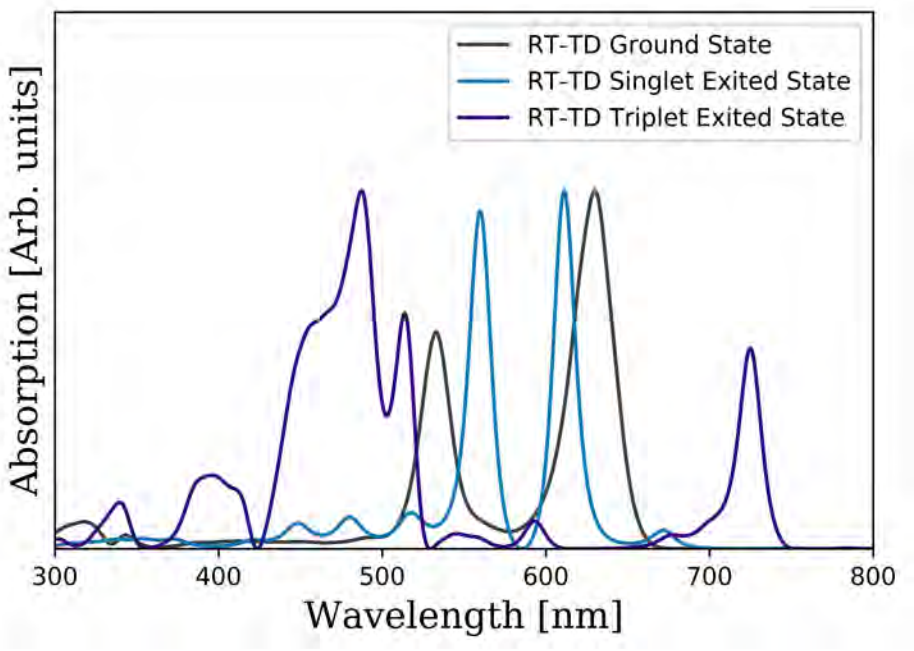

Figure 59: RTTD-DFT dipole response of the C_{4h} regioisomer of $\beta SnCl_2Pc$ in the UV/Vis region.

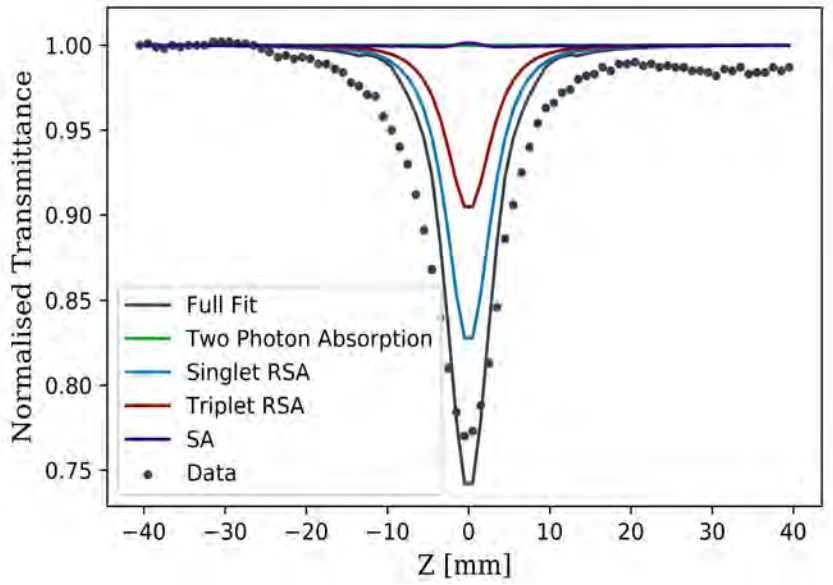

Figure 60: The five level model fit of $\beta SnCl_2Pc$'s C_{4h} regioisomer at a focal intensity of 0.7×10^{12} W.m^{-2}.

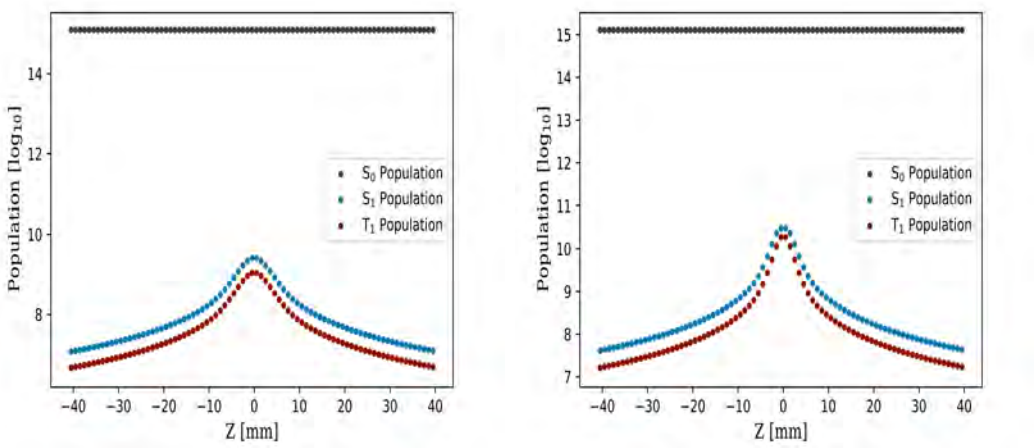

Figure 61: The five level model populations of $\beta SnCl_2Pc$'s C_{4h} regioisomer at a focal intensity of 0.7×10^{12} W.m^{-2} (left), and 8×10^{12} W.m^{-2} (right).

for the $\alpha SnCl_2Pc$ regioisomers, though this does not correspond to that of the $Im[\gamma]$ for $\beta SnCl_2Pc$ regioisomers. The lower values for the values of the calculated excited state cross sections for the $\beta SnCl_2Pc$ regioisomers are lower than the equivalent regioisomers of $\alpha SnCl_2Pc$. This most probably due to smaller mesomeric effect the β substituents that will exhibited lower redshifting of the excited state absorption, than the α substituents of the $\alpha SnCl_2Pc$ regioisomers.

Table 31: Calculated cross sections from the five level model for the $\beta SnCl_2Pc$ regioisomers.

regioisomer	σ_{tpa} GM	σ_2 cm^2	σ_3 cm^2	σ_1 cm^2	$\sigma_{\text{eff}}/\sigma_1$
C_{4h}	111.86	9.01E-18	7.60E-17	3.05E-18	7.87
C_{2v}	50.93	7.11E-18	7.71E-17	1.21E-18	4.25
C_s	105.68	6.78E-18	7.77E-17	6.70E-18	3.45
D_{2h}	117.07	8.14E-18	7.81E-17	6.52E-18	6.08

Closed aperture z-scans were performed on the $\beta SnCl_2Pc$ regioisomers at the same Is that the open aperture z-scan were run at. The $\beta SnCl_2Pc$ regioisomers also showed the same n_2 inversion at higher values of I that was seen in the $\alpha SnCl_2Pc$ regioisomers. This can be demonstrated with the two most extreme values of I, shown in Figure 62. The theoretical values of γ were calculated with CPHF and shown in Table 32. As with the other regioisomers, the values of γ suggest that the sign of the ground state $Re[\gamma]$ of the $\beta SnCl_2Pc$ regioisomers should be negative, and this matches the closed aperture results. The change of sign nonlinear refraction index sign seen at higher

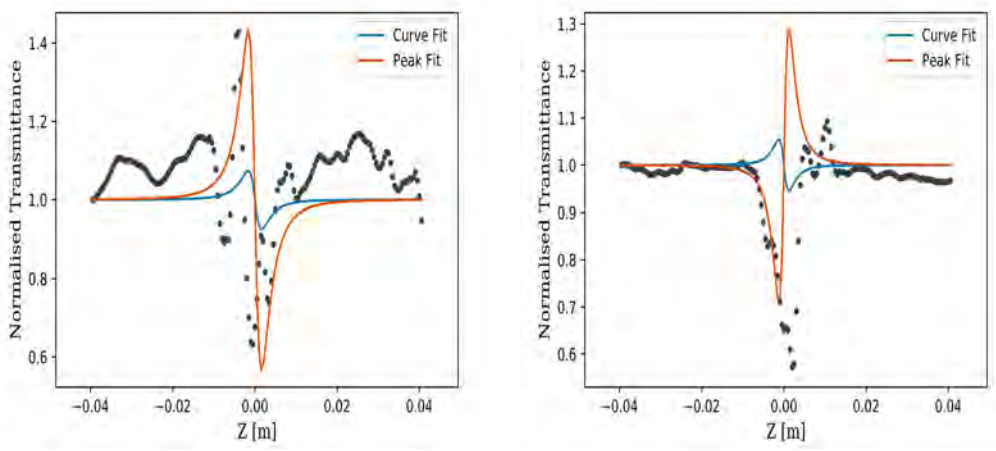

Figure 62: Closed aperture results for $\beta SnCl_2Pc$ C_{4h} regioisomer at a focal intensity of $1.2{\times}10^{12}$ W.m^{-2} (left), and $5.6{\times}10^{12}$ W.m^{-2} (right).

I, shown previously in Figure 62 and tabulated for all $\beta SnCl_2Pc$ regioisomers in Table 34, is attributed to the shift in the total populations of each state. Figure 63 shows the gradual shift of the $\beta SnCl_2Pc$ regioisomers mostly negative $Re[\gamma]$ to a $Re[\gamma]$ with a slightly positive majority. This is very similar to the trend seen with the other metalated regioisomers that also exhibited slightly positive nonlinear refraction at higher values of I .

Table 32: Theoretical values for γ, calculated with CPHF, for the $\beta SnCl_2Pc$ regioisomers.

regioisomer	γ_{S_0} esu ($\times 10^{-36}$)	γ_{T_1} esu ($\times 10^{-36}$)
C_{4h}	-1.10E+03	8.63E+02
C_{2v}	-1.18E+03	7.42E+02
C_s	-1.17E+03	8.08E+02
D_{2h}	-1.14E+03	8.17E+02

In order to determine the nonlinear refractive contribution from each state, the populations that were determined in the five level model, Figure 61, are used to calculate the respective refractive contribution of each state. Similar to the population dynamics of the $\alpha SnCl_2Pc$ regioisomers, the populations of the $\beta SnCl_2Pc$ regioisomers showed a much higher N_{totalE} than is seen in the free-base regioisomers. The calculated refractive cross sections, shown in Table 33, are similar to those seen in the $\alpha SnCl_2Pc$ regioisomers. However, as was seen with the absorption cross section, the area of each refractive cross section is smaller. This was similar to the comparison

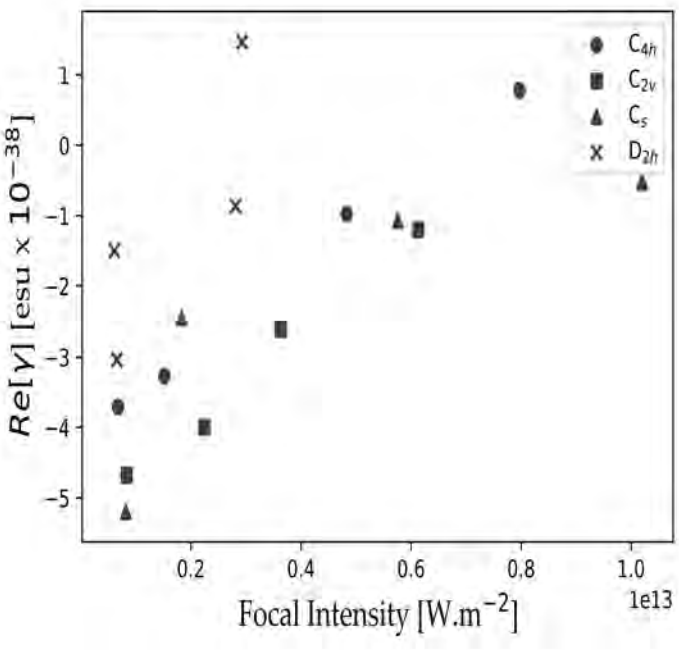

Figure 63: $Re[\gamma]$ for the regioisomers of $\beta SnCl_2Pc$ plotted against focal intensity.

of the cross sections of the βH_2Pc regioisomers when compared to the cross sections of the αH_2Pc regioisomers, the smaller absorption cross sections corresponded with smaller refraction cross sections, likely due to the wavelength of interaction being shifted away from a resonance wavelength. As found in the other Pc studied in this work, the Kerr effect was determined to be negligible.

Table 33: Calculated values of the refractive cross sections for the $\beta SnCl_2Pc$ regioisomers.

regioisomer	σ_{r1} cm^2	σ_{r2} cm^2	σ_{r3} cm^2
C_{4h}	-1.13E-19	3.48E-17	2.94E-17
C_{2v}	-1.23E-19	4.56E-17	3.76E-17
C_s	-1.62E-19	3.74E-17	3.18E-17
D_{2h}	-2.15E-19	4.45E-17	3.74E-17

Table 34: Parametric model results of the $\beta SnCl_2Pc$ regioisomers.

regioisomer	I W.m^{-2}	z_R m	β m.W^{-1}	$Im[\chi^{(3)}]$ esu	$Im[\gamma]$ esu	n_2 m^2.W^{-1}	$Re[\chi^{(3)}]$ esu	$Re[\gamma]$ esu	Δn	W
C_{4h}	1.52E+12	3.43E-03	1.49E-06	3.55E-11	2.48E-37	-8.33E-14	-4.68E-12	-3.27E-38	-2.10E-02	-1.82E-01
	4.83E+12	2.08E-03	2.76E-06	6.57E-11	1.88E-37	-6.07E-14	-3.41E-12	-9.78E-39	-4.88E-02	-1.74E-01
	7.97E+12	1.66E-03	1.15E-06	2.74E-11	1.88E-37	2.03E-14	1.14E-12	7.83E-39	1.62E-01	2.29E-01
	6.75E+11	4.78E-03	1.63E-06	3.88E-11	3.14E-37	-8.18E-14	-4.60E-12	-3.71E-38	-9.20E-03	9.24E-02
C_{2v}	2.24E+12	2.47E-03	1.05E-06	2.51E-11	1.93E-37	-9.25E-14	-5.20E-12	-4.00E-38	-3.45E-02	-3.22E-01
	3.63E+12	2.23E-03	2.37E-06	5.65E-11	1.78E-37	-1.48E-13	-8.30E-12	-2.61E-38	-8.93E-02	-3.41E-01
	6.13E+12	1.84E-03	9.69E-07	2.31E-11	1.74E-37	-2.82E-14	-1.58E-12	-1.20E-38	-1.73E-01	-2.64E-01
	8.32E+11	3.76E-03	9.24E-07	2.20E-11	1.95E-37	-9.37E-14	-5.27E-12	-4.68E-38	-1.30E-02	-1.40E-01
C_s	1.83E+12	3.34E-03	8.22E-07	1.96E-11	1.58E-37	-5.40E-14	-3.03E-12	-2.45E-38	-1.65E-02	-1.69E-01
	5.76E+12	2.07E-03	1.83E-06	4.34E-11	1.44E-37	-5.74E-14	-3.23E-12	-1.07E-38	-5.52E-02	-2.32E-01
	1.02E+13	1.37E-03	6.71E-07	1.60E-11	1.27E-37	-1.17E-14	-6.56E-13	-5.22E-39	-1.98E-02	-2.00E-01
	8.17E+11	3.22E-03	1.23E-06	2.93E-11	2.74E-37	-1.56E-13	-8.76E-12	-8.20E-38	-2.12E-02	-2.52E-01
D_{2h}	6.08E+11	8.63E-03	9.67E-07	2.30E-11	1.96E-37	-3.14E-14	-1.76E-12	-1.50E-38	-3.18E-03	-7.36E-02
	2.81E+12	2.82E-03	5.03E-07	1.20E-11	4.18E-38	-4.41E-14	-2.48E-12	-8.65E-39	-2.07E-02	-1.95E-01
	2.93E+12	4.25E-03	2.79E-07	6.63E-12	5.55E-38	3.13E-14	1.76E-12	1.47E-38	9.16E-02	3.47E-01
	6.53E+11	4.45E-03	1.29E-07	3.08E-12	3.03E-38	-5.49E-14	-3.09E-12	-3.04E-38	-5.98E-03	-1.60E-01

4.5 Analysis

Having completed the nonlinear studies of all four structural isomers and their respective regioisomers the trends observed between the data sets were analysed. This was done in order understand the significance of the regio-substitution the trends of nonlinear behaviour for all regioisomers across all structural isomers.

4.5.1 Imaginary Component of the 3rd Order Susceptibility $Im[\gamma]$

The values of $Im[\gamma]$ showed a trend in the αH_2Pc, $\alpha SnCl_2Pc$, and $\beta SnCl_2Pc$ regioisomers with only the regioisomers of the βH_2Pc showing a significant deviation. Shown in Figure 64 are the averages of $Im[\gamma]$ for all I for each of the regioisomers, and the trend seen in each of the αH_2Pc, $\alpha SnCl_2Pc$, and $\beta SnCl_2Pc$ structural isomers is evident. When averaging the values for each regioisomer, it was found that the C_{4h} regioisomer has the largest average of $Im[\gamma]$ (2.91×10^{-37} esu), followed by the C_{2v} regioisomer (1.96×10^{-37} esu), then the C_s regioisomer (1.80×10^{-37} esu), and finally the D_{2h} regioisomer (1.57×10^{-37} esu). This was similar to trends seen in literature for the free-base regioisomers[50].

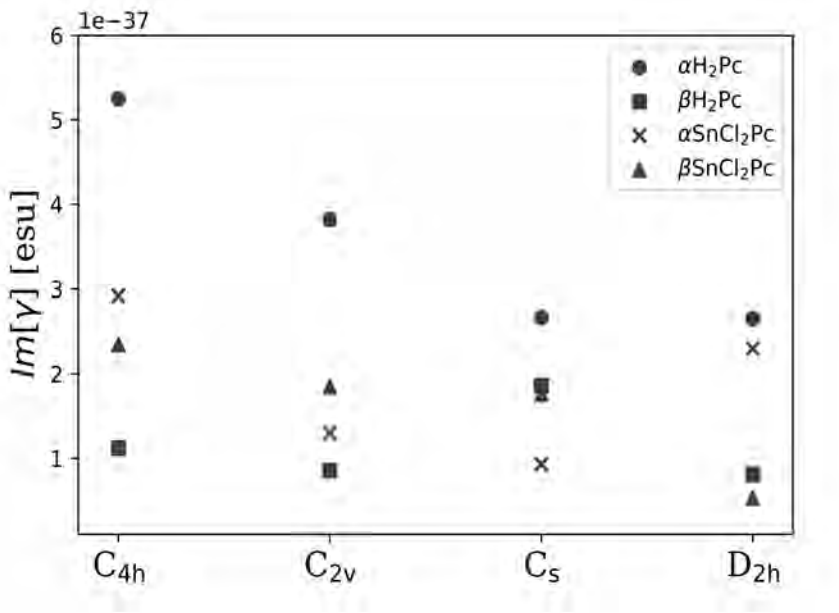

Figure 64: Averaged values of $Im[\gamma]$ for all regioisomers at 532 nm.

4.5.2 Excited State Absorption

The excited state absorption was found to be the dominant factor in the nonlinear absorption seen in all regioisomers. Due to the very small σ_1 of 1×10^{-18} cm^2 to 7×10^{-18} cm^2, the regioisomers were almost transparent at the wavelength of the 532 nm beam used in this study. With the values of σ_2 and σ_3 found to be of the order 10^{-17} cm^2, this resulted in the ratio of ground state to excited state absorption being high, as shown in Figure 65. As was shown in the population studies of each structural isomer, the relative populations are highly dependent on the value of I, and as the values of σ_3 were found to be 3-4 time higher than those of σ_2, this would result in the increase of σ_{eff}/σ_1 as I was increased. This presents several problems for using Equation 35 as a parameter of significance. While reporting σ_2/σ_1 or σ_3/σ_1 might appear to circumvent this issue, the population dynamics are a significant consideration in the total nonlinear absorption and can be more significant than the cross sectional area of either σ_2 or σ_3. The values of σ_{eff}/σ_1, recorded from a simulation at an I of 2×10^{12} W.m^{-2}, are used for Figure 65, though due to the similar population dynamics of all the regioisomers, the trend seen here is retained up to an I of 10×10^{12} W.m^{-2}. Due to the long-lived T_1 state, it is expected that the $\alpha SnCl_2Pc$ and $\beta SnCl_2Pc$ regioisomers would possess higher values of σ_{eff}/σ_1 at $I > 10 \times 10^{12}$ W.m^{-2}. This is due to 10×10^{12} W.m^{-2} being where the T_1 state populations are found to exceed the S_1 state populations. From inspection of Figure 65 the trend found for the regioisomers appears to be similar to those found in the $Im[\gamma]$ results. However, due to the effects of σ_3 in the $\alpha SnCl_2Pc$ and $\beta SnCl_2Pc$'s D_{2h} regioisomer as well as the anomalous behaviour of the βH_2Pc's D_{2h} regioisomer the trend differs. The regioisomer with the highest σ_{eff}/σ_1 is the C_{4h} regioisomer, with an average of 7.67, followed by the D_{2h} regioisomer with an average ratio of 6.18, then the C_{2v} regioisomer with an average of 5.73, and the regioisomer with the smallest average is found to be C_s, with an average ratio of 4.14.

4.5.3 Parametric Nonlinear Refraction

While the nonlinear absorption of the regioisomers showed little to no variation in $Im[\gamma]$, the $Re[\gamma]$ were found to vary greatly with respect to I, as shown by the graphs of $Re[\gamma]$ for each structural isomer, see Figures 42, 49, 63, and 56. This created difficulties in calculating the effective differences between each regioisomer, as averaging across multiple I was not possible. This was further complicated by the closed aperture z-scan data being very noisy, due to the small aperture magnifying any small deflection in the beam path. The noisy data interfered with the curve fitting used in this work, often showing false peaks or masking present peaks. While repeated runs seemed to add additional peaks to the average, the resulting data was sufficiently smooth for fitting. The end result of the parametric nonlinear refraction fittings were values of $Re[\gamma]$ that were only valid for a particular value of I, and this precluded the comparisons of the regioisomers effects on $Re[\gamma]$.

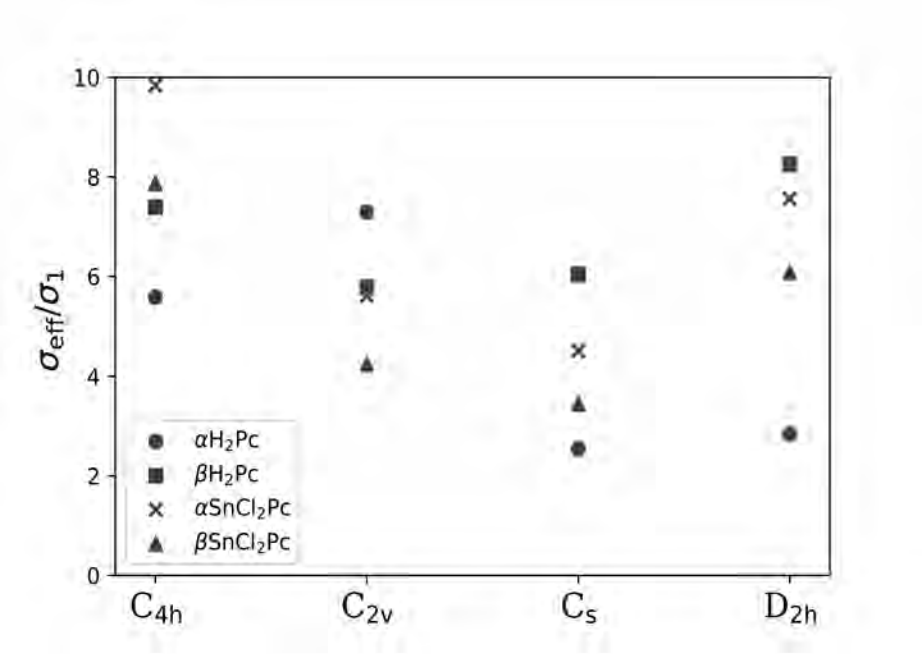

Figure 65: Averaged σ_{eff}/σ_1 at 2×10^{12} W.m^{-2} for all regioisomers at 532 nm.

4.5.4 Non-Parametric Nonlinear Refraction

Apparent from an inspection of Figures 42, 49, 56, and 63 is the decrease in the magnitude of the nonlinear refraction with an increase in I. Initially, this was attributed to thermal lensing, however, thermal lensing in chloroform would create the opposite effect, making the effective n_2 more negative not more positive, as seen in the figures. This left the contributions to the nonlinear refraction to be attributed to each of the molecular states present in the material. CPHF calculations were done on the ground state of each regioisomer, with the results shown in Figure 66, and while these confirmed that the nonlinear fraction due to S_0 was negative, the averaged theoretical values of γ did not trend in a manner seen for either the absorption cross sections nor the values of $Im[\gamma]$. The regioisomer with the largest average value of γ were found to be C_{2v} (-1.33$\times10^{-33}$ esu), followed by C_s (-1.31$\times10^{-33}$ esu), then C_{4h} (-1.30$\times10^{-33}$ esu), and finally D_{2h}(-1.20$\times10^{-33}$ esu). The average values of γ calculated for the regioisomers are very close in magnitude, differencing by at most 9% and this is attributed to the inaccuracies in the CPHF calculations in separating the region effects in each isomer.

To separate out the contribution of the refractive cross sections σ_{r1}, σ_{r2} and σ_{r3} the populations calculated in the five level model were applied to the nonparametric refraction model. The results for each cross sections are shown below, with Figure 67 showing the averages for the ground state refraction calculated for the regioisomers (the negative signs are kept to show the refractive change exhibited by the regioi-

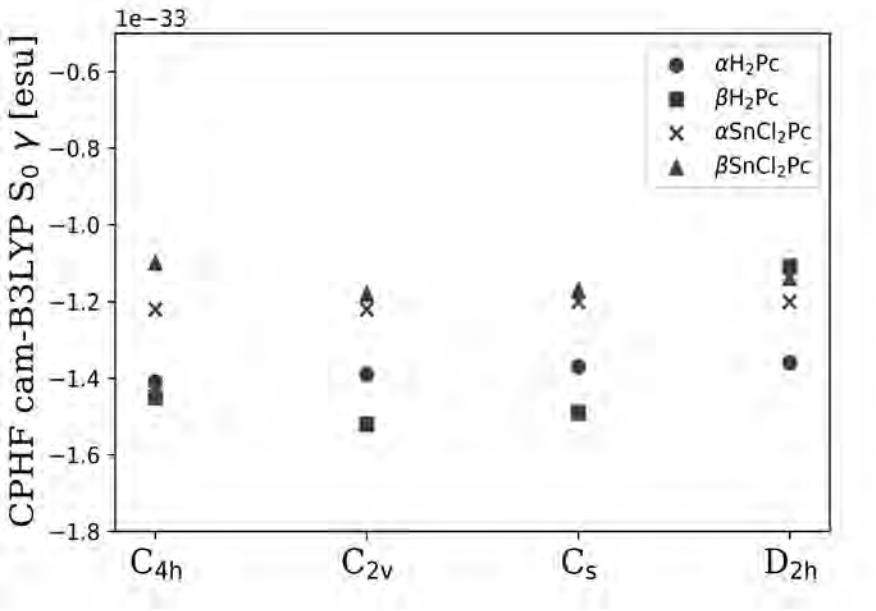

Figure 66: Averaged values of the theoretical values of γ for all regioisomers calculated with CPHF using a perturbation wavelength of 532 nm.

somers). When averaged, the observed trend in the regioisomers with regard to the values of σ_{r1} were found to be D_{2h}(-3.00×10^{-19} cm^2), followed by C_{4h}(-2.80×10^{-19} cm^2), then C_s(-2.62×10^{-19} cm^2), and finally C_{2v}(-2.36×10^{-19} cm^2). These values were relatively similar, with a maximum difference of around 20%, and the small trend seen here does not correlate with any trend in the nonlinear absorption. The averaged values of σ_{r2} calculated for all regioisomers are plotted in Figure 68. C_{2v}(-5.98×10^{-17} cm^2), D_{2h}(-3.00×10^{-17} cm^2), followed by C_{4h}(-2.80×10^{-17} cm^2), and then C_s(-2.62×10^{-17} cm^2). As was seen for the values of σ_{r1}, the small differences in the range of the points in Figure 68 suggest a minor trend, however it does not correlate with any observed prior trend.

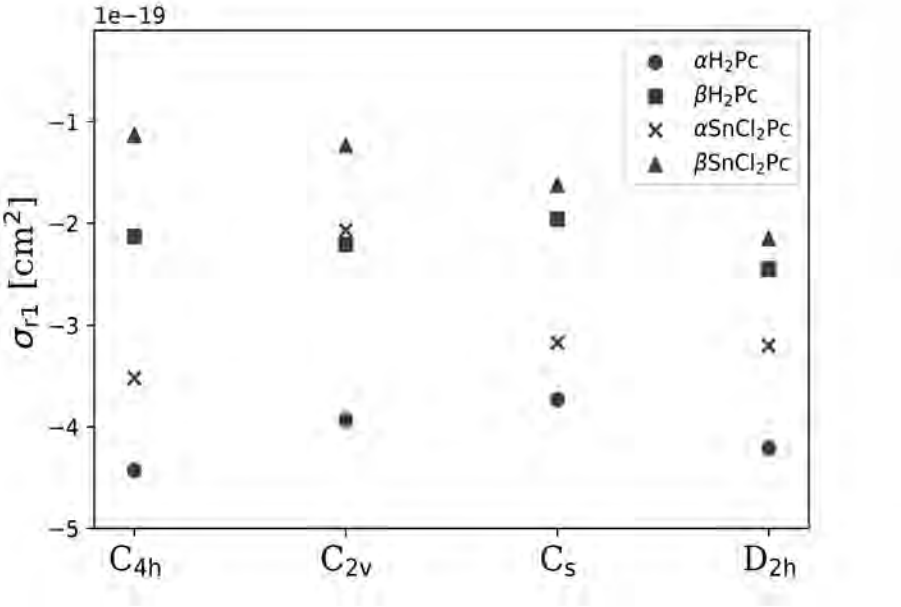

Figure 67: Averaged values of ground state refraction for all regioisomers at 532 nm.

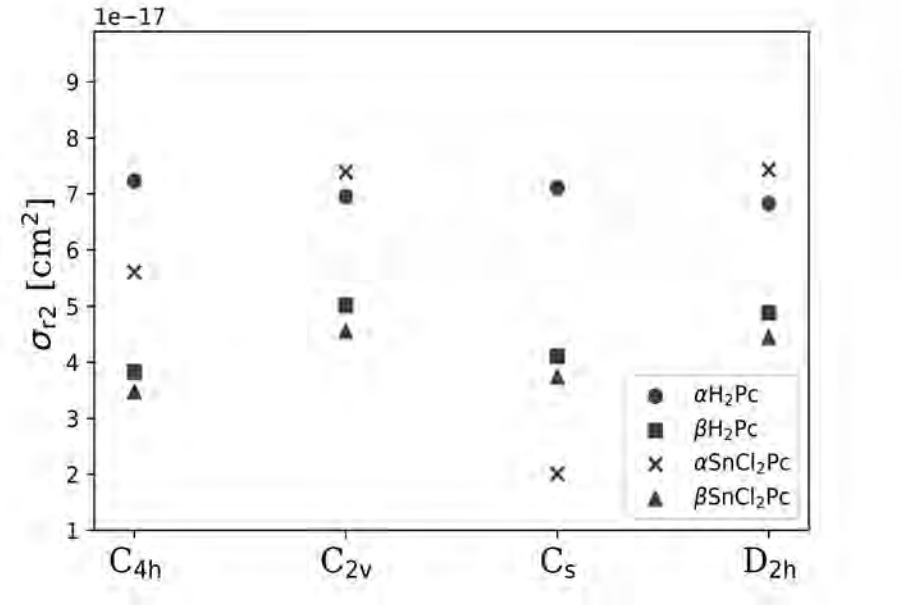

Figure 68: Averaged values of the singlet excited state refraction for all regioisomers at 532 nm.

5 Conclusion

References

[1] James Clerk. Maxwell. A Dynamical Theory of the Electromagnetic Field. *Philosophical transactions of the Royal Society of London*, 155:459–512., 1865.

[2] Edmund Taylor Whittaker. *A History of the Theories of Aether and Electricity from the Age of Descartes to the Close of the Nineteenth Century*. Longmans, Green and Company, 1910.

[3] Giorgos Demetriou. *Ultrafast Nonlinear Optics of Bulk and Two- Dimensional Materials for Infrared Applications Giorgos Demetriou Submitted for the degree of Doctor of Philosophy School of Engineering and Physical Sciences*. PhD thesis, 2016.

[4] Ying Xie, Fei Liang, Bo Zhang, Binghui Ge, Haohai Yu, Zheshuai Lin, Zeyan Wang, Huaijin Zhang, Baibiao Huang, and Jiyang Wang. Artificial Second-Order Nonlinear Optics in a Centrosymmetric Optical Material BiVO 4 : Breaking the Prerequisite for Nonlinear Optical Materials. *ACS Omega*, 4:1045–1052, 2019.

[5] John Kerr. LIV. A new relation between electricity and light: Dielectrified media birefringent (Second paper). *The London, Edinburgh, and Dublin Philosophical Magazine and Journal of Science*, 50(333):446–458, dec 1875.

[6] Elsa Garmire. Nonlinear optics in daily life. *Optics Express*, 21(25):30532, 2013.

[7] P A Franken, Alan E Hill, C W Peters, and G Weinreich. Generation of optical harmonics. *Physical Review Letters*, 7(4):118, 1961.

[8] F J McClung and R W Hellwarth. Giant optical pulsations from ruby. *Journal of Applied Physics*, 33(3):828–829, 1962.

[9] Herman A Haus. Mode-locking of lasers. *IEEE Journal of Selected Topics in Quantum Electronics*, 6(6):1173–1185, 2000.

[10] J Ihlemann and B Wolff-Rottke. Excimer laser micro machining of inorganic dielectrics. *Applied surface science*, 106:282–286, 1996.

[11] Timothy Ragan, Lolahon R Kadiri, Kannan Umadevi Venkataraju, Karsten Bahlmann, Jason Sutin, Julian Taranda, Ignacio Arganda-Carreras, Yongsoo Kim, H Sebastian Seung, and Pavel Osten. Serial two-photon tomography for automated ex vivo mouse brain imaging. *Nature methods*, 9(3):255, 2012.

[12] Robert R Alfano and S L Shapiro. Observation of self-phase modulation and small-scale filaments in crystals and glasses. *Physical Review Letters*, 24(11):592, 1970.

[13] Eric W Van Stryland and Mansoor Sheik-Bahae. Z-Scan Measurements of Optical Nonlinearities. In *Characterization Techniques and Tabulations for Organic Nonlinear Materials*, number 3, pages 655–692. 1998.

[14] Robert Boyd. *Nonlinear Optics*. Elsevier, third edit edition, 2008.

[15] Richard L Sutherland, Daniel G Mclean, and Sean Kirkpatrick. *Handbook of Nonlinear Optics*. 2003.

[16] D G Mclean. Nonlinear absorption study of a C 60 -toluene solution. *Optics Letters*, 18(11):858–860, 1993.

[17] G Maria. Elementary processes with two quantum transitions. *Annalen der Physik*, 479(7):466–479, 2009.

[18] M Drobizhev, N S Makarov, T Hughes, and A Rebane. Resonance Enhancement of Two-Photon Absorption in Fluorescent Proteins. *The Journal of Physical Chemistry B*, 111(50):14051–14054, 2007.

[19] D A Jarvis, I J Hutchinson, D I Bower, and I M Ward. Characterization of biaxial orientation in poly (ethylene terephthalate) by means of refractive index measurements and Raman and infra-red spectroscopies. *Polymer*, 21(1):41–54, 1980.

[20] Eric L Buckland and Robert W Boyd. Electrostrictive contribution to the intensity-dependent refractive index of optical fibers. *Optics letters*, 21(15):1117–1119, 1996.

[21] Stephen Ducharme and Jack Feinberg. Speed of the photorefractive effect in a BaTiO3 single crystal. *Journal of applied physics*, 56(3):839–842, 1984.

[22] Robert L Swofford, M E Long, and A C Albrecht. C–H vibrational states of benzene, naphthalene, and anthracene in the visible region by thermal lensing spectroscopy and the local mode model. *The Journal of Chemical Physics*, 65(1):179–190, 1976.

[23] R DeSalvo, Mansoor Sheik-Bahae, A A Said, David J Hagan, and Eric W Van Stryland. Z-scan measurements of the anisotropy of nonlinear refraction and absorption in crystals. *Optics letters*, 18(3):194–196, 1993.

[24] J. P. Gordon and H. Kogelnik. PMD fundamentals: Polarization mode dispersion in optical fibers. *Proceedings of the National Academy of Sciences*, 97(9):4541–4550, 2000.

[25] Walter Koechner. Thermal lensing in a Nd: YAG laser rod. *Applied optics*, 9(11):2548–2553, 1970.

[26] Antoine Coyac, Laurent Hespel, Nicolas Riviere, and Xavier Briottet. Performance assessment of simulated 3D laser images using Geiger-mode avalanche

photo-diode: tests on simple synthetic scenarios. In *Electro-Optical and Infrared Systems: Technology and Applications XII; and Quantum Information Science and Technology*, volume 9648, page 964805. International Society for Optics and Photonics, 2015.

[27] I C Khoo, S L Zhuang, and S Shepard. Self-focusing of a low power cw laser beam via optically induced birefringence in a nematic liquid-crystal film. *Applied Physics Letters*, 39(12):937–940, 1981.

[28] Miles A. Dahlen. The Phthalocyanines. *Industrial and engernering chemistry*, 31(7):839–847, 1939.

[29] Katsuhiro Shirota, Tsuyoshi Eida, Takao Yamamoto, and Mayumi Yamamoto. Phthalocyanine dyes, jun 1992.

[30] Rongrong Chen, Haixia Li, Deryn Chu, and Guofeng Wang. Unraveling oxygen reduction reaction mechanisms on carbon-supported Fe-phthalocyanine and Co-phthalocyanine catalysts in alkaline solutions. *The Journal of Physical Chemistry C*, 113(48):20689–20697, 2009.

[31] Norman Herron, Galen D Stucky, and Chadwick A Tolman. Shape selectivity in hydrocarbon oxidations using zeolite encapsulated iron phthalocyanine catalysts. *Journal of the Chemical Society, Chemical Communications*, (20):1521–1522, 1986.

[32] Helen J Mackintosh, Peter M Budd, and Neil B McKeown. Catalysis by microporous phthalocyanine and porphyrin network polymers. *Journal of Materials Chemistry*, 18(5):573–578, 2008.

[33] Koichi Fukasawa and Hirohiko Ishii. Light emitting diode, jun 2004.

[34] J Simon and C Sirlin. Mesomorphic molecular materials for electronics, opto-electronics, iono-electronics: octaalkyl-phthalocyanine derivatives. *Pure and applied chemistry*, 61(9):1625–1629, 1989.

[35] David González-rodríguez, Tomás Torres, Dirk M Guldi, José Rivera, and Maria Ángeles. Subphthalocyanines : New Tuneable Tectons for Intramolecular Electron and Energy Transfer Processes. (2):1–36, 2004.

[36] M Vogel, S Doka, Ch Breyer, M Ch Lux-Steiner, and K Fostiropoulos. On the function of a bathocuproine buffer layer in organic photovoltaic cells. *Applied Physics Letters*, 89(16):163501, 2006.

[37] P Peumans and S R Forrest. Very-high-efficiency double-heterostructure copper phthalocyanine/C60 photovoltaic cells. *Applied Physics Letters*, 79(1):126–128, 2001.

[38] Raymond Bonnett. Photosensitizers of the porphyrin and phthalocyanine series for photodynamic therapy. *Chemical Society Reviews*, 24(1):19–33, 1995.

[39] John D Spikes. Phthalocyanines as photosensitizers in biological systems and for the photodynamic therapy of tumors. *Photochemistry and photobiology*, 43(6):691–699, 1986.

[40] Michael Hanack, Danilo Dini, Markus Barthel, and Sergej Vagin. Conjugated Macrocycles as Active Materials in Nonlinear Optical Processes : Optical Limiting Effect with Phthalocyanines and Related Compounds. *The Chemical Record*, 2(3):129–148, 2002.

[41] Jacek Waluk and Josef Michl. The Perimeter Model and Magnetic Circular Dichroism of Porphyrin Analogues. *Journal of Organic Chemistry*, 56(8):2729–2735, 1991.

[42] Gema De Torre, Monica Nicolau, and Tomas Torres. *Supramolecular Photosensitive and Eledroactive Materials*. Academic Press, 2001.

[43] Martin Gouterman. Spectra of Porphyrins. *Journal of Molecular Spectroscopy*, 6(1):138–&, 1961.

[44] David O Oluwole, Njemuwa Nwaji, Lindokhuhle C Nene, Lesedi Mokone, Edith Dube, and Tebello Nyokong. Novel nano-dyad of homoleptic sandwich-type phthalocyanines with nitrogen doped graphene quantum dots for nonlinear optics. *New Journal of Chemistry*, 42(12):10124–10133, 2018.

[45] Chen Jing, Ruolin Wang, Hanlin Ou, Ang Li, Yingli An, Shutao Guo, and Linqi Shi. Axial modification inhibited H-aggregation of phthalocyanines in polymeric micelles for enhanced PDT efficacy. *Chemical communications*, 54(32):3985–3988, 2018.

[46] Sean M. O'Flaherty, Stephanie V. Hold, Michael J. Cook, Tomas Torres, Yu Chen, Michael Hanack, and Werner J. Blau. Molecular engineering of peripherally and axially modified phthalocyanines for optical limiting and nonlinear optics. *Advanced Materials*, 15(1):19–32, 2003.

[47] Gerd Löbbert. Phthalocyanines. *Ullmann's Encyclopedia of Industrial Chemistry*, 2000.

[48] S Schumann, R A Hatton, and T S Jones. Organic photovoltaic devices based on water-soluble copper phthalocyanine. *The Journal of Physical Chemistry C*, 115(11):4916–4921, 2011.

[49] John Mack and Martin J Stillman. Transition Assignments in the Ultraviolet - Visible Absorption and Magnetic Circular Dichroism Spectra of Phthalocyanines. *Inorganic Chemistry*, 40(4):812–814, 2001.

[50] Grace N. Ngubeni, Jonathan Britton, John Mack, Edward New, Ian Hancox, Marc Walker, Tebello Nyokong, Tim S. Jones, and Samson Khene. Spectroscopic and nonlinear optical properties of the four positional isomers of 4α-(4-tert-butylphenoxy)phthalocyanine. *J. Mater. Chem. C*, 3:10705–10714, 2015.

[51] Marcel Louzada, Jonathan Britton, Tebello Nyokong, and Samson Khene. Solvent Effect on the Third-Order Nonlinear Optical Properties of α-and β-Tertbutyl Phenoxy-Substituted Tin (IV) Chloride Phthalocyanines. *The Journal of Physical Chemistry A*, 121(38):7165–7175, 2017.

[52] Mopelola Idowu and Tebello Nyokong. Synthesis, photophysics and photochemistry of tin(IV) phthalocyanine derivatives. *Journal of Photochemistry and Photobiology A: Chemistry*, 199(2-3):282–290, 2008.

[53] María a. Díaz-García. Nonlinear optical properties of phthalocyanines and related compounds. *Journal of Porphyrins and Phthalocyanines*, 13:652–667, 2009.

[54] Hari Singh Nalwa, Michael Hanack, Georg Pawlowski, and Michael Klaus Engel. Third-order nonlinear optical properties of porphyrazine, phthalocyanine and naphthalocyanine germanium derivatives: Demonstrating the effect of p-conjugation length on third-order optical nonlinearity of two-dimensional molecules. *Chemical Physics*, 245:17–26, 1999.

[55] Mitsuhiko Morisue, Kazuya Ogawa, Kenji Kamada, Koji Ohta, and Yoshiaki Kobuke. Strong two-photon and three-photon absorptions in the antiparallel dimer of a porphyrin–phthalocyanine tandem. *Chemical Communications*, 46(12):2121–2123, 2010.

[56] Reji Philip, M Ravikanth, and G Ravindra Kumar. Studies of third order optical nonlinearity in iron (III) phthalocyanine μ-oxo dimers using picosecond four-wave mixing. *Optics communications*, 165(1-3):91–97, 1999.

[57] Shaoli Fang, Hirokazu Tada, and Shinro Mashiko. Enhancement of the third-order nonlinear optical susceptibility in epitaxial vanadyl-phthalocyanine films grown on KBr. *Applied physics letters*, 69(6):767–769, 1996.

[58] D Mwanza, M Louzada, J Britton, E Sekhosana, S Khene, T Nyokong, and P Mashazi. The effect of the cobalt and manganese central metal ions on the nonlinear optical properties of tetra (4-propargyloxyphenoxy) phthalocyanines. *New Journal of Chemistry*, 42(12):9857–9864, 2018.

[59] Denisha Gounden, Grace N. Ngubeni, Marcel S. Louzada, Samson Khene, Jonathan Britton, and Nolwazi Nombona. Synthesis, spectroscopic and DFT characterization of 4β-(4-tert-Butylphenoxy)phthalocyanine Positional Isomers for Non-linear Optical Absorption. *South African Journal of Chemistry*, 70:49–59, 2017.

[60] John Mack, Martin J. Stillman, and Nagao Kobayashi. Application of MCD spectroscopy to porphyrinoids. *Coordination Chemistry Reviews*, 251(3-4):429–453, 2007.

[61] Edward A Ough, Martin J Stillman, and Katherine A M Creber. Absorption and magnetic circular dichroism spectra of nitrogen homologues of magnesium and zinc phthalocyanine. *Canadian journal of chemistry*, 71(11):1898–1909, 1993.

[62] Mansoor Sheik-Bahae, Ali A. Said, Tai Huei Wei, David J. Hagan, and E. W. Van Stryland. Sensitive Measurement of Optical Nonlinearities Using a Single Beam. *IEEE Journal of Quantum Electronics*, 26(4):760–769, 1990.

[63] G. Tsigaridas, I. Polyzos, P. Persephonis, and V. Giannetas. A novel approach for analyzing open Z-scan experiments. *Optics Communications*, 266(1):284–289, 2006.

[64] Ameenah Al-Ahmadi. *Quantum Dots: a variety of new applications*. BoD–Books on Demand, 2012.

[65] G DelaTorre, P Vazquez, F Agullo-Lopez, and T Torres. Role of Structural Factors in the Nonlinear Optical Properties of Phthalocyanines and Related Compounds. *Chemical Reviews*, 104(9):3723–3750, 2004.

[66] S. Venugopal Rao, P.T. Anusha, T. Shuvan Prashant, D. Swain, and Surya P. Tewari. Ultrafast nonlinear optical properties and excited state dynamics of phthalocyanine thin films. *Spie Opto*, 7935:793517–793517–11, 2011.

[67] A. Slodek, D. Wöhrle, J. J. Doyle, and W. Blau. Metal Complexes of Phthalocyanines in Polymers as Suitable Materials for Optical Limiting. *Macromol. Symp.*, 235:9–18, 2006.

[68] Danilo Dini, Mario J F Calvete, Michael Hanack, Richard G S Pong, Steven R. Flom, and James S. Shirk. Nonlinear transmission of a tetrabrominated naphthalocyaninato indium chloride. *Journal of Physical Chemistry B*, 110(25):12230–12239, 2006.

[69] E Saievariranizad, Z Dehghani, and M Nadafan. Measurement of Ferronematic Liquid Crystal Using a Single Beam Method. *International Journal of Engineering Sciences & Research Technology*, 3(2):1043–1047, 2014.

[70] G. Tsigaridas, M. Fakis, I. Polyzos, P. Persephonis, and V. Giannetas. Z-scan technique through beam radius measurements. *Applied Physics B: Lasers and Optics*, 76(1):83–86, 2003.

[71] Vijender Singh and Praveen Aghamkar. Z-scan: A simple technique for determination of third-order optical nonlinearity. *AIP Conference Proceedings*, 2142(1):1675, 2015.

[72] Mauro Falconieri, Elia Palange, and Hugo L. Fragnito. Achievement of $\lambda/4000$ phase distortion sensitivity in the measurement of optical nonlinearities by using a modulated Z-scan technique. *Journal of Optics A: Pure and Applied Optics*, 4(4):404–407, 2002.

[73] Qiguang Yang, Jae Tae Seo, Santiel Creekmore, Doyle Temple, Andy Mott, Namkung Min, Ki Pung Yoo, Sun Young Kim, and Sungsoo Jung. Distortions in Z-scan spectroscopy. *Applied Physics Letters*, 82(1):19–21, 2003.

[74] Soma Venugopal Rao, Puliparambil Thilakan Anusha, Turaga Shuvan Prashant, Debasis Swain, and Surya P. Tewari. Ultrafast Nonlinear Optical and Optical Limiting Properties of Phthalocyanine Thin Films Studied Using Z-Scan. *Materials Sciences and Applications*, 02(05):299–306, 2011.

[75] Zihui Chen, Xinyu Zhou, Zhongyu Li, Lihong Niu, Jiaxiang Yi, and Fushi Zhang. The third-order optical nonlinearities of thiophene-bearing phthalocyanines studied by Z-scan technique. *Journal of Photochemistry and Photobiology A: Chemistry*, 218(1):64–68, 2011.

[76] Raul Rangel-Rojo, Shinji Yamada, Hiro Matsuda, Hitoshi Kasai, Yuko Komai, Shuji Okada, Hidetoshi Oikawa, and Hachiro Nakanishi. Refractive third-order nonlinearity in vanadium-oxide phthalocyanine micro-crystals. *Japanese journal of applied physics*, 38(1R):69, 1999.

[77] Danilo Dini, Mario J F Calvete, Michael Hanack, Richard G S Pong, Steven R Flom, and James S Shirk. Nonlinear Transmission of a Tetrabrominated Naphthalocyaninato Indium Chloride. pages 12230–12239, 2006.

[78] Dieter Wöhrle, Günter Schnurpfeil, Sergey G. Makarov, Alexander Kazarin, and Olga N. Suvorova. Practical applications of phthalocyanines - from dyes and pigments to materials for optical, electronic and photo-electronic devices. *Macroheterocycles*, 5(3):191–202, 2012.

[79] Yaunli Zhang. *Nonlinear Optical Characterisation of Bithiophenes with Phosphorus containing substituents*. PhD thesis, The University of Alabama at Birmingham, 2013.

[80] Lee W. Tutt and Thomas F. Boggess. A review of optical limiting mechanisms and devices using organics, fullerenes, semiconductors and other materials. *Progress in Quantum Electronics*, 17(4):299–338, 1993.

[81] Tsvetan G. Gantchev, Johan E. Van Lier, and Darel J. Hunting. Molecular models of zinc phthalocyanines: Semi-empirical molecular orbital computations and physicochemical properties studied by molecular mechanics simulations. *Radiation Physics and Chemistry*, 72(2-3):367–379, 2005.

[82] Marius A Albota, Chris Xu, and Watt W Webb. Two-photon fluorescence excitation cross sections of biomolecular probes from 690 to 960 nm. *Applied Optics*, 37(31):7352–7356, 1998.

[83] Joseph W Perry, Kamjou Mansour, Seth R Marder, Daniel Alvarez, J Kelly, and Ingrid Choong. Enhanced Reverse Saturable Absorption and Optical Limiting in Heavy-Atom Substituted Phthalocyanines. *Optics letters*, 19(9):625–627, 1994.

[84] Haifeng Wang, Terry B. Huff, Daniel A. Zweifel, Wei He, Philip S. Low, Alexander Wei, and Ji Xin Cheng. In vitro and in vivo two-photon luminescence imaging of single gold nanorods. *Proceedings of the National Academy of Sciences of the United States of America*, 102(44):15752–15756, 2005.

[85] Tai-Huei Wei, Tzer-Hsiang Huang, and Tsai-Chuan Wen. Mechanism of reverse saturable absorption in chloro-aluminum phthalocyanine solution studied with Z-scan. *Chemical Physics Letters*, 314(5-6):403–410, 1999.

[86] Youssef Mir, Johan E. Van Lier, Jean François Allard, Denis Morris, and Daniel Houde. Two-photon absorption cross section of excited phthalocyanines by a femtosecond Ti-sapphire laser. *Photochemical and Photobiological Sciences*, 8(3):391–395, 2009.

[87] Kayode Sanusi, Edith Antunes, and Tebello Nyokong. Optical nonlinearities in non-peripherally substituted pyridyloxy phthalocyanines: A combined effect of symmetry, ring-strain and demetallation. *Dalton Transactions*, 43(3):999–1010, 2014.

[88] Kamjou Mansour, Daniel Alvarez Jr, Kelly J Perry, Ingrid Choong, Seth R Marder, and Joseph W Perry. Dynamics of optical limiting in heavy-atom-substituted phthalocyanines. In *Organic and Biological Optoelectronics*, volume 1853, pages 132–141. International Society for Optics and Photonics, 1993.

[89] Yunjing Li, Timothy M. Pritchett, Jiandong Huang, Meirong Ke, Pin Shao, and Wenfang Sun. Photophysics and nonlinear absorption of peripheral-substituted zinc phthalocyanines. *Journal of Physical Chemistry A*, 112(31):7200–7207, 2008.

[90] Tai Huei Wei, Tzer Hsiang Huang, and Mu Shih Lin. Signs of nonlinear refraction in chloroaluminum phthalocyanine solution. *Applied Physics Letters*, 72(20):2505–2507, 1998.

[91] R H Stolen and A Ashkin. Optical Kerr effect in glass waveguide. *Applied Physics Letters*, 22(6):294–296, 1973.

[92] Peng Wang, Shuang Zhang, Peiji Wu, Cheng Ye, Hongwei Liu, and Fu Xi. Optical limiting properties of optically active phthalocyanine derivatives. *Chemical Physics Letters*, 340(3-4):261–266, 2001.

[93] Chenjuan He, Yu Chen, Yuxin Nie, and Duoyuan Wang. Third order optical nonlinearities of eight-β-octa-octyloxy-phthalocyanines. *Optics Communications*, 271(1):253–256, 2007.

[94] D.J. Fox M.J. Frisch, G.W. Trucks, H.B. Schlegel, G.E. Scuseria, M.A. Robb, J.R. Cheeseman, G. Scalmani, V. Barone, B. Mennucci, G.A. Petersson, H. Nakatsuji, M. Caricato, X. Li, H.P. Hratchian, A.F. Izmaylov, J. Bloino, G. Zheng, J.L. Sonnenberg, M. Hada, M. Ehar. Guassian09, 2009.

[95] Chengteh Lee, Weitao Yang, and Robert G Parr. Development of the Colle-Salvetti correlation-energy formula into a functional of the electron density. *Physical review B*, 37(2):785, 1988.

[96] Thom H Dunning Jr. Gaussian basis sets for use in correlated molecular calculations. I. The atoms boron through neon and hydrogen. *The Journal of chemical physics*, 90(2):1007–1023, 1989.

[97] Takeshi Yanai, David P Tew, and Nicholas C Handy. A new hybrid exchange–correlation functional using the Coulomb-attenuating method (CAM-B3LYP). *Chemical Physics Letters*, 393(1-3):51–57, 2004.

[98] Yan Zhao and Donald G Truhlar. The M06 suite of density functionals for main group thermochemistry, thermochemical kinetics, noncovalent interactions, excited states, and transition elements: two new functionals and systematic testing of four M06-class functionals and 12 other function. *Theoretical Chemistry Accounts*, 120(1-3):215–241, 2008.

[99] Shaohui Zheng, Yongping Tian, Xue Chen, and Mengyue Xiao. Design of a sub phthalocyanine-based hybrid donor of photovoltaic materials and its theoretical investigation. In *AIP Conference Proceedings*, volume 1864, page 20003. AIP Publishing LLC, 2017.

[100] Alexey V Yagodin, Alexander G Martynov, Yulia G Gorbunova, and Aslan Yu Tsivadze. Synthesis, electronic structure and NH-tautomerism of novel mono- and dibenzoannelated phthalocyanines. *Dyes and Pigments*, page 108564, 2020.

[101] Ricky A. Kendall, Edoardo Aprà, David E. Bernholdt, Eric J. Bylaska, Michel Dupuis, George I. Fann, Robert J. Harrison, Jialin Ju, Jeffrey A. Nichols, Jarek Nieplocha, T. P. Straatsma, Theresa L. Windus, and Adrian T. Wong. High performance computational chemistry: an overview of NWChem a distributed parallel application. *Computer Physics Communications*, 128(1):260–283, 2000.

[102] Frank Neese. Software update: the ORCA program system, version 4.0. *Wiley Interdisciplinary Reviews: Computational Molecular Science*, 8(1):1–6, 2018.

[103] John Mack and Martin J Stillman. Band Deconvolution Analysis of the Absorption and Magnetic Circular Dichroism Spectral Data of ZnPc(-2) Recorded at Cryogenic Temperatures. *Journal of Physical Chemistry*, 99(20):7935–7945, 1995.

[104] Christopher J Cramer and Donald G Truhlar. Density functional theory for transition metals and transition metal chemistry. *Physical Chemistry Chemical Physics*, 11(46):10757–10816, 2009.

[105] Sudong Park and Byungki Ryu. Hybrid-Density Functional Theory Study on Band Structures of Tetradymite-Bi2Te3, Sb2Te3, Bi2Se3, and Sb2Se3 Thermoelectric Materials Sudong. *Journal of the Korean Pysical Society*, 68(1):115–120, 2016.

[106] C L Yaws. Correlation Constants for Chemical Compounds. *Chem. Eng*, 83(17):79–87, 1976.

[107] Jianji Wang, Yong Tian, Yang Zhao, and Kelei Zhuo. A volumetric and viscosity study for the mixtures of 1-n-butyl-3-methylimidazolium tetrafluoroborate ionic liquid with acetonitrile, dichloromethane, 2-butanone and N, N–dimethylformamide. *Green Chemistry*, 5(5):618–622, 2003.

[108] Abimbola Ogunsipe, Ji-Yao Chen, and Tebello Nyokong. Photophysical and photochemical studies of zinc (II) phthalocyanine derivatives—effects of substituents and solvents. *New Journal of Chemistry*, 28(7):822–827, 2004.

[109] Abimbola Ogunsipe and Tebello Nyokong. Photophysical and photochemical studies of sulphonated non-transition metal phthalocyanines in aqueous and non-aqueous media. *Journal of Photochemistry and Photobiology A: Chemistry*, 173(2):211–220, 2005.

[110] Abraham Savitzky and Marcel J E Golay. Smoothing and differentiation of data by simplified least squares procedures. *Analytical chemistry*, 36(8):1627–1639, 1964.

[111] Matthew Newville, Till Stensitzki, Daniel B Allen, Michal Rawlik, Antonino Ingargiola, and Andrew Nelson. LMFIT: Non-linear least-square minimization and curve-fitting for Python. *Astrophysics Source Code Library*, 2016.

[112] Rainer Storn and Kenneth Price. Differential evolution-a simple efficient adaptive scheme for global optimization. Technical report, 1995.

Appendix A

TD-DFT Calulations

Table 35: Calculated ground state absorption the αH_2Pc constitutional isomers using M06-HF.

Phthalocyanine	Transition	Assignment	Energy eV	Wavelength nm	Oscilator Strength	Exp. Wavelength nm	Exp. Log(e)
C4h	HOMO(149)->LUMO(150)	a->-a	1.7732	699.22	0.5471	720.5	5.14
	HOMO(149)->UMO(151)	a->-s	1.8513	669.7	0.5967	689.5	5.07
	OMO(145) ->UMO(151)	s->-s	3.85	322.04	0.2652	418	3.12
	OMO(145) ->LUMO(150)	s->-a	4.0204	308.39	0.1218	360	4.11
	OMO(147) ->LUMO(150)		4.2494	291.77	0.4429	322	4.8
C2v	HOMO(149)->LUMO(150)	a->-a	1.78	696	0.5484	723	5.16
	HOMO(149)->UMO(151)	a->-s	1.86	667	0.5961	691	5.11
	OMO(145) ->UMO(151)	s->-s	4.27	290	0.5821	419	3.08
	OMO(145) ->LUMO(150)	s->-a	4.36	284	0.15	361	4.12
	OMO(147) ->LUMO(150)		4.46	278	0.349	331	4.89
Cs	HOMO(149)->LUMO(150)	a->-a	1.77	702	0.5459	725	5.02
	HOMO(149)->UMO(151)	a->-s	1.85	670	0.5991	692.5	4.97
	OMO(145) ->UMO(151)	s->-s	4.25	292	0.5486	409	4.12
	OMO(145) ->LUMO(150)	s->-a	4.38	283	0.3139	325	4.61
D2h	HOMO(149)->LUMO(150)	a->-a	1.76	705	0.5343	728	5.03
	HOMO(149)->UMO(151)	a->-s	1.86	666	0.6012	695	4.99
	OMO(145) ->UMO(151)	s->-s	3.89	319	0.3671	409	4.12
	OMO(145) ->LUMO(150)	s->-a	4.27	290	0.6349	325	4.61

Table 36: Calculated ground state absorption for the βH_2Pc constitutional isomers using M06-HF.

Phthalocyanine	Transition	Assignment	Energy eV	Wavelength nm	Oscilator Strength	Exp. Wavelength nm	Exp. Log(e)
C4h	HOMO(149)->LUMO(150)	a->-a	1.83	677	0.509	704	5.01
	HOMO(149)->UMO(151)	a->-s	1.92	644	0.5673	668	4.93
	OMO(146) ->UMO(151)	s->-s	4.33	290	0.5926	401	4.01
	OMO(146) ->LUMO(150)	s->-a	4.44	286	1.1785	340	4.38
C2v	HOMO(149)->LUMO(150)	a->-a	1.83	677	0.509	704	4.69
	HOMO(149)->UMO(151)	a->-s	1.92	644	0.5673	668.5	4.62
	OMO(146) ->UMO(151)	s->-s	4.32	286	0.7151	399	4.02
	OMO(146) ->LUMO(150)	s->-a	4.44	278	1.0787	341	4.36
Cs	HOMO(149)->LUMO(150)	a->-a	1.82	677	0.5142	704	4.95
	HOMO(149)->UMO(151)	a->-s	1.92	644	0.5663	668.5	4.89
	OMO(146) ->UMO(151)	s->-s	4.33	285	0.7151	399	4.33
	OMO(146) ->LUMO(150)	s->-a	4.45	278	1.0787	342	4.66
D2h	HOMO(149)->LUMO(150)	a->-a	1.73	716	0.4945	705	4.85
	HOMO(149)->UMO(151)	a->-s	1.88	661	0.5512	670	4.8
	OMO(146) ->UMO(151)	s->-s	4.19	296	0.7057	399	4.42
	OMO(146) ->LUMO(150)	s->-a	4.35	285	1.1497	342	4.7

Table 37: Calculated ground state absorption for the αH_2Pc constitutional isomers using CAM-B3LYP.

Phthalocyanine	Transition	Assignment	Energy eV	Wavelength nm	Oscilator Strength	Exp. Wavelength nm	Exp. Log(e)
C4h	HOMO(149)->LUMO(150)	a->-a	1.87	663	0.5149	720.5	5.14
	HOMO(149)->UMO(151)	a->-s	1.91	650	0.5518	689.5	5.07
	OMO(147) ->LUMO(150)	s->-s	3.51	353	0.1187	418	3.12
	OMO(147) ->UMO(151)	s->-a	3.7	335	0.1812	360	4.11
C2v	HOMO(149)->LUMO(150)	a->-a	1.87	665	0.5131	723	5.16
	HOMO(149)->UMO(151)	a->-s	1.9	652	0.5519	691	5.11
	OMO(147) ->LUMO(150)	s->-s	3.61	343	0.0745	419	3.08
	OMO(147) ->UMO(151)	s->-a	3.71	334	0.1159	361	4.12
Cs	HOMO(149)->LUMO(150)	a->-a	1.86	666	0.5113	725	5.02
	HOMO(149)->UMO(151)	a->-s	1.9	652	0.556	692.5	4.97
	OMO(147) ->LUMO(150)	s->-s	3.52	352	0.0955	409	4.12
	OMO(147) ->UMO(151)	s->-a	3.66	339	0.1076	325	4.61
D2h	HOMO(149)->LUMO(150)	a->-a	1.85	670	0.5006	728	5.03
	HOMO(149)->UMO(151)	a->-s	1.92	646	0.5589	695	4.99
	OMO(147) ->LUMO(150)	s->-s	3.72	334	0.1935	409	4.12
	OMO(147) ->UMO(151)	s->-a	3.84	323	0.1782	325	4.61

Table 38: Calculated ground state absorption for the βH_2Pc constitutional isomers using CAM-B3LYP.

Phthalocyanine	Transition	Assignment	Energy eV	Wavelength nm	Oscilator Strength	Exp. Wavelength nm	Exp. Log(e)
C4h	HOMO(149)->LUMO(150)	a->-a	1.95	637	0.4786	704	5.01
	HOMO(149)->UMO(151)	a->-s	2	621	0.5197	668	4.93
	OMO(146) ->UMO(151)	s->-s	4	310	0.6444	401	4.01
	OMO(146) ->LUMO(150)	s->-a	4.08	304	0.943	340	4.38
C2v	HOMO(149)->LUMO(150)	a->-a	1.96	633	0.4778	704	4.69
	HOMO(149)->UMO(151)	a->-s	1.99	623	0.512	668.5	4.62
	HOMO(149)->UMO(152)		3.9	318	0.2912		
	OMO(146) ->UMO(151)	s->-s	3.93	315	0.1423	399	4.02
	OMO(146) ->LUMO(150)	s->-a	3.97	312	0.2574	341	4.36
Cs	HOMO(149)->LUMO(150)	a->-a	1.94	638	0.4821	704	4.95
	HOMO(149)->UMO(151)	a->-s	1.99	622	0.517	668.5	4.89
	HOMO(149)->UMO(152)		3.9	318	0.1635		
	OMO(146) ->UMO(151)	s->-s	3.96	313	0.2647	399	4.33
	OMO(146) ->LUMO(150)	s->-a	3.99	310	0.3619	342	4.66
D2h	HOMO(149)->LUMO(150)	a->-a	1.85	670	0.4602	705	4.85
	HOMO(149)->UMO(151)	a->-s	1.96	633	0.505	670	4.8
	OMO(146) ->UMO(151)	s->-s	3.83	324	0.2708	399	4.42
	OMO(146) ->LUMO(150)	s->-a	3.92	316	1.1052	342	4.7

Table 39: Calculated ground state absorption for the $\alpha SnCl_2Pc$ constitutional isomers using M06-HF.

Phthalocyanine	Transition	Assignment	Energy eV	Wavelength nm	Oscilator Strength	Exp. Wavelength nm	Exp. Log(e)
C4h	HOMO(311)->LUMO(312)	a->-a	1.7859	694.23	0.5278	739	5.29
	HOMO(311)->UMO(313)	a->-s	1.7945	690.91	0.6239	739	5.29
	OMO(300) ->LUMO(312)	s->-s	4.4852	276.43	0.0171	414	4.32
	OMO(300) ->UMO(313)	s->-a	4.7165	262.87	0.0112	339	4.93
C2v	HOMO(311)->LUMO(312)	a->-a	1.7794	696.78	0.635	741	5.49
	HOMO(311)->UMO(313)	a->-s	1.781	696.16	0.6299	741	5.49
	OMO(300) ->LUMO(312)	s->-s	3.9486	314	0.4378	420	4.21
	OMO(300) ->UMO(313)	s->-a	3.9573	313.31	0.5853	353	4.87
Cs	HOMO(311)->LUMO(312)	a->-a	1.7753	698.37	0.7266	741	4.91
	HOMO(311)->UMO(313)	a->-s	1.7852	694.5	0.546	741	4.91
	OMO(300) ->LUMO(312)	s->-s	3.9525	313.68	0.4767	414	4.29
	OMO(300) ->UMO(313)	s->-a	3.9631	312.85	0.571	357	4.38
D2h	HOMO(311)->LUMO(312)	a->-a	1.7671	701.63	0.8201	741	4.84
	HOMO(311)->UMO(313)	a->-s	1.7864	694.03	0.4592	741	4.84
	OMO(300) ->LUMO(312)	s->-s	3.9598	313.11	0.7329	414	4.35
	OMO(300) ->UMO(313)	s->-a	3.9699	312.31	0.441	350	4.3

Table 40: Calculated ground state absorption for the $\beta SnCl_2Pc$ constitutional isomers using M06-HF.

Phthalocyanine	Transition	Assignment	Energy eV	Wavelength nm	Oscilator Strength	Exp. Wavelength nm	Exp. Log(e)
C4h	HOMO(311)->LUMO(312)	a->-a	1.8031	687.63	0.6686	711	5.29
	HOMO(311)->UMO(313)	a->-s	1.8032	687.57	0.6683	711	5.29
	OMO(302) ->LUMO(312)	s->-s	3.9587	313.2	0.3926	414	4.32
	OMO(302) ->UMO(313)	s->-a	3.9592	313.15	0.3974	339	4.93
C2v	HOMO(311)->LUMO(312)	a->-a	1.8081	685.71	0.6658	711	5.6
	HOMO(311)->UMO(313)	a->-s	1.8156	682.86	0.665	711	5.6
	OMO(302) ->LUMO(312)	s->-s	3.946	314.2	0.1608	420	4.79
	OMO(302) ->UMO(313)	s->-a	3.9918	310.59	0.212	361	4.96
Cs	HOMO(311)->LUMO(312)	a->-a	1.7897	692.77	0.6487	711	5.41
	HOMO(311)->UMO(313)	a->-s	1.825	679.37	0.6832	711	5.41
	OMO(302) ->LUMO(312)	s->-s	3.9246	315.92	0.378	420	4.54
	OMO(302) ->UMO(313)	s->-a	3.9801	311.51	0.2029	361	4.76
D2h	HOMO(311)->LUMO(312)	a->-a	1.7673	701.53	0.6304	711	5.22
	HOMO(311)->UMO(313)	a->-s	1.8394	674.04	0.7008	711	5.22
	OMO(302) ->LUMO(312)	s->-s	3.9063	317.4	0.4076	454	4.56
	OMO(302) ->UMO(313)	s->-a	4.0431	306.65	0.0235	353	4.71

Table 41: Calculated ground state absorption for the $\alpha SnCl_2Pc$ constitutional isomers using CAM-B3LYP.

Phthalocyanine	Transition	Assignment	Energy eV	Wavelength nm	Oscilator Strength	Exp. Wavelength nm	Exp. Log(e)
C4h	HOMO(311)->LUMO(312)	a->-a	1.867	664.1	0.49	739	5.29
	HOMO(311)->UMO(313)	a->-s	1.880	659.4	0.61	739	5.29
	OMO(300) ->LUMO(312)	s->-s	3.776	328.3	0.12	414	4.32
	OMO(300) ->UMO(313)	s->-a	3.719	333.4	0.24	339	4.93
C2v	HOMO(311)->LUMO(312)	a->-a	1.856	668.2	0.60	741	5.49
	HOMO(311)->UMO(313)	a->-s	1.856	668.1	0.60	741	5.49
	OMO(300) ->LUMO(312)	s->-s	3.571	347.2	0.18	420	4.21
	OMO(300) ->UMO(313)	s->-a	3.617	342.8	0.02	353	4.87
Cs	HOMO(311)->LUMO(312)	a->-a	1.853	669.0	0.70	741	4.91
	HOMO(311)->UMO(313)	a->-s	1.858	667.2	0.52	741	4.91
	OMO(300) ->LUMO(312)	s->-s	3.731	332.3	0.12	414	4.29
	OMO(300) ->UMO(313)	s->-a	3.765	329.3	0.02	357	4.38
D2h	HOMO(311)->LUMO(312)	a->-a	1.847	671.4	0.79	741	4.84
	HOMO(311)->UMO(313)	a->-s	1.857	667.7	0.43	741	4.84
	OMO(300) ->LUMO(312)	s->-s	3.701	335.0	0.19	414	4.35
	OMO(300) ->UMO(313)	s->-a	3.775	328.5	0.02	350	4.3

Table 42: Calculated ground state absorption for the $\beta SnCl_2Pc$ constitutional isomers using CAM-B3LYP.

Phthalocyanine	Transition	Assignment	Energy eV	Wavelength nm	Oscilator Strength	Exp. Wavelength nm	Exp. Log(e)
C4h	HOMO(311)->LUMO(312)	a->-a	1.8951	654.24	0.6368	711	5.29
	HOMO(311)->UMO(313)	a->-s	1.8952	654.18	0.6364	711	5.29
	OMO(302) ->LUMO(312)	s->-s	3.4394	360.48	0.1136	414	4.32
	OMO(302) ->UMO(313)	s->-a	3.4407	360.34	0.115	339	4.93
C2v	HOMO(311)->LUMO(312)	a->-a	1.8984	653.08	0.6317	711	5.6
	HOMO(311)->UMO(313)	a->-s	1.9012	652.15	0.6282	711	5.6
	OMO(302) ->LUMO(312)	s->-s	3.4099	363.6	0.0026	420	4.79
	OMO(302) ->UMO(313)	s->-a	3.4301	361.46	0.0019	361	4.96
Cs	HOMO(311)->LUMO(312)	a->-a	1.8787	659.95	0.6059	711	5.41
	HOMO(311)->UMO(313)	a->-s	1.916	647.09	0.6572	711	5.41
	OMO(302) ->LUMO(312)	s->-s	3.4213	362.39	0.0079	420	4.54
	OMO(302) ->UMO(313)	s->-a	3.443	360.1	0.0948	361	4.76
D2h	HOMO(311)->LUMO(312)	a->-a	1.8579	667.34	0.5791	711	5.22
	HOMO(311)->UMO(313)	a->-s	1.9338	641.15	0.684	711	5.22
	OMO(302) ->LUMO(312)	s->-s	3.4316	361.3	0.0542	454	4.56
	OMO(302) ->UMO(313)	s->-a	3.4445	359.95	0.1324	353	4.71

Appendix B

Code

The first code used in this work is an implementation of Tsigaridas's open aperture z-scan fitting and a general implementation of a closed aperture z-scan fit. The code asks for a parent directory in which the results of both are separated into different folders. The code reads the laser pulse energy from the name of each open apeture data set and expects a corresponding closed aperture data set with the same energy. The results from the fit are saved in the parent folder, along with a text document listing the NLO properties that were calculated. The code used in this work is shown in Listing 1.

```
import pandas as pd
import numpy as np
from scipy.optimize import curve_fit
import matplotlib.pyplot as plt
import math as m
import os
from scipy.signal import savgol_filter
import glob
import gc
from itertools import cycle
import tkinter as tk
from tkinter import filedialog

font = {'family' :'serif',
        'color':  'black',
        'weight': 'normal',
        'size': 12,
```

```
18         }
19
20 tk.Tk().withdraw() #Folder with results
21 path= tk.filedialog.askdirectory()
22
23
24 frac=np.arange(1,5)
25 Isomers=['Alpha','Beta']
26 #print(frac)
27 isomers=['\\alpha','\\beta']
28 label=['C$_{4h}$','C$_{2v}$','C$_{s}$','D$_{2h}$']
29 Concentrations=np.empty((2,4,4))
30
31 #pmill = pd.read_csv(('C:/Users/General/GoogleD work/Coding/Z-Scan/
      Permille.csv'), header=None)
32 Conc = pd.read_csv((path+'Concentrations.csv'),delimiter=',', header
      =None)
33 #Seperate all concentraotions into an array [Isomer, Power, Fraction
      ]
34 for FRAC in np.arange(4):
35     conc=Conc.iloc[:,10+FRAC]
36     for ISO in np.arange(2):
37         for POW in np.arange(4):
38 #             print(conc[POW +1+(5*ISO)])
39             Concentrations[ISO,POW,FRAC]=conc[POW +1+(5*ISO)]
40 MAC=np.empty((8))#create array for molar attenuation coef at 532 nm
      [a1,a2,a3,a4,b1,b2,b3,b4]
41 Acs=(Conc.iloc[:,6])
42 myIterator = cycle(['t','b'])
43 f= open(path+"Latex.txt","a+")
44 f.write('\\clearpage\n')
45 for ISO in np.arange(4):
46     MAC[ISO]=Acs[ISO+1]
47     MAC[ISO+4]=Acs[ISO+6]
48 results=np.empty((16,10))
49 for number,Iso in enumerate(Isomers):
50     for ik in frac:
51         num=ik
52         IND=number+ik
53         print(IND)
54         Cpath=path+Iso+'/Frac'+ str(num) +'/Closed/'
55         Opath=path+Iso+'/Frac'+ str(num) +'/Open/'
56         Cfiles=glob.glob(Cpath+'./*')
57         Ofiles=glob.glob(Opath+'./*')
58 #         Ofiles=Ofiles[:-1]
59         Energy=np.empty_like(Ofiles)
60         sep='F'
61         rest=np.empty_like(Ofiles)
62         for p,n, in enumerate(Ofiles):
63             rest[p]= os.path.basename(Ofiles[p]).split(sep,1)[0]
64             rest[p]=rest[p].replace(',','.')
```

```
65              Energy[p] =np.float_(rest[p])
66          print(Energy)
67          os.chdir(path+Iso+'/Frac'+str(ik))
68          n2S=np.empty((np.size(Ofiles),2))
69          b2S=np.empty((np.size(Ofiles),4))
70          for n in np.arange(len(Ofiles)):
71              data = pd.read_csv((Ofiles[n]),delim_whitespace=True,
    header=None)
72              print(n)
73              d2=data.iloc[:,1]
74              Tm=d2.tolist()#This is the amp(ydata)
75              d1=data.iloc[:,0]
76              zmm=d1.tolist()#This is The z value (xdata)
77              z=np.array(zmm)/1000
78              z0I = Tm.index(min(Tm))
79              z0=z[z0I]
80              ####These two just used to cal concentration or
    absorption, depending on the measurents takem
81              cmol = Concentrations[number, n, ik-1]
82              MolarArrCoeff = MAC[IND] #[Mol/m]
83              ab = MolarArrCoeff*(0.2)*cmol #[cm^-1] due to cuvet
    being 2 mm wide
84              ######
85              wvl = (532*(10**(-9))) ##wavelength [m]
86              k = (1/wvl) ##wavenumber 1/m
87              alphac = 0.2 ## base absorption at laser wavelength in m
    ^-1
88              alpha = alphac*100
89              Refrac = 1.49 ## refractive index of solvent [unitless]
90              L = 2*(10**(-3)) ## sample length [m]
91              E= float(Energy[n])*10**(-6)#Energy of each pulse [J]
92              P0=E/(10*10**(-9))#Power of pulse [W(J/s)]
93              Leff = (1- np.exp(-alpha*L))/alpha
94              esu = 1.39555*10**(-8)#convertion ratio to electrostatic
     units from m2V2
95              eta0 = 8.85*10**(-12) #permitivity of free space
96              c= 2.998*10**8 #speed of light in vac [m/s]
97              lff = ((Refrac**2) +2)/3# Lorentz field factor (normaly
    just 'f')
98              NA = 6.02*10**23 #Avogadro's number
99              #Gp = np.arctan(z/zr) ##the gouy shift(not used but kept
     in case)
100
101             ##pre fitted constants from Tsi for a gaussian pulse
102             a0 =  15.66
103             a1 = -37.45
104             a2 =  30.76
105             a3 = -8.97
106             c0 = -2.301
107             c1 =  2.156
108             c2 = -1.563
```

```
109             ####################################
110             C1 = [index for index, value in enumerate(Tm) if value
    >= 0.75]#find the Tm idesis
111             C2 = [index for index, value in enumerate(Tm) if value
    <= 0.75]
112             q0=np.zeros([np.size(Tm)]) #create an empty array for q0
113
114             ##Bi conditional q0 values dep on absorption
115             for i in np.arange(0,np.size(C1)):
116                 q0[C1[i]]=a0 + a1*Tm[C1[i]] + a2*Tm[C1[i]]**2 +a3*Tm
    [C1[i]]**3
117             for i in np.arange(0,np.size(C2)):
118                 q0[C2[i]]=c0 + c1*Tm[C2[i]]**c2
119
120             #The function of the fitted data
121             def Zfun(z,Q0,zr):
122                 return (Q0/(1+(((z-z0)**2)/(zr)**2)) )
123
124             Fit = curve_fit(Zfun,z,q0,bounds=(0, np.inf))
125
126             zr=(Fit[0][1])
127             Zi=np.zeros(np.size(z))#making an empty array for next
    step
128             for i in np.arange(0,np.size(z)):   #re-evaluate the eqn
     with fitted values
129                 Zi[i] = Zfun(z[i],Fit[0][0],(Fit[0][1]))
130
131             fig1=plt.figure()
132             ax1=fig1.add_subplot(111)
133             ax1.scatter(z,q0,marker=".",c='xkcd:charcoal grey')
134             ax1.plot(z,Zi,c='xkcd:nice blue',label='q0')
135             plt.xlabel('Z [m]',font)
136             plt.ylabel('q0',font)
137             handles1, labels1 = ax1.get_legend_handles_labels()
138             ax1.legend(handles1, labels1)
139 #             fig1.savefig(Energy[n].replace('.',',')+'F'+str(n+1)+'O
    '+'.png', format='png', dpi=1200)
140             fig1.clf()
141             plt.close(fig1)
142             gc.collect()
143             beta= (wvl*Fit[0][0]*(Fit[0][1]))/(2*P0*Leff) #cm/W
144             ImX=(0.001)*((Refrac**2)*eta0*(c**2)*wvl*beta)/(4*(np.pi
    )**2)#esu units taken from R.Boyd
145 #             ImX(stnunits= ((Refrac**2)*eta0*c*wvl*beta)/(2*np.pi) #
    Imaginarry c.o. succeptability. from DOI: 10.1039/B210707D
146             ImY = ImX/((1ff**4)*cmol*NA)
147             I0=(2*P0)/(zr*wvl) #Intesity at focus
148             ###function for open appeture
149             #Q0 = (2*beta*P0*Leff)/(wvl*zr)
150
151             #
```

```
152             ###function for closed appeture
153         #
    ------------------------------------------------------------------------------

154
155             data2 = pd.read_csv((Cfiles[n*2]),delim_whitespace=True,
     header=None)
156             Para =  pd.read_csv((Cfiles[n*2 +1]),delimiter=('S'),
    header=None)
157             d2=data2.iloc[:,1]
158             CTmr=d2.tolist()#This is the amp(ydata)
159             CTm=  savgol_filter(CTmr, 7, 2)
160             d1=data2.iloc[:,0]
161             Czmm=d1.tolist()#This is The z value (xdata)
162             zr=zr
163             z2=np.array(Czmm)/1000
164         #   next bit creats offset for the zero point
165             z0I = CTmr.index(min(CTmr))
166             z0m=z2[z0I]
167             z0L = CTmr.index(max(CTmr))
168             z0M=z2[z0L]
169             diff=np.round((np.abs(z0L-z0I))/2)
170             mv=z0L+diff
171     #         zC=z2[np.int(mv)]
172             zC=z0
173     #         Z2 cahnges by 0.005 per index
174     #         65 is the index of the minima of the fit curve
175     #         0.0015*6 is the diff detwean max and min of fit
176
177             zC = np.abs(zC)
178             z2=(np.array(Czmm)/1000)+zC
179     #         print('Beta=',beta)
180             S=Para.iloc[0,1]
181
182             #making an empty array for next step
183             CZi=np.zeros(np.size(z2))
184             def CZFun(z2,Phi):
185 #                print(Phi)
186                 return 1 + ((4*Phi*(z2/(zr)))/(((z2/(zr))**2 +9)*((
    z2/(zr))**2 +1)))
187             #for i in np.arange(0,np.size(z2)):   #equation that is
    fitted
188
189             FitC = curve_fit(CZFun,z2,CTm,bounds=(-np.inf, np.inf))
190             Phi=(FitC[0][0])
191
192             ##making an empty array for next step
193             for i in np.arange(0,np.size(z2)):   #re-evaluate the
    eqn with fitted values
194                 CZi[i] = CZFun(z2[i],FitC[0][0])
195     #
```

```
196          #         DeltaTP=0.406 * (1-S)**0.25 *(2pi/lambda)*n2*I0*Leff
197          #         1/n2=0.406 * (1-S)**0.25 *(2pi/lambda)*I0*Leff/Delt
198          #         1/n2=0.406 * (1-S)**0.25 *(2pi/lambda)*(2*P0/np.pi*wo
         **2)*Leff/Delt
199          #         Eqn relating n2 to the height diff in closed apeture
         refraction
200          #         From "Measurement of Ferronematic Liquid Crystal Using
         a Single Beam Method"
201          #         By E. SaievarIranizad, Z. Dehghani and M. Nadafan
202          #         thus we make a second fitted refraction index we will
         call n2P
203                   DeltaTP=max(CTmr)-min(CTmr)
204
205                   #Peak measuring does not contain a means of determing th
          sign of n2 so it must be done manualy
206                   nsign=0
207                   if CTmr.index(min(CTmr))-CTmr.index(max(CTmr))<0:
208                       nsign=1
209                   else:
210                       nsign=-1
211
212                   PhiP=DeltaTP/(0.406*(1-S)**0.25)*nsign
213                   #n2p=[m]/[W] UNITS
214                   n2P=(wvl*PhiP)/(2*np.pi*I0*Leff) #cm^2/W
215                   n2P2=DeltaTP/((0.406*(1-S)**0.25)*(2*np.pi/wvl)*(2*P0/(
         zr*wvl))*Leff)
216                   CzP=np.zeros(np.size(z2))
217
218
219
220                   for i in np.arange(0,np.size(z2)):   #re-evaluate the
         eqn with fitted values
221                       CzP[i] = CZFun(z2[i],PhiP)
222
223                   ReX=0.0001*((Refrac**2)*eta0*(c**2)*n2P)/((np.pi)) #Esu
         UNTIS
224                   ReY = ReX/((lff**4)*cmol*NA)
225                   Dn=I0*n2P
226                   W=Dn/(wvl*ab)
227                   fig2=plt.figure()
228                   ax2=fig2.add_subplot(111)
229                   plt.scatter((z2),CTm,marker=".",c='xkcd:charcoal grey')
230                   plt.plot((z2),CZi,c='xkcd:nice blue',label='Curve Fit')
231                   plt.plot((z2),CzP,c='xkcd:deep orange',label='Peak Fit')
232                   plt.xlabel('Z [m]',font)
233                   plt.ylabel('Normalised Transmittance',font)
234                   handles2, labels2 = ax2.get_legend_handles_labels()
235                   ax2.legend(handles2, labels2)
236                   fig2.savefig(Energy[n].replace('.',',')+'F'+str(n+1)+'C'
```

```
      +'.png', format='png', dpi=1200)
237               plt.close(fig2)
238               fig2.clf()
239               plt.close(fig2)
240               gc.collect()
241
242               n2=(wvl*Phi)/(2*np.pi*I0*Leff*(1-S)**0.25)
243               n2S[n,0]=n2
244               n2S[n,1]=n2P
245               b2S[n,0]=zr
246               b2S[n,1]=beta
247               b2S[n,2]=ImX
248               b2S[n,3]=ImY
249               print('n=',n,'ik=',ik,n+(ik-1)*4)
250               results[n+(ik-1)*4 ,0]=I0
251               results[n+(ik-1)*4,5]=n2P
252               results[n+(ik-1)*4,1]=zr
253               results[n+(ik-1)*4,2]=beta
254               results[n+(ik-1)*4,3]=ImX
255               results[n+(ik-1)*4,4]=ImY
256               results[n+(ik-1)*4,6]=ReX
257               results[n+(ik-1)*4,7]=ReY
258               results[n+(ik-1)*4,8]=Dn
259               results[n+(ik-1)*4,9]=W
260               np.savetxt("N2.txt",n2S)
261               np.savetxt("Beta.txt",b2S)
262 #              print("n2P2=",n2P2,"Phi=",Phi)
263 #              print("n2P=",n2P,"PhiP=",PhiP)
264               f.write('\\begin{figure}['+str(next(myIterator))+']\n\\
      includegraphics[height=0.4\\textheight,width=\\linewidth]{Images/
      Zscan/Snpc/'+str(Iso)+'/'+'Frac'+str(ik)+'/'+Energy[n].replace('.
      ',',')+'F'+str(n+1)+'O'+'.png}\n\\caption{Open apeture Zscan of
      the '+label[num-1]+' isomer of the $'+isomers[number]+'$SnCl\\
      textsubscript{2}Pc at '+str(np.around(I0/1e12,decimals=1))+'$\\
      times10^{12}$ W.m$^{-2}$.}\n\label{fig:Sn'+str(Iso)+str(ik)+
      Energy[n].replace('.',',')+'Ouj}\n\end{figure}\n')
265               f.write('\\begin{figure}['+str(next(myIterator))+']\n\\
      includegraphics[height=0.4\\textheight,width=\\linewidth]{Images/
      Zscan/Snpc/'+str(Iso)+'/'+'Frac'+str(ik)+'/'+Energy[n].replace('.
      ',',')+'F'+str(n+1)+'C'+'.png}\n\\caption{Closed apeture Zscan of
       the '+label[num-1]+' isomer of the $'+isomers[number]+'$SnCl\\
      textsubscript{2}Pc at '+str(np.around(I0/1e12,decimals=1))+'$\\
      times10^{12}$ W.m$^{-2}$.}\n\label{fig:Sn'+str(Iso)+str(ik)+
      Energy[n].replace('.',',')+'Cuj}\n\end{figure}\n')
266      np.savetxt(path+str(Iso)+'/'+str(Iso)+'Results.txt',results)
267      f.write('\\clearpage\n')
268 f.close()
```

Listing 1: Parametric model

The second code used in this work has two sub-functions, OA and OAp2. Both require 12 inputs: Beam energy, σ_0, σ_1, σ_2, σ_{TPA}, τ_{21}, τ_{23} , τ_{31}, concentration of solution (or active species crystal density), Z_R, position relative to focus (units m), and photon count at the position. OA returns the ratio of photons transmitted relative to photon count at the position. OAp2 returns the ratio of photons transmitted relative to photon count at the position, the final populations of each state, and the relative absorption due to each state. Due to the limitations on data transfer between each device, OA should be used to solve the unknown variables and OAp2 should only be used once all the inputs are determined. The code used in this work is shown in Listing 2.

```
1 import pyopencl as cl
2 import numpy as np
3 import time
4 from scipy import signal
5 import matplotlib as mpl
6 import pyopencl.cltypes
7 import matplotlib.pyplot as plt
```

```
 8 import math as m
 9 from vpulse import vpulse
10 import os
11 import matplotlib.animation as animation
12 import time
13 from vpulse import vpulse
14 #
15 #
16 #
      #=============================================================================

17 #Energies=[4.586e-05]
18 #Sigmas = [0.0869,0.17316967493463287, 0.4425360786610155,
      250.33147339267891
19 #Taus    =[5*10**(-9),5*10**(-4),5*10**(-7)]
20 #Zr      =0.00135
21 #os.environ['PYOPENCL_COMPILER_OUTPUT'] = '1'
22 #Concentrations=0.0297
23 #
      ###============================================================================

24 ###
25 ###
26 ###def Openapp(Powers,Sigmas,Taus, Concentrations,Zr):
27 #
      ###============================================================================

28 #Zpos=np.arange(-40,40,1)
29 #
      ##============================================================================

30 #VP=vpulse(Zr,Zpos,Energies[1],15,10e-9)
31 KERNEL_CODE ="""
32 #define N %(mat_size)d
33 __kernel
34 void dmv_cl(__global float *I,global float *RC, __global float *N1,
      __global float *N2,  __global float *N3,__global float *N10,
      __global float *N20, __global float *N30, __global float *IO,
      __global float *TPA,__global float *RSA,__global float *RTA)
35 {
36   int xid = get_global_id(0);
37   int yid = get_global_id(1);
38   int sx  = get_global_size(0);
39   int sy  = get_global_size(1);
40
41   int sv  = sy*sx;
42   int vid = sx*yid +xid;
43
44   TPA[vid]=0;
45   RSA[vid]=0;
46   RTA[vid]=0;
```

```
47  I[vid]=0;
48
49  float N1k1 ;float N1k2 ;float N1k3 ;float N1k4;
50  float N2k1 ;float N2k2 ;float N2k3 ;float N2k4;
51  float N3k1 ;float N3k2 ;float N3k3 ;float N3k4;
52  float N1tem;float N2tem;float N3tem;float Totl;
53  float Corr ;float Item ;
54
55  IO[vid]  = 0;
56  //Move populations into their buffers
57  N1O[sy*yid +xid]=N1[vid];
58  N2O[sy*yid +xid]=0;
59  N3O[sy*yid +xid]=0;
60
61  for (int j = 0; j < RC[8]-1; ++j)
62  {
63      int tid = j*sx*sy +sx*yid +xid;
64
65      // make the time index a float for equations
66      float i = j;
67      float M =1;
68
69      N1k1= -RC[0]*IO[tid]*IO[tid]*  N1O[tid]                          -RC
    [1]*IO[tid]   *  N1O[tid]                        +RC[4]* N2O[tid]
                        +RC[5]* N3O[tid];
70      N1k2= -RC[0]*IO[tid]*IO[tid]*( N1O[tid] + N1k1*(RC[7]/2))  -RC
    [1]*IO[tid]   * (N1O[tid] + N1k1*(RC[7]/2))  +RC[4]*(N2O[tid]  +
    N1k1*(RC[7]/2))    +RC[5]*(N3O[tid]  + N1k1*(RC[7]/2));
71      N1k3= -RC[0]*IO[tid]*IO[tid]*( N1O[tid] + N1k2*(RC[7]/2))  -RC
    [1]*IO[tid]   * (N1O[tid] + N1k2*(RC[7]/2))  +RC[4]*(N2O[tid]  +
    N1k2*(RC[7]/2))    +RC[5]*(N3O[tid]  + N1k2*(RC[7]/2));
72      N1k4= -RC[0]*IO[tid]*IO[tid]*( N1O[tid] + N1k3*(RC[7])  )  -RC
    [1]*IO[tid]   * (N1O[tid] + N1k3*(RC[7])  )  +RC[4]*(N2O[tid]  +
    N1k3*(RC[7]))      +RC[5]*(N3O[tid]  + N1k3*(RC[7]));
73
74      N2k1=  RC[0]*IO[tid]*IO[tid]*  N1O[tid]                          +RC
    [1]*IO[tid]   * N1O[tid]                        -RC[4]* N2O[tid]
                        -RC[6]* N2O[tid];
75      N2k2=  RC[0]*IO[tid]*IO[tid]*( N1O[tid] + N2k2*(RC[7]/2))  +RC
    [1]*IO[tid]   *( N1O[tid] + N2k1*(RC[7]/2))  -RC[4]*(N2O[tid]  +
    N2k1*(RC[7]/2))    -RC[6]*(N2O[tid]  + N2k1*(RC[7]/2));
76      N2k3=  RC[0]*IO[tid]*IO[tid]*( N1O[tid] + N2k2*(RC[7]/2))  +RC
    [1]*IO[tid]   *( N1O[tid] + N2k2*(RC[7]/2))  -RC[4]*(N2O[tid]  +
    N2k2*(RC[7]/2))    -RC[6]*(N2O[tid]  + N2k2*(RC[7]/2));
77      N2k4=  RC[0]*IO[tid]*IO[tid]*( N1O[tid] + N2k3*(RC[7])  )  +RC
    [1]*IO[tid]   *( N1O[tid] + N2k3*(RC[7])  )  -RC[4]*(N2O[tid]  +
    N2k3*(RC[7]))      -RC[6]*(N2O[tid]  + N2k3*(RC[7])) ;
78
79      N3k1=                                                          RC
    [6]* N2O[tid]                                -RC[5]* N3O[tid];
80      N3k2=                                                          RC
```

```
[6]*(N2O[tid]             + N3k1*(RC[7]/2)) -RC[5]*(N3O[tid]  +
N3k1*(RC[7]/2));
81      N3k3=                                                    RC
[6]*(N2O[tid]             + N3k2*(RC[7]/2)) -RC[5]*(N3O[tid]  +
N3k2*(RC[7]/2));
82      N3k4=                                                    RC
[6]*(N2O[tid]             + N3k3*(RC[7]))   -RC[5]*(N3O[tid]  +
N3k3*(RC[7]));
83
84      N1tem= N1O[tid] + (RC[7]/6)*((N1k1 + 2*N1k2 + 2*N1k3 + N1k4));
85      N2tem= N2O[tid] + (RC[7]/6)*((N2k1 + 2*N2k2 + 2*N2k3 + N2k4));
86      N3tem= N3O[tid] + (RC[7]/6)*((N3k1 + 2*N3k2 + 2*N3k3 + N3k4));
87
88      N1O[tid +sv] = N1tem;
89      N2O[tid +sv] = N2tem;
90      N3O[tid +sv] = N3tem;
91
92      //Subtraction step
93
94      //IO[tid+sv]=1;//IO[tid]+1;//-RC[0]*IO[tid]*IO[tid]* N1O[tid]
    - IO[tid]* N1O[tid]*RC[1] - RC[2]*IO[tid]* N2O[tid] - RC[3]*IO[
    tid]* N3O[tid];
95
96      //2dguassian  = (1)*(exp(-( ((x-x0)^2/2sigmax^2)  +  ((y-y0)
    ^2/2sigmay^2) )))  ;
97      //IO[tid]= (1)*(exp(-( (( (i-RC[8]/2)*(i-RC[8]/2))/(RC[9]*RC
    [9]*2))  +  (((yid-sy/2)*(yid-sy/2))/(2*RC[10]*RC[10]) ))));
98      // ((1)*(exp(-( (( (i-RC[8]/2)*(i-RC[8]/2))/(RC[9]*RC[9]*2))
    +  (((yid-sy/2)*(yid-sy/2))/(2*RC[10]*RC[10]) )))));
99      //(xid %% sx >= 1) returns 1 on all other indecis with xid=sx
    so left most column =0 , the flip flop need all those values to
    be written one up
100     //(xid %% sx <= 1)    Yields  [10000000] , the reverse of the
    previous
101     //                              |10000000|
102     //                              |10000000|
103     //                              |10000000|
104     //                              [........]
105     //(xid %% sx == sx-1) Yields  [00000001]
106     //                              |00000001|
107     //                              |00000001|
108     //                              |00000001|
109     //                              [........]
110
111
112     IO[(xid %% sx >= 1)*(sv * (j+1) + yid * sx + xid-1) +(xid %%
    sx < 1)*(sv * (j+1) + yid * sx + xid + sx-1) ] = IO[(sv *j  + yid
     * sx + xid)];
113
114     //Record Absorption of each species
115     TPA[vid]=TPA[vid]+ RC[0]*IO[tid]*IO[tid]* N1O[tid];
```

```
116       RSA[vid]=RSA[vid]+ RC[2]*IO[tid]*          N2O[tid];
117       RTA[vid]=RTA[vid]+ RC[3]*IO[tid]*          N3O[tid];
118       //Catch pulse in dedicated buffer, though we only care about
      the final slice
119       I[vid]=I[vid]+IO[vid+j*sx*sy];
120       //Change pulse due to pops
121       IO[tid +sv]=IO[tid + sv]-RC[0]*IO[tid+sv]*IO[tid+sv]* N1O[tid]
       - IO[tid+sv]* N1O[tid]*RC[1]- RC[2]*IO[tid+sv]* N2O[tid] - RC
      [3]*IO[tid+sv]* N3O[tid];
122       //Insert guassian at time/pos
123       IO[tid + sv]=IO[tid + sv]*(xid %% sx != sx-1) +(xid %% sx ==
      sx-1)*((RC[11]/(2*3.14159*RC[10]*RC[9]))*(exp(-(((i-RC[8]/2)*(i-
      RC[8]/2)/(RC[9]*RC[9]*2))    +  (((yid-sy/2)*(yid-sy/2))/(2*RC
      [10]*RC[10])))));
124
125       //
126 }
127 }
128 """
129 platform_list = cl.get_platforms()
130 platform = platform_list[3]
131 # device
132 device_list = platform.get_devices()
133 device = device_list[0]
134 # context
135 ctx = cl.Context([device])
136 # command queue
137 queue = cl.CommandQueue(ctx)
138
139
140 def OA (Energies,Sigmas0,Sigmas1,Sigmas2,SigmasT,Taus0,Taus1,Taus2,
      Concentrations,Zr,Zpos,VP):
141     E=Energies
142     print(type(E))
143     NM=np.arange(np.size(Zpos))
144     MData= np.zeros(np.size(Zpos)).astype(np.float32)
145     Inp = np.zeros(np.size(Zpos)).astype(np.float32)
146     Oup= np.zeros(np.size(Zpos)).astype(np.float32)
147     print('S1:',Sigmas1,'S3:',Sigmas2,'ST:',SigmasT)
148     # Work Size
149     n = 15
150     kernel_params = {"mat_size": n}
151     program = cl.Program(ctx, KERNEL_CODE % kernel_params).build()
152     c=2.99792458e8 #Speed of light in vac in m/s
153     #Sample width is 2mm, therefore the system unit is 2mm/n
154     #SDim is now difined as the spatial step size
155     SDim = 0.002/n
156     #The NdYag we use q-switches for a 10ns FDHM thus the full pulse
       take 30ns (amplitude after/before this is negligible)
157     #Taking speed of light to be 299792458 m/s we find set
158     TDim = SDim/c #to the time of each step in units C
```

```
159     #Thus the time step is now equal to 1, but it has units TDim
160     #The NdYag we use q-switches for a 10ns FDHM thus the full pulse
        take 30ns (amplitude after this is negligible)
161     #Converting this to TDim (0.00000001*SDim/C) we get the the time
        of the laserpulse in TDim
162     Pulsetime = 10*(10**(-9)) ##seconds
163     Sigt=Pulsetime/2.3548 #FWHT = 2.3548*Sigma
164     Sg = Sigt/TDim
165     #The NdYag we use q-switches for a 10ns FDHM thus the full pulse
        take 30ns (amplitude after/before this is negligible)
166     #Taking speed of light to be 299792458 m/s we find set
167     TDim = SDim/c #to the time of each step in units C
168     #Sg is the std for time dimension(z axsis) of the laser pulse,
      the spatial dim std is given by the position of
169     #the sample in the zscan setup and is a function of its position
        and its Rayleigh length.Zr =(pi*Wo^2)/lamnda
170     # We normally get Zr from the parametric fit, but it can be done
        manually
171     wl = 532.00e-9 # wavelenght of our laser (Ndyag 2nd harmonic)
172 #   Zr = Zr #in mm
173     w0 = np.sqrt((Zr*wl)/np.pi) #w0 is the beamwidth at z0 (FWHM)
174     for nm in NM:
175         z= Zpos[nm]*0.001 #define the position of the sample along
      the guassian beam profile
176         wz = w0*(np.sqrt(1+(z/Zr)**2)) # this is the beam radius in
      terms of z(the sample pos)
177 #         print(wz)
178
179         #Now we define the std for the x and y dim as
180         Syg = ((2*wz)/2.3548)/SDim #in the system dimensions
181         #Sxg = (2*wz)/2.3548/SDim # this is not used in the slice
      model at the moment
182         #Light travels 0.299792458 m/ns and thus the pulse is
      8.99377374 m long
183         #Since the cuvette is 2mm wide, the system must cylce 9m
      /0.002m (or 4500 )times
184
185         Cn=4500
186         ConcSD=((Concentrations*10**3)*SDim**3)*6.022140857*1e23 #
      convert concentration to mol/L then to molec/system unit
187 #         print('Conc=',ConcSD)
188         #This is constant for all values of n, as n only defines the
        spatial/temporal resolution
189         #The pulse then is defined as 4500*n long and n (for a 2d
      slice) wide making it rather large and must be sliced up for the
190         #compute device to handle.
191         #The Total loop iterations then is Cn*n +2n as the device
      must be iterated over the sample with resolution n
192         #4500  times(dead zone before and after pulse) but since the
        tails of the pulse are so low we omit this
193         h=6.626070040e-34 #Planc in J.s
```

```
194         Photons=(E*wl)/(h*c) #number of photons in the 10 ns pulse
    at 532nm
195 #         print('Phot',np.log10(Photons))
196         #The integral of a 3d mulivariate guassian function is given
     as ((height of peak)*(sigmax)*(sigmay)*(sigmaz))/(4pi^2)
197         #In this case the to intagral is equal to the total number
    of photons in the function, so rearanging:
198         H = (Photons*(4*np.pi**2))/(Syg*Syg*Sg) #Std in x and y are
    equivalent (we hope)
199 #         print('H=',H)
200 #         P=0.94*(E/(Pulsetime))*10**6
201         #Finally the intesnity of each pulse is given as I(r,z)= (2*
    P/pi*wz^2)*e^((-2*r^2)/wz^2) with P
202         #P the total power of each pulse(constant for all positions)
203 #         Iposm= ((2*P)/(np.pi*(wz**2)))*np.exp((-2*(wz**2))/(w0**2))
     #Intesnity at pos z in W/m2
204 #         print(Iposm)
205 #         Ipos=Iposm*(SDim**2) #conversion to system units
206 #         print('Sx=',Syg)
207 #         print('h=',H)
208 #         print('p=',Photons)
209         #
    ------------------------------------------------------------------------

210         #rate constants:
211         #as the TDim is not an si unit all values must be converted
    before hand (spatial values stay the same though)
212         sigma12 = (Sigmas0*(1e-20))/SDim**2   #SPA ground state
    absorption cross section
213         sigma24 = (Sigmas1*(1e-20))/SDim**2   #S1 ESA cross section
214         sigma35 = (Sigmas2*(1e-20))/SDim**2   #T1 ESA cross section
215         tpa12   = SigmasT*((10**(-58)))/((SDim**5)/c) #G to S1 two
    photon crossection in GM [1GM=1e?50 cm4*s/photon= 1e-58 m4*s/
    photon;]
216 #         print(tpa12)
217         tau21 = 1/((Taus0)/TDim) #S1  lifetime
218         tau23 = 1/((Taus1)/TDim) #ISC lifetime
219         tau31 = 1/((Taus2)/TDim) #T1  lifetime
220
221
222 #         print(tpa12,sigma12,sigma24,sigma35,tau21,tau23,tau31,1,n*
    Cn,Sg,Syg,H)
223         RC=np.array([tpa12,sigma12,sigma24,sigma35,tau21,tau23,tau31
    ,1,n*Cn,Sg,Syg,H], dtype=cl.cltypes.float)
224         #RC=(0.tpa12.1.sigma12,2.sigma24,3.sigma35,4.tau21,5.tua23
    ,6.tau31,7.stepsize,8.totalsteps=n*Cn,9.Sg,10.Syg,11.IPos)
225 #         print("TPA=",SigmasT,"S24=",sigma24,"S35=",sigma35)
226         # platform
227
228 #         print(RC)
229         # data
```

```
230         N1 = np.ones((n,n))*ConcSD
231         N2 = np.zeros((n,n))
232         N3 = np.zeros((n,n))
233         I  = np.ones((n,n))
234 
235         Tim= Cn*n
236         #---------------------------------------
237 
238 
239         # host buffers
240         h_N1O = np.zeros((Tim,n,n)).astype(np.float32)
241         h_N2O = np.zeros((Tim,n,n)).astype(np.float32)
242         h_N3O = np.zeros((Tim,n,n)).astype(np.float32)
243         h_IO  = np.zeros((Tim,n,n)).astype(np.float32)
244         h_N1  = np.real(N1).astype(np.float32)
245         h_N2  = np.real(N2).astype(np.float32)
246         h_N3  = np.real(N3).astype(np.float32)
247         h_TPAb  = np.zeros((n,n)).astype(np.float32) #Buffer for
    recording amount of each absorption
248         h_RSAb  = np.zeros((n,n)).astype(np.float32)
249         h_RTAb  = np.zeros((n,n)).astype(np.float32)
250         h_I    = np.real(I).astype(np.float32)
251 
252 
253         # device buffers
254         mf = cl.mem_flags
255         RC_buf     = cl.Buffer(ctx, mf.READ_ONLY  | mf.COPY_HOST_PTR
    , hostbuf=RC  )
256         d_I_buf    = cl.Buffer(ctx, mf.READ_ONLY  | mf.COPY_HOST_PTR
    , hostbuf=h_I )
257         d_N1_buf   = cl.Buffer(ctx, mf.READ_ONLY  | mf.COPY_HOST_PTR
    , hostbuf=h_N1)
258         d_N2_buf   = cl.Buffer(ctx, mf.READ_ONLY  | mf.COPY_HOST_PTR
    , hostbuf=h_N2)
259         d_N3_buf   = cl.Buffer(ctx, mf.READ_ONLY  | mf.COPY_HOST_PTR
    , hostbuf=h_N3)
260         d_TPAb_buf = cl.Buffer(ctx, mf.WRITE_ONLY, size= h_N1.nbytes
    ) #Buffer for recording amount of each absorption On GPGPu device
261         d_RSAb_buf = cl.Buffer(ctx, mf.WRITE_ONLY, size= h_N2.nbytes
    )
262         d_RTAb_buf = cl.Buffer(ctx, mf.WRITE_ONLY, size= h_N3.nbytes
    )
263         d_N1O_buf  = cl.Buffer(ctx, mf.READ_WRITE, size= h_N1.nbytes
    *Tim)
264         d_N2O_buf  = cl.Buffer(ctx, mf.READ_WRITE, size= h_N2.nbytes
    *Tim)
265         d_N3O_buf  = cl.Buffer(ctx, mf.READ_WRITE, size= h_N3.nbytes
    *Tim)
266         d_IO_buf   = cl.Buffer(ctx, mf.READ_WRITE, size= h_I.nbytes*
    Tim)
267 
```

```
268
269         event = program.dmv_cl(queue, h_N1.shape, None, d_I_buf,
        RC_buf, d_N1_buf,d_N2_buf,d_N3_buf,d_N1O_buf,d_N2O_buf,d_N3O_buf,
        d_IO_buf,d_TPAb_buf,d_RSAb_buf,d_RTAb_buf)
270         event.wait()
271         #    #Copy data across only used in population study
272 #         cl.enqueue_copy(queue, h_N2O,  d_N2O_buf)
273 #         cl.enqueue_copy(queue, h_N1O,  d_N1O_buf)
274 #         cl.enqueue_copy(queue, h_N3O,  d_N3O_buf)
275 #         cl.enqueue_copy(queue, h_IO,   d_IO_buf)
276         cl.enqueue_copy(queue, h_I,    d_I_buf)
277         cl.enqueue_copy(queue, h_TPAb, d_TPAb_buf)
278         cl.enqueue_copy(queue, h_RSAb, d_RSAb_buf)
279         cl.enqueue_copy(queue, h_RTAb, d_RTAb_buf)
280 #         print("PTPA=",SigmasT,"PS24=",sigma24,"PS35=",sigma35)
281         queue.flush()
282         queue.finish()
283         #Absorption ratio
284         Oup[nm]=np.sum(h_I[:,0])
285         Inp[nm]=np.sum(h_I[:,-1])
286
287 #         print('Photons:',Photons,'Inp:',Inp,'Mdata:',MData)#his is
        a value pertaining to the amount of photons in the system vs the
        pulse
288 #         print('In=',Inp)
289 #         print('Out=',Oup[nm])
290         MData[nm]=Oup[nm]/VP[nm] #h is the total photon count for
        the beam, this model assumes negligible absorption(i.e. linear)
        outside the area of interest
291
292         print(MData[nm]/MData[0],Zpos[nm])
293 #         print('Photons:',np.log10(Photons),'Inp:',np.log10(Inp),'
        Mdata:',MData[nm]/MData[0])#his is a value pertaining to the
        amount of photons in the system vs the pulse
294     for n in reversed(np.arange((np.size(MData)))):
295         MData[n]=MData[n]/MData[0]
296     # could not get it in to for loop without an exception(and
        making the formloop go backwards was longer than adding this line
        )
297     MData[np.isnan(MData)] = 0
298     return MData
299
300 def OAp2 (Energies,Sigmas0,Sigmas1,Sigmas2,SigmasT,Taus0,Taus1,Taus2
        , Concentrations,Zr,Zpos,VP):
301     E=float(Energies)
302     NM=np.arange(np.size(Zpos))
303     MData= np.zeros(np.size(Zpos)).astype(np.float32)
304     Pop= np.zeros((np.size(Zpos),3)).astype(np.float32)
305
306     Inp = np.zeros(np.size(Zpos)).astype(np.float32)
307     Oup= np.zeros(np.size(Zpos)).astype(np.float32)
```

```
308     Absr= np.zeros((np.size(Zpos),3)).astype(np.float32)
309     print('S1:',Sigmas1,'S3:',Sigmas2,'ST:',SigmasT)
310     # Work Size
311     n = 15
312     kernel_params = {"mat_size": n}
313     program = cl.Program(ctx, KERNEL_CODE % kernel_params).build()
314     c=2.99792458e8 #Speed of light in vac in m/s
315     #Sample width is 2mm, therefore the system unit is 2mm/n
316     #SDim is now difined as the spatial step size
317     SDim = 0.002/n
318     #The NdYag we use q-switches for a 10ns FDHM thus the full pulse
        take 30ns (amplitude after/before this is negligible)
319     #Taking speed of light to be 299792458 m/s we find set
320     TDim = SDim/c #to the time of each step in units C
321     #Thus the time step is now equal to 1, but it has units TDim
322     #The NdYag we use q-switches for a 10ns FDHM thus the full pulse
        take 30ns (amplitude after this is negligible)
323     #Converting this to TDim (0.00000001*SDim/C) we get the the time
        of the laserpulse in TDim
324     Pulsetime = 10*(10**(-9)) ##seconds
325     Sigt=Pulsetime/2.3548 #FWHT = 2.3548*Sigma
326     Sg = Sigt/TDim
327     #The NdYag we use q-switches for a 10ns FDHM thus the full pulse
        take 30ns (amplitude after/before this is negligible)
328     #Taking speed of light to be 299792458 m/s we find set
329     TDim = SDim/c #to the time of each step in units C
330     #Sg is the std for time dimension(z axsis) of the laser pulse,
      the spatial dim std is given by the position of
331     #the sample in the zscan setup and is a function of its position
        and its Rayleigh length.Zr =(pi*Wo^2)/lamnda
332     # We normally get Zr from the parametric fit, but it can be done
        manually
333     wl = 532e-9 # wavelenght of our laser (Ndyag 2nd harmonic)
334 #   Zr = Zr #in mm
335     w0 = np.sqrt((Zr*wl)/np.pi) #w0 is the beamwidth at z0 (FWHM)
336     for nm in NM:
337         z= Zpos[nm]*0.001 #define the position of the sample along
      the guassian beam profile
338         wz = w0*(np.sqrt(1+(z/Zr)**2)) # this is the beam radius in
      terms of z(the sample pos)
339 #        print(wz)
340
341         #Now we define the std for the x and y dim as
342         Syg = ((2*wz)/2.3548)/SDim #in the system dimensions
343         #Sxg = (2*wz)/2.3548/SDim # this is not used in the slice
      model at the moment
344         #Light travels 0.299792458 m/ns and thus the pulse is
      8.99377374 m long
345         #Since the cuvette is 2mm wide, the system must cylce 9m
      /0.002m (or 4500 )times
346
```

```
347         Cn=4500
348         ConcSD=((Concentrations*10**3)*SDim**3)*6.022140857*1e23 #
        convert concentration to mol/L then to molec/system unit
349 #         print('Conc=',ConcSD)
350         #This is constant for all values of n, as n only defines the
         spatial/temporal resolution
351         #The pulse then is defined as 4500*n long and n (for a 2d
        slice) wide making it rather large and must be sliced up for the
352         #compute device to handle.
353         #The Total loop iterations then is Cn*n +2n as the device
        must be iterated over the sample with resolution n
354         #4500  times(dead zone before and after pulse) but since the
         tails of the pulse are so low we omit this
355         h=6.626070040e-34 #Planc in J.s
356         Photons=(E*wl)/(h*c) #number of photons in the 10 ns pulse
        at 532nm
357 #         print('Phot',np.log10(Photons))
358         #The integral of a 3d mulivariate guassian function is given
         as ((height of peak)*(sigmax)*(sigmay)*(sigmaz))/(4pi^2)
359         #In this case the to intagral is equal to the total number
        of photons in the function, so rearanging:
360         H = (Photons*(4*np.pi**2))/(Syg*Syg*Sg) #Std in x and y are
        equivalent (we hope)
361 #         print('H=',H)
362 #         P=0.94*(E/(Pulsetime))*10**6
363         #Finally the intesnity of each pulse is given as I(r,z)= (2*
        P/pi*wz^2)*e^((-2*r^2)/wz^2) with P
364         #P the total power of each pulse(constant for all positions)
365 #         Iposm= ((2*P)/(np.pi*(wz**2)))*np.exp((-2*(wz**2))/(w0**2))
         #Intesnity at pos z in W/m2
366 #         print(Iposm)
367 #         Ipos=Iposm*(SDim**2) #conversion to system units
368 #         print('Sx=',Syg)
369 #         print('h=',H)
370 #         print('p=',Photons)
371         #
        ------------------------------------------------------------------------

372         #rate constants:
373         #as the TDim is not an si unit all values must be converted
        before hand (spatial values stay the same though)
374         sigma12 = (Sigmas0*(1e-20))/SDim**2   #SPA ground state
        absorption cross section
375         sigma24 = (Sigmas1*(1e-20))/SDim**2   #S1 ESA cross section
376         sigma35 = (Sigmas2*(1e-20))/SDim**2   #T1 ESA cross section
377         tpa12   = SigmasT*((10**(-58)))/((SDim**5)/c) #G to S1 two
        photon crossection in GM [1GM=1e?50 cm4*s/photon= 1e-58 m4*s/
        photon;]
378 #         print(tpa12)
379         tau21 = 1/((Taus0)/TDim) #S1  lifetime
380         tau23 = 1/((Taus1)/TDim) #ISC lifetime
```

```
381         tau31 = 1/((Taus2)/TDim) #T1  lifetime
382
383
384 #         print(tpa12,sigma12,sigma24,sigma35,tau21,tau23,tau31,1,n*
    Cn,Sg,Syg,H)
385         RC=np.array([tpa12,sigma12,sigma24,sigma35,tau21,tau23,tau31
    ,1,n*Cn,Sg,Syg,H], dtype=cl.cltypes.float)
386         #RC=(0.tpa12.1.sigma12,2.sigma24,3.sigma35,4.tau21,5.tua23
    ,6.tau31,7.stepsize,8.totalsteps=n*Cn,9.Sg,10.Syg,11.IPos)
387 #         print("TPA=",SigmasT,"S24=",sigma24,"S35=",sigma35)
388         # platform
389
390 #         print(RC)
391         # data
392         N1 = np.ones((n,n))*ConcSD
393         N2 = np.zeros((n,n))
394         N3 = np.zeros((n,n))
395         I  = np.ones((n,n))
396
397         Tim= Cn*n
398         #---------------------------------------
399
400
401         # host buffers
402         h_N1O = np.zeros((Tim,n,n)).astype(np.float32)
403         h_N2O = np.zeros((Tim,n,n)).astype(np.float32)
404         h_N3O = np.zeros((Tim,n,n)).astype(np.float32)
405         h_IO  = np.zeros((Tim,n,n)).astype(np.float32)
406         h_N1  = np.real(N1).astype(np.float32)
407         h_N2  = np.real(N2).astype(np.float32)
408         h_N3  = np.real(N3).astype(np.float32)
409         h_TPAb  = np.zeros((n,n)).astype(np.float32) #Buffer for
    recording amount of each absorption
410         h_RSAb  = np.zeros((n,n)).astype(np.float32)
411         h_RTAb  = np.zeros((n,n)).astype(np.float32)
412         h_I    = np.real(I).astype(np.float32)
413
414
415         # device buffers
416         mf = cl.mem_flags
417         RC_buf      = cl.Buffer(ctx, mf.READ_ONLY  | mf.COPY_HOST_PTR
    , hostbuf=RC  )
418         d_I_buf     = cl.Buffer(ctx, mf.READ_ONLY  | mf.COPY_HOST_PTR
    , hostbuf=h_I )
419         d_N1_buf    = cl.Buffer(ctx, mf.READ_ONLY  | mf.COPY_HOST_PTR
    , hostbuf=h_N1)
420         d_N2_buf    = cl.Buffer(ctx, mf.READ_ONLY  | mf.COPY_HOST_PTR
    , hostbuf=h_N2)
421         d_N3_buf    = cl.Buffer(ctx, mf.READ_ONLY  | mf.COPY_HOST_PTR
    , hostbuf=h_N3)
422         d_TPAb_buf = cl.Buffer(ctx, mf.WRITE_ONLY, size= h_N1.nbytes
```

```
    ) #Buffer for recording amount of each absorption On GPGPu device
423         d_RSAb_buf = cl.Buffer(ctx, mf.WRITE_ONLY, size= h_N2.nbytes
    )
424         d_RTAb_buf = cl.Buffer(ctx, mf.WRITE_ONLY, size= h_N3.nbytes
    )
425         d_N1O_buf  = cl.Buffer(ctx, mf.READ_WRITE, size= h_N1.nbytes
    *Tim)
426         d_N2O_buf  = cl.Buffer(ctx, mf.READ_WRITE, size= h_N2.nbytes
    *Tim)
427         d_N3O_buf  = cl.Buffer(ctx, mf.READ_WRITE, size= h_N3.nbytes
    *Tim)
428         d_IO_buf   = cl.Buffer(ctx, mf.READ_WRITE, size= h_I.nbytes*
    Tim)
429
430
431         event = program.dmv_cl(queue, h_N1.shape, None, d_I_buf,
    RC_buf, d_N1_buf,d_N2_buf,d_N3_buf,d_N1O_buf,d_N2O_buf,d_N3O_buf,
    d_IO_buf,d_TPAb_buf,d_RSAb_buf,d_RTAb_buf)
432         event.wait()
433         #    #Copy data across only used in population study
434         cl.enqueue_copy(queue, h_N2O,  d_N2O_buf)
435         cl.enqueue_copy(queue, h_N1O,  d_N1O_buf)
436         cl.enqueue_copy(queue, h_N3O,  d_N3O_buf)
437         cl.enqueue_copy(queue, h_IO,   d_IO_buf)
438         cl.enqueue_copy(queue, h_I,    d_I_buf)
439         cl.enqueue_copy(queue, h_TPAb, d_TPAb_buf)
440         cl.enqueue_copy(queue, h_RSAb, d_RSAb_buf)
441         cl.enqueue_copy(queue, h_RTAb, d_RTAb_buf)
442
443
444         queue.flush()
445         queue.finish()
446         #Absorption ratio
447         Oup[nm]=np.sum(h_I[:,0])
448         Inp[nm]=np.sum(h_I[:,-1])
449
450 #        print('Photons:',Photons,'Inp:',Inp,'Mdata:',MData)#his is
    a value pertaining to the amount of photons in the system vs the
    pulse
451 #        print('In=',Inp)
452 #        print('Out=',Oup[nm])
453         MData[nm]=Oup[nm]/VP[nm] #h is the total photon count for
    the beam, this model assumes negligible absorption(i.e. linear)
    outside the area of interest
454
455 #        print(MData[nm]/MData[0],Zpos[nm])
456
457         #        Geting the pop at each pos, though this is only the
    pop at the pulse peak (t/2)
458         Gpop=np.sum(h_N1O[Tim//2,:,:])
459         Spop=np.sum(h_N2O[Tim//2,:,:])
```

```
460         Tpop=np.sum(h_N3O[Tim//2,:,:])
461 #          print(Gpop,Spop,Tpop)
462         Pop[nm,:]=[Gpop,Spop,Tpop]
463
464 #       Next we gen the relative absorption of each process, this we
        get from arrays i build into the kernel
465         AbsTPA=np.sum(h_TPAb)
466         AbsSSA=np.sum(h_RSAb)
467         AbsTSA=np.sum(h_RTAb)
468 #       These three buffers are sums of all photonic interactions
    for each process for a single pulse
469 #       to get the ratio of absorption as a function of the NLO
    behavior they must be normalised with the
470 #       modeled input photon count
471         Absr[nm,:]=[VP[nm]-AbsTPA,VP[nm]-AbsSSA,VP[nm]-AbsTSA]/VP[nm
    ]
472
473     for n in reversed(np.arange((np.size(MData)))):
474         MData[n]=MData[n]/MData[0]
475         Absr[n,:]=Absr[n,:]/Absr[0,:]
476     # could not get it in to for loop without an exception(and
    making the formloop go backwards was longer than adding this line
    )
477     return MData,Pop,Absr
478
```

Listing 2: Five Level Model

Supplementary Data

Supporting data

February 17, 2020

List of Figures

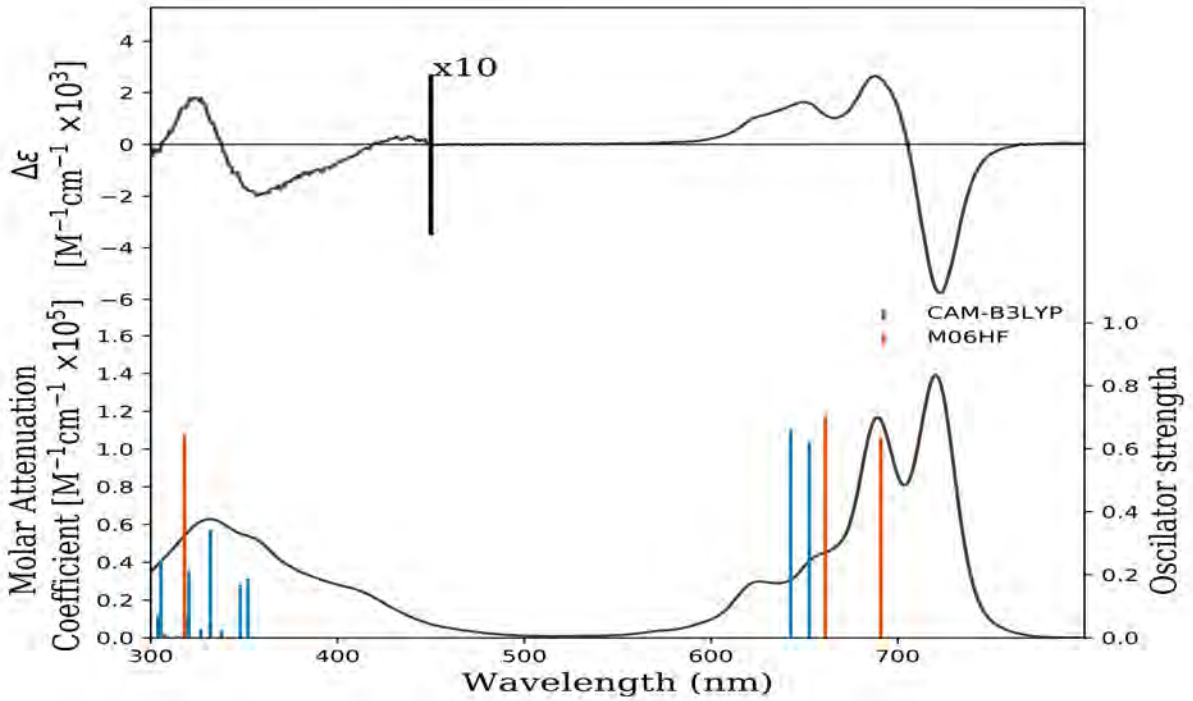

Figure 1: Ground State Absorption of H2-Alpha Fraction 1.

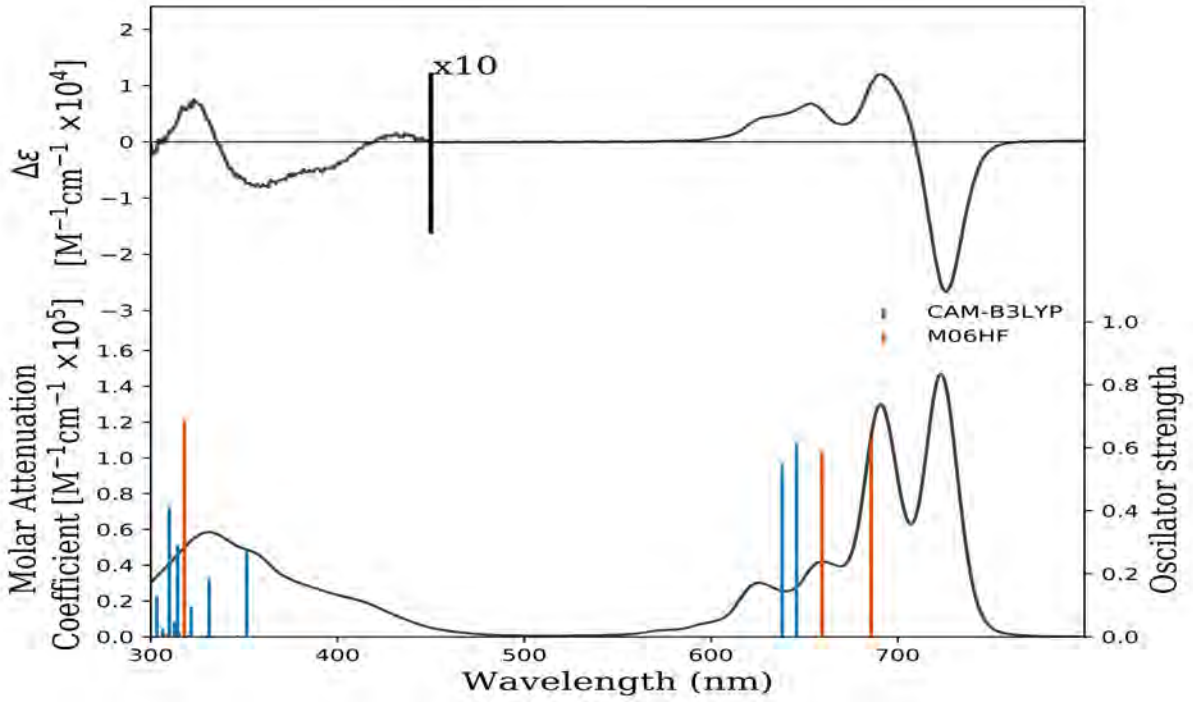

Figure 2: Ground State Absorption of H2-Alpha Fraction 2.

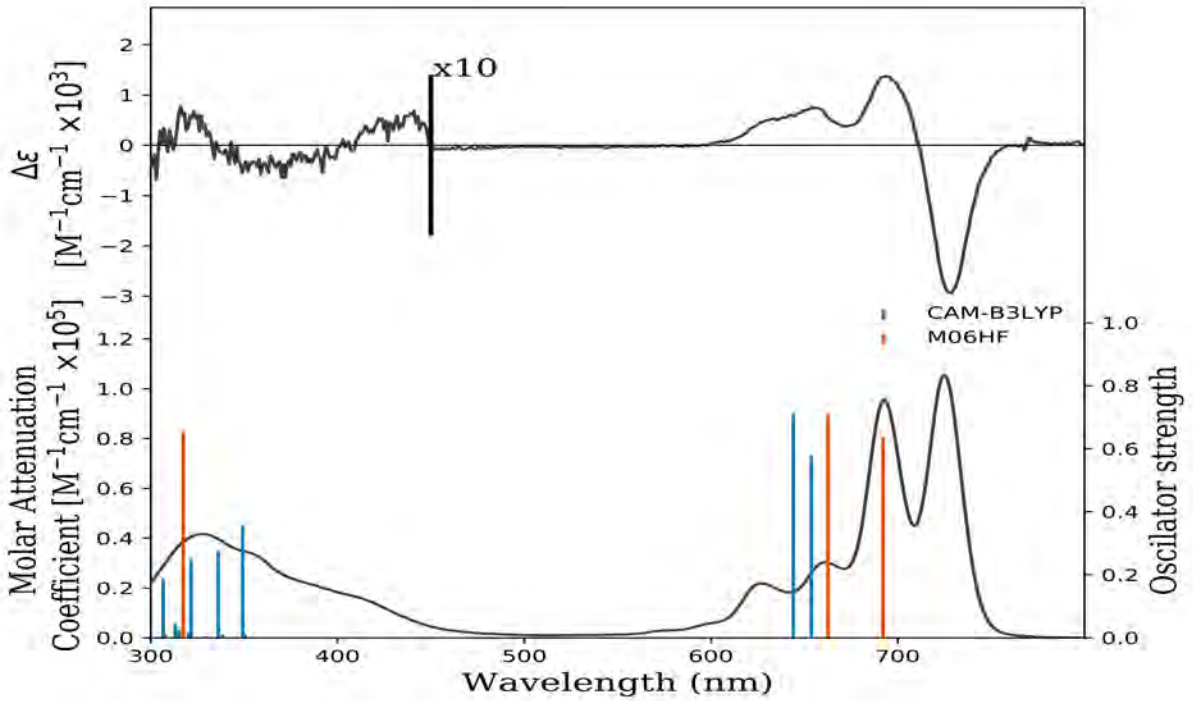

Figure 3: Ground State Absorption of H2-Alpha Fraction 3.

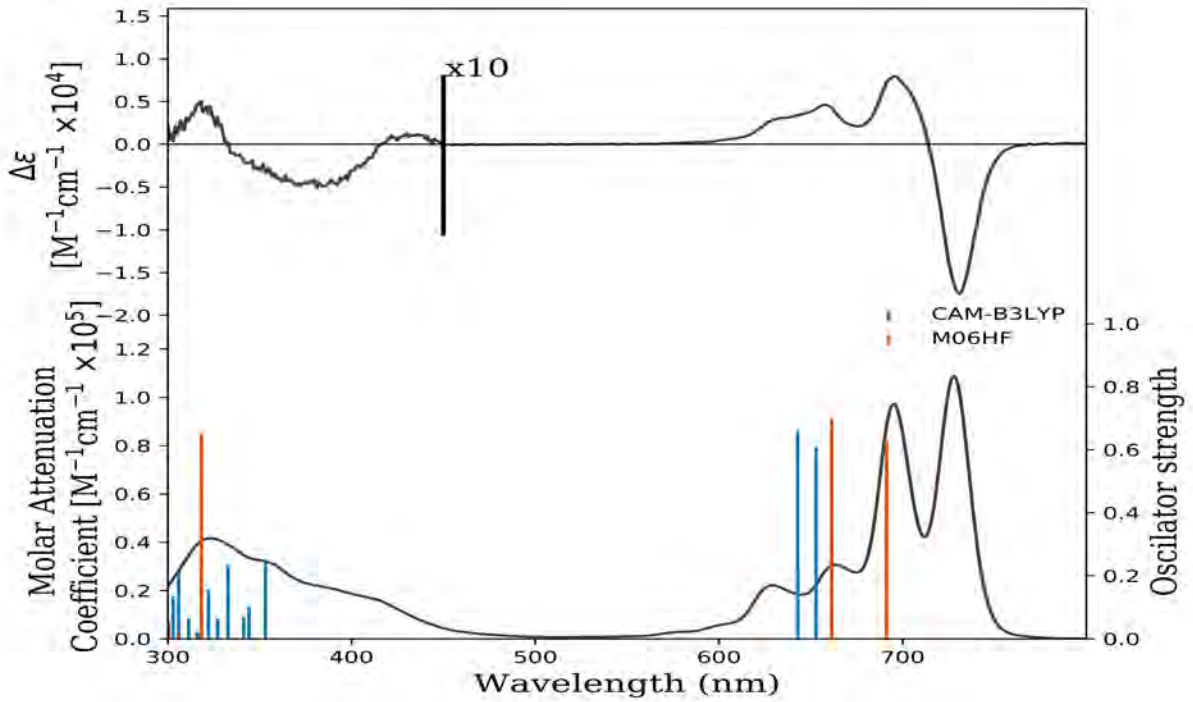

Figure 4: Ground State Absorption of H2-Alpha Fraction 4.

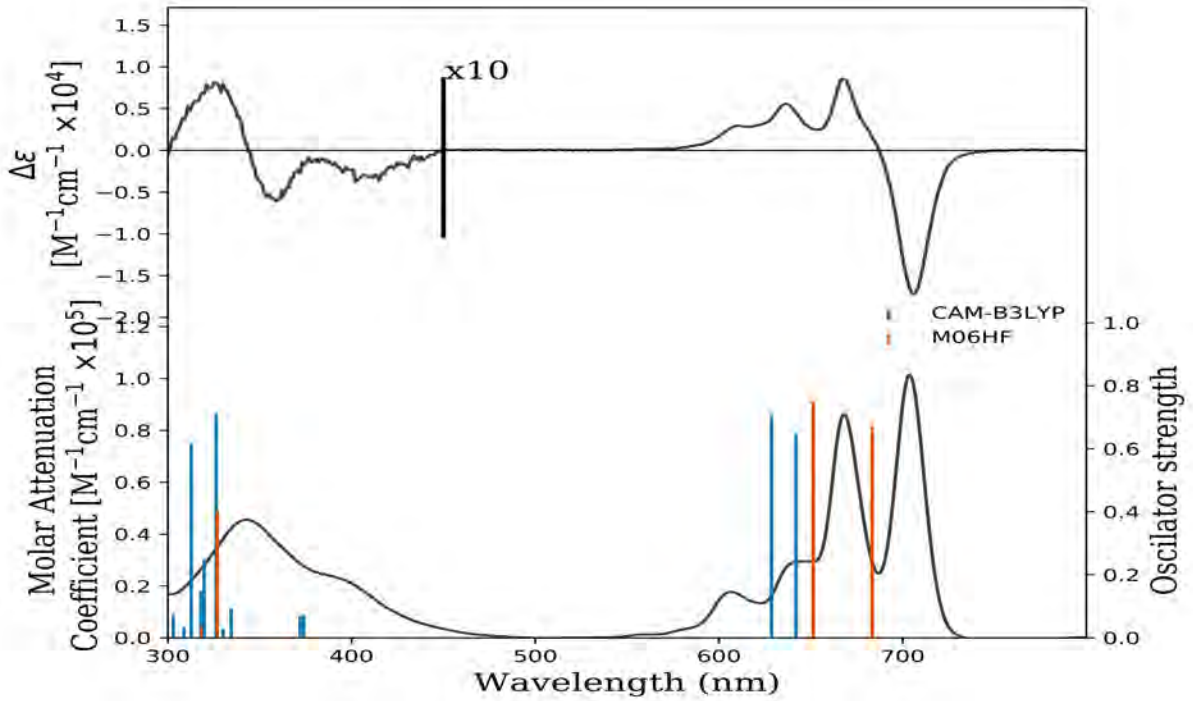

Figure 5: Ground State Absorption of H2-Beta Fraction 1.

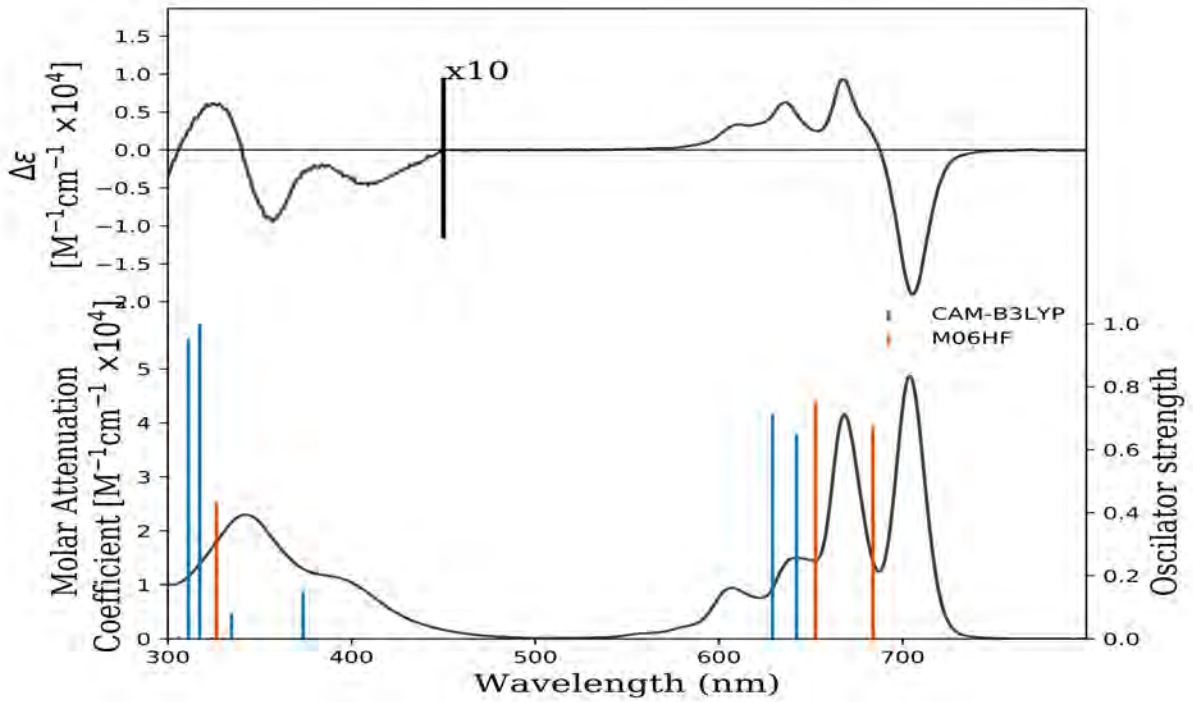

Figure 6: Ground State Absorption of H2-Beta Fraction 2.

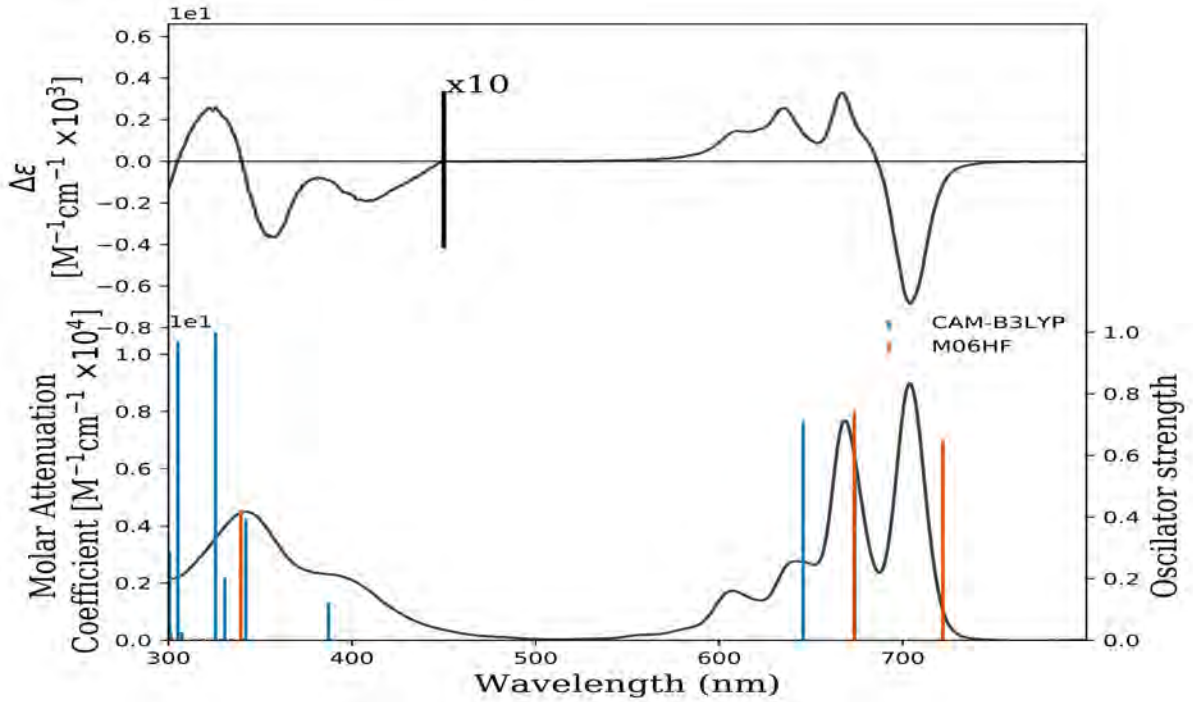

Figure 7: Ground State Absorption of H2-Beta Fraction 3.

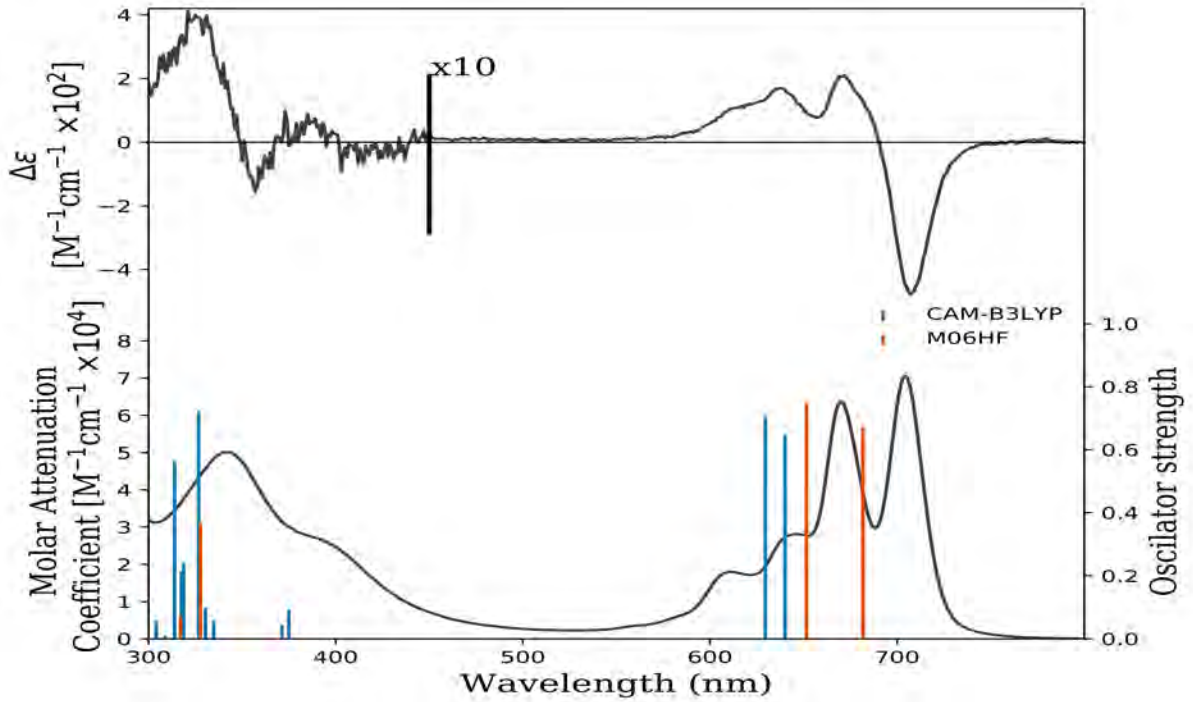

Figure 8: Ground State Absorption of H2-Beta Fraction 4.

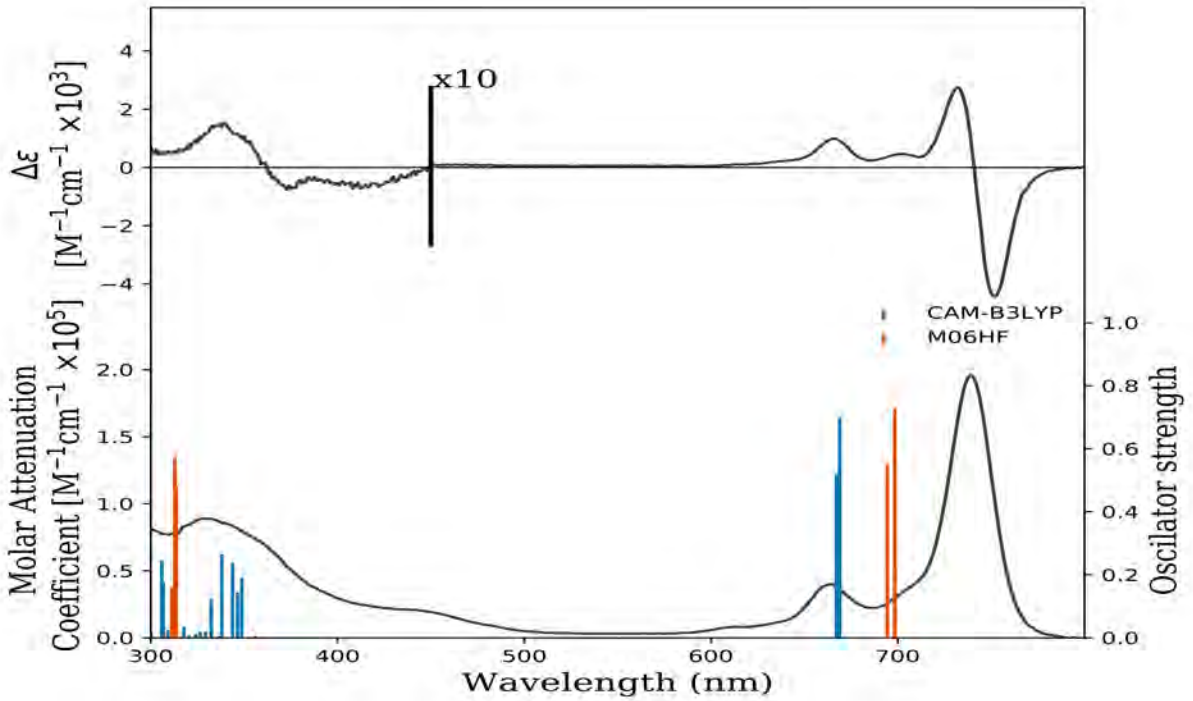

Figure 9: Ground State Absortption of $SnCl_2$-Alpha Fraction 1.

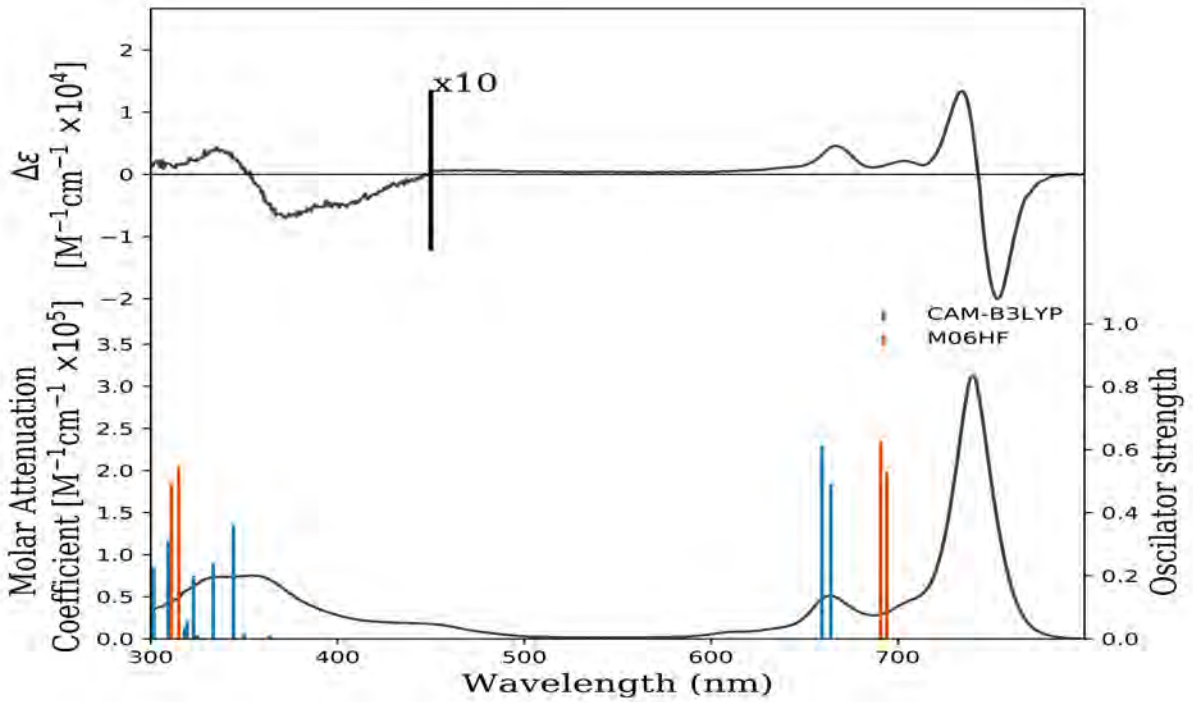

Figure 10: Ground State Absortption of $SnCl_2$-Alpha Fraction 2.

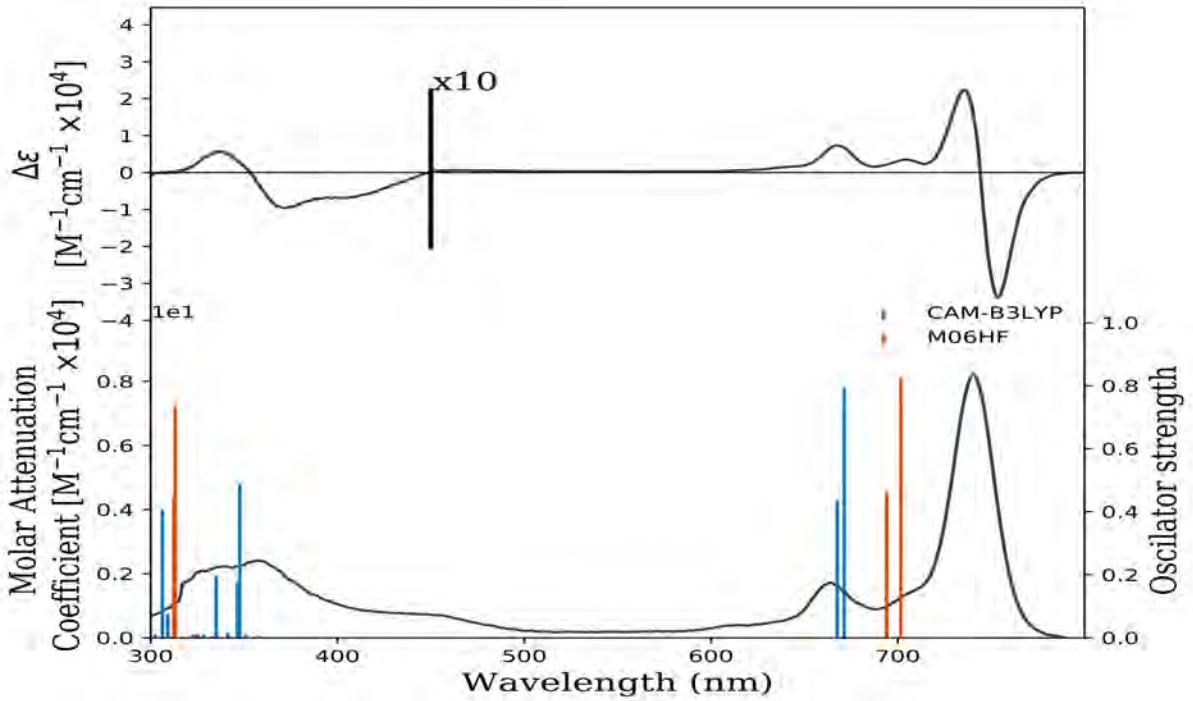

Figure 11: Ground State Absortption of $SnCl_2$-Alpha Fraction 3.

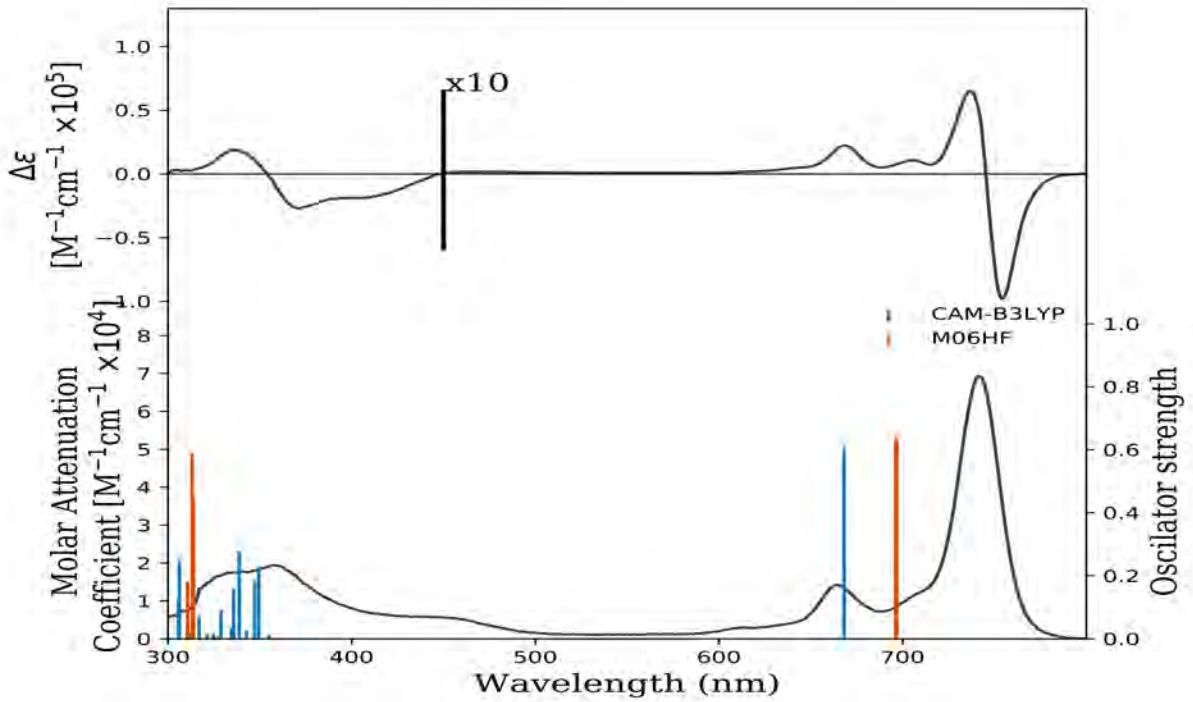

Figure 12: Ground State Absortption of $SnCl_2$-Alpha Fraction 4.

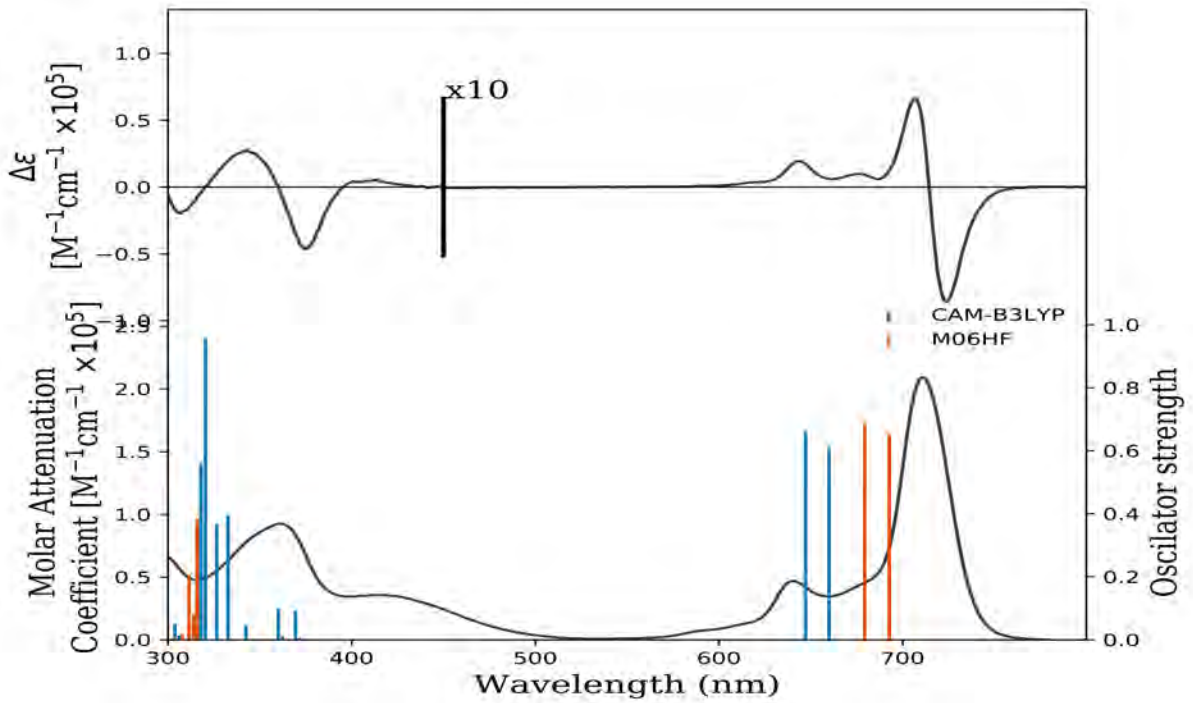

Figure 13: Ground State Absortption of $SnCl_2$-Beta Fraction 1.

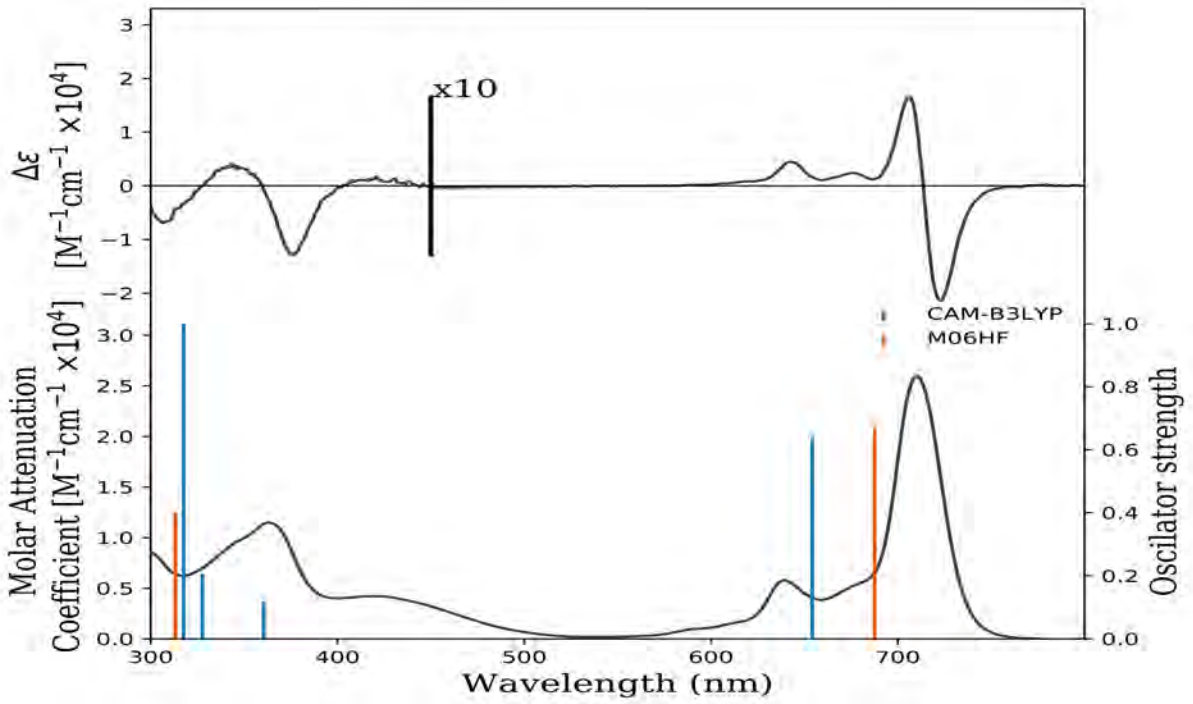

Figure 14: Ground State Absortption of $SnCl_2$-Beta Fraction 2.

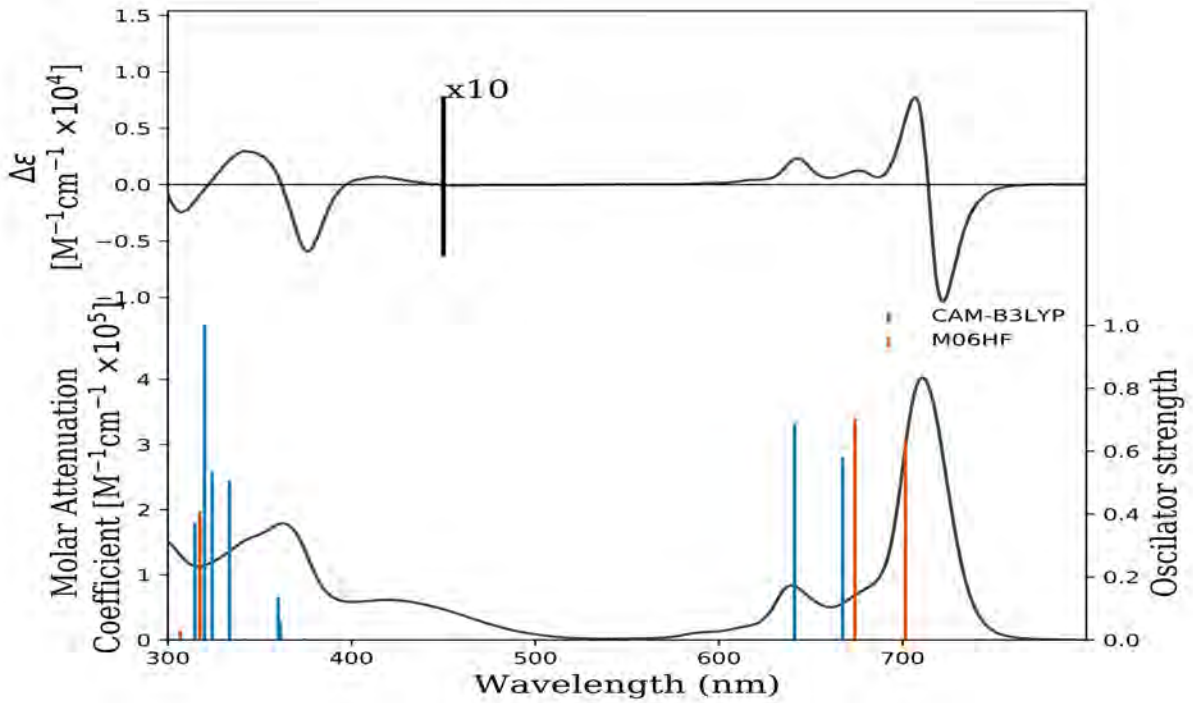

Figure 15: Ground State Absortption of $SnCl_2$-Beta Fraction 3.

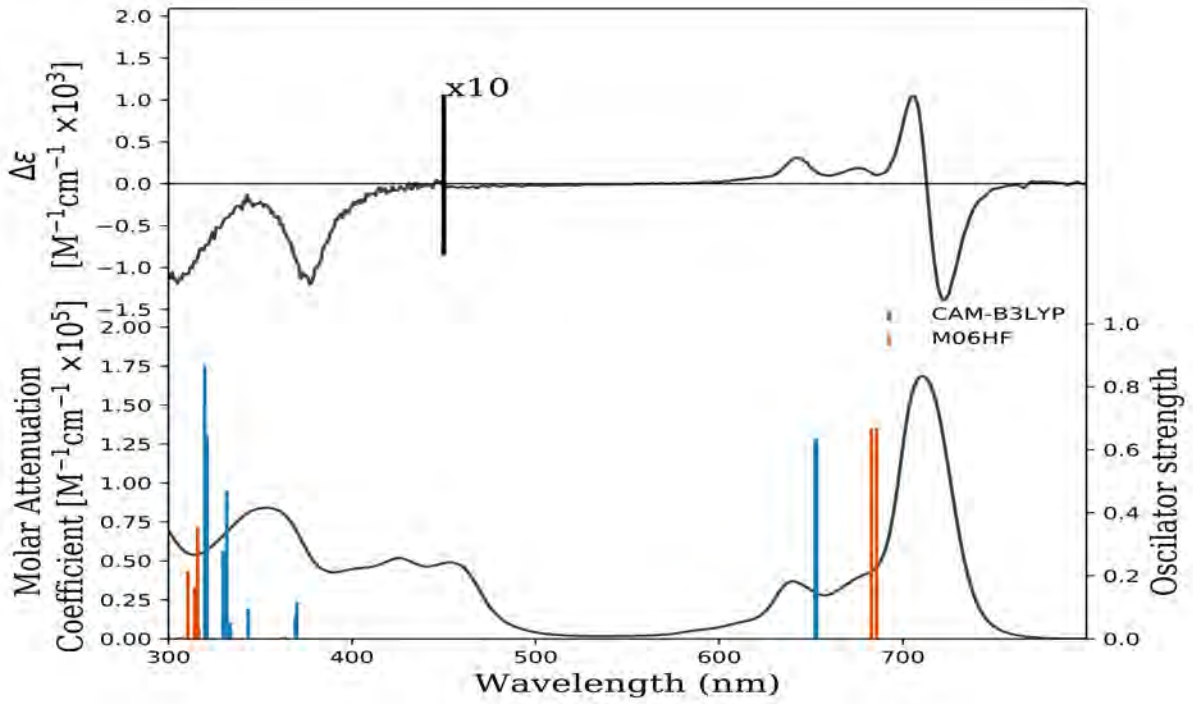

Figure 16: Ground State Absortption of $SnCl_2$-Beta Fraction 4.

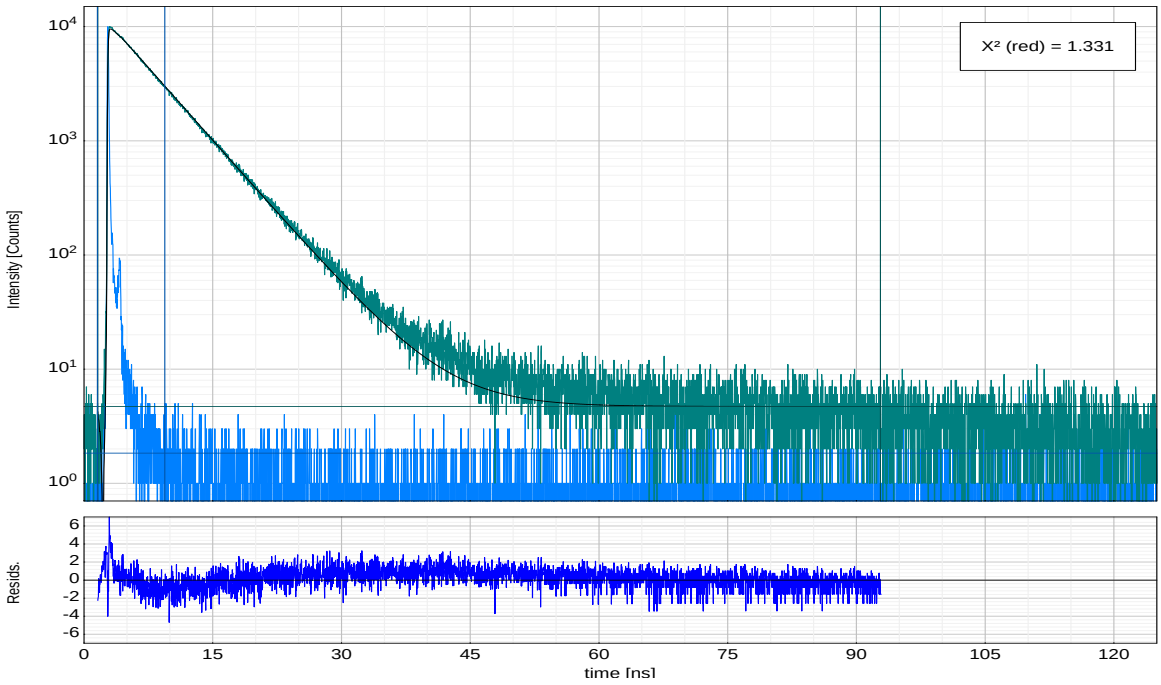

Figure 17: Fluorescence Decay of H2-Alpha Fraction 1.

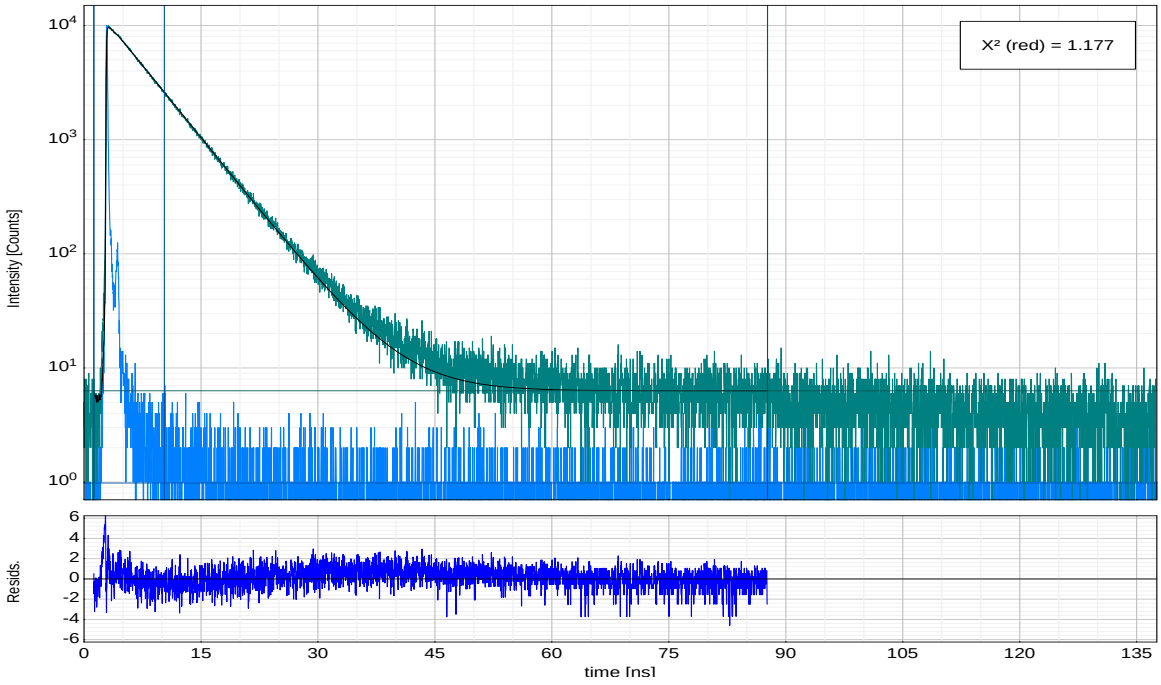

Figure 18: Fluorescence Decay of H2-Alpha Fraction 2.

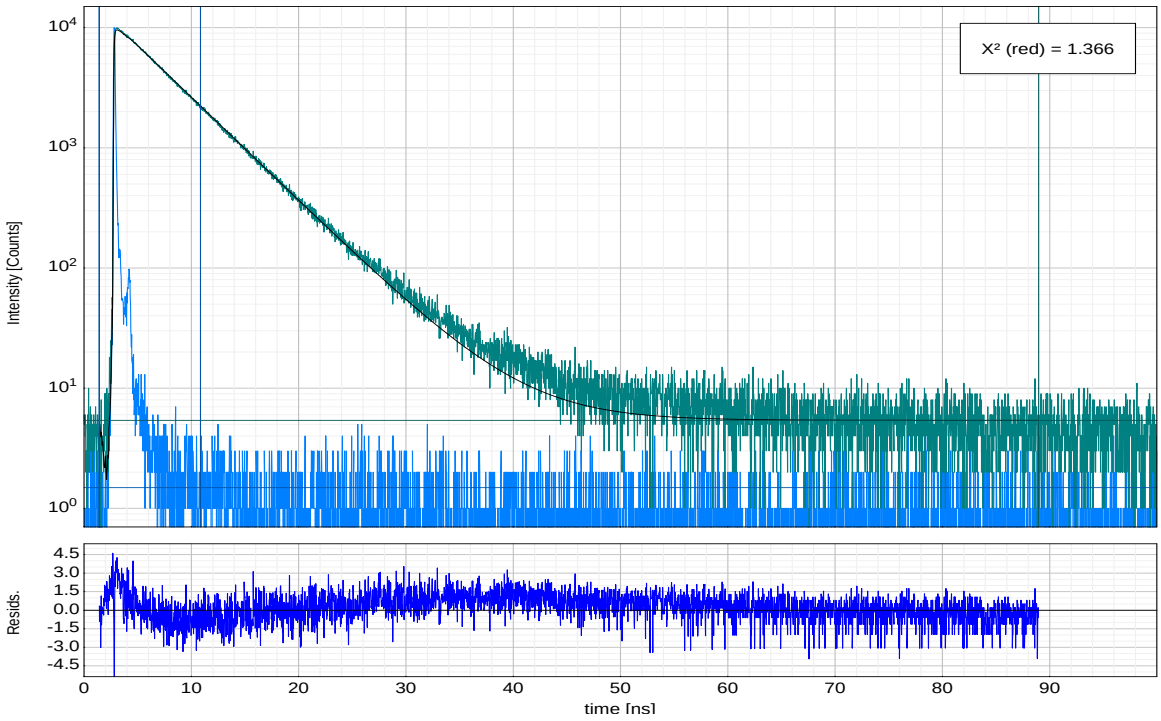

Figure 19: Fluorescence Decay of H2-Alpha Fraction 3.

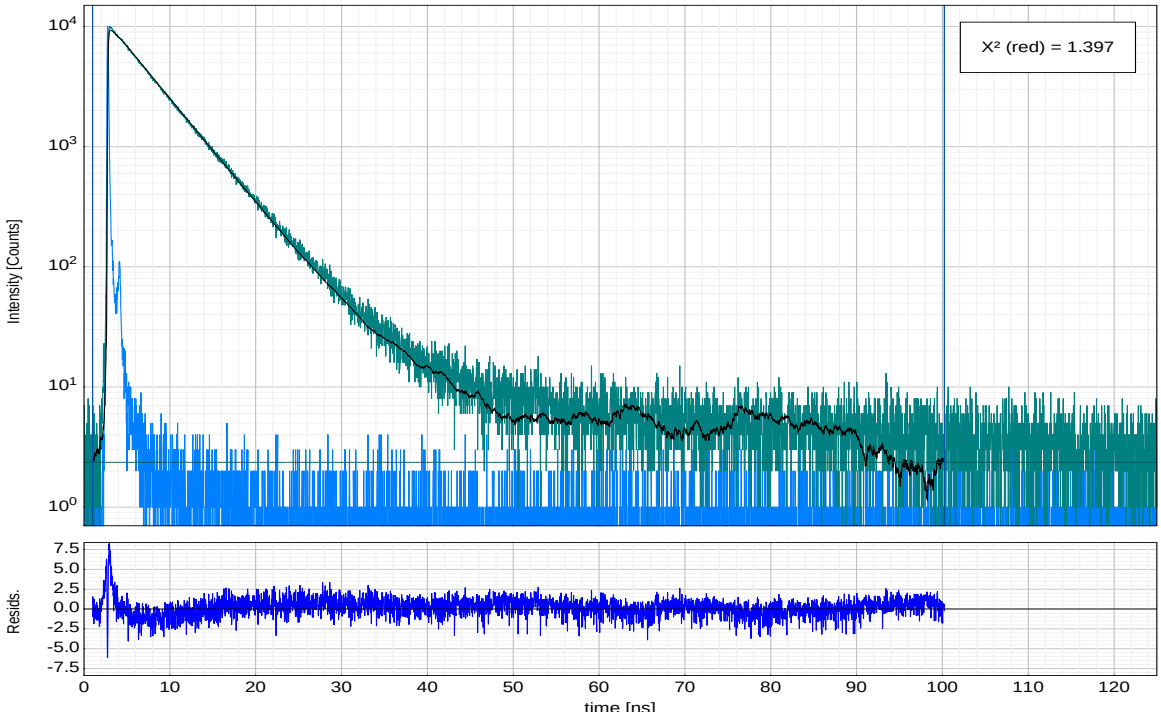

Figure 20: Fluorescence Decay of H2-Alpha Fraction 4.

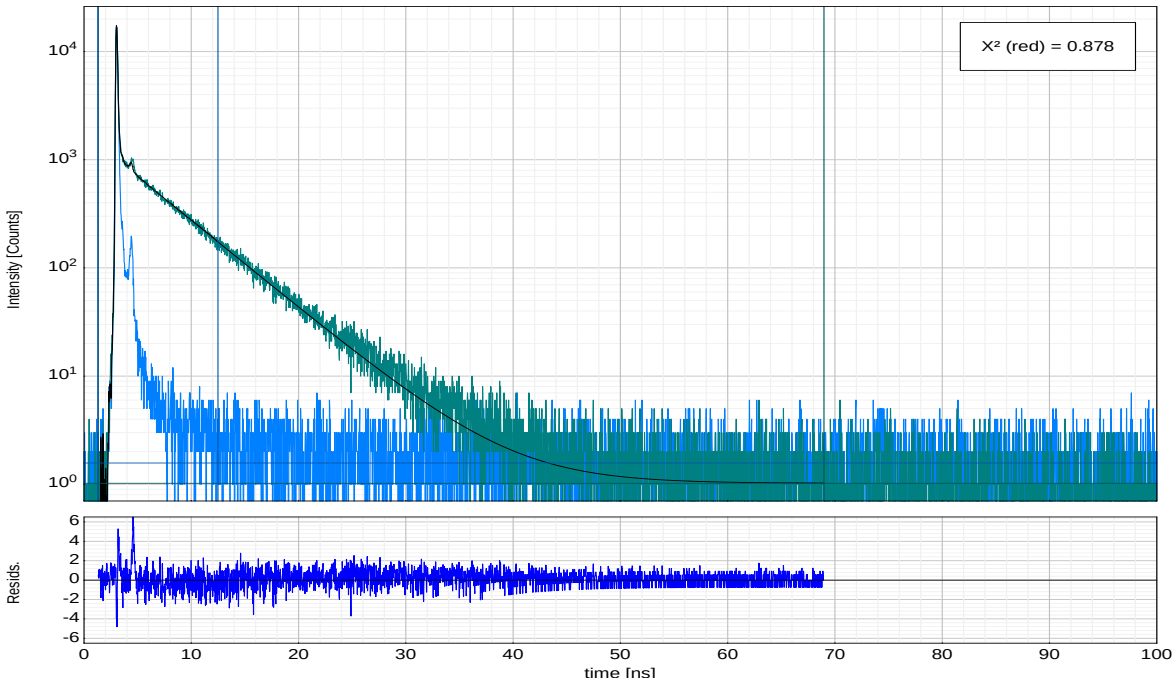

Figure 21: Fluorescence Decay of H2-Beta Fraction 1.

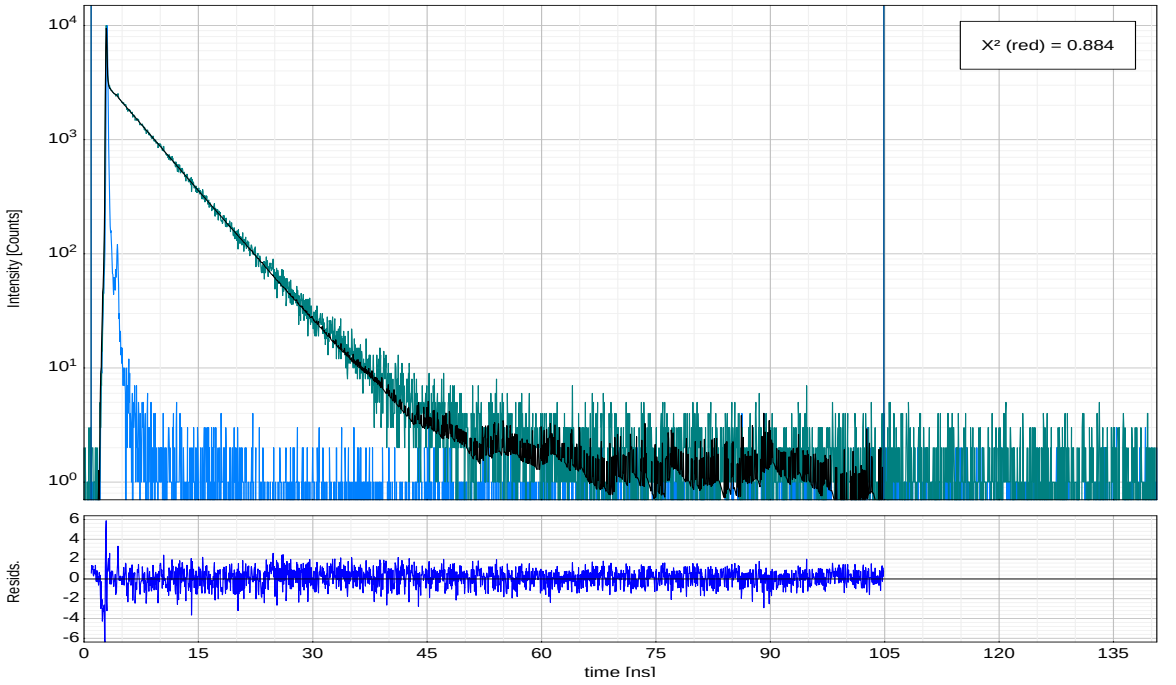

Figure 22: Fluorescence Decay of H2-Beta Fraction 2.

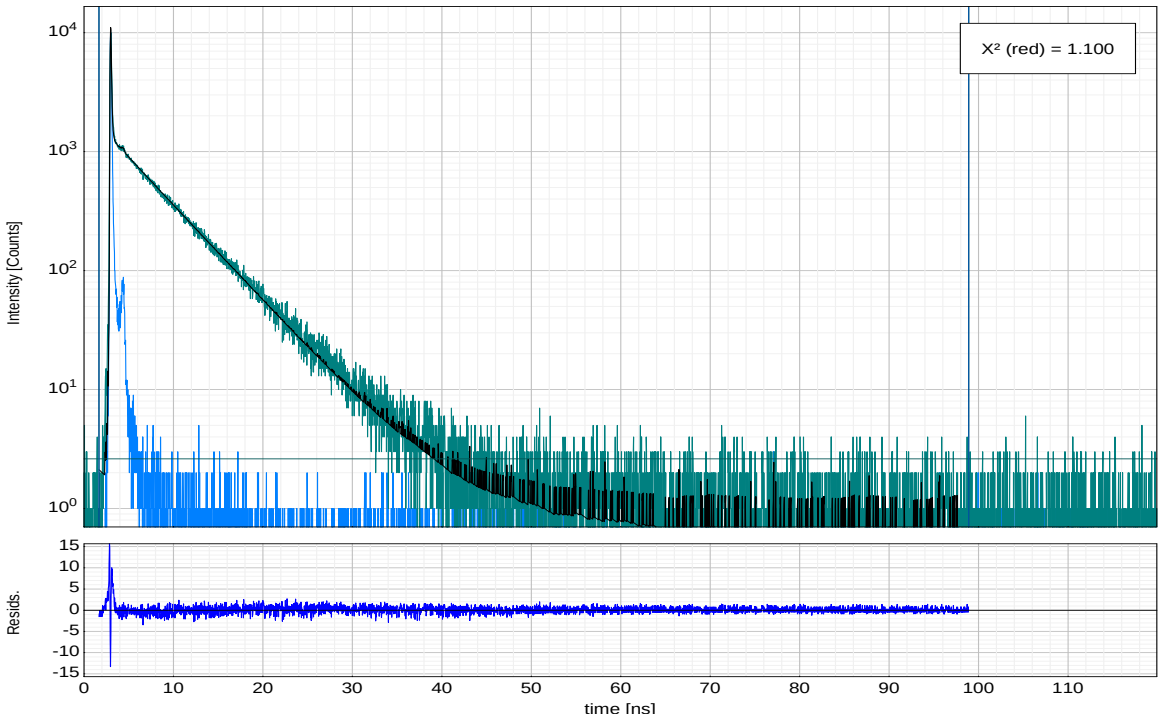

Figure 23: Fluorescence Decay of H2-Beta Fraction 3.

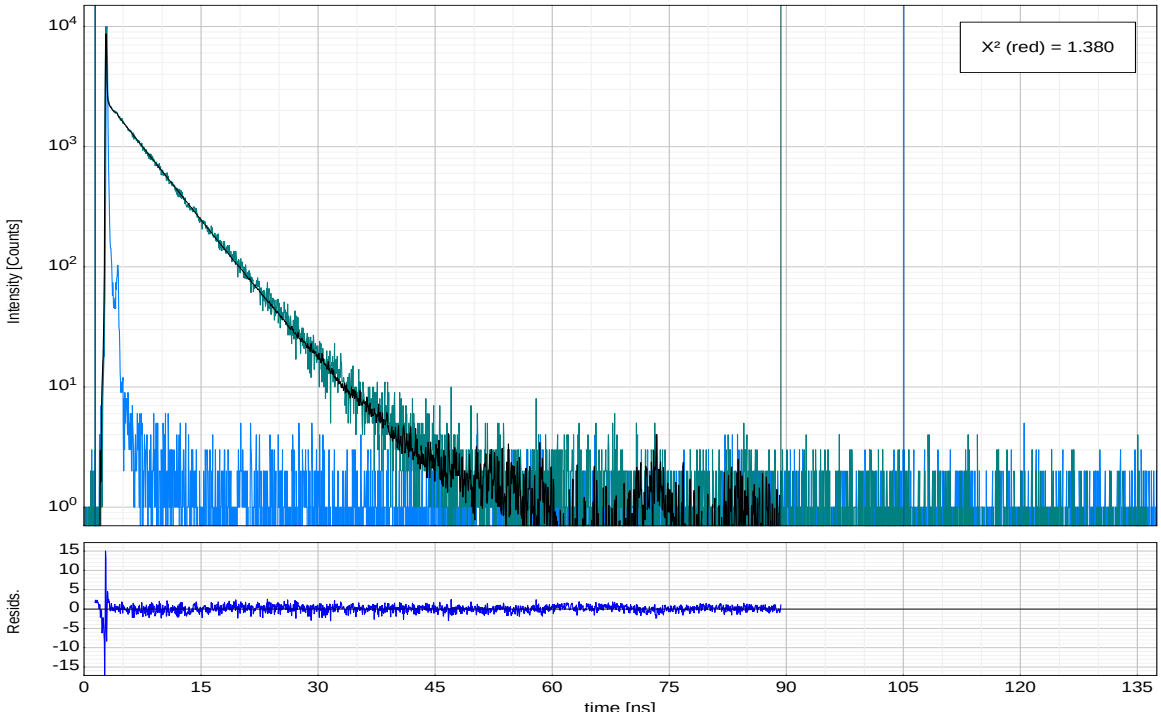

Figure 24: Fluorescence Decay of H2-Beta Fraction 4.

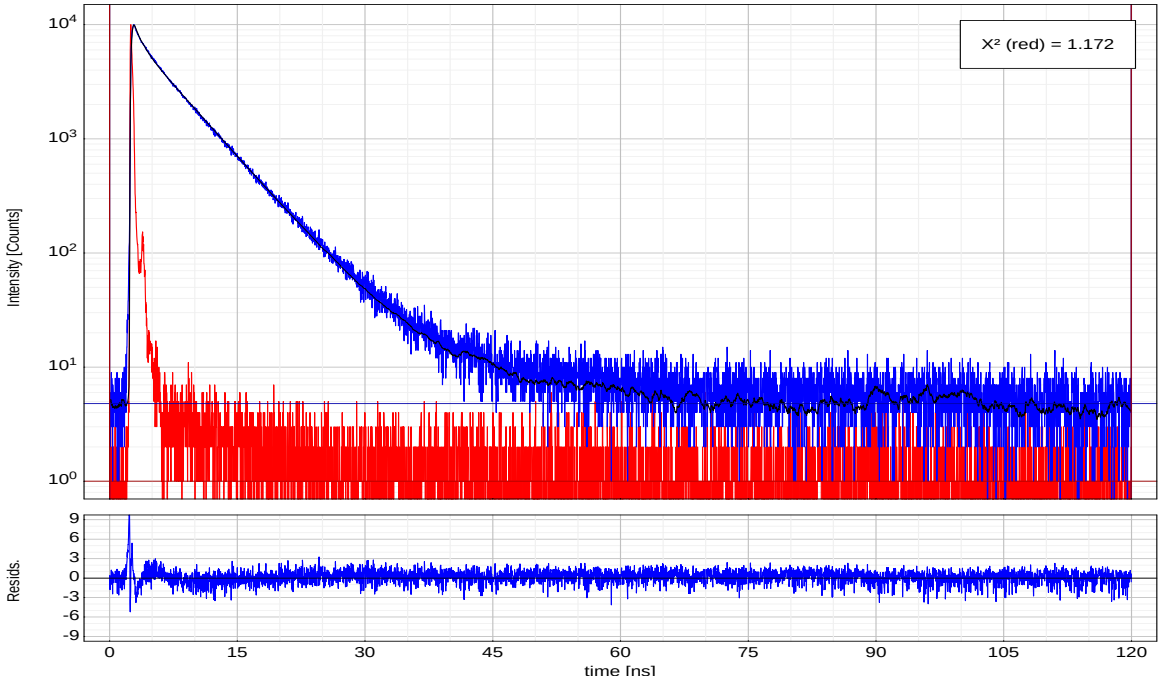

Figure 25: Fluorescence Decay of $SnCl_2$-Alpha Fraction 1.

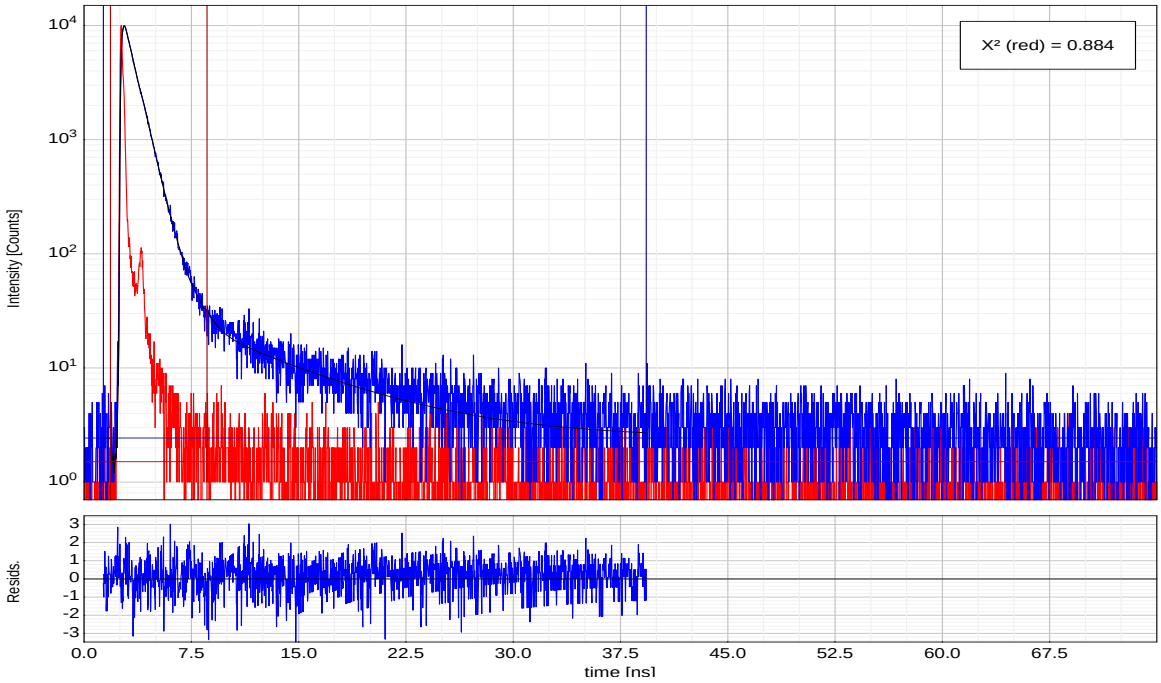

Figure 26: Fluorescence Decay of $SnCl_2$-Alpha Fraction 2.

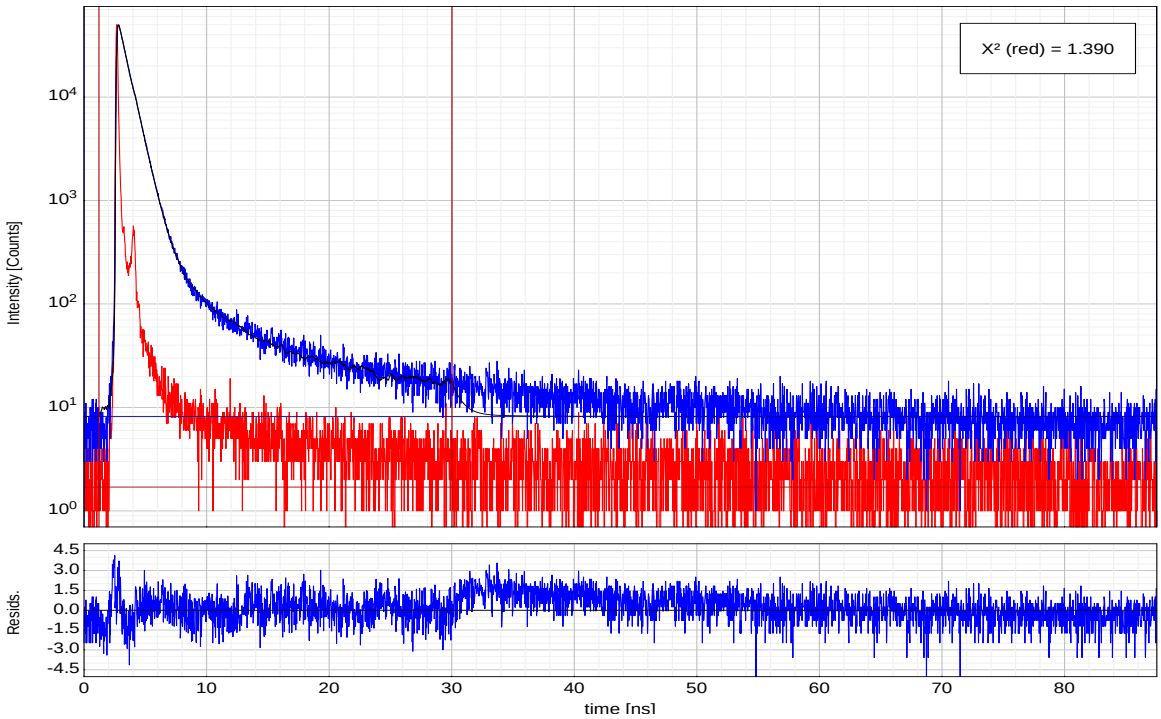

Figure 27: Fluorescence Decay of $SnCl_2$-Alpha Fraction 3.

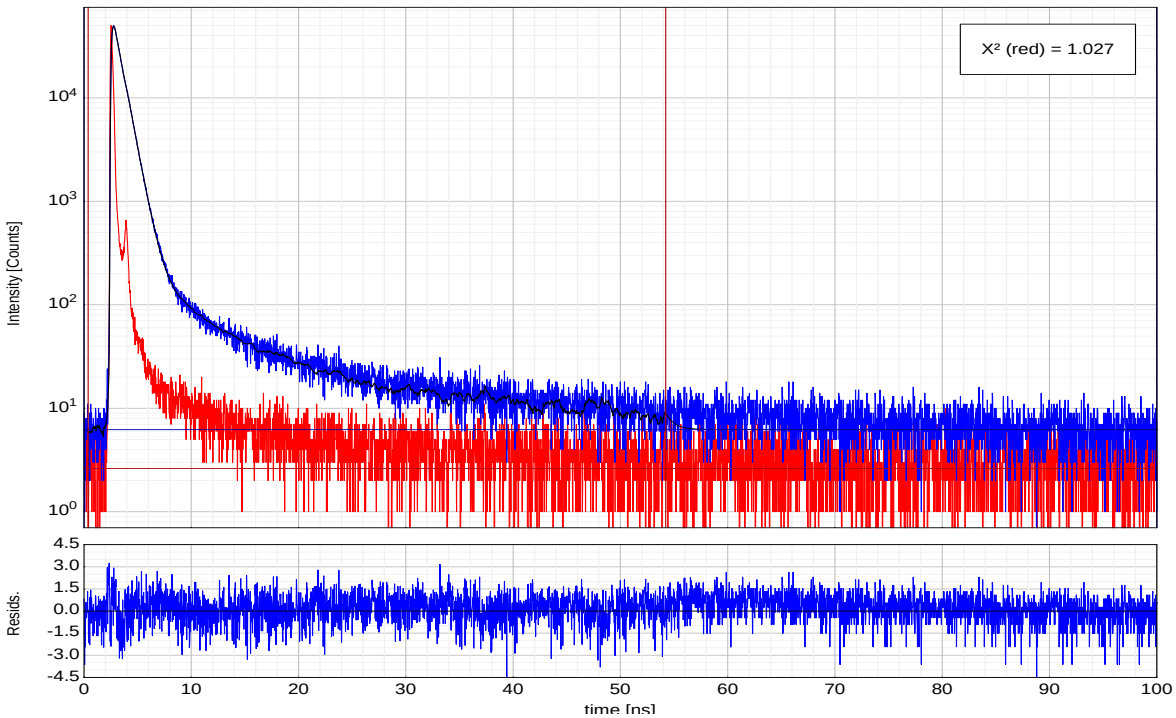

Figure 28: Fluorescence Decay of $SnCl_2$-Alpha Fraction 4.

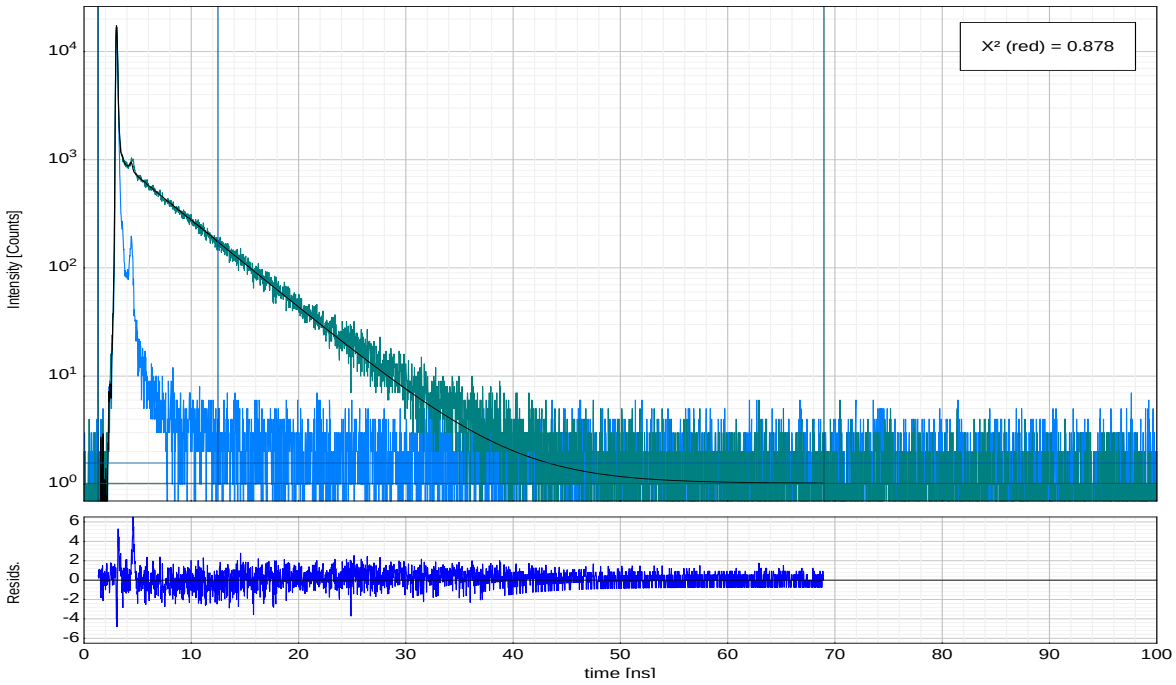

Figure 29: Fluorescence Decay of $SnCl_2$-Beta Fraction 1.

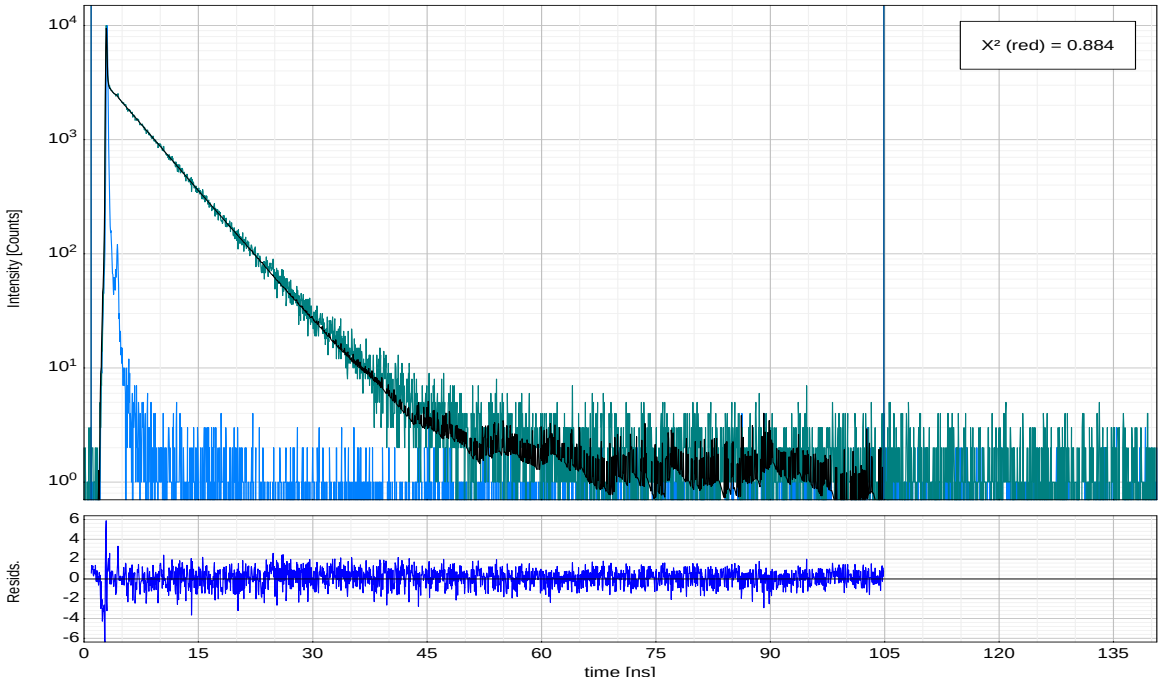

Figure 30: Fluorescence Decay of $SnCl_2$-Beta Fraction 2.

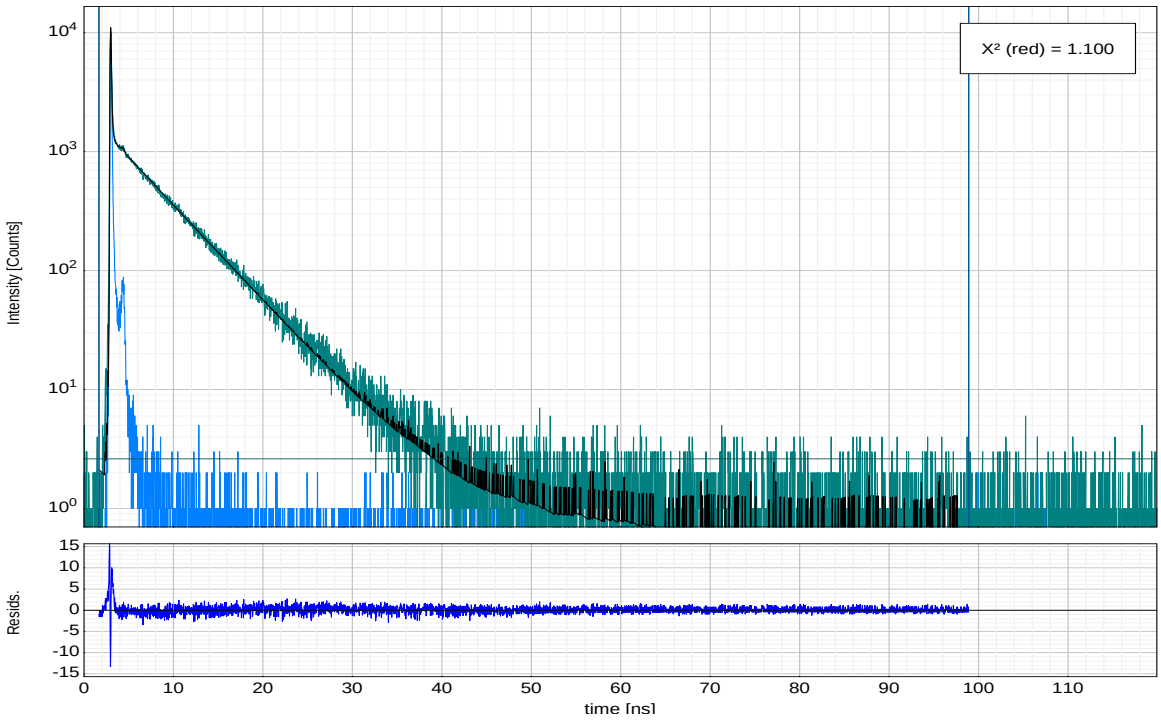

Figure 31: Fluorescence Decay of $SnCl_2$-Beta Fraction 3.

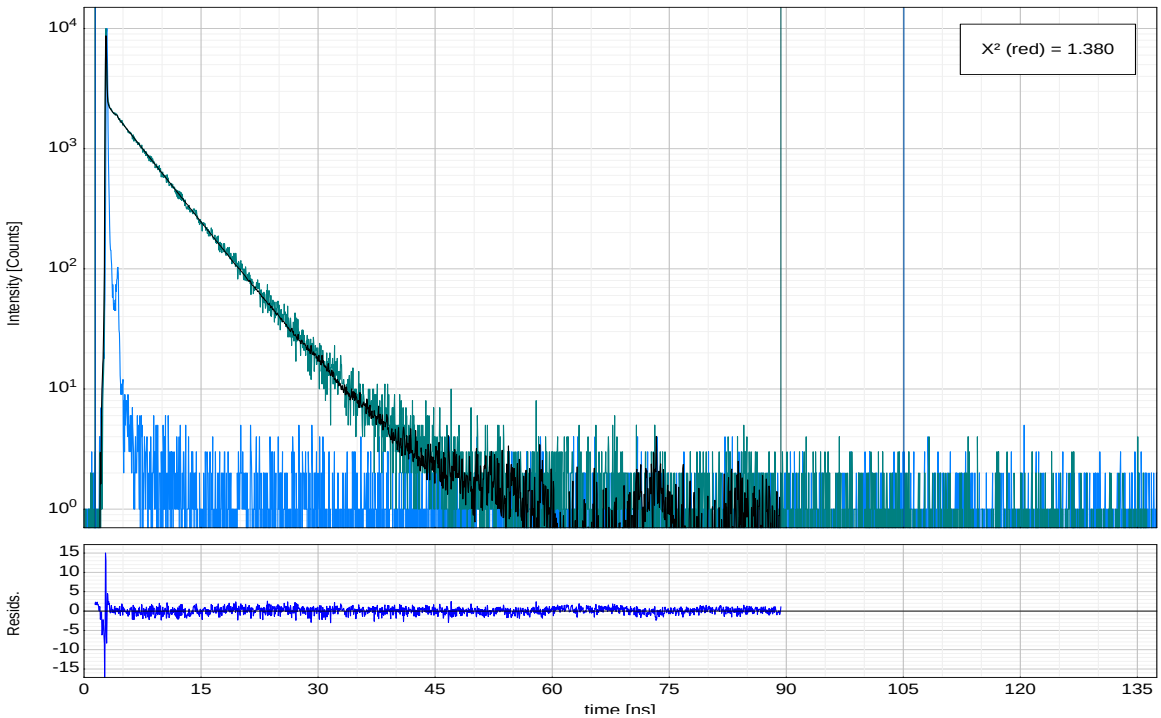

Figure 32: Fluorescence Decay of $SnCl_2$-Beta Fraction 4.

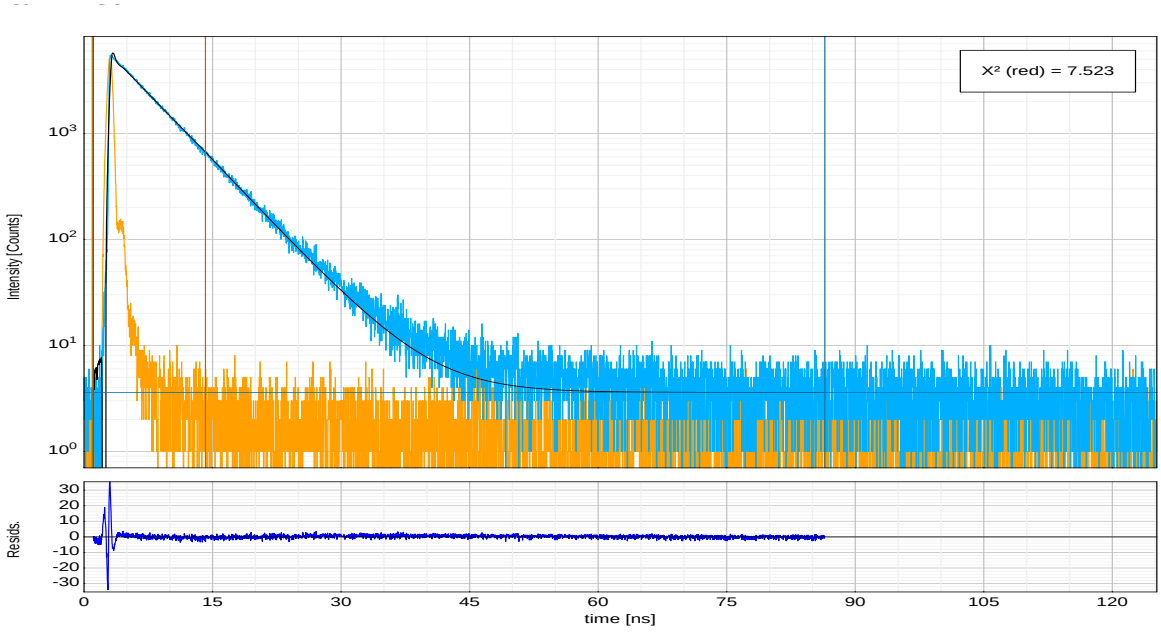

Figure 33: Fluorescence Isometric Decay of H2-Alpha Fraction 1.

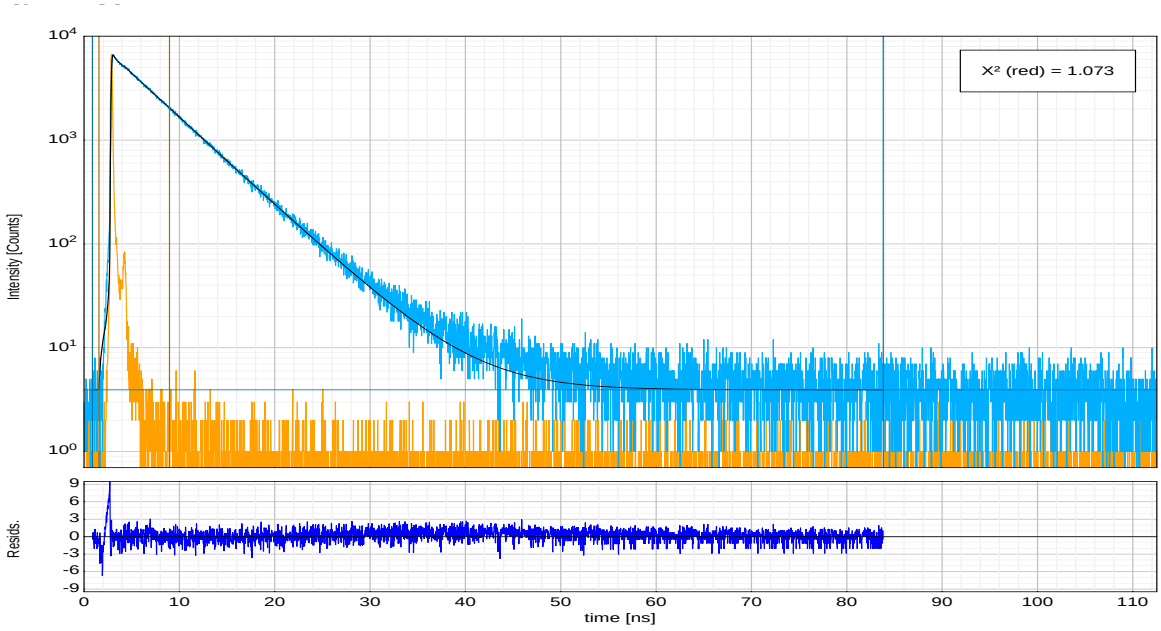

Figure 34: Fluorescence Isometric Decay of H2-Alpha Fraction 2.

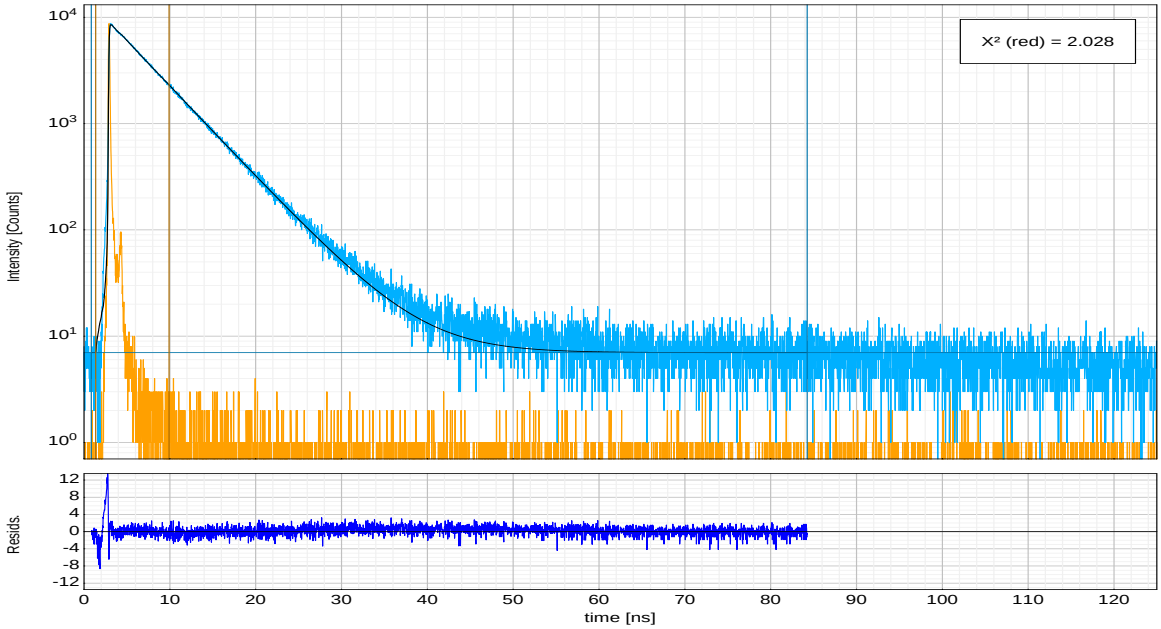

Figure 35: Fluorescence Isometric Decay of H2-Alpha Fraction 3.

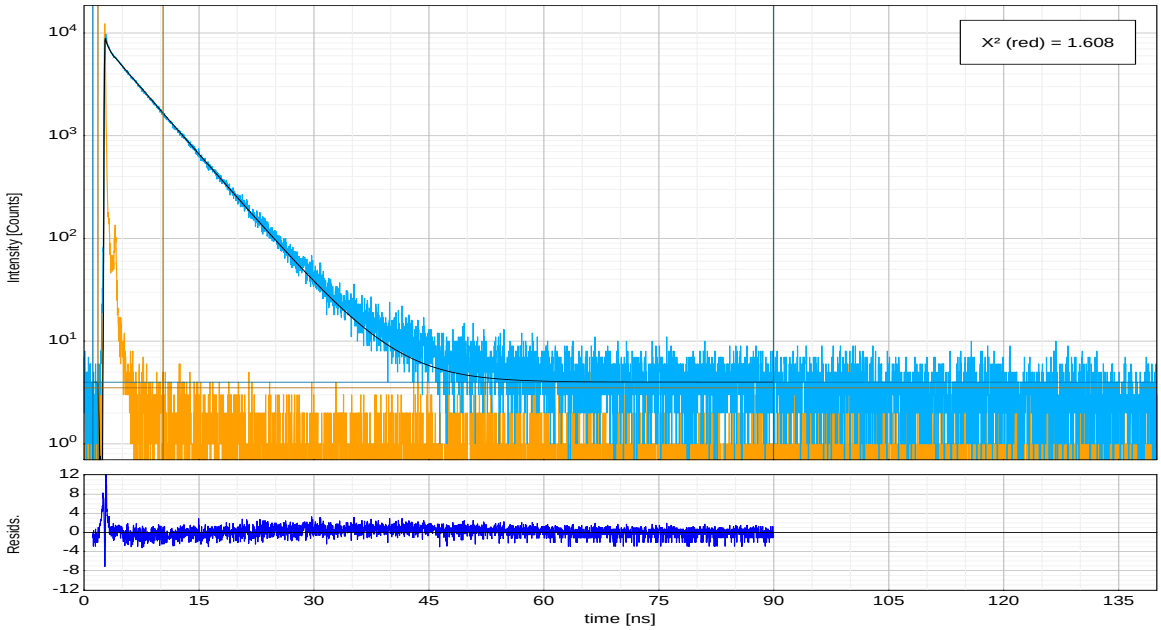

Figure 36: Fluorescence Isometric Decay of H2-Alpha Fraction 4.

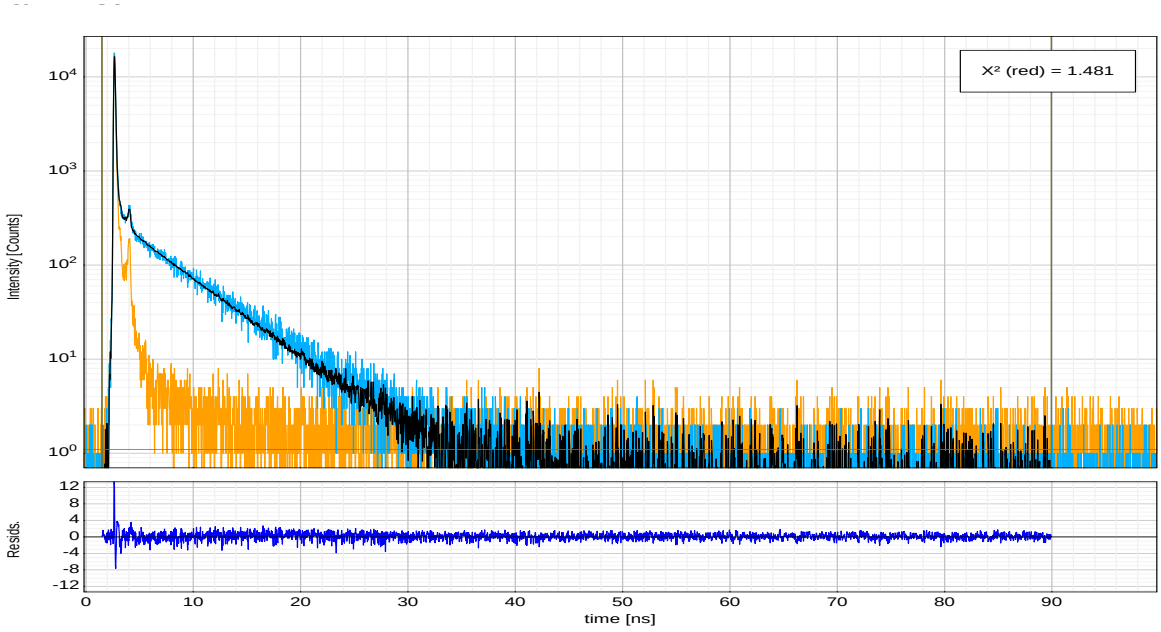

Figure 37: Fluorescence Isometric Decay of H2-Beta Fraction 1.

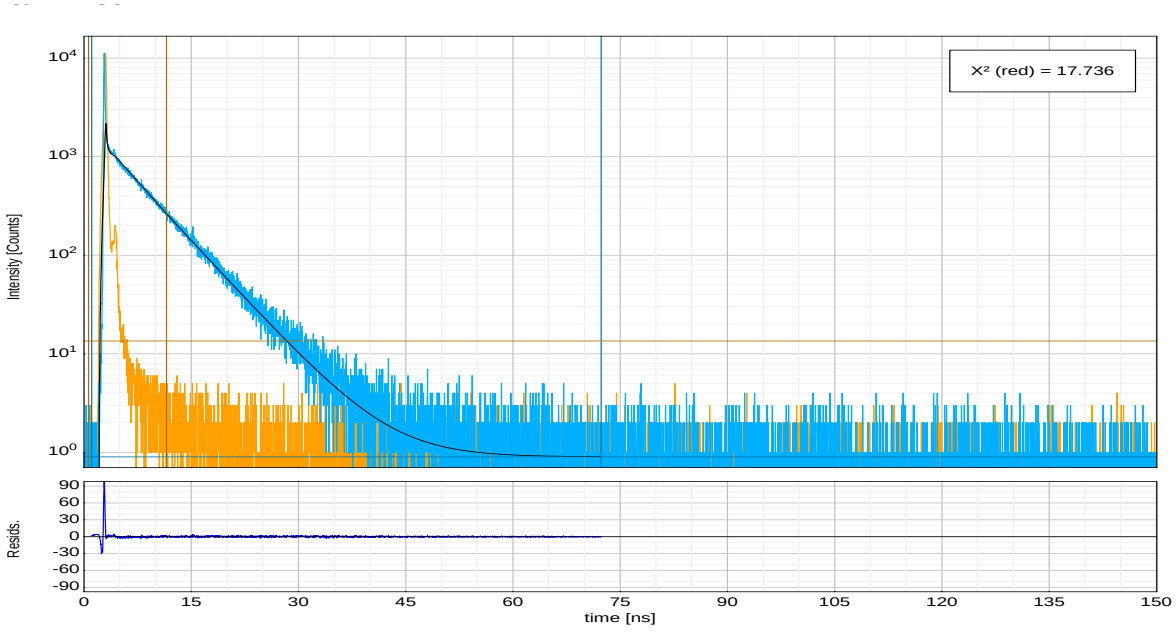

Figure 38: Fluorescence Isometric Decay of H2-Beta Fraction 2.

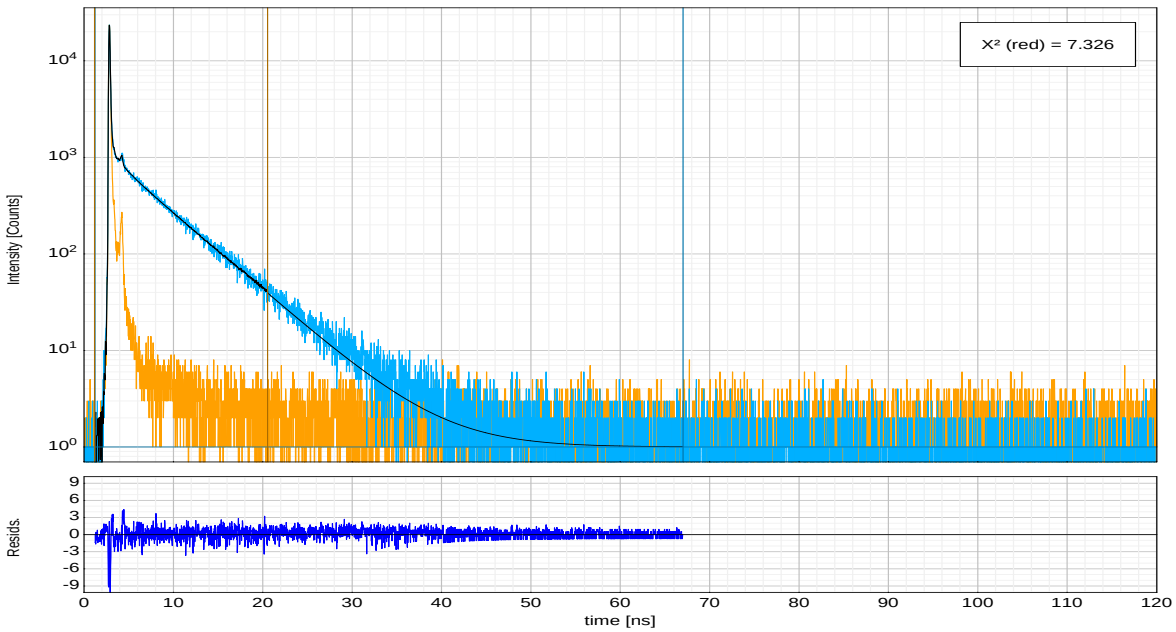

Figure 39: Fluorescence Isometric Decay of H2-Beta Fraction 3.

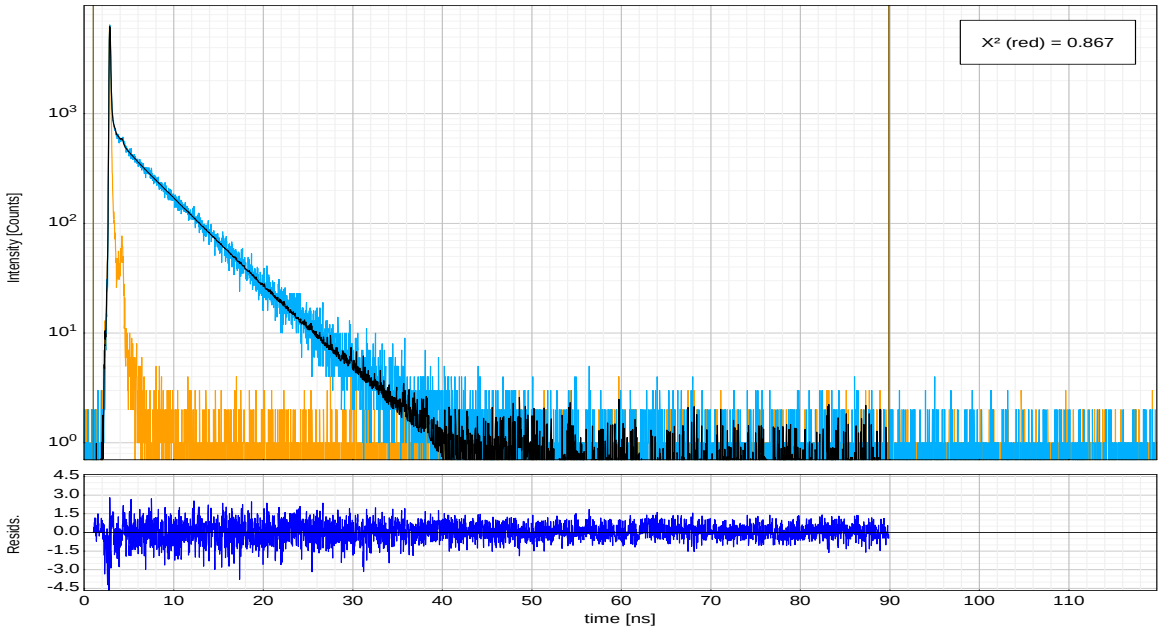

Figure 40: Fluorescence Isometric Decay of H2-Beta Fraction 4.

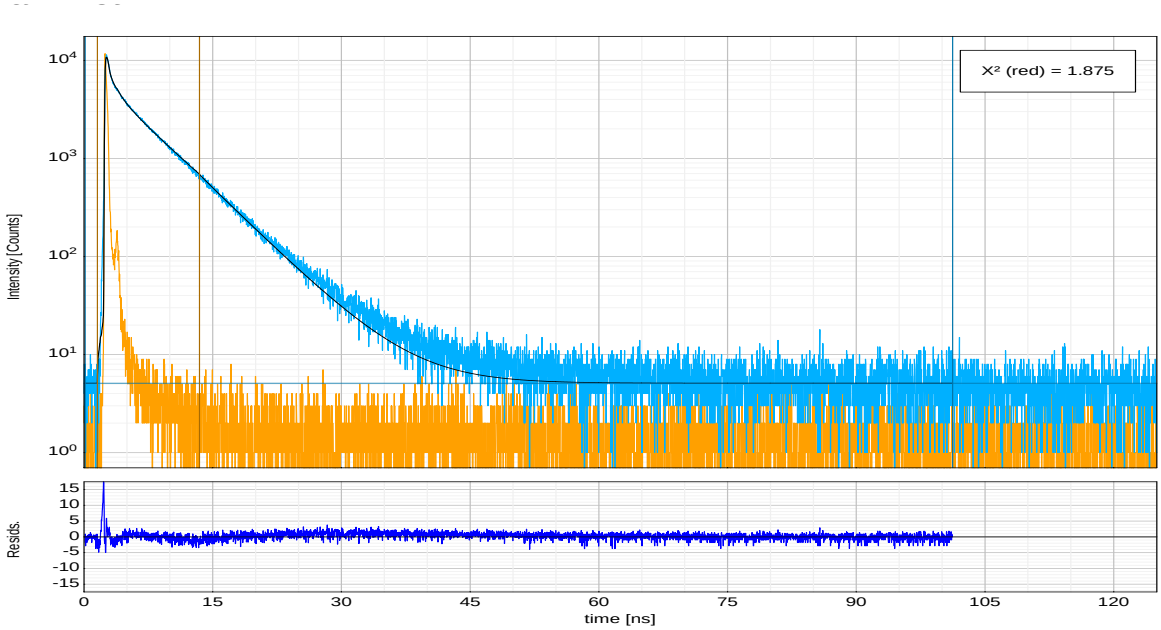

Figure 41: Fluorescence Isometric Decay of $SnCl_2$-Alpha Fraction 1.

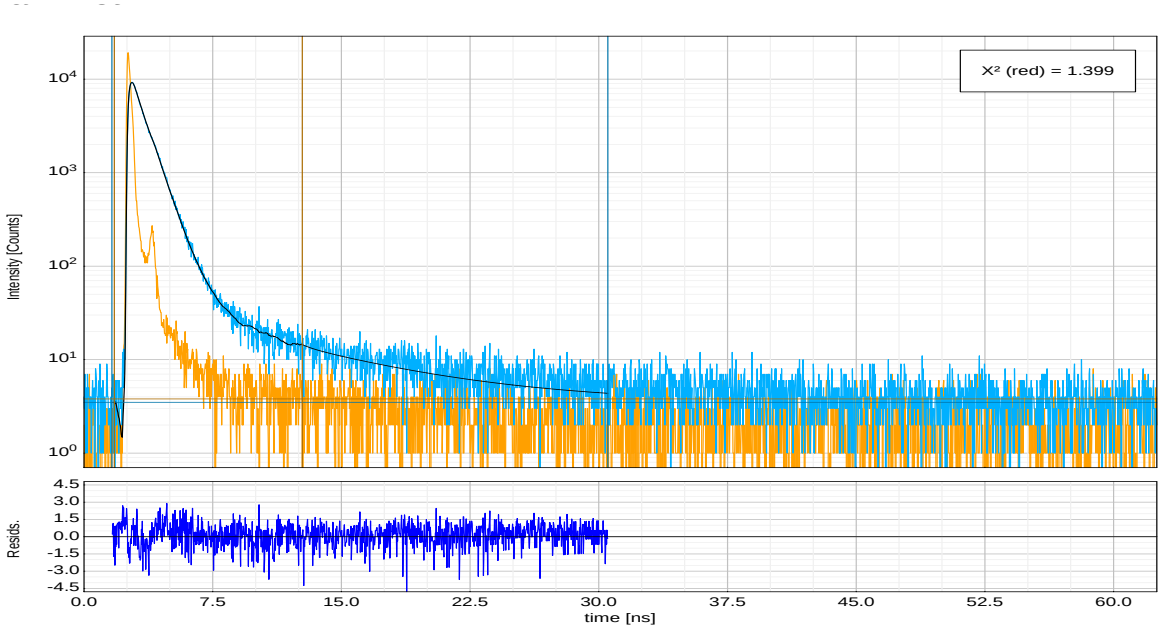

Figure 42: Fluorescence Isometric Decay of $SnCl_2$-Alpha Fraction 2.

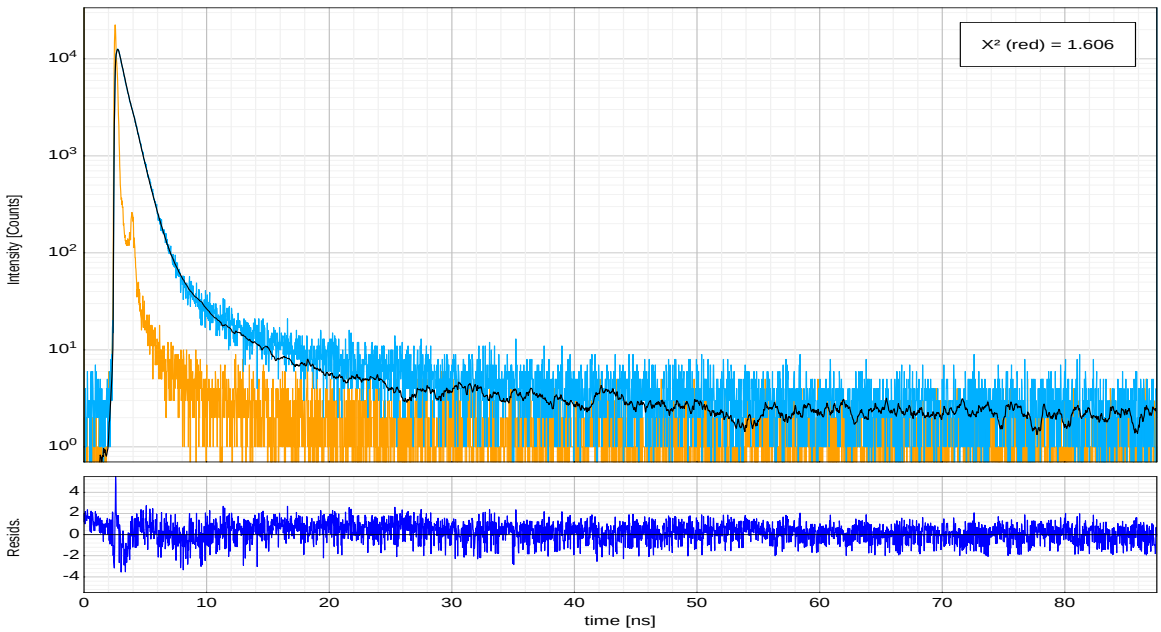

Figure 43: Fluorescence Isometric Decay of $SnCl_2$-Alpha Fraction 3.

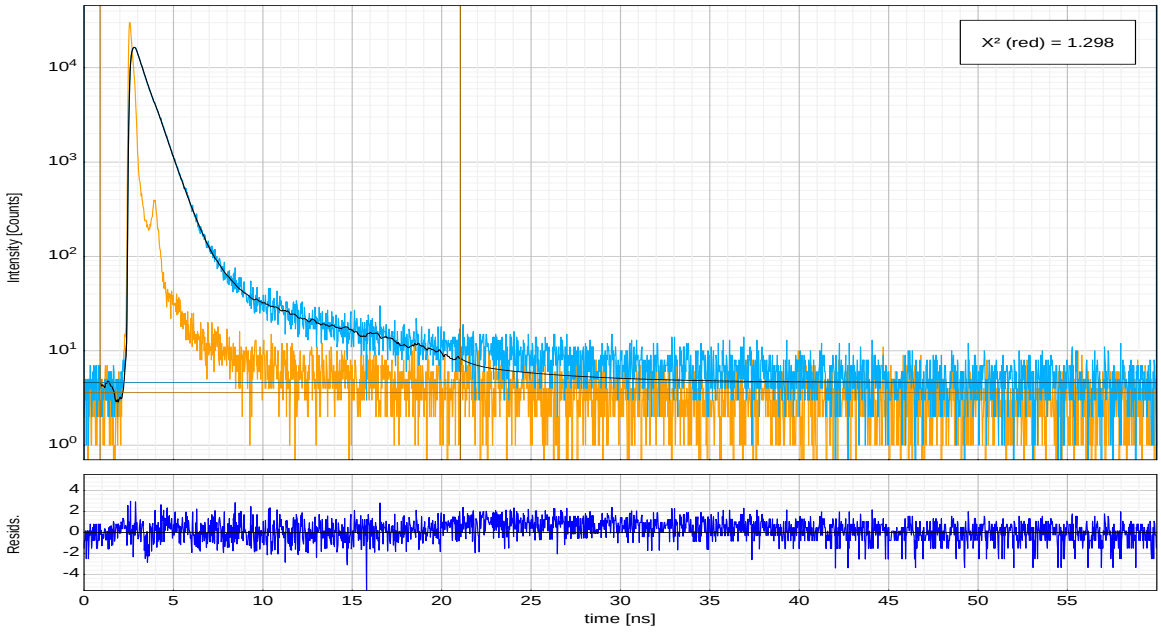

Figure 44: Fluorescence Isometric Decay of $SnCl_2$-Alpha Fraction 4.

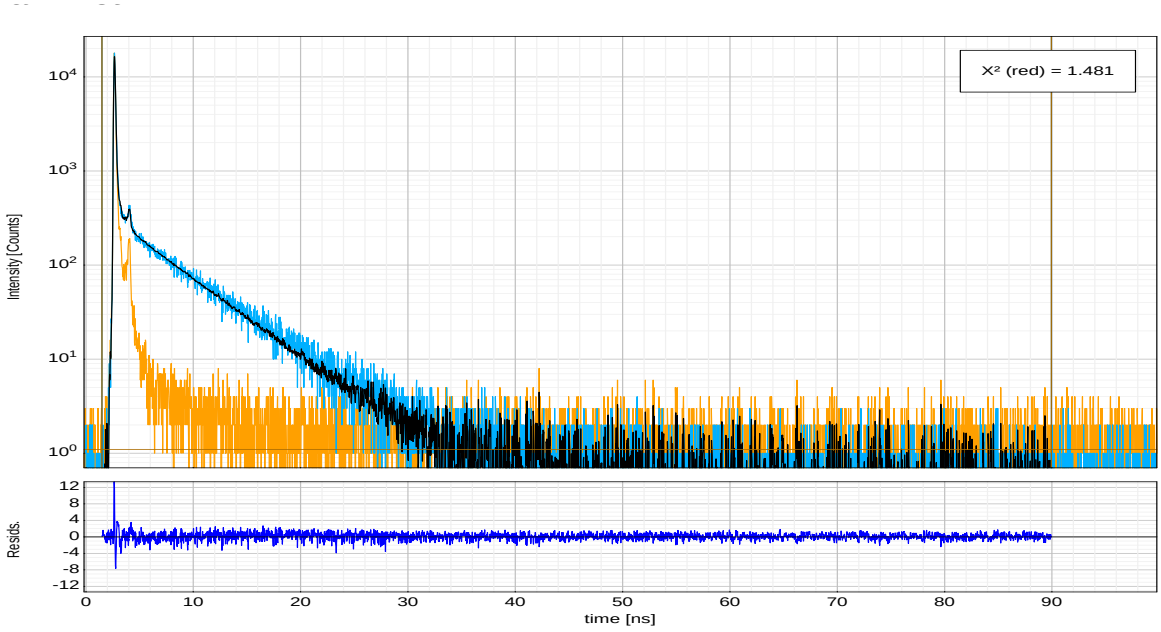

Figure 45: Fluorescence Isometric Decay of $SnCl_2$-Beta Fraction 1.

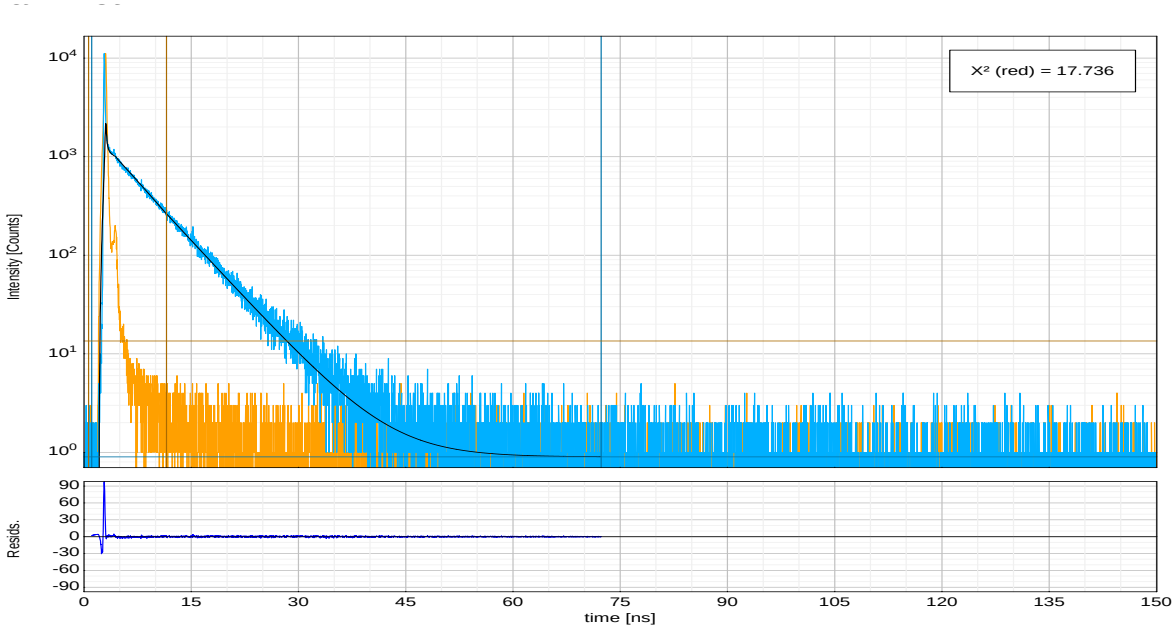

Figure 46: Fluorescence Isometric Decay of $SnCl_2$-Beta Fraction 2.

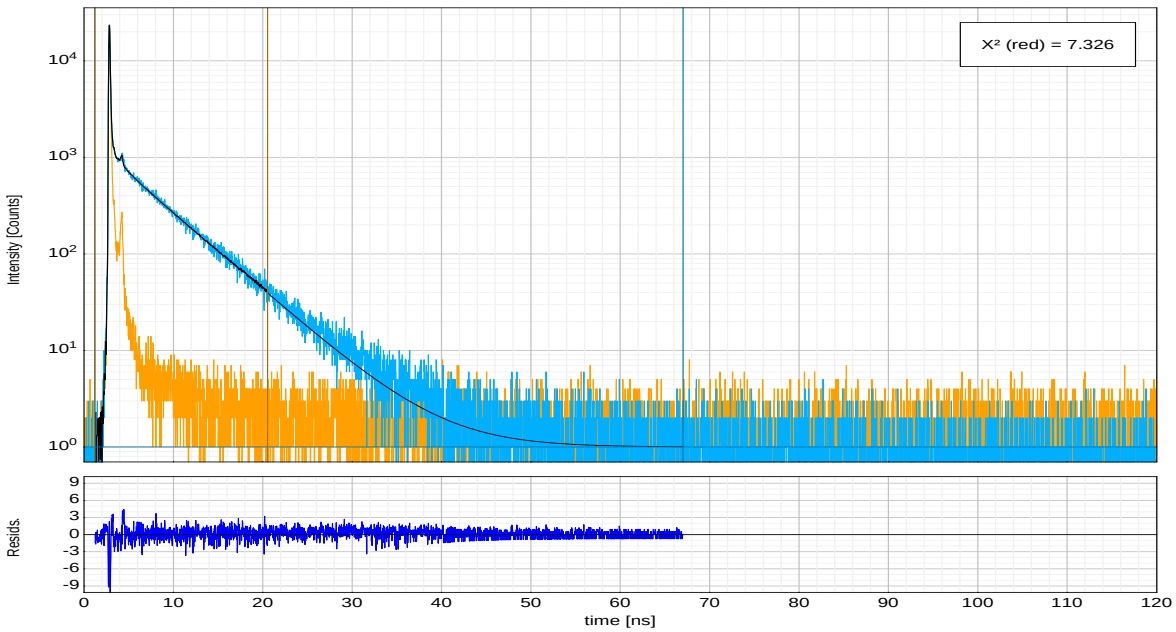

Figure 47: Fluorescence Isometric Decay of $SnCl_2$-Beta Fraction 3.

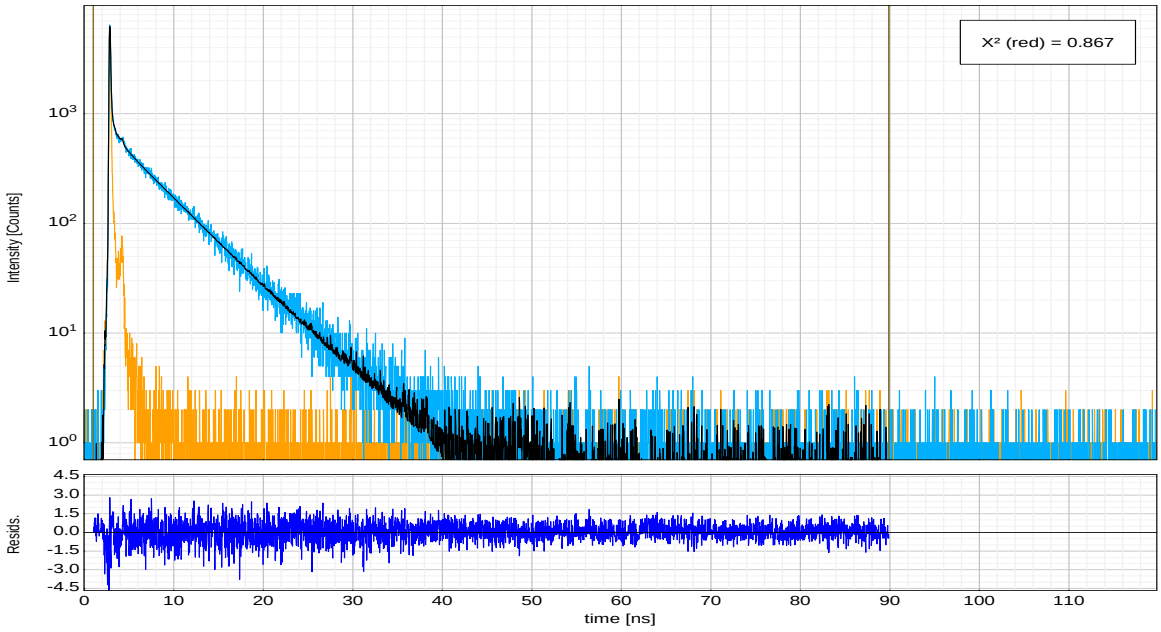

Figure 48: Fluorescence Isometric Decay of $SnCl_2$-Beta Fraction 4.

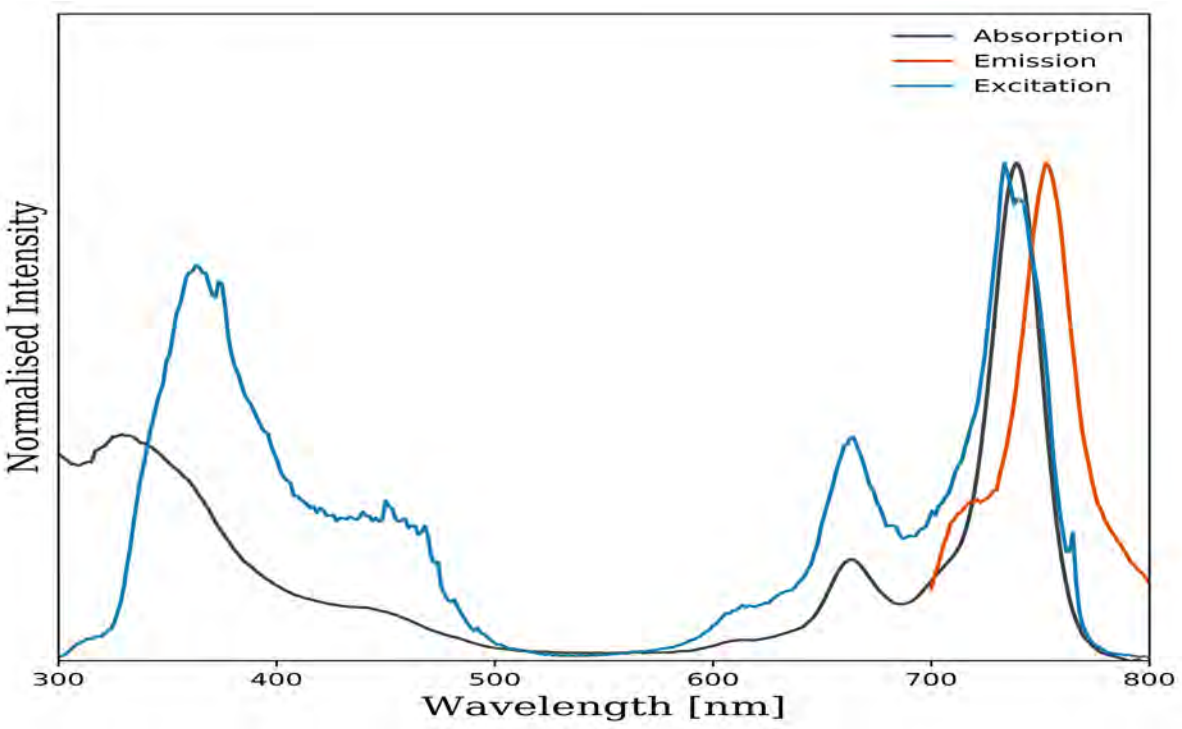

Figure 49: Fluorescence Excitation and Emission Spectra of C_{4h} $\alpha SnCl_2Pc$

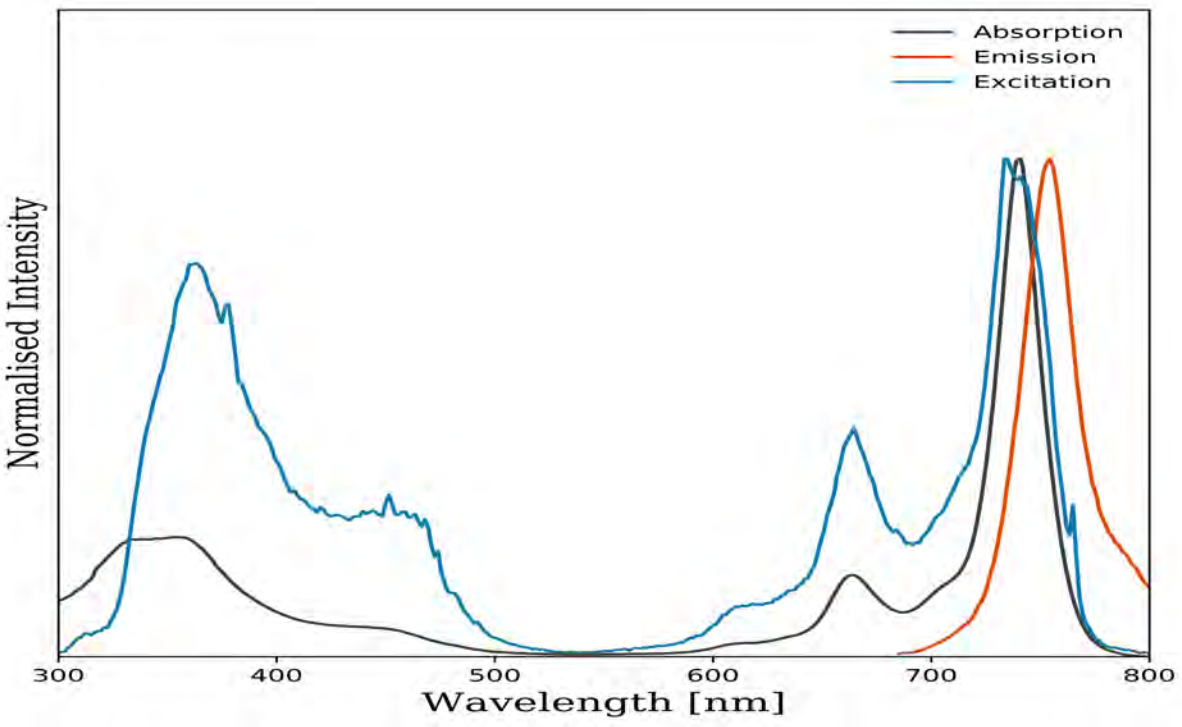

Figure 50: Fluorescence Excitation and Emission Spectra of C_{2v} $\alpha SnCl_2Pc$

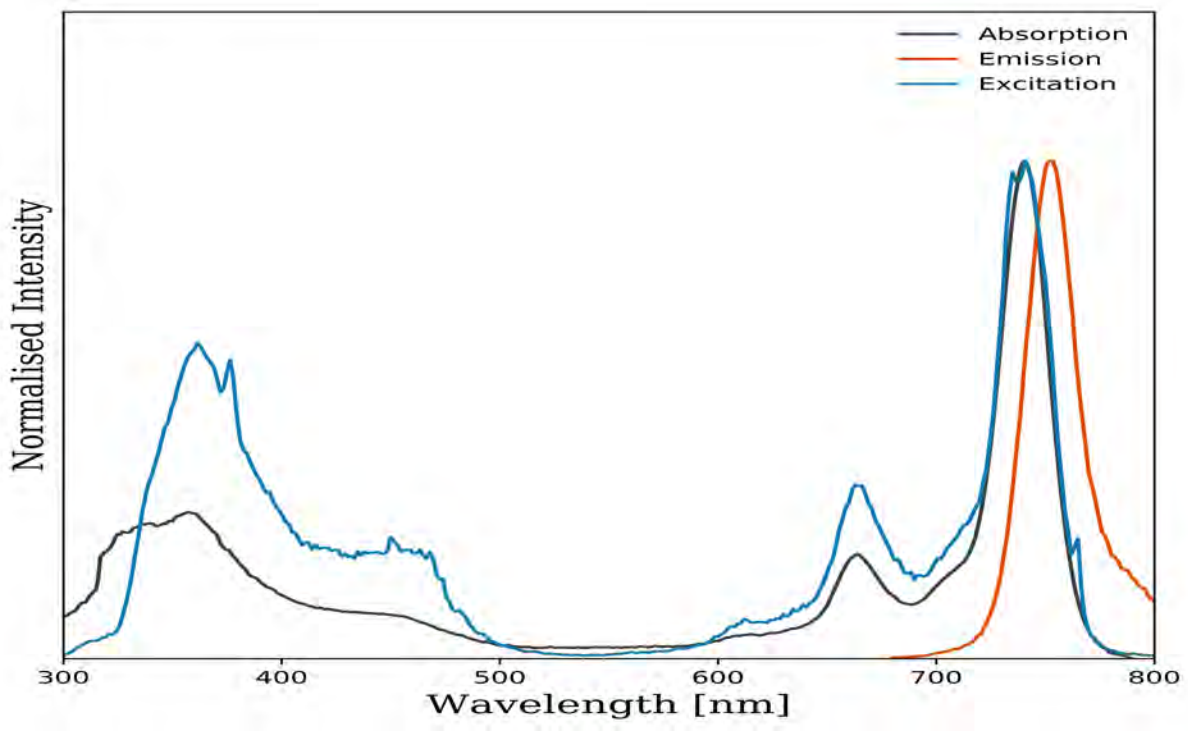

Figure 51: Fluorescence Excitation and Emission Spectra of C_s $\alpha SnCl_2Pc$

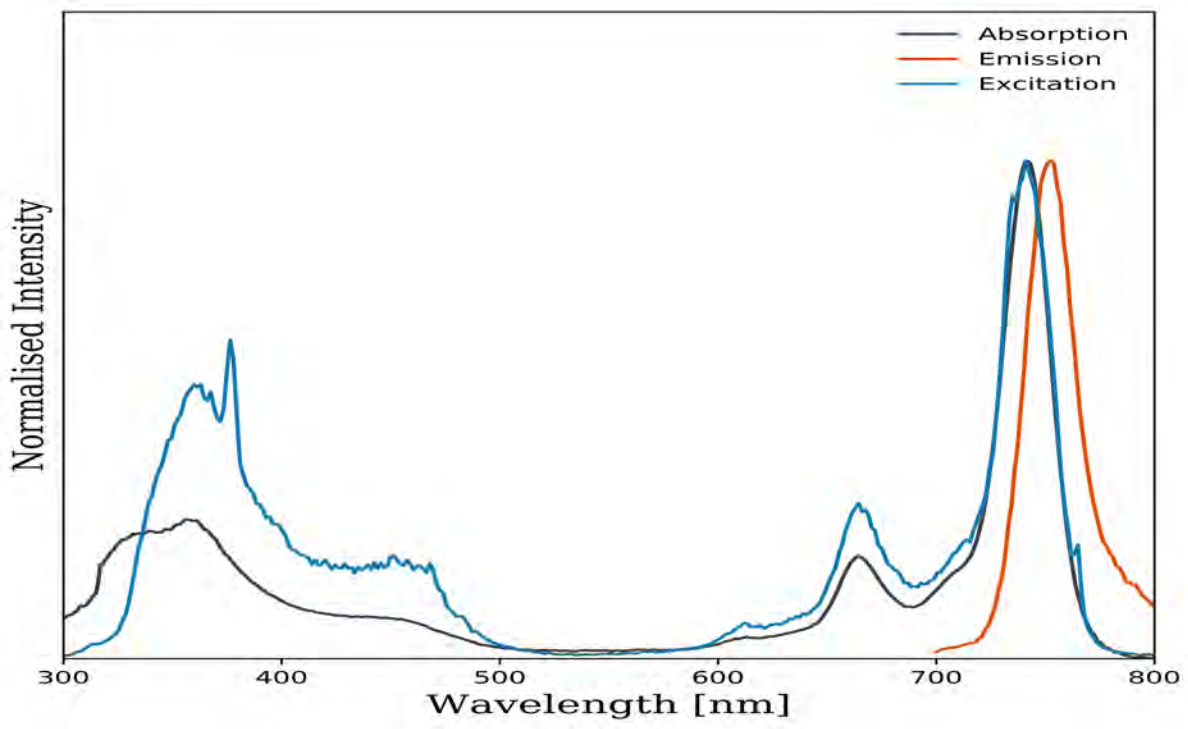

Figure 52: Fluorescence Excitation and Emission Spectra of D_{2h} $\alpha SnCl_2Pc$

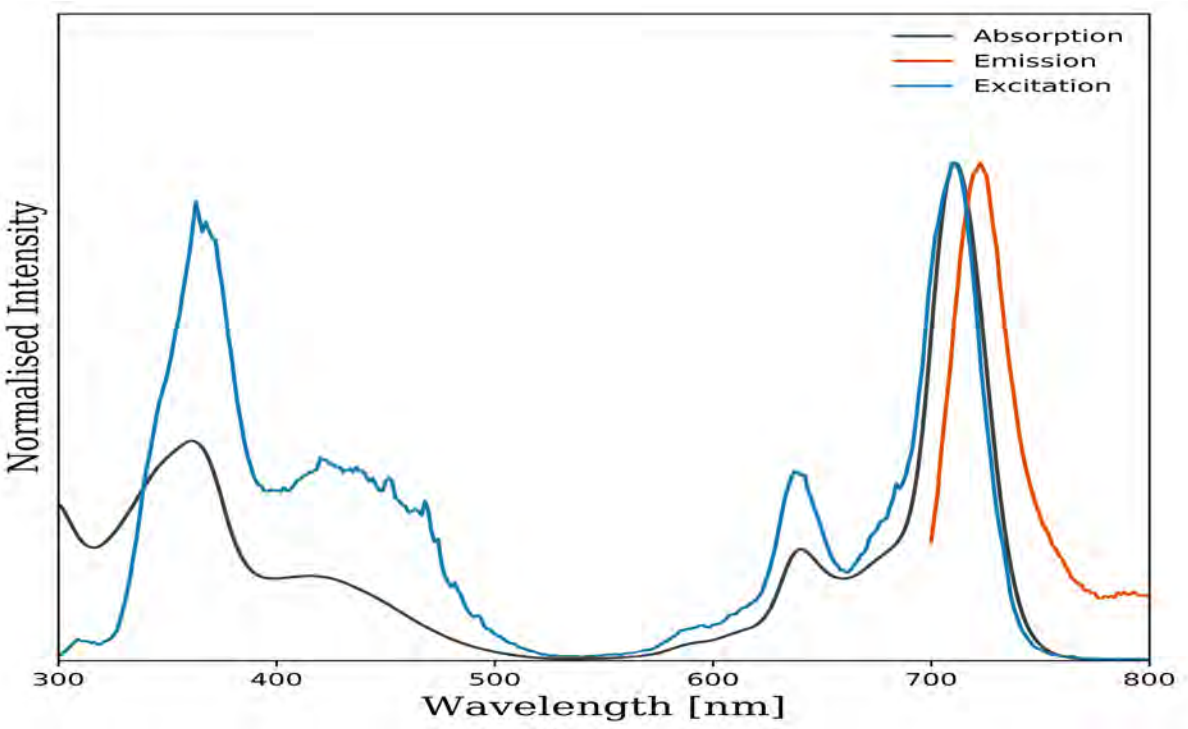

Figure 53: Fluorescence Excitation and Emission Spectra of C_{4h} $\beta SnCl_2Pc$

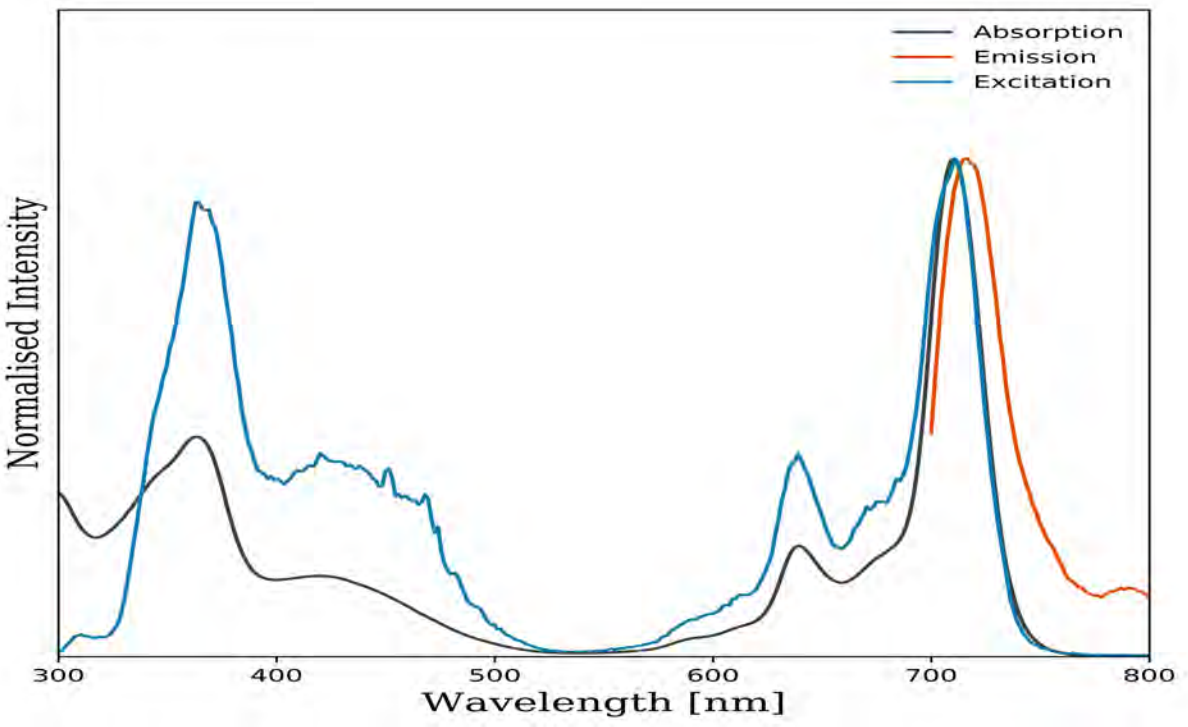

Figure 54: Fluorescence Excitation and Emission Spectra of C_{2v} $\beta SnCl_2Pc$

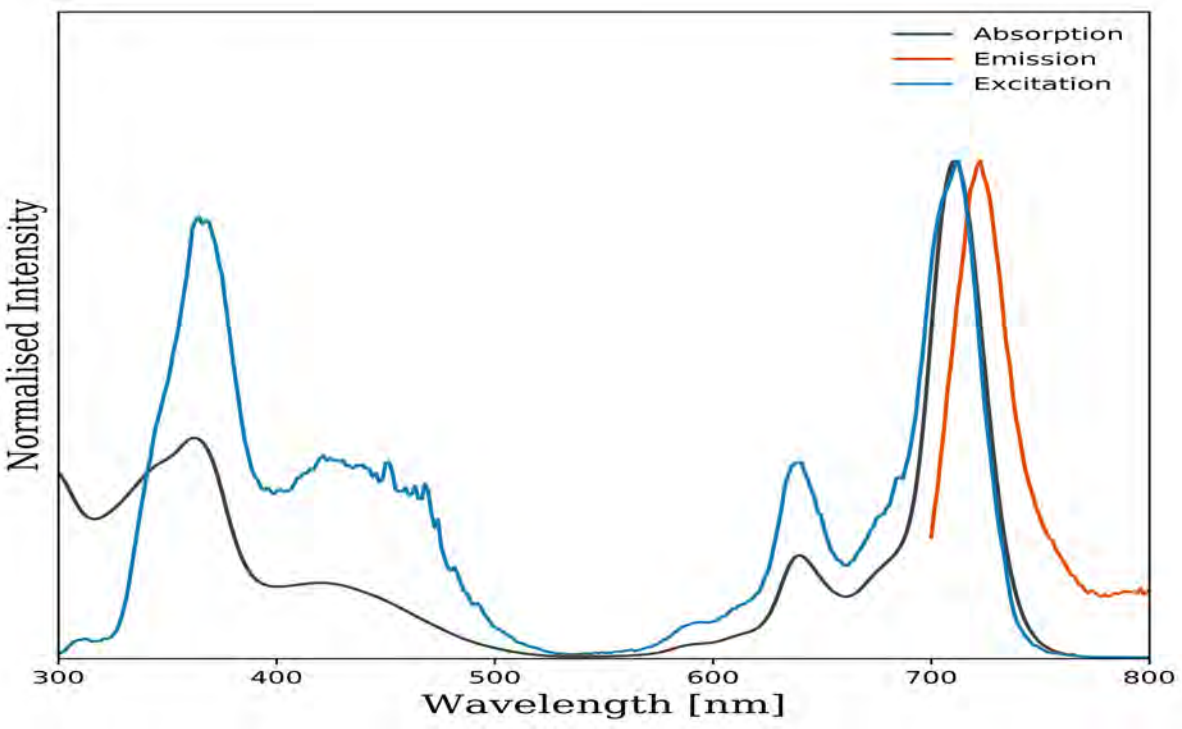

Figure 55: Fluorescence Excitation and Emission Spectra of C_s $\beta SnCl_2Pc$

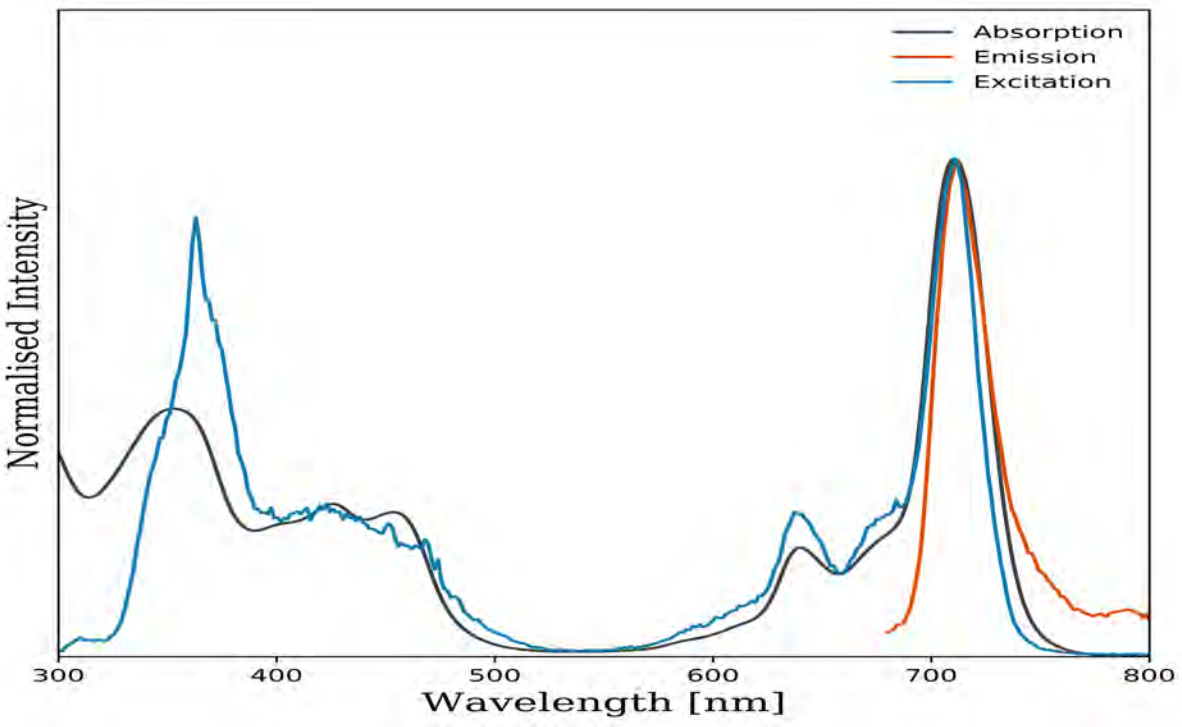

Figure 56: Fluorescence Excitation and Emission Spectra of D_{2h} $\beta SnCl_2Pc$

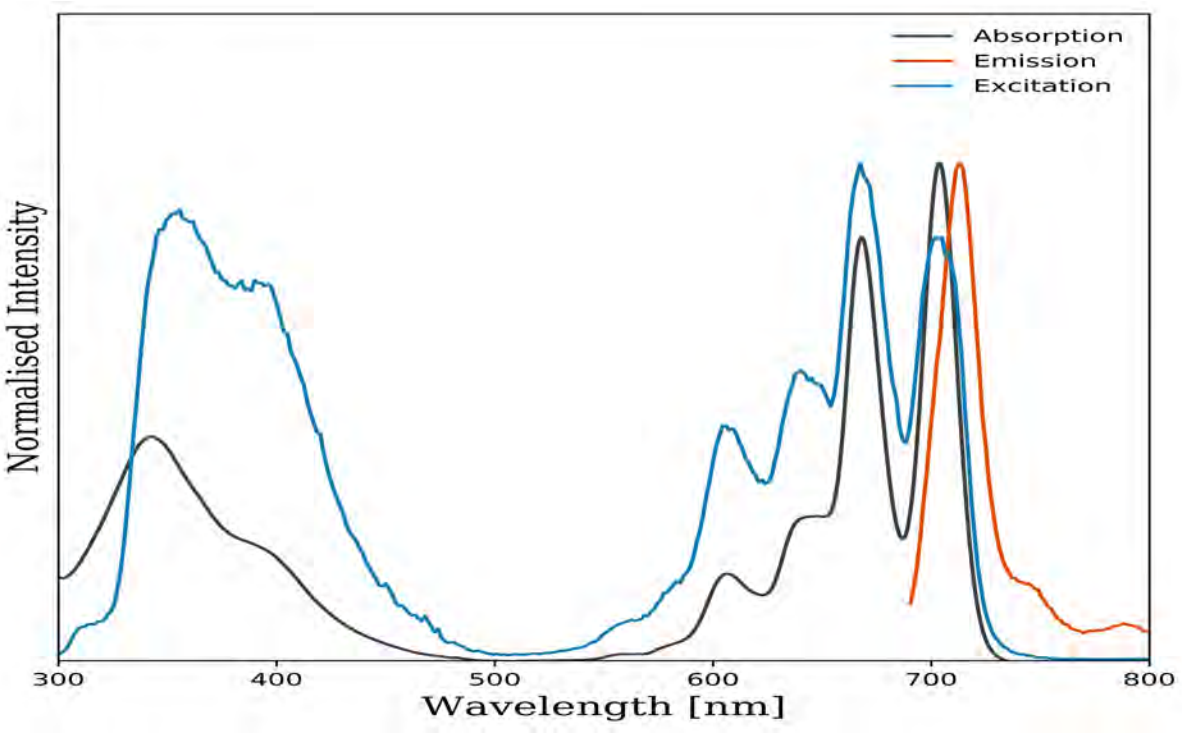

Figure 57: Fluorescence Excitation and Emission Spectra of C_{4h} βH_2Pc

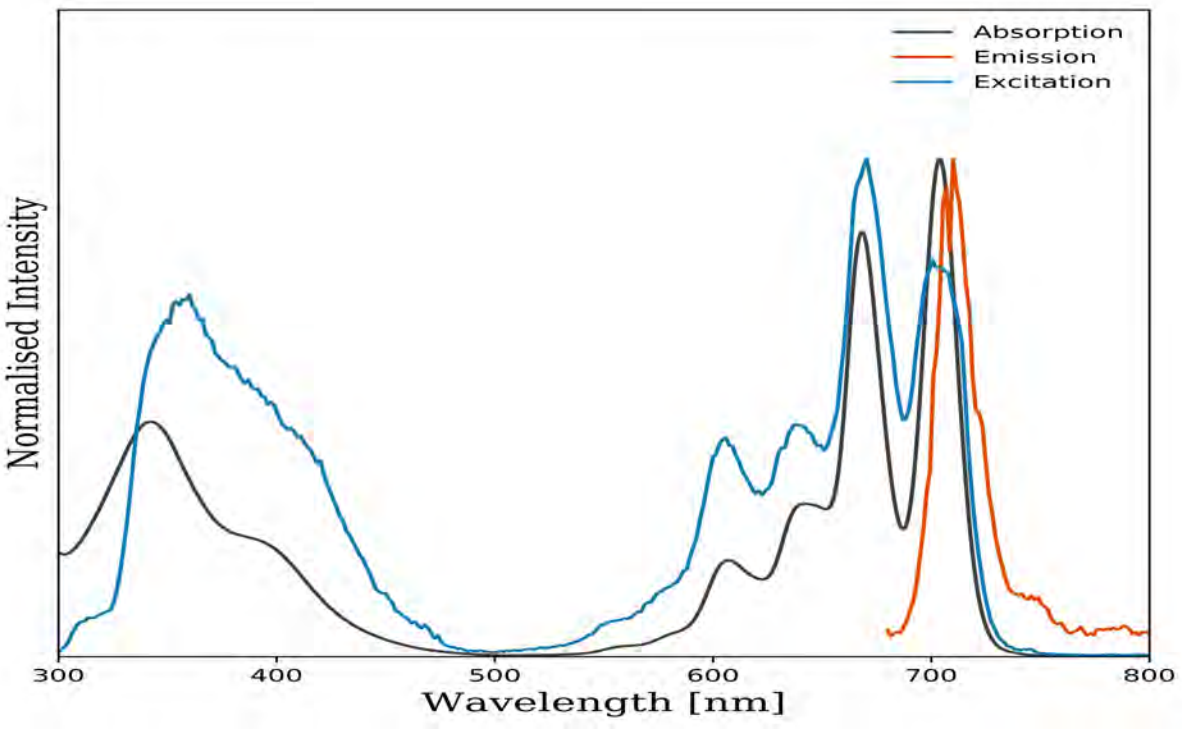

Figure 58: Fluorescence Excitation and Emission Spectra of C_{2v} βH_2Pc

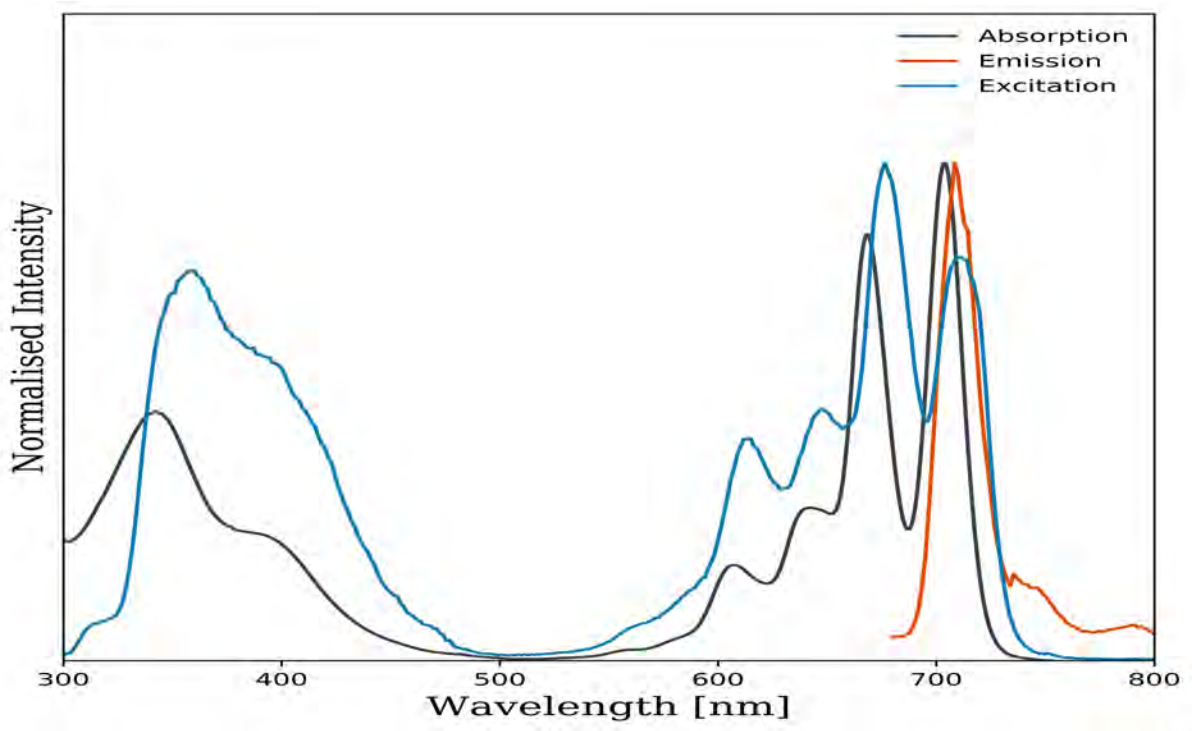

Figure 59: Fluorescence Excitation and Emission Spectra of C_s βH_2Pc

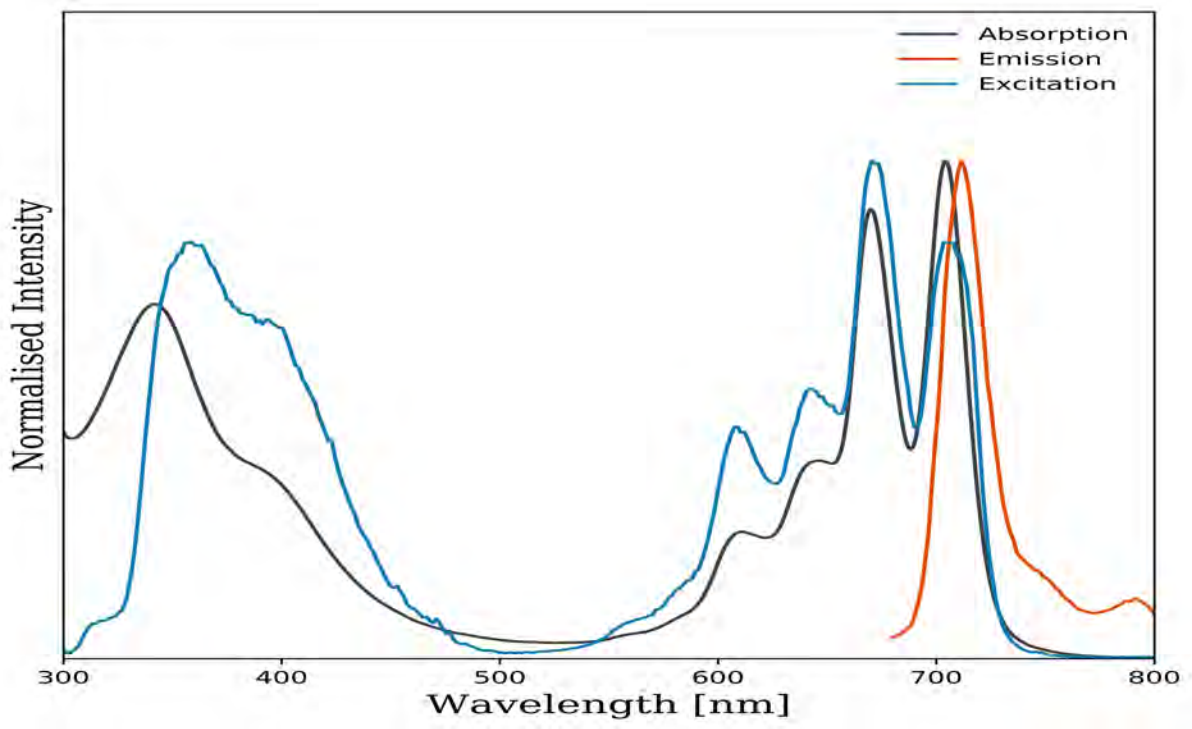

Figure 60: Fluorescence Excitation and Emission Spectra of D_{2h} βH_2Pc

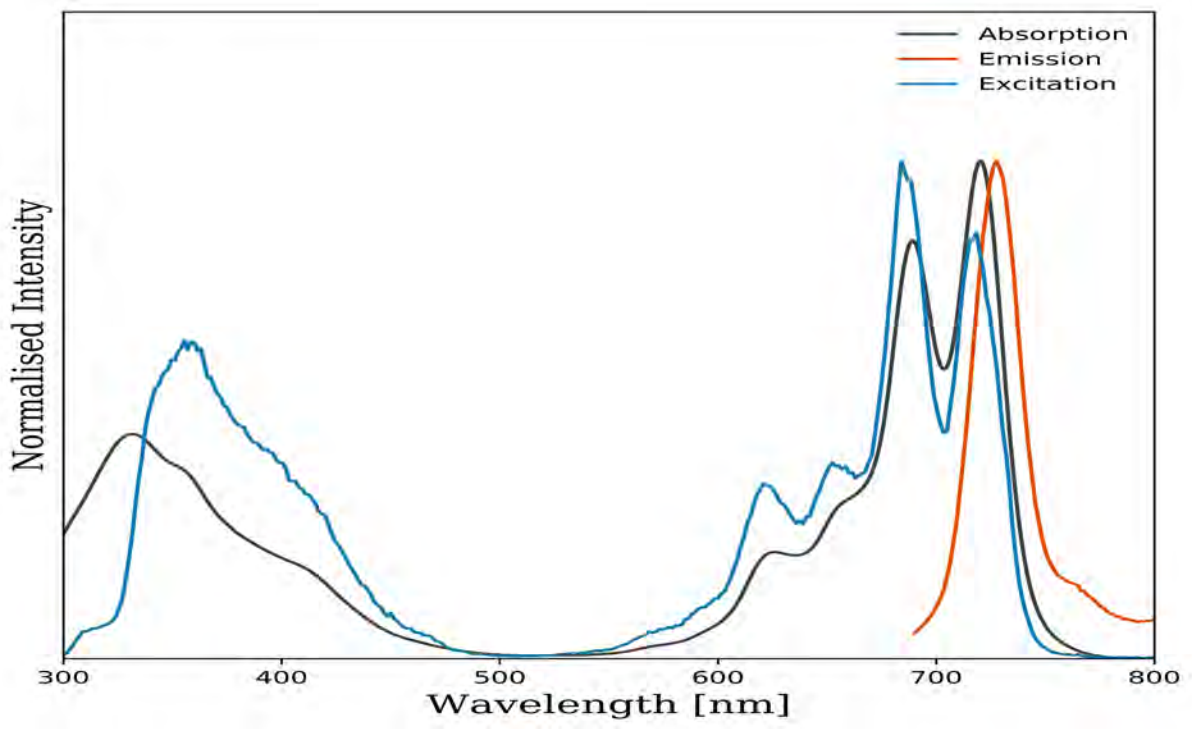

Figure 61: Fluorescence Excitation and Emission Spectra of C_{4h} αH_2Pc

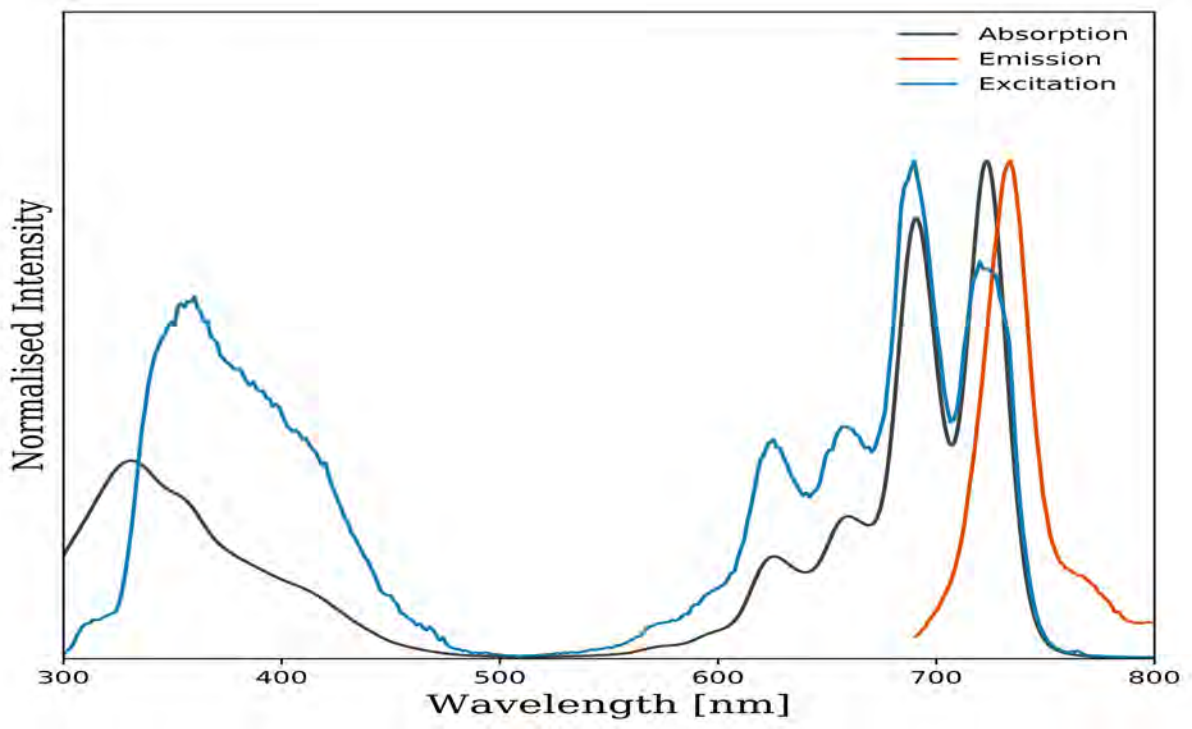

Figure 62: Fluorescence Excitation and Emission Spectra of C_{2v} αH_2Pc

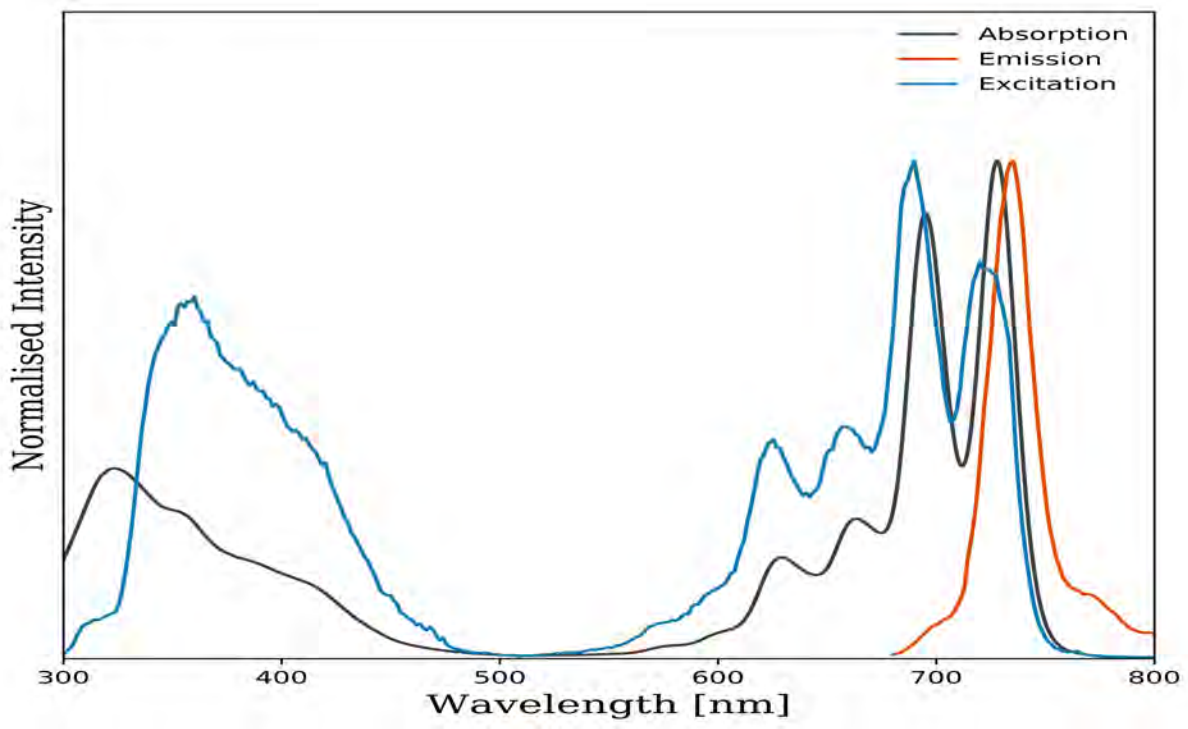

Figure 63: Fluorescence Excitation and Emission Spectra of C_s αH_2Pc

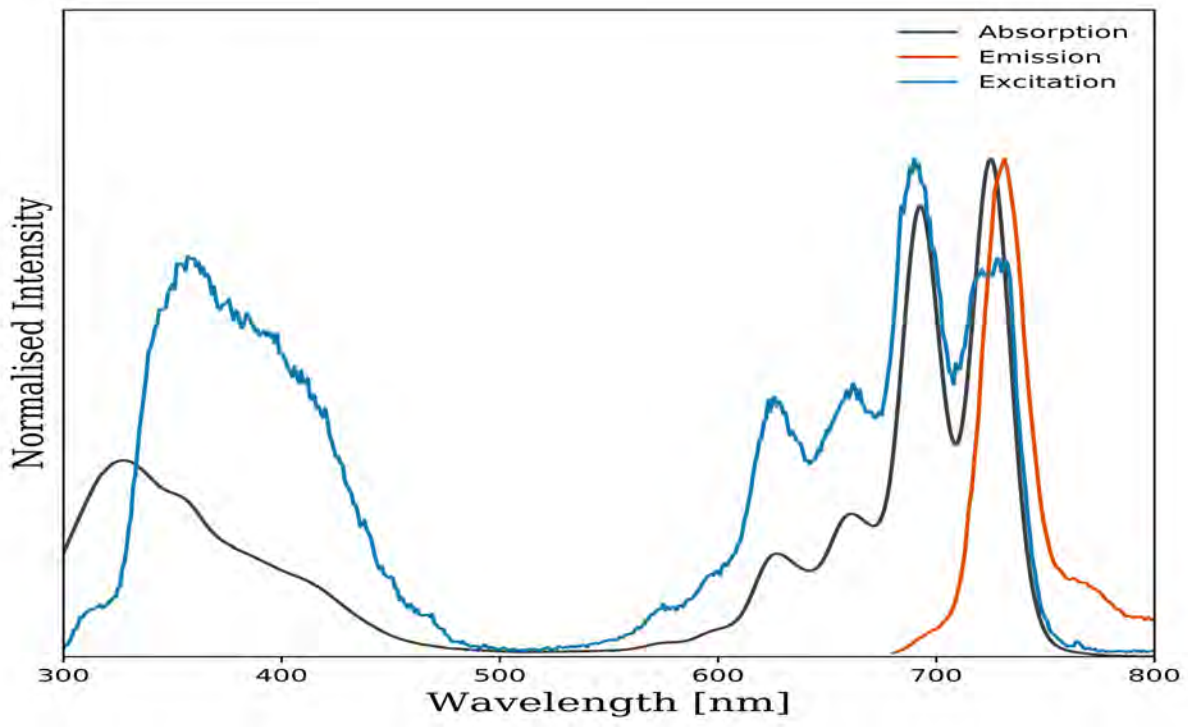

Figure 64: Fluorescence Excitation and Emission Spectra of D_{2h} αH_2Pc

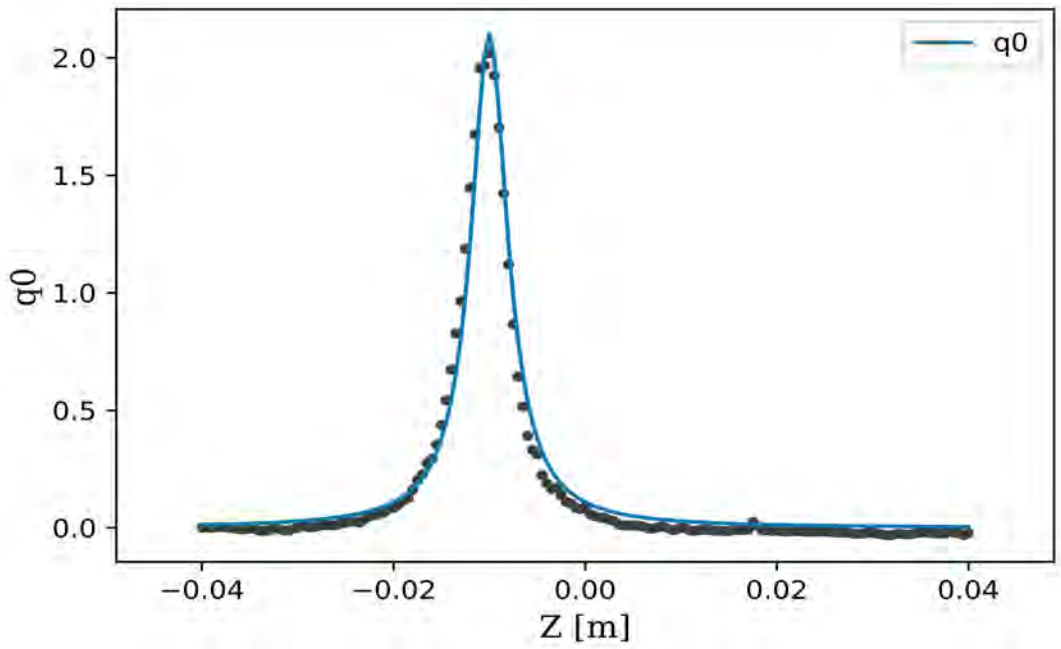

Figure 65: Open apeture Zscan of the C_{4h} isomer of the $\alpha SnCl_2Pc$ at 2.2×10^{12} W.m^{-2}.

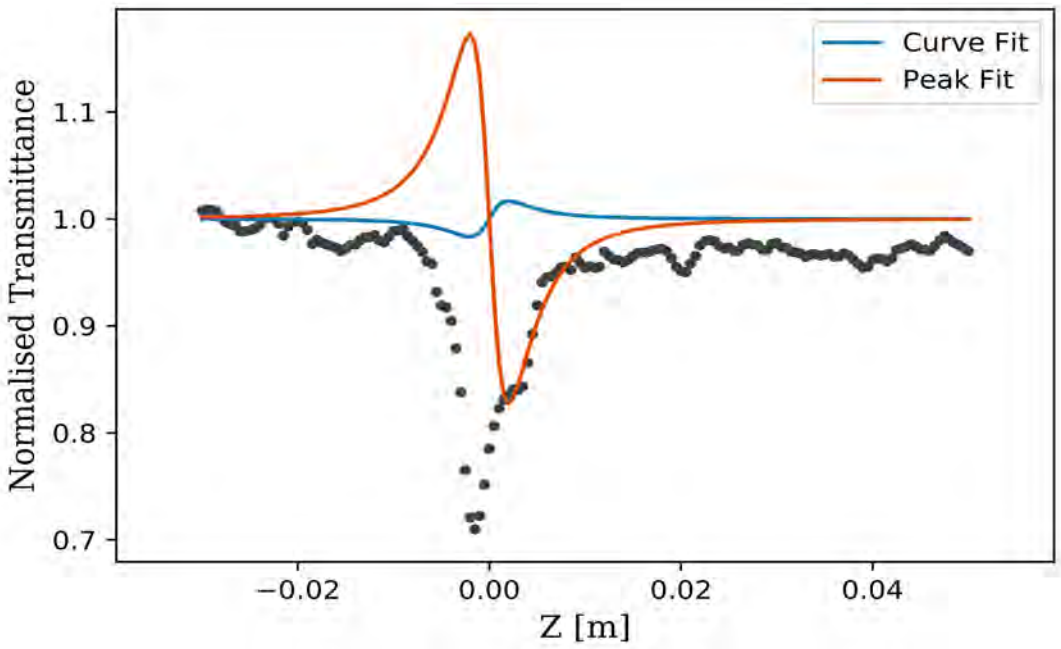

Figure 66: Closed apeture Zscan of the C_{4h} isomer of the $\alpha SnCl_2Pc$ at 2.2×10^{12} W.m^{-2}.

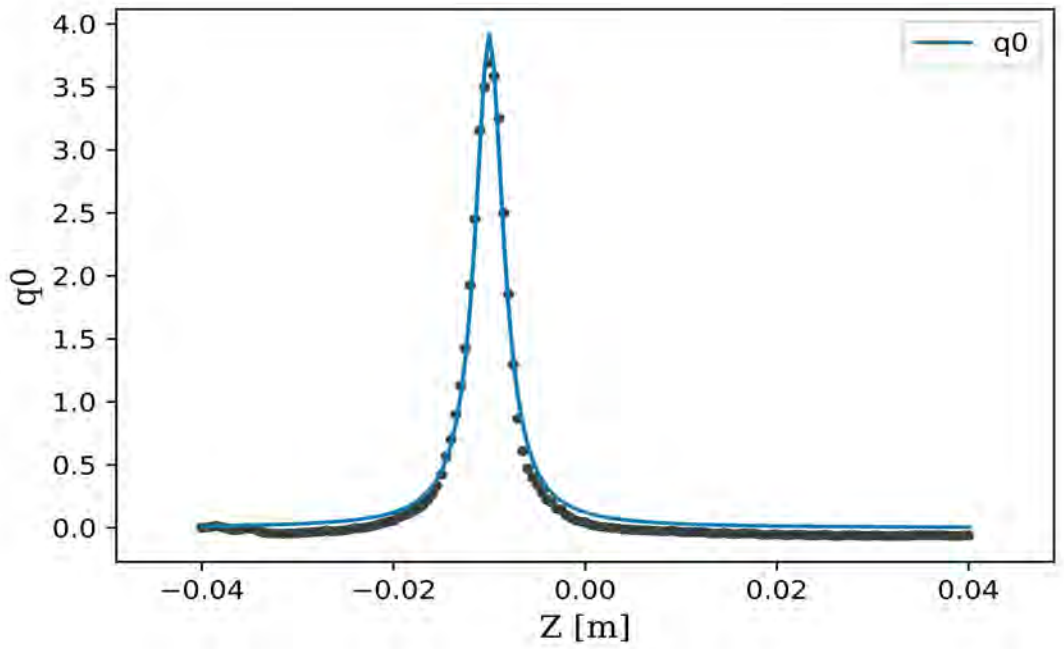

Figure 67: Open apeture Zscan of the C_{4h} isomer of the $\alpha SnCl_2Pc$ at 4.2×10^{12} W.m^{-2}.

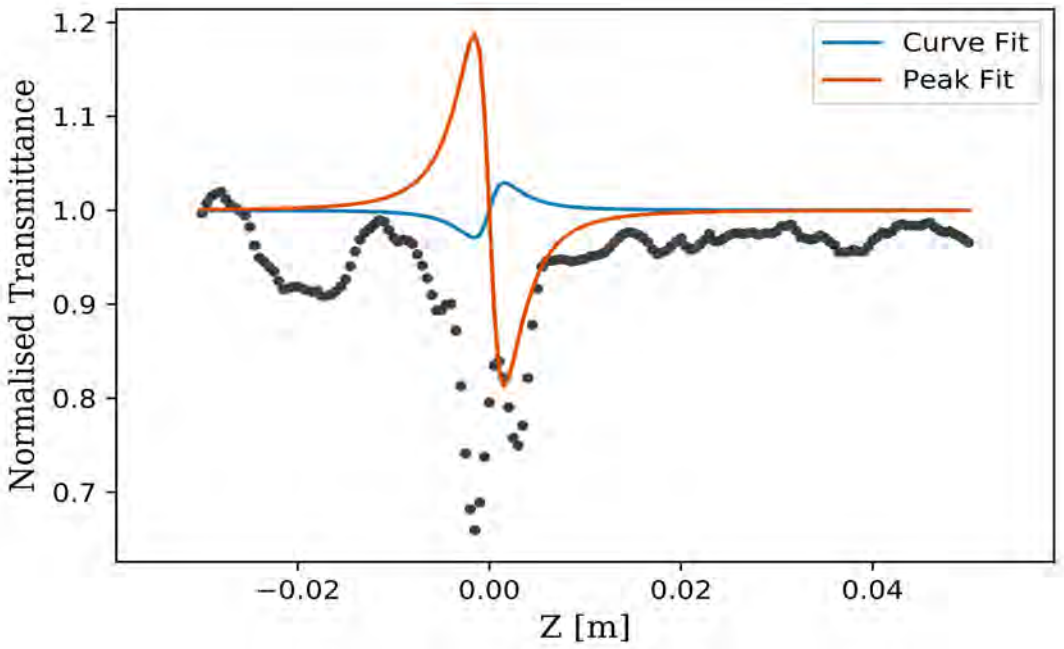

Figure 68: Closed apeture Zscan of the C_{4h} isomer of the $\alpha SnCl_2Pc$ at 4.2×10^{12} W.m^{-2}.

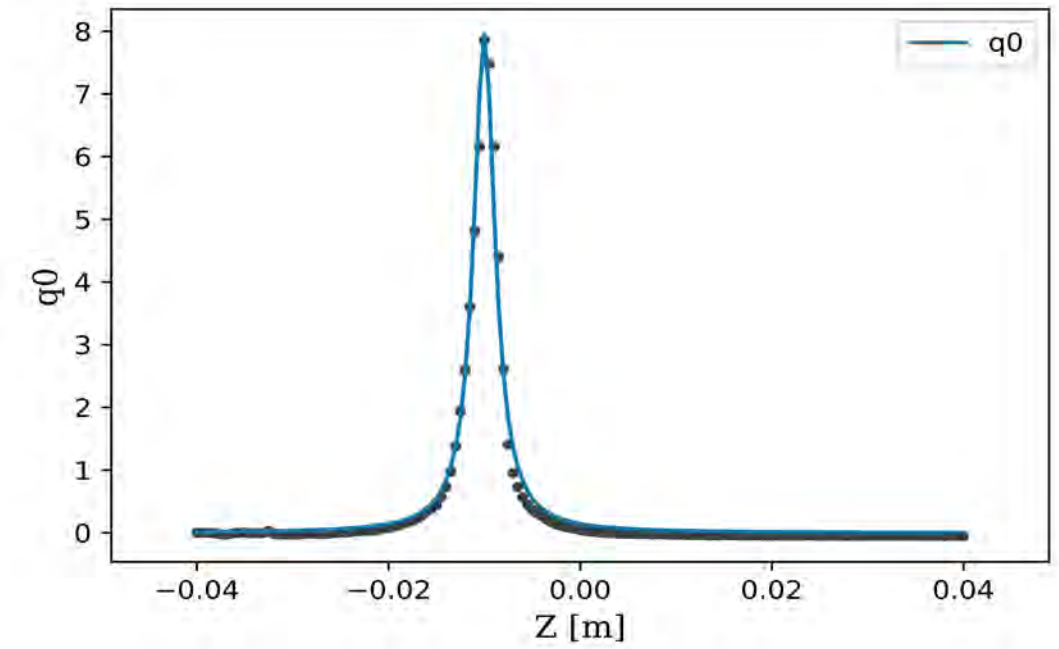

Figure 69: Open apeture Zscan of the C_{4h} isomer of the $\alpha SnCl_2Pc$ at 7.5×10^{12} W.m^{-2}.

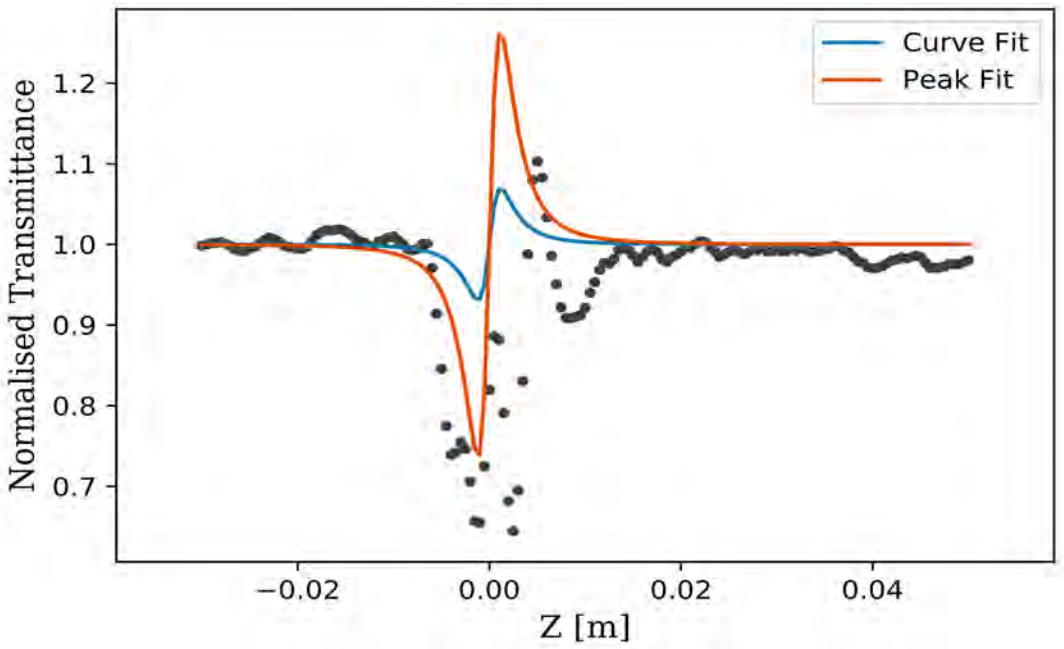

Figure 70: Closed apeture Zscan of the C_{4h} isomer of the $\alpha SnCl_2Pc$ at 7.5×10^{12} W.m^{-2}.

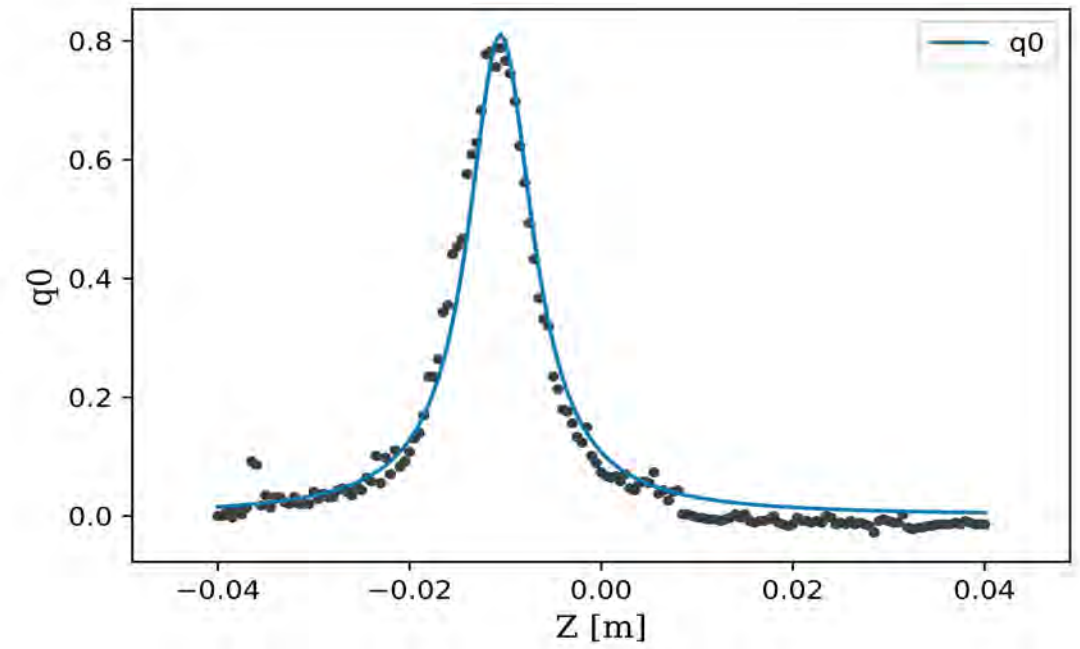

Figure 71: Open apeture Zscan of the C_{4h} isomer of the $\alpha SnCl_2Pc$ at $0.8{\times}10^{12}$ W.m^{-2}.

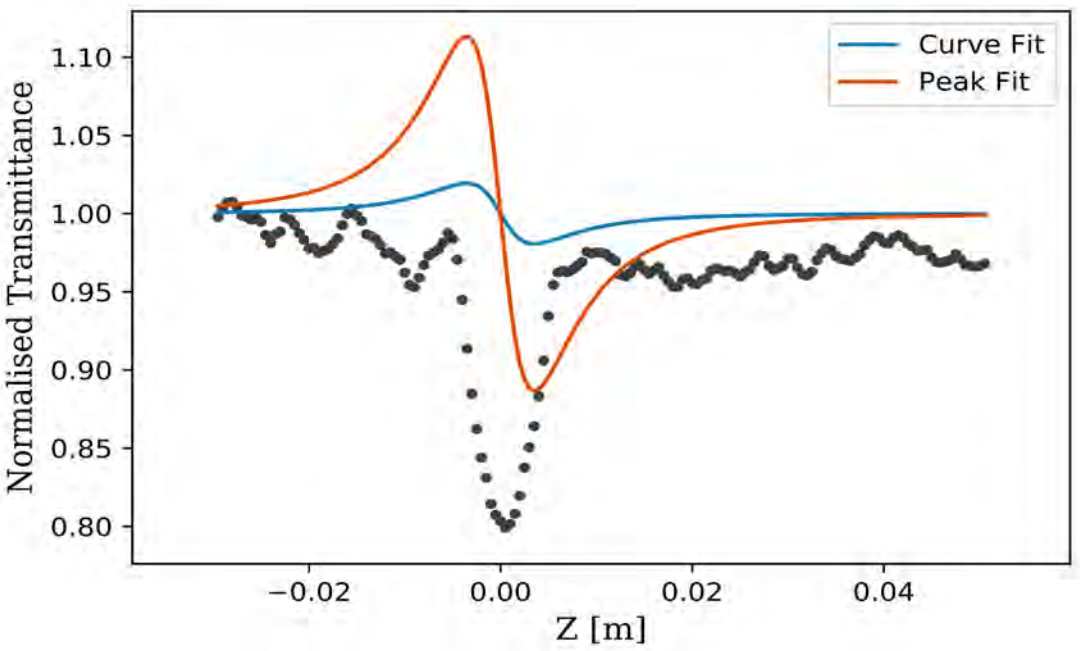

Figure 72: Closed apeture Zscan of the C_{4h} isomer of the $\alpha SnCl_2Pc$ at $0.8{\times}10^{12}$ W.m^{-2}.

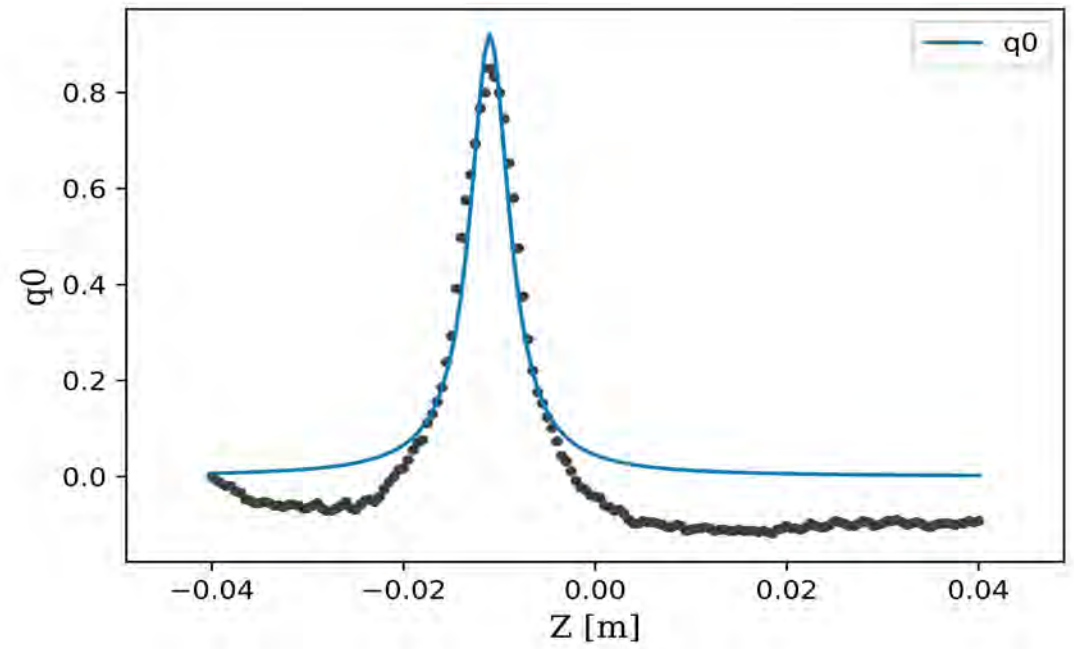

Figure 73: Open apeture Zscan of the C_{2v} isomer of the $\alpha SnCl_2Pc$ at 1.9×10^{12} W.m^{-2}.

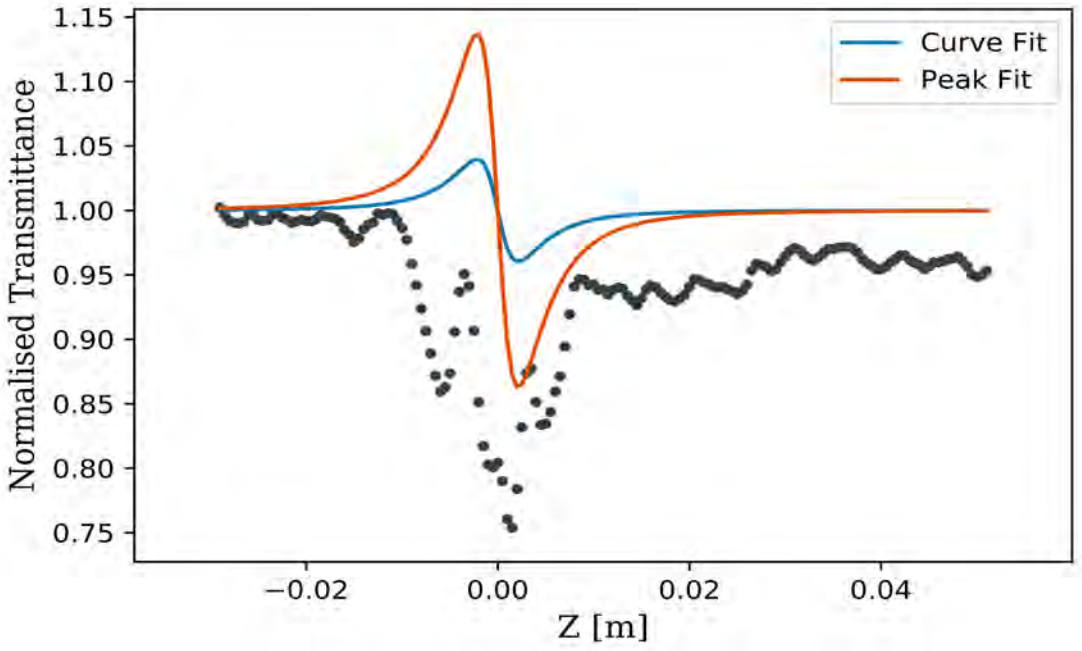

Figure 74: Closed apeture Zscan of the C_{2v} isomer of the $\alpha SnCl_2Pc$ at 1.9×10^{12} W.m^{-2}.

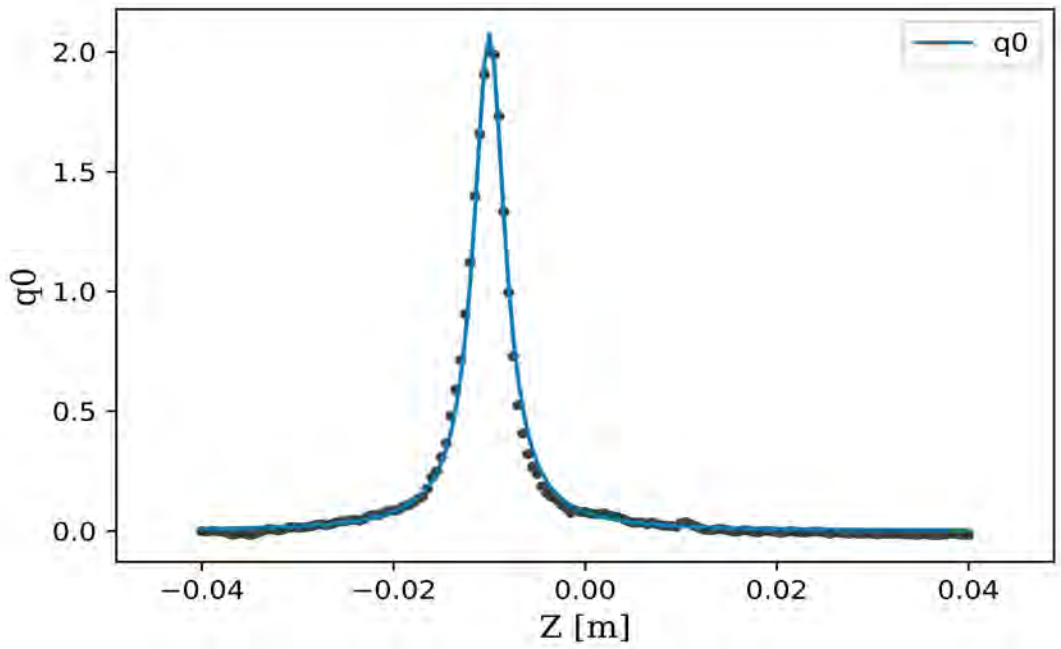

Figure 75: Open apeture Zscan of the C_{2v} isomer of the $\alpha SnCl_2Pc$ at 3.5×10^{12} W.m^{-2}.

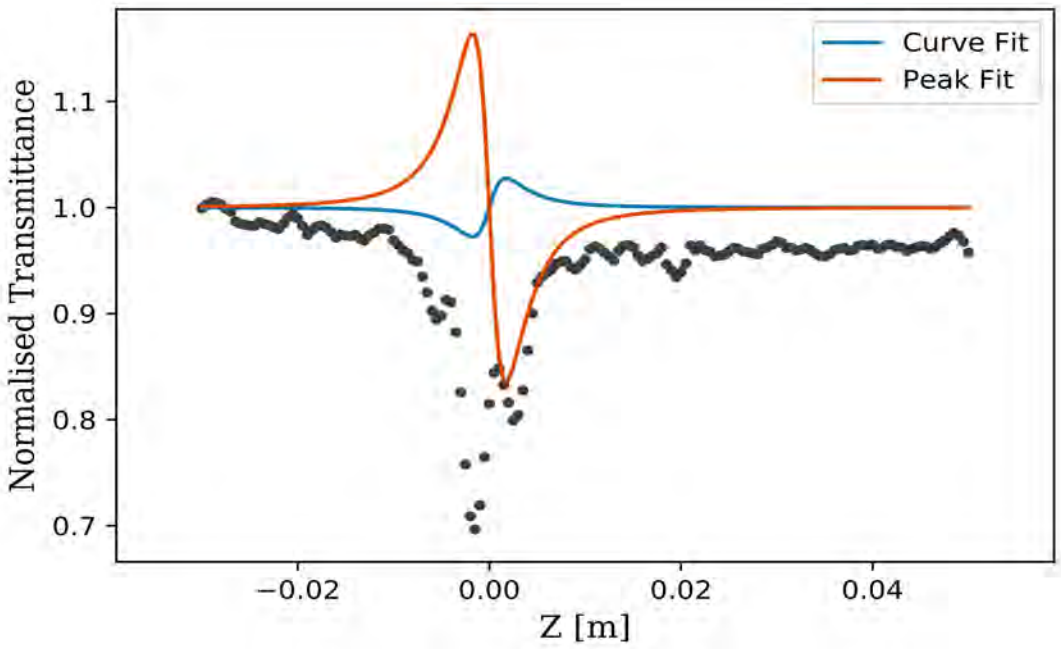

Figure 76: Closed apeture Zscan of the C_{2v} isomer of the $\alpha SnCl_2Pc$ at 3.5×10^{12} W.m^{-2}.

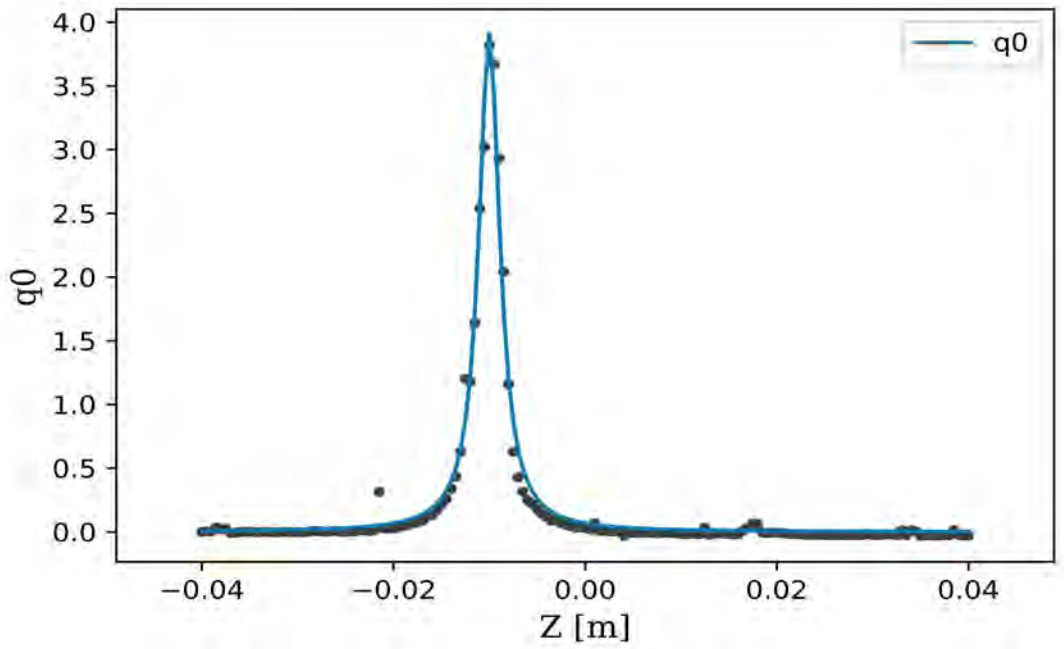

Figure 77: Open apeture Zscan of the C_{2v} isomer of the $\alpha SnCl_2Pc$ at 7.7×10^{12} W.m^{-2}.

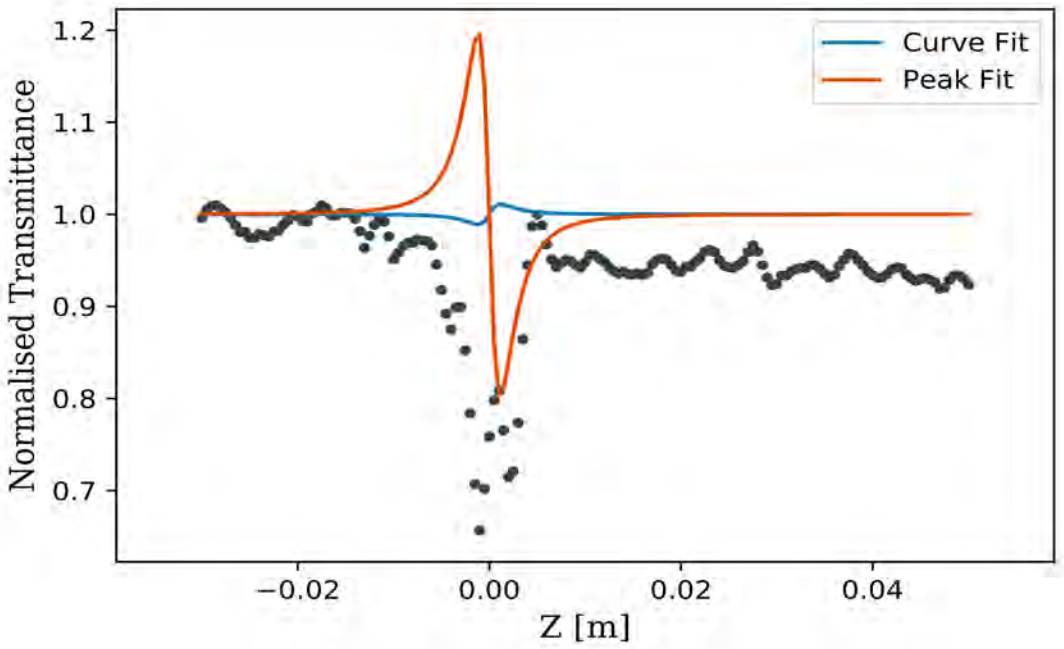

Figure 78: Closed apeture Zscan of the C_{2v} isomer of the $\alpha SnCl_2Pc$ at 7.7×10^{12} W.m^{-2}.

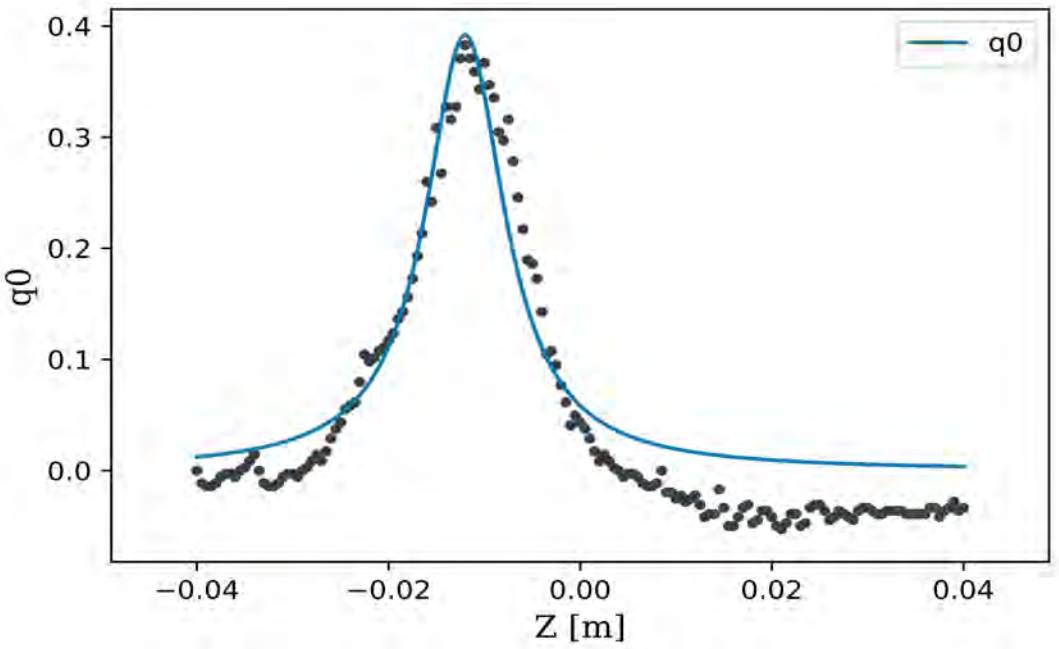

Figure 79: Open apeture Zscan of the C_{2v} isomer of the $\alpha SnCl_2Pc$ at 0.5×10^{12} W.m^{-2}.

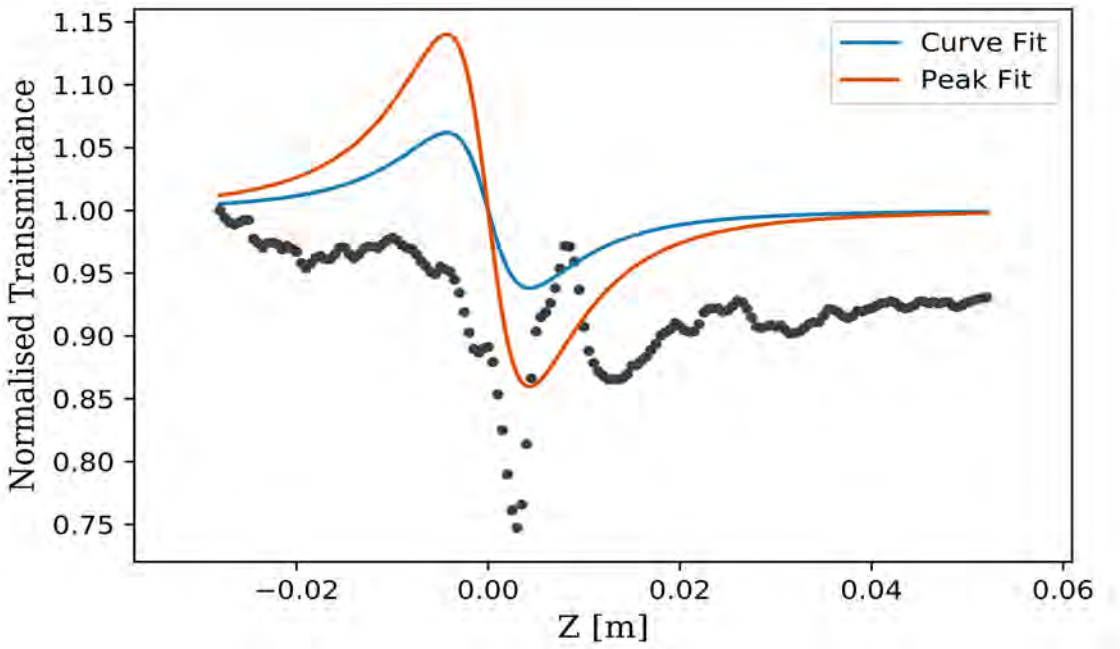

Figure 80: Closed apeture Zscan of the C_{2v} isomer of the $\alpha SnCl_2Pc$ at 0.5×10^{12} W.m^{-2}.

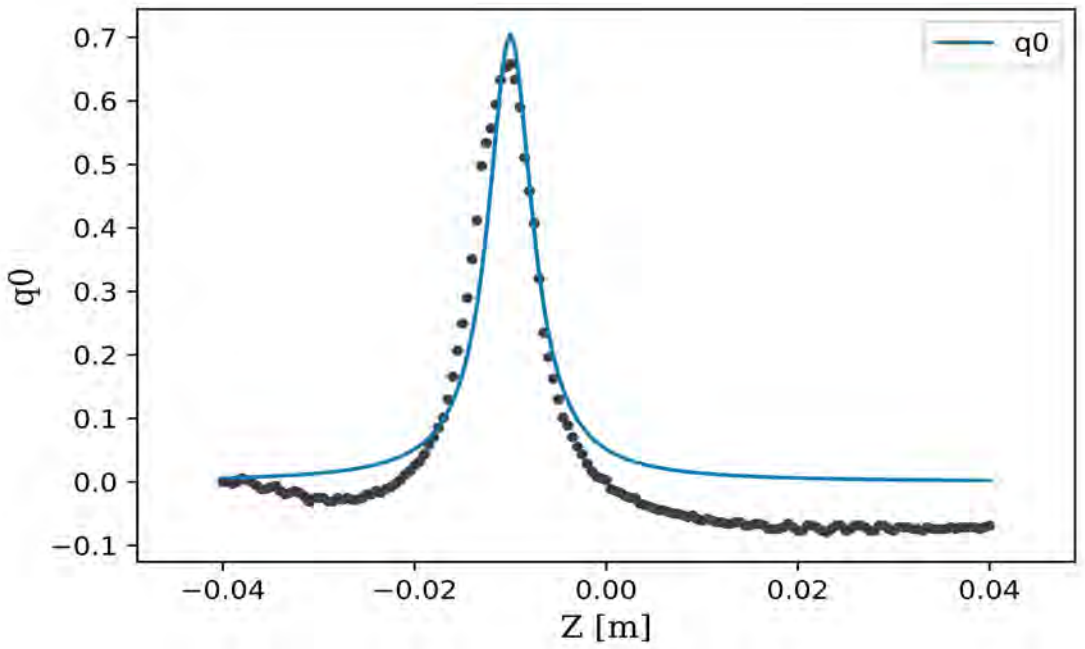

Figure 81: Open apeture Zscan of the C_s isomer of the $\alpha SnCl_2Pc$ at 1.9×10^{12} W.m^{-2}.

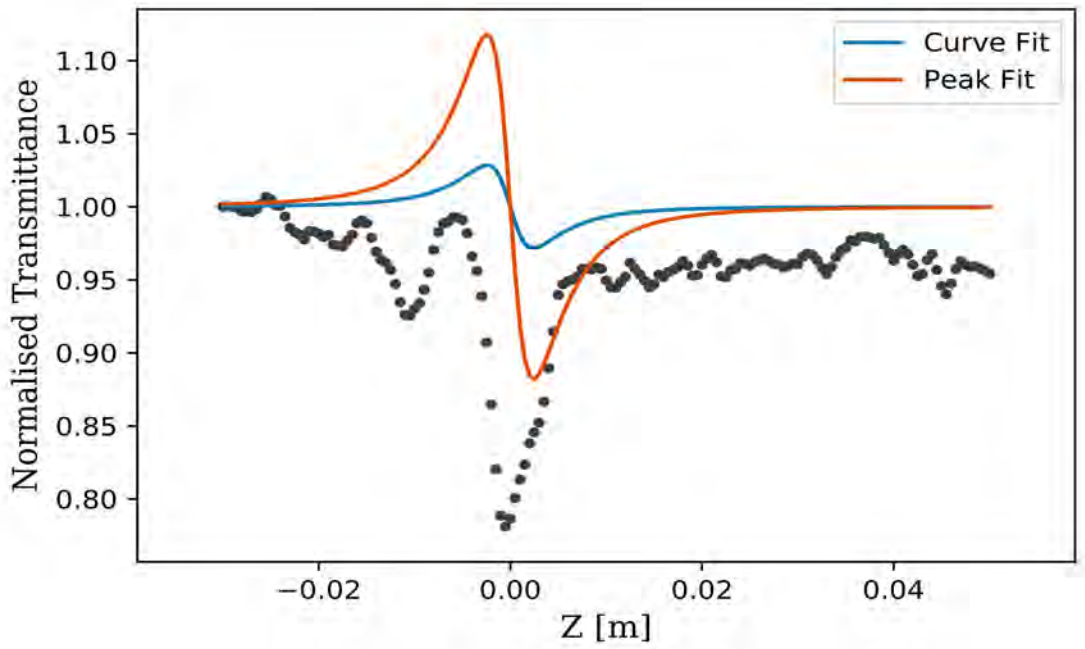

Figure 82: Closed apeture Zscan of the C_s isomer of the $\alpha SnCl_2Pc$ at 1.9×10^{12} W.m^{-2}.

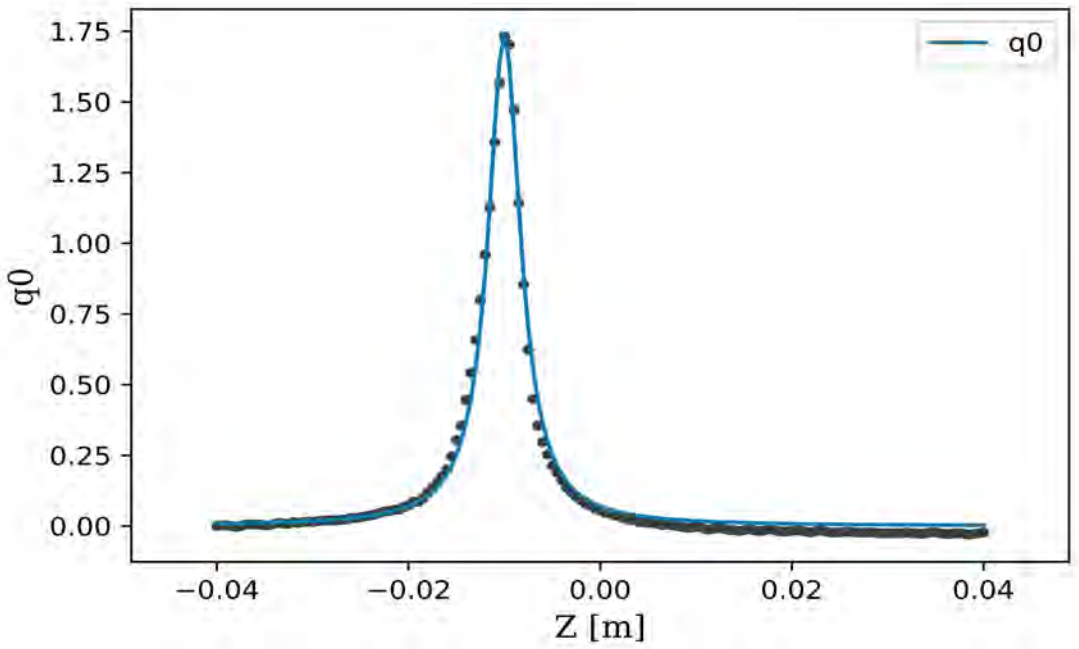

Figure 83: Open apeture Zscan of the C_s isomer of the $\alpha SnCl_2Pc$ at 4.0×10^{12} W.m^{-2}.

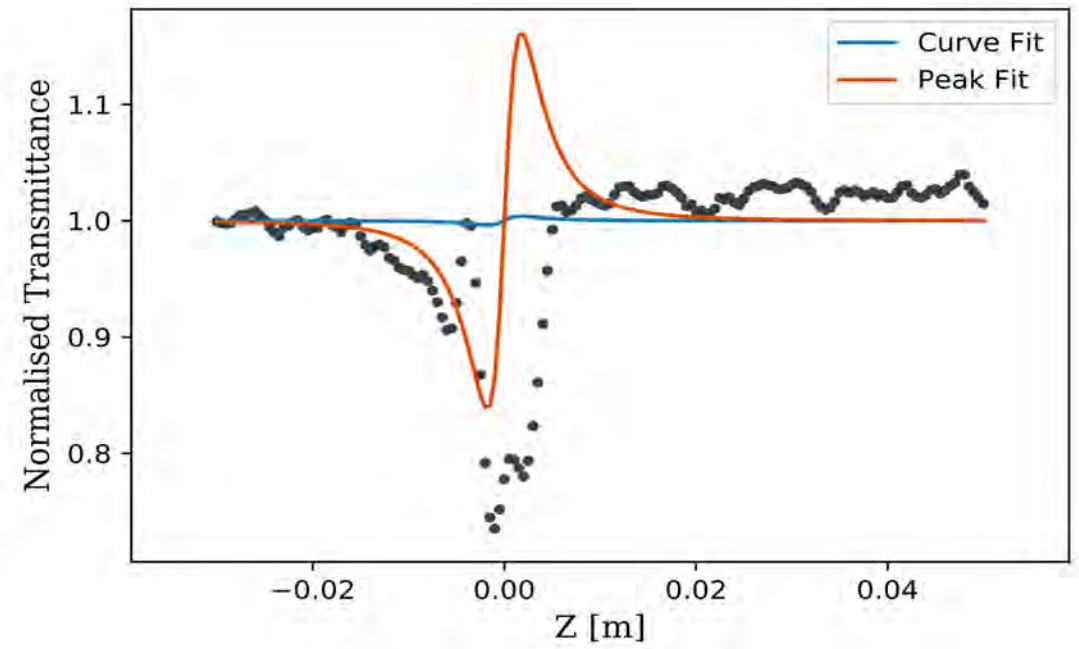

Figure 84: Closed apeture Zscan of the C_s isomer of the $\alpha SnCl_2Pc$ at 4.0×10^{12} W.m^{-2}.

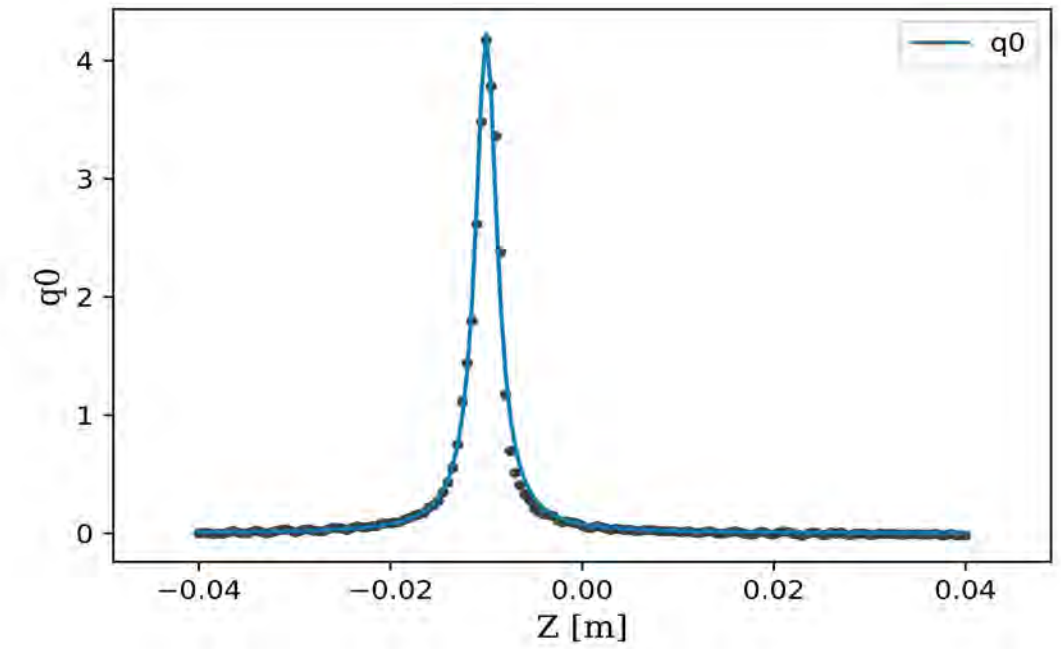

Figure 85: Open apeture Zscan of the C_s isomer of the $\alpha SnCl_2Pc$ at 9.4×10^{12} W.m^{-2}.

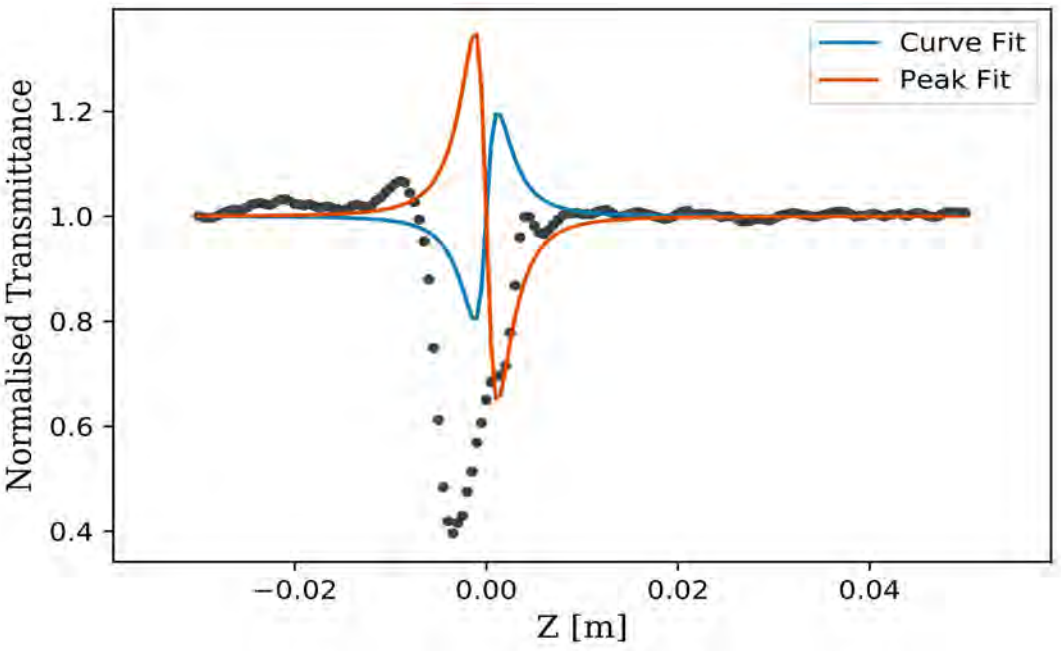

Figure 86: Closed apeture Zscan of the C_s isomer of the $\alpha SnCl_2Pc$ at 9.4×10^{12} W.m^{-2}.

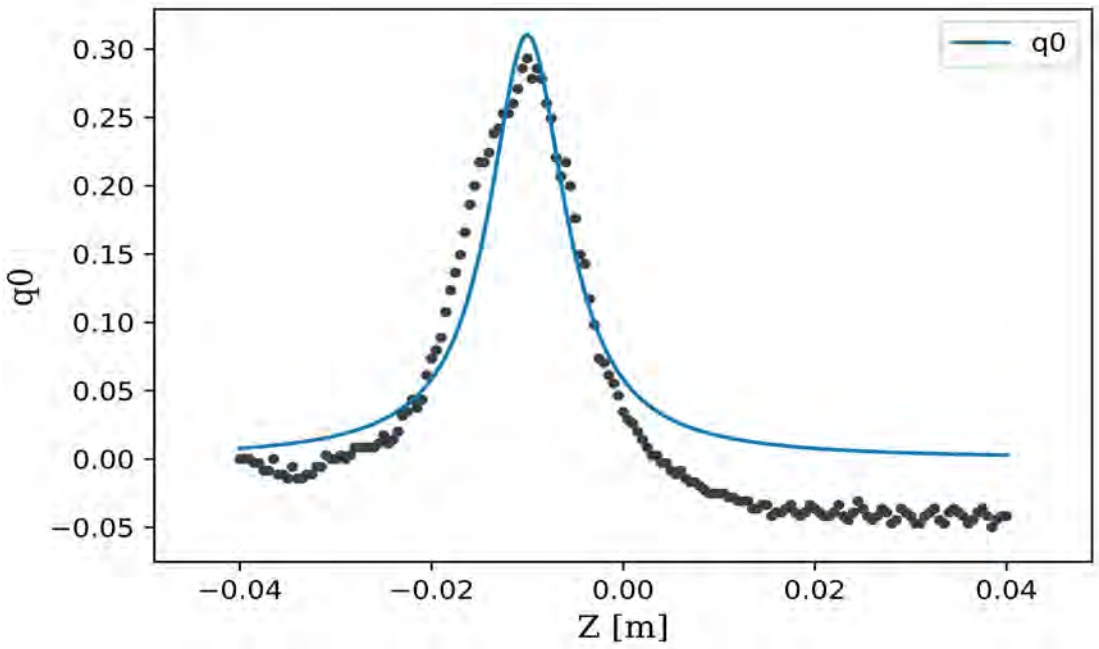

Figure 87: Open apeture Zscan of the C_s isomer of the $\alpha SnCl_2Pc$ at 0.7×10^{12} W.m^{-2}.

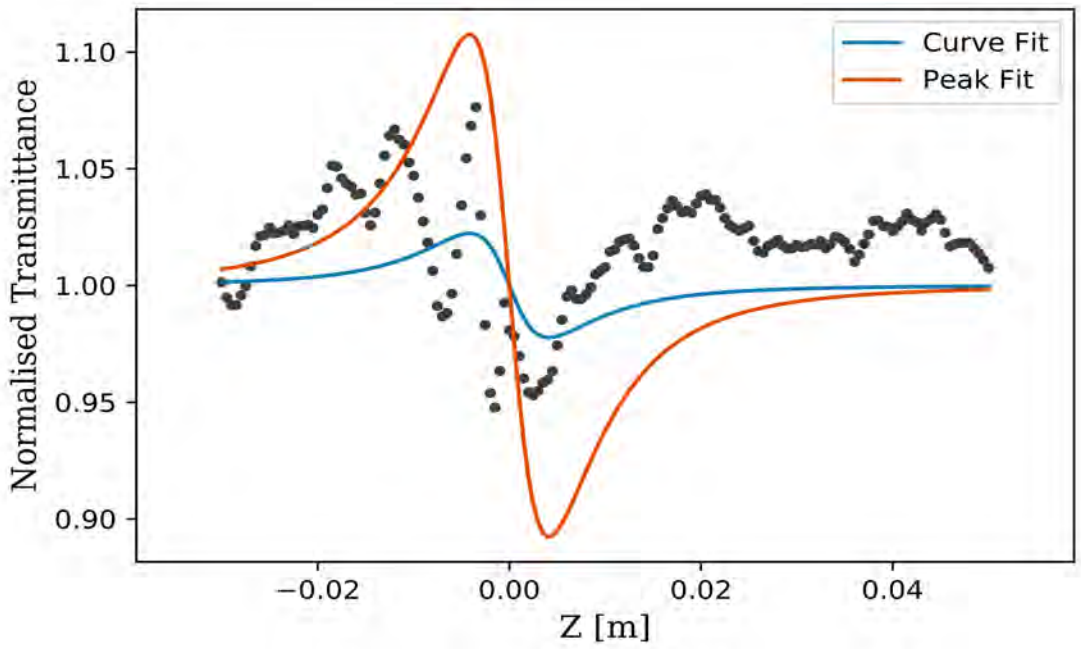

Figure 88: Closed apeture Zscan of the C_s isomer of the $\alpha SnCl_2Pc$ at 0.7×10^{12} W.m^{-2}.

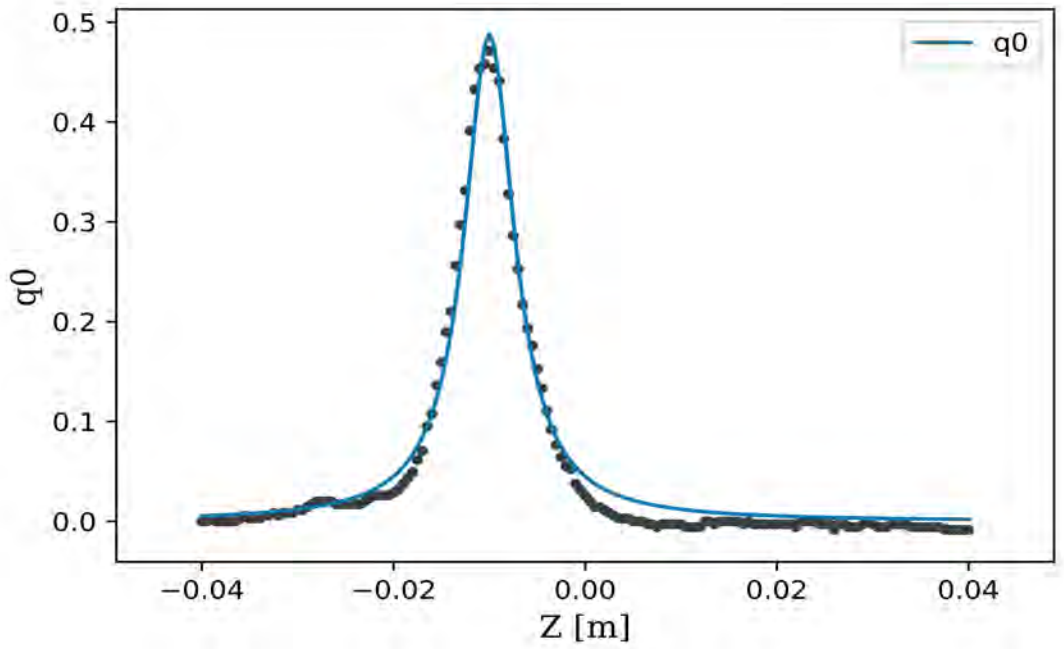

Figure 89: Open apeture Zscan of the D_{2h} isomer of the $\alpha SnCl_2Pc$ at 1.7×10^{12} W.m^{-2}.

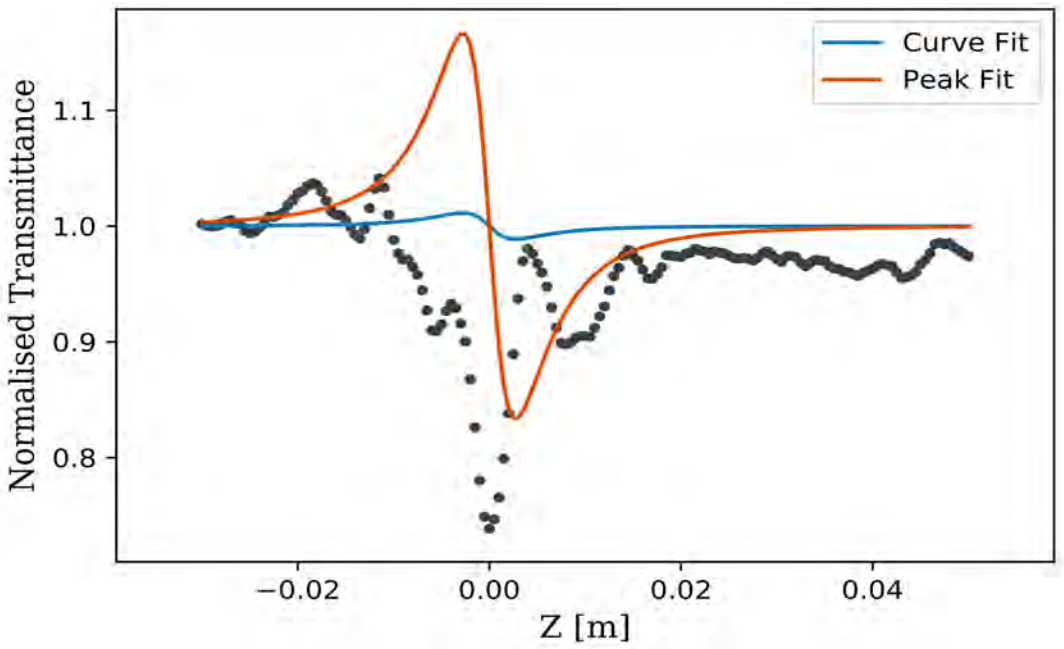

Figure 90: Closed apeture Zscan of the D_{2h} isomer of the $\alpha SnCl_2Pc$ at 1.7×10^{12} W.m^{-2}.

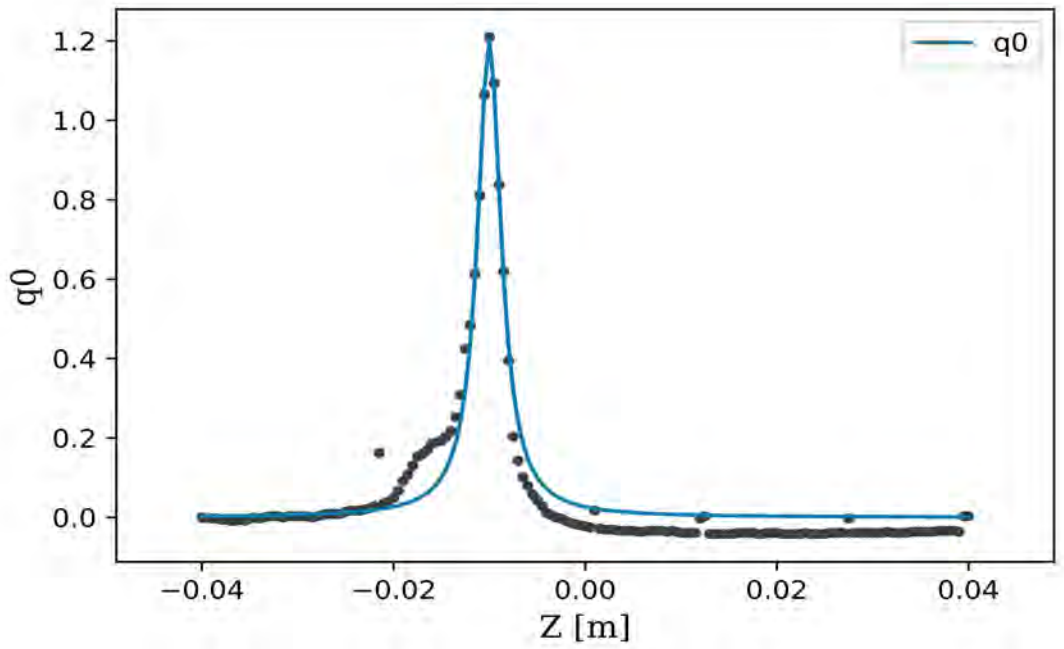

Figure 91: Open apeture Zscan of the D_{2h} isomer of the $\alpha SnCl_2Pc$ at 6.6×10^{12} W.m^{-2}.

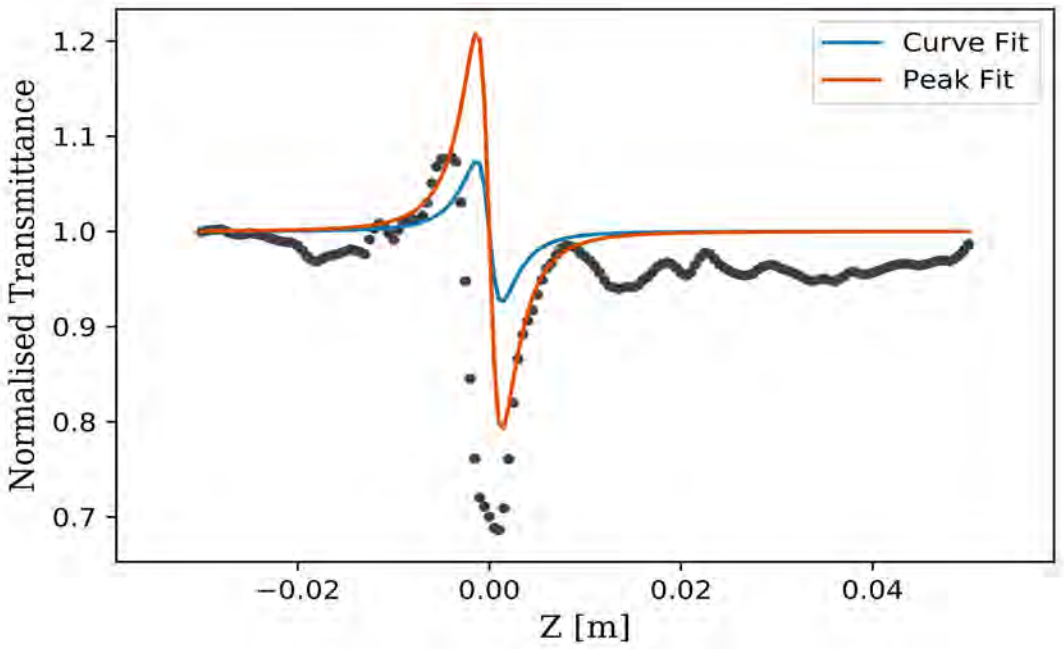

Figure 92: Closed apeture Zscan of the D_{2h} isomer of the $\alpha SnCl_2Pc$ at 6.6×10^{12} W.m^{-2}.

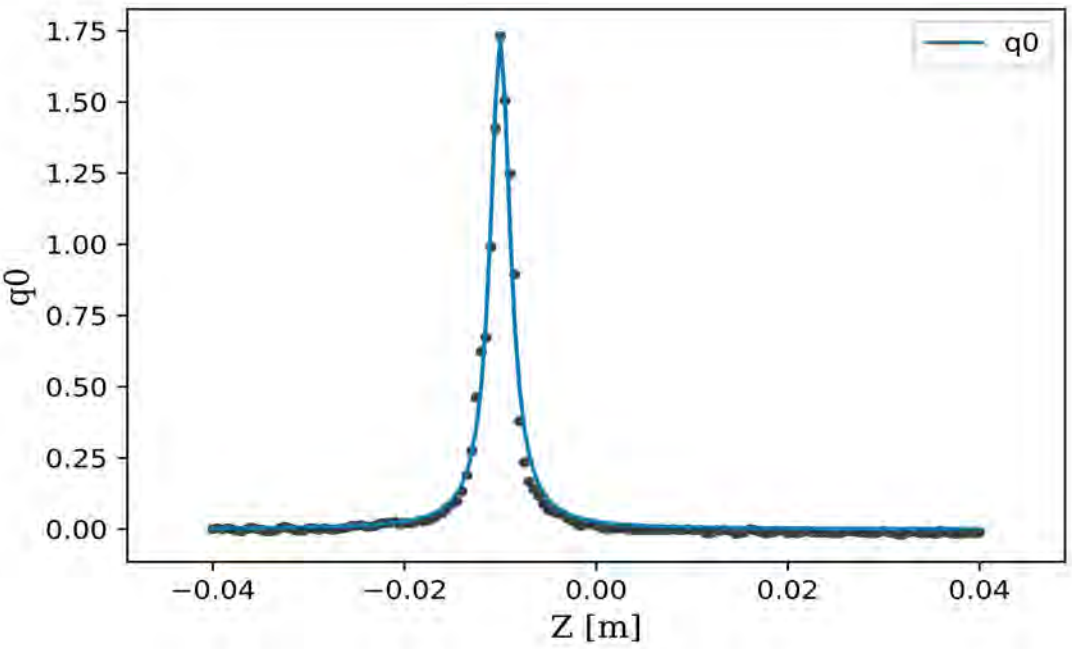

Figure 93: Open apeture Zscan of the D_{2h} isomer of the $\alpha SnCl_2Pc$ at 9.6×10^{12} W.m^{-2}.

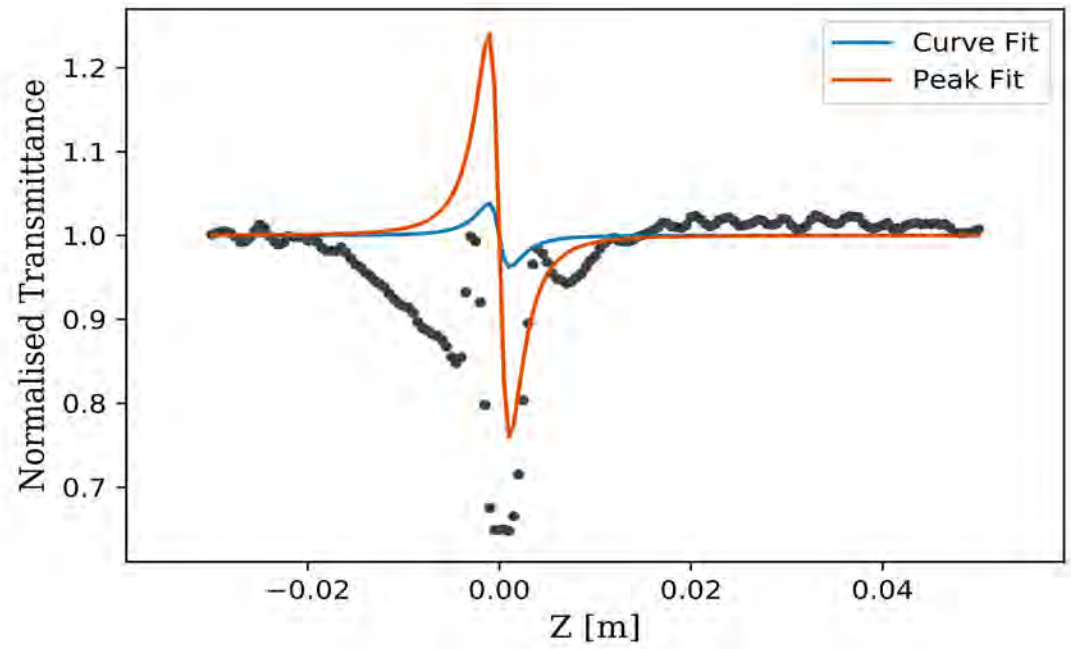

Figure 94: Closed apeture Zscan of the D_{2h} isomer of the $\alpha SnCl_2Pc$ at 9.6×10^{12} W.m^{-2}.

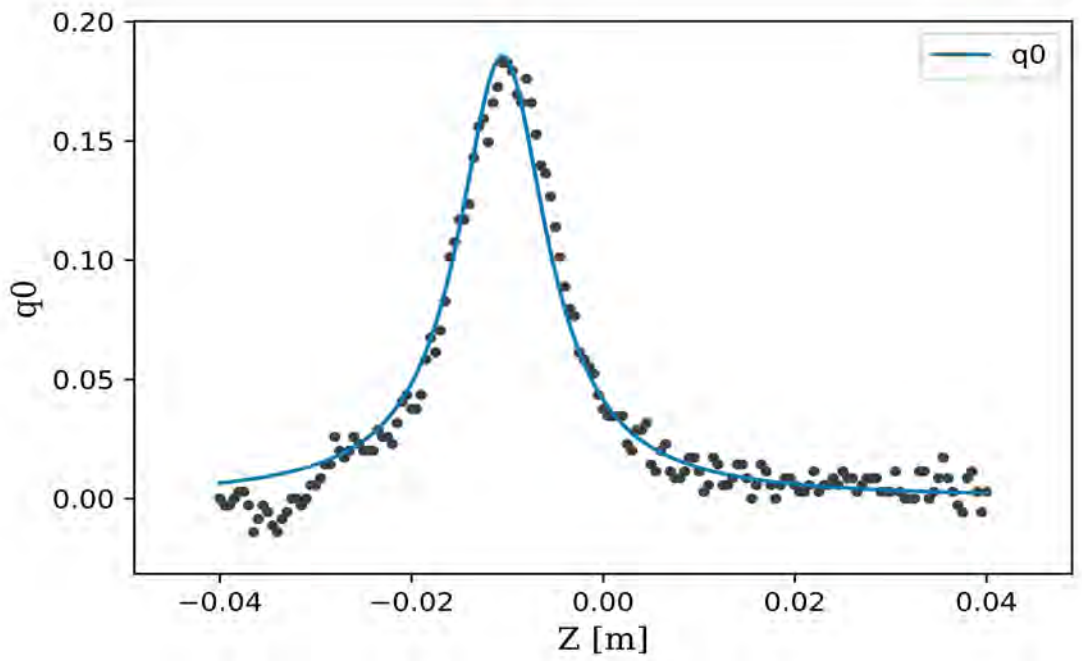

Figure 95: Open apeture Zscan of the D_{2h} isomer of the $\alpha SnCl_2Pc$ at 0.5×10^{12} W.m^{-2}.

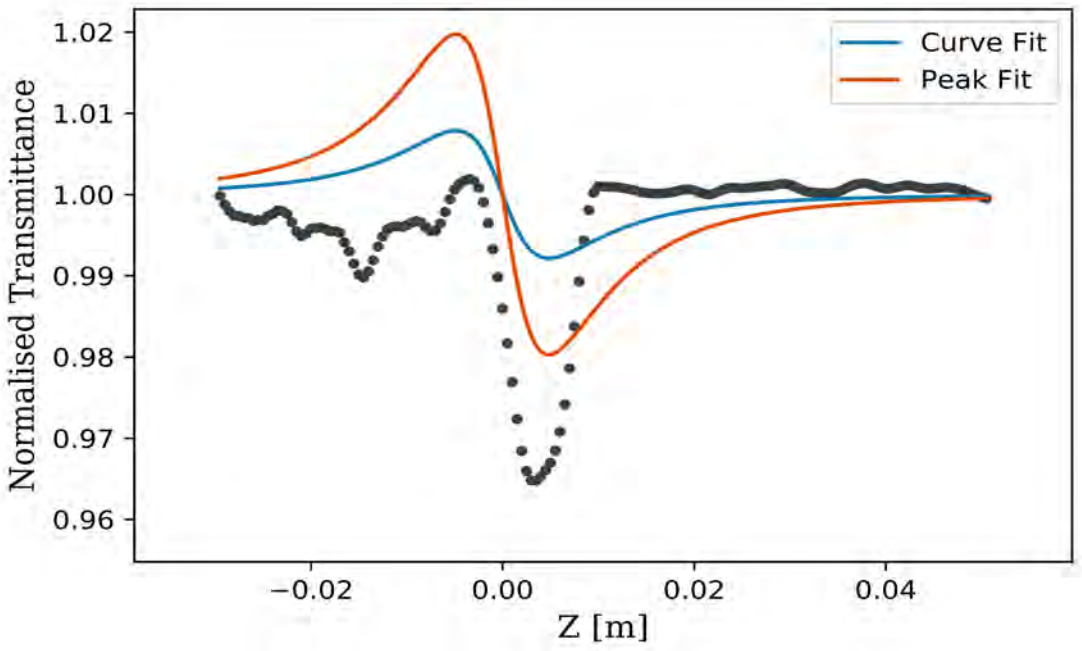

Figure 96: Closed apeture Zscan of the D_{2h} isomer of the $\alpha SnCl_2Pc$ at 0.5×10^{12} W.m^{-2}.

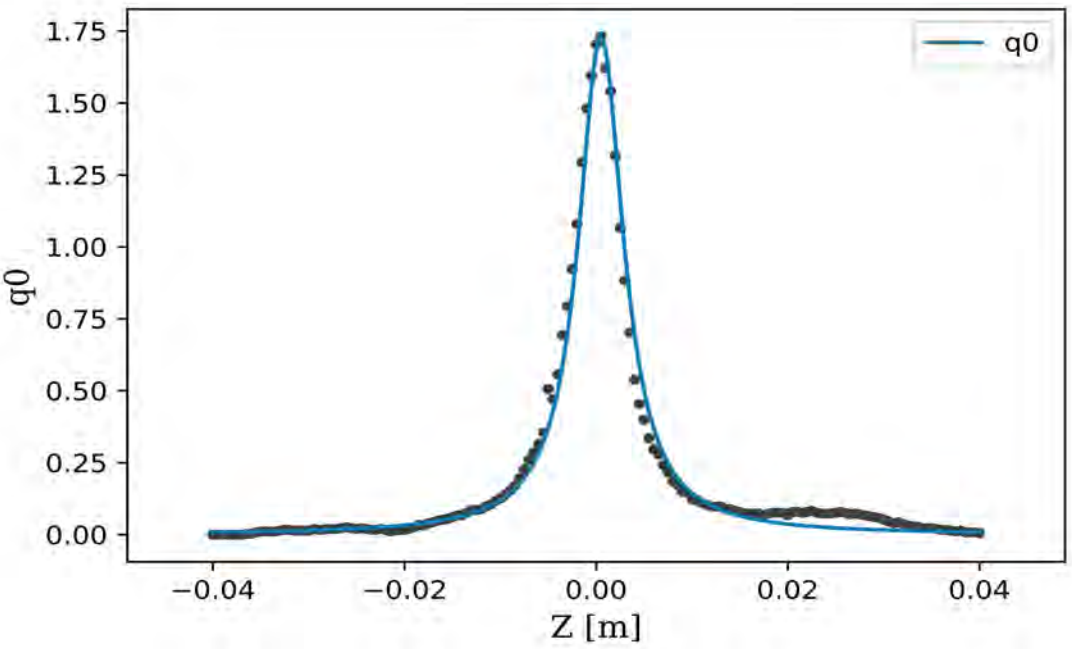

Figure 97: Open apeture Zscan of the C_{4h} isomer of the $\beta SnCl_2Pc$ at 1.5×10^{12} W.m^{-2}.

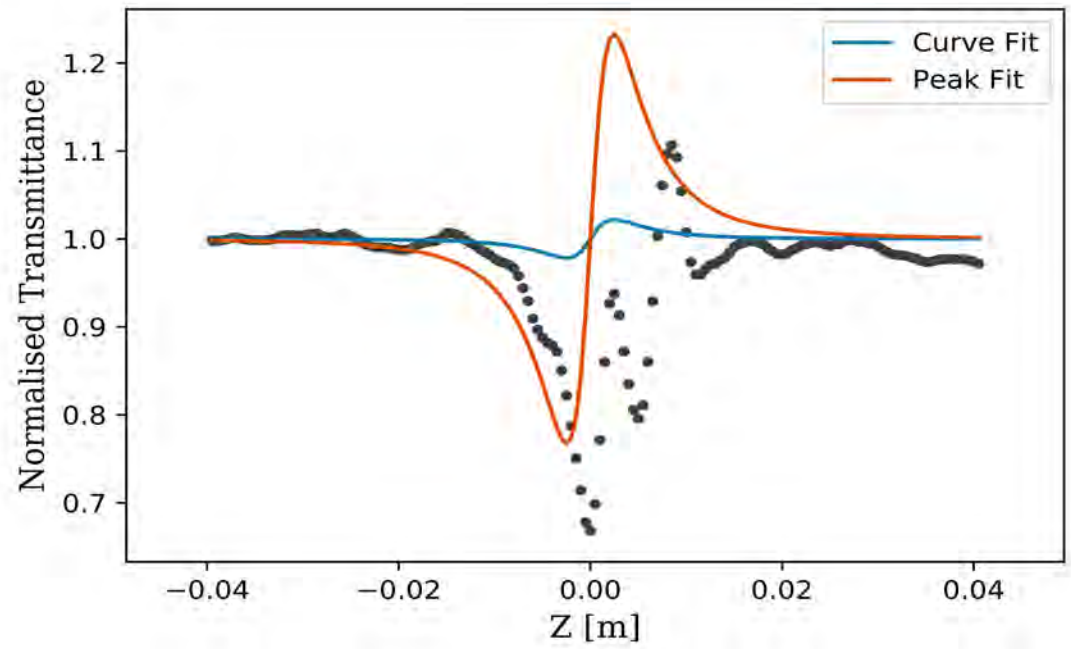

Figure 98: Closed apeture Zscan of the C_{4h} isomer of the $\beta SnCl_2Pc$ at 1.5×10^{12} W.m^{-2}.

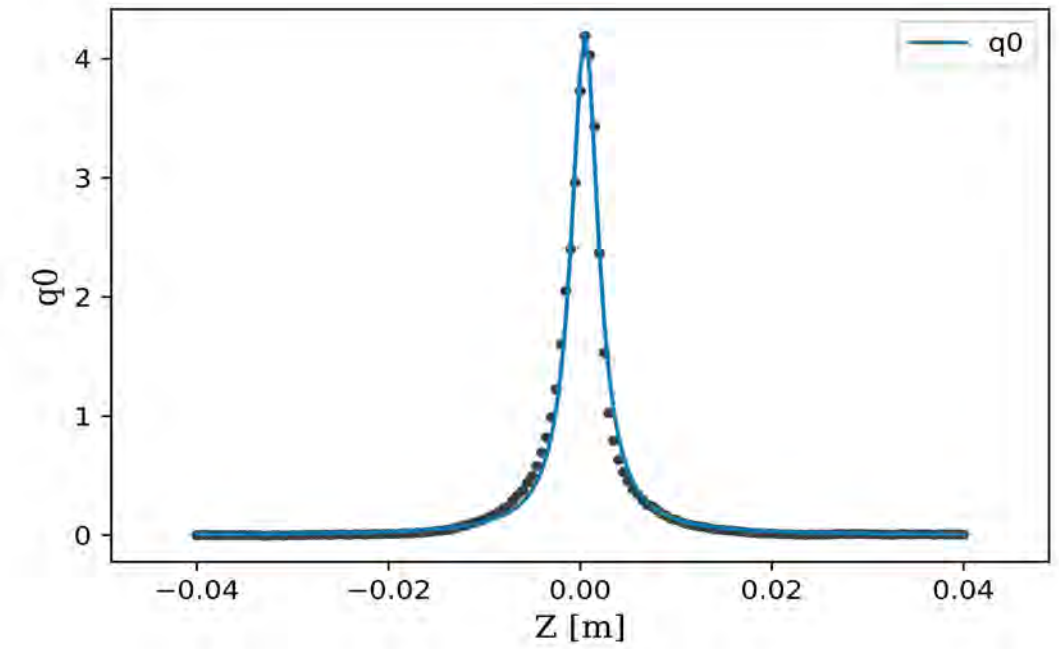

Figure 99: Open apeture Zscan of the C_{4h} isomer of the $\beta SnCl_2Pc$ at 4.8×10^{12} W.m^{-2}.

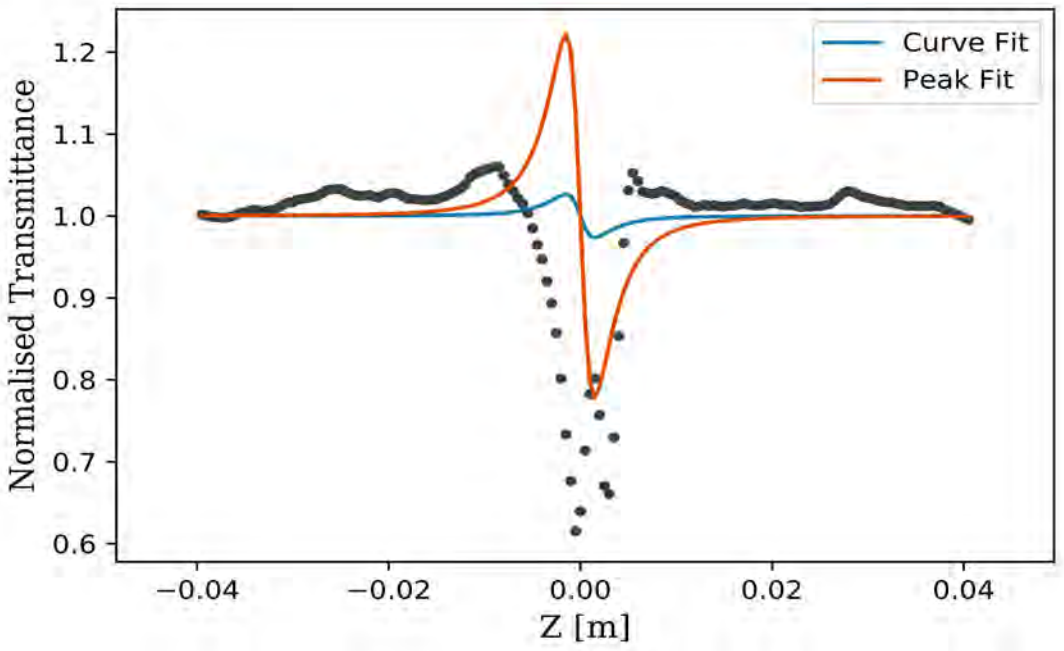

Figure 100: Closed apeture Zscan of the C_{4h} isomer of the $\beta SnCl_2Pc$ at 4.8×10^{12} W.m^{-2}.

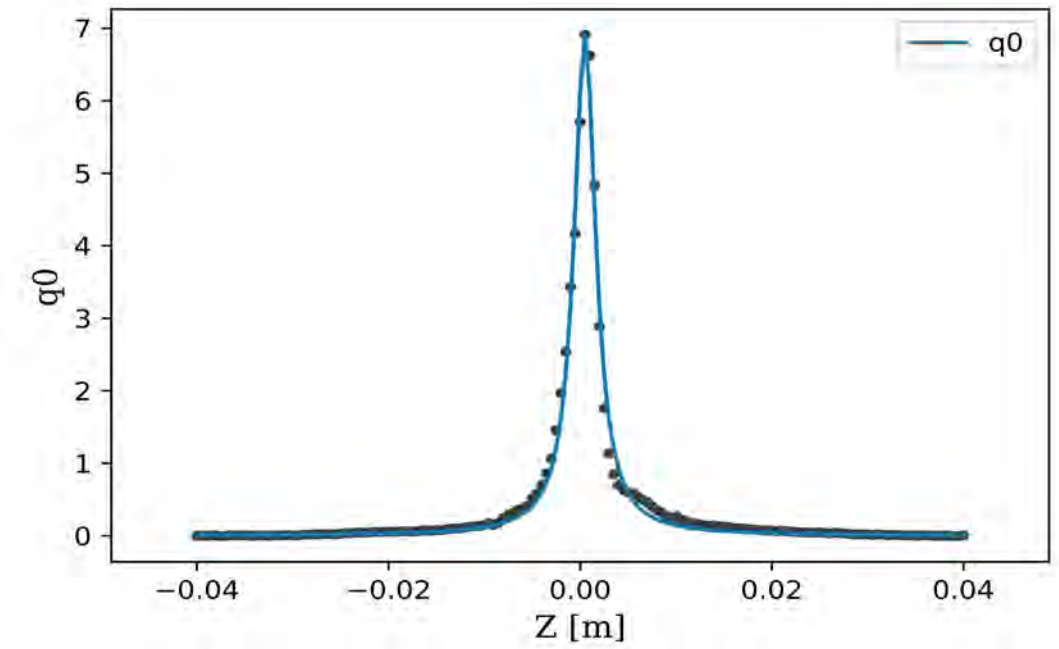

Figure 101: Open apeture Zscan of the C_{4h} isomer of the $\beta SnCl_2Pc$ at 8.0×10^{12} W.m^{-2}.

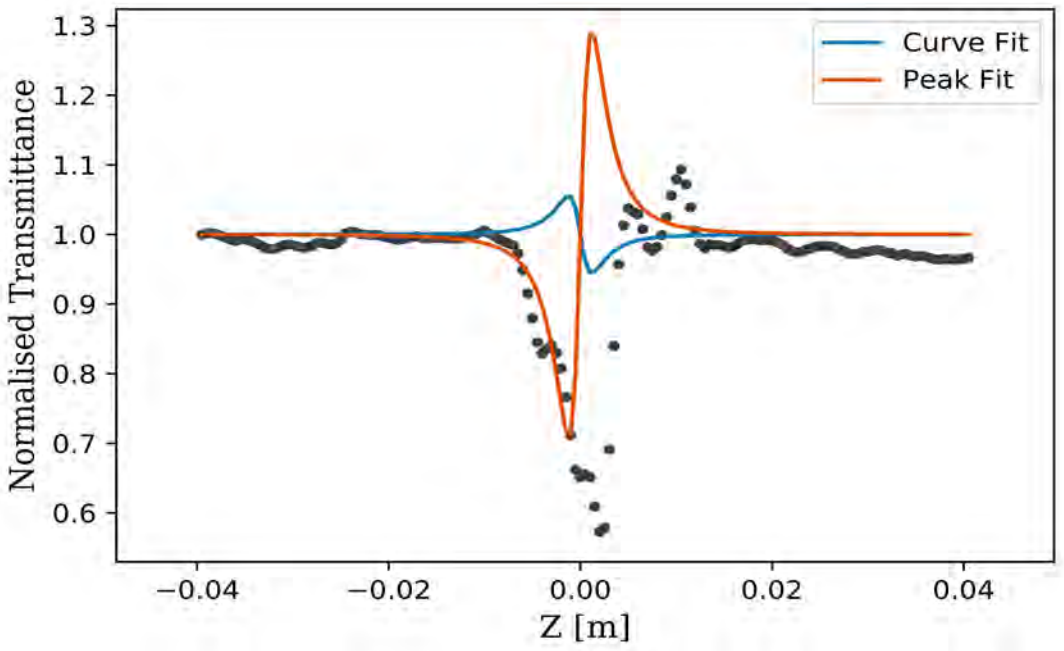

Figure 102: Closed apeture Zscan of the C_{4h} isomer of the $\beta SnCl_2Pc$ at 8.0×10^{12} W.m^{-2}.

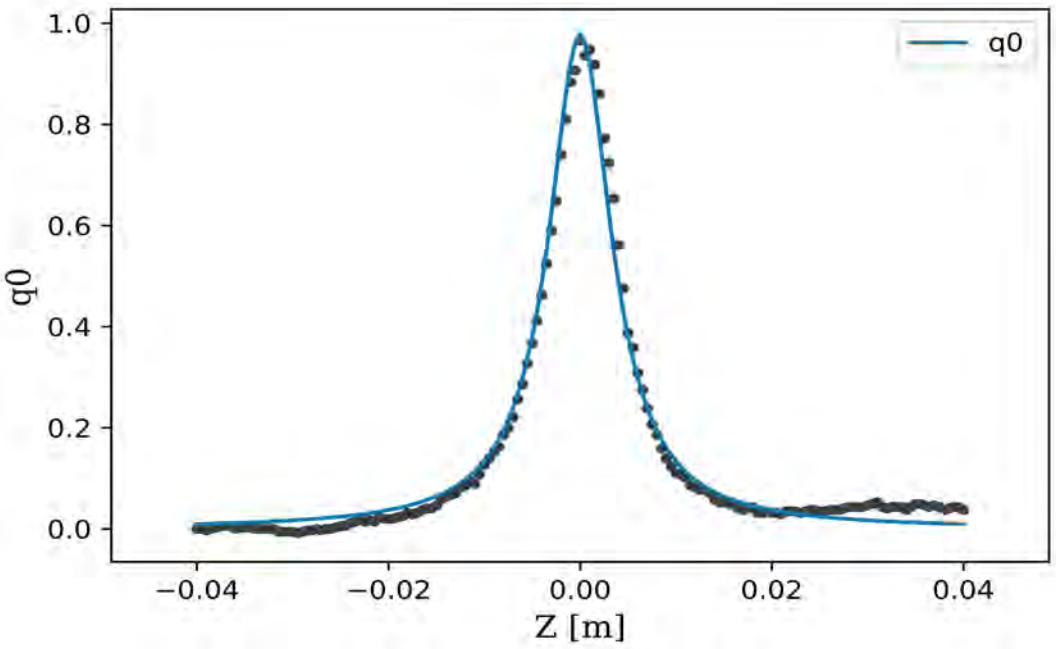

Figure 103: Open apeture Zscan of the C_{4h} isomer of the $\beta SnCl_2Pc$ at 0.7×10^{12} W.m^{-2}.

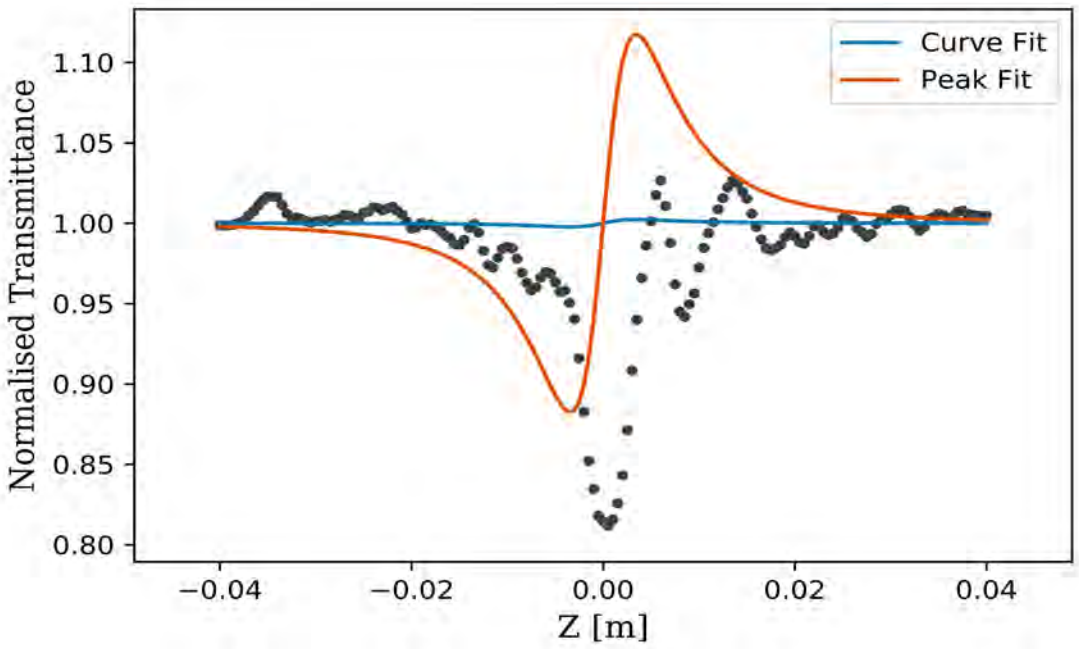

Figure 104: Closed apeture Zscan of the C_{4h} isomer of the $\beta SnCl_2Pc$ at 0.7×10^{12} W.m^{-2}.

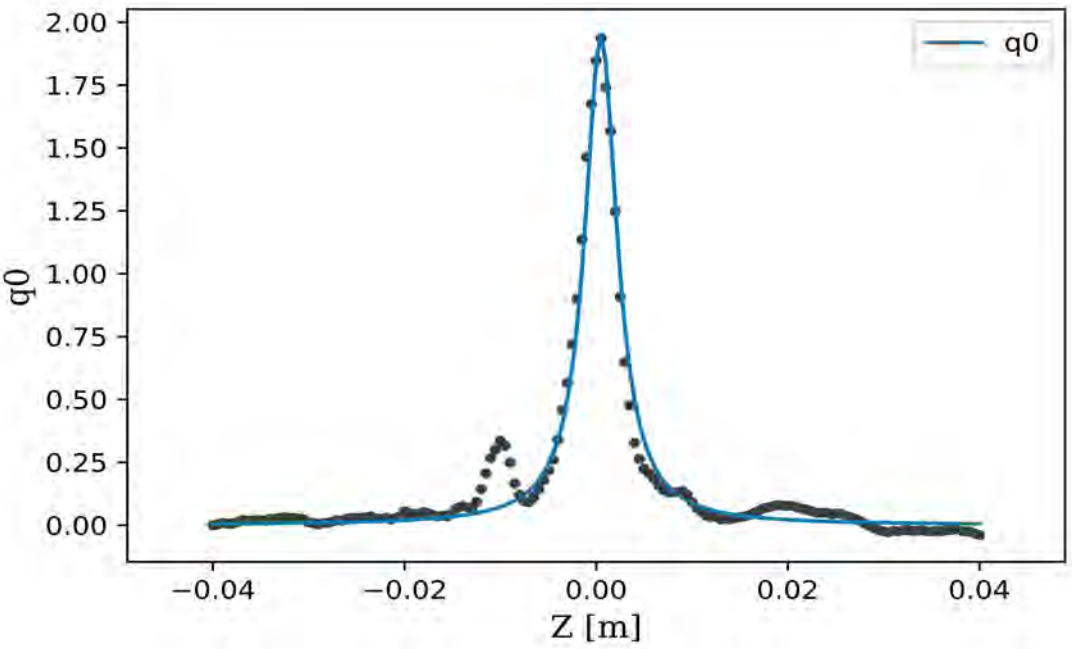

Figure 105: Open apeture Zscan of the C_{2v} isomer of the $\beta SnCl_2Pc$ at 2.2×10^{12} W.m^{-2}.

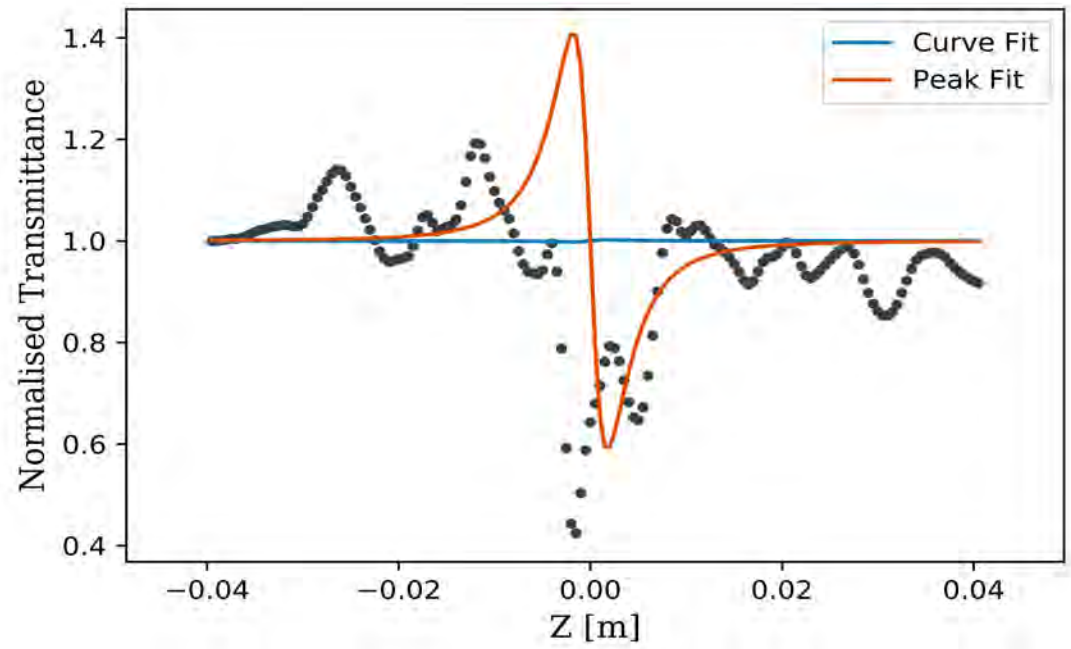

Figure 106: Closed apeture Zscan of the C_{2v} isomer of the $\beta SnCl_2Pc$ at 2.2×10^{12} W.m^{-2}.

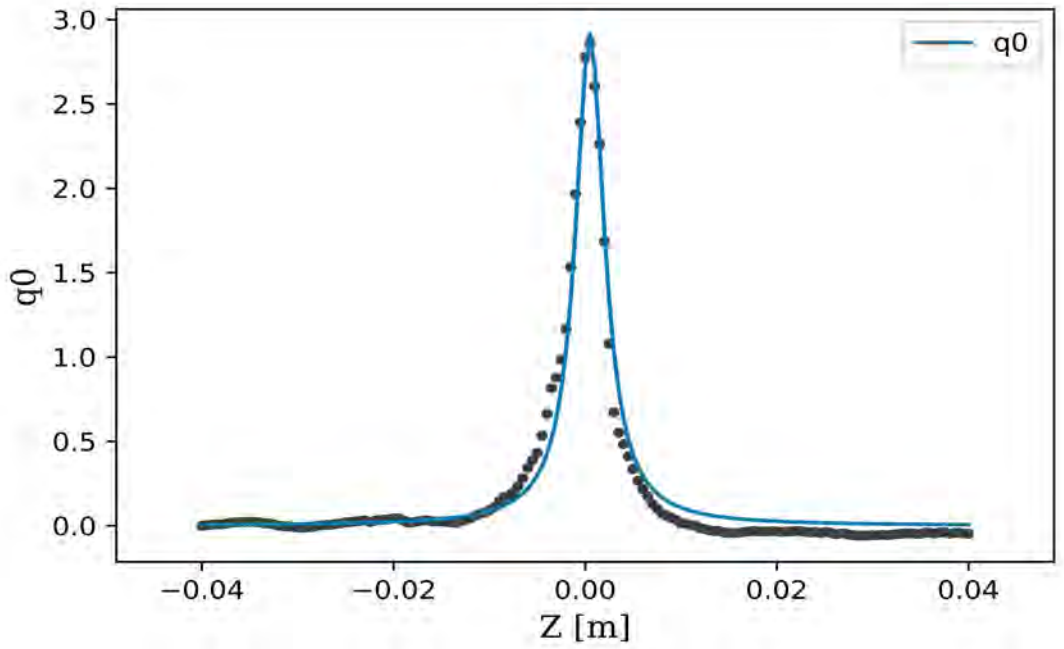

Figure 107: Open apeture Zscan of the C_{2v} isomer of the $\beta SnCl_2Pc$ at 3.6×10^{12} W.m^{-2}.

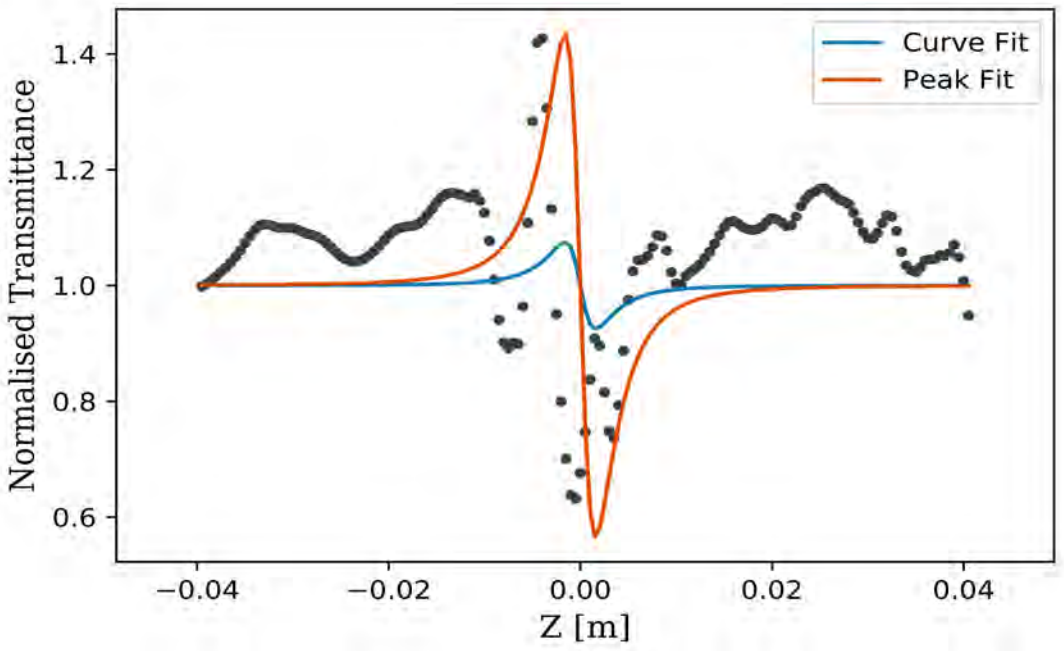

Figure 108: Closed apeture Zscan of the C_{2v} isomer of the $\beta SnCl_2Pc$ at 3.6×10^{12} W.m^{-2}.

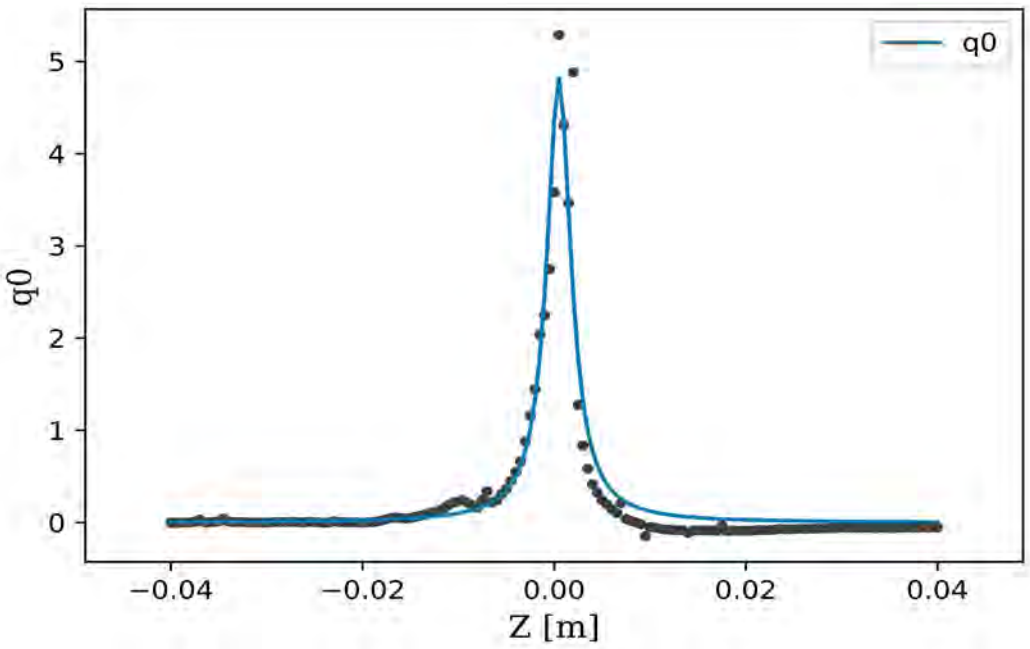

Figure 109: Open apeture Zscan of the C_{2v} isomer of the $\beta SnCl_2Pc$ at 6.1×10^{12} W.m^{-2}.

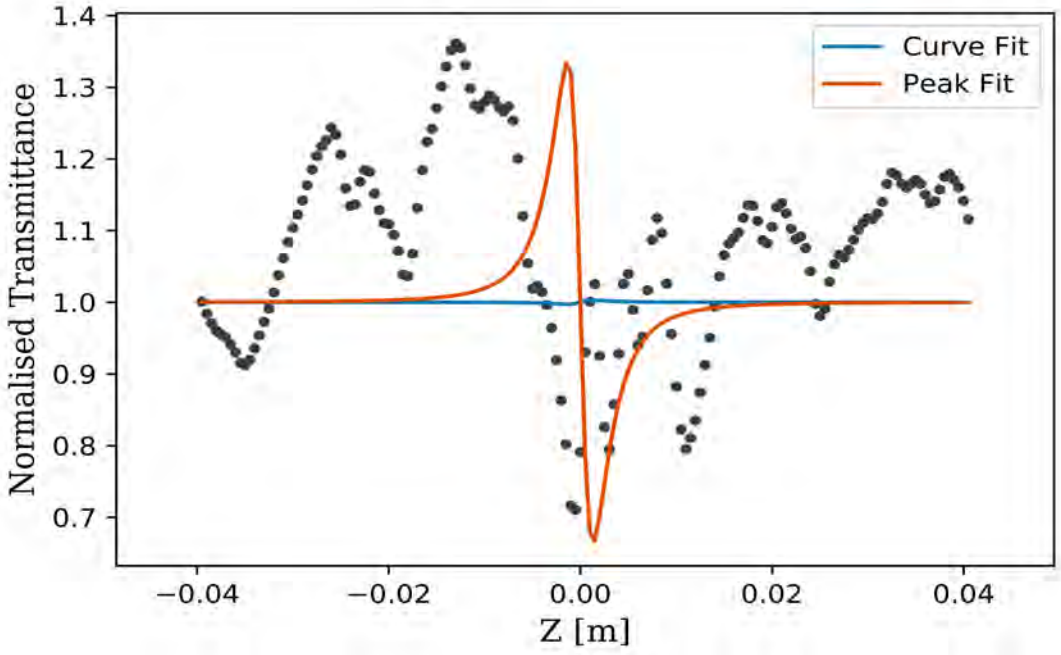

Figure 110: Closed apeture Zscan of the C_{2v} isomer of the $\beta SnCl_2Pc$ at 6.1×10^{12} W.m^{-2}.

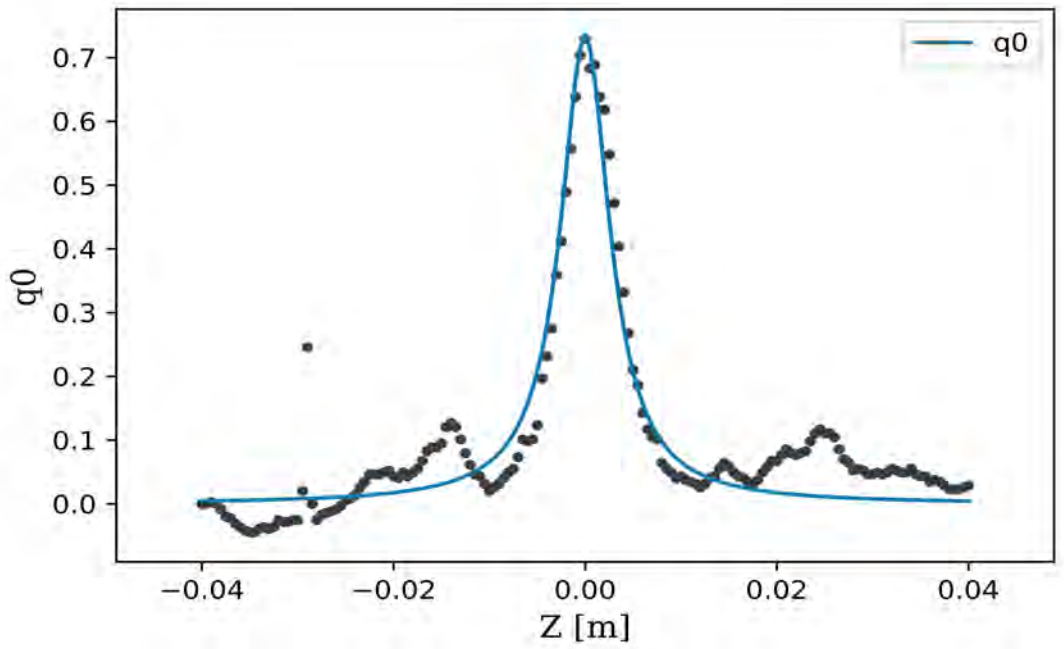

Figure 111: Open apeture Zscan of the C_{2v} isomer of the $\beta SnCl_2Pc$ at $0.8{\times}10^{12}$ W.m^{-2}.

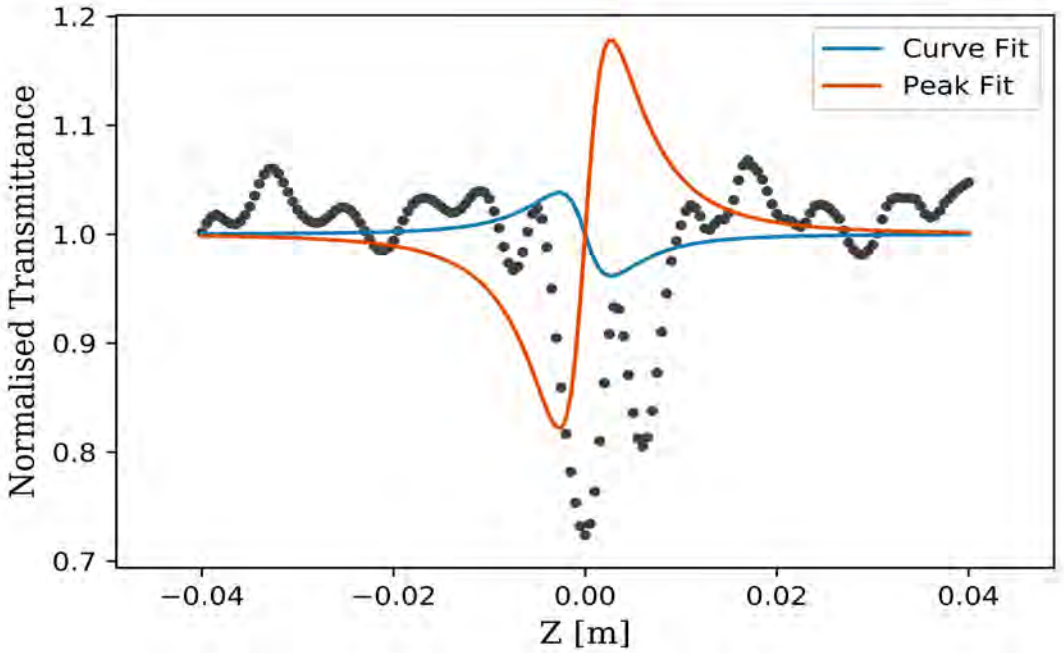

Figure 112: Closed apeture Zscan of the C_{2v} isomer of the $\beta SnCl_2Pc$ at $0.8{\times}10^{12}$ W.m^{-2}.

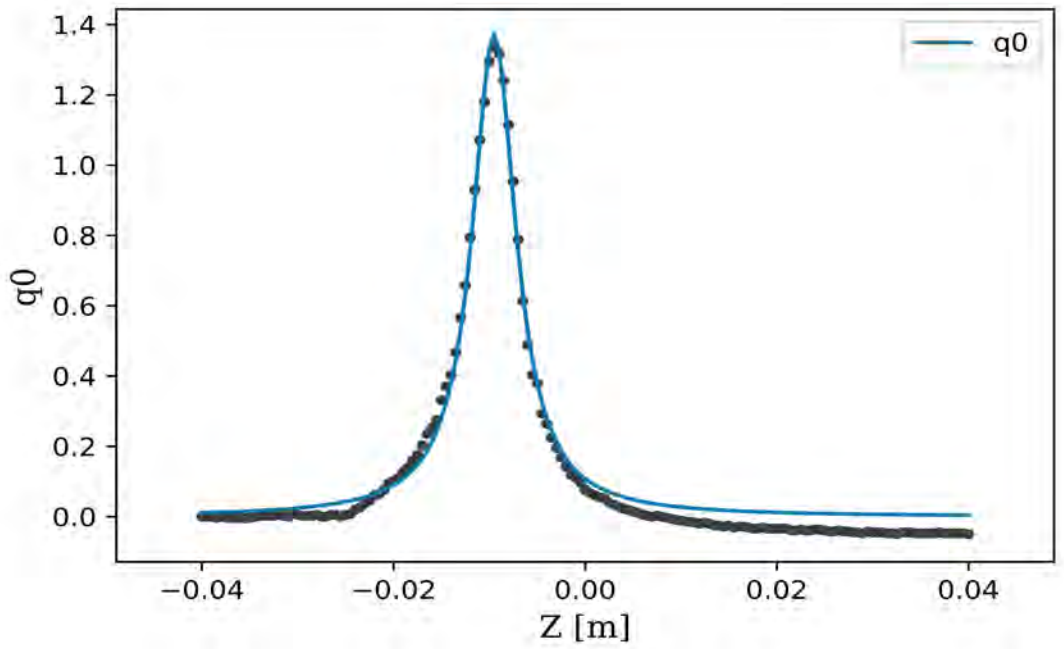

Figure 113: Open apeture Zscan of the C_s isomer of the $\beta SnCl_2Pc$ at 1.8×10^{12} W.m^{-2}.

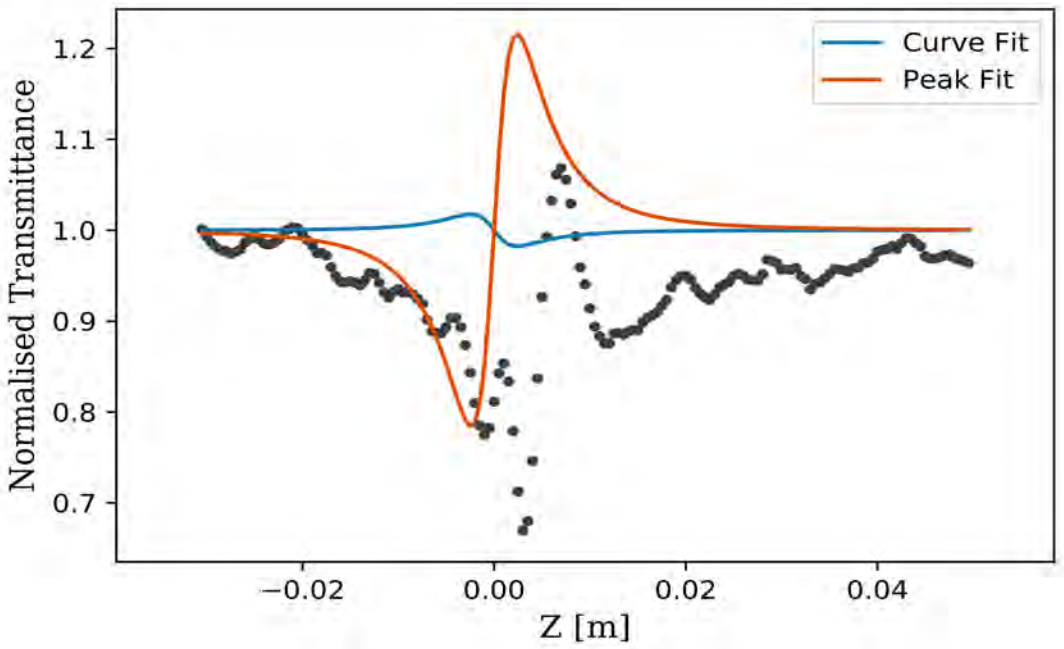

Figure 114: Closed apeture Zscan of the C_s isomer of the $\beta SnCl_2Pc$ at 1.8×10^{12} W.m^{-2}.

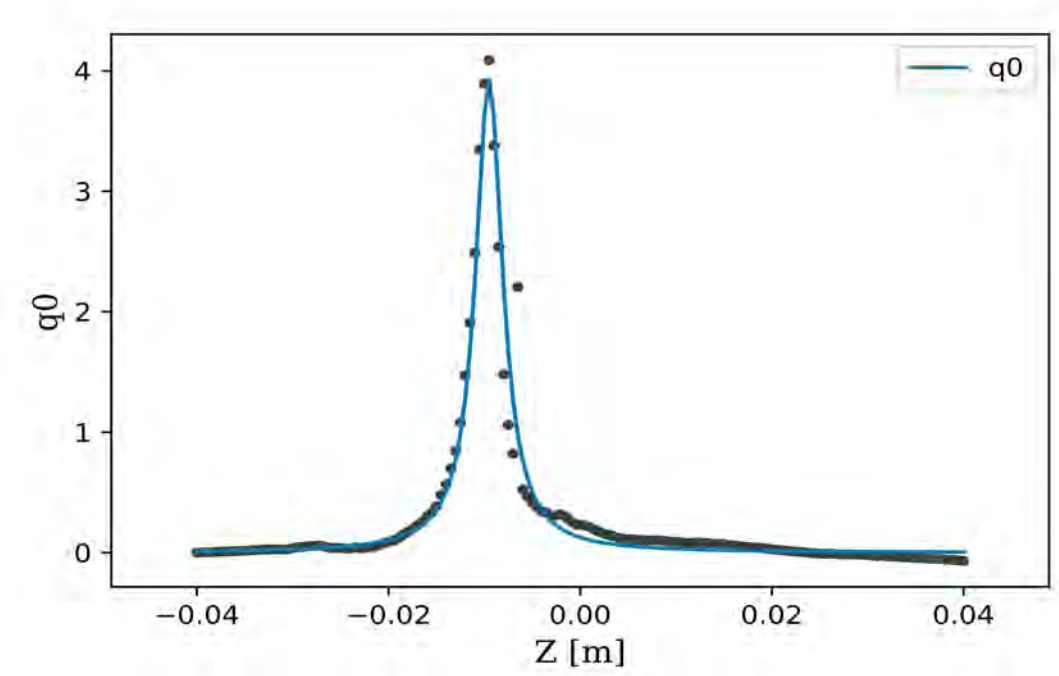

Figure 115: Open apeture Zscan of the C_s isomer of the $\beta SnCl_2Pc$ at 5.8×10^{12} W.m^{-2}.

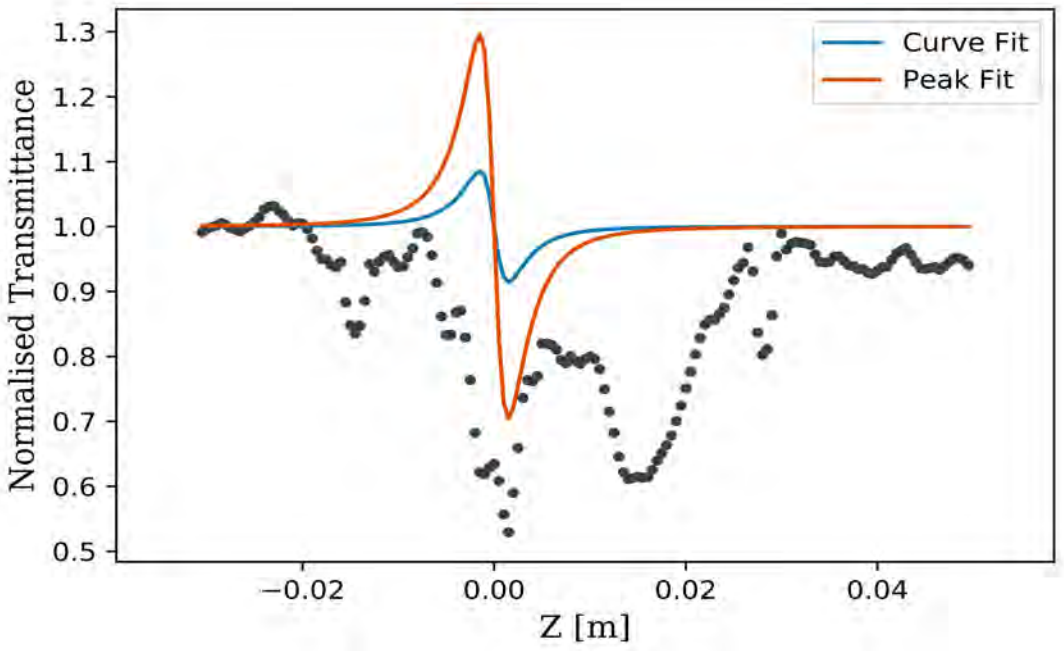

Figure 116: Closed apeture Zscan of the C_s isomer of the $\beta SnCl_2Pc$ at 5.8×10^{12} W.m^{-2}.

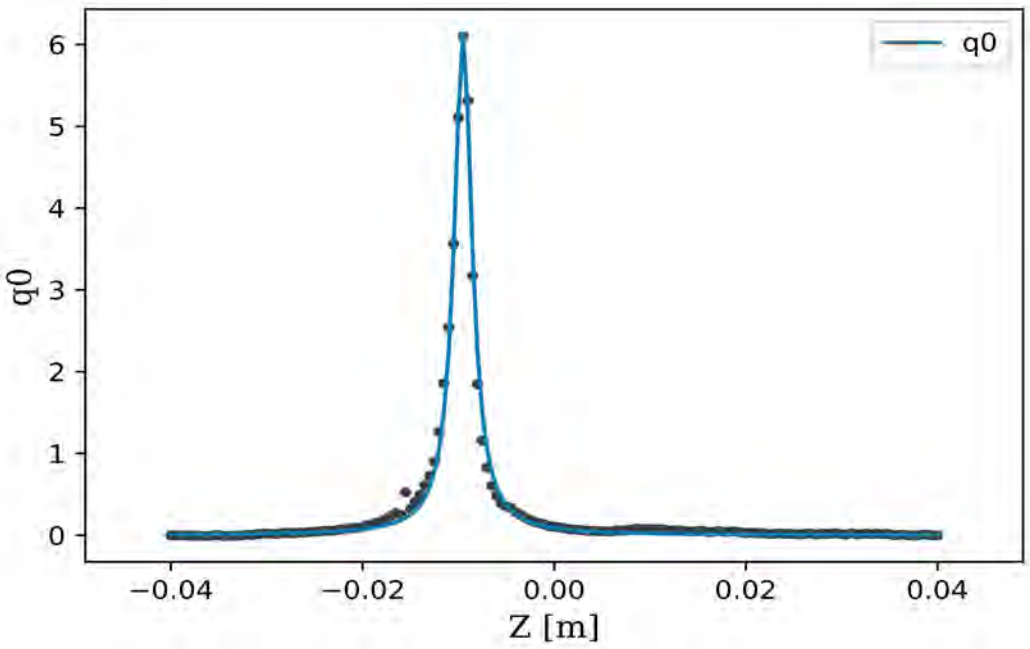

Figure 117: Open apeture Zscan of the C_s isomer of the $\beta SnCl_2Pc$ at 10.2×10^{12} W.m^{-2}.

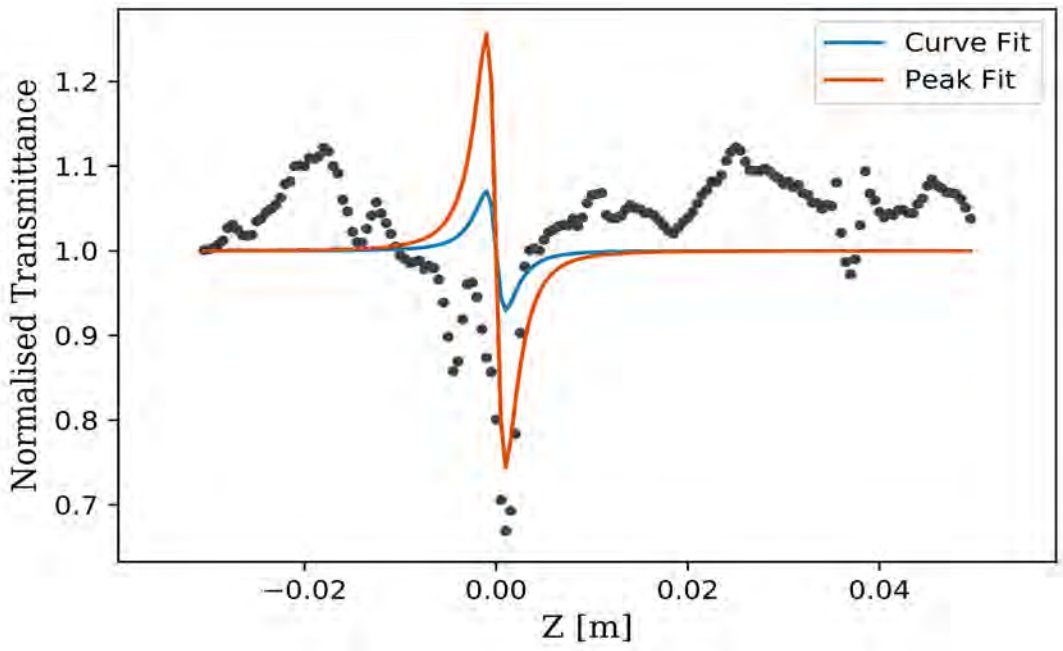

Figure 118: Closed apeture Zscan of the C_s isomer of the $\beta SnCl_2Pc$ at 10.2×10^{12} W.m^{-2}.

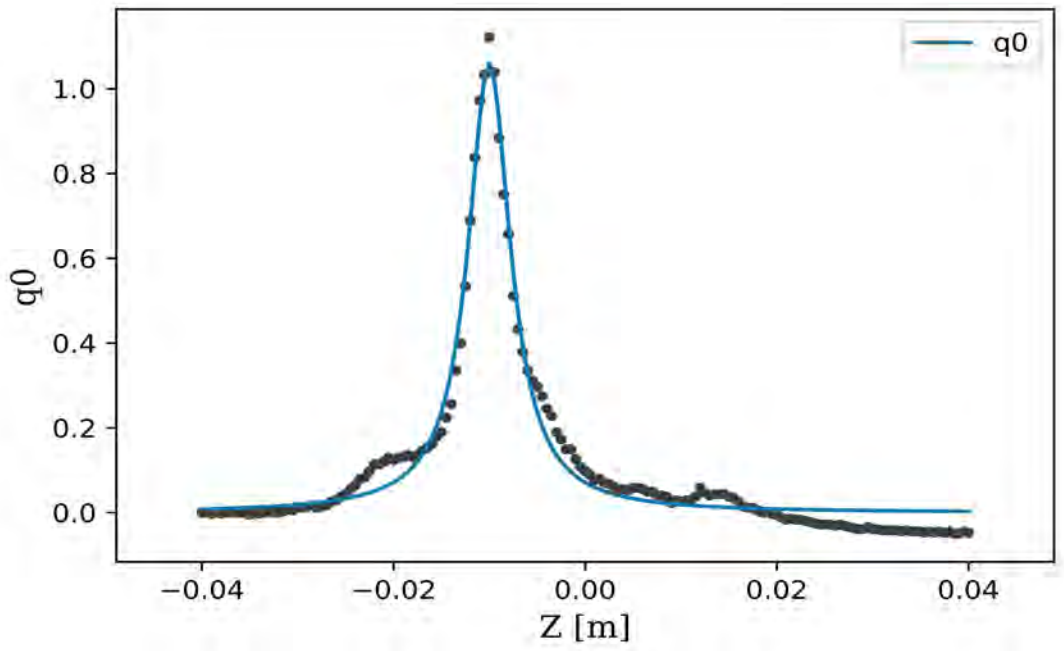

Figure 119: Open apeture Zscan of the C_s isomer of the $\beta SnCl_2Pc$ at 0.8×10^{12} W.m^{-2}.

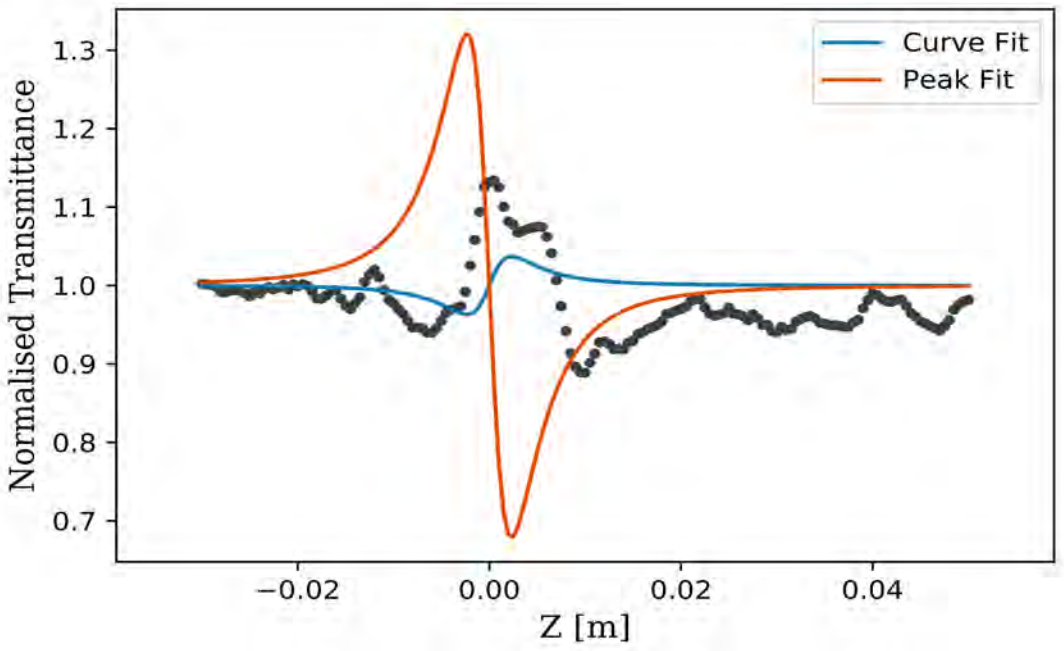

Figure 120: Closed apeture Zscan of the C_s isomer of the $\beta SnCl_2Pc$ at 0.8×10^{12} W.m^{-2}.

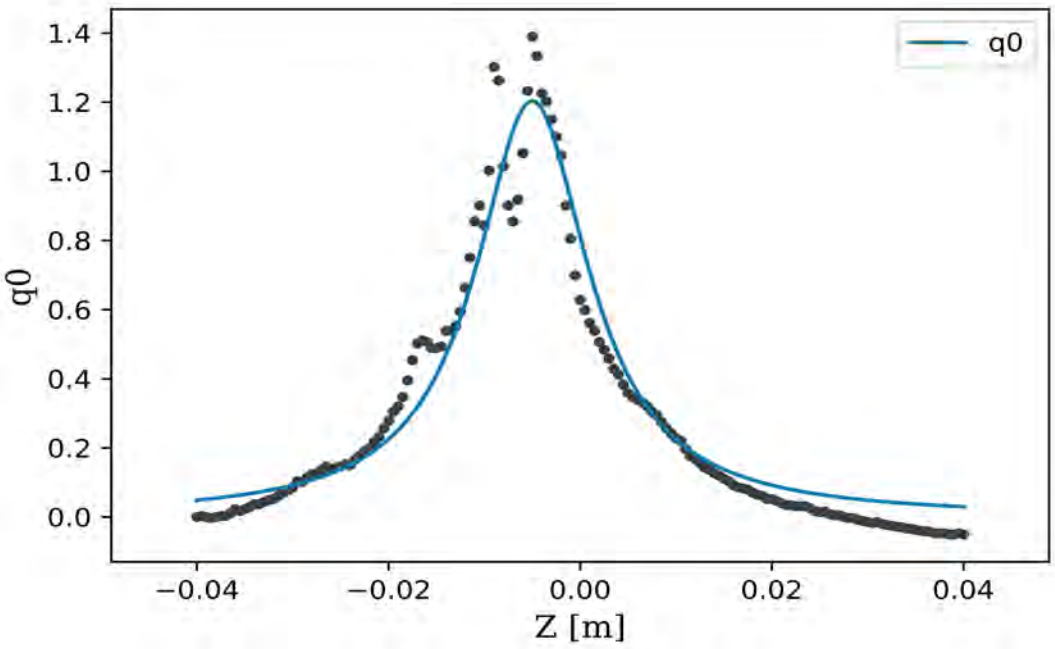

Figure 121: Open apeture Zscan of the D_{2h} isomer of the $\beta SnCl_2Pc$ at 0.6×10^{12} W.m^{-2}.

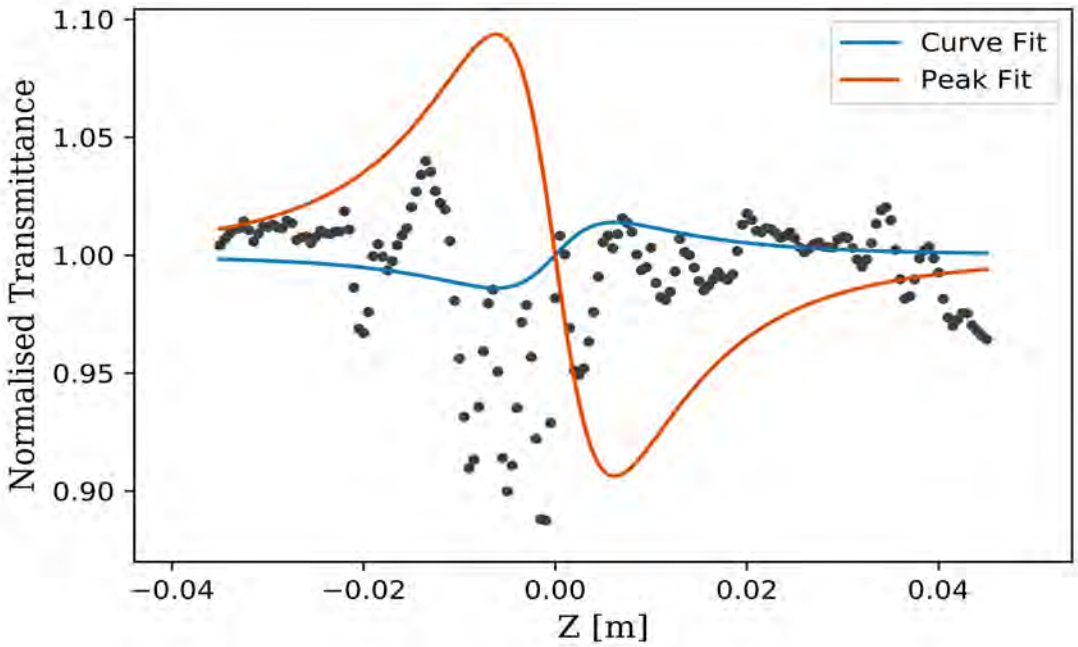

Figure 122: Closed apeture Zscan of the D_{2h} isomer of the $\beta SnCl_2Pc$ at 0.6×10^{12} W.m^{-2}.

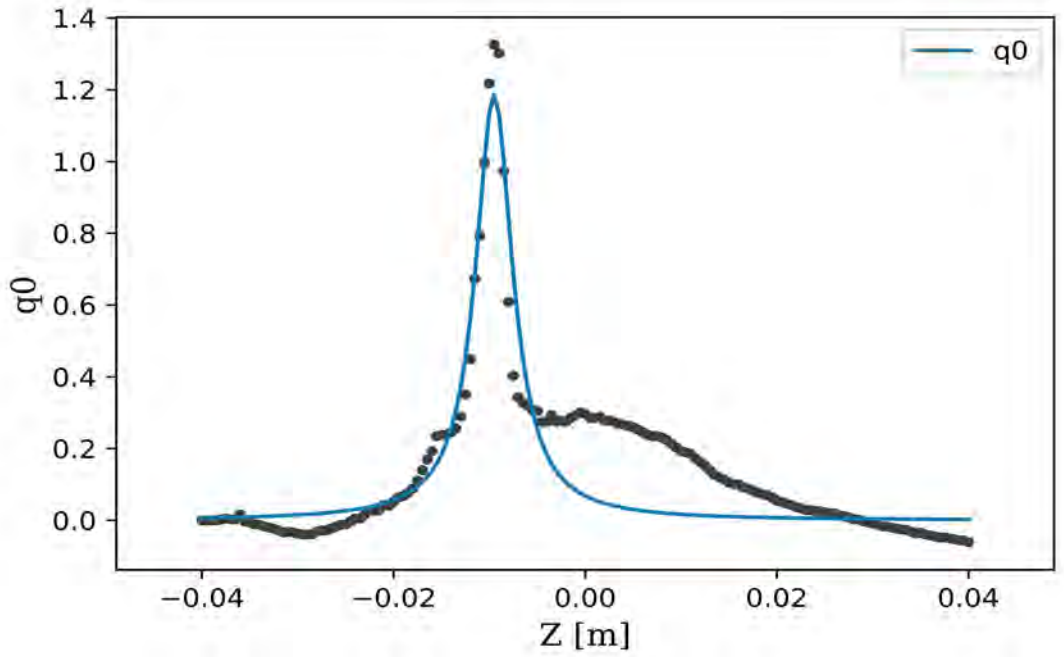

Figure 123: Open apeture Zscan of the D_{2h} isomer of the $\beta SnCl_2Pc$ at 2.8×10^{12} W.m^{-2}.

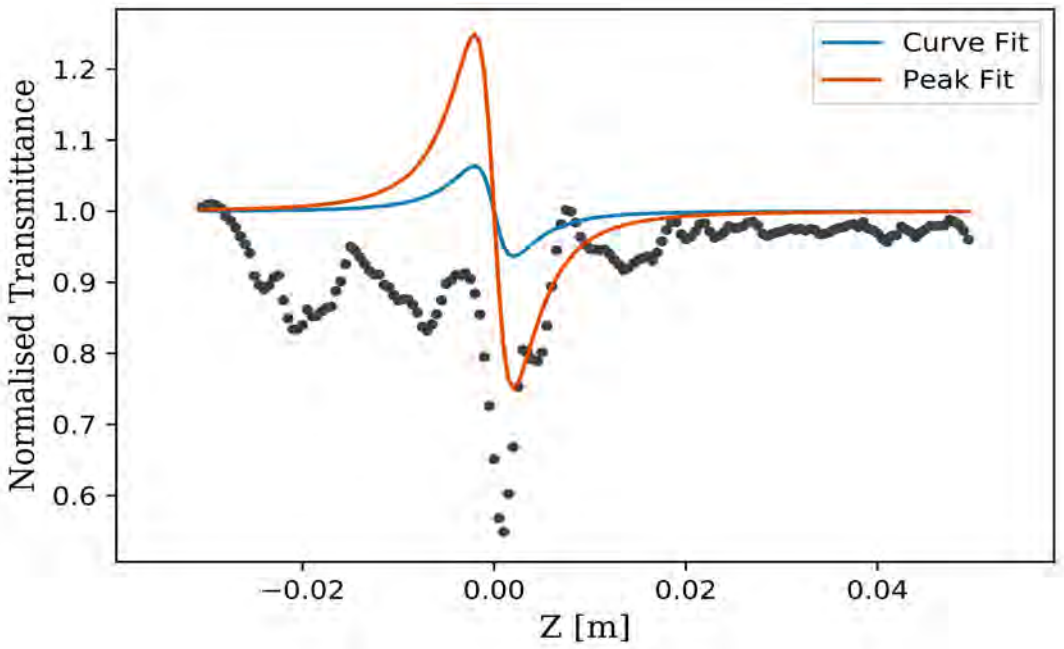

Figure 124: Closed apeture Zscan of the D_{2h} isomer of the $\beta SnCl_2Pc$ at 2.8×10^{12} W.m^{-2}.

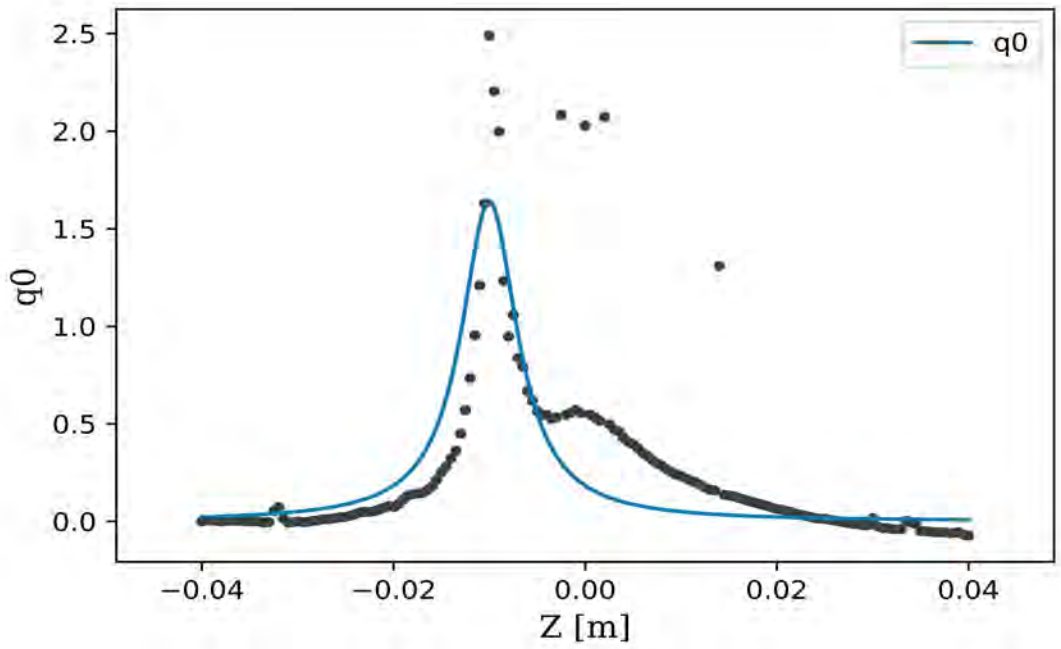

Figure 125: Open apeture Zscan of the D_{2h} isomer of the $\beta SnCl_2Pc$ at 2.9×10^{12} W.m^{-2}.

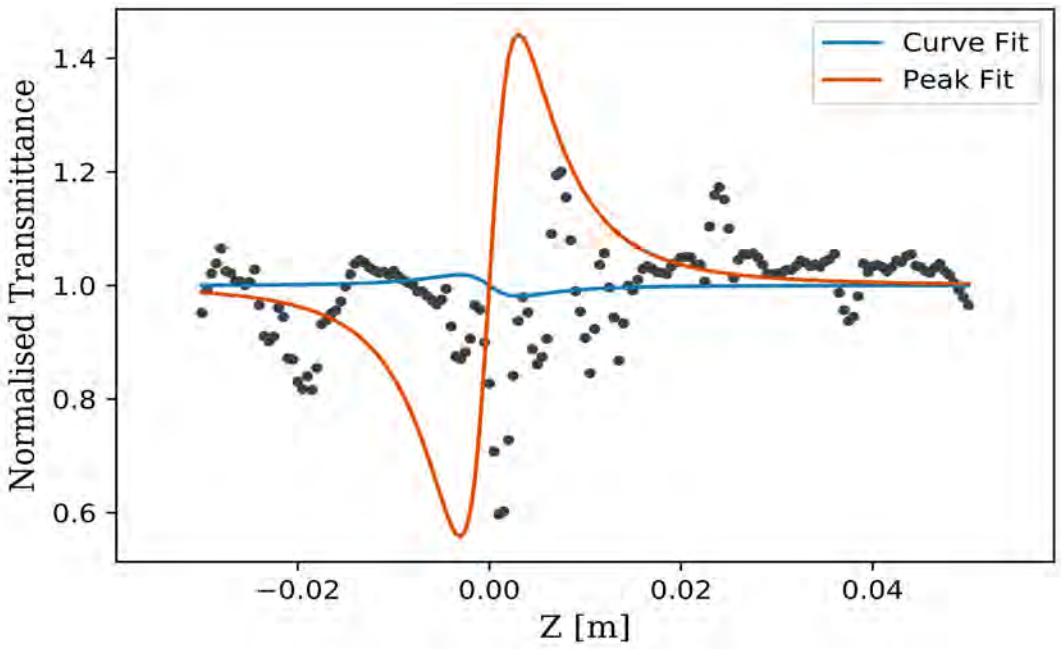

Figure 126: Closed apeture Zscan of the D_{2h} isomer of the $\beta SnCl_2Pc$ at 2.9×10^{12} W.m^{-2}.

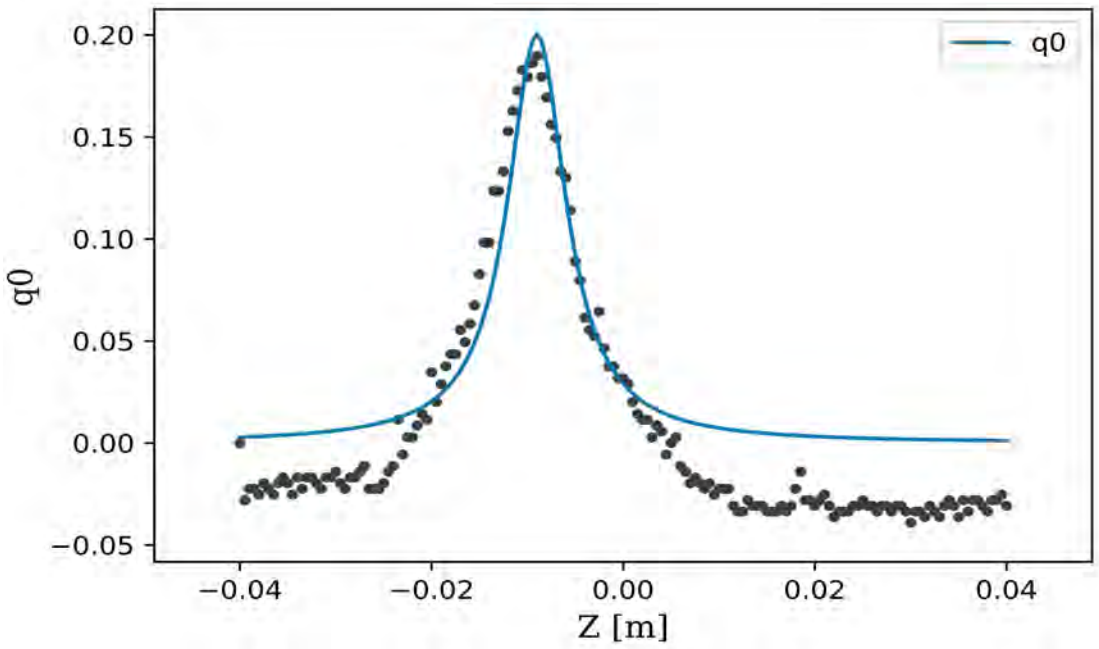

Figure 127: Open apeture Zscan of the D_{2h} isomer of the $\beta SnCl_2Pc$ at 0.7×10^{12} W.m^{-2}.

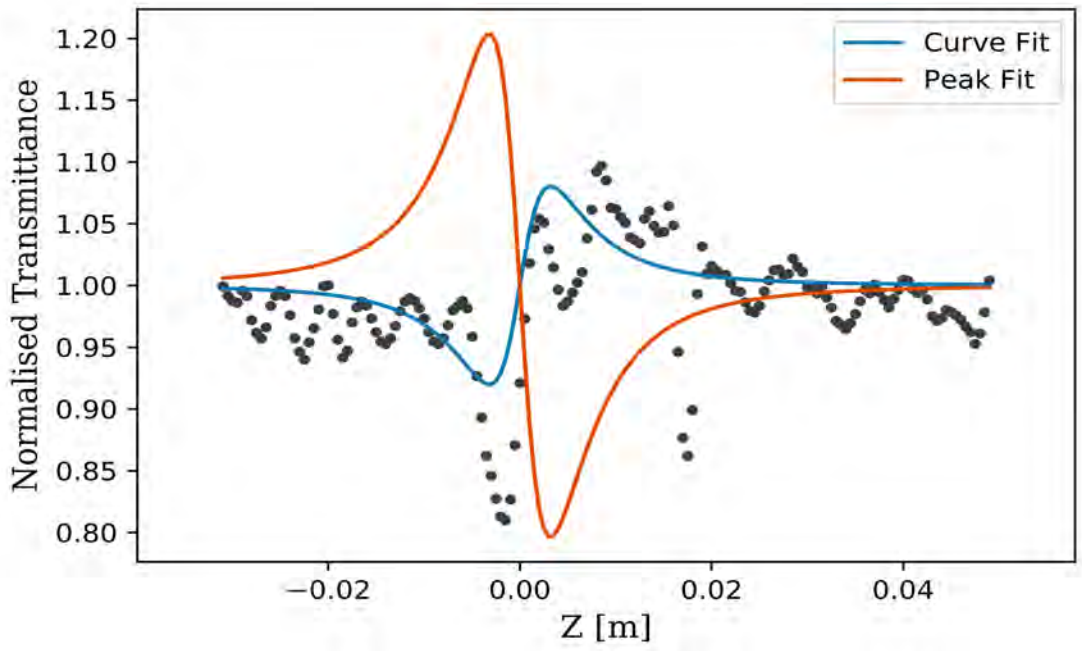

Figure 128: Closed apeture Zscan of the D_{2h} isomer of the $\beta SnCl_2Pc$ at 0.7×10^{12} W.m^{-2}.

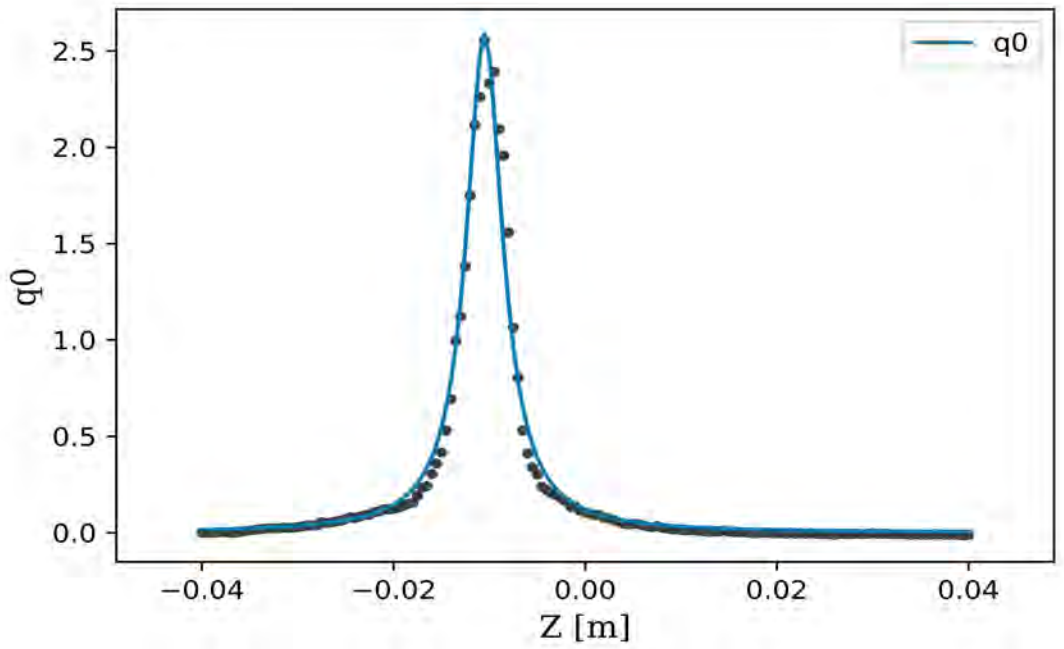

Figure 129: Open apeture Zscan of the C_{4h} isomer of the αH_2Pc at 1.6×10^{12} W.m^{-2}.

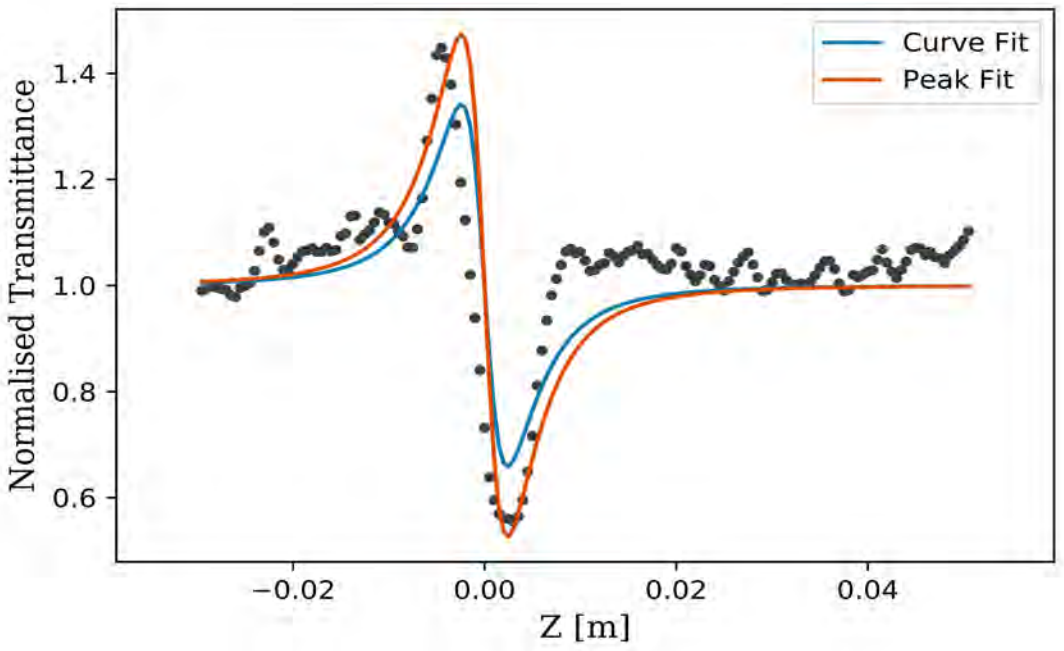

Figure 130: Closed apeture Zscan of the C_{4h} isomer of the αH_2Pc at 1.6×10^{12} W.m^{-2}.

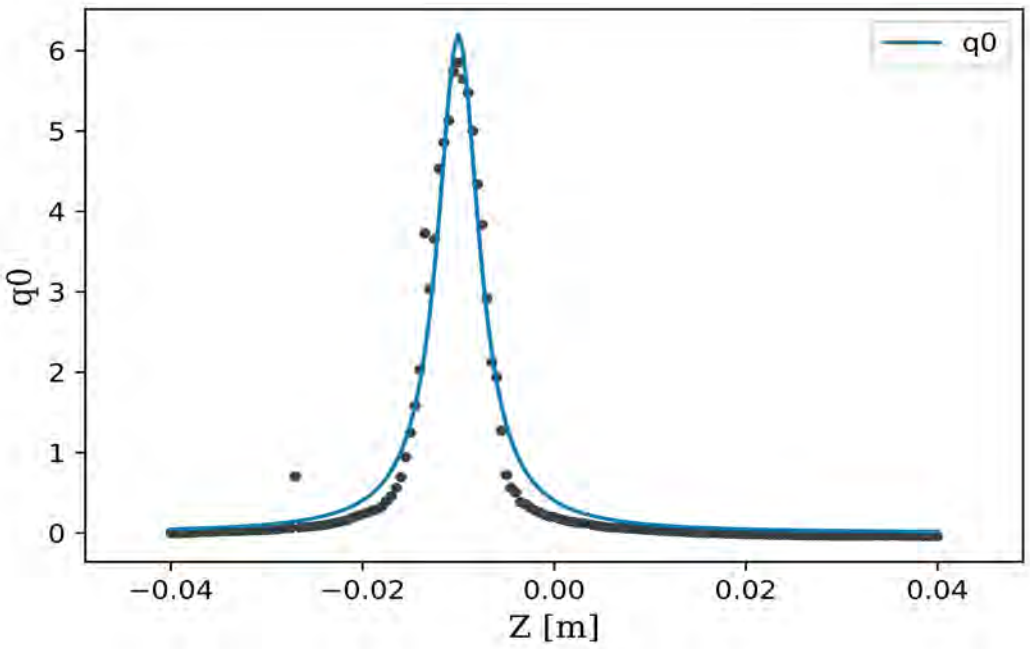

Figure 131: Open apeture Zscan of the C_{4h} isomer of the αH_2Pc at 3.2×10^{12} W.m^{-2}.

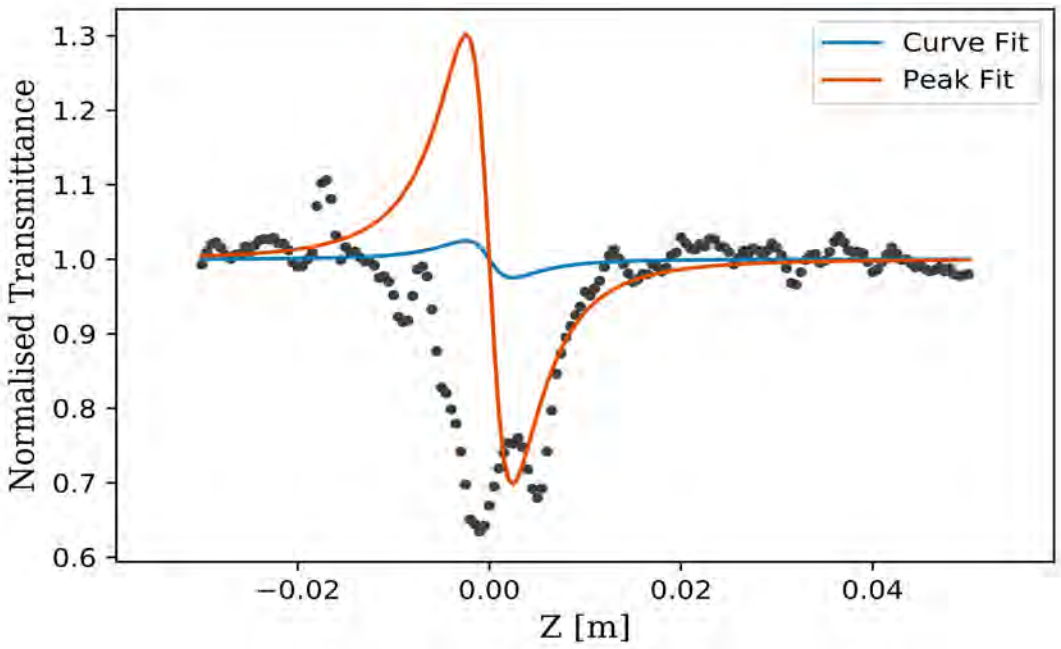

Figure 132: Closed apeture Zscan of the C_{4h} isomer of the αH_2Pc at 3.2×10^{12} W.m^{-2}.

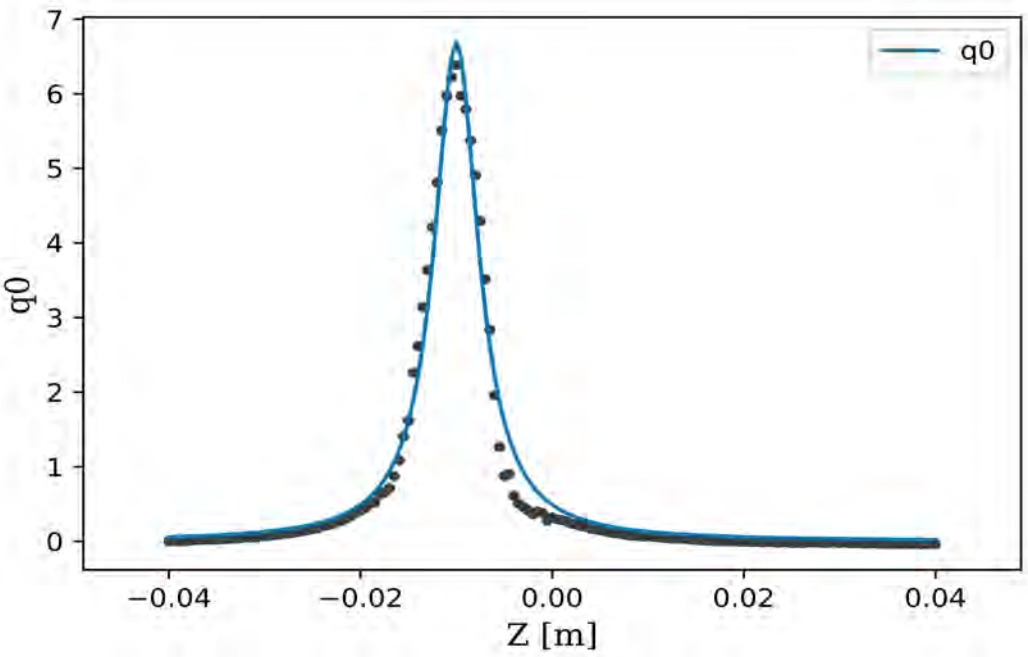

Figure 133: Open apeture Zscan of the C_{4h} isomer of the αH_2Pc at 4.6×10^{12} W.m^{-2}.

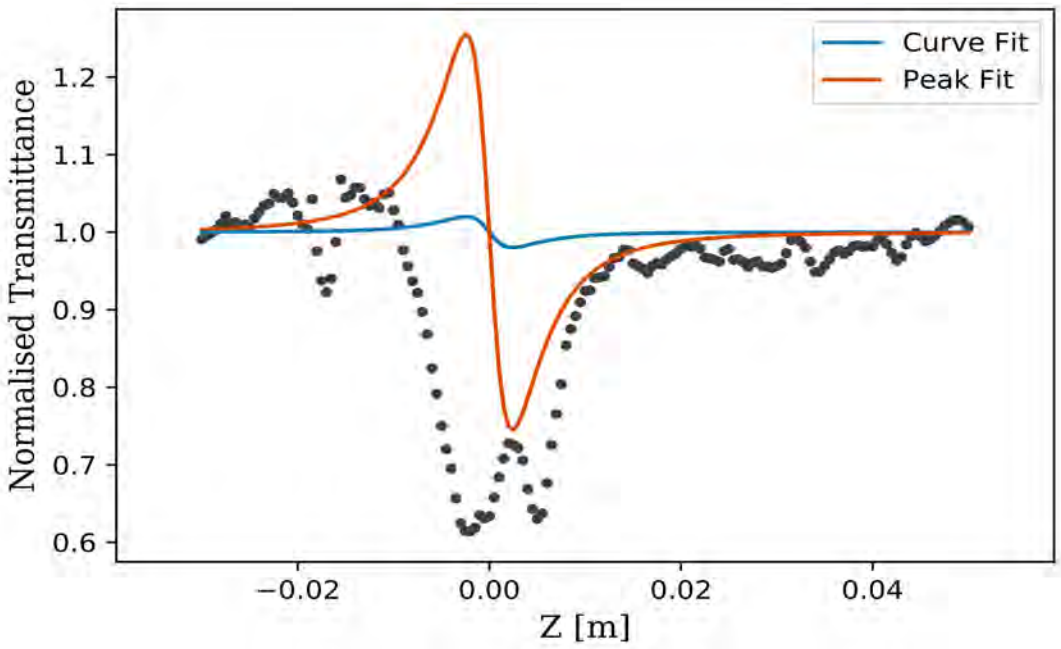

Figure 134: Closed apeture Zscan of the C_{4h} isomer of the αH_2Pc at 4.6×10^{12} W.m^{-2}.

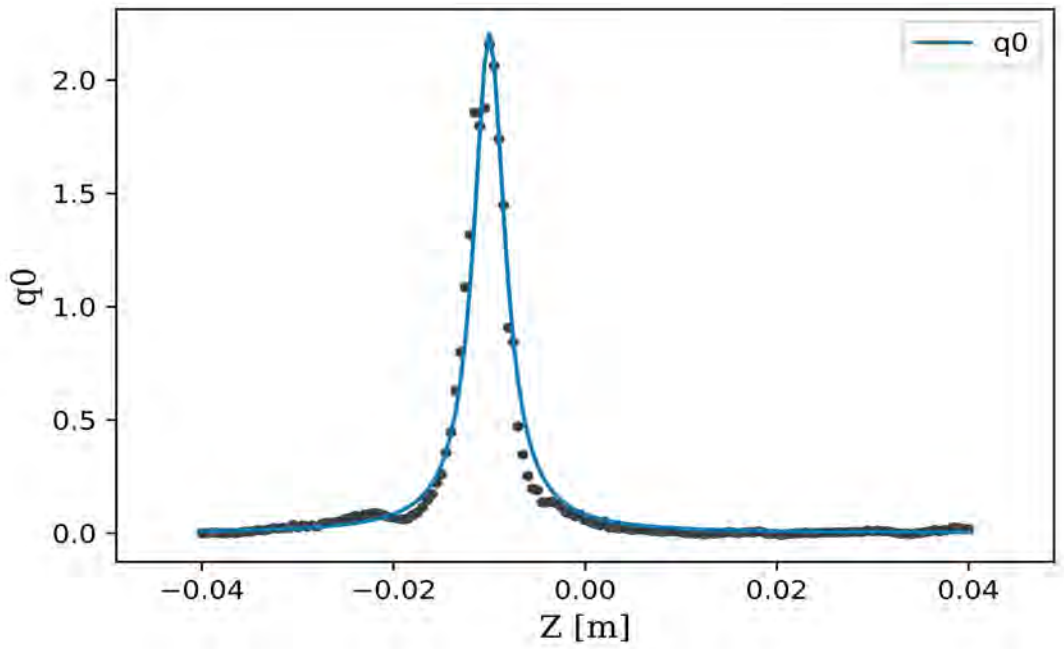

Figure 135: Open apeture Zscan of the C_{4h} isomer of the αH_2Pc at 1.1×10^{12} W.m^{-2}.

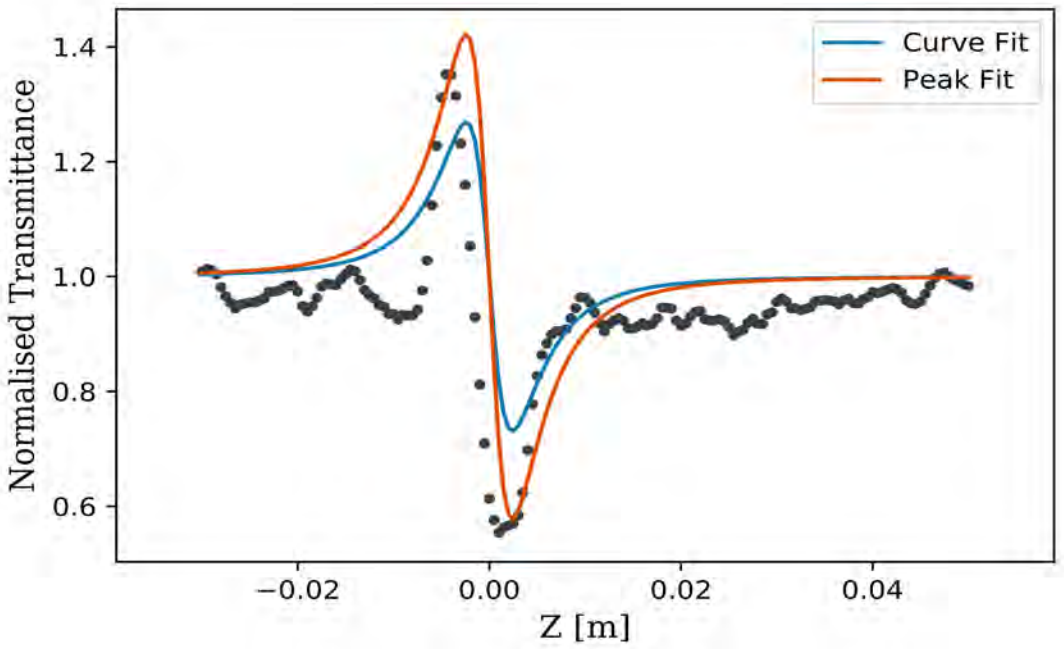

Figure 136: Closed apeture Zscan of the C_{4h} isomer of the αH_2Pc at 1.1×10^{12} W.m^{-2}.

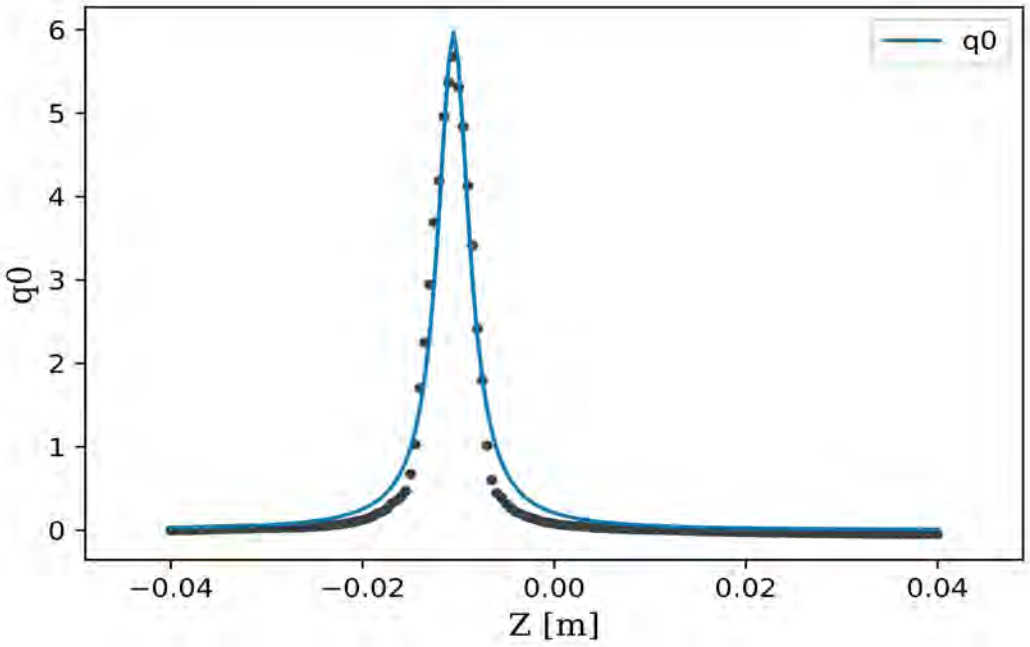

Figure 137: Open apeture Zscan of the C_{2v} isomer of the αH_2Pc at 2.8×10^{12} W.m^{-2}.

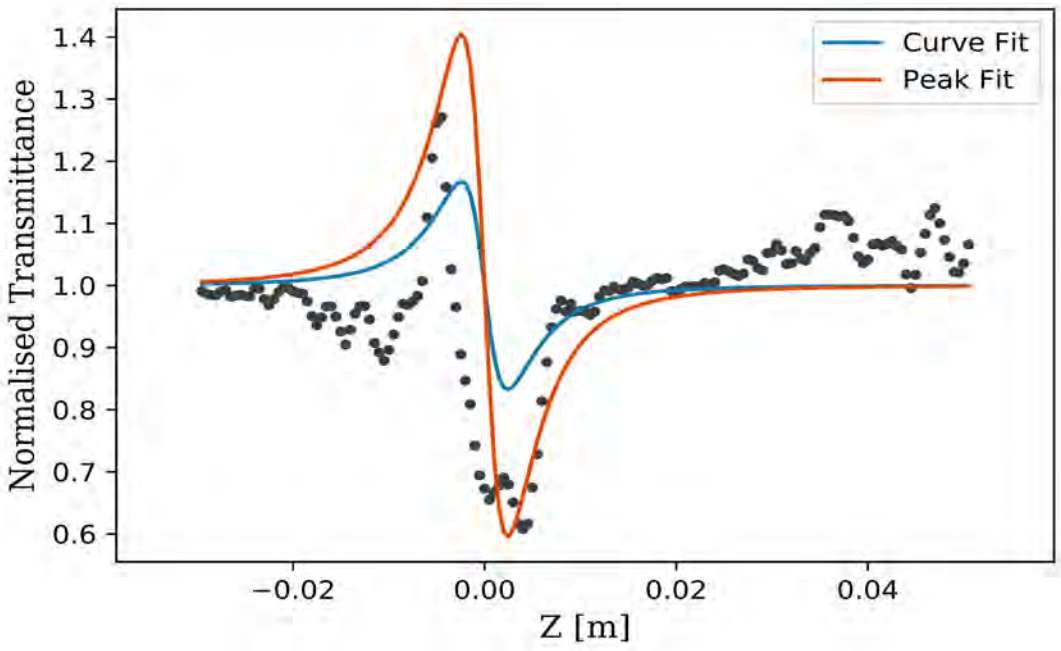

Figure 138: Closed apeture Zscan of the C_{2v} isomer of the αH_2Pc at 2.8×10^{12} W.m^{-2}.

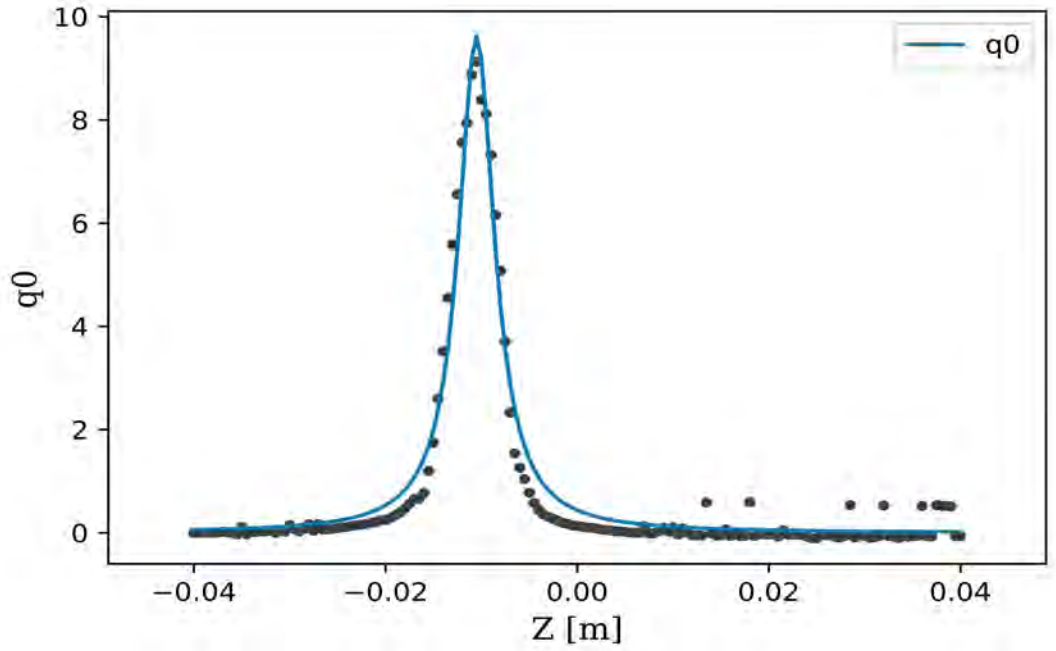

Figure 139: Open apeture Zscan of the C_{2v} isomer of the αH_2Pc at 4.9×10^{12} W.m^{-2}.

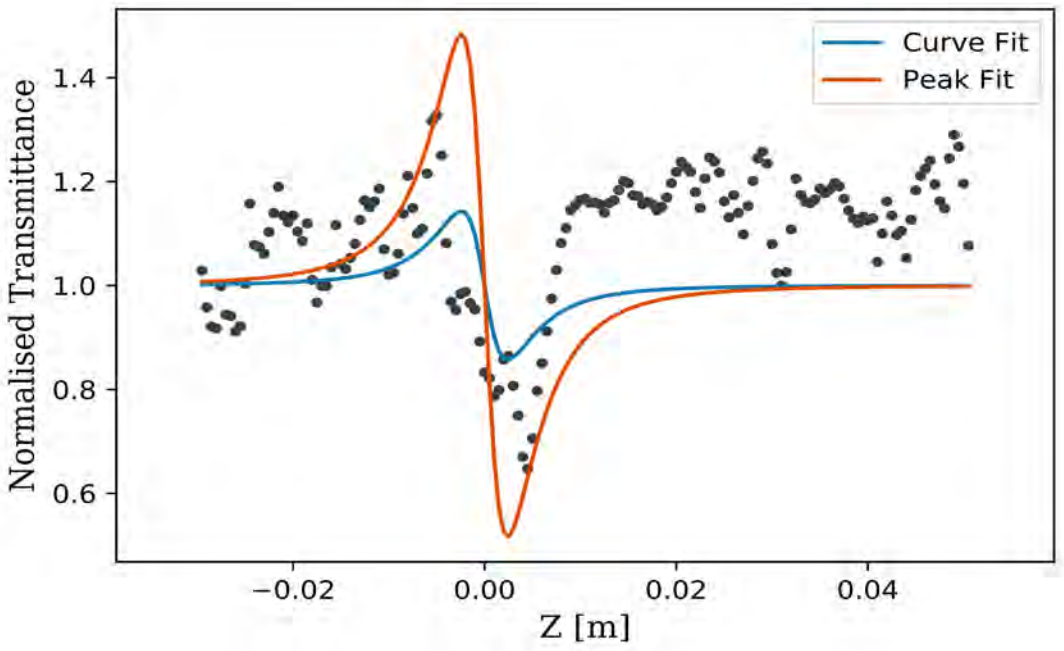

Figure 140: Closed apeture Zscan of the C_{2v} isomer of the αH_2Pc at 4.9×10^{12} W.m^{-2}.

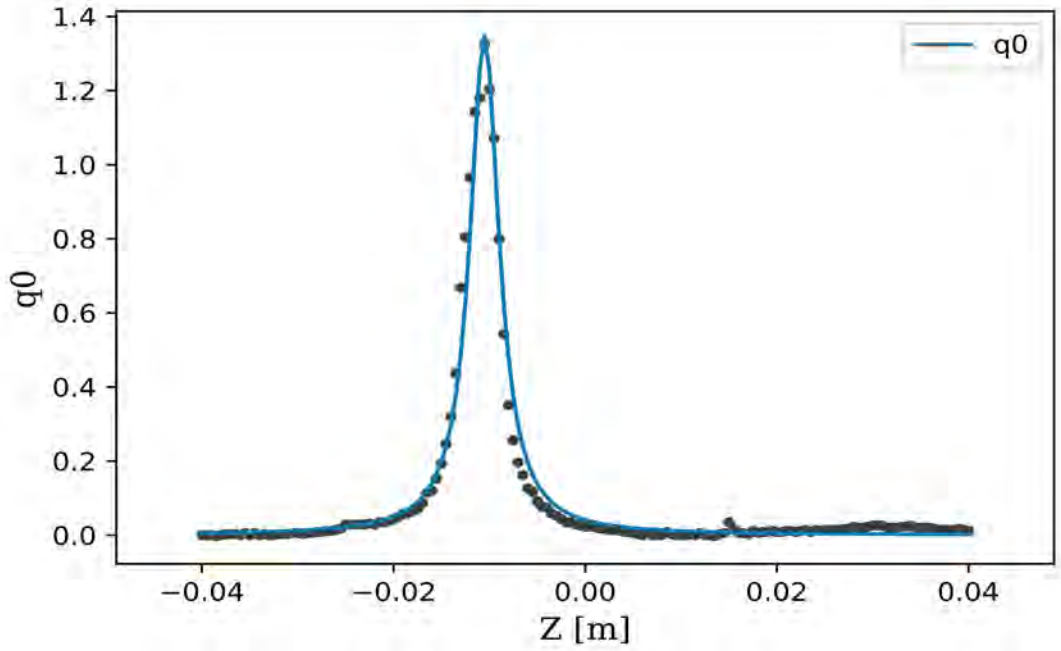

Figure 141: Open apeture Zscan of the C_{2v} isomer of the αH_2Pc at 1.0×10^{12} W.m^{-2}.

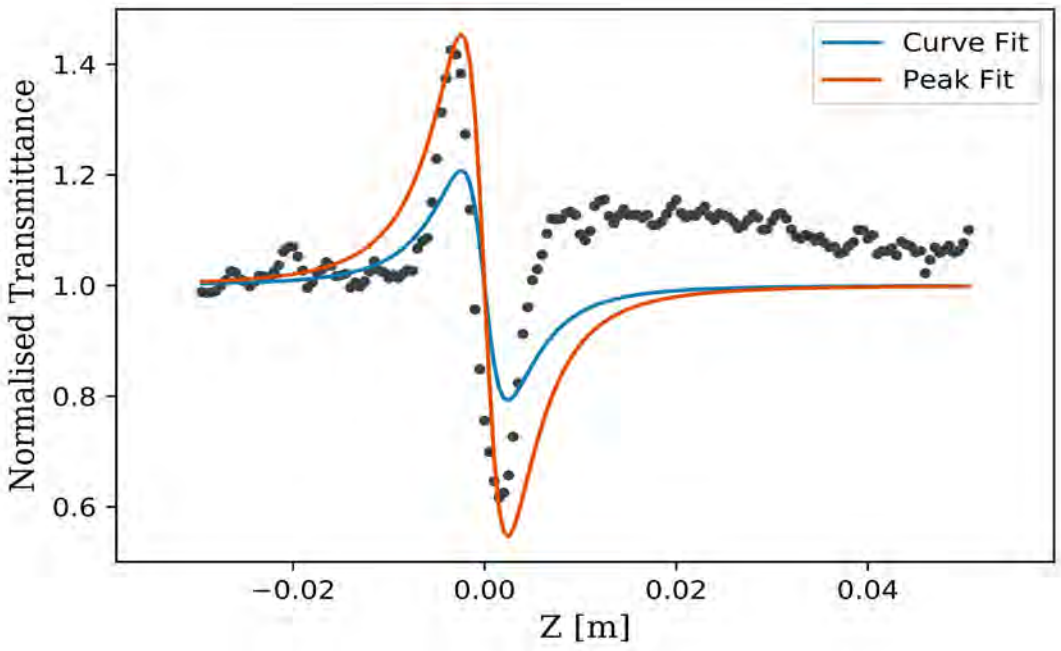

Figure 142: Closed apeture Zscan of the C_{2v} isomer of the αH_2Pc at 1.0×10^{12} W.m^{-2}.

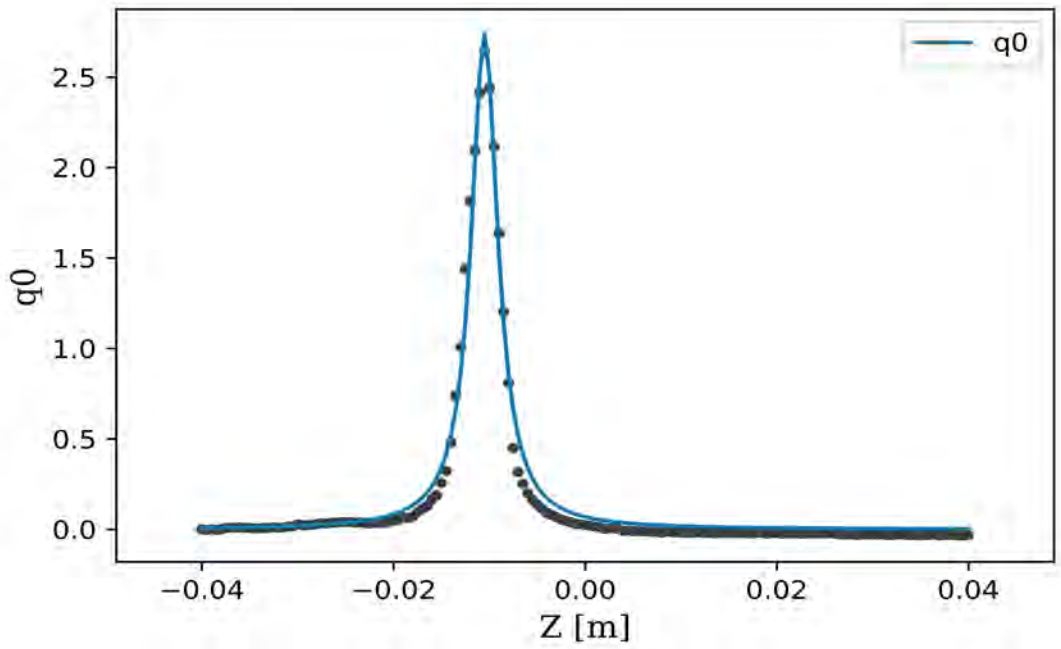

Figure 143: Open apeture Zscan of the C_{2v} isomer of the αH_2Pc at 1.7×10^{12} W.m^{-2}.

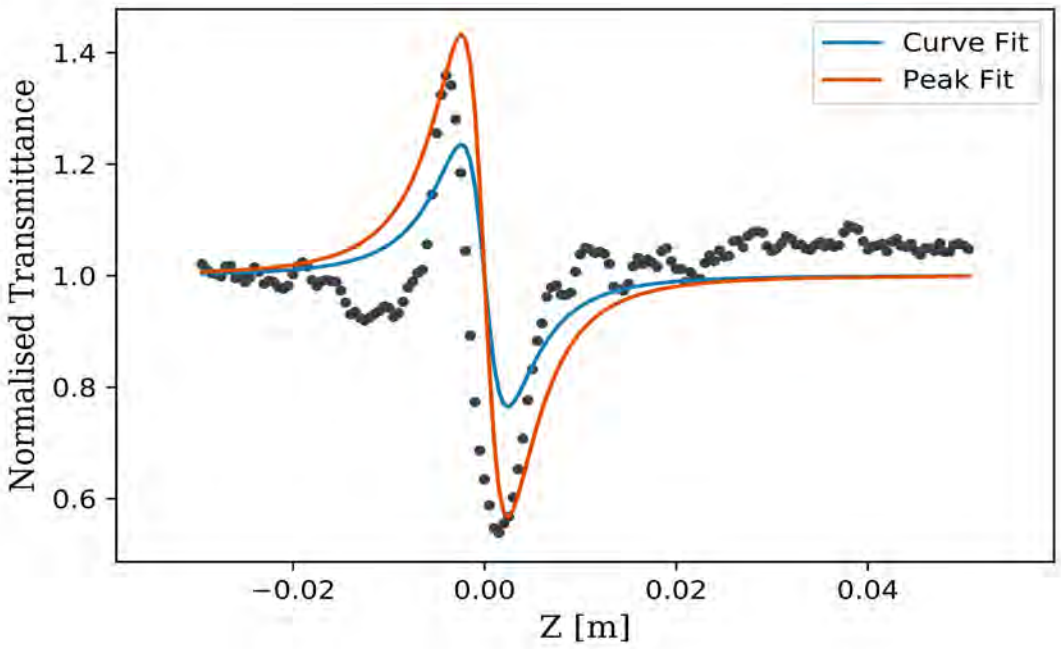

Figure 144: Closed apeture Zscan of the C_{2v} isomer of the αH_2Pc at 1.7×10^{12} W.m^{-2}.

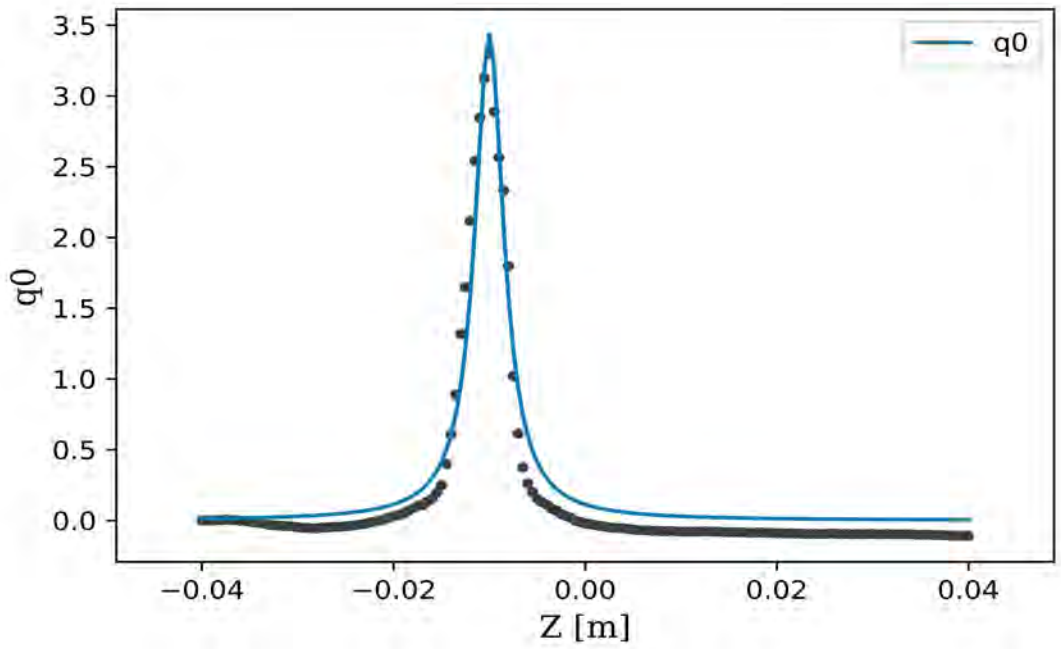

Figure 145: Open apeture Zscan of the C_s isomer of the αH_2Pc at 3.0×10^{12} W.m^{-2}.

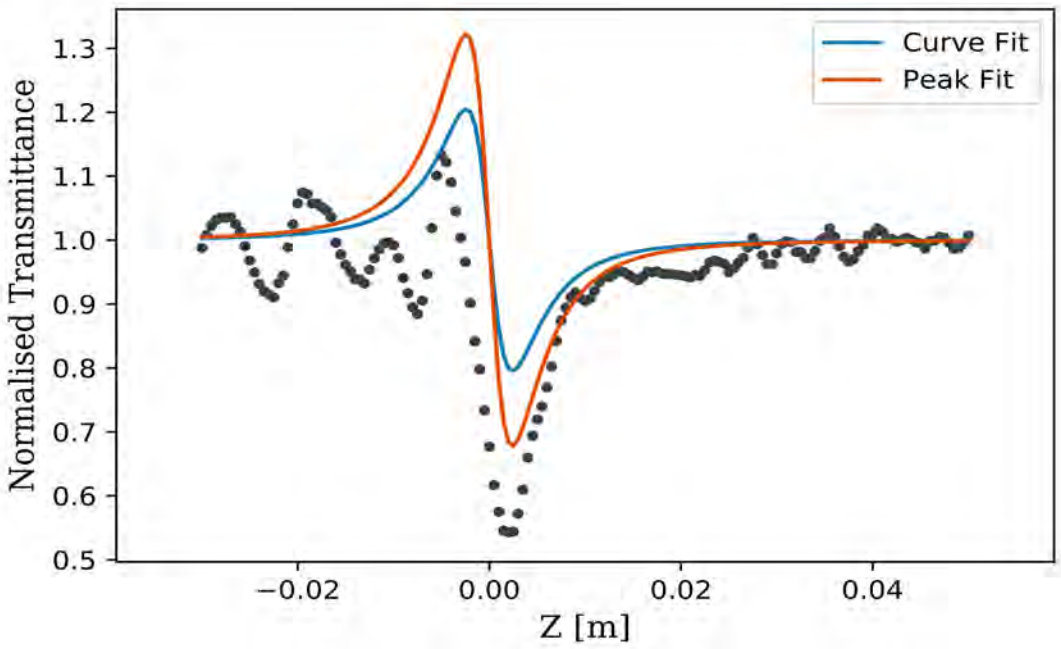

Figure 146: Closed apeture Zscan of the C_s isomer of the αH_2Pc at 3.0×10^{12} W.m^{-2}.

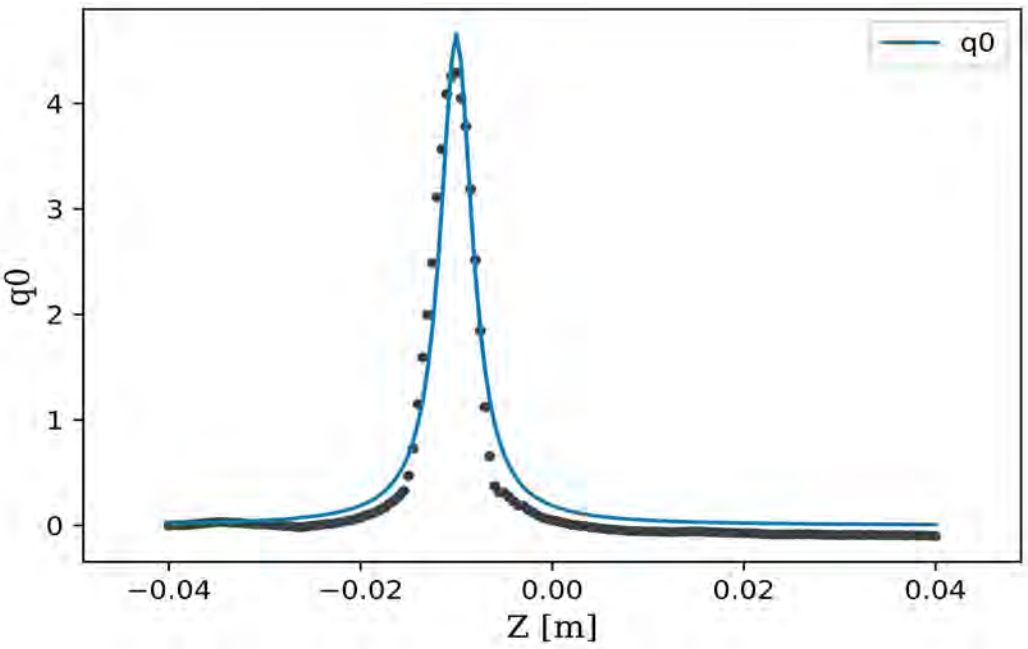

Figure 147: Open apeture Zscan of the C_s isomer of the αH_2Pc at 4.1×10^{12} W.m^{-2}.

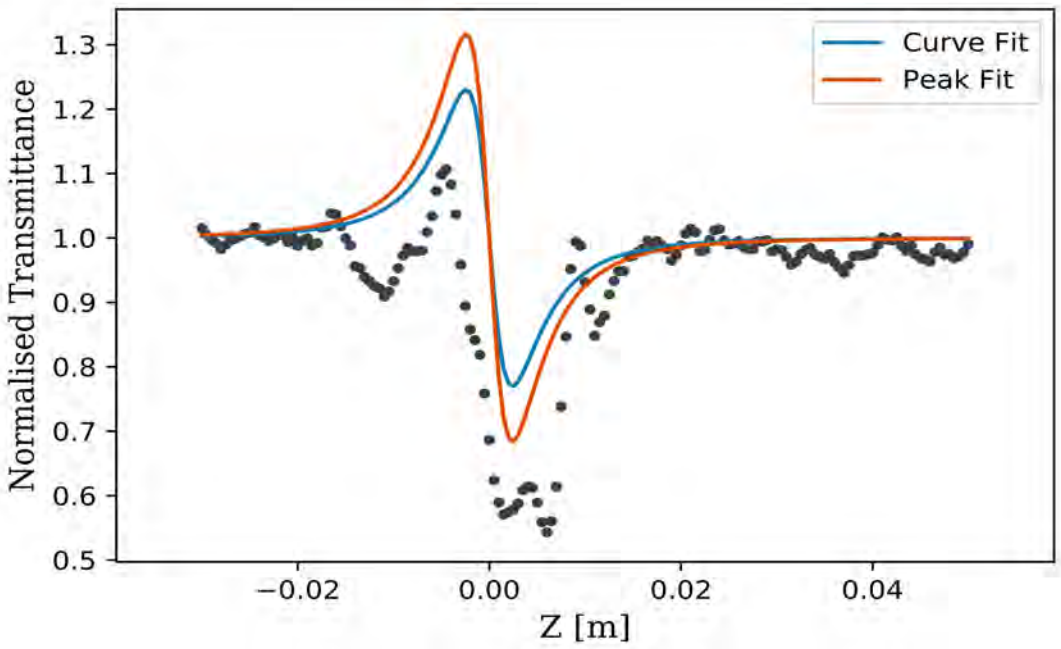

Figure 148: Closed apeture Zscan of the C_s isomer of the αH_2Pc at 4.1×10^{12} W.m^{-2}.

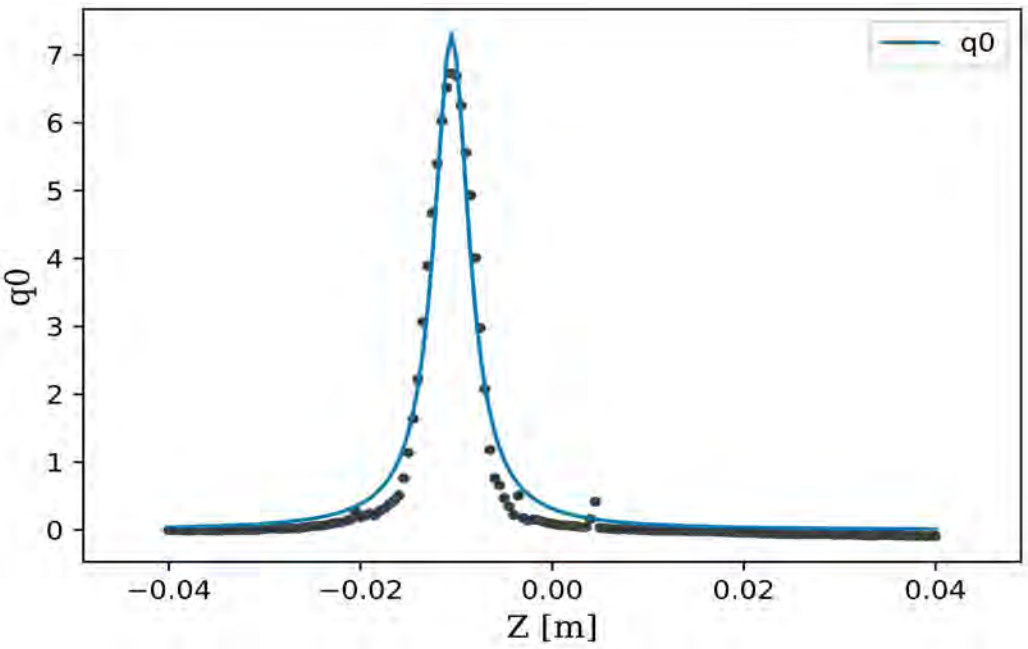

Figure 149: Open apeture Zscan of the C_s isomer of the αH_2Pc at 5.4×10^{12} W.m^{-2}.

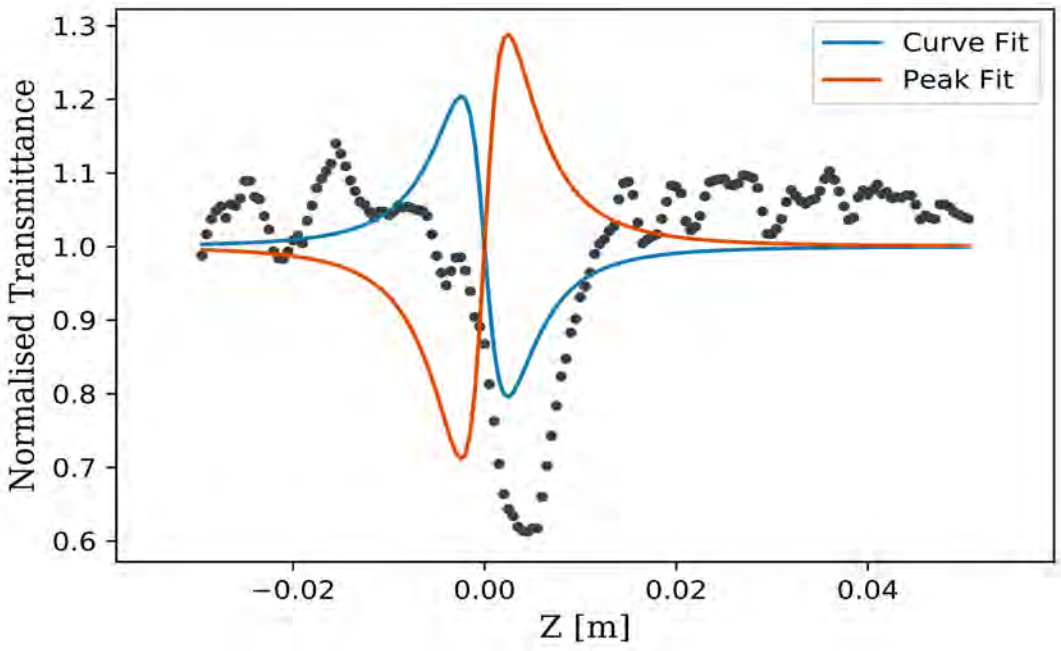

Figure 150: Closed apeture Zscan of the C_s isomer of the αH_2Pc at 5.4×10^{12} W.m^{-2}.

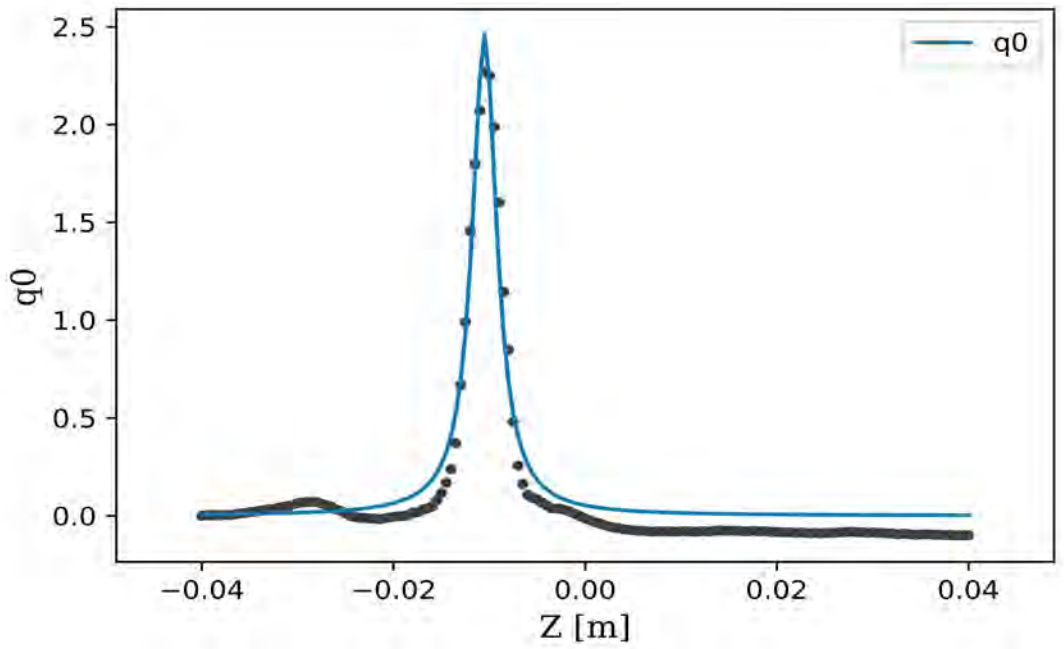

Figure 151: Open apeture Zscan of the C_s isomer of the αH_2Pc at 2.1×10^{12} W.m^{-2}.

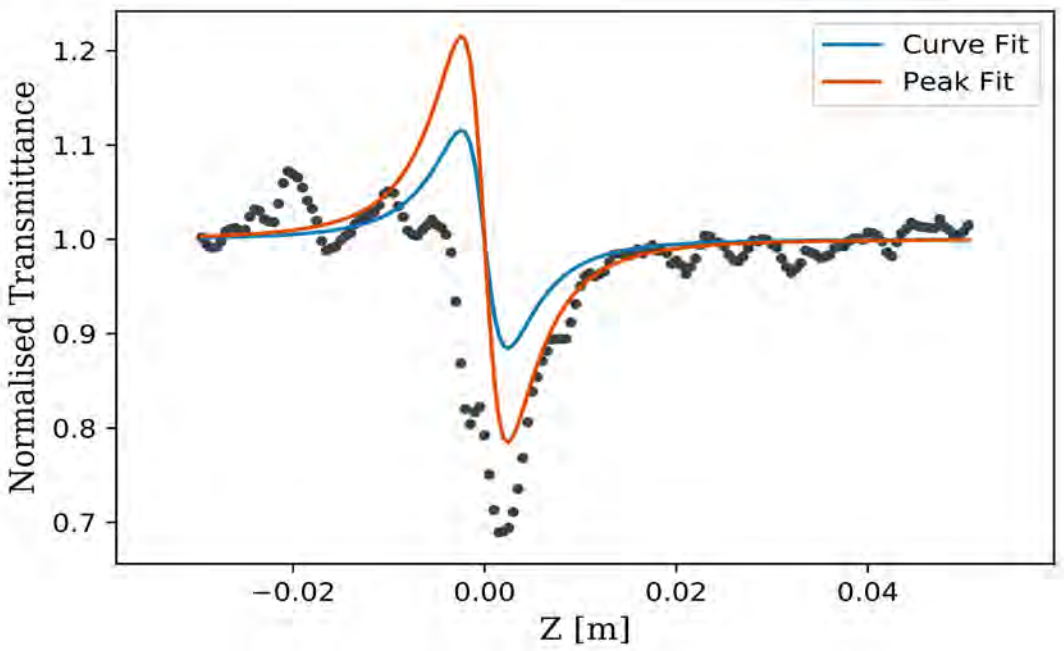

Figure 152: Closed apeture Zscan of the C_s isomer of the αH_2Pc at 2.1×10^{12} W.m^{-2}.

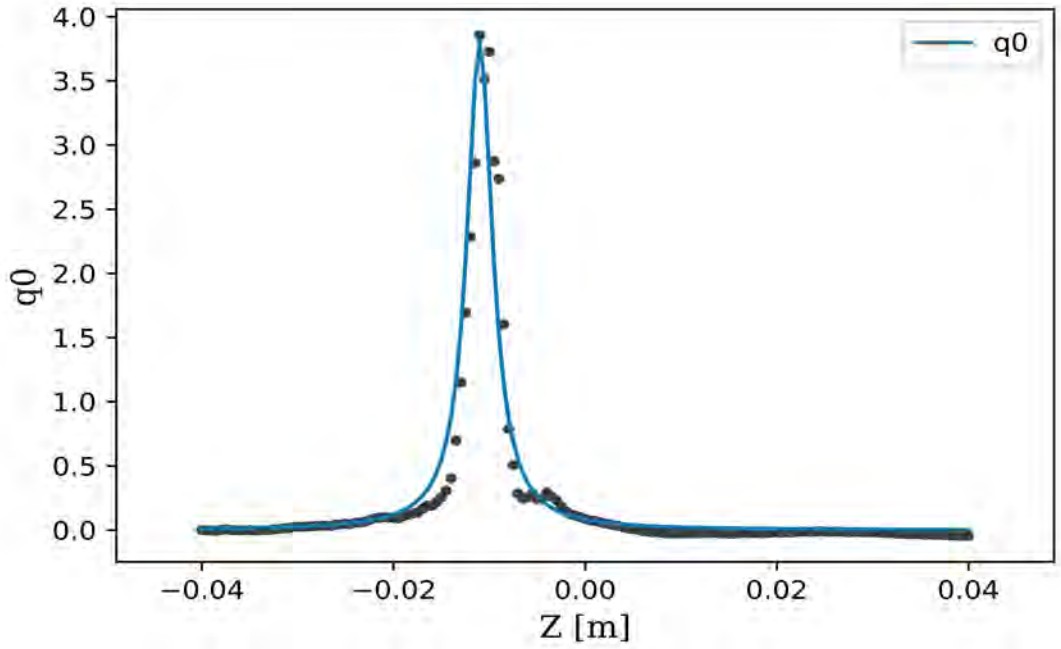

Figure 153: Open apeture Zscan of the D_{2h} isomer of the αH_2Pc at 2.3×10^{12} W.m^{-2}.

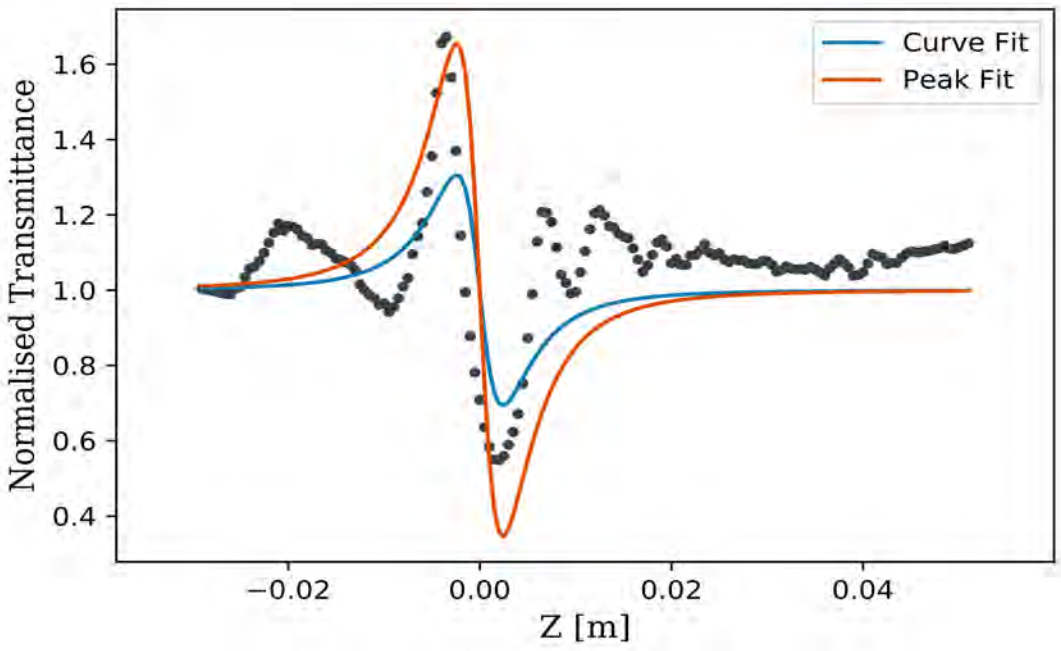

Figure 154: Closed apeture Zscan of the D_{2h} isomer of the αH_2Pc at 2.3×10^{12} W.m^{-2}.

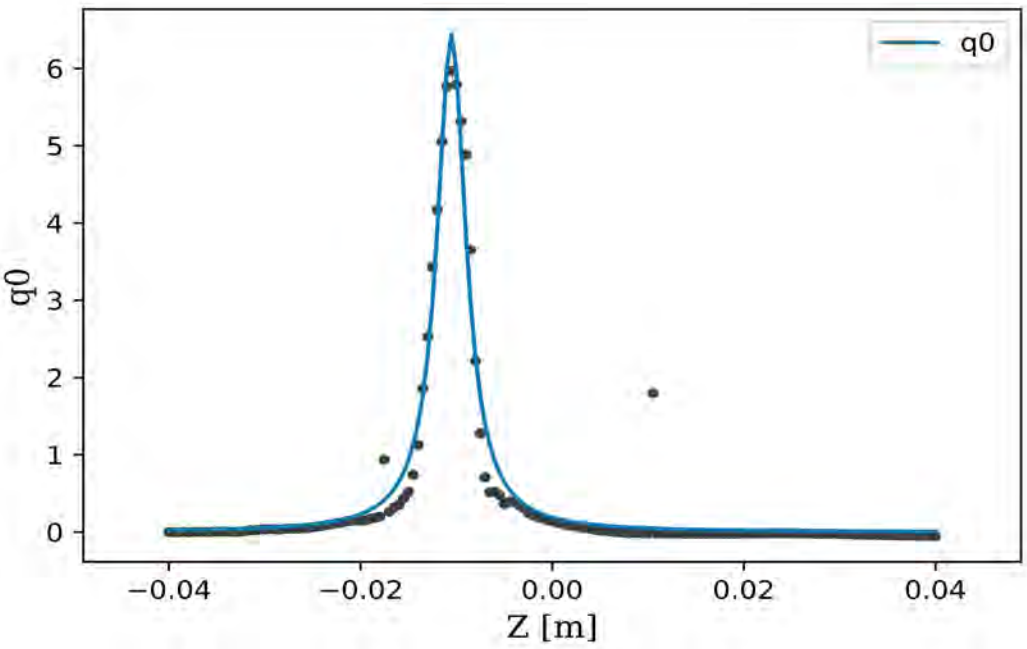

Figure 155: Open apeture Zscan of the D_{2h} isomer of the αH_2Pc at 4.4×10^{12} W.m^{-2}.

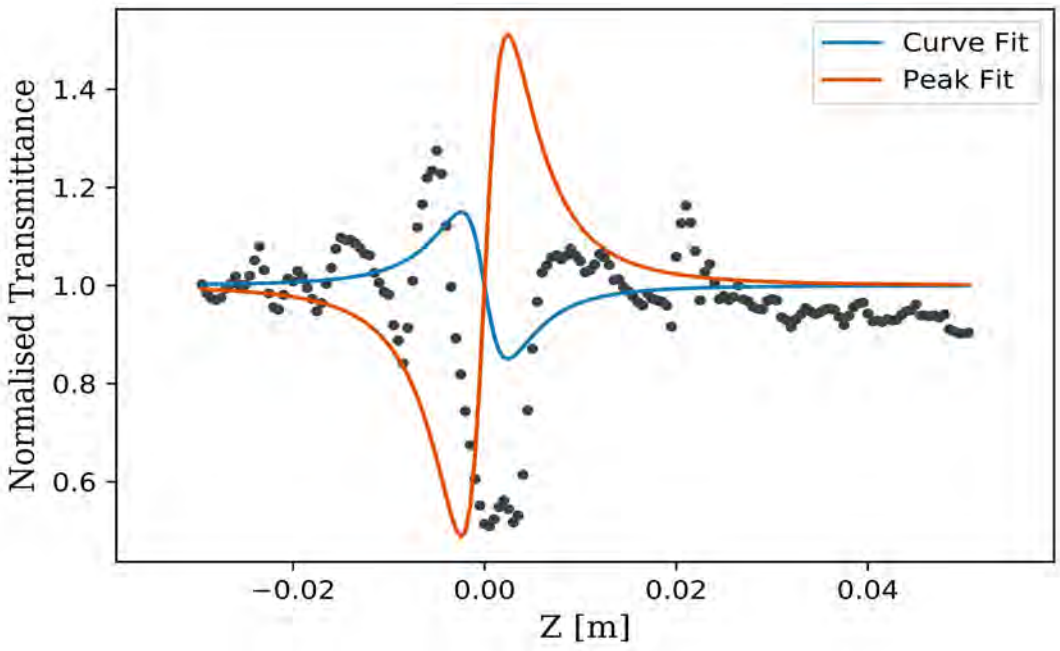

Figure 156: Closed apeture Zscan of the D_{2h} isomer of the αH_2Pc at 4.4×10^{12} W.m^{-2}.

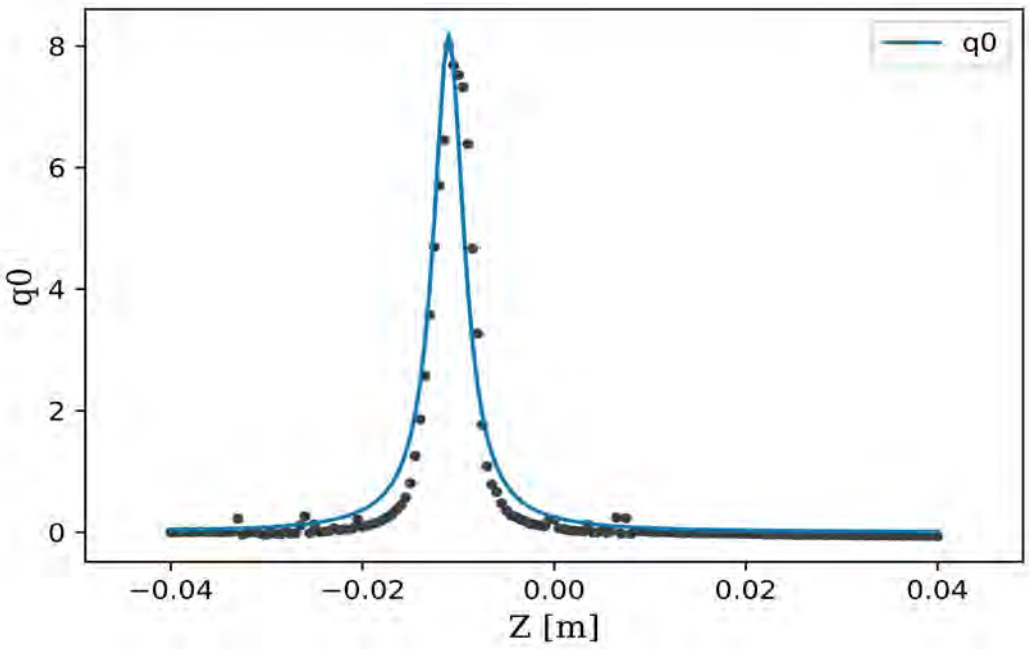

Figure 157: Open apeture Zscan of the D_{2h} isomer of the αH_2Pc at 6.4×10^{12} W.m^{-2}.

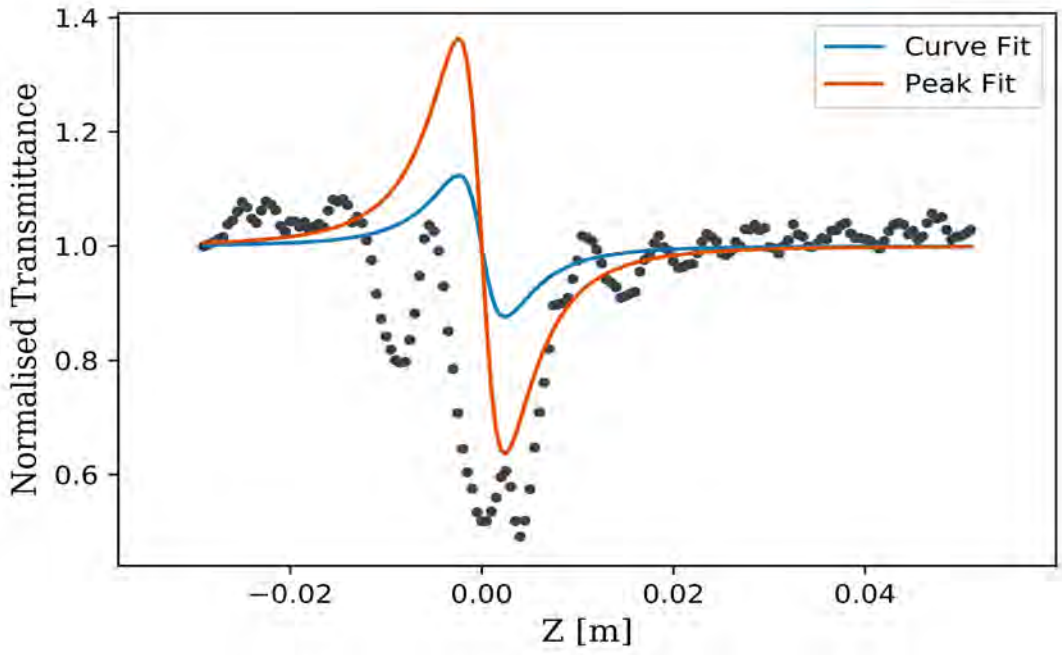

Figure 158: Closed apeture Zscan of the D_{2h} isomer of the αH_2Pc at 6.4×10^{12} W.m^{-2}.

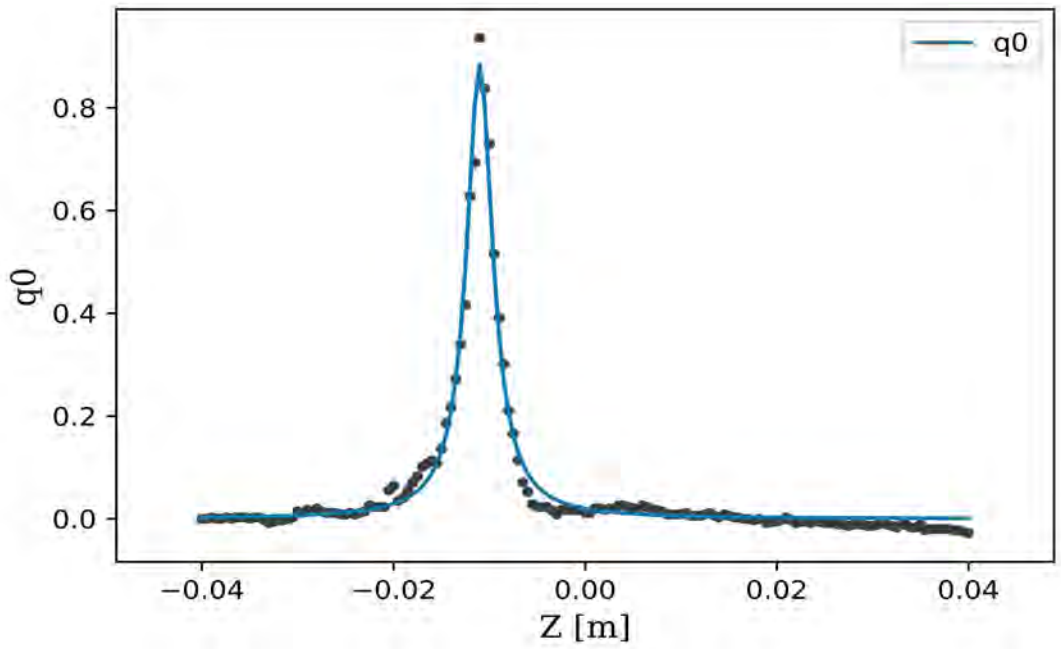

Figure 159: Open apeture Zscan of the D_{2h} isomer of the αH_2Pc at $1.4{\times}10^{12}$ W.m^{-2}.

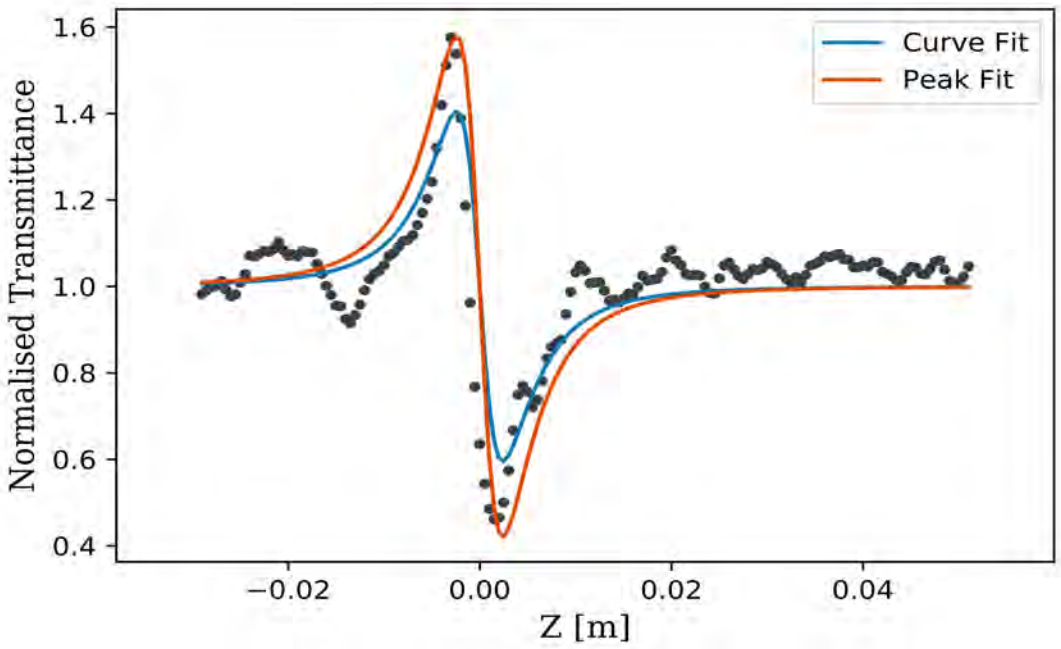

Figure 160: Closed apeture Zscan of the D_{2h} isomer of the αH_2Pc at $1.4{\times}10^{12}$ W.m^{-2}.

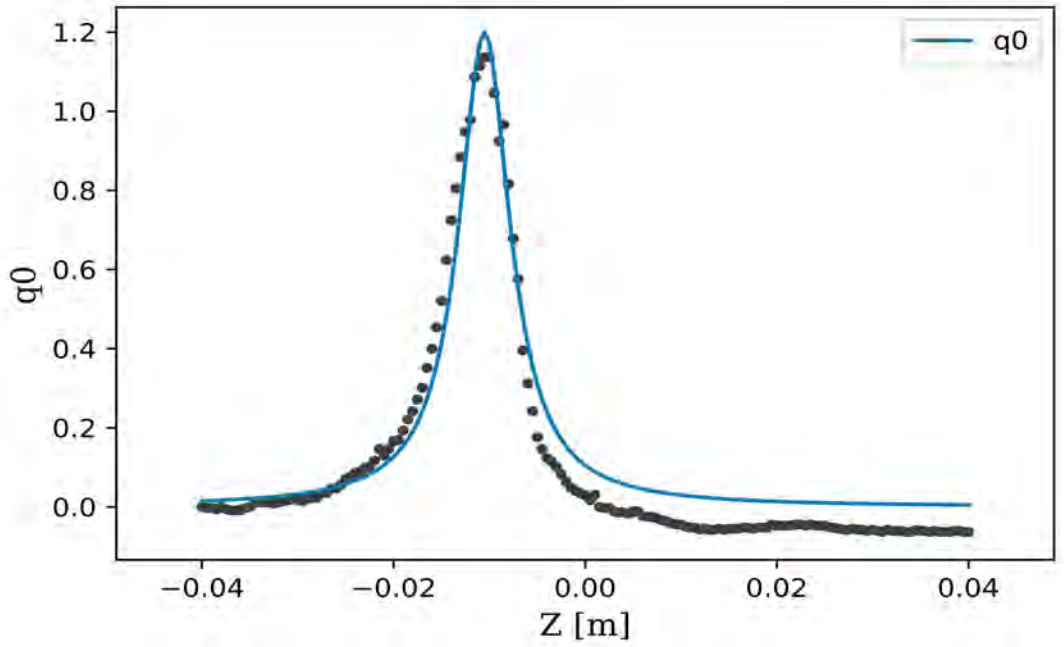

Figure 161: Open apeture Zscan of the C_{4h} isomer of the βH_2Pc at 2.0×10^{12} W.m^{-2}.

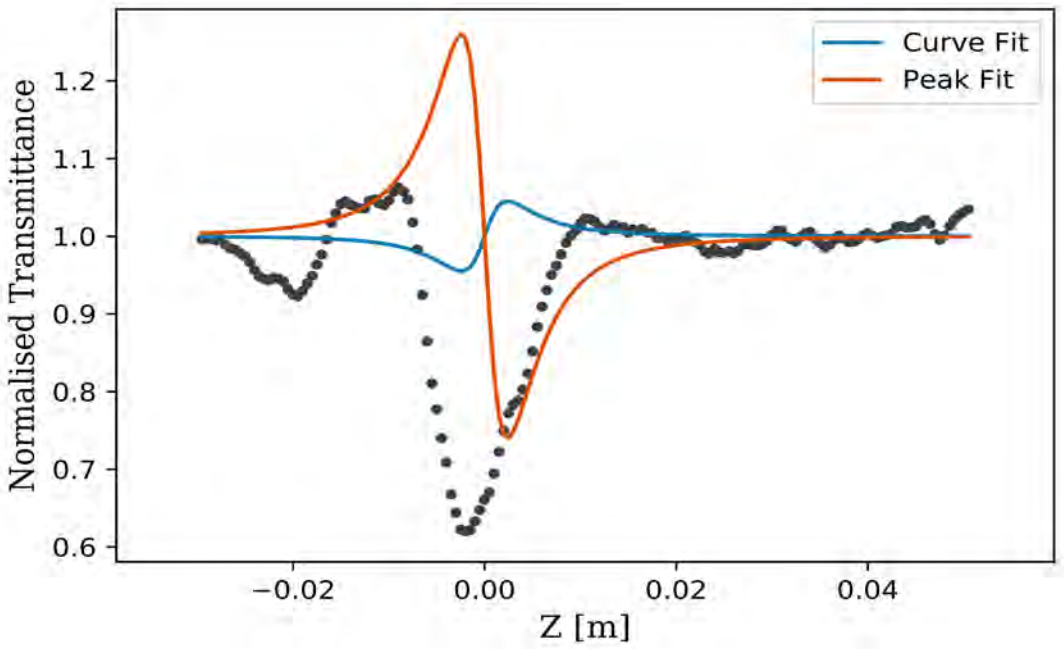

Figure 162: Closed apeture Zscan of the C_{4h} isomer of the βH_2Pc at 2.0×10^{12} W.m^{-2}.

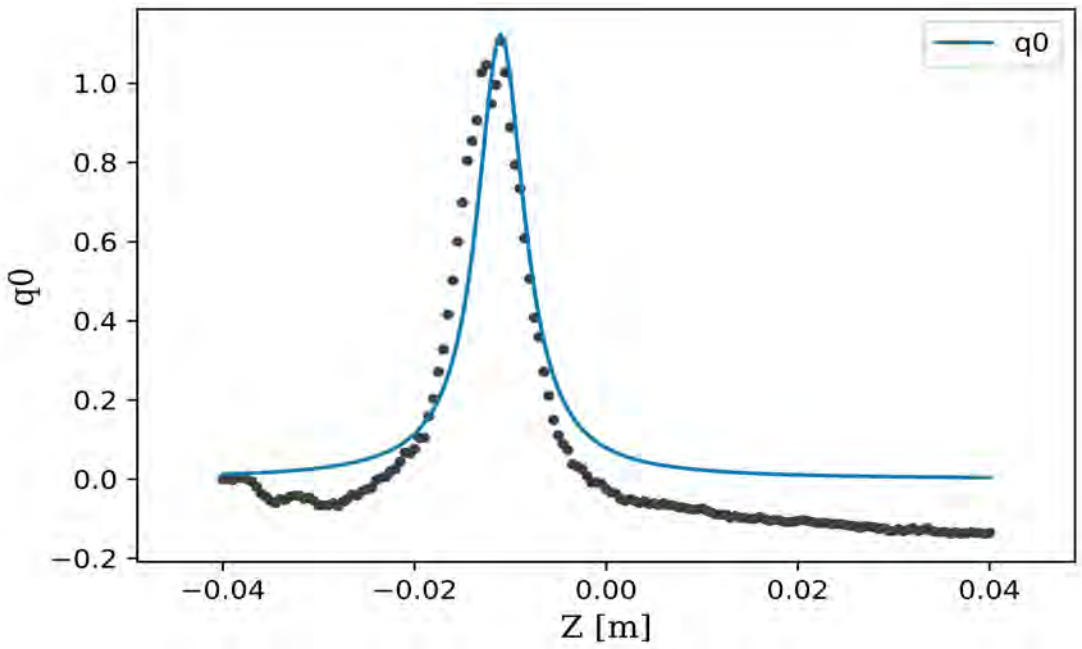

Figure 163: Open apeture Zscan of the C_{4h} isomer of the βH_2Pc at 2.5×10^{12} W.m^{-2}.

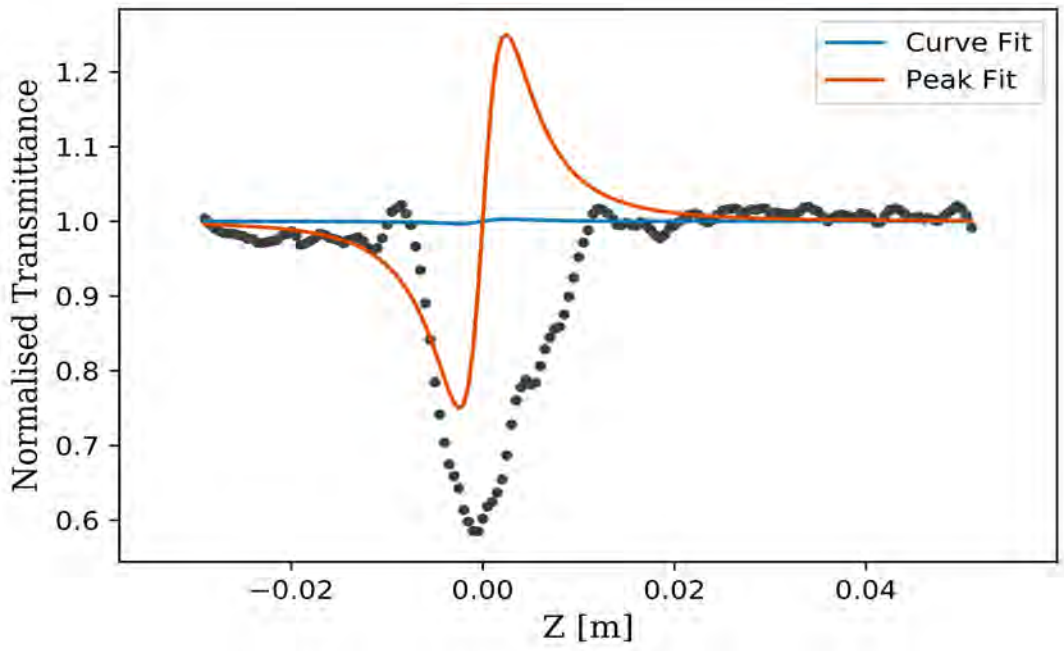

Figure 164: Closed apeture Zscan of the C_{4h} isomer of the βH_2Pc at 2.5×10^{12} W.m^{-2}.

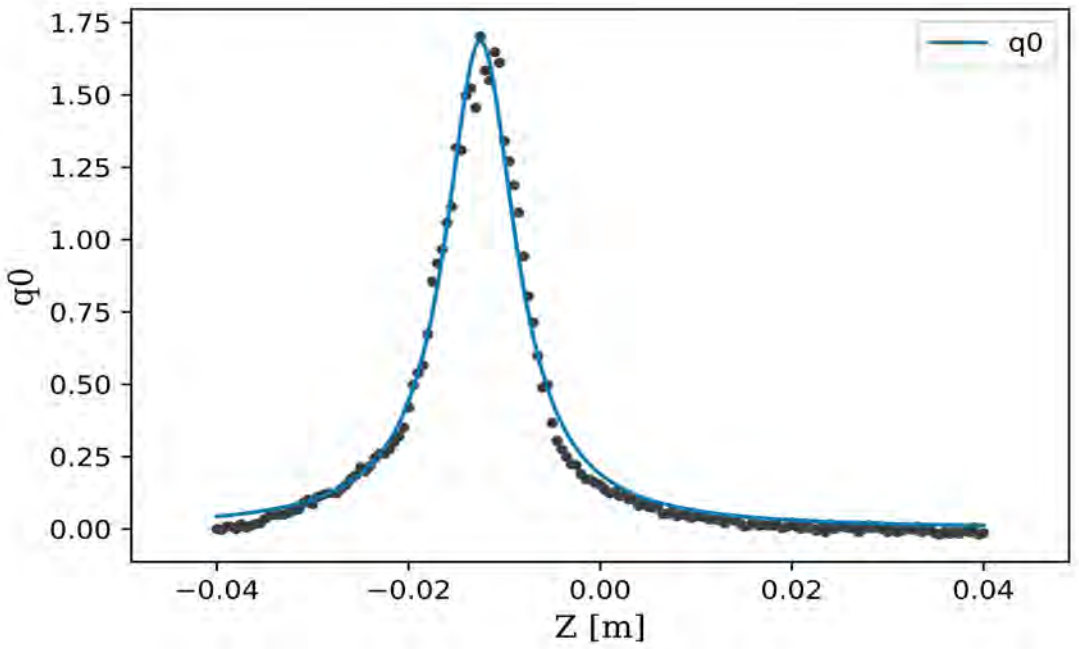

Figure 165: Open apeture Zscan of the C_{4h} isomer of the βH_2Pc at 3.5×10^{12} W.m^{-2}.

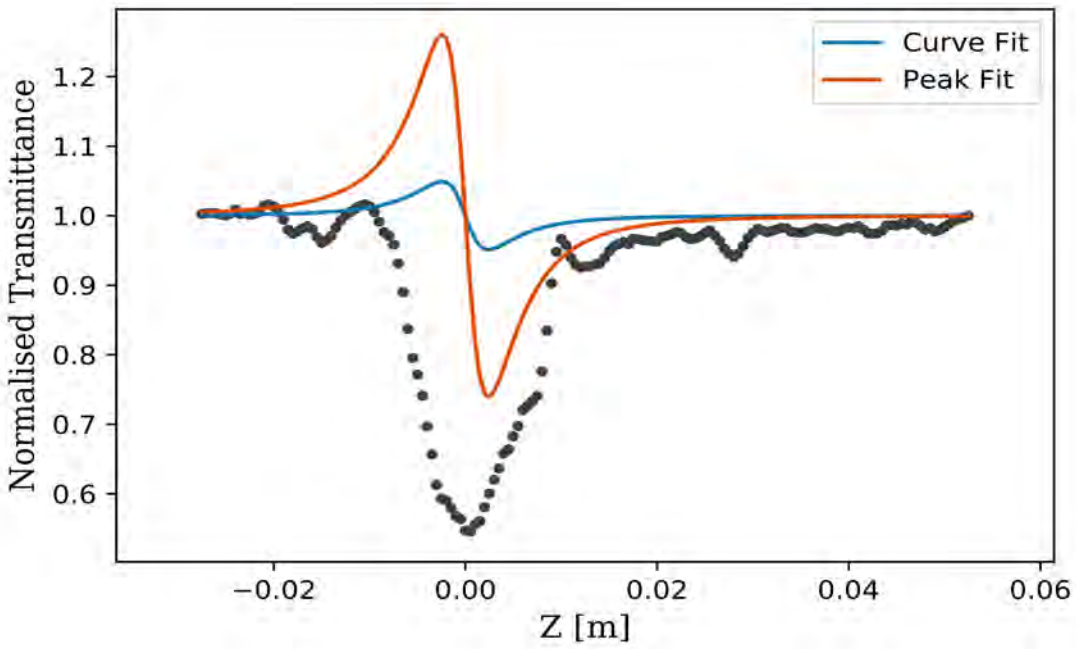

Figure 166: Closed apeture Zscan of the C_{4h} isomer of the βH_2Pc at 3.5×10^{12} W.m^{-2}.

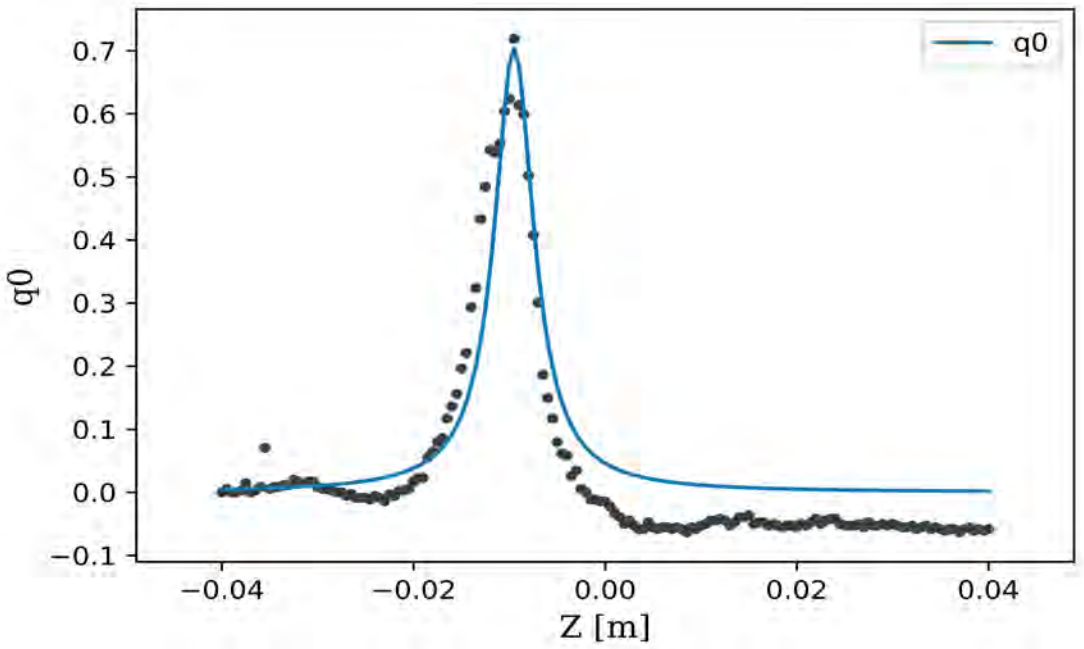

Figure 167: Open apeture Zscan of the C_{4h} isomer of the βH_2Pc at 1.3×10^{12} W.m^{-2}.

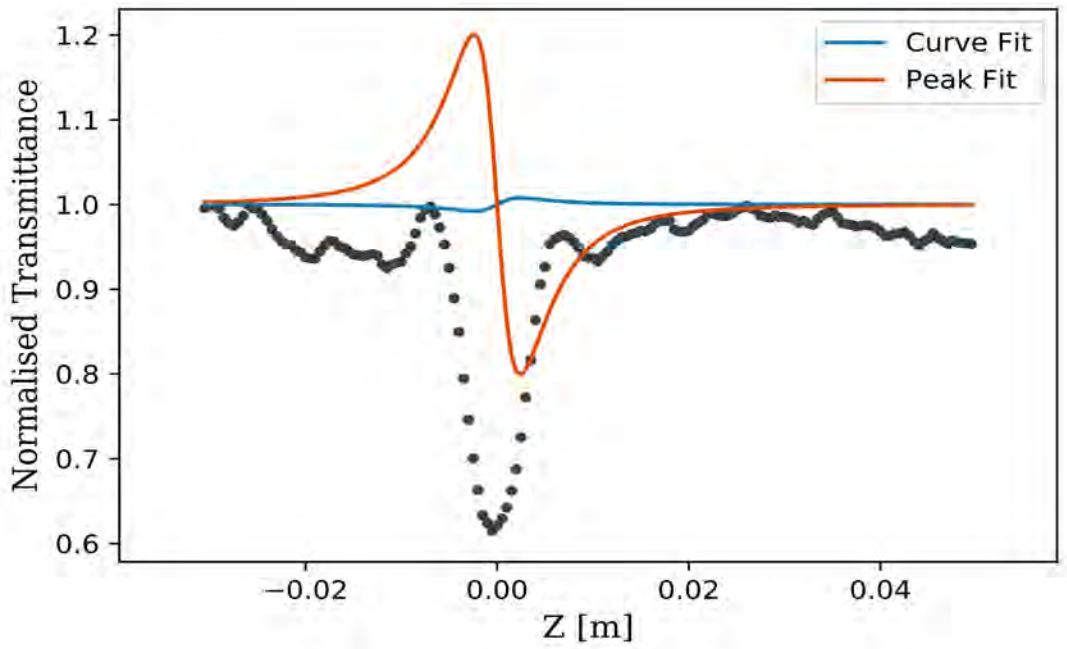

Figure 168: Closed apeture Zscan of the C_{4h} isomer of the βH_2Pc at 1.3×10^{12} W.m^{-2}.

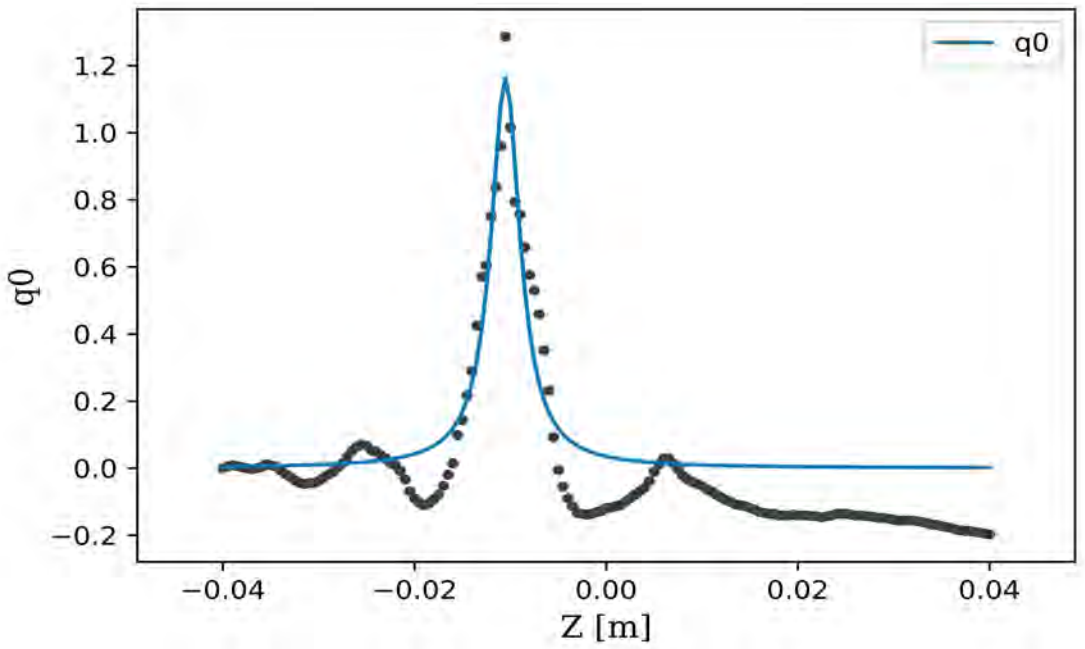

Figure 169: Open apeture Zscan of the C_{2v} isomer of the βH_2Pc at 3.8×10^{12} W.m^{-2}.

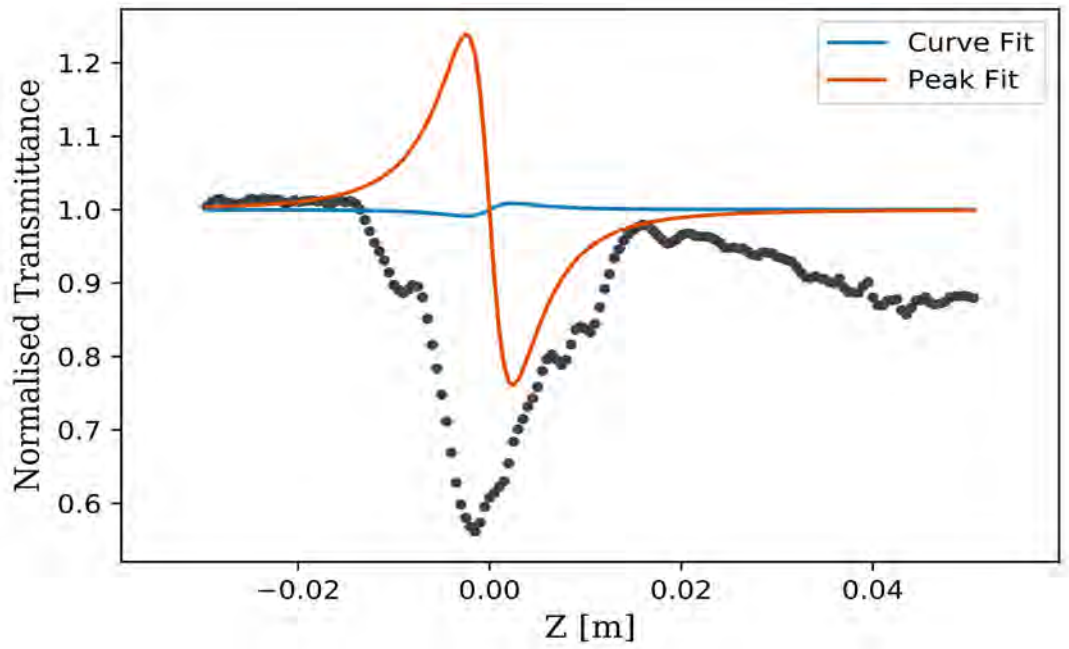

Figure 170: Closed apeture Zscan of the C_{2v} isomer of the βH_2Pc at 3.8×10^{12} W.m^{-2}.

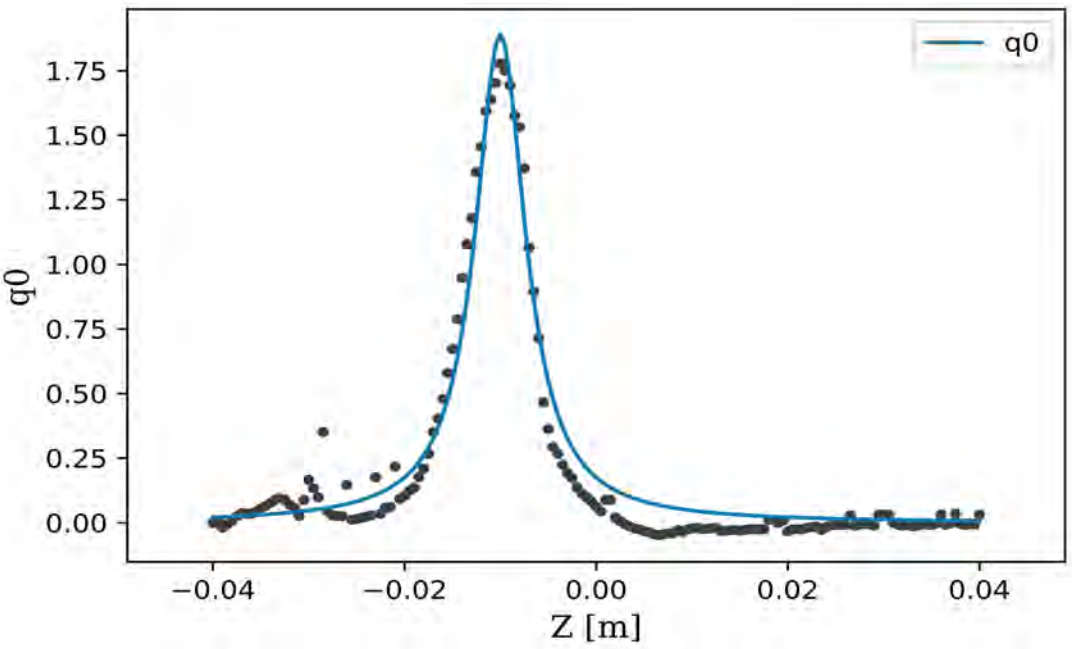

Figure 171: Open apeture Zscan of the C_{2v} isomer of the βH_2Pc at 3.7×10^{12} W.m^{-2}.

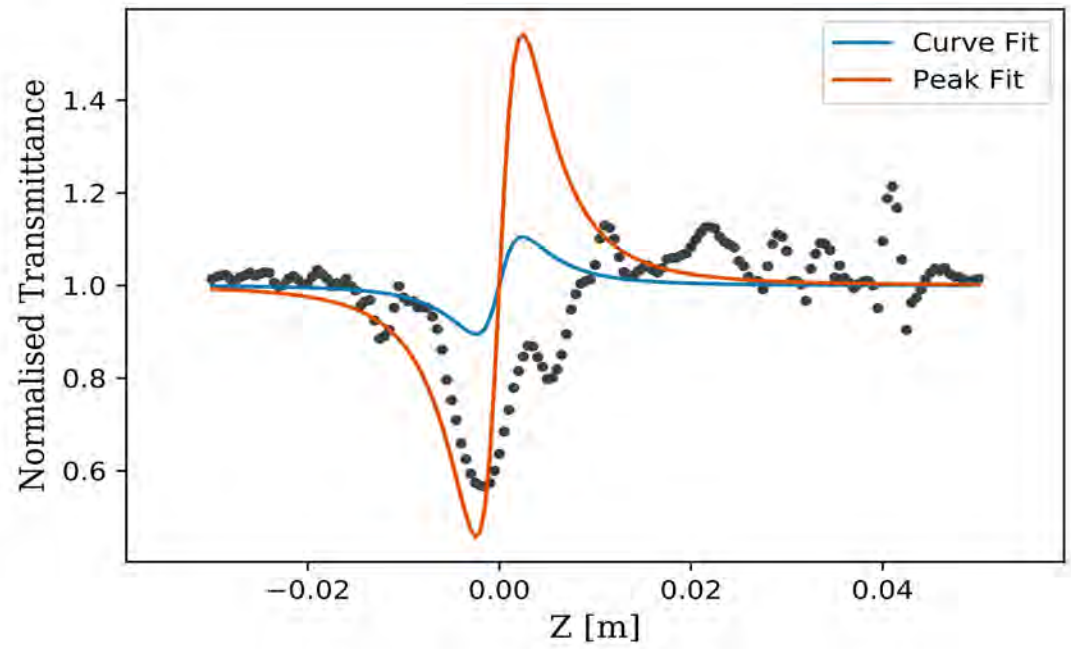

Figure 172: Closed apeture Zscan of the C_{2v} isomer of the βH_2Pc at 3.7×10^{12} W.m^{-2}.

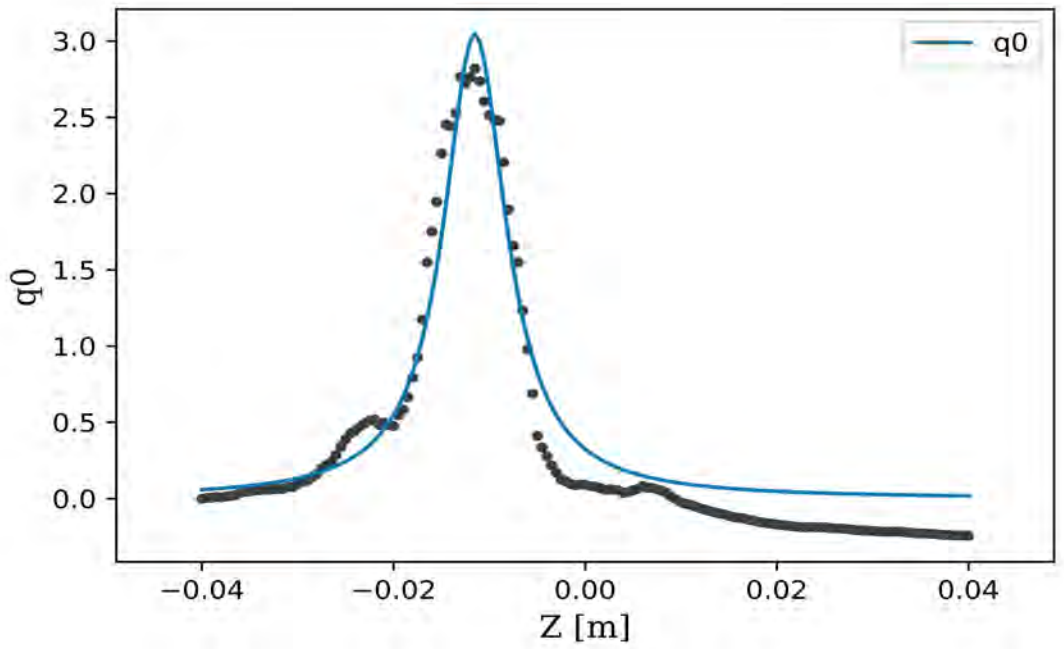

Figure 173: Open apeture Zscan of the C_{2v} isomer of the βH_2Pc at 6.4×10^{12} W.m^{-2}.

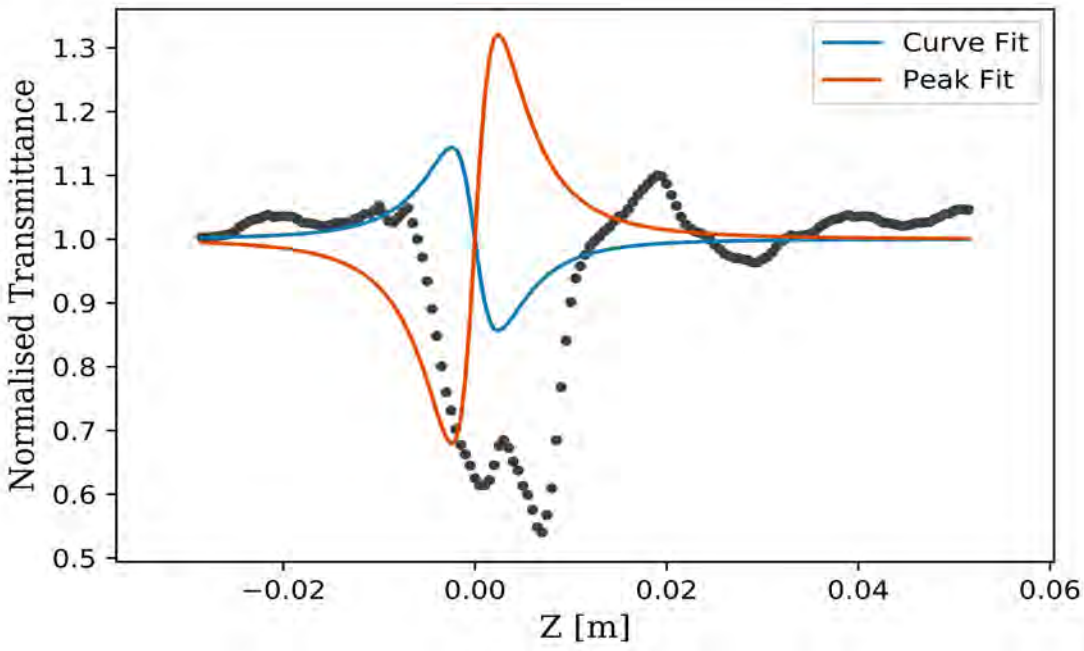

Figure 174: Closed apeture Zscan of the C_{2v} isomer of the βH_2Pc at 6.4×10^{12} W.m^{-2}.

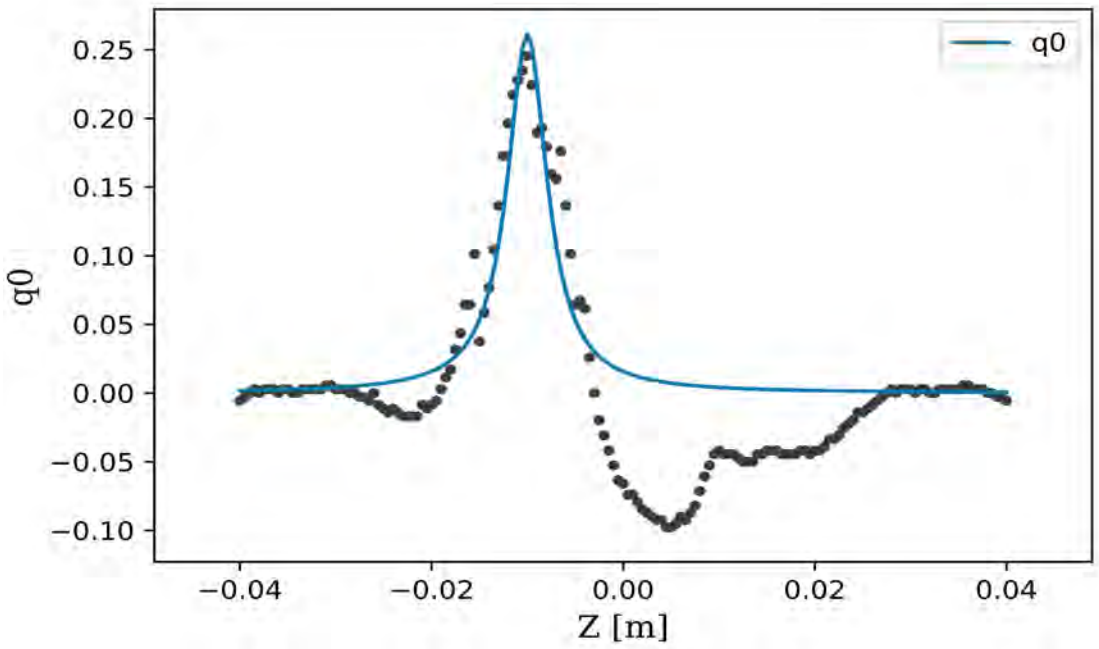

Figure 175: Open apeture Zscan of the C_{2v} isomer of the βH_2Pc at 1.1×10^{12} W.m^{-2}.

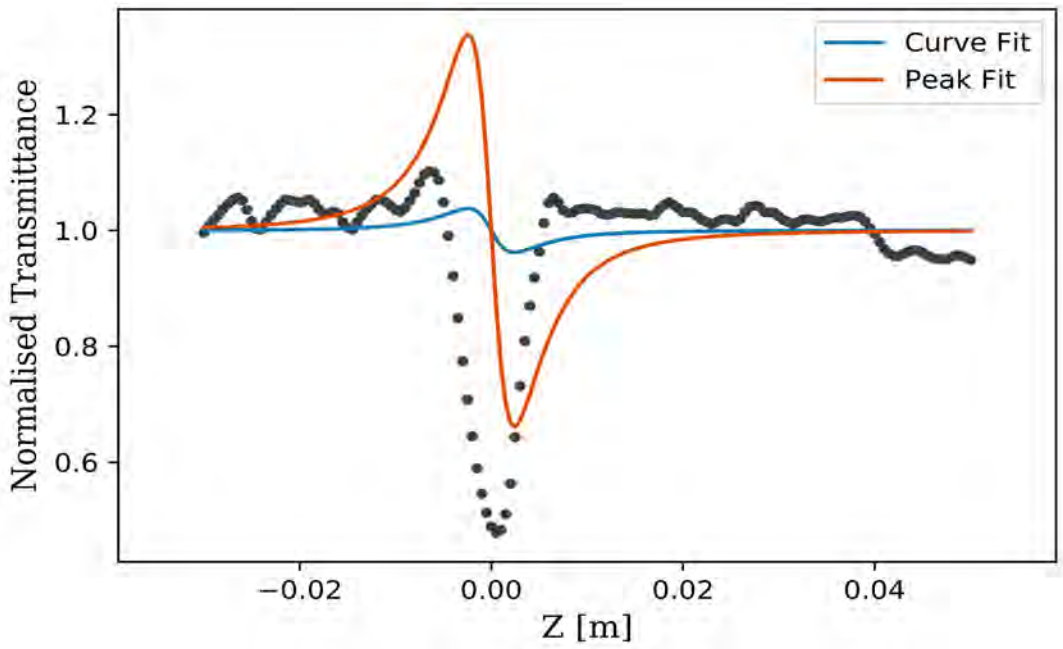

Figure 176: Closed apeture Zscan of the C_{2v} isomer of the βH_2Pc at 1.1×10^{12} W.m^{-2}.

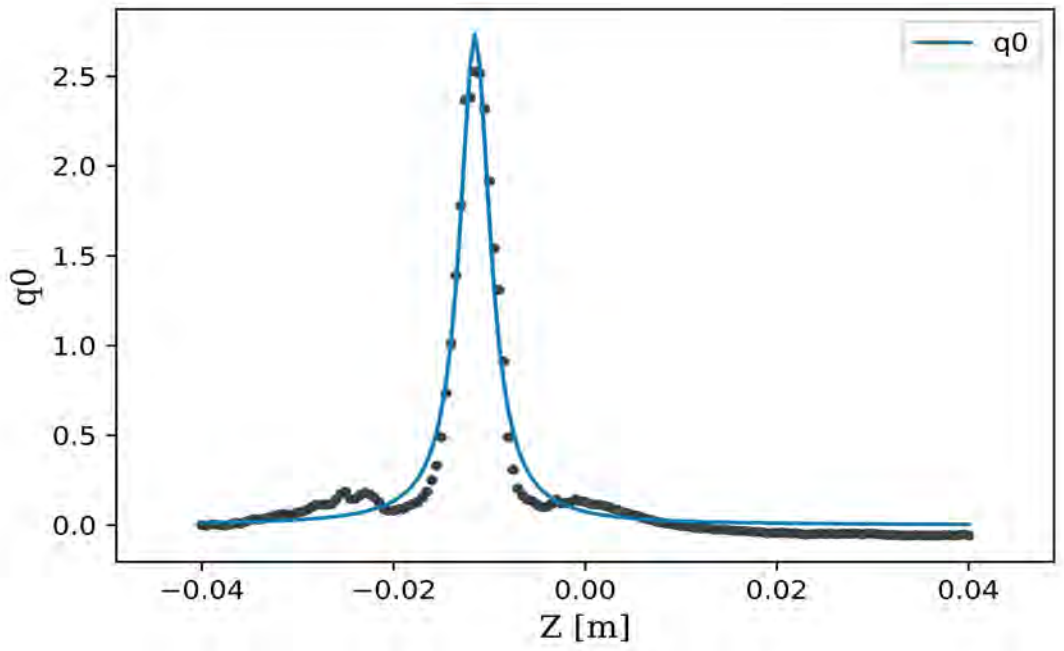

Figure 177: Open apeture Zscan of the C_s isomer of the βH_2Pc at 3.0×10^{12} W.m^{-2}.

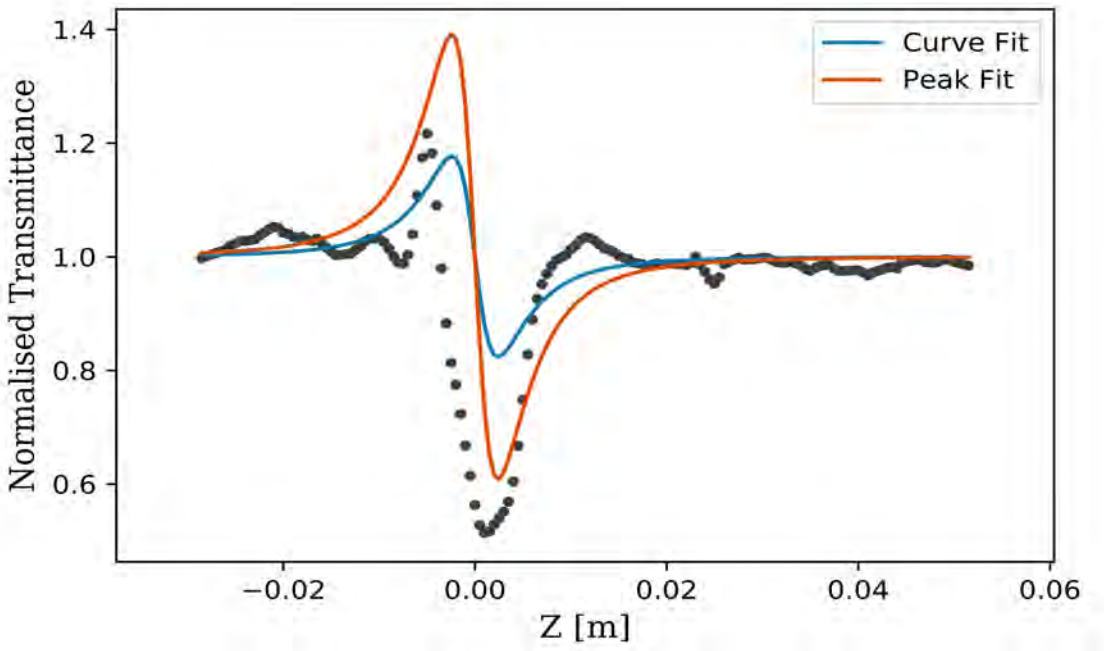

Figure 178: Closed apeture Zscan of the C_s isomer of the βH_2Pc at 3.0×10^{12} W.m^{-2}.

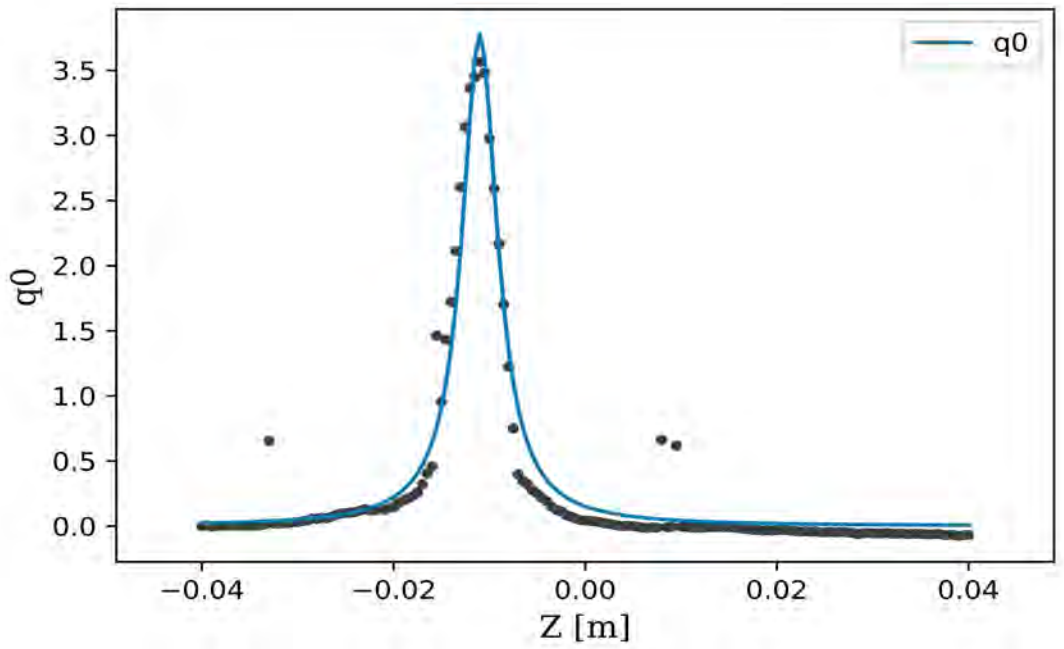

Figure 179: Open apeture Zscan of the C_s isomer of the βH_2Pc at 3.6×10^{12} W.m^{-2}.

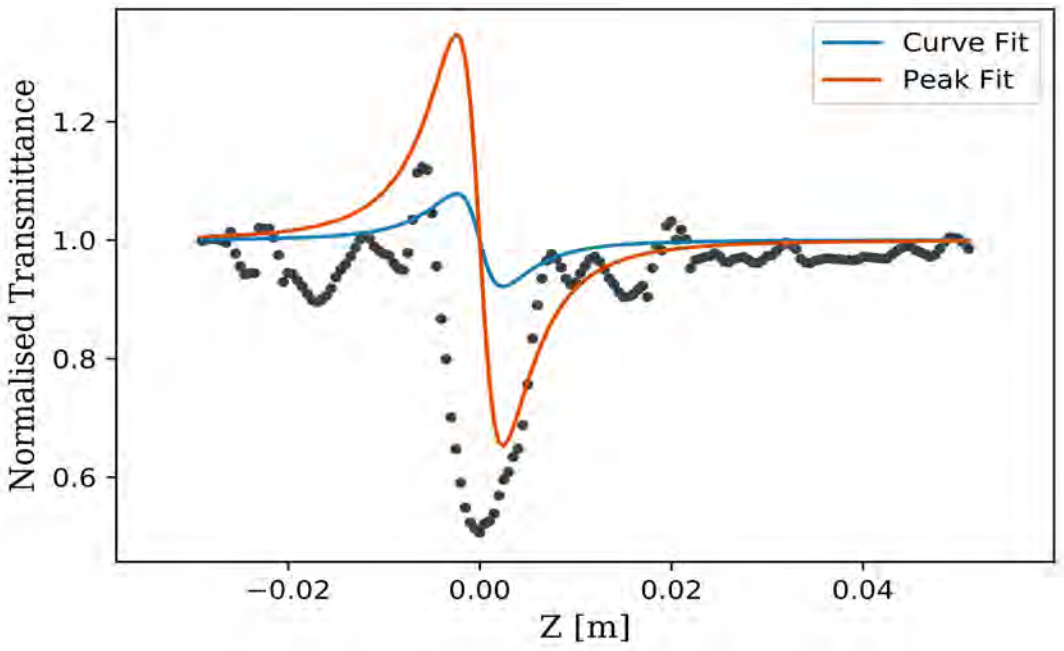

Figure 180: Closed apeture Zscan of the C_s isomer of the βH_2Pc at 3.6×10^{12} W.m^{-2}.

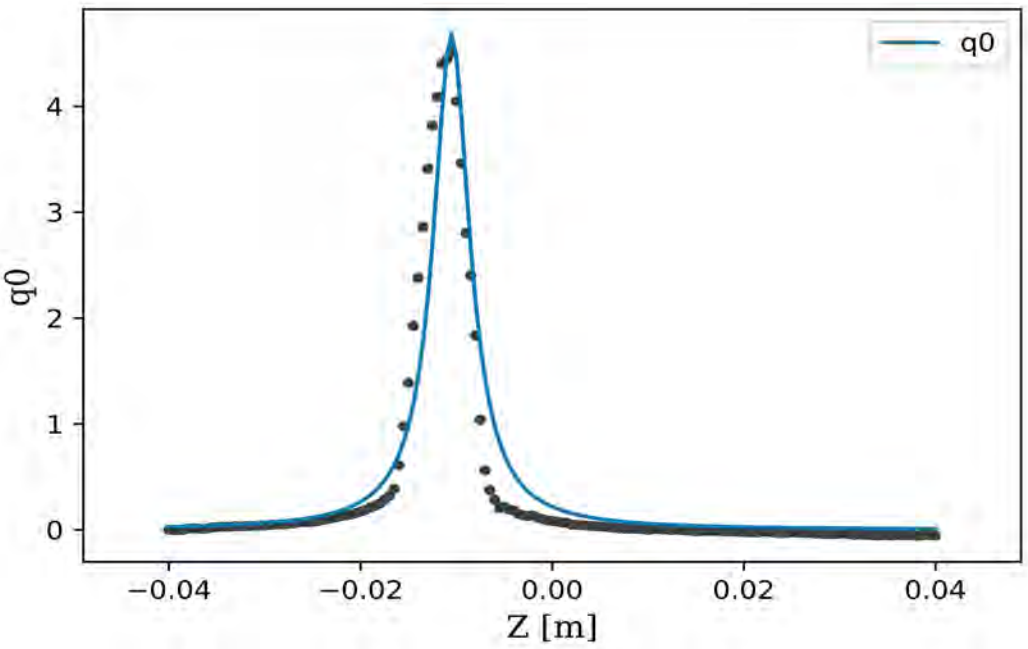

Figure 181: Open apeture Zscan of the C_s isomer of the βH_2Pc at 5.2×10^{12} W.m^{-2}.

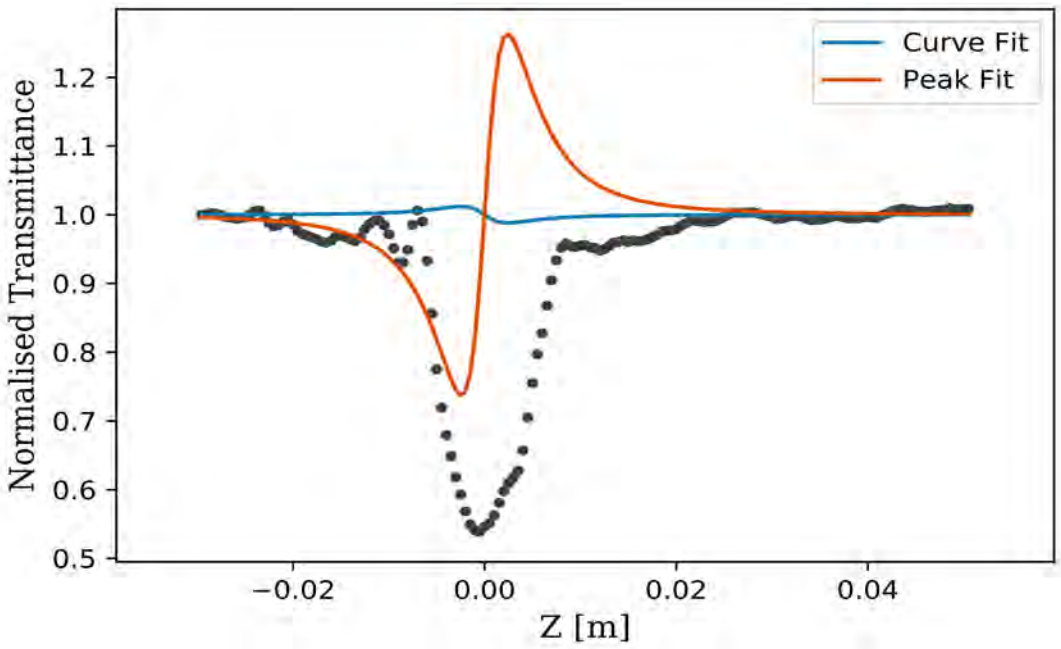

Figure 182: Closed apeture Zscan of the C_s isomer of the βH_2Pc at 5.2×10^{12} W.m^{-2}.

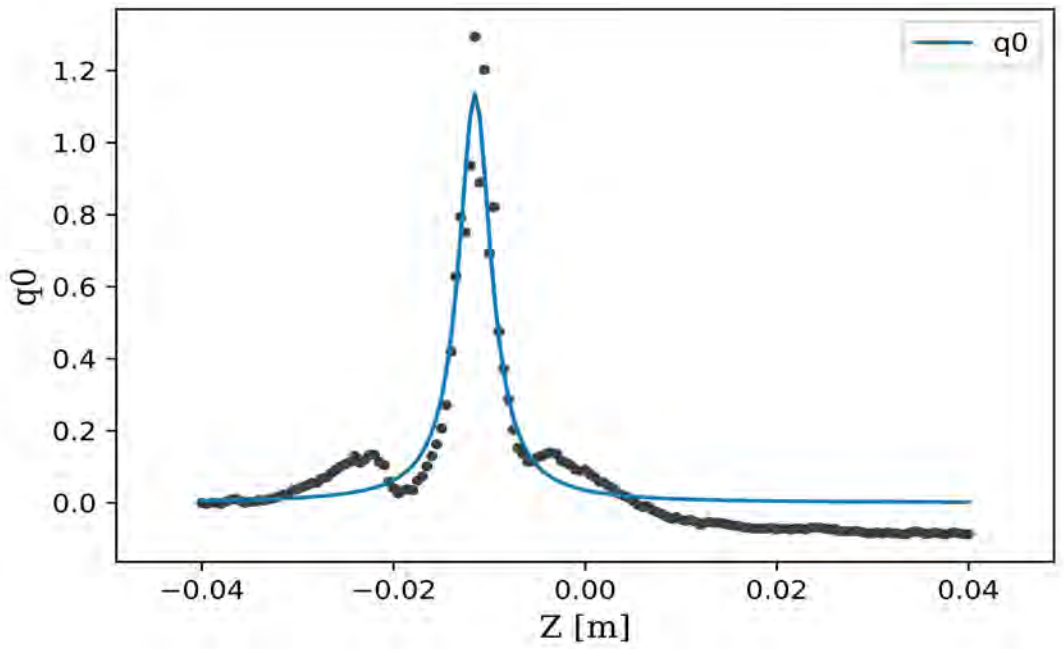

Figure 183: Open apeture Zscan of the C_s isomer of the βH_2Pc at $1.8{\times}10^{12}$ W.m^{-2}.

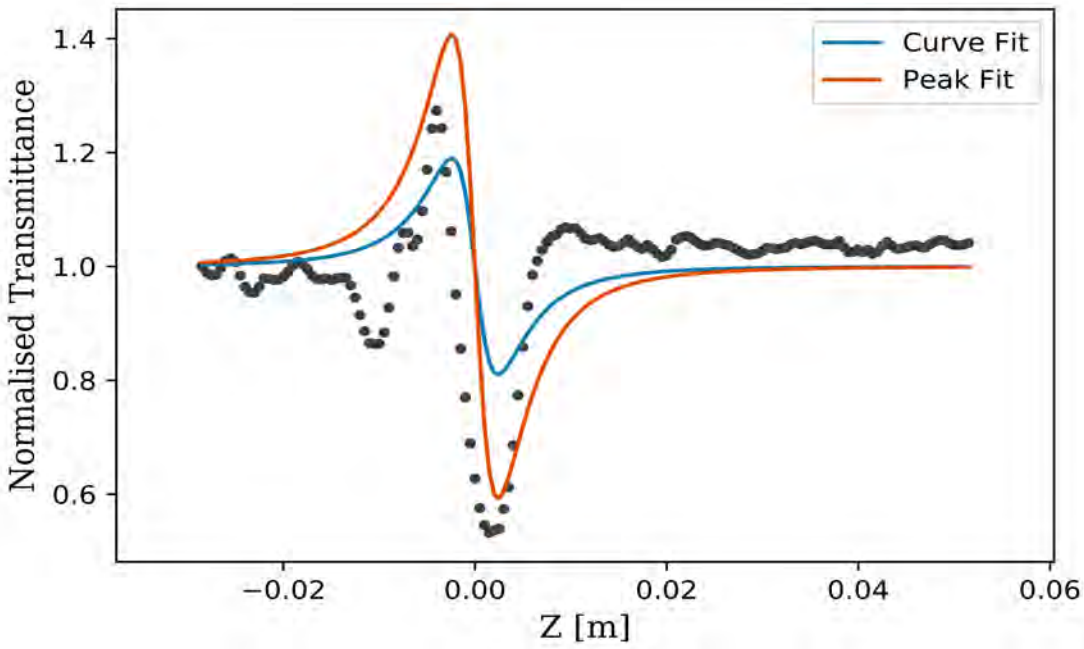

Figure 184: Closed apeture Zscan of the C_s isomer of the βH_2Pc at $1.8{\times}10^{12}$ W.m^{-2}.

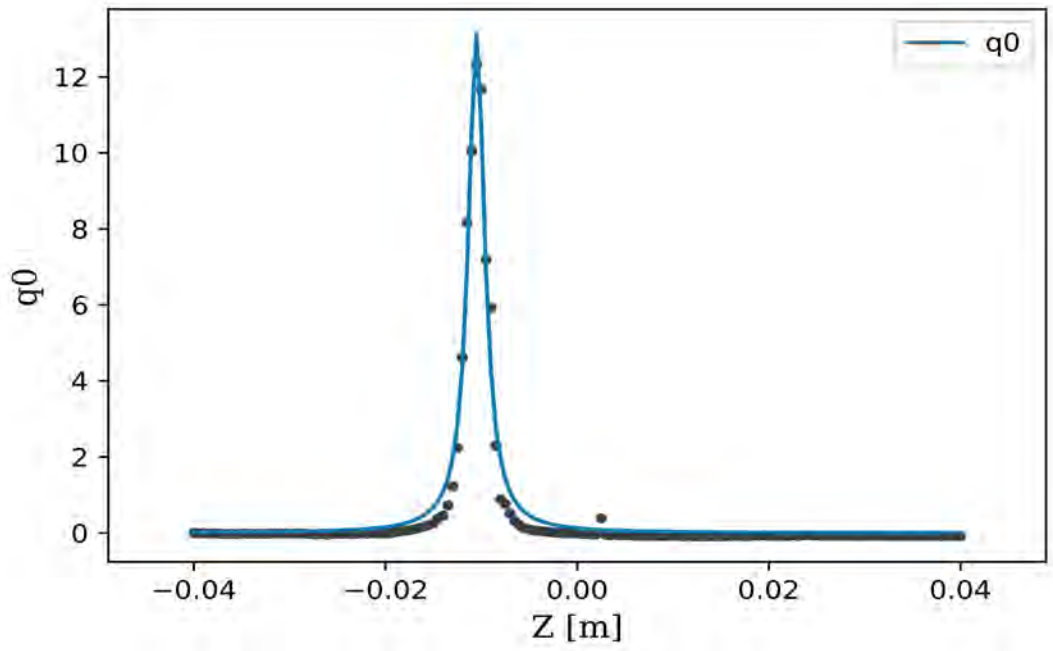

Figure 185: Open apeture Zscan of the D_{2h} isomer of the βH_2Pc at 3.7×10^{12} W.m^{-2}.

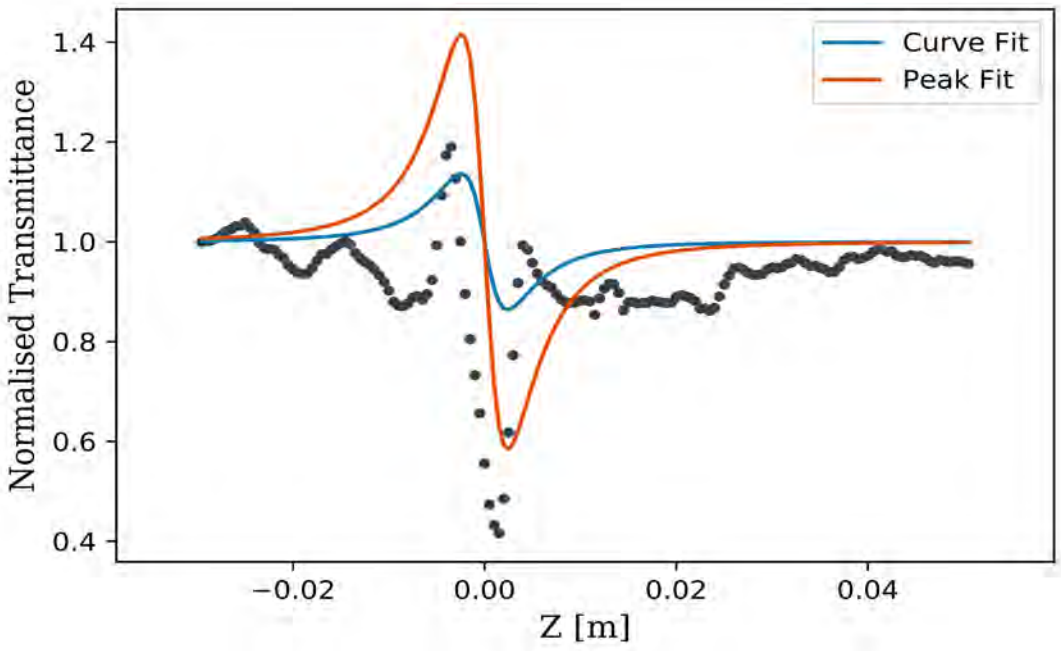

Figure 186: Closed apeture Zscan of the D_{2h} isomer of the βH_2Pc at 3.7×10^{12} W.m^{-2}.

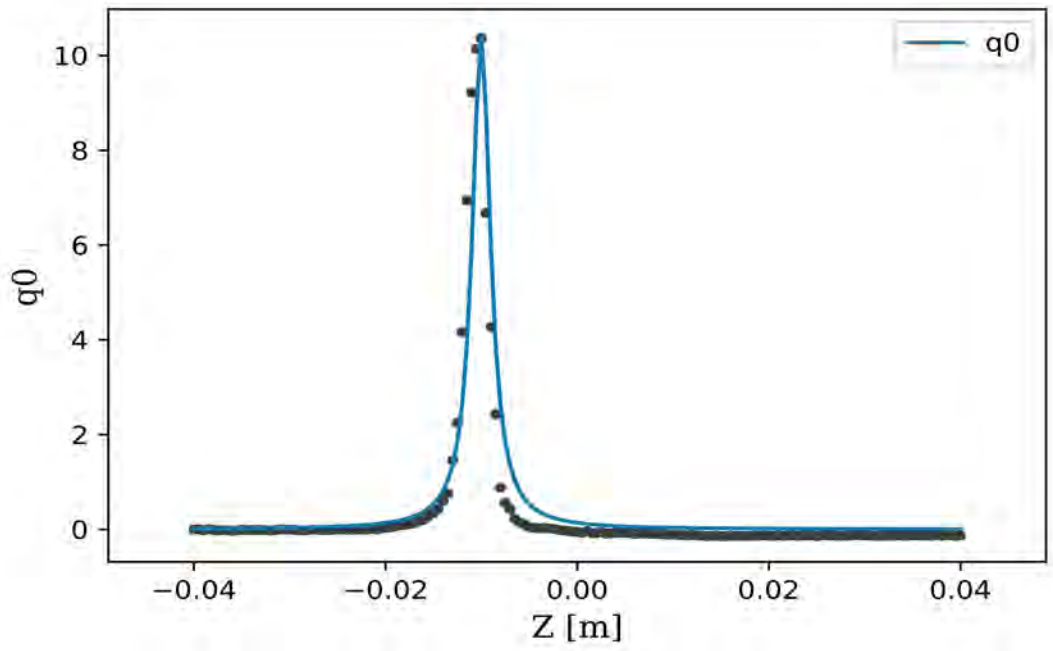

Figure 187: Open apeture Zscan of the D_{2h} isomer of the βH_2Pc at 4.3×10^{12} W.m^{-2}.

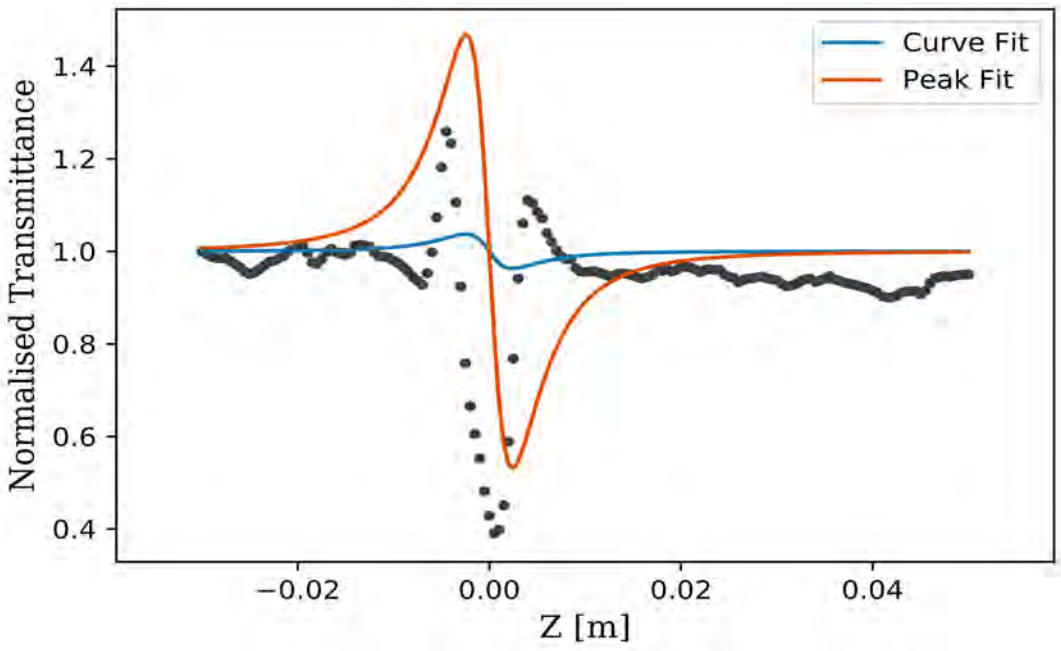

Figure 188: Closed apeture Zscan of the D_{2h} isomer of the βH_2Pc at 4.3×10^{12} W.m^{-2}.

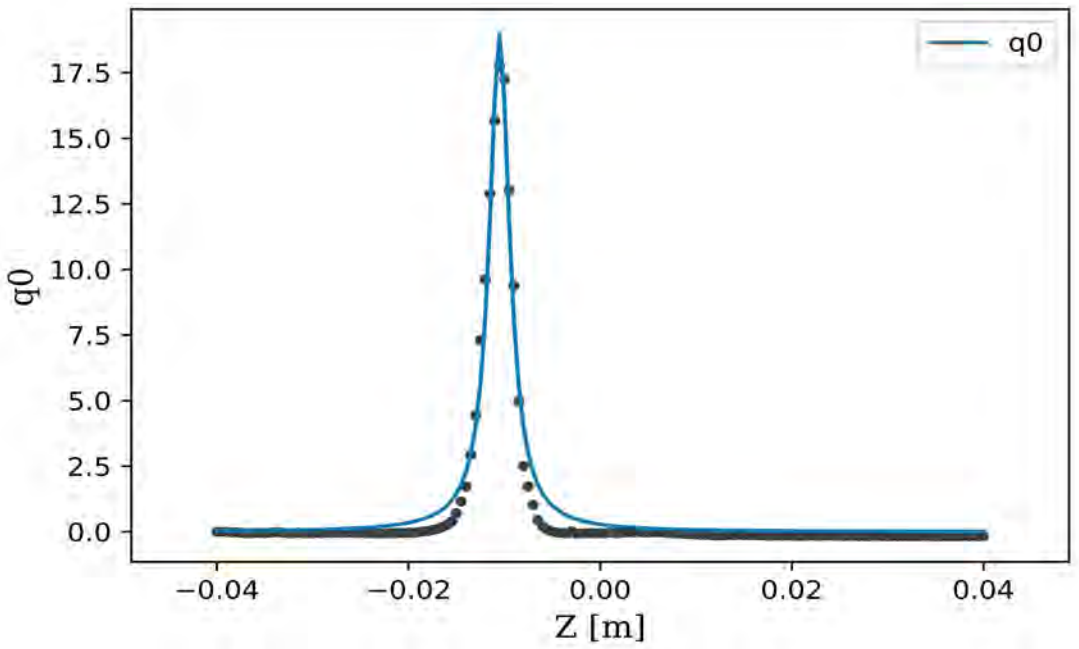

Figure 189: Open apeture Zscan of the D_{2h} isomer of the βH_2Pc at 9.8×10^{12} W.m^{-2}.

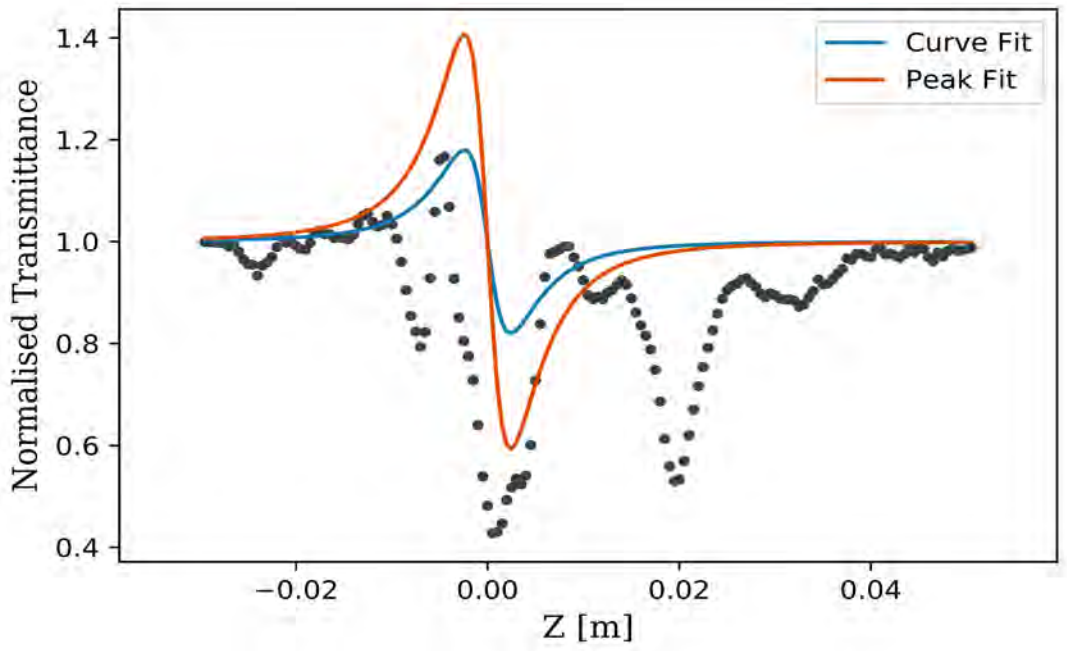

Figure 190: Closed apeture Zscan of the D_{2h} isomer of the βH_2Pc at 9.8×10^{12} W.m^{-2}.

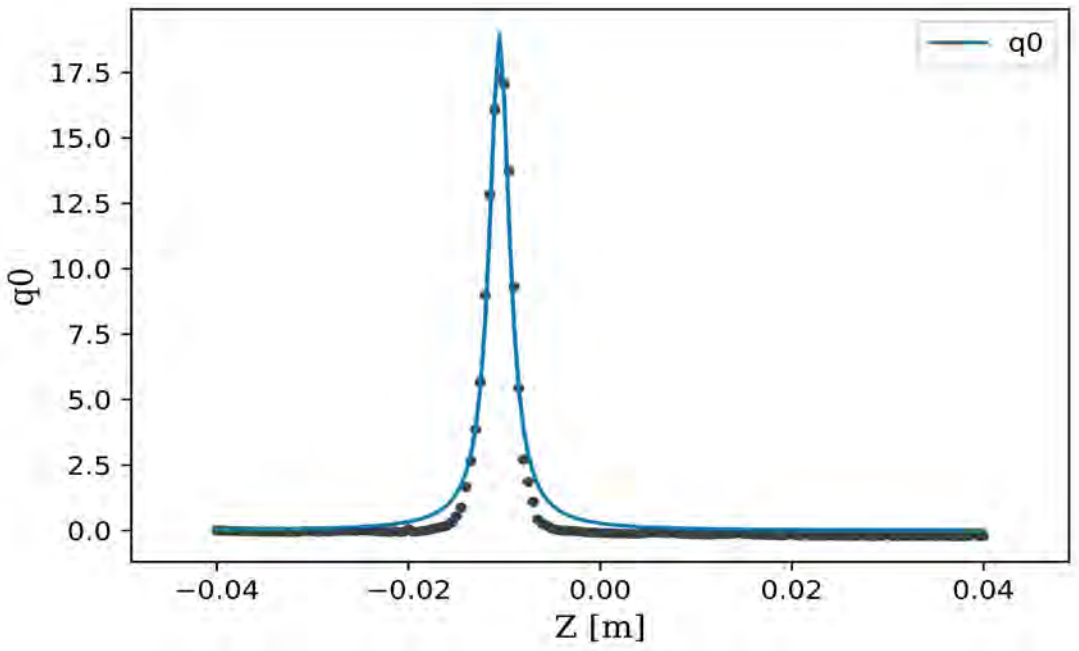

Figure 191: Open apeture Zscan of the D_{2h} isomer of the βH_2Pc at 13.5×10^{12} W.m^{-2}.

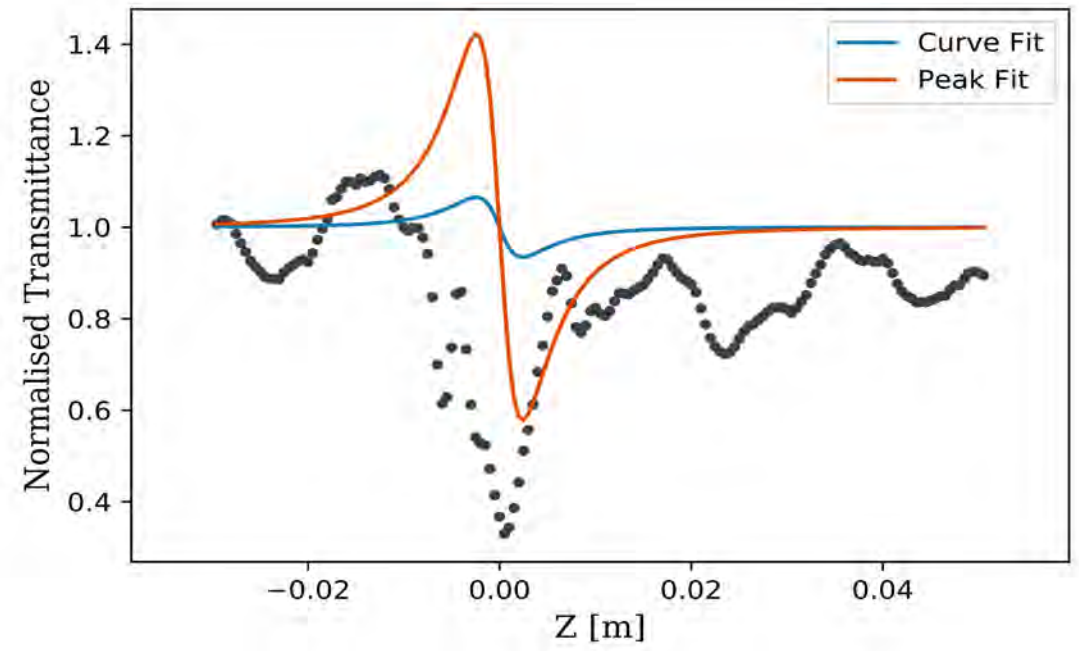

Figure 192: Closed apeture Zscan of the D_{2h} isomer of the βH_2Pc at 13.5×10^{12} W.m^{-2}.

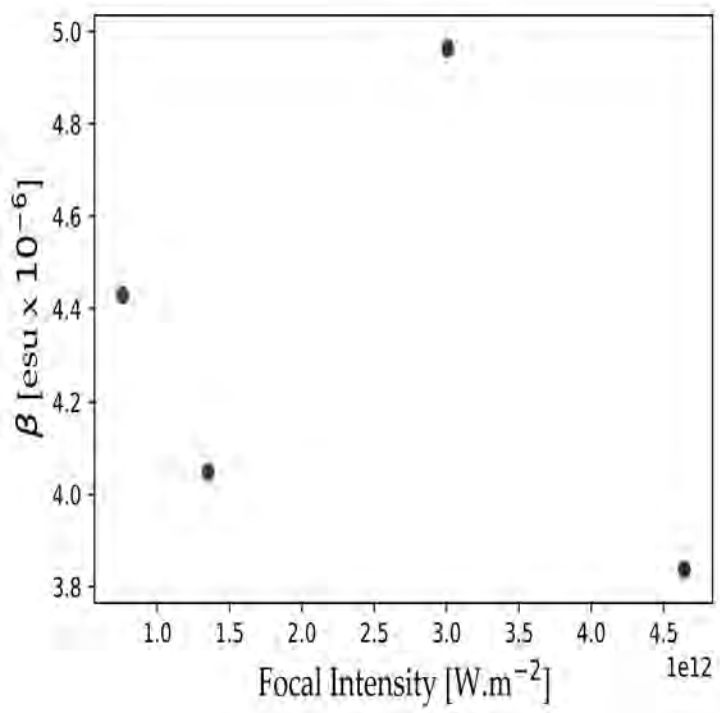

Figure 193: Nonlinear absorption coefficients for the C_{4h} constitutional isomer of αH_2Pc plotted against focal intensity.

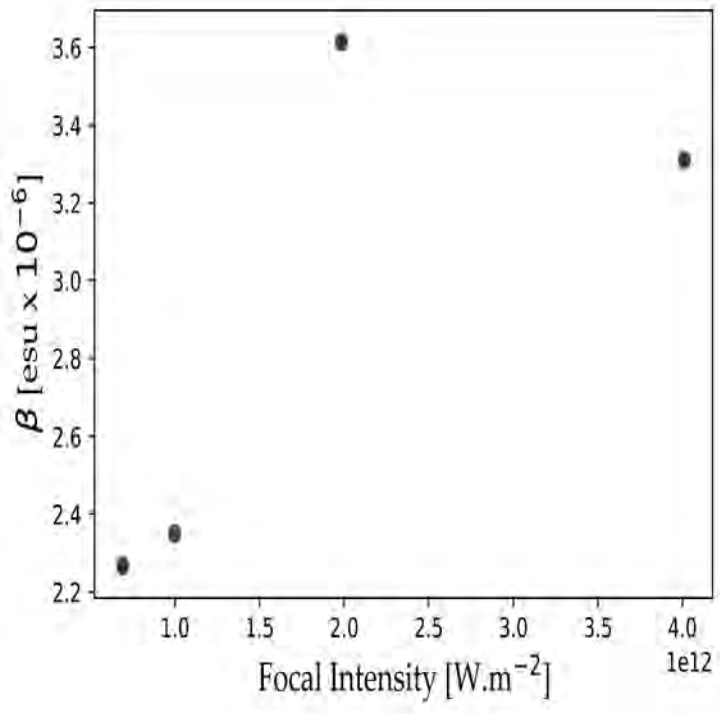

Figure 194: Nonlinear absorption coefficients for the C_{2v} constitutional isomer of αH_2Pc plotted against focal intensity.

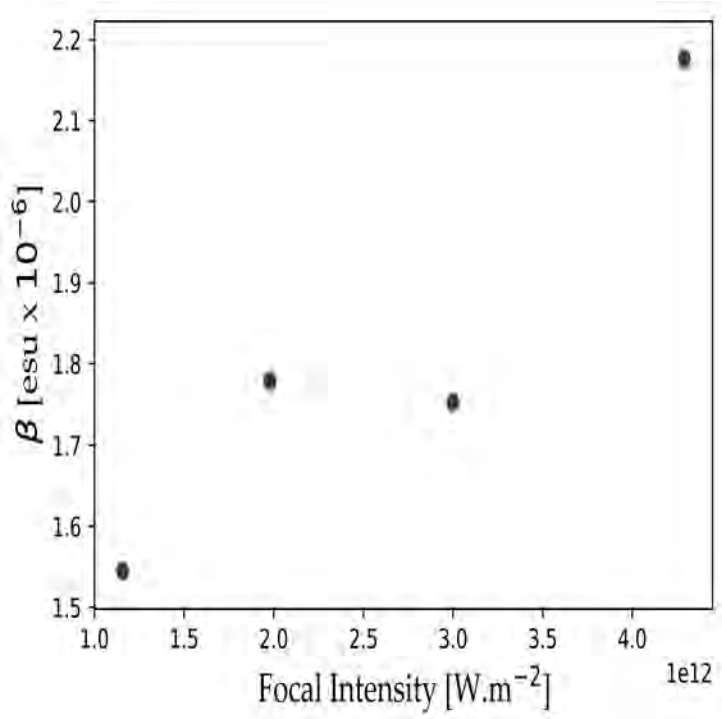

Figure 195: Nonlinear absorption coefficients for the C_s constitutional isomer of αH_2Pc plotted against focal intensity.

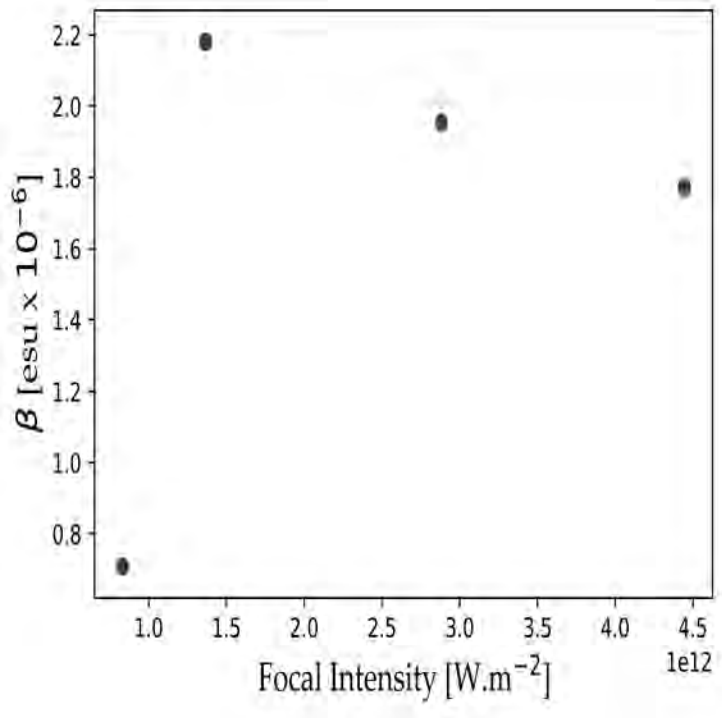

Figure 196: Nonlinear absorption coefficients for the D_{2h} constitutional isomer of αH_2Pc plotted against focal intensity.

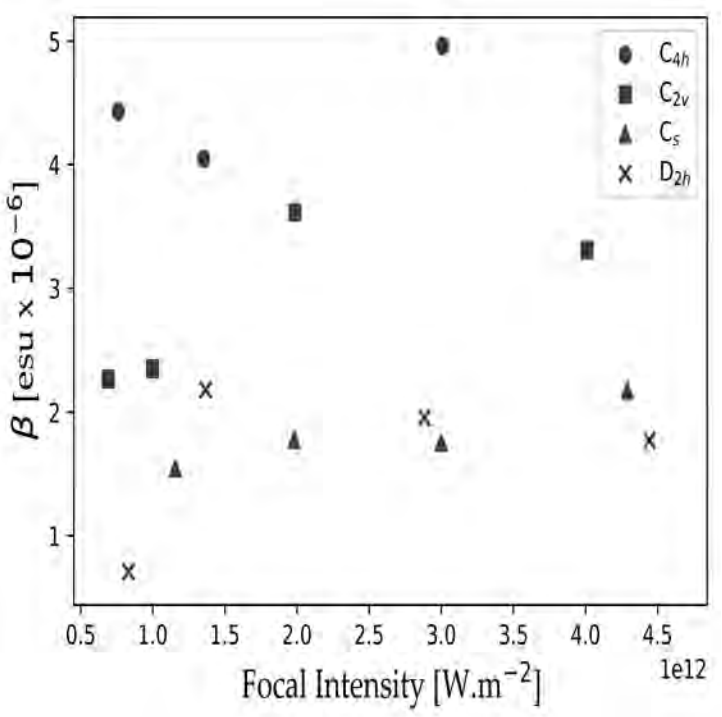

Figure 197: Nonlinear absorption coefficients for the constitutional isomers of αH_2Pc plotted against focal intensity.

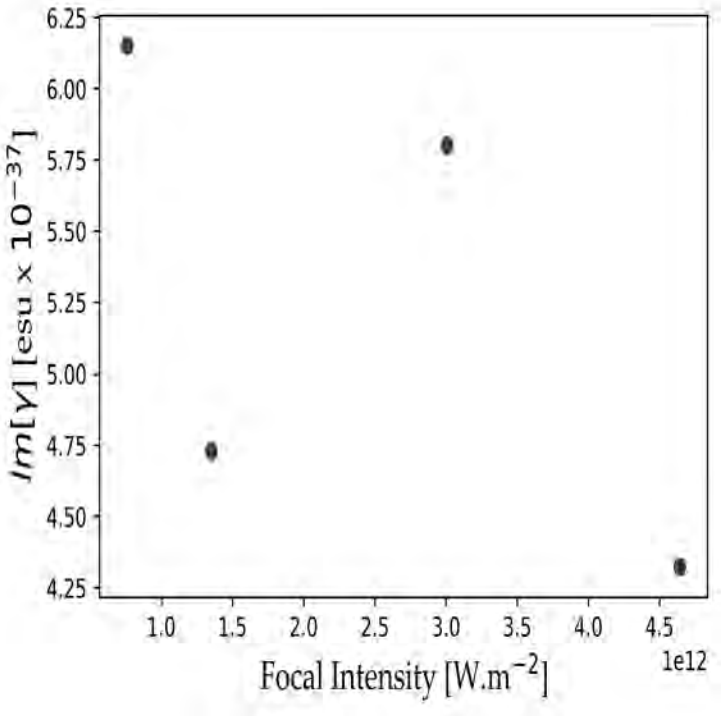

Figure 198: Imaginary component of the second-order hyperpolarisability for the C_{4h} constitutional isomer of αH_2Pc plotted against focal intensity.

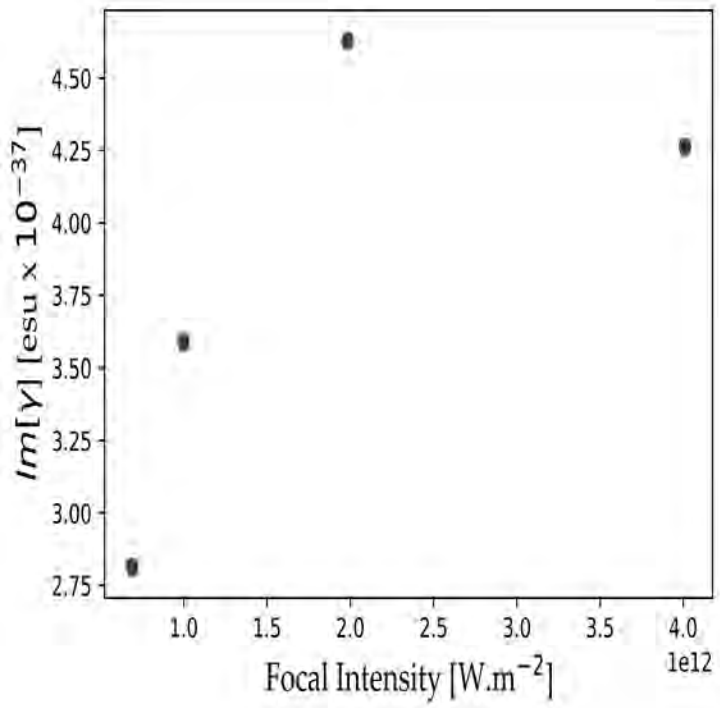

Figure 199: Imaginary component of the second-order hyperpolarisability for the C_{2v} constitutional isomer of αH_2Pc plotted against focal intensity.

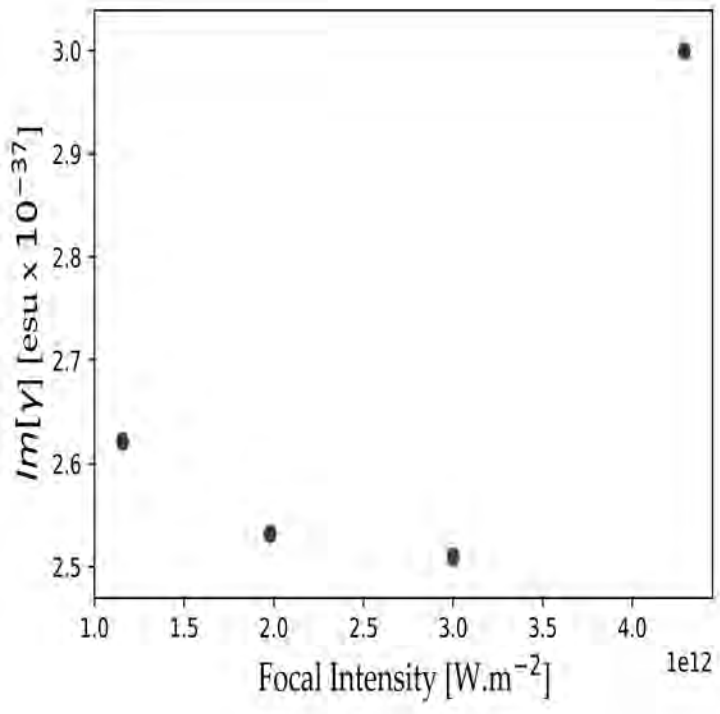

Figure 200: Imaginary component of the second-order hyperpolarisability for the C_s constitutional isomer of αH_2Pc plotted against focal intensity.

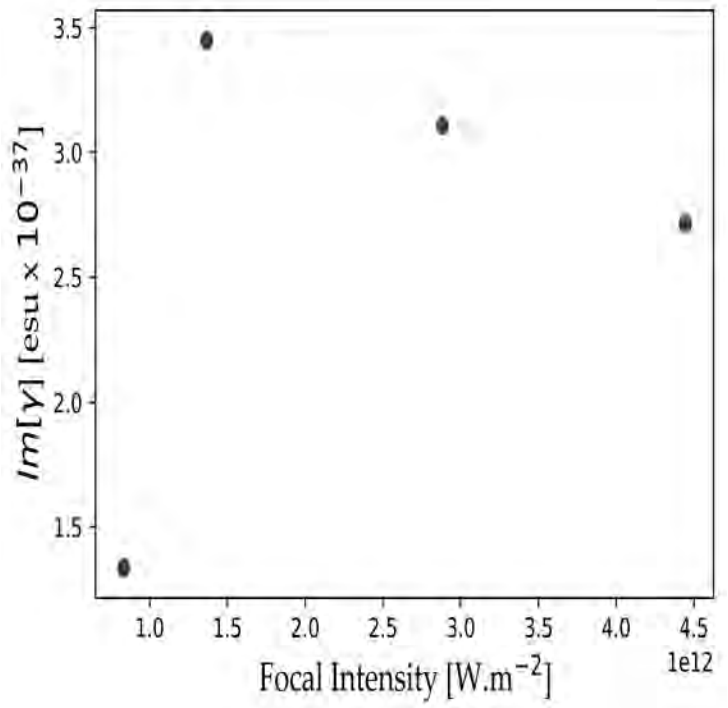

Figure 201: Imaginary component of the second-order hyperpolarisability for the D_{2h} constitutional isomer of αH_2Pc plotted against focal intensity.

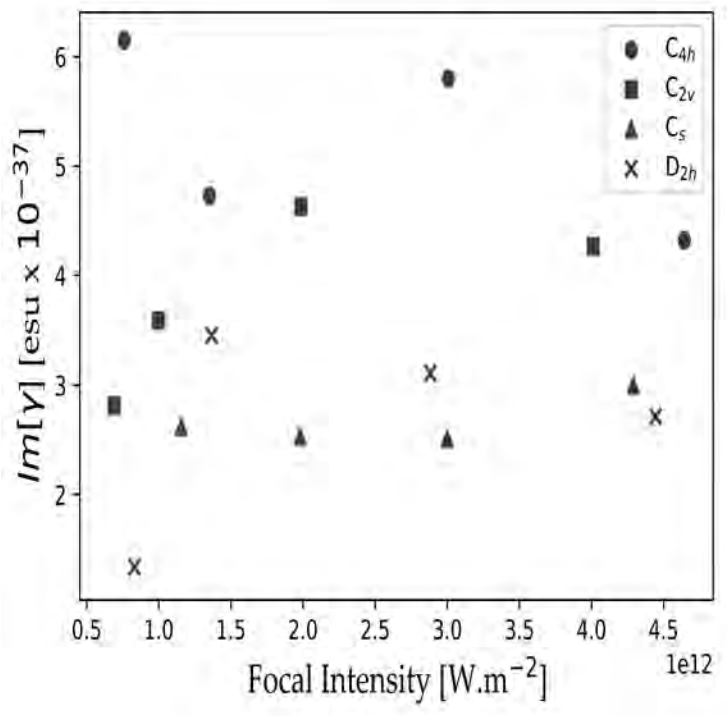

Figure 202: Imaginary component of the second-order hyperpolarisability for the constitutional isomers of αH_2Pc plotted against focal intensity.

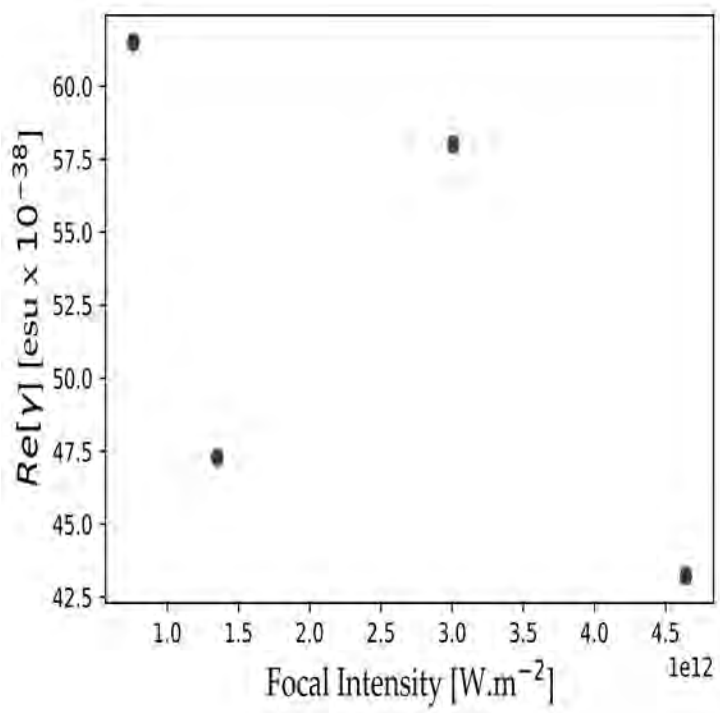

Figure 203: Real component of the second-order hyperpolarisability for the C_{4h} constitutional isomer of αH_2Pc plotted against focal intensity.

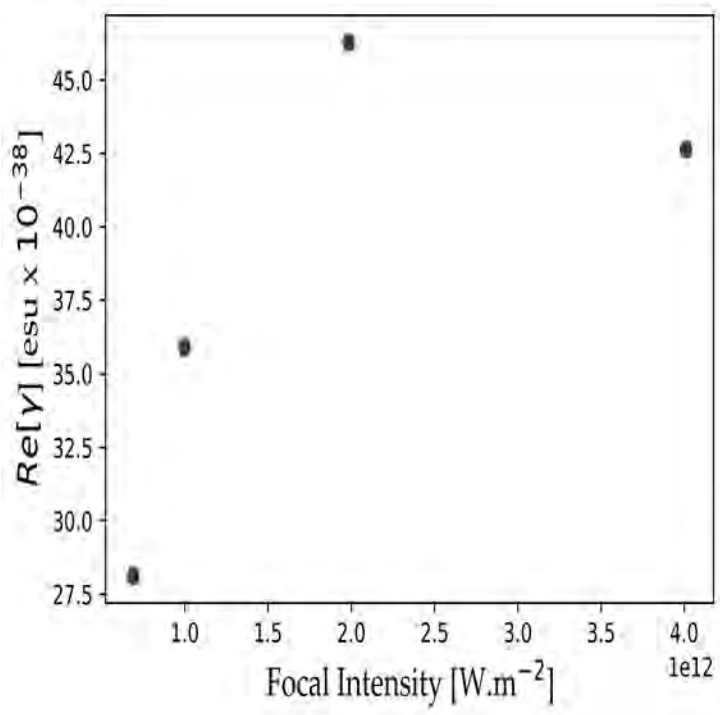

Figure 204: Real component of the second-order hyperpolarisability for the C_{2v} constitutional isomer of αH_2Pc plotted against focal intensity.

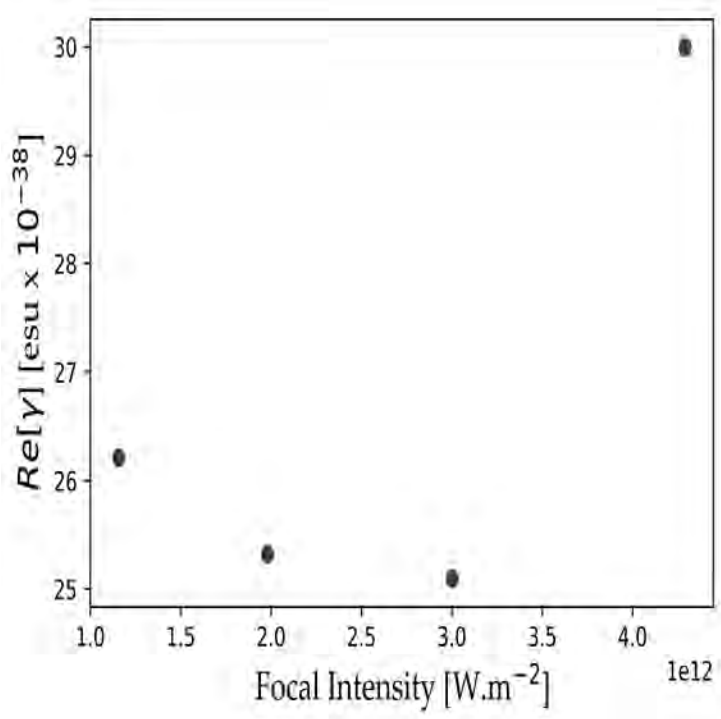

Figure 205: Real component of the second-order hyperpolarisability for the C_s constitutional isomer of αH_2Pc plotted against focal intensity.

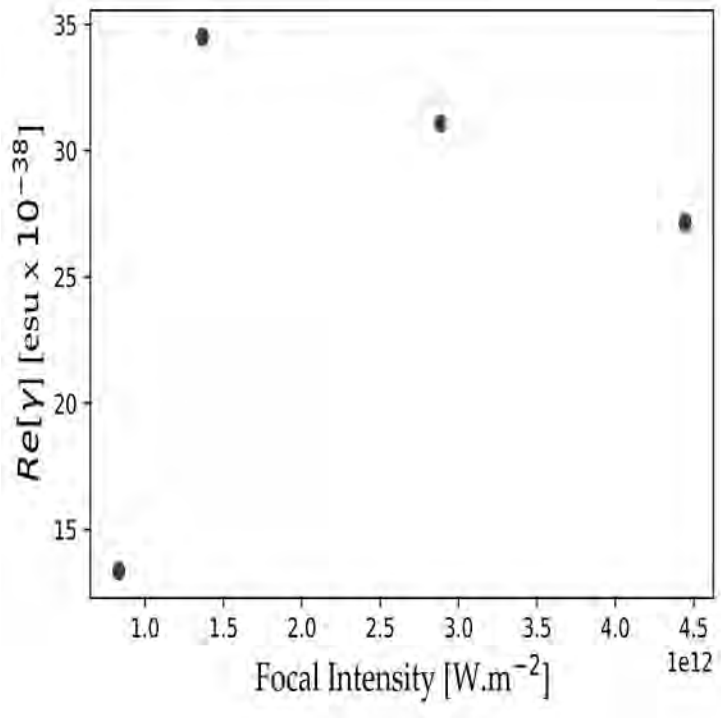

Figure 206: Real component of the second-order hyperpolarisability for the D_{2h} constitutional isomer of αH_2Pc plotted against focal intensity.

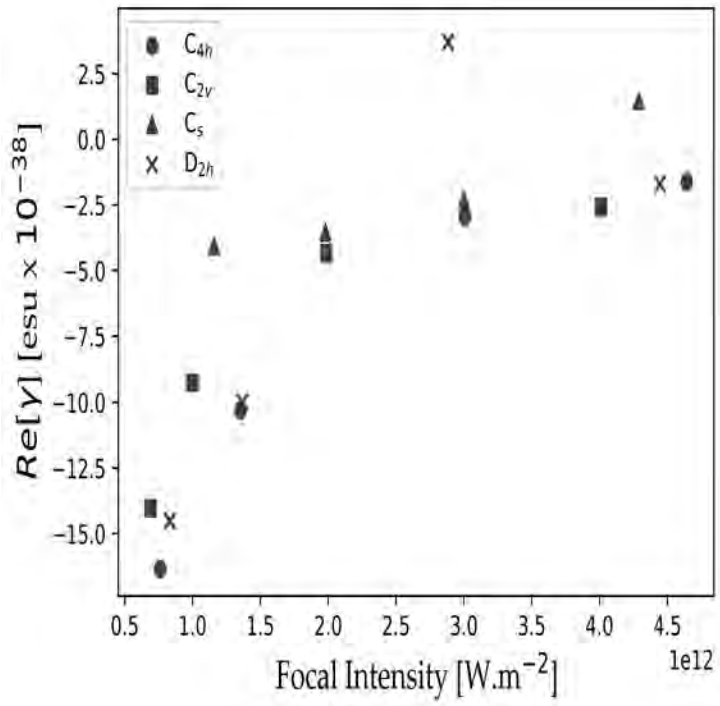

Figure 207: Real component of the second-order hyperpolarisability for the constitutional isomers of αH_2Pc plotted against focal intensity.

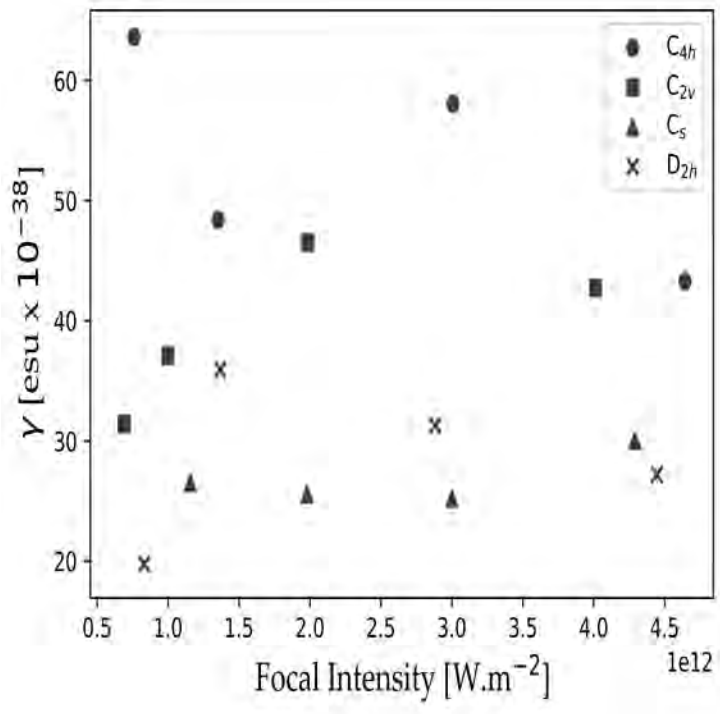

Figure 208: Total second-order hyperpolarisability for the constitutional isomers of αH_2Pc plotted against focal intensity.

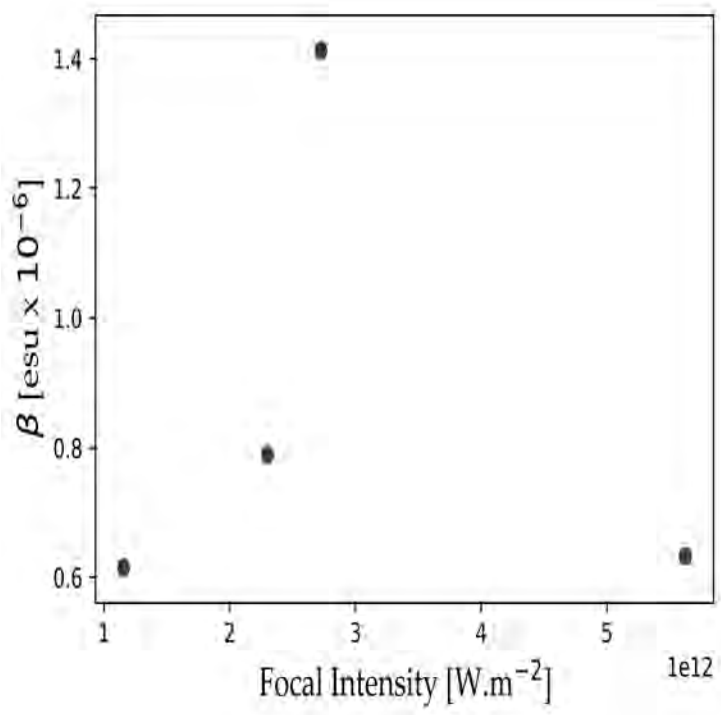

Figure 209: Nonlinear absorption coefficients for the C_{4h} constitutional isomer of βH_2Pc plotted against focal intensity.

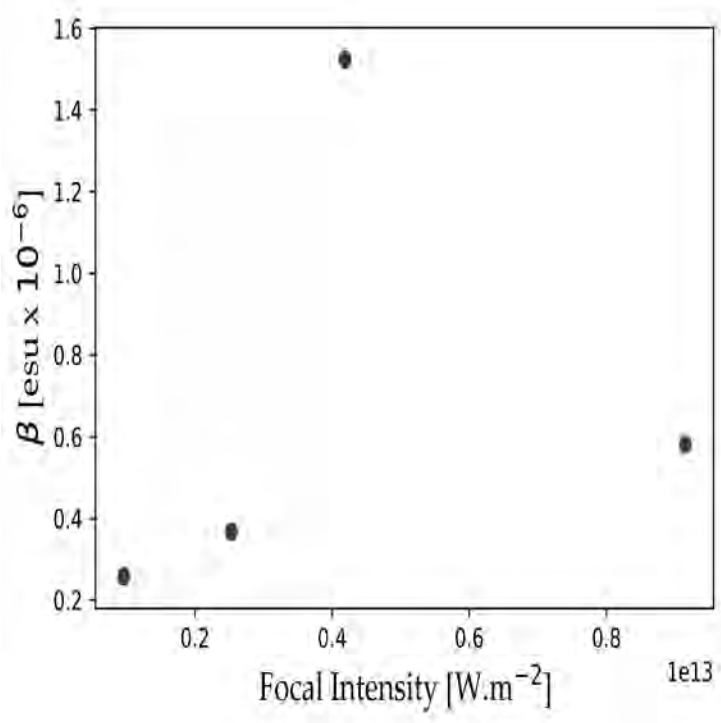

Figure 210: Nonlinear absorption coefficients for the C_{2v} constitutional isomer of βH_2Pc plotted against focal intensity.

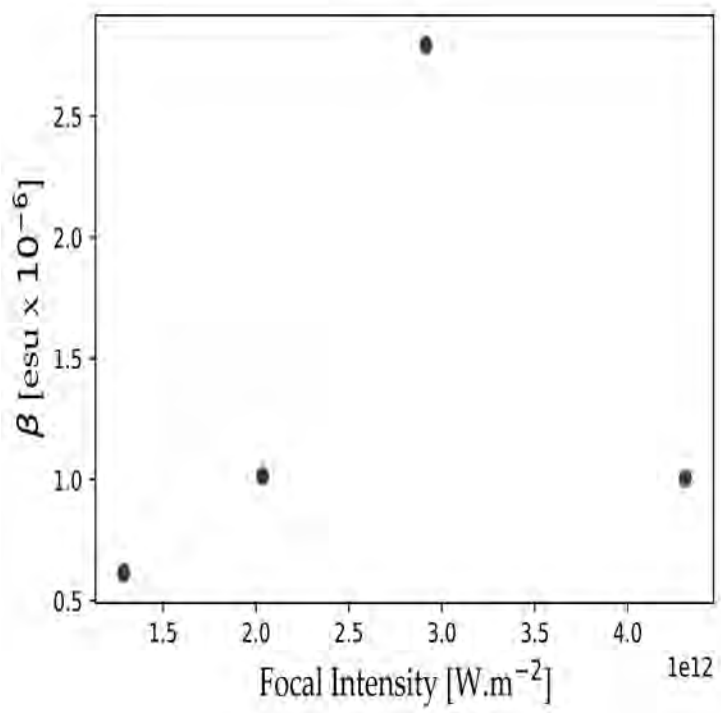

Figure 211: Nonlinear absorption coefficients for the C_s constitutional isomer of βH_2Pc plotted against focal intensity.

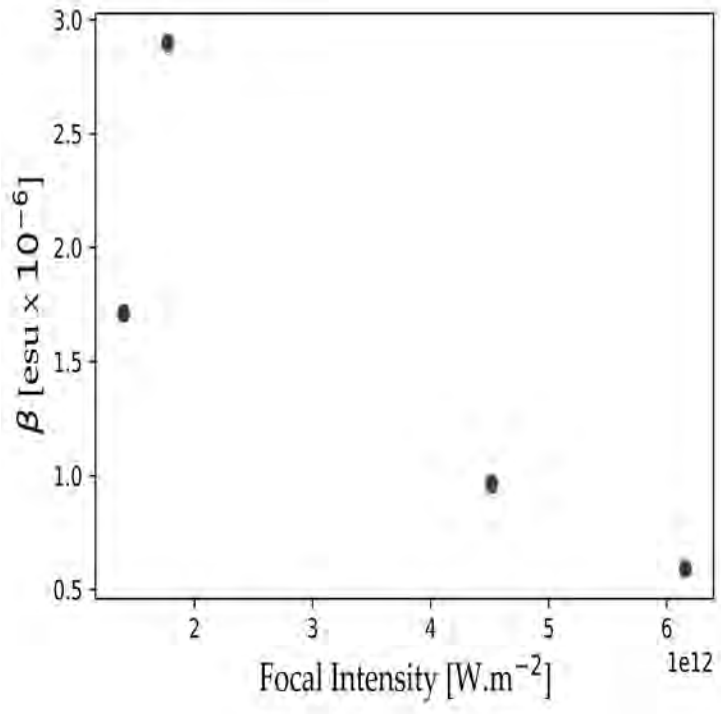

Figure 212: Nonlinear absorption coefficients for the D_{2h} constitutional isomer of βH_2Pc plotted against focal intensity.

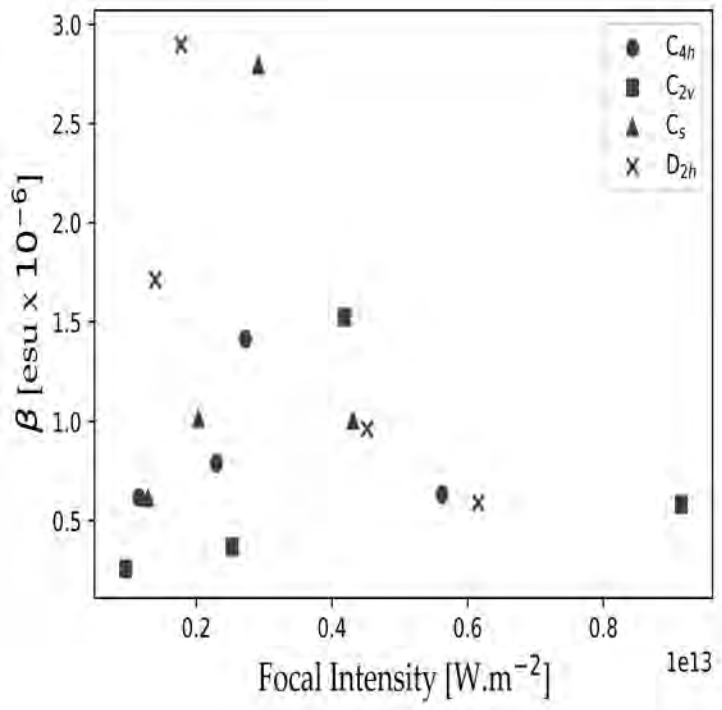

Figure 213: Nonlinear absorption coefficients for the constitutional isomers of βH_2Pc plotted against focal intensity.

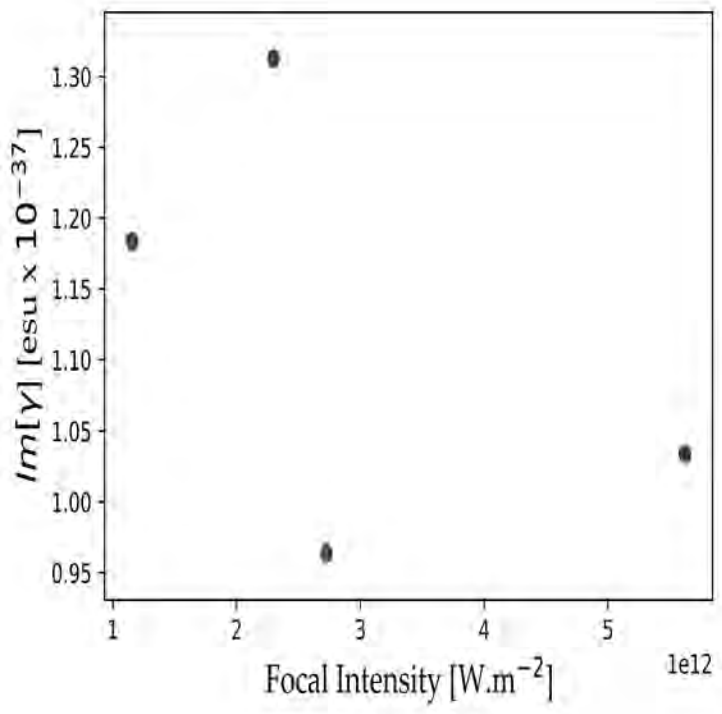

Figure 214: Imaginary component of the second-order hyperpolarisability for the C_{4h} constitutional isomer of βH_2Pc plotted against focal intensity.

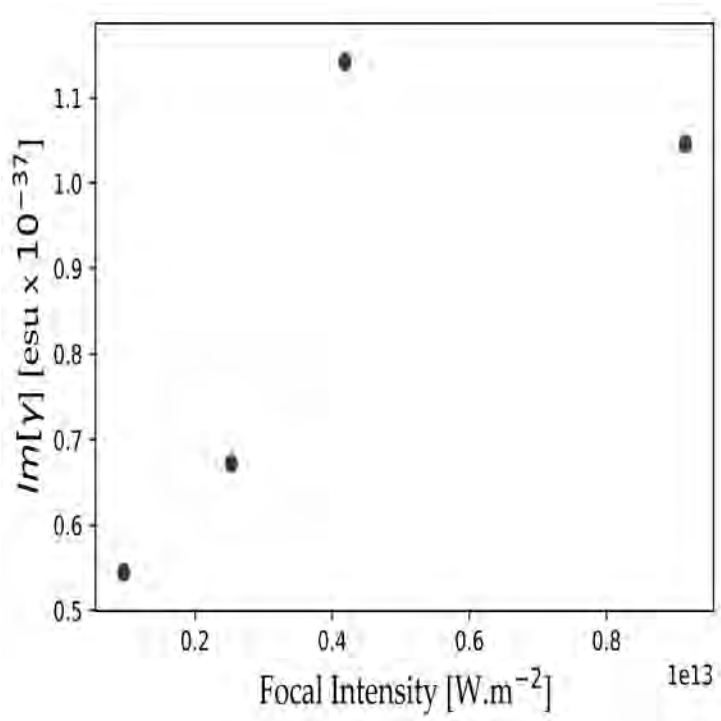

Figure 215: Imaginary component of the second-order hyperpolarisability for the C_{2v} constitutional isomer of βH_2Pc plotted against focal intensity.

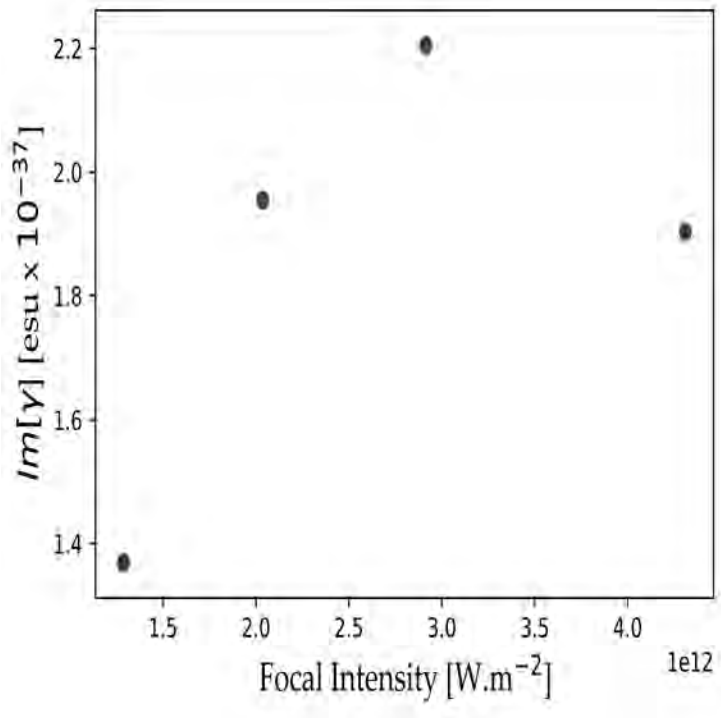

Figure 216: Imaginary component of the second-order hyperpolarisability for the C_s constitutional isomer of βH_2Pc plotted against focal intensity.

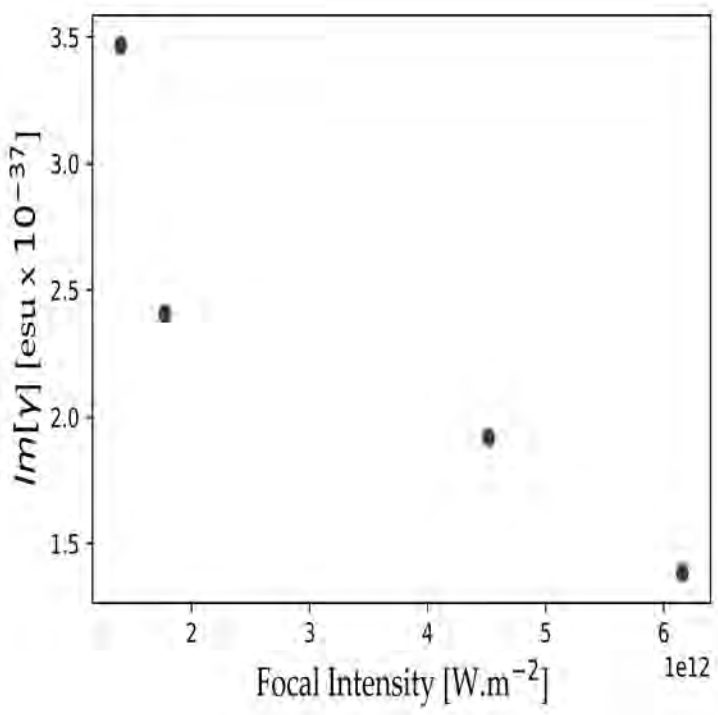

Figure 217: Imaginary component of the second-order hyperpolarisability for the D_{2h} constitutional isomer of βH_2Pc plotted against focal intensity.

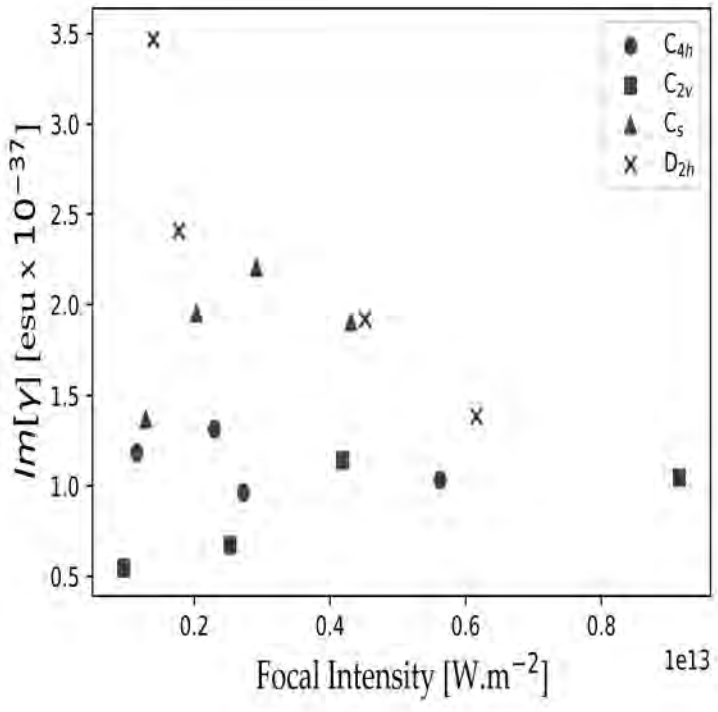

Figure 218: Imaginary component of the second-order hyperpolarisability for the constitutional isomers of βH_2Pc plotted against focal intensity.

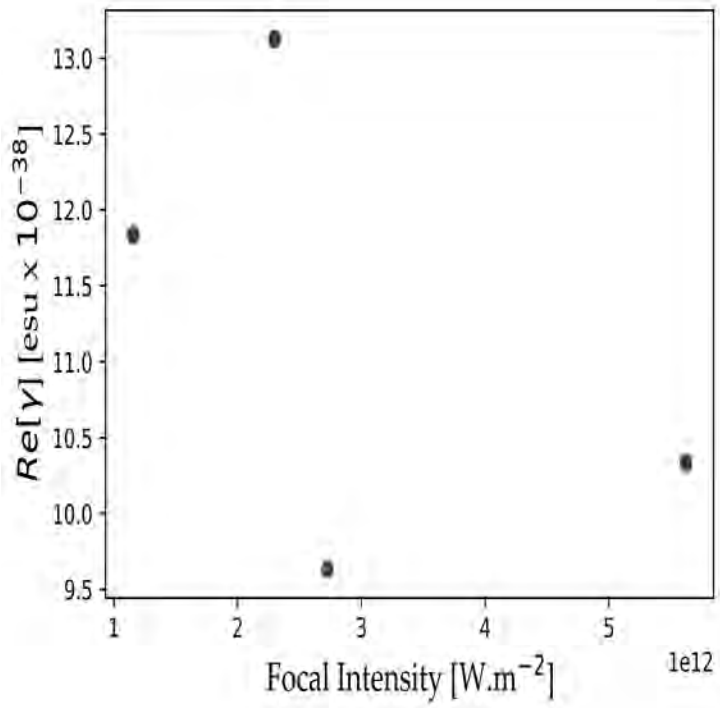

Figure 219: Real component of the second-order hyperpolarisability for the C_{4h} constitutional isomer of βH_2Pc plotted against focal intensity.

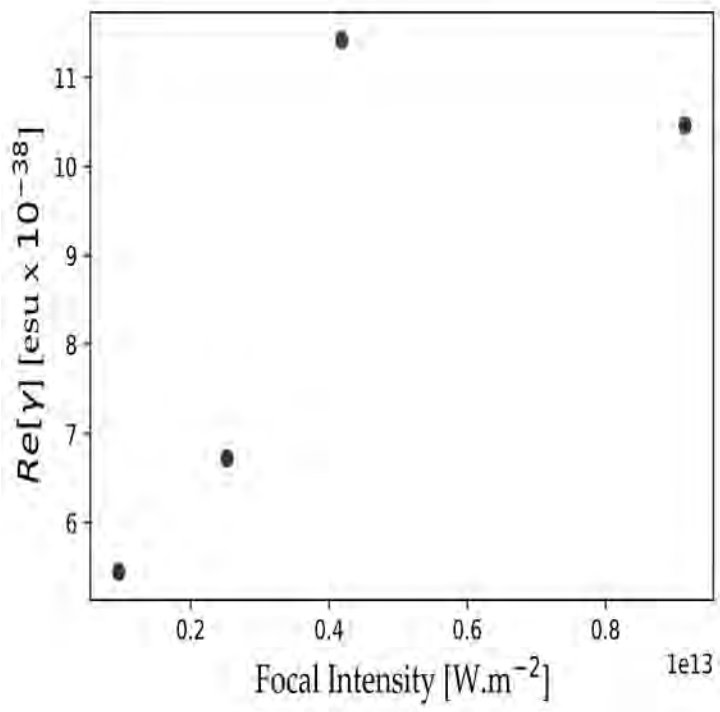

Figure 220: Real component of the second-order hyperpolarisability for the C_{2v} constitutional isomer of βH_2Pc plotted against focal intensity.

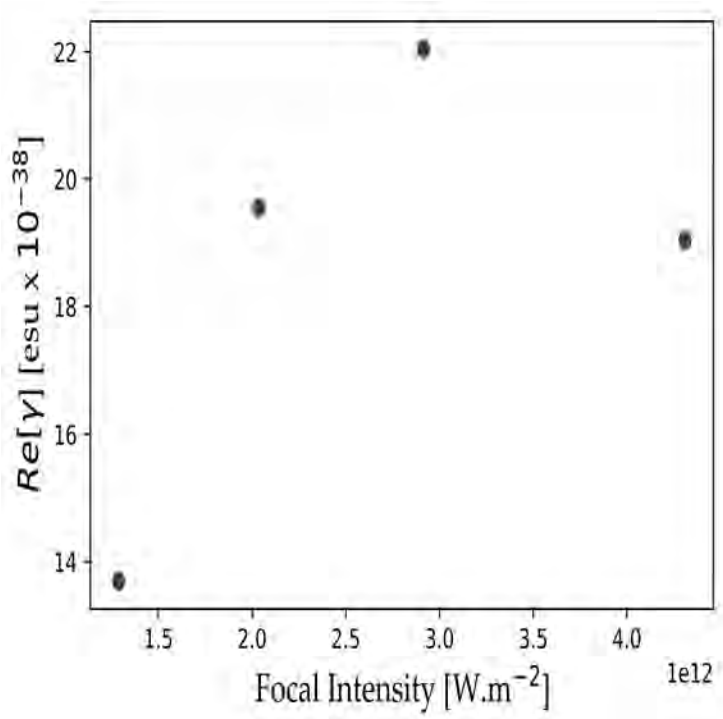

Figure 221: Real component of the second-order hyperpolarisability for the C_s constitutional isomer of βH_2Pc plotted against focal intensity.

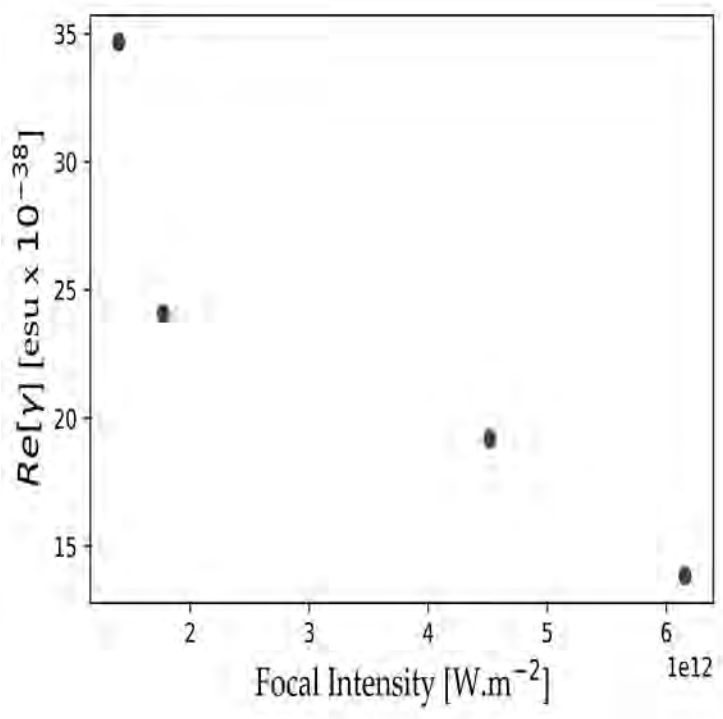

Figure 222: Real component of the second-order hyperpolarisability for the D_{2h} constitutional isomer of βH_2Pc plotted against focal intensity.

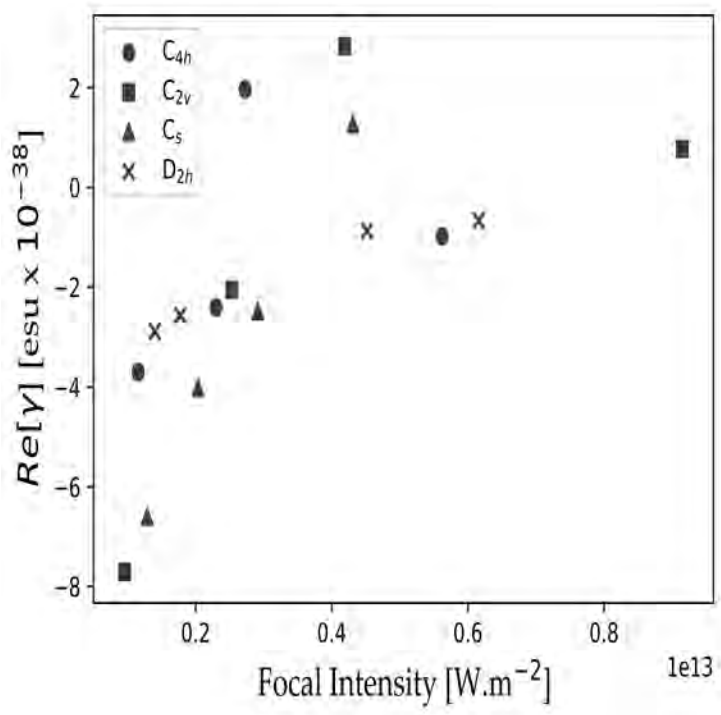

Figure 223: Real component of the second-order hyperpolarisability for the constitutional isomers of βH_2Pc plotted against focal intensity.

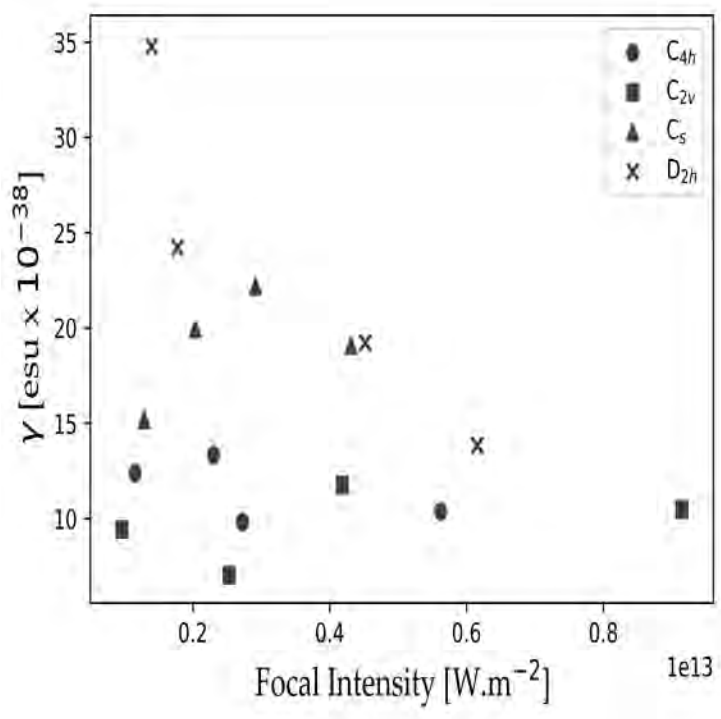

Figure 224: Total second-order hyperpolarisability for the constitutional isomers of βH_2Pc plotted against focal intensity.

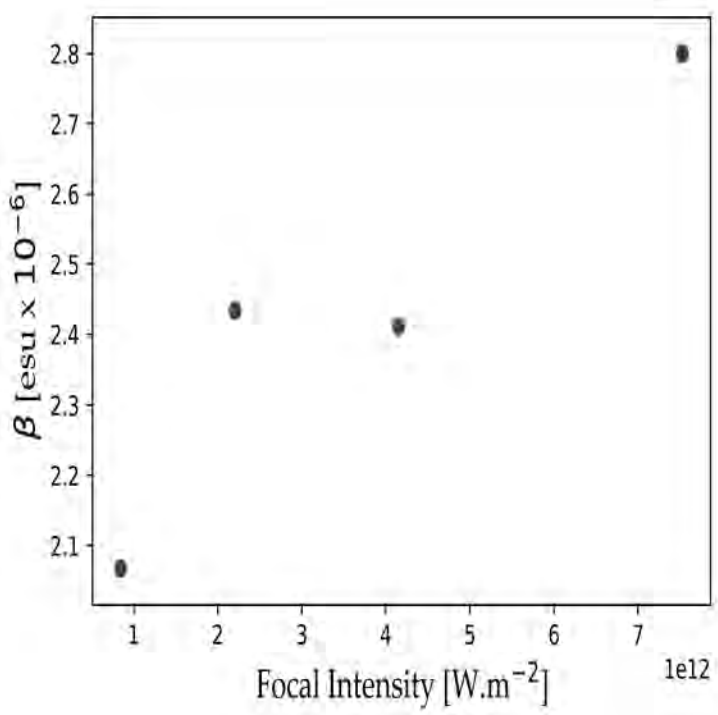

Figure 225: Nonlinear absorption coefficients for the C_{4h} constitutional isomer of αSn_2Pc plotted against focal intensity.

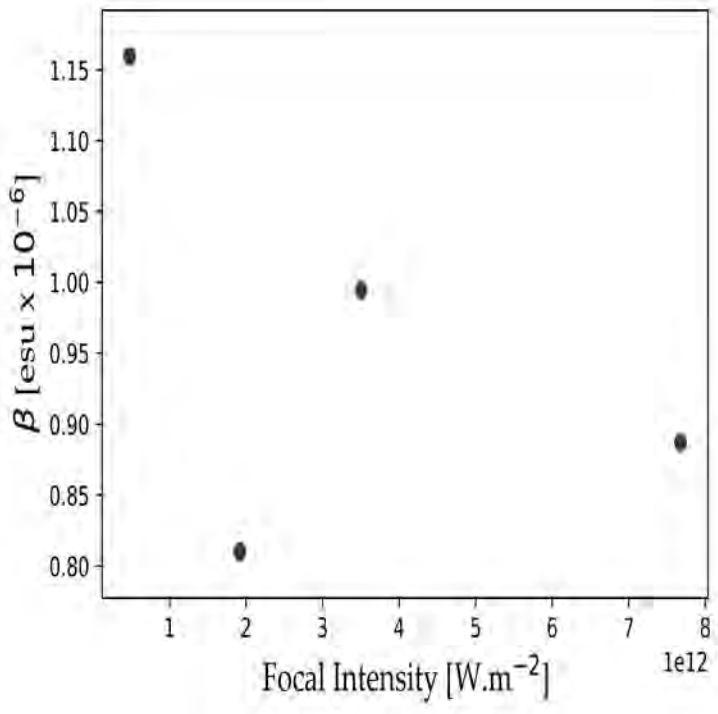

Figure 226: Nonlinear absorption coefficients for the C_{2v} constitutional isomer of αSn_2Pc plotted against focal intensity.

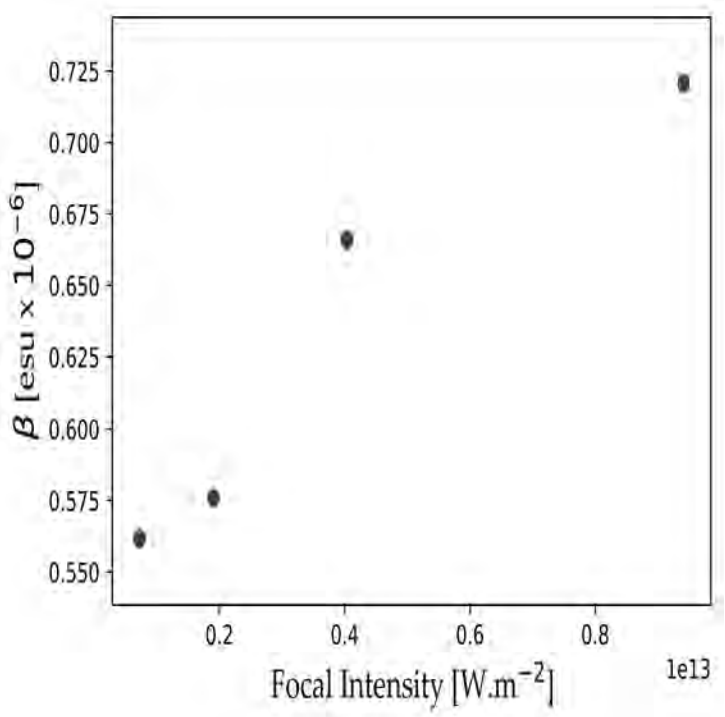

Figure 227: Nonlinear absorption coefficients for the C_s constitutional isomer of αSn_2Pc plotted against focal intensity.

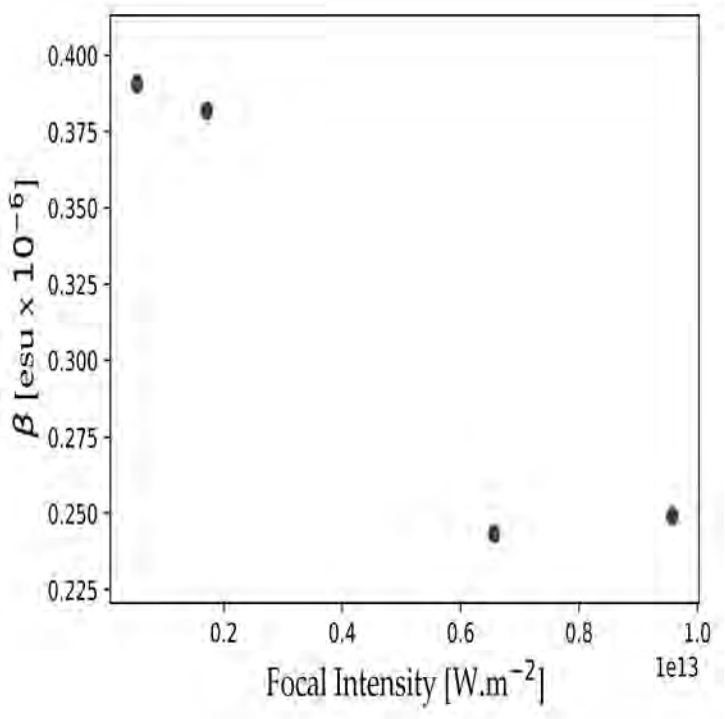

Figure 228: Nonlinear absorption coefficients for the D_{2h} constitutional isomer of αSn_2Pc plotted against focal intensity.

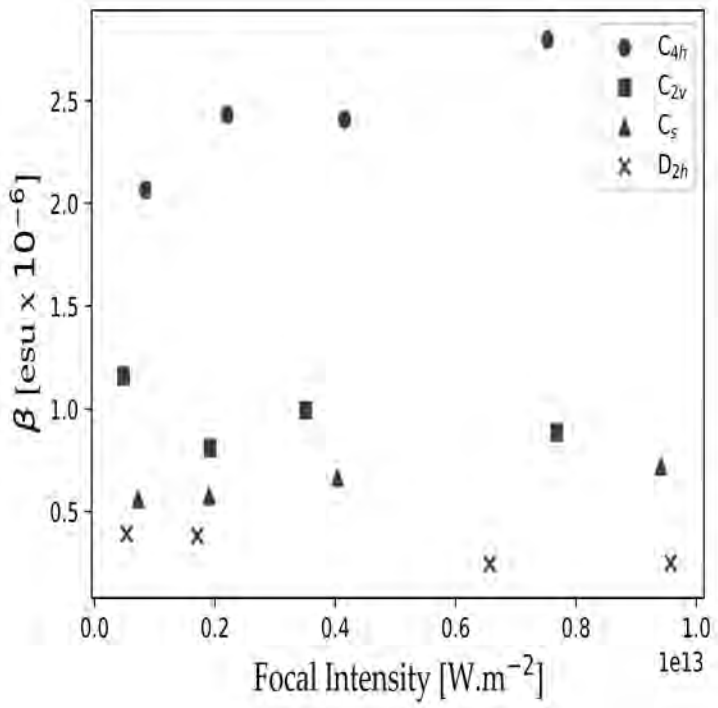

Figure 229: Nonlinear absorption coefficients for the constitutional isomers of αSn_2Pc plotted against focal intensity.

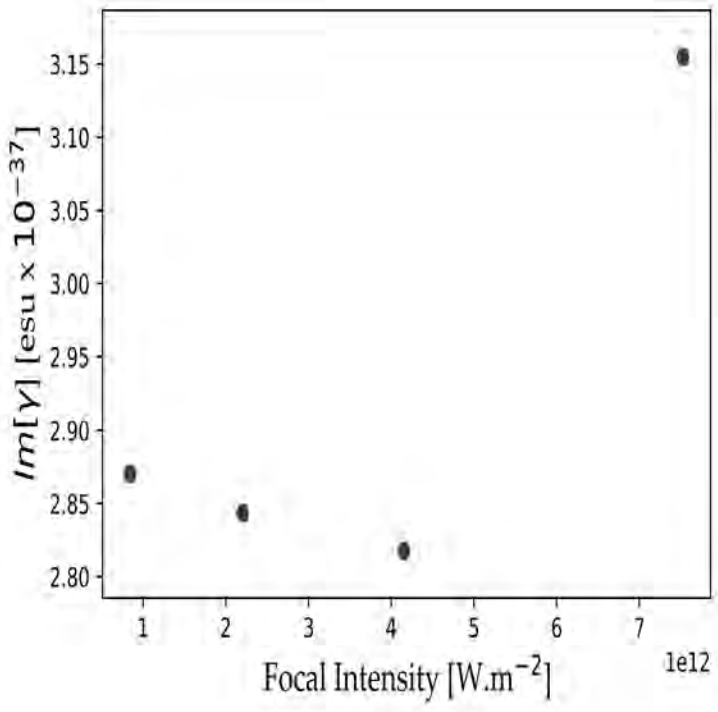

Figure 230: Imaginary component of the second-order hyperpolarisability for the C_{4h} constitutional isomer of αSn_2Pc plotted against focal intensity.

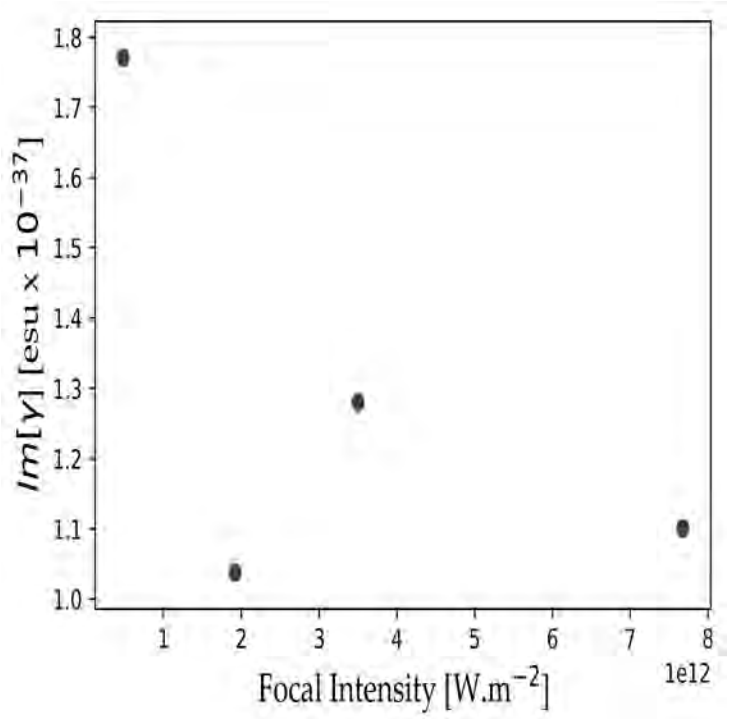

Figure 231: Imaginary component of the second-order hyperpolarisability for the C_{2v} constitutional isomer of αSn_2Pc plotted against focal intensity.

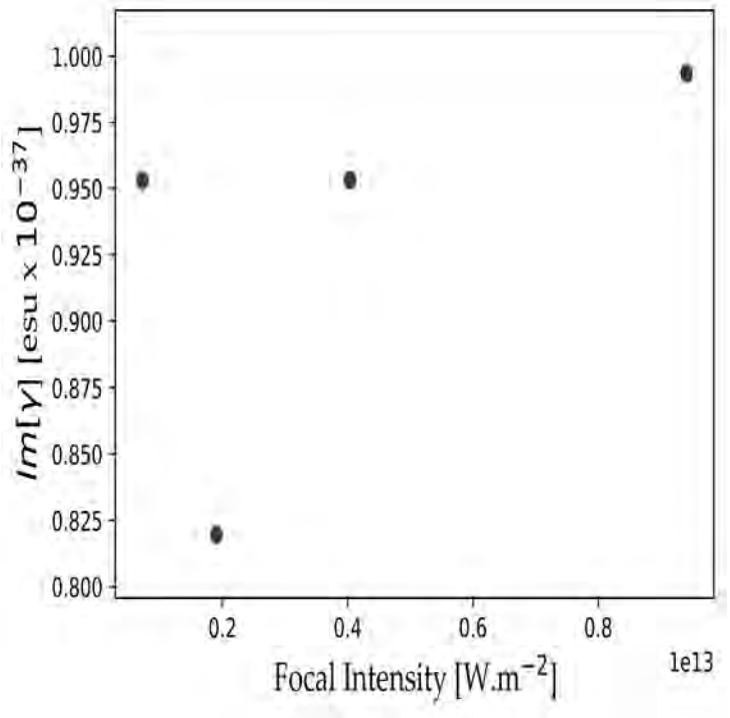

Figure 232: Imaginary component of the second-order hyperpolarisability for the C_s constitutional isomer of αSn_2Pc plotted against focal intensity.

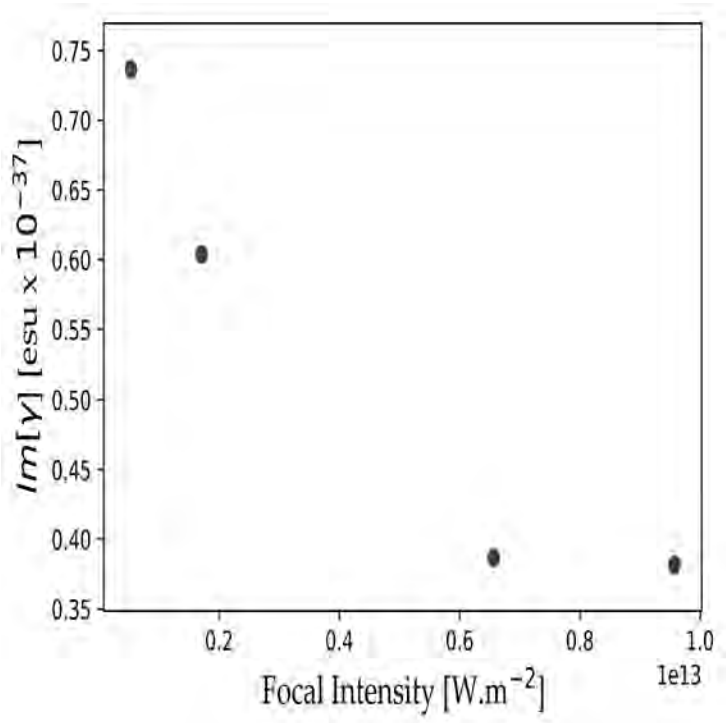

Figure 233: Imaginary component of the second-order hyperpolarisability for the D_{2h} constitutional isomer of αSn_2Pc plotted against focal intensity.

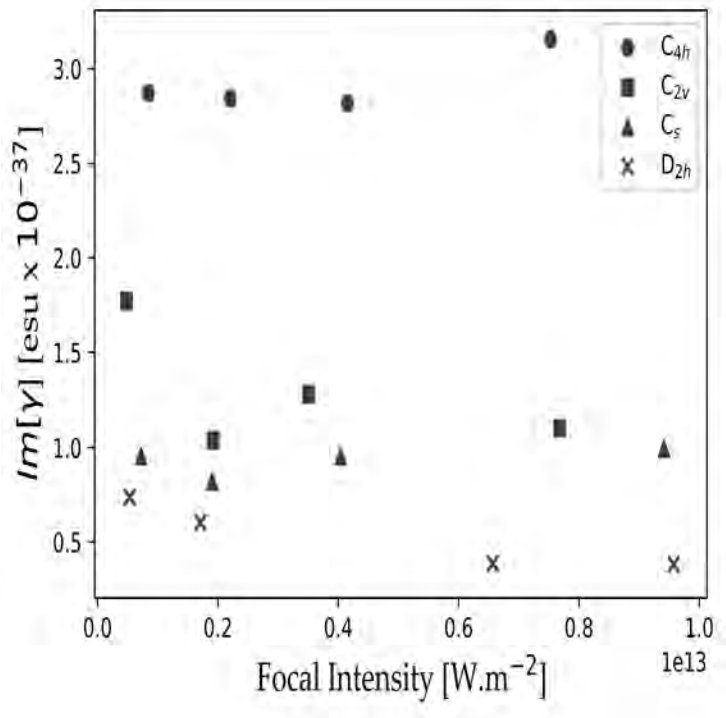

Figure 234: Imaginary component of the second-order hyperpolarisability for the constitutional isomers of αSn_2Pc plotted against focal intensity.

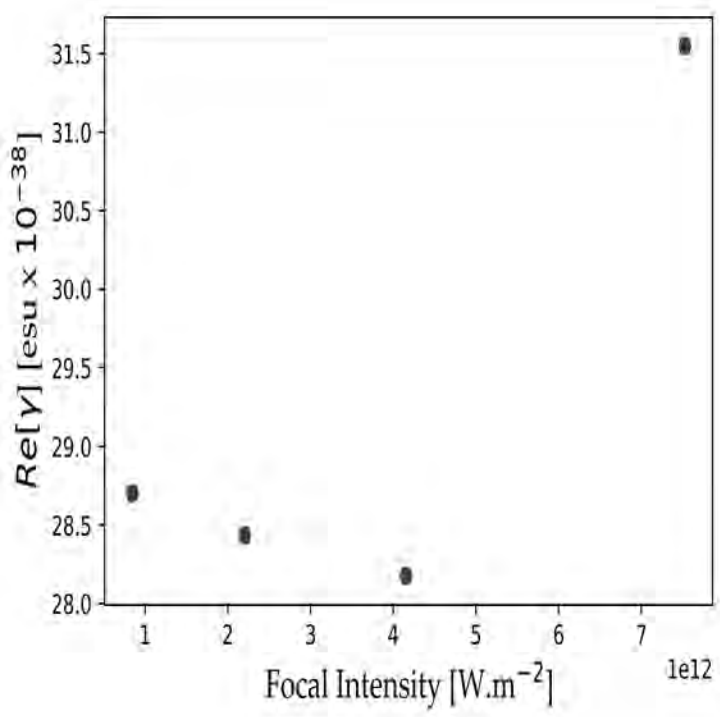

Figure 235: Real component of the second-order hyperpolarisability for the C_{4h} constitutional isomer of αSn_2Pc plotted against focal intensity.

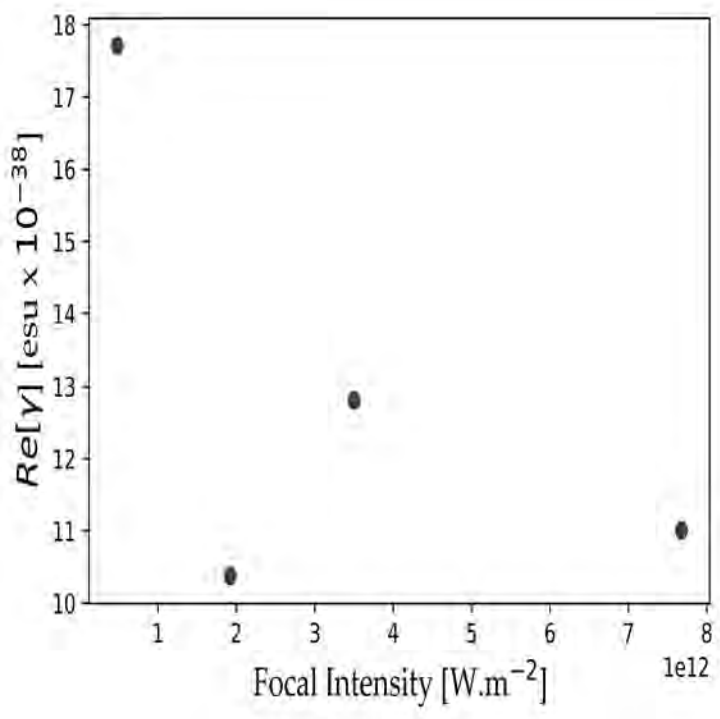

Figure 236: Real component of the second-order hyperpolarisability for the C_{2v} constitutional isomer of αSn_2Pc plotted against focal intensity.

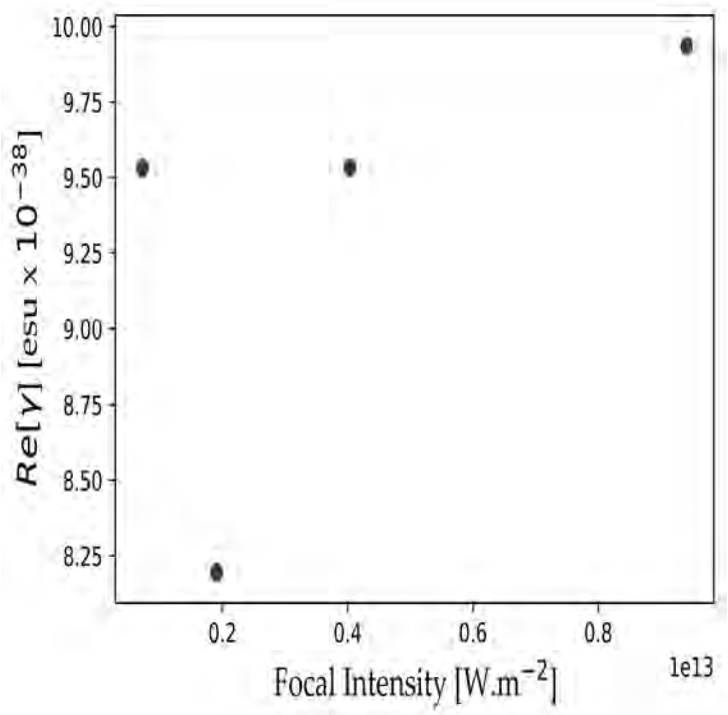

Figure 237: Real component of the second-order hyperpolarisability for the C_s constitutional isomer of αSn_2Pc plotted against focal intensity.

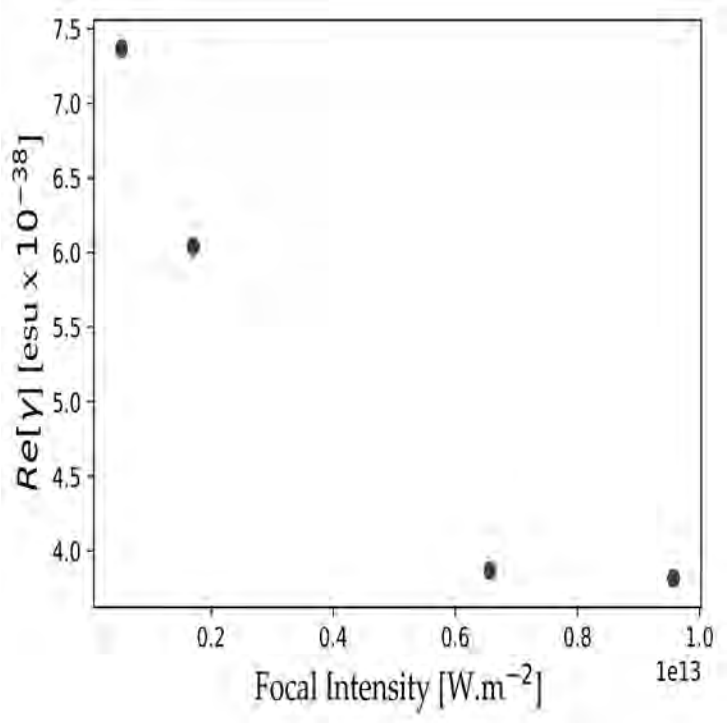

Figure 238: Real component of the second-order hyperpolarisability for the D_{2h} constitutional isomer of αSn_2Pc plotted against focal intensity.

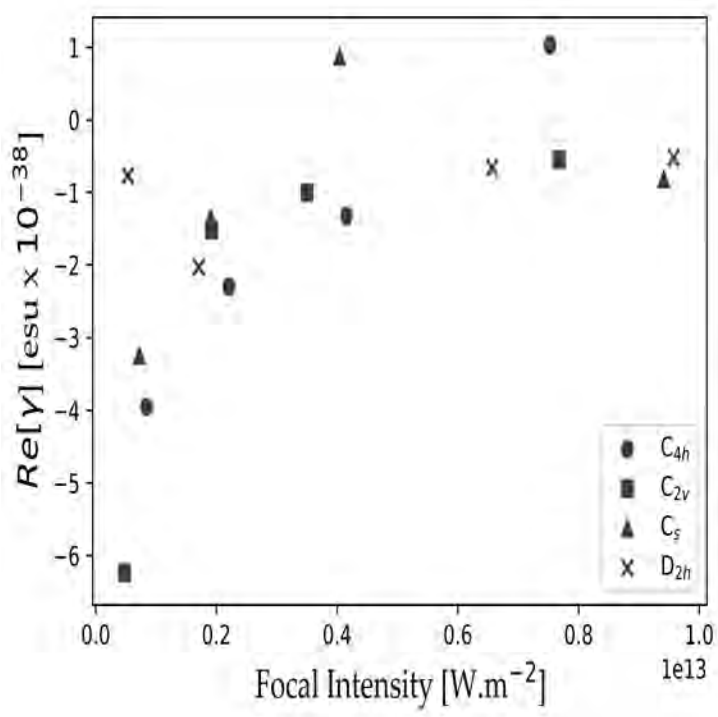

Figure 239: Real component of the second-order hyperpolarisability for the constitutional isomers of αSn_2Pc plotted against focal intensity.

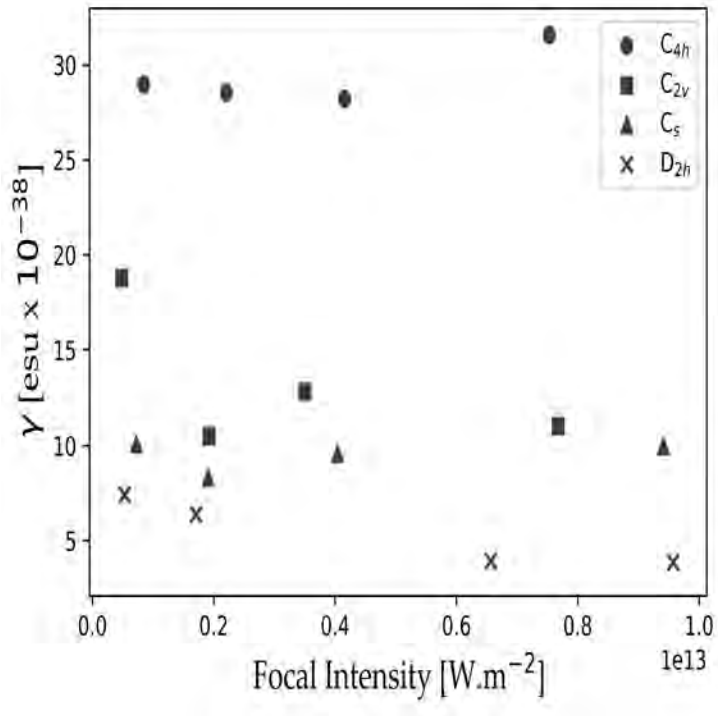

Figure 240: Total second-order hyperpolarisability for the constitutional isomers of αSn_2Pc plotted against focal intensity.

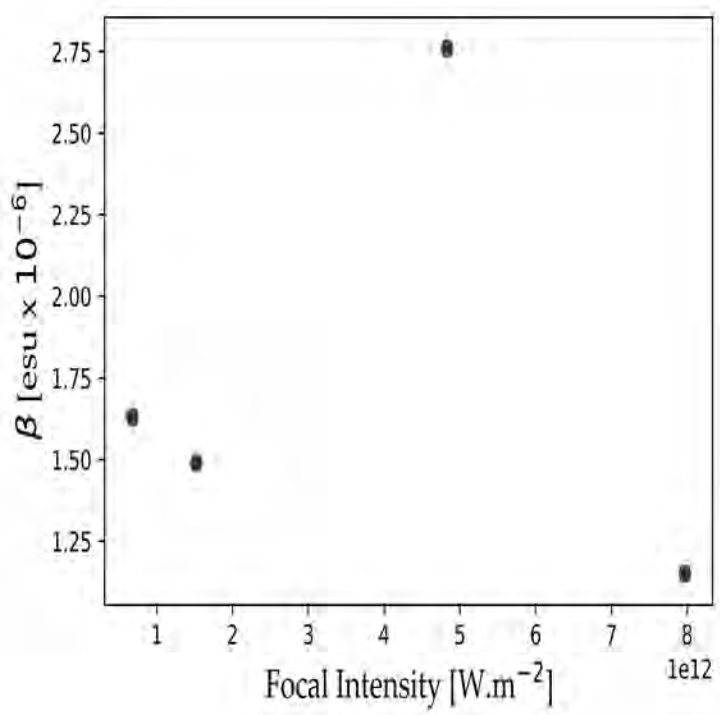

Figure 241: Nonlinear absorption coefficients for the C_{4h} constitutional isomer of βSn_2Pc plotted against focal intensity.

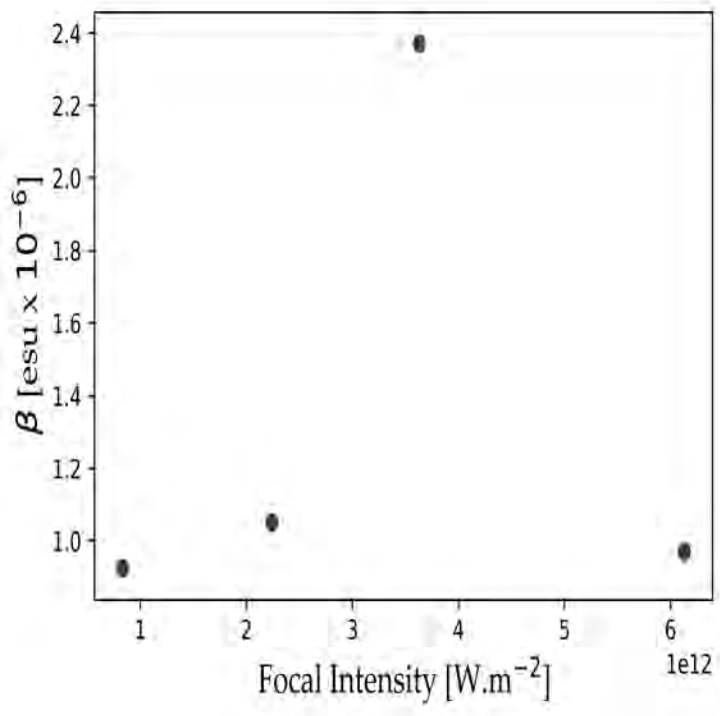

Figure 242: Nonlinear absorption coefficients for the C_{2v} constitutional isomer of βSn_2Pc plotted against focal intensity.

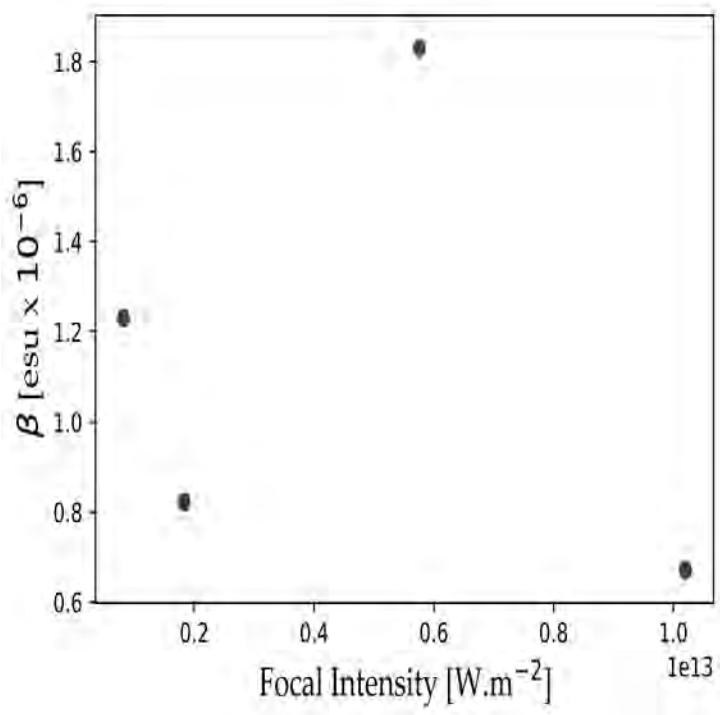

Figure 243: Nonlinear absorption coefficients for the C_s constitutional isomer of βSn_2Pc plotted against focal intensity.

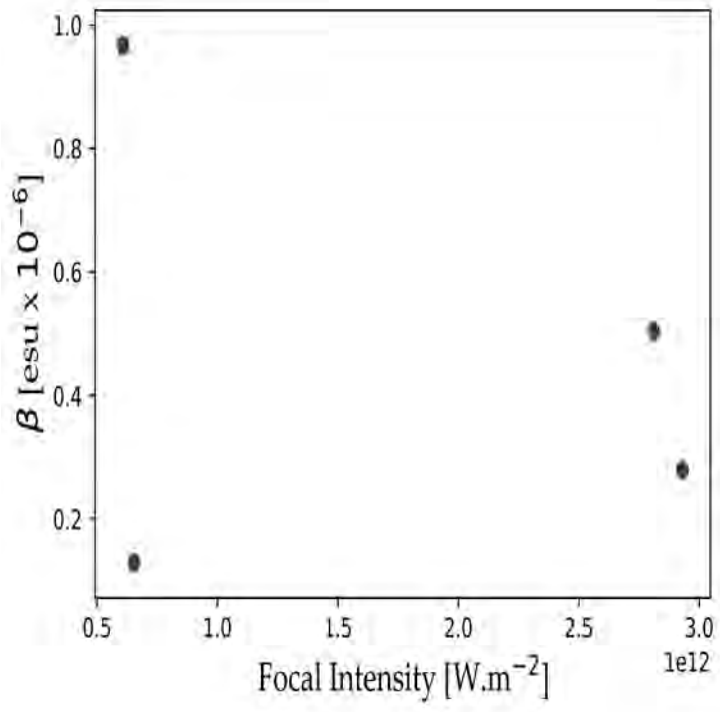

Figure 244: Nonlinear absorption coefficients for the D_{2h} constitutional isomer of βSn_2Pc plotted against focal intensity.

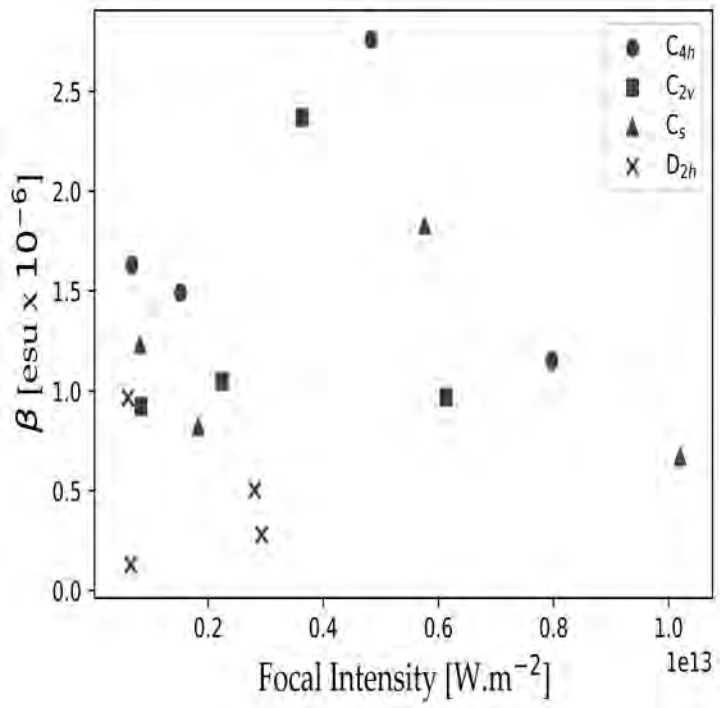

Figure 245: Nonlinear absorption coefficients for the constitutional isomers of βSn_2Pc plotted against focal intensity.

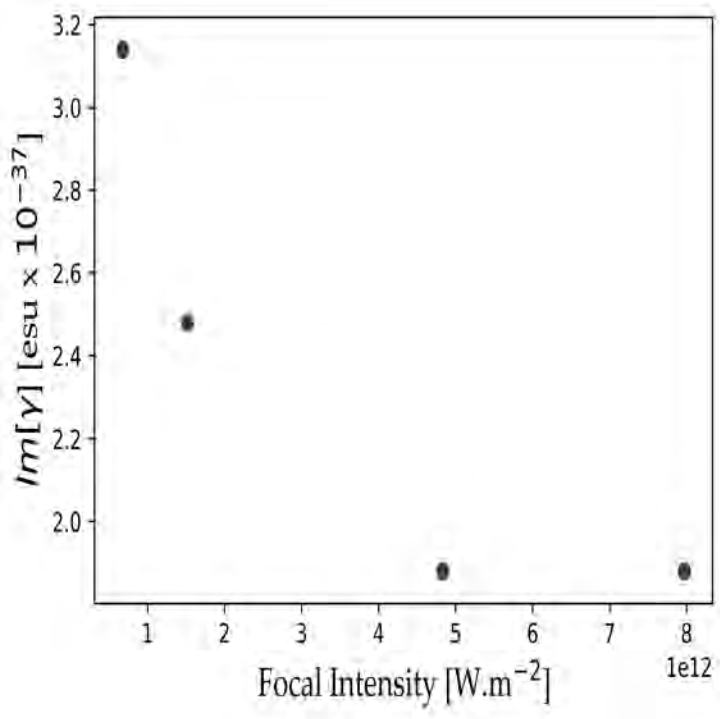

Figure 246: Imaginary component of the second-order hyperpolarisability for the C_{4h} constitutional isomer of βSn_2Pc plotted against focal intensity.

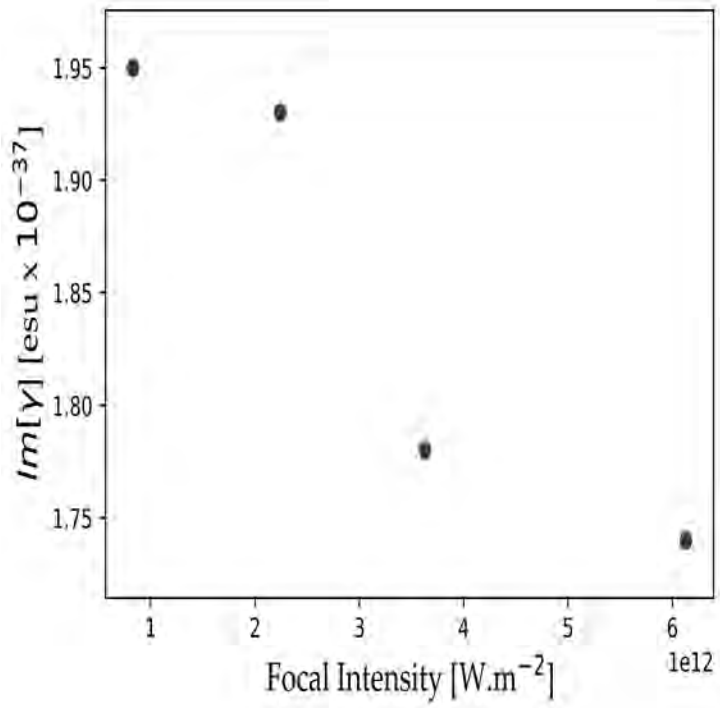

Figure 247: Imaginary component of the second-order hyperpolarisability for the C_{2v} constitutional isomer of βSn_2Pc plotted against focal intensity.

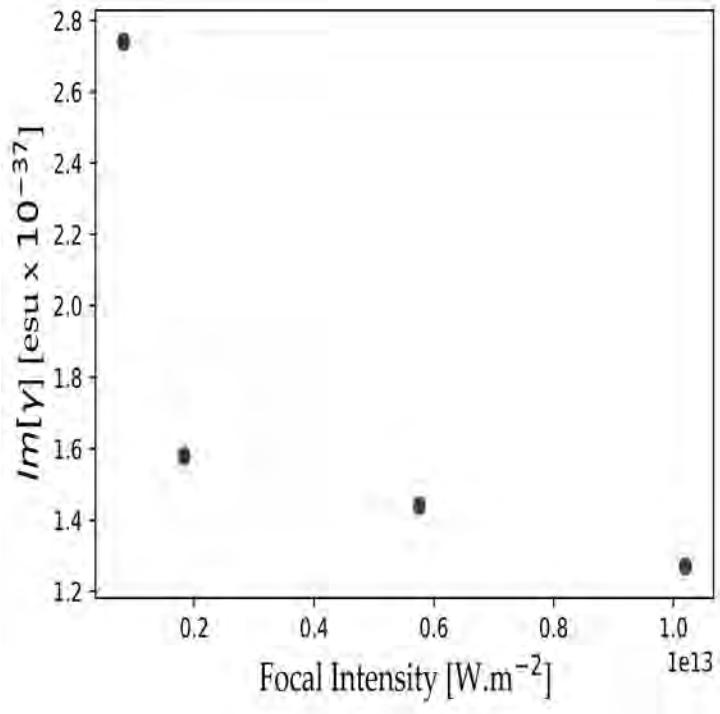

Figure 248: Imaginary component of the second-order hyperpolarisability for the C_s constitutional isomer of βSn_2Pc plotted against focal intensity.

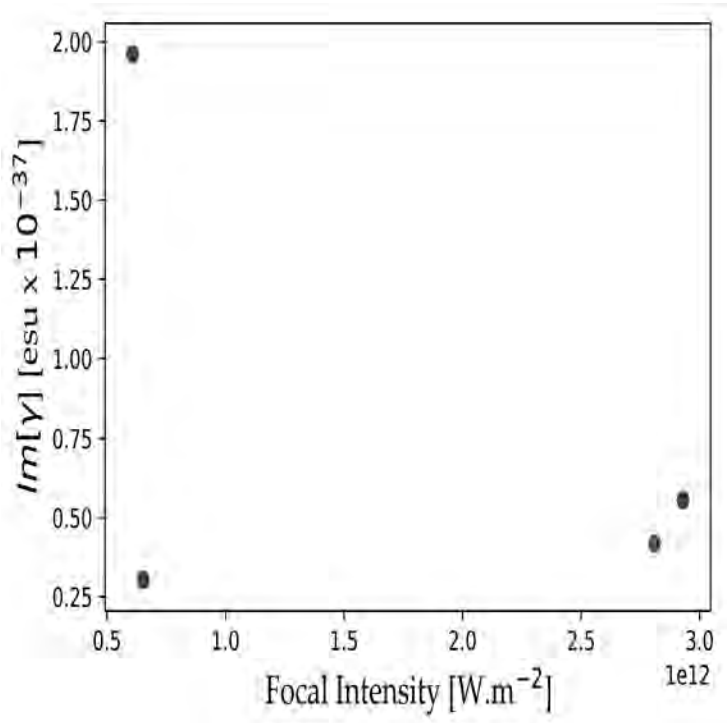

Figure 249: Imaginary component of the second-order hyperpolarisability for the D_{2h} constitutional isomer of βSn_2Pc plotted against focal intensity.

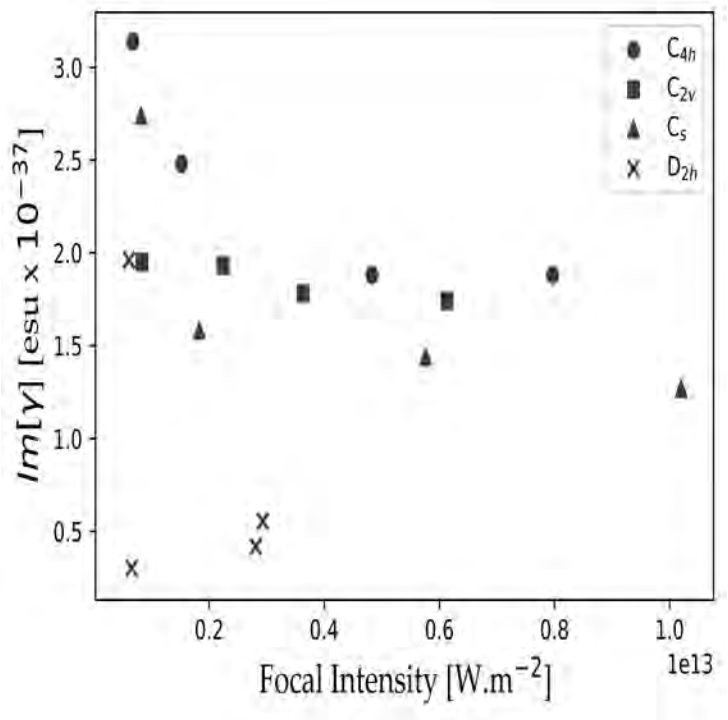

Figure 250: Imaginary component of the second-order hyperpolarisability for the constitutional isomers of βSn_2Pc plotted against focal intensity.

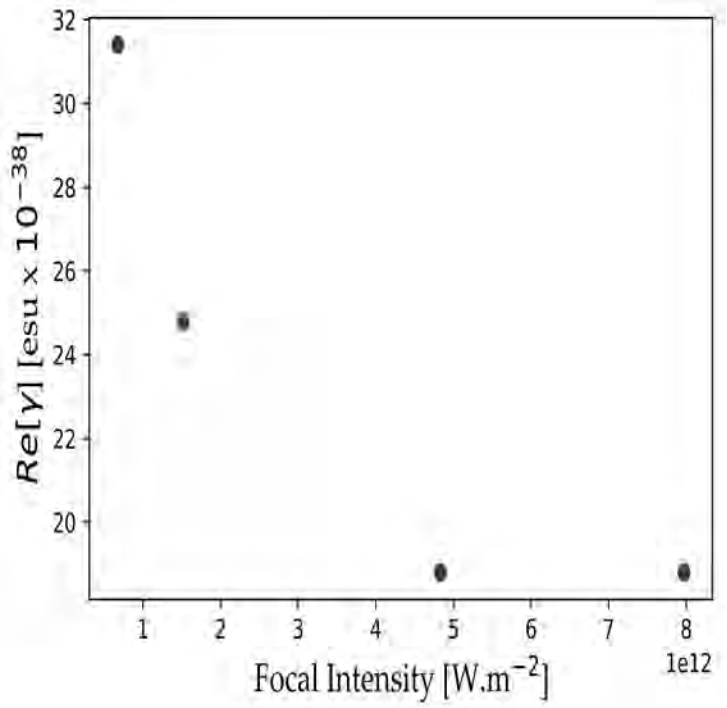

Figure 251: Real component of the second-order hyperpolarisability for the C_{4h} constitutional isomer of βSn_2Pc plotted against focal intensity.

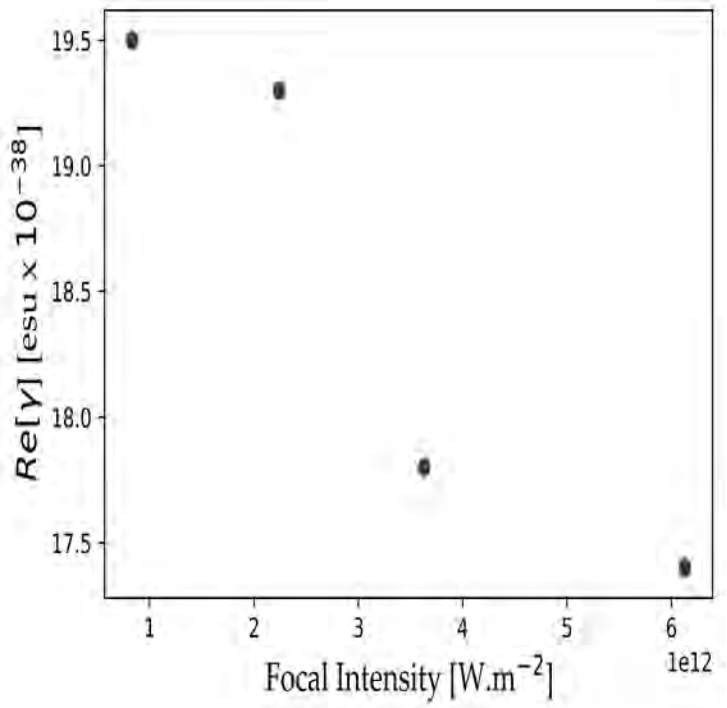

Figure 252: Real component of the second-order hyperpolarisability for the C_{2v} constitutional isomer of βSn_2Pc plotted against focal intensity.

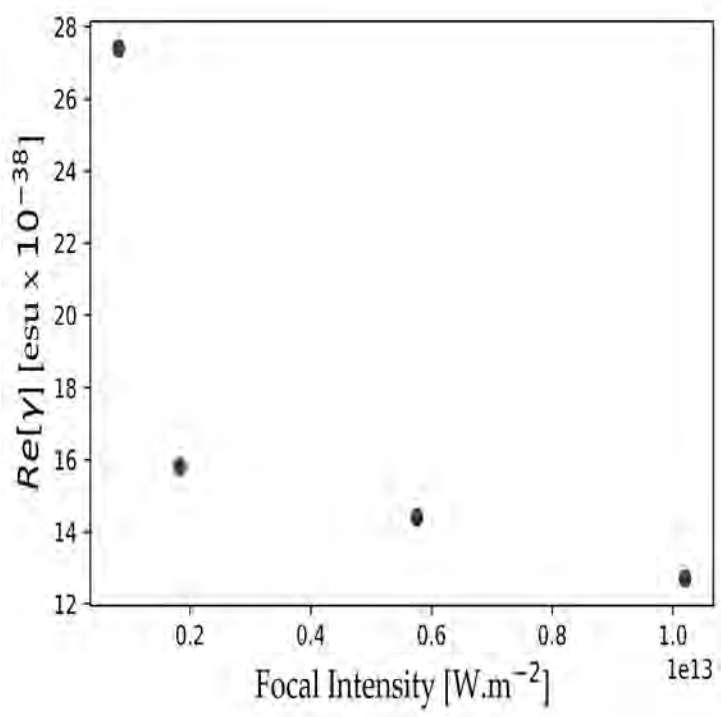

Figure 253: Real component of the second-order hyperpolarisability for the C_s constitutional isomer of βSn_2Pc plotted against focal intensity.

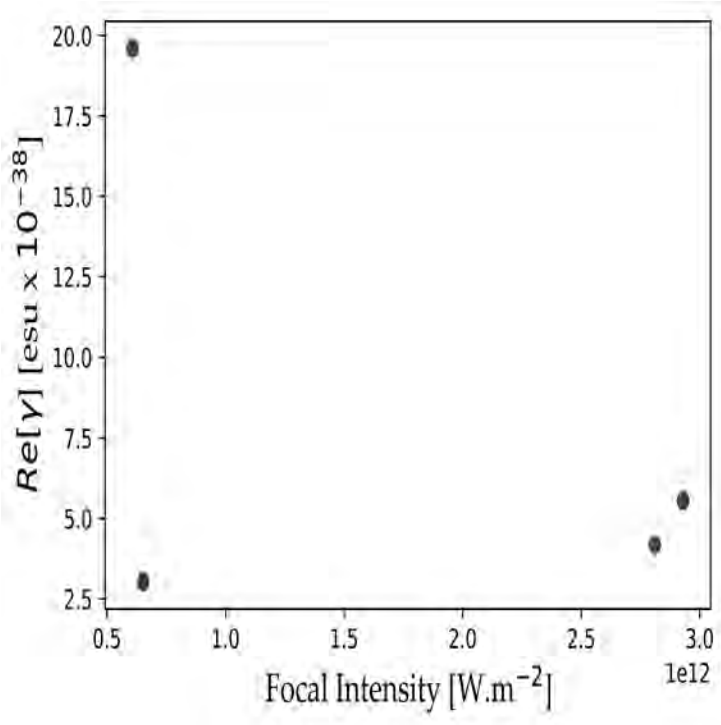

Figure 254: Real component of the second-order hyperpolarisability for the D_{2h} constitutional isomer of βSn_2Pc plotted against focal intensity.

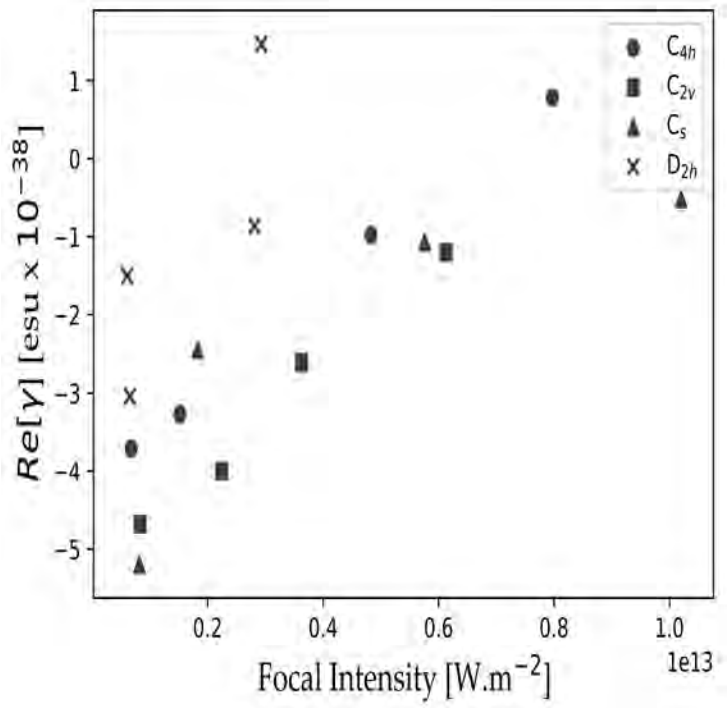

Figure 255: Real component of the second-order hyperpolarisability for the constitutional isomers of βSn_2Pc plotted against focal intensity.

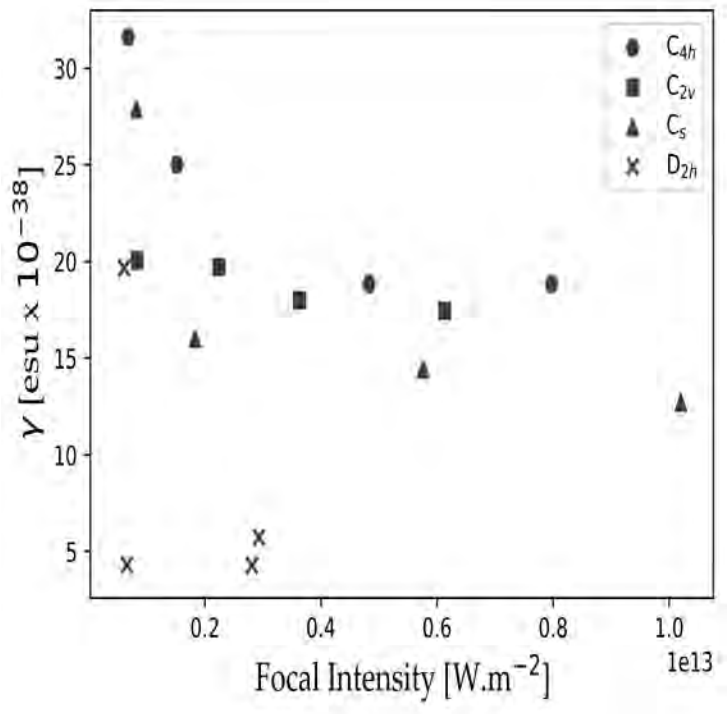

Figure 256: Total second-order hyperpolarisability for the constitutional isomers of βSn_2Pc plotted against focal intensity.

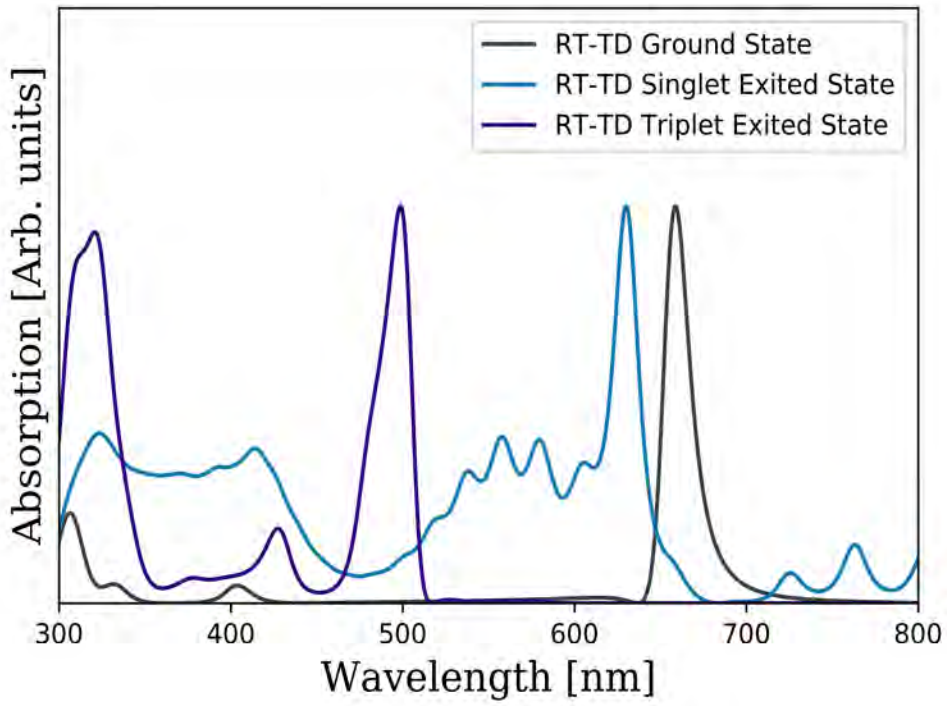

Figure 257: RTTD-DFT dipole response of the C_{4h} constitutional isomer of αH_2Pc in the UV/Vis region.

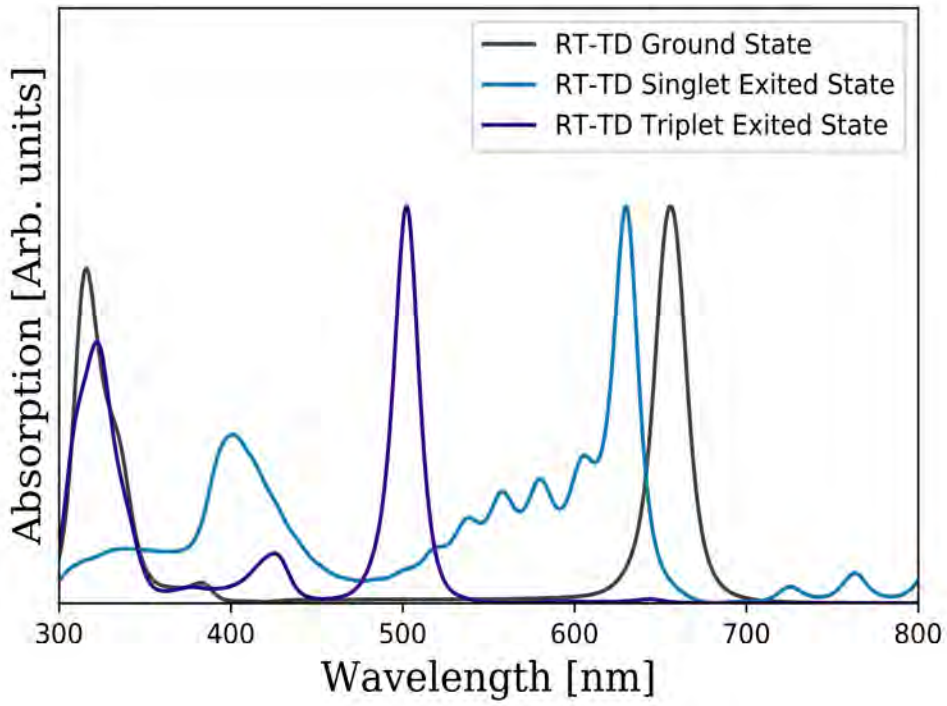

Figure 258: RTTD-DFT dipole response of the C_{2v} constitutional isomer of αH_2Pc in the UV/Vis region.

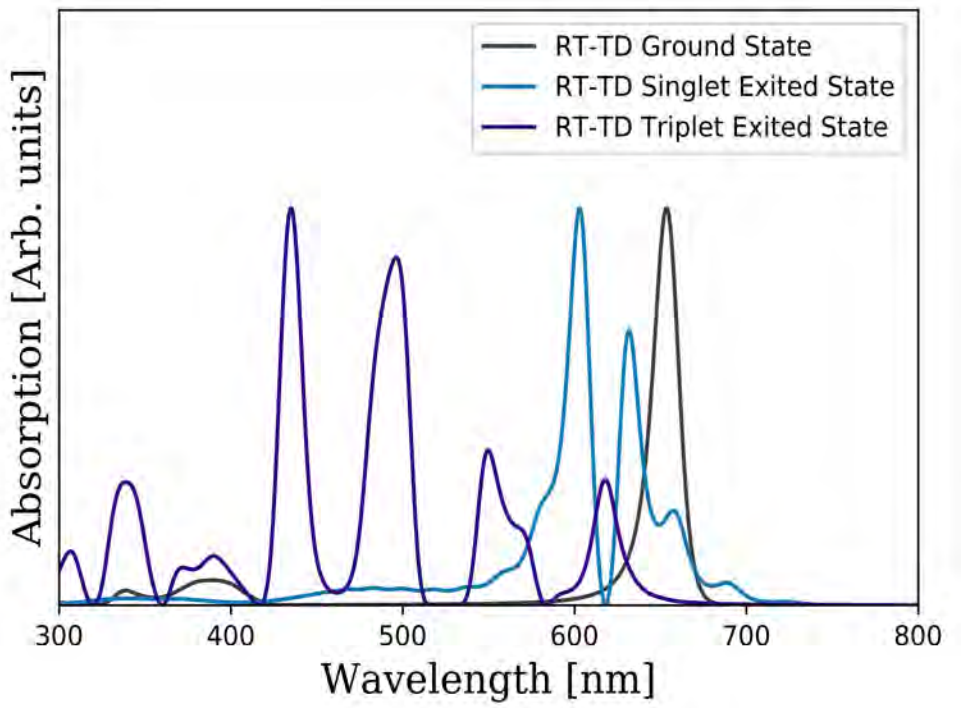

Figure 259: RTTD-DFT dipole response of the C_s constitutional isomer of αH_2Pc in the UV/Vis region.

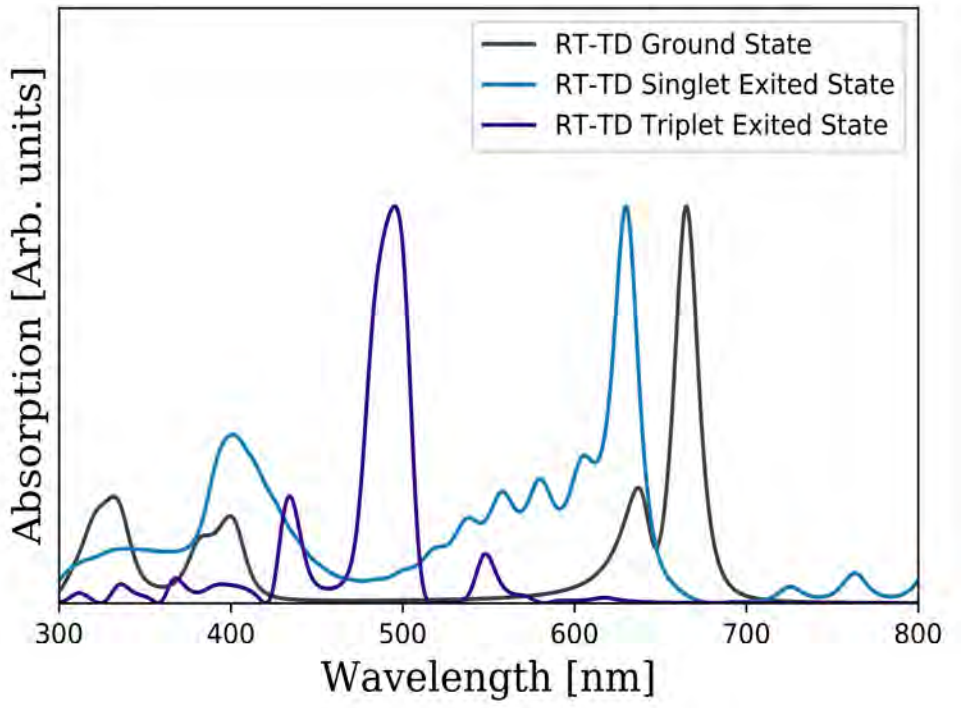

Figure 260: RTTD-DFT dipole response of the D_{2h} constitutional isomer of αH_2Pc in the UV/Vis region.

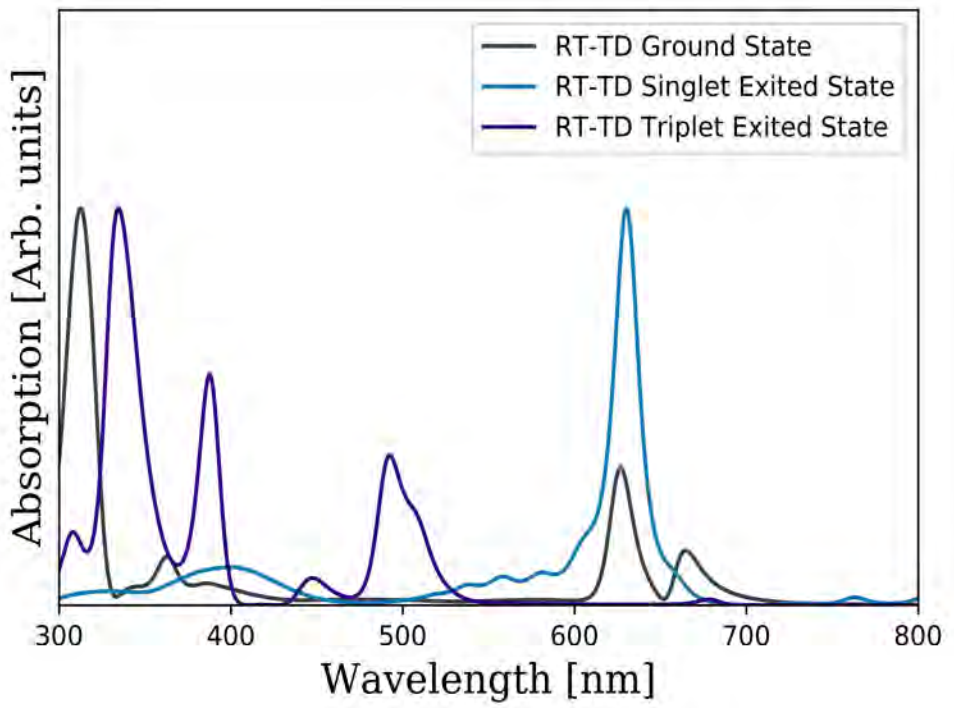

Figure 261: RTTD-DFT dipole response of the C_{4h} constitutional isomer of βH_2Pc in the UV/Vis region.

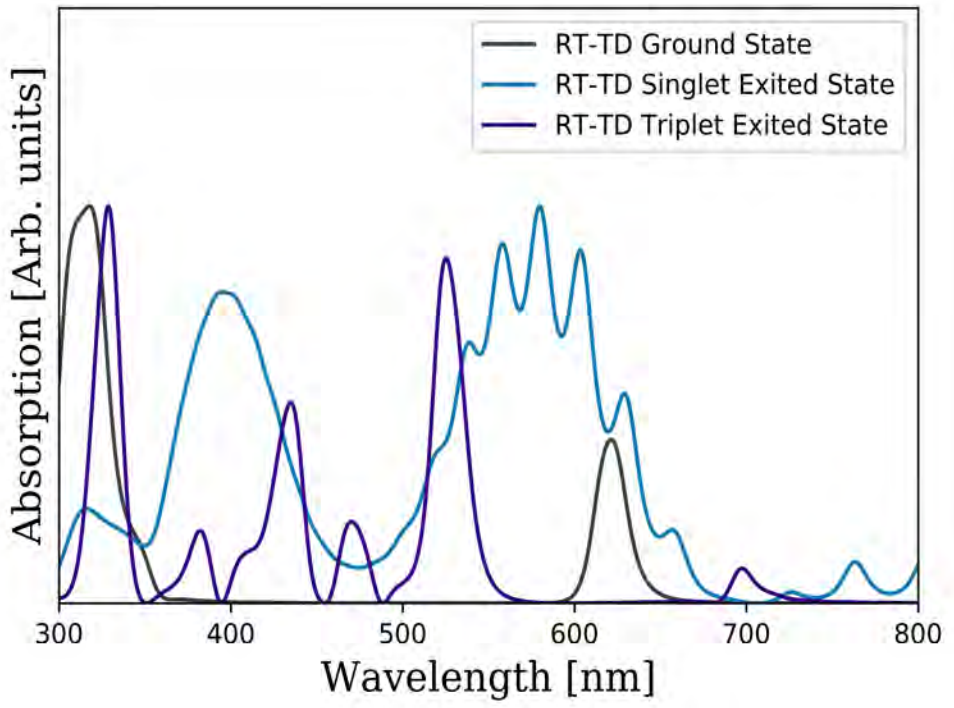

Figure 262: RTTD-DFT dipole response of the C_{2v} constitutional isomer of βH_2Pc in the UV/Vis region.

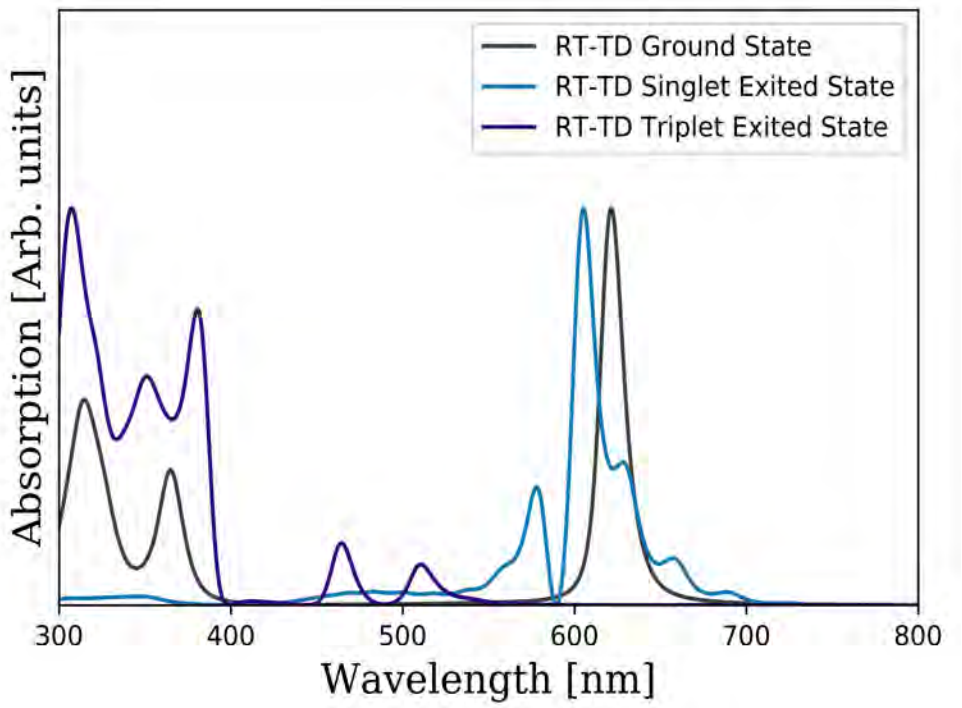

Figure 263: RTTD-DFT dipole response of the C_s constitutional isomer of βH_2Pc in the UV/Vis region.

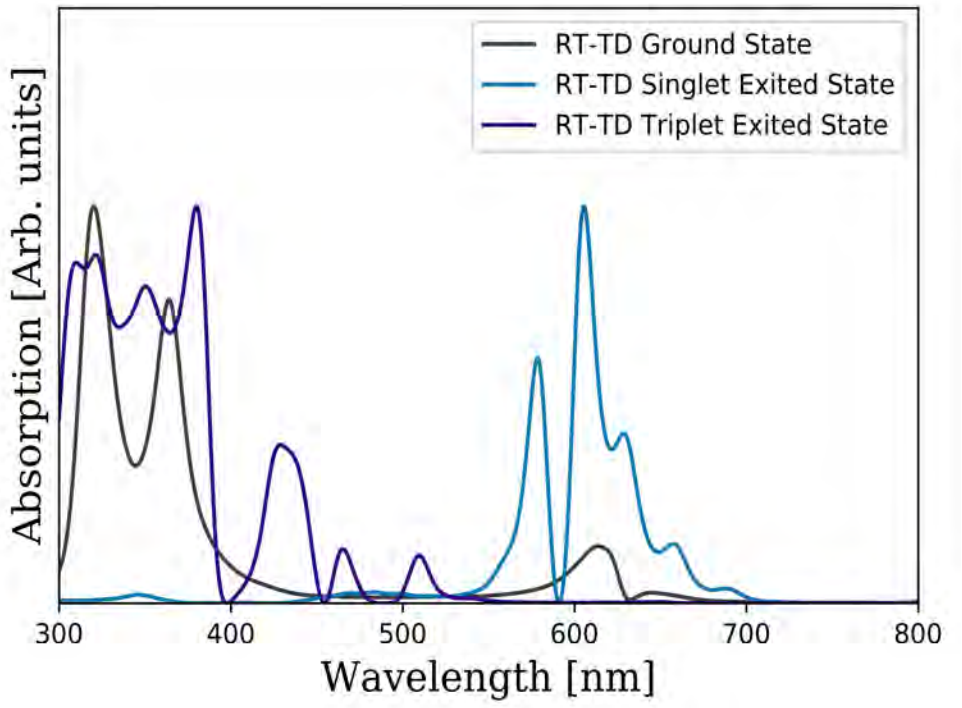

Figure 264: RTTD-DFT dipole response of the D_{2h} constitutional isomer of βH_2Pc in the UV/Vis region.

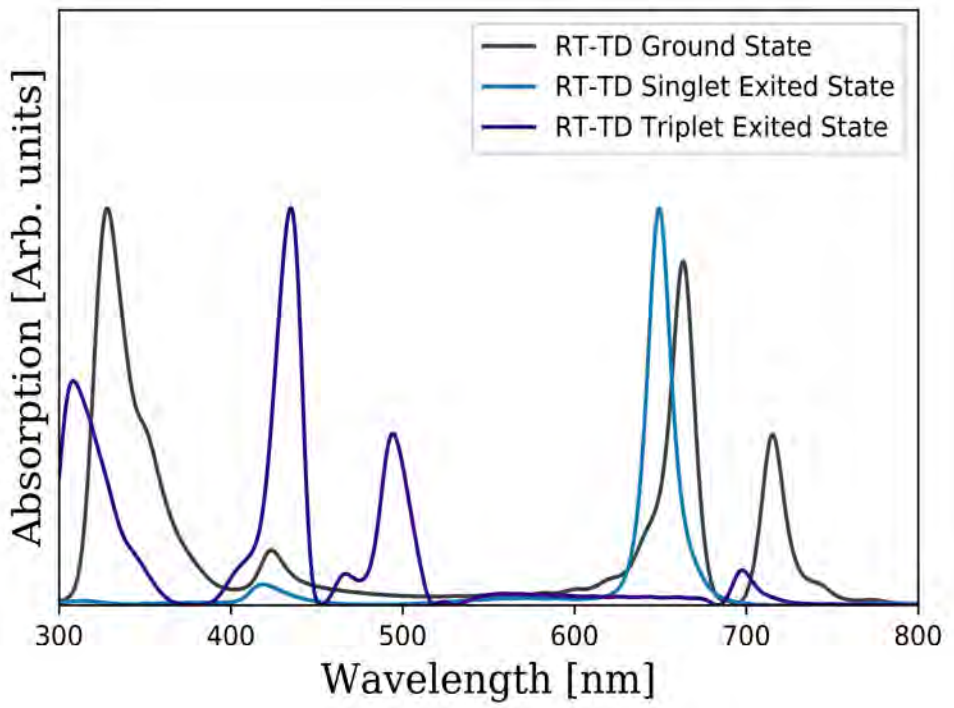

Figure 265: RTTD-DFT dipole response of the C_{4h} constitutional isomer of $\alpha SnCl_2Pc$ in the UV/Vis region.

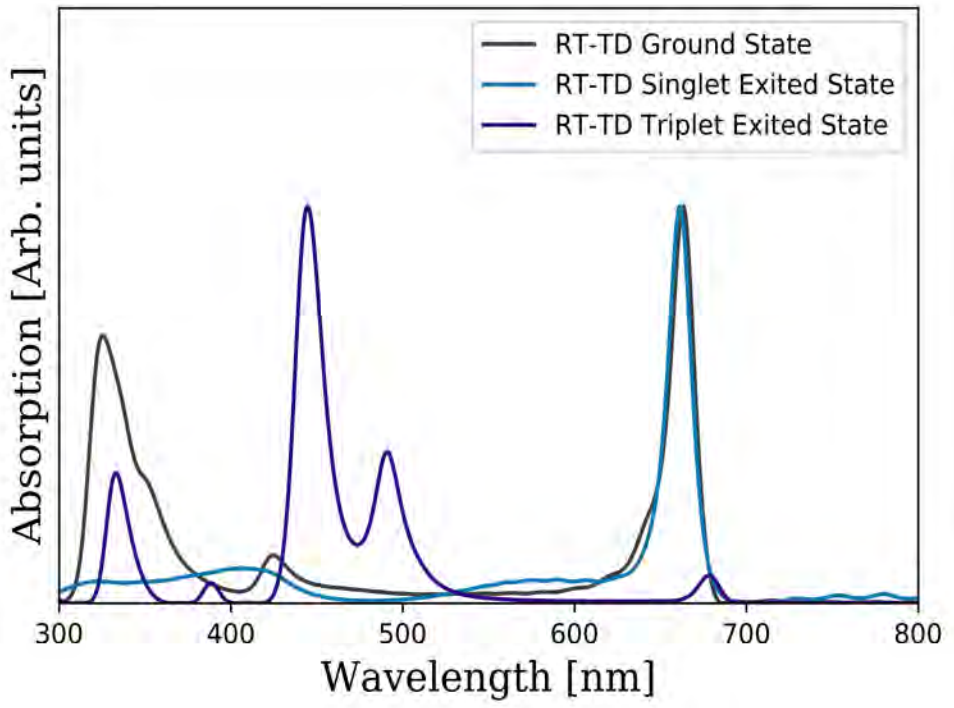

Figure 266: RTTD-DFT dipole response of the C_{2v} constitutional isomer of $\alpha SnCl_2Pc$ in the UV/Vis region.

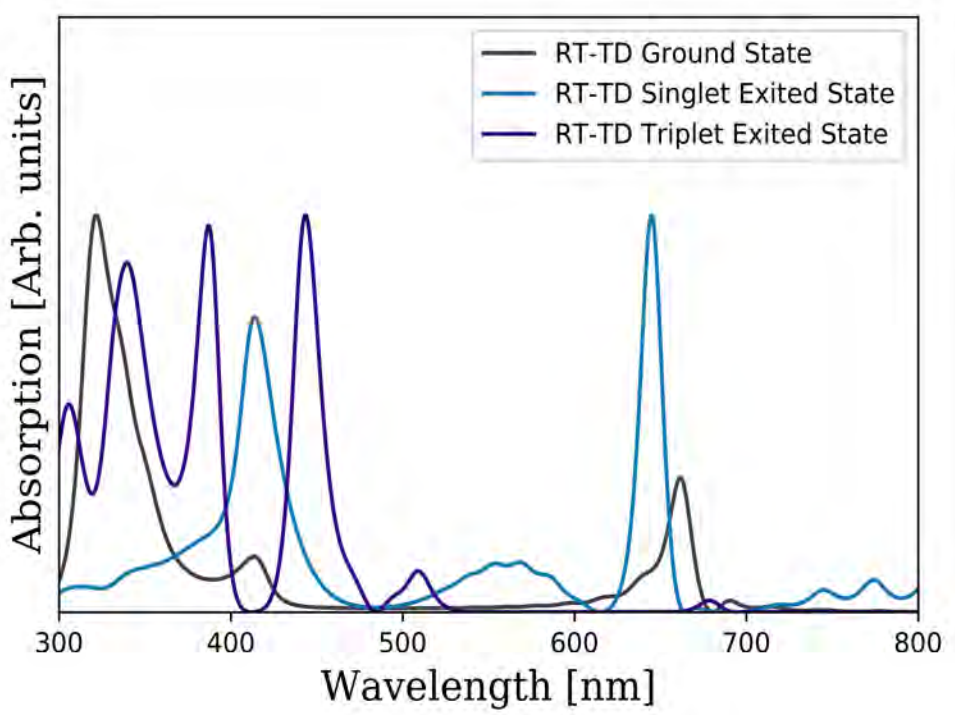

Figure 267: RTTD-DFT dipole response of the C_s constitutional isomer of $\alpha SnCl_2Pc$ in the UV/Vis region.

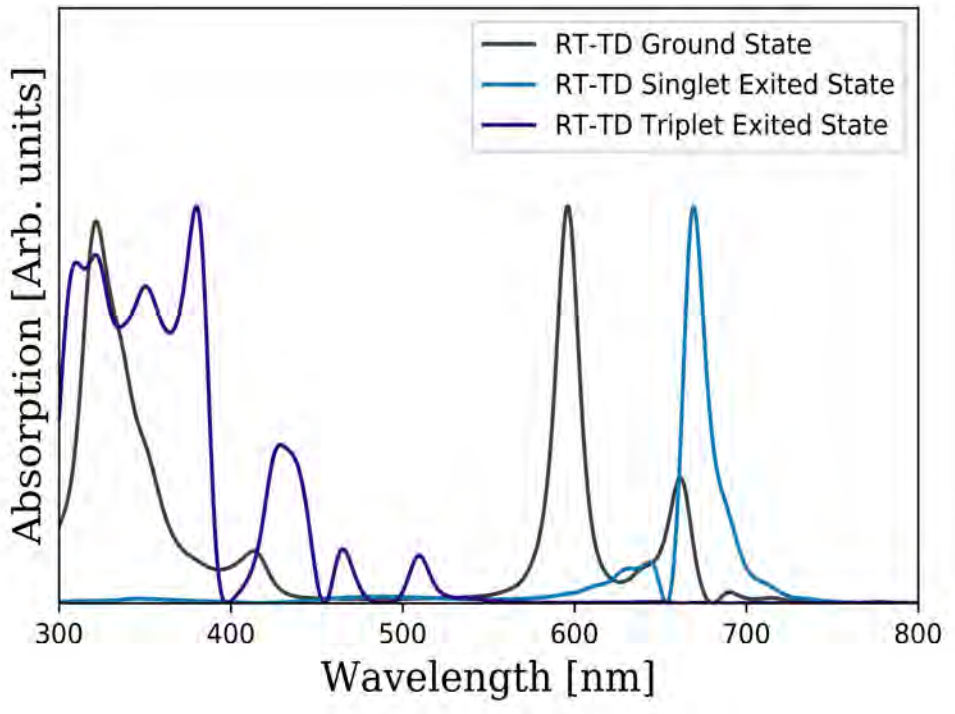

Figure 268: RTTD-DFT dipole response of the D_{2h} constitutional isomer of $\alpha SnCl_2Pc$ in the UV/Vis region.

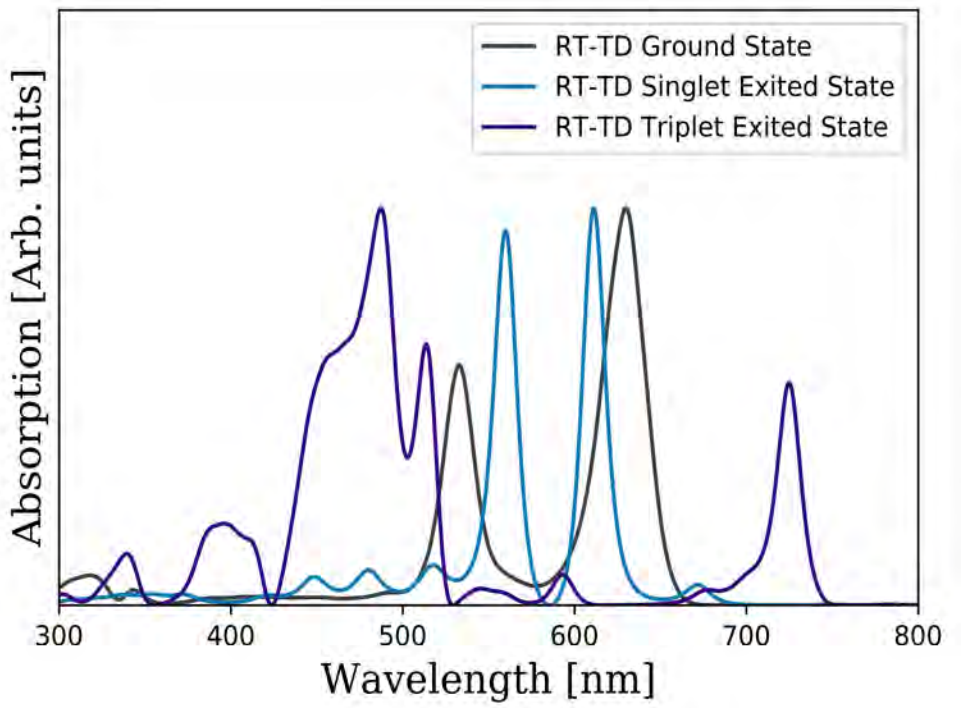

Figure 269: RTTD-DFT dipole response of the C_{4h} constitutional isomer of $\beta SnCl_2Pc$ in the UV/Vis region.

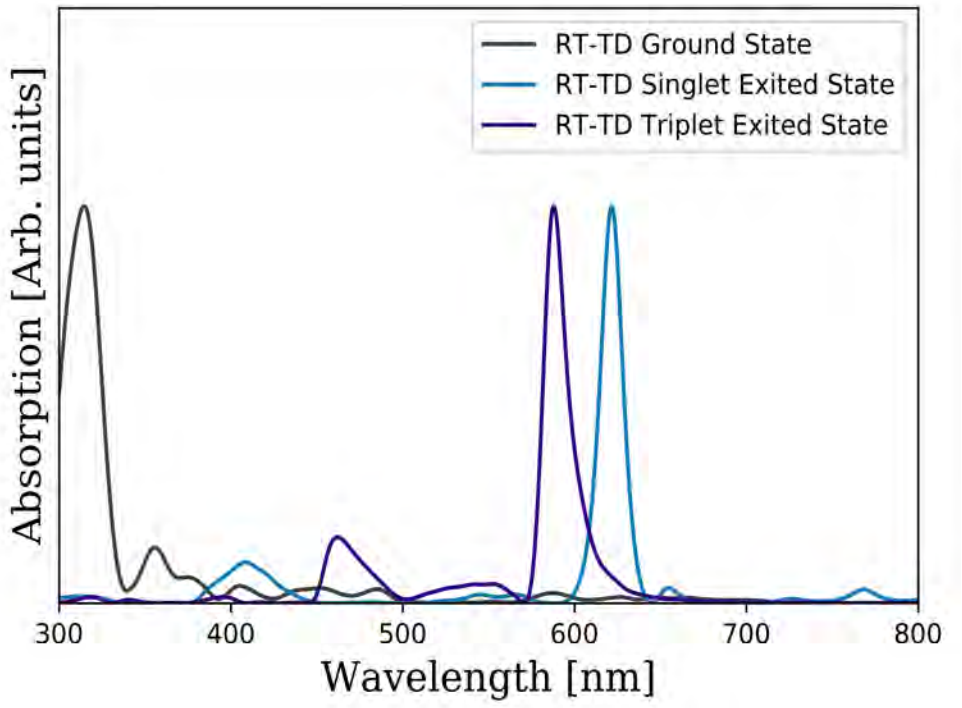

Figure 270: RTTD-DFT dipole response of the C_{2v} constitutional isomer of $\beta SnCl_2Pc$ in the UV/Vis region.

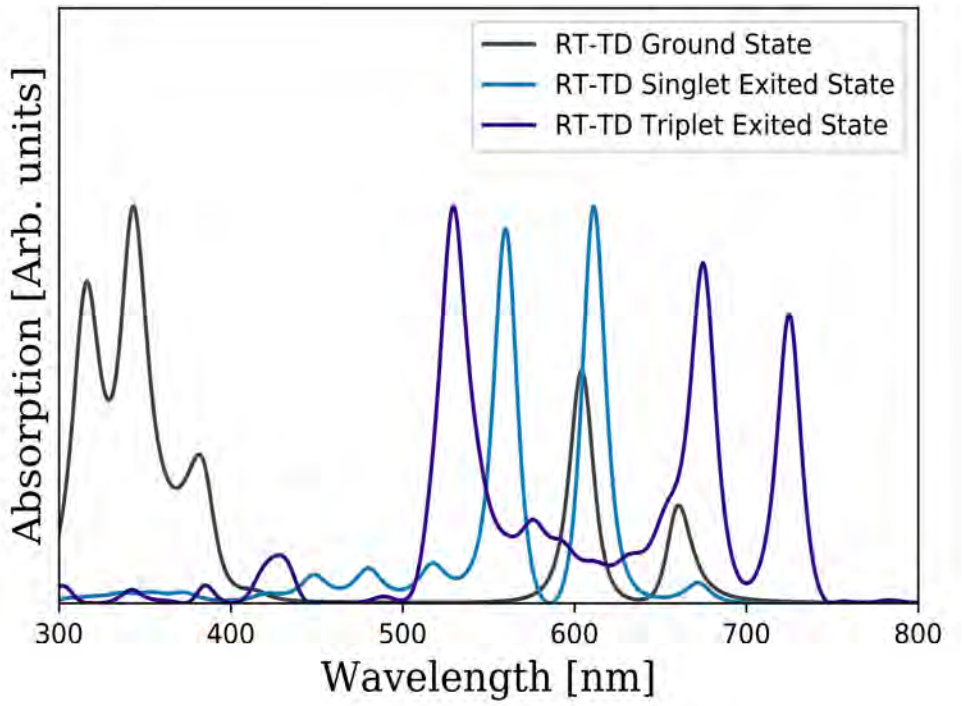

Figure 271: RTTD-DFT dipole response of the C_s constitutional isomer of $\beta SnCl_2Pc$ in the UV/Vis region.

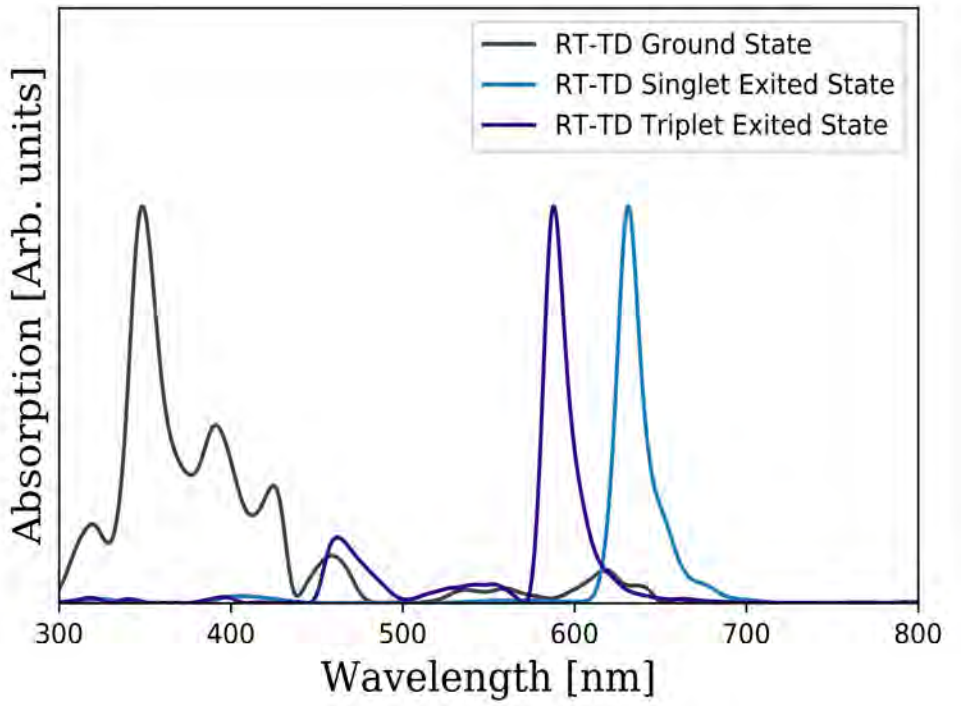

Figure 272: RTTD-DFT dipole response of the D_{2h} constitutional isomer of $\beta SnCl_2Pc$ in the UV/Vis region.

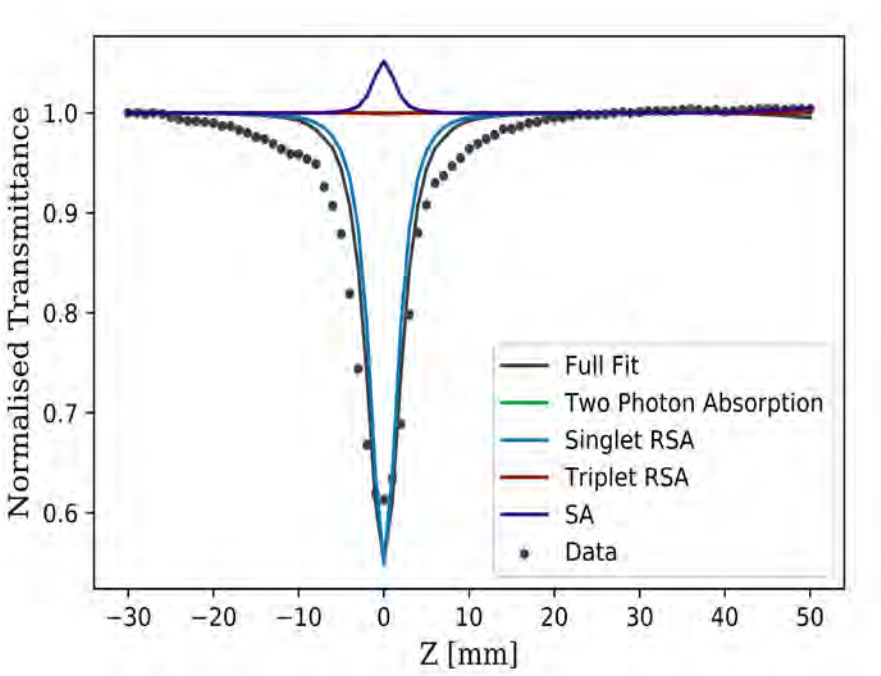

Figure 273: The five level model fit of αH_2Pc's C_{4h} stereoisomer at a focal intensity of $1.4{\times}10^{12}$ W.m^{-2}.

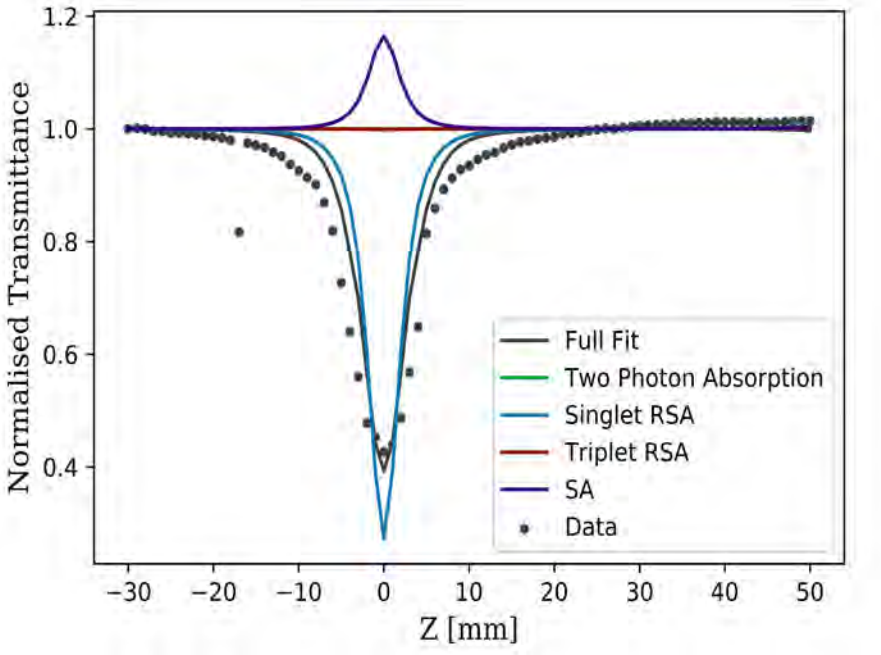

Figure 274: The five level model fit of αH_2Pc's C_{4h} stereoisomer at a focal intensity of $3.0{\times}10^{12}$ W.m^{-2}.

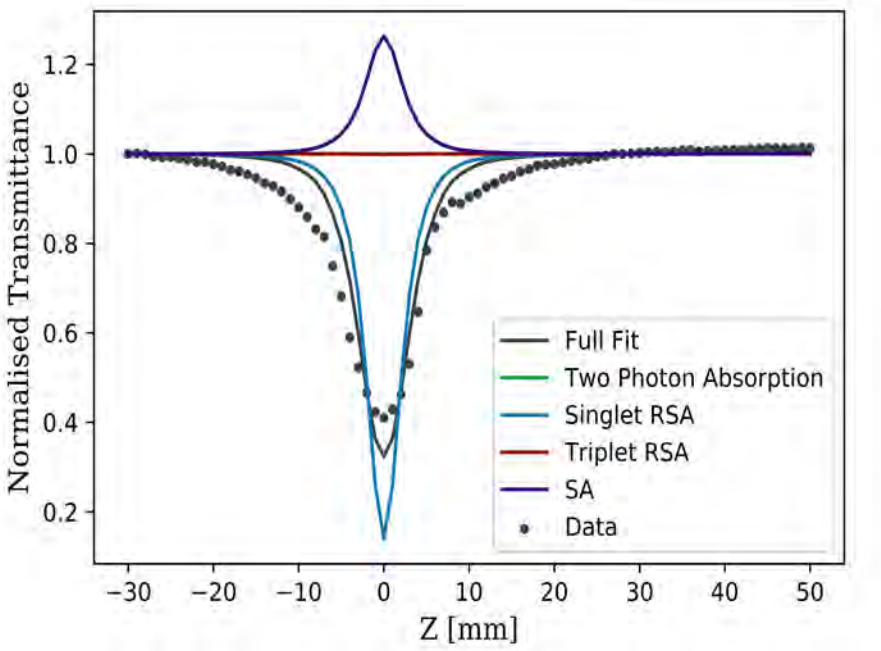

Figure 275: The five level model fit of αH_2Pc's C_{4h} stereoisomer at a focal intensity of 4.6×10^{12} W.m^{-2}.

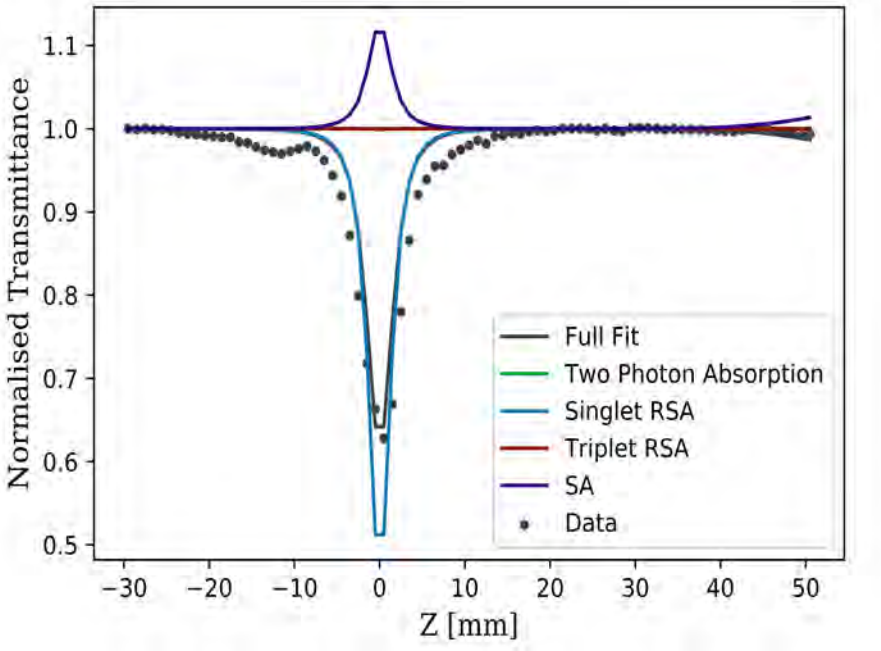

Figure 276: The five level model fit of αH_2Pc's C_{4h} stereoisomer at a focal intensity of 0.8×10^{12} W.m^{-2}.

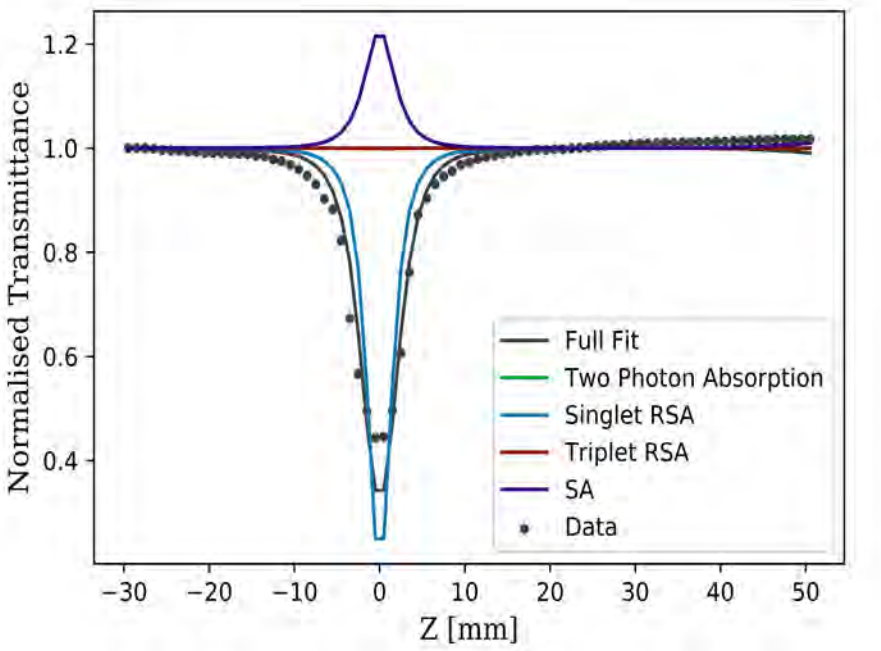

Figure 277: The five level model fit of αH_2Pc's C_{2v} stereoisomer at a focal intensity of 1.4×10^{12} W.m^{-2}.

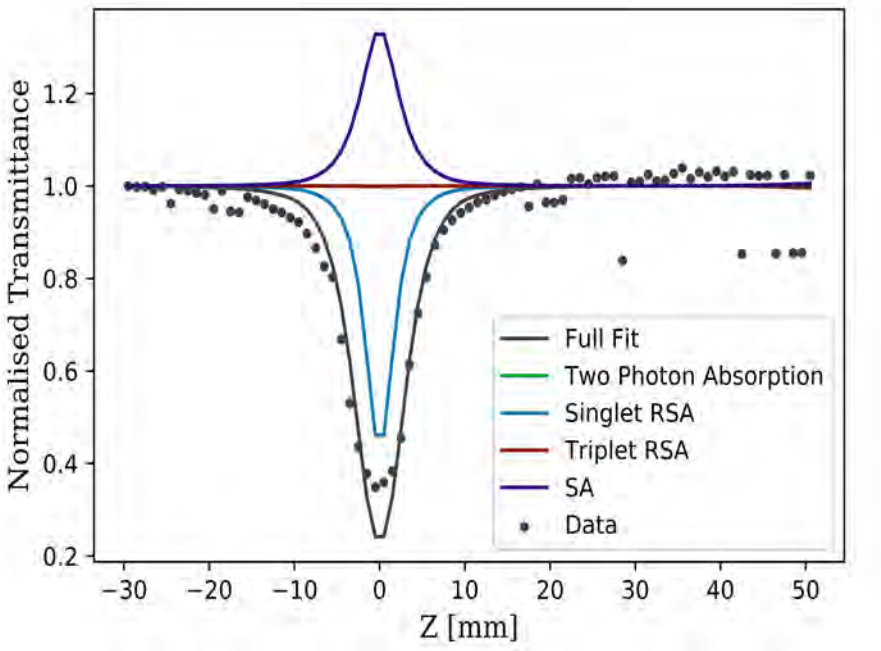

Figure 278: The five level model fit of αH_2Pc's C_{2v} stereoisomer at a focal intensity of 3.0×10^{12} W.m^{-2}.

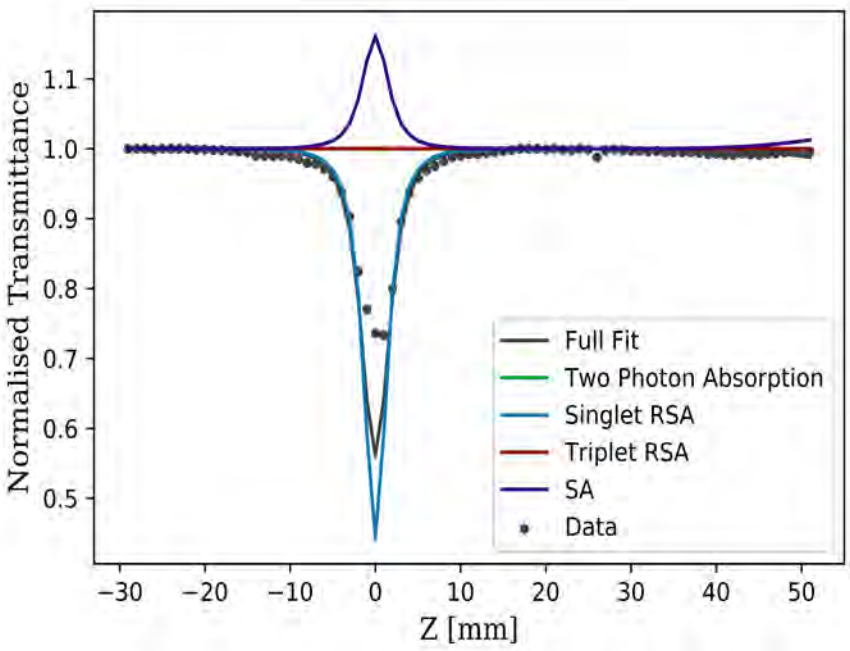

Figure 279: The five level model fit of αH_2Pc's C_{2v} stereoisomer at a focal intensity of 4.6×10^{12} W.m^{-2}.

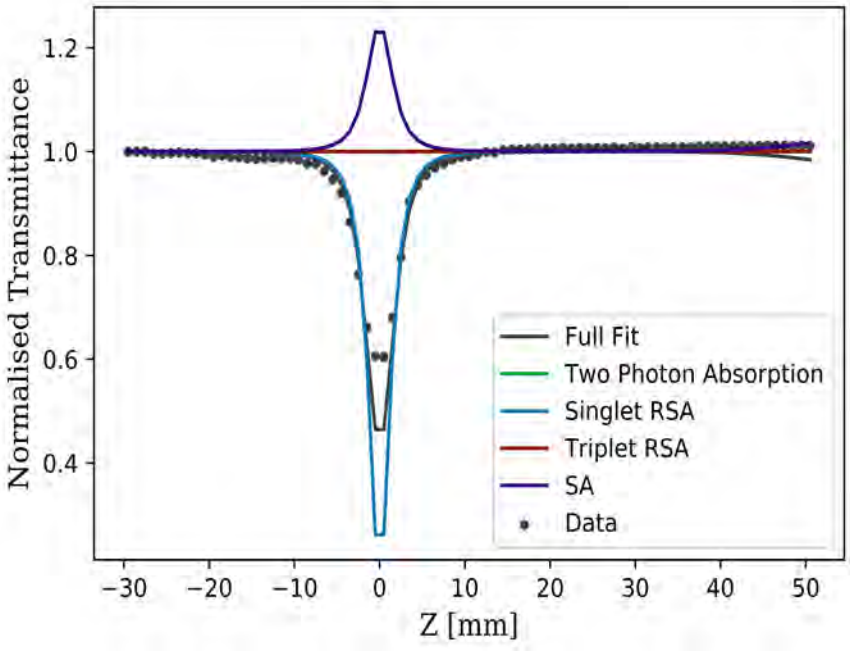

Figure 280: The five level model fit of αH_2Pc's C_{2v} stereoisomer at a focal intensity of 0.8×10^{12} W.m^{-2}.

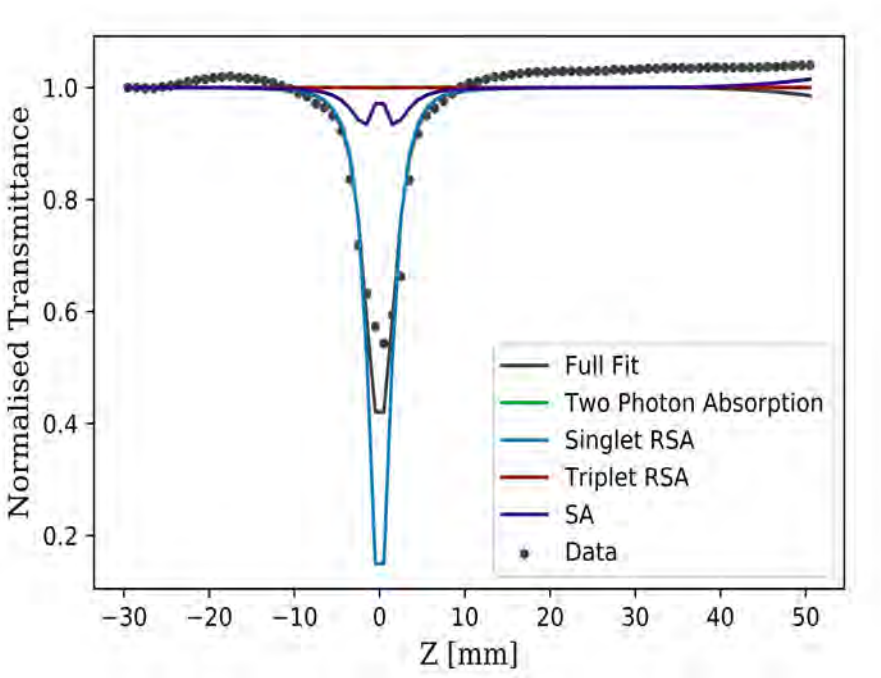

Figure 281: The five level model fit of αH_2Pc's C_s stereoisomer at a focal intensity of 1.4×10^{12} W.m^{-2}.

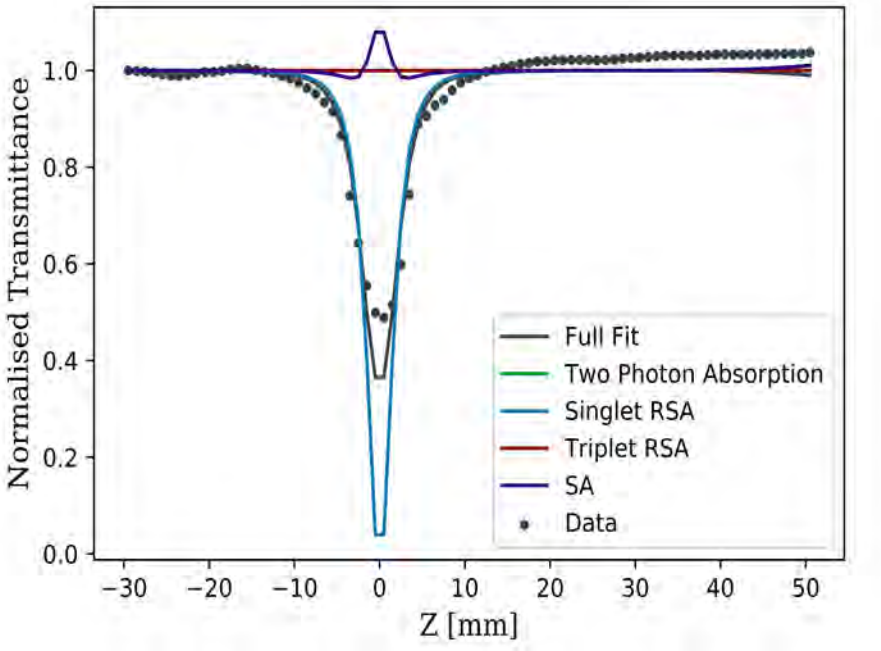

Figure 282: The five level model fit of αH_2Pc's C_s stereoisomer at a focal intensity of 3.0×10^{12} W.m^{-2}.

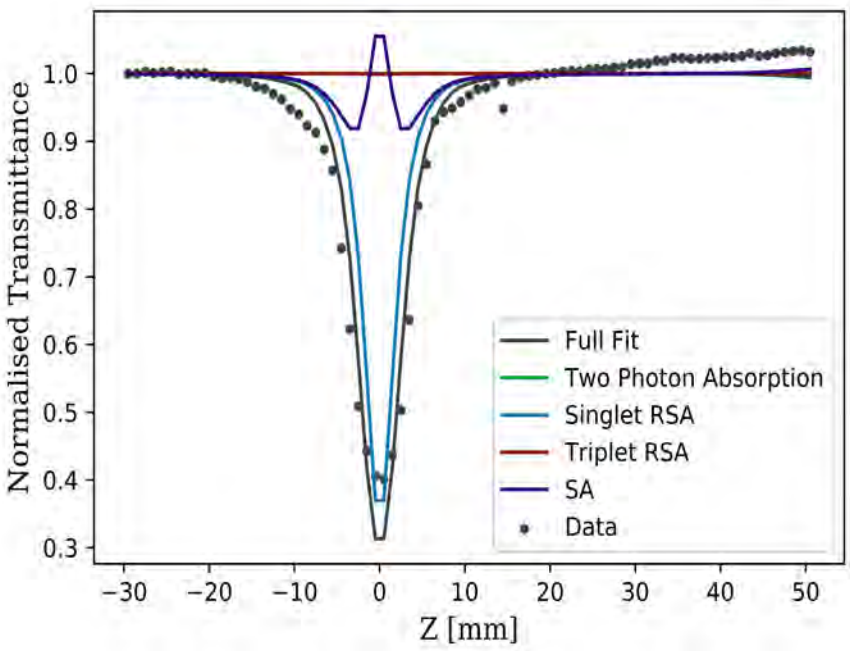

Figure 283: The five level model fit of αH_2Pc's C_s stereoisomer at a focal intensity of 4.6×10^{12} W.m^{-2}.

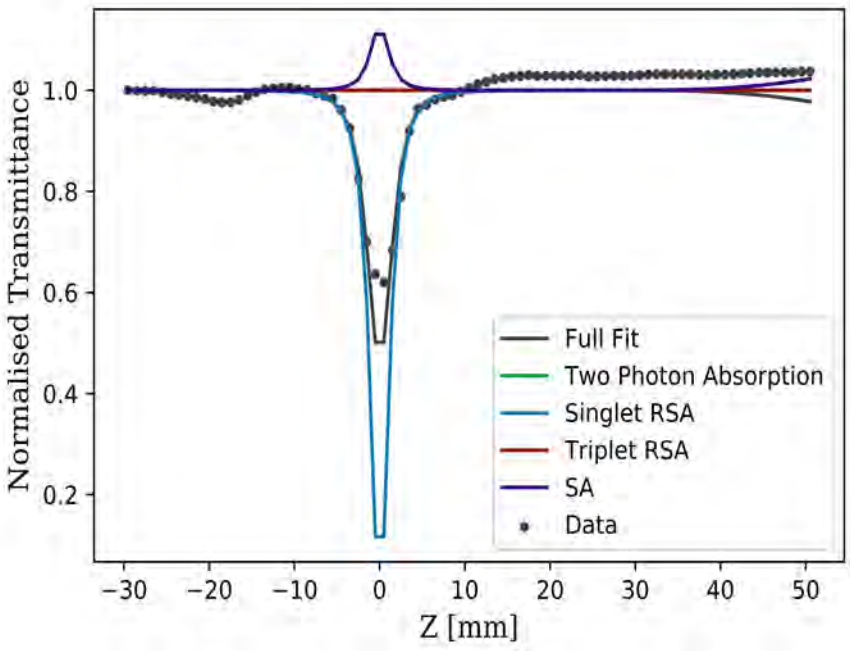

Figure 284: The five level model fit of αH_2Pc's C_s stereoisomer at a focal intensity of 0.8×10^{12} W.m^{-2}.

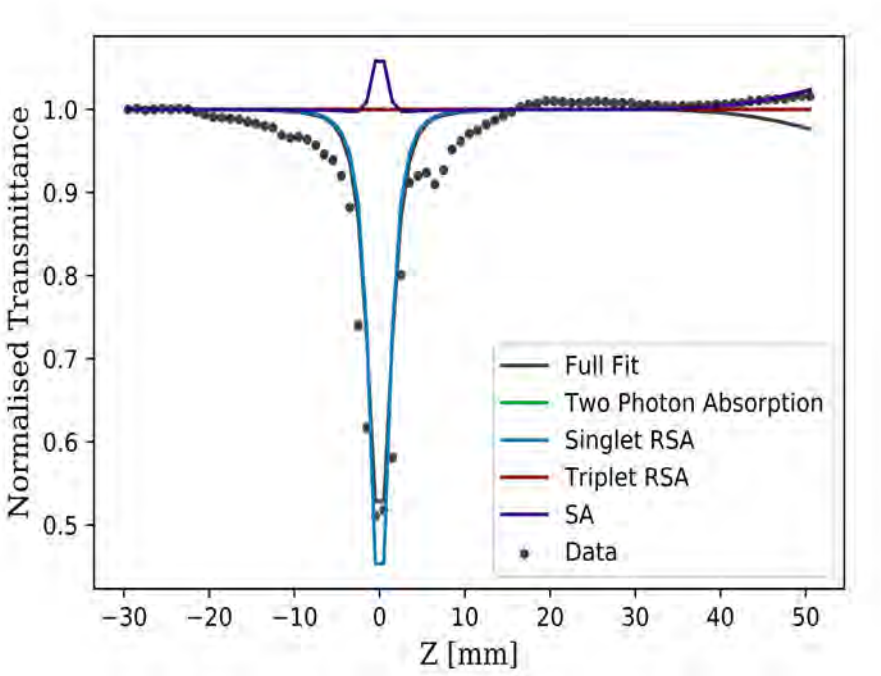

Figure 285: The five level model fit of αH_2Pc's D_{2h} stereoisomer at a focal intensity of 1.4×10^{12} W.m^{-2}.

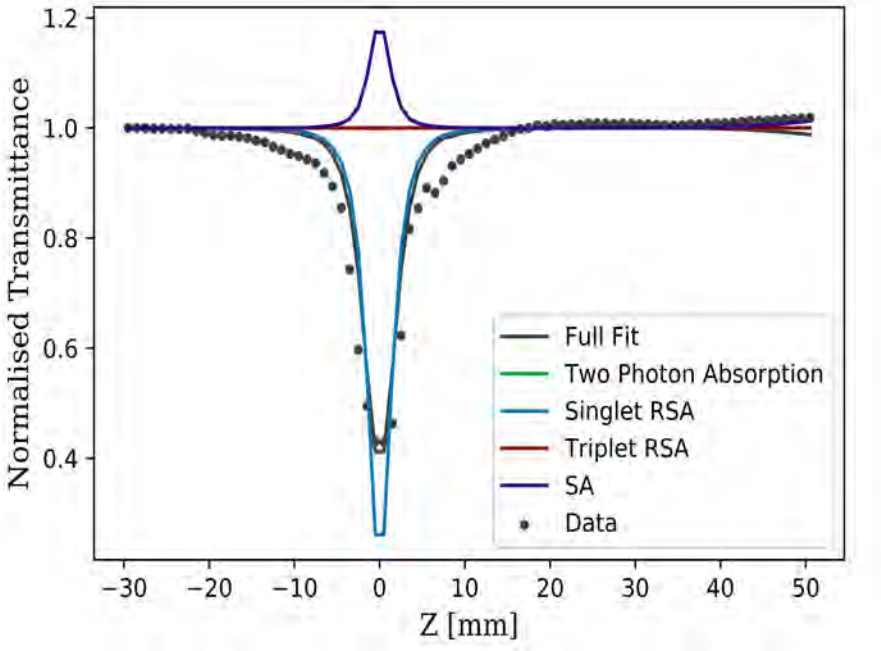

Figure 286: The five level model fit of αH_2Pc's D_{2h} stereoisomer at a focal intensity of 3.0×10^{12} W.m^{-2}.

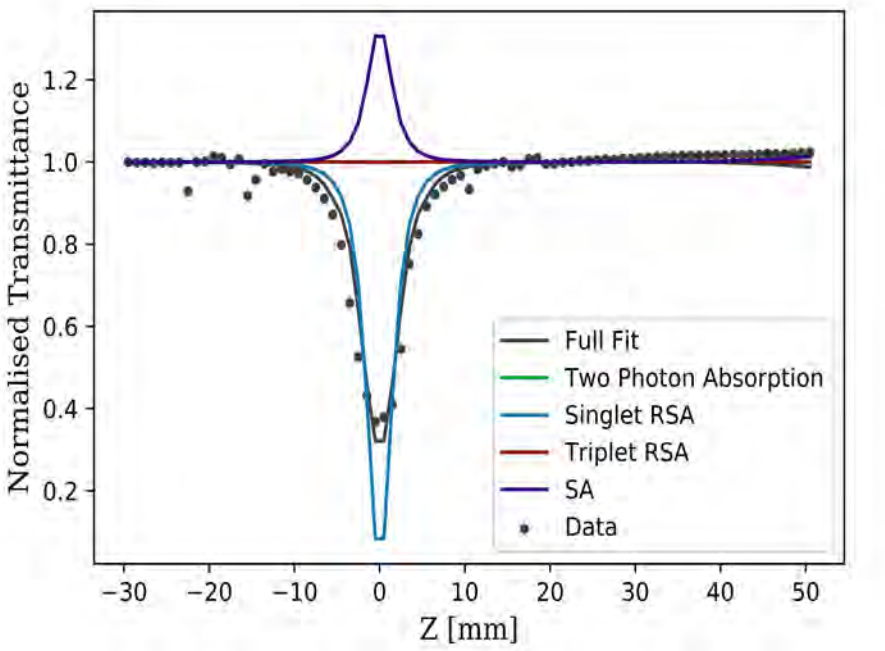

Figure 287: The five level model fit of αH_2Pc's D_{2h} stereoisomer at a focal intensity of 4.6×10^{12} W.m^{-2}.

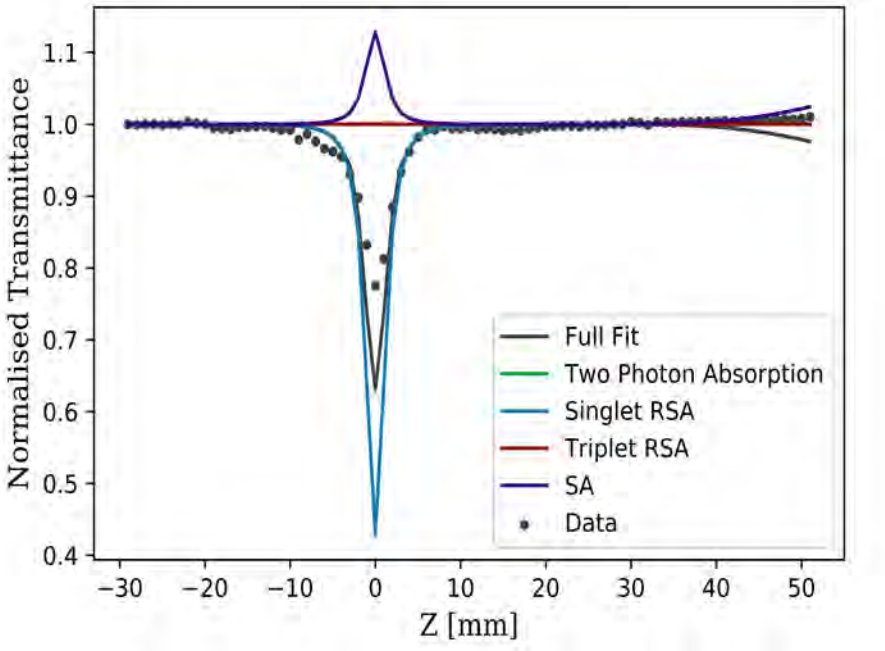

Figure 288: The five level model fit of αH_2Pc's D_{2h} stereoisomer at a focal intensity of 0.8×10^{12} W.m^{-2}.

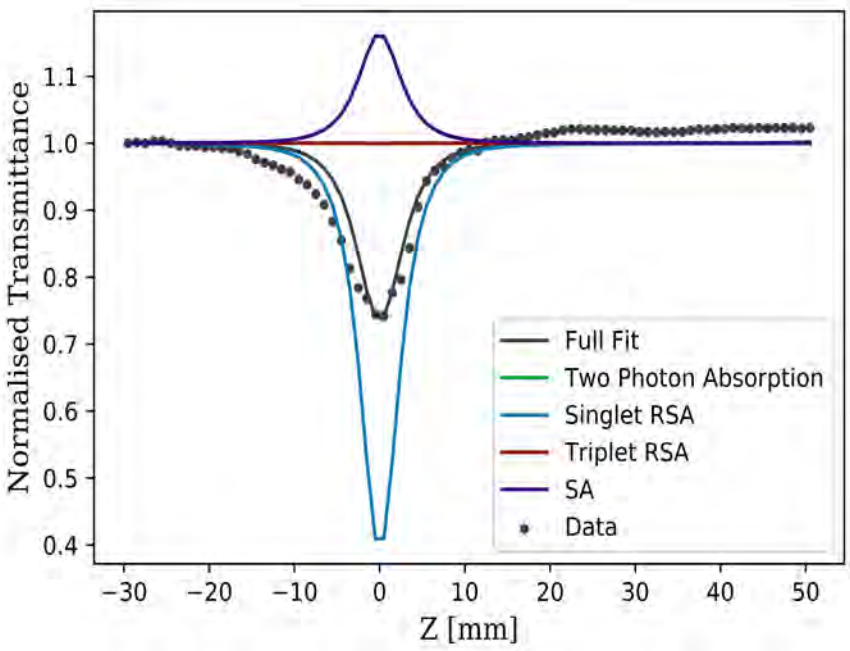

Figure 289: The five level model fit of βH_2Pc's C_{4h} stereoisomer at a focal intensity of 2.3×10^{12} W.m^{-2}.

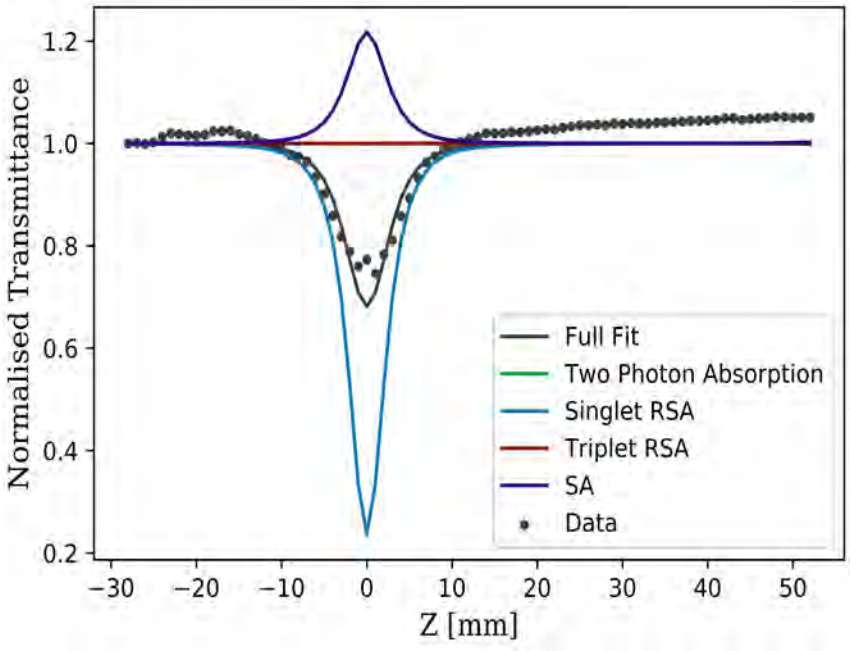

Figure 290: The five level model fit of βH_2Pc's C_{4h} stereoisomer at a focal intensity of 2.7×10^{12} W.m^{-2}.

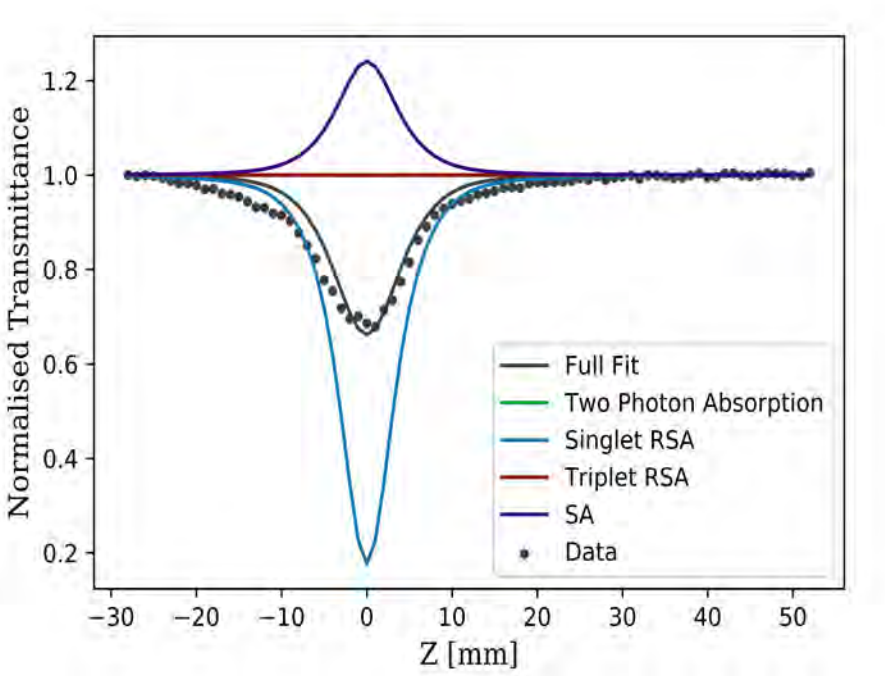

Figure 291: The five level model fit of βH_2Pc's C_{4h} stereoisomer at a focal intensity of 5.6×10^{12} W.m^{-2}.

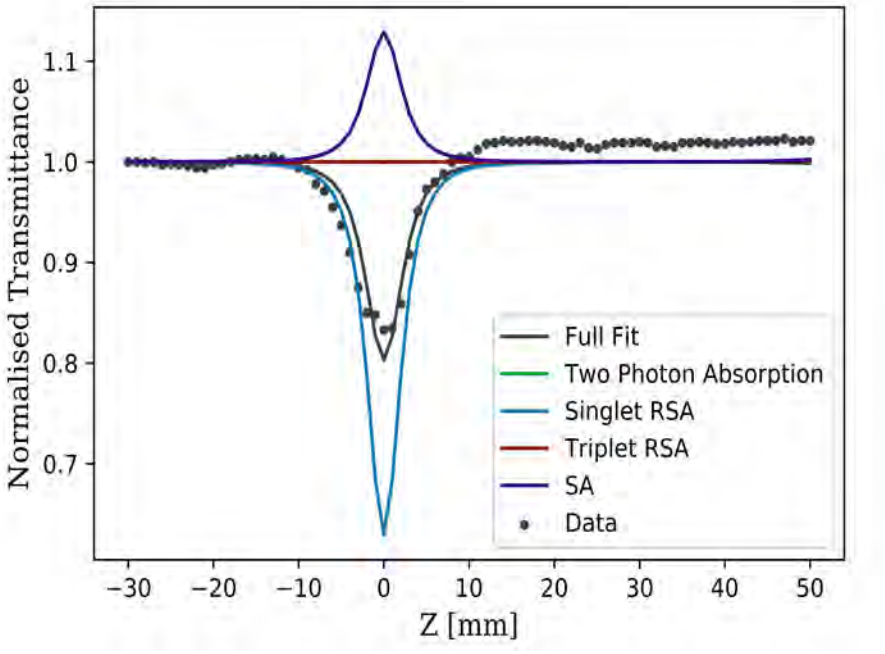

Figure 292: The five level model fit of βH_2Pc's C_{4h} stereoisomer at a focal intensity of 1.2×10^{12} W.m^{-2}.

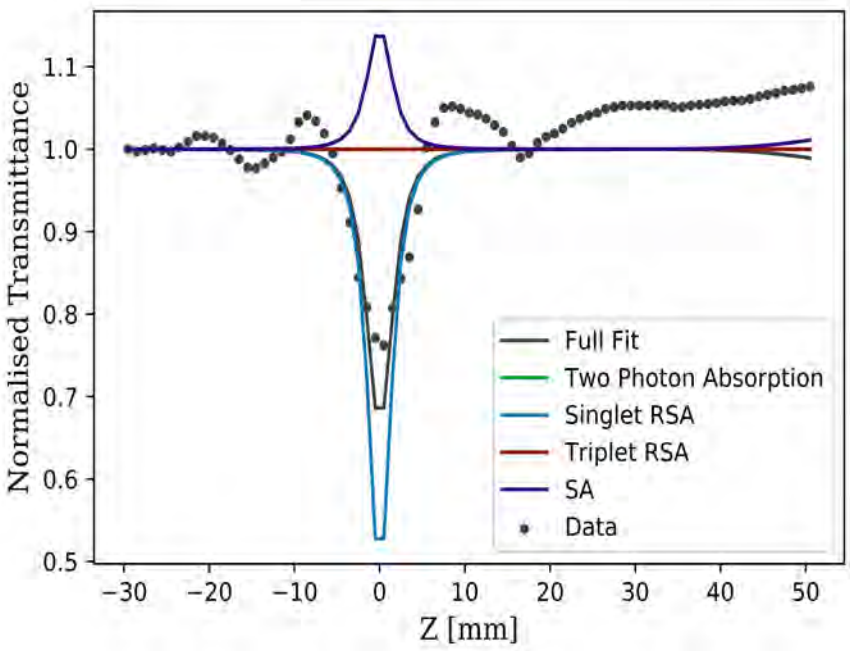

Figure 293: The five level model fit of βH_2Pc's C_{2v} stereoisomer at a focal intensity of 2.3×10^{12} W.m^{-2}.

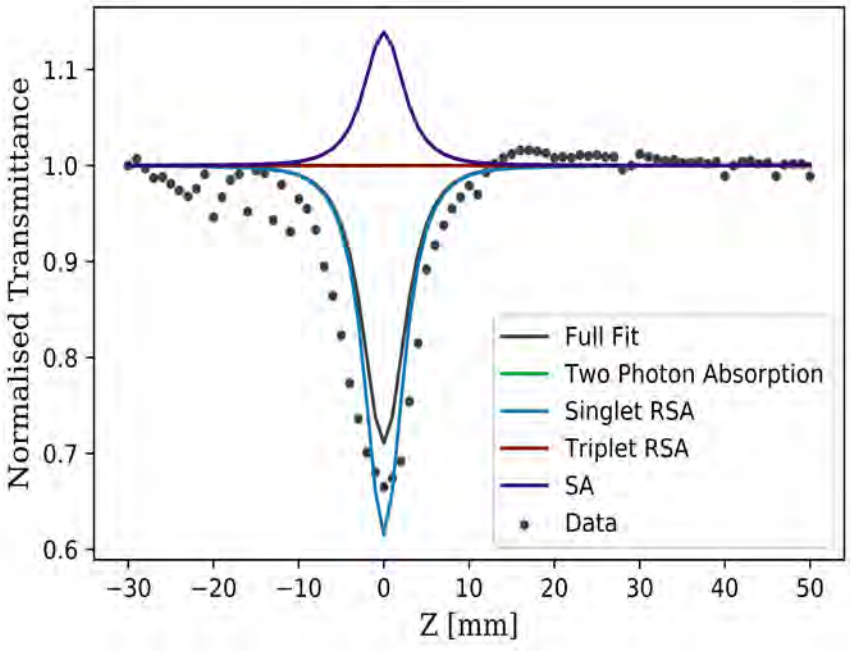

Figure 294: The five level model fit of βH_2Pc's C_{2v} stereoisomer at a focal intensity of 2.7×10^{12} W.m^{-2}.

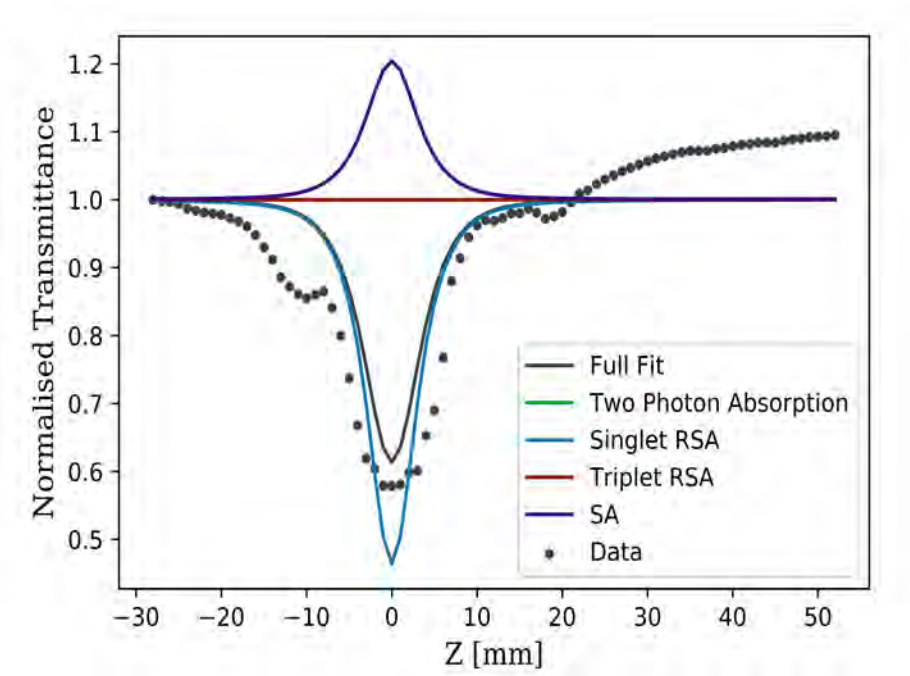

Figure 295: The five level model fit of βH_2Pc's C_{2v} stereoisomer at a focal intensity of 5.6×10^{12} W.m^{-2}.

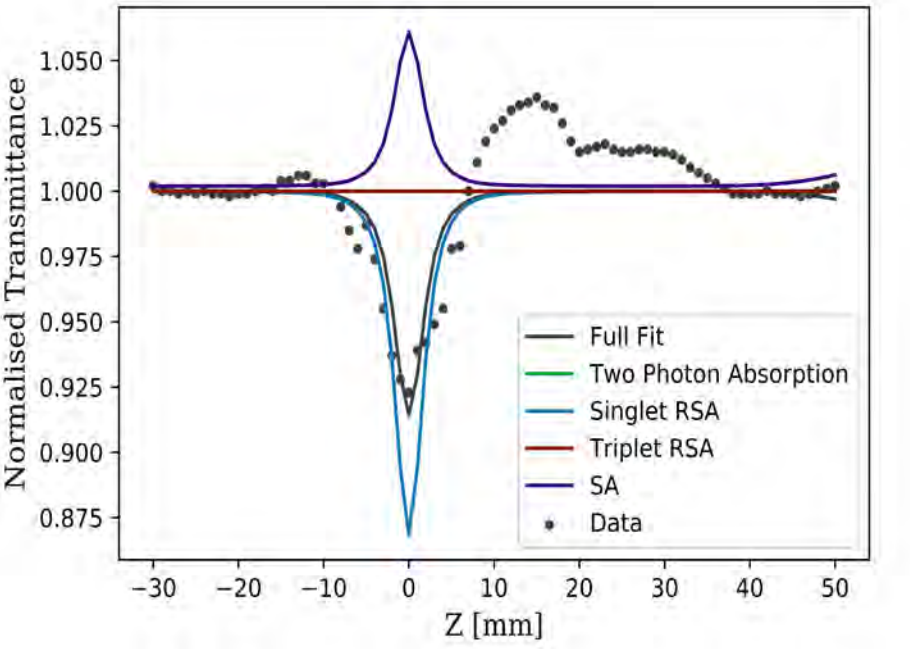

Figure 296: The five level model fit of βH_2Pc's C_{2v} stereoisomer at a focal intensity of 1.2×10^{12} W.m^{-2}.

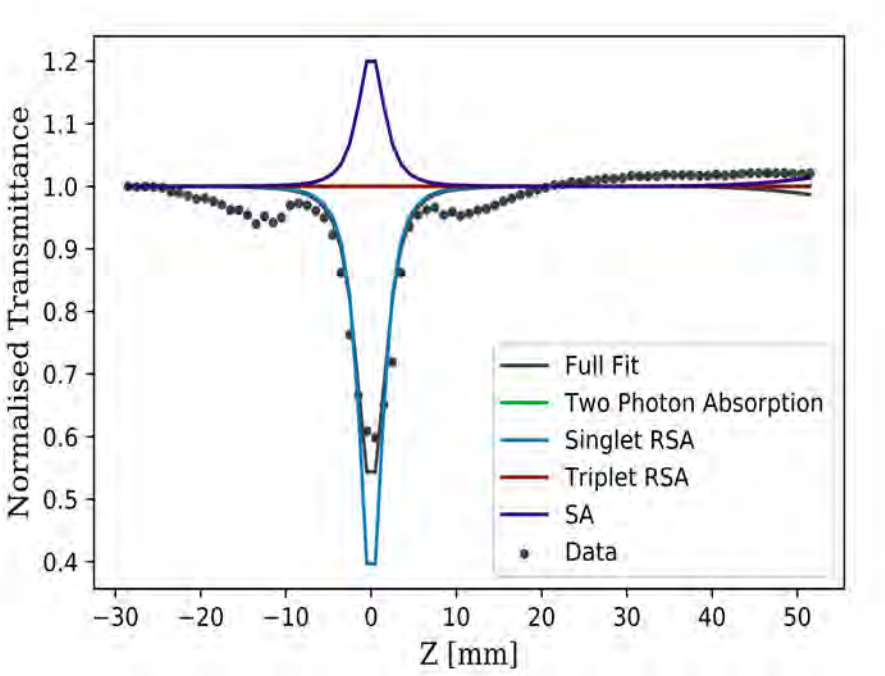

Figure 297: The five level model fit of βH_2Pc's C_s stereoisomer at a focal intensity of 2.3×10^{12} W.m^{-2}.

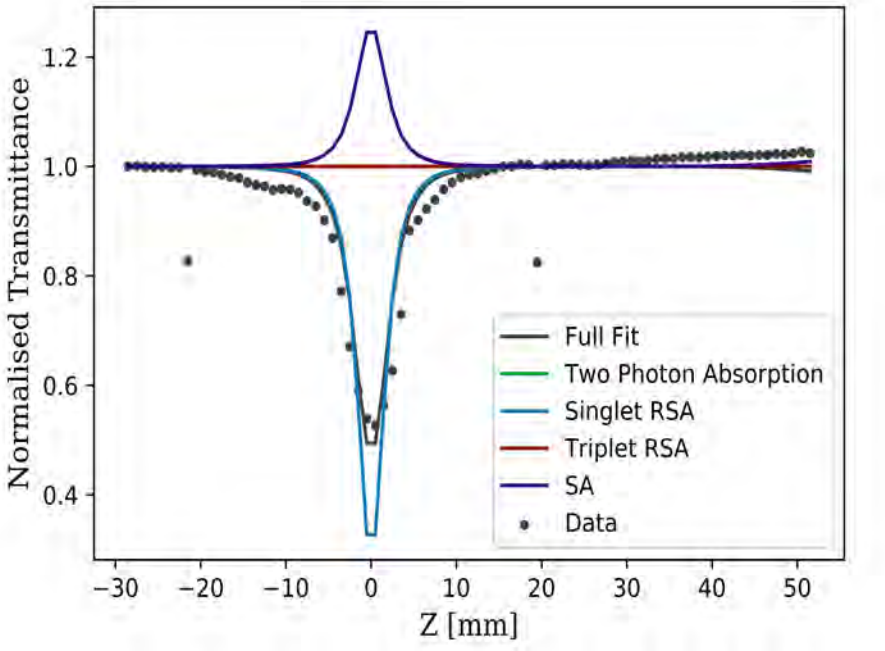

Figure 298: The five level model fit of βH_2Pc's C_s stereoisomer at a focal intensity of 2.7×10^{12} W.m^{-2}.

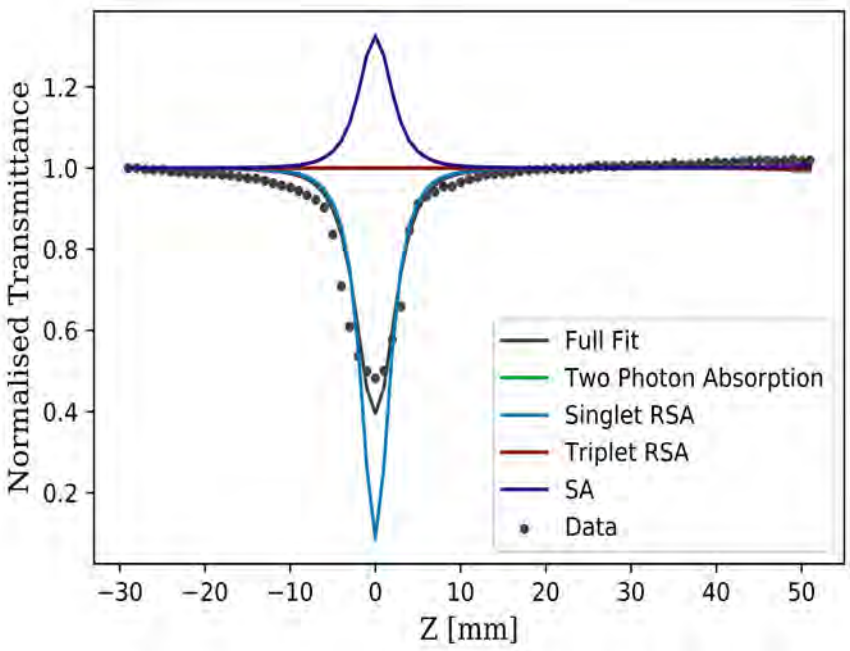

Figure 299: The five level model fit of βH_2Pc's C_s stereoisomer at a focal intensity of 5.6×10^{12} W.m^{-2}.

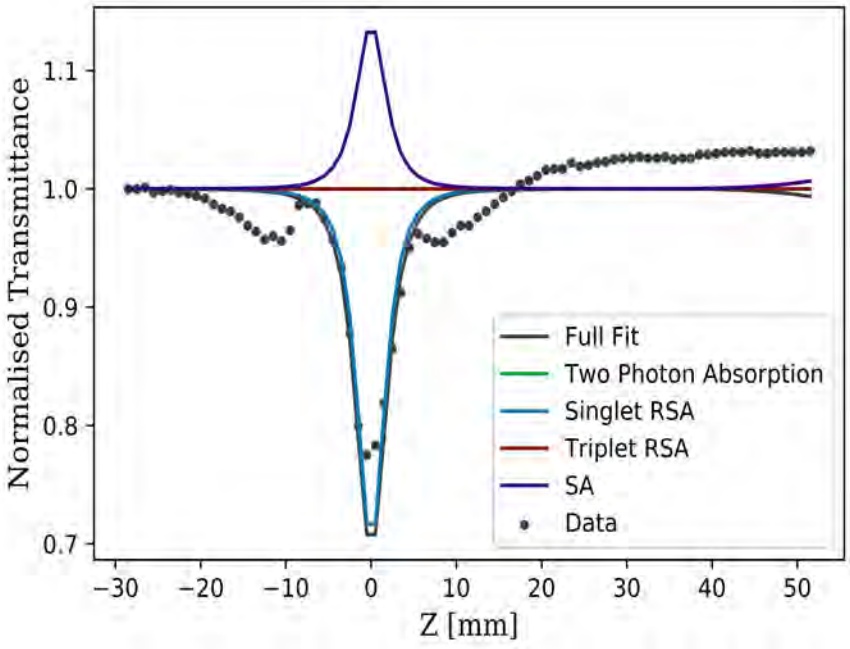

Figure 300: The five level model fit of βH_2Pc's C_s stereoisomer at a focal intensity of 1.2×10^{12} W.m^{-2}.

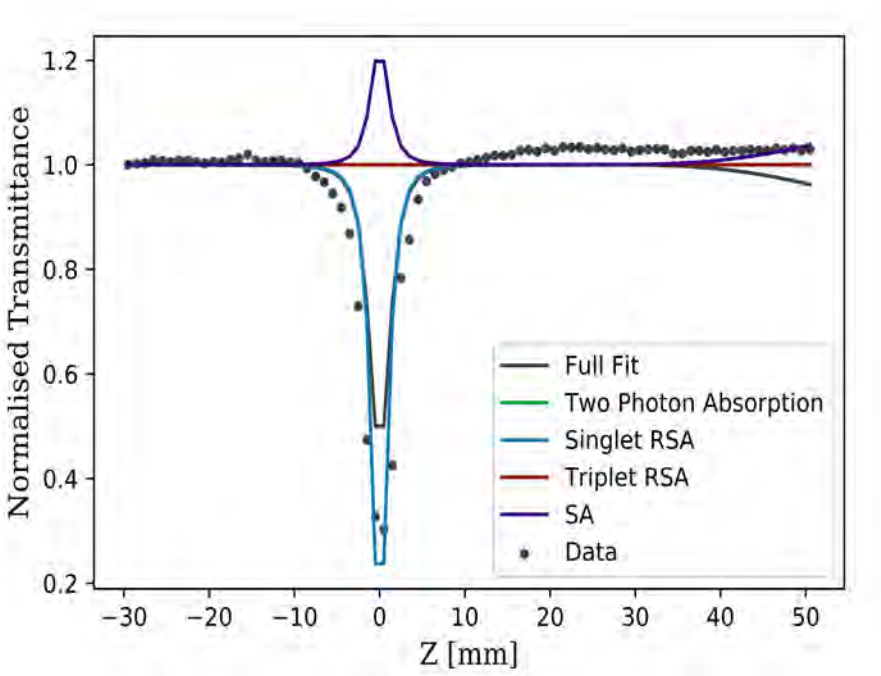

Figure 301: The five level model fit of βH_2Pc's D_{2h} stereoisomer at a focal intensity of 2.3×10^{12} W.m^{-2}.

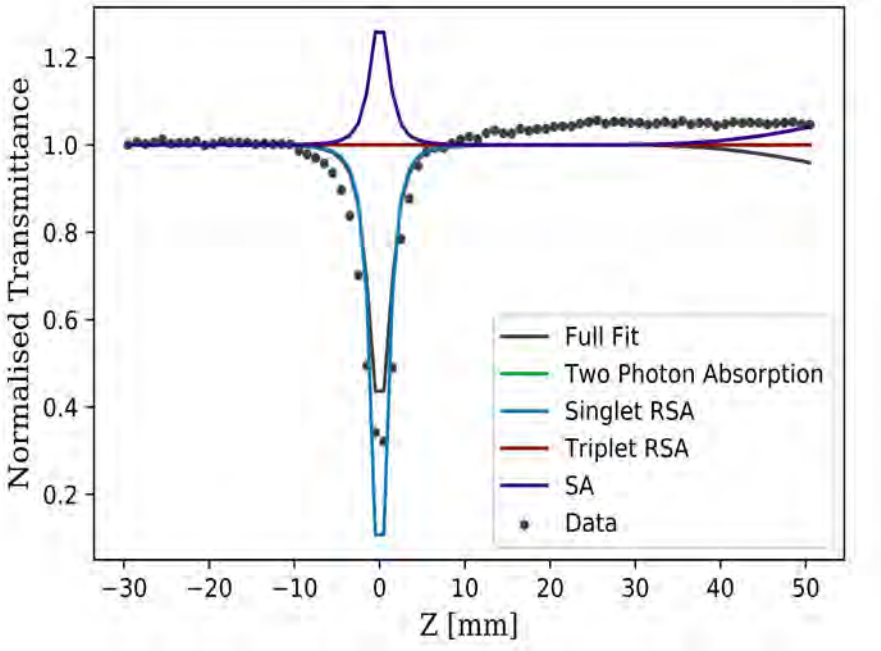

Figure 302: The five level model fit of βH_2Pc's D_{2h} stereoisomer at a focal intensity of 2.7×10^{12} W.m^{-2}.

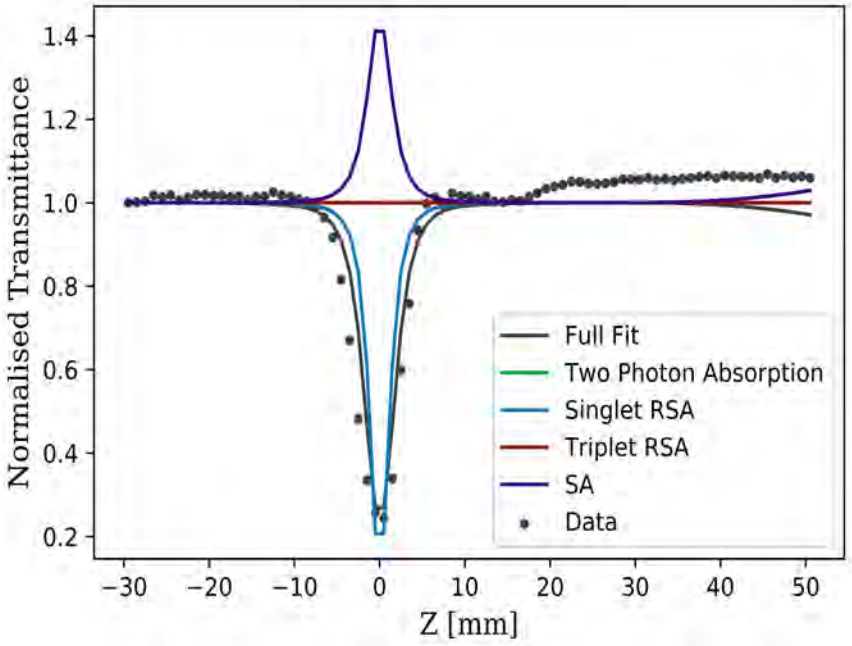

Figure 303: The five level model fit of βH_2Pc's D_{2h} stereoisomer at a focal intensity of 5.6×10^{12} W.m^{-2}.

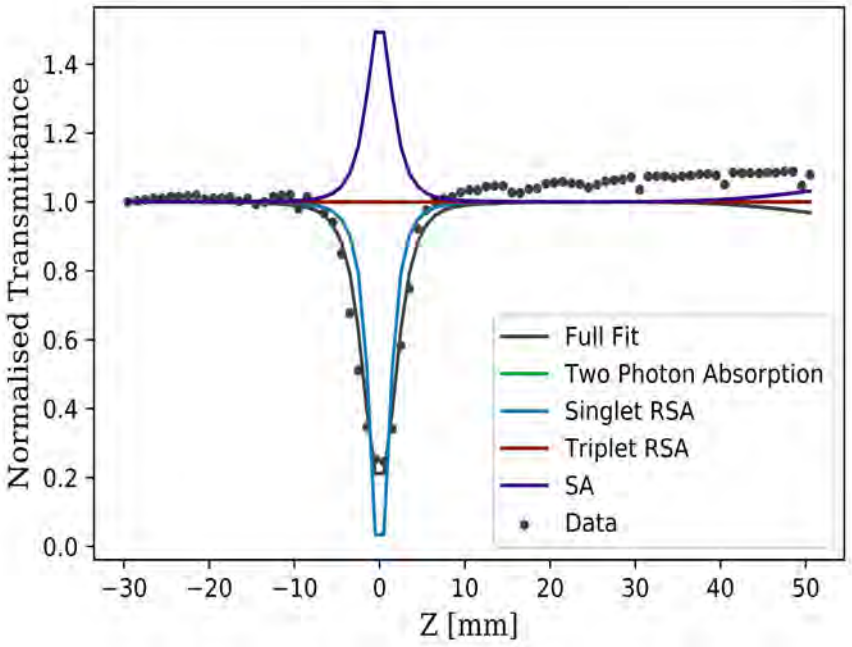

Figure 304: The five level model fit of βH_2Pc's D_{2h} stereoisomer at a focal intensity of 1.2×10^{12} W.m^{-2}.

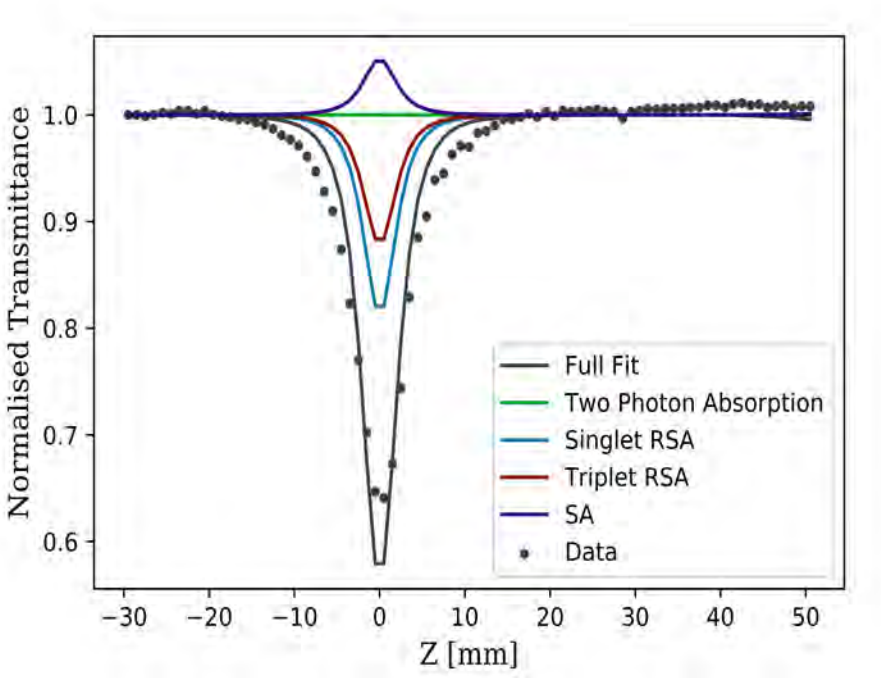

Figure 305: The five level model fit of $\alpha SnCl_2Pc$'s C_{4h} stereoisomer at a focal intensity of 2.2×10^{12} W.m^{-2}.

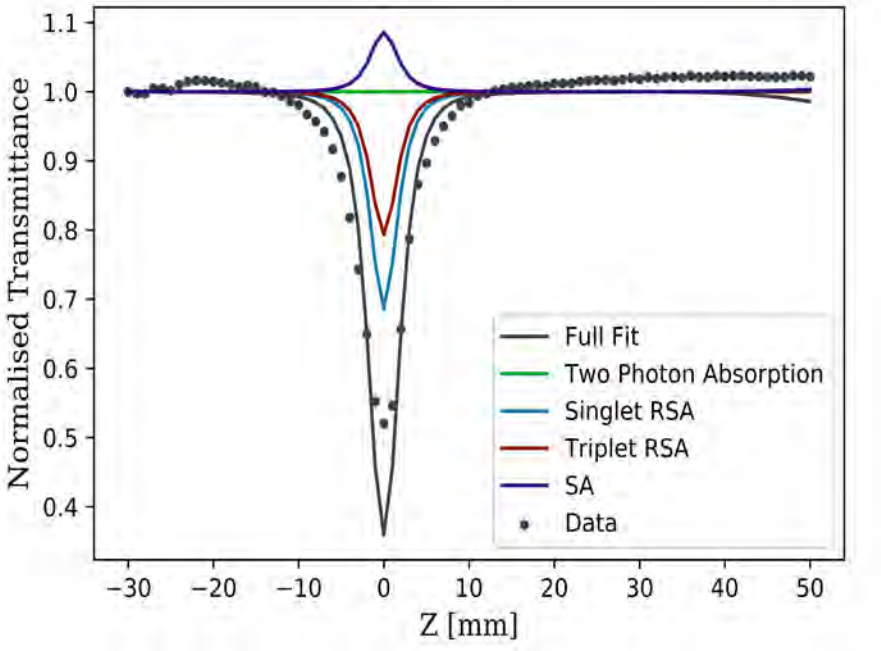

Figure 306: The five level model fit of $\alpha SnCl_2Pc$'s C_{4h} stereoisomer at a focal intensity of 4.2×10^{12} W.m^{-2}.

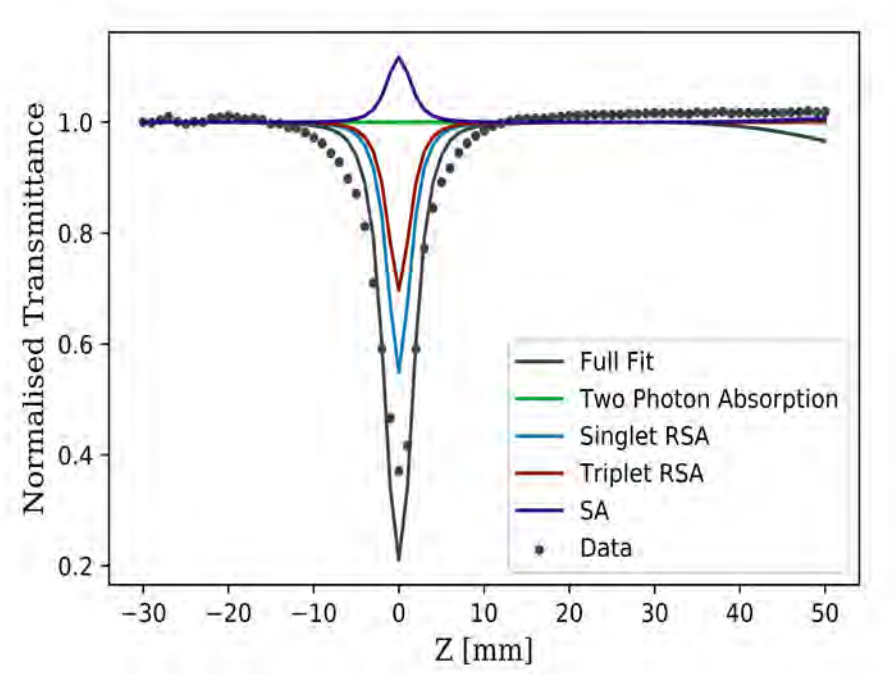

Figure 307: The five level model fit of $\alpha SnCl_2Pc$'s C_{4h} stereoisomer at a focal intensity of 7.5×10^{12} W.m^{-2}.

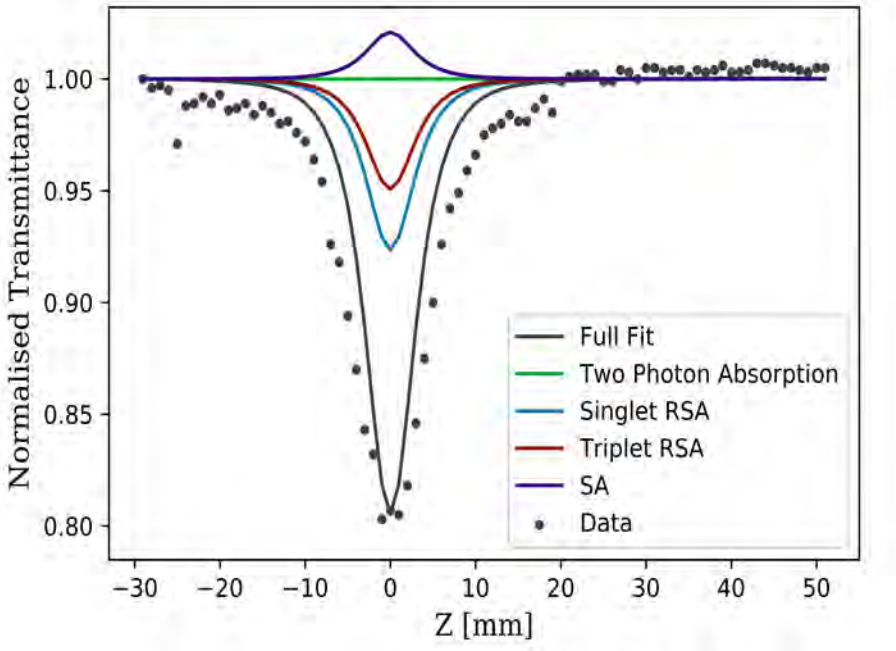

Figure 308: The five level model fit of $\alpha SnCl_2Pc$'s C_{4h} stereoisomer at a focal intensity of 0.8×10^{12} W.m^{-2}.